2006

A NUMERICAL STUDY OF A NEW SPRAY APPLICATOR

Vedanth Srinivasan
University of Kentucky, vedanth@uky.edu

Recommended Citation

Srinivasan, Vedanth, "A NUMERICAL STUDY OF A NEW SPRAY APPLICATOR" (2006). *University of Kentucky Doctoral Dissertations*. 388.
https://uknowledge.uky.edu/gradschool_diss/388

ABSTRACT OF DISSERTATION

Vedanth Srinivasan

The Graduate School
University of Kentucky
2006

A NUMERICAL STUDY OF A NEW SPRAY APPLICATOR

ABSTRACT OF DISSERTATION

A dissertation submitted in partial fulfillment of the
requirements for the degree of Doctor of Philosophy in the
College of Engineering
at the University of Kentucky

By

Vedanth Srinivasan
Lexington, Kentucky

Director: Dr. Kozo Saito, Professor of Mechanical Engineering

Lexington, Kentucky

2006

ABSTRACT OF DISSERTATION

A NUMERICAL STUDY OF A NEW SPRAY APPLICATOR

This study focuses on the design and development of a new spray applicator design utilizing effects of imposed pressure oscillations in conjunction with cavitation collapse energy to create distribution of fine droplets. An oscillating horn placed inside the nozzle performing high frequency oscillations is envisioned to provide the necessary pressure perturbations on the exiting liquid jet, while the nozzle geometry design in configured to amplify cavitation process. Initially, a two-zone approach modeling the nozzle interior and exterior in a separate fashion and later, a coupled strategy is proposed.

Parametric studies describing the effect of horn stroke length, frequency, its position inside the nozzle in combination with different nozzle designs and liquid flow rates are explored to identify their contribution in obtaining desired cavitation characteristics. In this regard, incorporation of a backward facing step profile within the nozzle shows strong capability of generating the required cavitation and flow field distribution at the nozzle exit.

The velocity modulations occuring at the nozzle exit due to oscillating horn structure result in a wide gamut of liquid structures specific to the imposed oscillation frequency and modulation amplitude. The disintegration characteristics of these modulated liquid jets are studied using a Volume-of-Fluid (VOF) interface capturing approach based on finite volume methodology employing an interface compression scheme. VOF methods are validated against experimental results and then subsequently used to study scaling parameters governing the modulated liquid jets.

To perform coupled interior-exterior nozzle computations with cavitation, two new cavitation models are presented: First, a model based on Homogeneous Equilibrium assumptions for tracking cavitation events in a compressible framework is presented. Owing to its inability to simulate incompressible cavitating flows, a new cavitation event tracking model based on a Cavitation-Induced-Momentum-Defect (CIMD) correction approach is formulated utilizing a scalar transport model for vapor volume fraction with relevant transport, diffusion and source terms. Validations of both the models against experimental observations are detailed.

Coupled internal-external liquid flow computations from the proposed atomizer design using a VOF-CIMD strategy shows strong potential for rapid drop formation in the presence of cavitation effects. A prototype model of a new spray applicator design is presented.

KEYWORDS: CFD, Sprays, Cavitation, Breakup, Atomizer.

Vedanth Srinivasan

December 1, 2006

NUMERICAL STUDY OF A NEW SPRAY APPLICATOR

By

Vedanth Srinivasan

Dr. Kozo Saito

Director of Dissertation

Dr. L.S. Stephens

Director of Graduate Studies

December 1, 2006

DISSERTATION

Vedanth Srinivasan

The Graduate School

University of Kentucky

2006

NUMERICAL STUDY OF A NEW SPRAY APPLICATOR

DISSERTATION

A dissertation submitted in partial fulfillment of the
requirements for the degree of Doctor of Philosophy in the
College of Engineering
at the University of Kentucky

By
Vedanth Srinivasan
Lexington, Kentucky

Director: Dr. Kozo Saito, Professor of Mechanical Engineering

Lexington, Kentucky
2006

To

My Mom, Dad and loving sister

Acknowledgments

I wish to express my gratitude to my mentor and supervisor, Professor Kozo Saito for his continued support and invaluable guidance throughout my graduate career. I am indebted to Dr. Abraham Salazar for his invaluable insights and constructive criticisms. I have been greatly benefited from his numerous comments and helpful discussions.

Furthermore, I would like to acknowledge post doctoral scholars Dr. Kazunori Kuwana, Dr. Tianxiang Li, Dr. Valerio Viti, Dr. Keng Hoo Chuah for their collaboration and companionship throughout my program. Specially, I would like to thank Dr. Hoo for his discussions ranging from Heat transfer, molecular dynamics, CFD to international politics, religion and language. My discussions with Dr.Viti on various subjects spanning compressible flows, aerosols to career development certainly helped me mold myself to the competitive environment. Dr. Kuwana's solution perspective has always accelerated by thinking and Dr.Li's insight and collaboration has offered me several new frontiers to think (worry) about. Definitely, Dr. Omar's research outlook has always been a source of inspiration and moral support.

I would also like to thank my colleagues in the IAES group for their company. Many thanks to visting post doctoral scholars Dr. Kazutaka Kitagawa and Dr. Tamio Ida for their strong support during my research program.

I am very appreciative of the support provided by the super computing facility at the University of Kentucky.

I would also like to extend my sincere thanks to Mr. Rich Alloo for his valuable comments and finally, the financial support provided by Toyota Motor Corporation, Japan which made my work possible, is gratefully acknowledged.

I am so very thankful to my parents, my sister, my grandfather and grandmother for motivating me under all circumstances. Undoubtedly, this would work would have been impossible if not for the divine intervention of Lord Venkateshwara.

Table of Contents

Chapter 3 58

Numerical Simulation of Modulated Liquid Jets 58

Chapter 4 166

Numerical study of cavitating atomizer 166

Chapter 7 429

Conclusions and Future Recommendations 429

List of Tables

List of Figures

List of Files

Vedanth.pdf	28.3 MB

Chapter 1

Introduction

1.1 Background and Motivation

The process of disintegration of liquid jets has long been investigated by a myriad of researchers due to its profound impact on a wide spectrum of applications ranging from automotive, aerospace to agriculture and food processing [1]. Despite several studies being devoted to fully comprehend the breakup process, no complete description of this non-linear process is yet available. A direct consequence of the liquid disintegration process results in drop formation, which are characteristic to the nature of the process utilized in breaking the liquid jet [2-5]. Droplet properties such as their size and velocity distribution are of particular interest in applications where the droplet-ambient interaction plays a decisive role in characterizing the efficiency of the system such as in a spray painting, spray combustion etc [1, 2, 6]. For example, impingement of non-uniform droplet size distribution of paint particles in a spray booth can lead to severe coating problems and in the potential development of unwanted characteristics such as scratch, corrosion etc. In combustors, droplet characteristics critically dictate the burning rates and hence, are major contributors to reduced emissions and efficient energy generation processes [1, 6-8]. Particularly, small droplet sizes are desired in spray combustion for rapid heat transfer and vaporization [8].

In order to control and predict the behavior of the droplet entities, a thorough understanding of the spray generation process is essential. Investigations reveal that most of the conventional atomizers available in the industry today have major uncontrollable behavior attributed to turbulence (pressure atomizers, twin-fluid, effervescent sprayers), wave instabilities (rotary cup sprayers) etc., that are inherent to the system. Another major concern is the utilization of energy resources for the spray generation process. In a typical pressure sprayer, the droplet sizes are controlled directly by the magnitude of pressure applied within the nozzle. Although, smaller droplet sizes are obtained by use of high pressure, the increase in pressure requirement, on the other hand, necessitates increase in the energy input in the system. However, this process is not monotonic in the sense that beyond finite applied pressure limits, the drop sizes do not exhibit any change in their characteristics [1]. Similar energy demand exist in the case of twin-fluid sprayers, rotary sprayers etc. Although the power requirement is alleviated in certain ultrasonic spray applicators, very low velocity sprays are generated questioning their ability to cope up with applications requiring higher penetration and increased flow rate [1]. In this spirit, the current study is devoted to the development of a low-energy, high-flow rate atomizer design to produce fine droplets with narrow size distribution in a controllable fashion. In the current study, a novel concept of aggravating naturally occurring perturbation-enhancing-mechanisms, such as cavitation, within the nozzles and focusing them onto the exiting liquid jets to promote the breakup process is utilized. As a result, careful control of the disturbance factors within the nozzle would reflect on the drop size distribution in the spraying environment.

The requirement of drop size and their production rate is completely dependent on the system under investigation. For process such as inkjet printing, lubrication, pharmaceutical process, very low liquid rates, of the order of 0.001 l/min are desired, while processes encountered in spray combustion, spray drying, spray forming etc., invoke large flow rate requirements [1, 9, 10]. Scaling up of small scale spray devices to produce a reasonably mono-disperse spray with increased flow rates may fail due to the distinguishing disintegration mechanisms (such as capillary, aerodynamic mechanisms) specific to the operation scale [1, 2-5]. In the current work, design and development of spraying mechanisms to accommodate flow rates 25 cc/min and higher are discussed. Most of the sprays generated for industrial applications predominantly depend on the process of liquid jet/sheet atomization, wherein the diameter of the droplets are much smaller than the liquid jet or sheet thickness itself and hence, a high surface to volume ratio in the liquid phase [1].

1.2 Process of drop generation: The atomization mechanism

Atomization is defined as the disintegration of liquid into small drops or droplets [1, 2, 10]. The process results in suspension of fine droplets or solid particles immersed in a surrounding gas field and are often termed as a spray, mist, or aerosol. Atomization of a liquid into discrete droplets can be brought about by use of diverse forcing methods: aerodynamic, mechanical, ultrasonic, or electrostatic etc. For example, the breakup of a liquid into droplets can be achieved by the impingement with a gas in two-fluid atomization, by centrifugal forces in rotary atomization, by ultrasonic vibrations utilizing a piezoelectric transducer in ultrasonic atomization, or by electrostatic/electromagnetic fields in electrostatic/electromagnetic atomization. Atomization processes may also be classified according to the energy used to produce the instability on the liquid element. For example, pressure energy in the case of pressure atomization, centrifugal energy for rotary atomization, gaseous/fluid energy for two-fluid atomization, and vibratory energy for ultrasonic or acoustic atomization [1]. Most practical atomization processes for normal liquids include: (a) pressure atomization, (b) two-fluid atomization, and (c) rotary atomization. Similar useful atomization processes for normal liquids have been developed in special applications, including: (a) effervescent atomization, (b) electrostatic atomization, (c) ultrasonic atomization, (d) whistle atomization, etc. These processes may be loosely classified into two major categories in terms of the relative velocity between the liquid being atomized and the surrounding gas flow. In the first category, a liquid at high velocity is discharged into a still or relatively slow-moving gas. Notable processes in this category include, pressure and rotary atomization. In the second category, a relatively slow-moving liquid is exposed to a stream of gas at high velocity such as in the case of two-fluid and whistle atomization. A summary of various atomization methods with associated droplet size distribution and distinct characteristics are listed in Table 1.1.

Table 1.1 List of conventional atomizers

Method		**Droplet size (μm)**	**Application**	**Advantage**	**Limitation**
Pressure Atomization	*Plain Orifice*	*20-250*	Diesel engines, after burners	Simple, rugged, cheap	Narrow spray angle, solid spray cone
	Simplex	*25-200*	Gas turbines, industrial furnaces, combustors	Simple, cheap, Wide spray angles	Increased pressure supply, Very sensitive to applied pressure
	Duplex	*20-250*	Gas turbine combustors, afterburners	Simple, cheap, Wide spray angle, Good atomization over a wide range of liquid flow rates	Increased liquid flow rate leads to narrow spray angle
	Dual-orifice	*20-250*	Variety of gas turbines, industrial combustors	Good atomization, Constant spray angle	Poor atomization in transient stage, design complexity, Passage blockage
	Spill return	*25-200*	Combustors, Slurry operation	Simple, good atomization over a range of flow rates	Flow rate dependent spray angle, higher power consumption
	Fan spray	*100-1000*	High pressure painting,	Good atomization, elliptical spray	High supply pressure

			coating, combustors	pattern	
Rotary Atomization	*Spinning disk*	*10-250*	Spray drying, chemical processes	Good monodispersity of droplets, independent control of atomization and flow rate	Satellite droplets, 360° spray pattern
	Rotary Cup	*10-300*	Spray painting drying, cooling, Industrial furnaces	Capable of handling slurries, high viscosity materials	Requirement for airblast and high power requirement
Two-fluid atomization (air assisted)	*Internal mixing*	*50-400*	Industrial furnaces, gas turbines, spray drying	Good atomization, low clogging, handle high viscosity liquids	High air power,other auxiliary device
	External mixing	*20-140*	Industrial furnaces, gas turbines, chemical processes	Good atomization, no risk of liquid backup into air line	Requirement for external source of high pressure air, limited air/liquid ratios
Two-fluid atomization (air blast)	*Plain-Jet*	*15-150*	Industrial gas turbines	Simple, cheap, good atomization	Narrow spray angle
	Pre-filming	*25-150*	Wide range of aircraft engines	Good atomization at high ambient pressures, wide spray angles	Poor atomization at low air velocities
Effervescent atomization		*25-350*	Combustors, spray drying, cooling	Simple, good atomization, low risk of plugging, soot reduction	Requirement for separate air supply
Electrostatic atomization		*0.1-1000* *300-600* *100-250*	Paint spraying, oil burners	Fine and uniform droplets	Very low flow rates, Sensitive dependence on liquid

					electrical properties
Ultrasonic atomization	*Nebulizers*	*1-5 (55 KHz)* *30-60 (50 KHz)*	Medical spray, Spray cooling, drying	Very fine uniform droplets, low spray rates	Incapable of handling high flow rates

Based on the elaborated experimental database concerning disintegration of liquid jets, it can be easily assessed that the mean droplet size and pattern distribution depend on many variables, such as operating conditions, liquid properties, and nozzle geometry [1, 2]. Some insights on the droplet generation processes reveal that a combination of high injection pressures with low ambient pressure and/or small orifice diameter leads to small droplet sizes, while an increase in liquid viscosity and/or surface tension usually hinders the liquid disintegration process[1, 2]. While high viscosity causes large droplet sizes, poor atomization, high spray jet penetration, low evaporation rates, heterogeneous mixing and imperfect combustion, surface tension effects oppose liquid surface distortion [1, 2, 11].

In the industrial scenario, another major concern attributed to the high-flow rate spray atomizers is the characteristic spray cone generated by them [2, 12]. For example, plain-orifice atomizers form spray cones ranging typically from 5° to 15° [13-16]. This angle is mainly affected by the turbulence and properties (viscosity and surface tension) of the liquid jet, and to a lesser extent by the diameter and diameter-to-length ratio of the orifice [2, 5, 12]. An increase in the turbulence enlarges the cone angle by increasing the ratio of radial-to-axial velocity components of the liquid jet [12]. On the other hand, the rotary sprayers can accommodate higher spray cone angles of the order of 120^{o} and higher, due to the nature of operation [17]. Similarly, effect of relative velocity between the liquid jet and surrounding air [18] and their propagation direction [19] have been identified to play a crucial role.

1.2.1 Requirements of a good atomization

The basic requirement in atomization applications is a narrow droplet size distribution [1], even a mono-size distribution in some spray drying and aerosol spray applications [10]. Small droplet size is desired in spray combustion for rapid heat transfer and vaporization. An ideal atomizer should possess the capability of providing energy-efficient and cost-effective atomization over a wide range of liquid flow rates and should be able to accommodate fluctuations in liquid flow rates. It should also be capable of scaling up for design flexibility, and not be susceptible to damages during manufacture, maintenance and installation. For spray combustion, an ideal atomizer should produce a uniform radial and circumferential fuel distribution, and be free of flow instabilities [1].

As detailed in Table (1.1), pressure atomizers offer humble solutions to spray formation due to their inexpensive prototyping and simple mode of operation, although their spray characteristics such as drop sizes and spray angle are highly questionable.

1.2.2 On pressure atomizers

Pressure atomization is probably one of the most commonly used techniques in general spray application areas. In pressure atomization of a liquid, pressure energy within the nozzle is converted to kinetic energy to accelerate the liquid to a high velocity relative to surrounding ambience [18, 19]. Depending on the atomizer design and geometry, a liquid may be accelerated in different forms, such as a liquid jet in pressure jet atomization, a swirling liquid sheet in pressure-swirl atomization, or a fan liquid sheet in fan spray atomization [1]. Further, different modifications can be applied to suit the requirements as seen in Table (1.1). Both Newtonian and Non-Newtonian liquids can be sprayed, although addressing the shear rate effects on drop sizes encountered in Non-Newtonian liquids are very complicated.

1.2.3 Pressure sprayer enhancements

1.2.3.1 Vibration atomization

In an attempt to improve the atomization behavior of simple pressure sprayers, periodic vibrations were imposed to the exiting liquid jet. The technique, vibration atomization, relies on superimposing the liquid to be sprayed with finite amplitude pressure waves either using mechanical or acoustic wave means [20]. Use of acoustic vibrations has been explored to reduce combustion emission in some cases [21]. The instability resulting from such a superposition interacts with the surface tension forces and results in drop formation. The drop sizes, then, can be precisely controlled by monitoring the vibrator device characteristics. In most cases, the vibratory mechanism is achieved by use of a piezo-electric transducer. The method is built on the capillary mechanism [2] and hence imposes high frequency requirement and low flow velocity scales to obtain fine drop formation. The resultant sprays from these atomizers are limited to very low flow rates of the order of 0.0025 l/min to 0.1 l/min (by use of entrainment devices used in several aerosol and pharmaceutical applications). Further, ultrasonic atomizers are critical to the viscous nature of the liquid, since higher viscosity impedes surface wave instabilities leading to large drop sizes [20]. In other developments, influence of vibration technique in enhancing liquid sheet atomization emanating from a pressure sprayer has been reported [22, 23].

1.2.3.2 Velocity-modulated atomizers

In a similar mechanism to that of vibration methodology, pressure sprayer characteristics were improved by use of high amplitude velocity-modulation mechanisms. The velocity-modulation atomizers [24-28], as they are called, impose direct high-amplitude perturbation to the liquid jets exiting through a cylindrical hole or a planar orifice. Using Newtonian type spraying liquid such as water, droplet sizes of the order of 1.5 to 3.4 times the jet diameter, in case of mono-disperse sprays, were achieved with a velocity range of 4-26 m/s. However, the system was restricted to low Reynolds number and liquid flow rates. Increase in the flow rate resulted in a narrow drop size distribution, with large Sauter mean diameters [21].

In view of the complexity including cost-effectiveness, ease of operation and maintenance, the capability of producing a mono disperse spray, covering the required range of droplet sizes, accommodating various liquid properties, and achieving sufficient production rates associated with several atomizer configurations such as the effervescent, rotary cup and ultrasonic based atomizers, a novel concept of spray generator based on a pressure sprayer enhancement strategy for low viscosity liquids such as water is developed in this study. Further, this spray applicator concept is presently tested only with a Newtonian liquid assumption which might be violated in many industrial liquids.

1.3 Novel spray applicator concept

The nature of the breakup process and the drop characteristics of liquid jets (planar/cylindrical) emanating from pressure sprayers have been identified to be affected by a myriad of forces such as turbulence, cavitation, swirl components, aerodynamic interactions and fluid properties among others [1-4]. Some of the major phenomena acting to enhance liquid disintegration such as pressure oscillation effects, cavitation and other internal nozzle phenomena described by several pioneering work in the pressure spraying environment are not explicitly accounted during the design of an atomizer. Rather, the atomizer designs by themselves are sometimes capable of generating these perturbations in a non-orderly fashion whose effects are hard to establish [2]. This is sometimes due to the harmful effects created by these mechanisms reducing the life cycle of the devices. However, the role played by these forces, in particular the cavitation and pressure fluctuations, in aggravating the spray formation, inducing heightened hydrodynamic instabilities in liquid jets, cannot be ruled out. To this effect, the current study is dedicated to design and development of a novel atomizer design where the role of cavitation is explicitly configured in addition to a pressure modulation on the exiting liquid jets to enhance its breakup into fine droplet sizes. Note that a cylindrical liquid jet is characterized by a single characteristic length, its diameter, while an emanating liquid sheet requires specification of its width and thickness across the orifice. Further, using planar nozzles can potentially evoke unwarranted perturbations owing to flow asymmetry within the nozzle. The research presented here concerns disintegration enhancement of round liquid jets for potential use in spray combustors, spray drying and spray painting environments.

1.4. Proposed approach for creating efficient atomization

The high energy associated with the cavitation bubbles was utilized in the design of ultrasonically cavitating interrupted cylindrical liquid jets used for metal erosion purposes [29-32]. The design produced cavitation bubble clusters [33, 34] inside the nozzle, due to high frequency oscillations of a solid horn, which exits the nozzle in an immersed fashion within high speed water jets. As the cavitation bubbles hit the surface, they triggered a microjet formation mechanism which generated a high intensity pulse resulting in erosive action [29-31]. In the current study, the principle of cavitation generation by use of a high frequency horn motion is employed. However, contrary to the interrupted cavitating jet type, the present design enforces the collapse of these high intensity cavitation clusters near a small diameter nozzle exit to enhance the atomization of liquid jets to create uniform distribution of fine droplets with narrow drop size distribution. In this regard, the primary objective lies in the creation of a controlled source of cavitation zones, which can then propagate and collapse near the nozzle exit to create fine spray region outside the nozzle. A schematic of the proposed ultrasonically cavitating atomizer concept is detailed in Fig. (1.1).

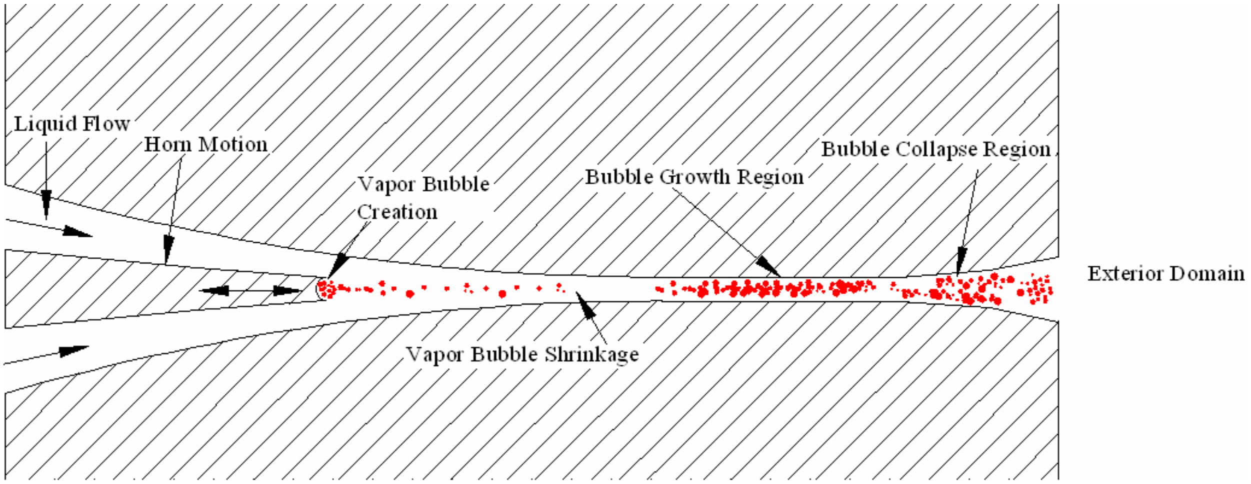

Figure 1.1: Schematic representation of coupled horn vibration and cavitation dynamics.

As described in Fig. (1.1), the ultrasonic horn motion creates low pressure region, depending on its location, resulting in the activation of cavitation nuclei. The design of nozzle is crucial in maintaining sufficient low pressure region for the growth of the cavitation nuclei [33, 34]. This requirement can be readily achieved by creating sufficient flow acceleration process that reflects on lowered pressure zones [34]. The cavitation clusters convected by the accelerating flow collapse on reaching the nozzle exit owing to the increased pressure content in the nozzle exterior ambience. In the near nozzle exit regions, the pressure perturbations generated by the cavitation bubbles collapse act as a strong deformation force within the liquid jet against the surface forces resulting in the creation of finer droplets [34]. Hence, to achieve the objective of generating fine droplets it is necessary that the cavitation bubbles be produced at a constant rate. In many atomization nozzles, occurrence of cavitation is strongly related to the geometry effects. Cavitation can occur if the geometry is aligned such that it creates very low pressure regions, such as recirculating regions inside the nozzle, sharp corners with suddenly enlarging geometries etc [1, 2]. Despite the nature of cavitation inception mechanism, their strength created in these zones is highly unsteady and dependent on the transient flow chracteristics. In this concern, design of the interior nozzle domain is crucial in order to maximize the perturbations, caused by cavitation clusters, in the exiting liquid jets.

In addition to the cavitation effects generated by the current design, the pressure pulsation effects superimposed on the nozzle flow due to the horn motion can manifest into a wide variety of liquid structures. The characteristics of these pressure pulses, immersed in the exiting liquid jets, contribute to the overall hydrodynamic instability of the liquid jets. In sum, the current design advocates enhancement of liquid jet instabilities by offering pressure pulsation effects through the use of ultrasonic horn vibrations within the nozzle in combination with intense cavitation cluster collapse energy to maximize the liquid disintegration process.

1.5. Design of a Cavitating Atomizer

The conceptual design of the proposed atomizer with an oscillating horn for cavitation cluster generation and to serve the purpose of modulating the exiting liquid jet is shown in Fig. (1.2). In the proposed design of the cavitating atomizer, a horn tip performing oscillations at very high frequencies is placed inside the nozzle close to the exit. The high frequency oscillations of the horn structure result in pressure depression near the horn surface which then acts as a primary source for the cavitation clusters [31]. The clusters of bubbles incepted in these regions are swept by the flow towards the nozzle exit where they collapse to intensify the atomization process [1, 2, 31].

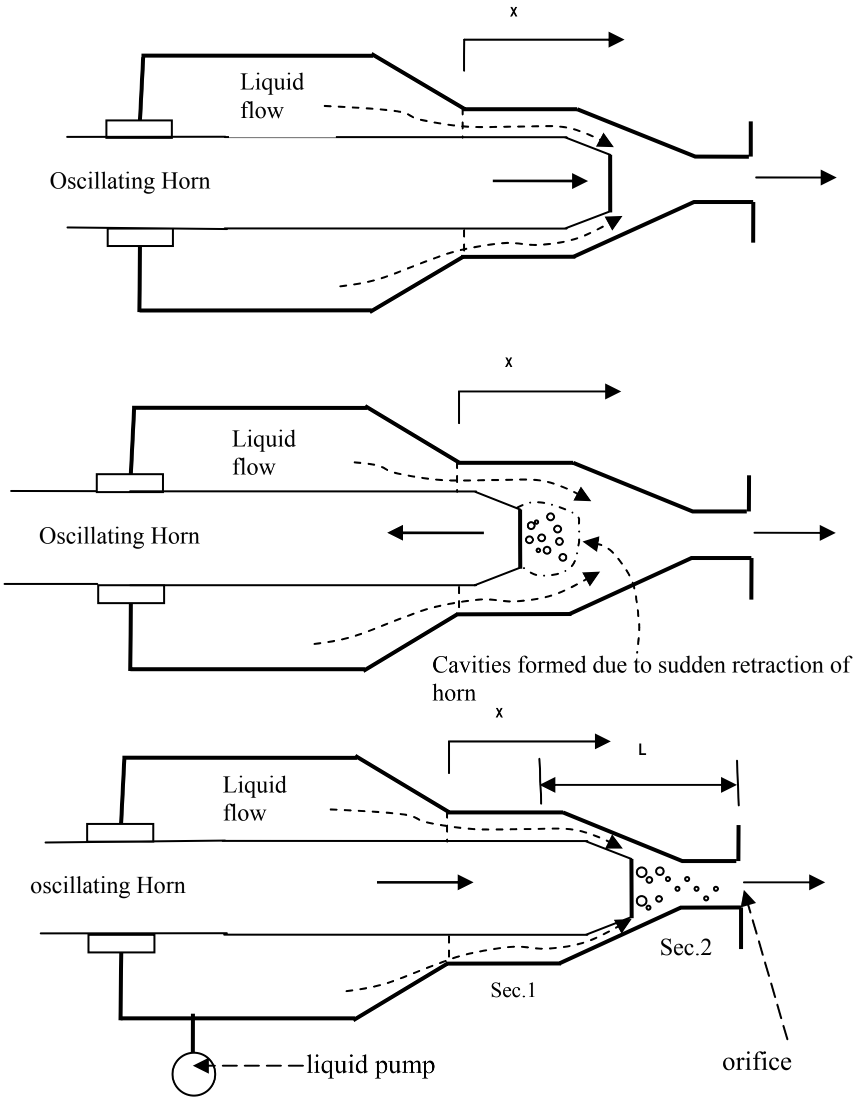

Figure 1.2: Schematic of the proposed atomizer

1.6 Design and Development of a new Spray applicator: A numerical approach

In order to design and develop the prototype, two strategies can be adopted: First, series of detailed experimentation process incorporating different nozzle design and horn parameters can be carried out. However, it should be admitted that experimentation of such process require sophisticated measurement techniques in addition to the added expense of building different models for testing purposes. Large scale tests to identify the primary factor, cavitation dynamics, influencing the design cannot be processed due to the non-scalability of the cavitation process [2, 31]. Several researchers have reported difficulties in visualizing cavitation in real scale nozzles and no concrete models to identify their effects on jet breakup has been addressed yet. Given the tall order of difficulties in following an experimentation strategy, the other alternative, the numerical approach, tends to prevail comfortably over its experimental counterpart.

In the recent decades, several numerical models have been developed to monitor and track events of cavitation typically encountered in nozzles. Adding, similar tools to understand the breakup of liquid jets emanating from nozzles into ambience have been constructed. These models provide approximate behavior of the multiphase fluid dynamic system to sufficient accuracy, at the favorable expense of lowered cost and effort. By means of a relevant numerical tool, several prototype designs can be tested to characterize their fundamental response to particular design parameter. These advantages offered by the numerical strategy provide sufficient support for their adoption in the design and development of the newly proposed spray applicator.

Several complexities involved in the application of a numerical model to the current system design have not been previously explored. A brief list of some of the intricacies involved in applying numerical models in designing a novel atomizer is listed here: Presence of a moving structure inside a nozzle is a classic example of fluid structure interaction with an added complexity of cavitation. The tracking of liquid jet disintegration process at the downstream of nozzle exit requires very detailed understanding of the involved numerical methodologies. Further, very few attempts have been made to simulate a combined internal-external coupled nozzle flow calculation with cavitation effects but were devoid of any moving structure induced oscillatory effects.

1.6.1 Numerical methodology

To overcome the difficulties cited in Section 1.6, a two zone approach is proposed: a detailed study of the internal cavitating-nozzle flow phenomena incorporating detailed effects of nozzle geometry, horn operation parameters and fluid flow properties are carried out. This methodology is relevant to the current situation since the cavitation bubble cluster swept by the flow from the oscillating tip influences the flow field distribution at the nozzle exit. Hence, performing a Computational Fluid Dynamics (CFD) simulation of the internal portion of the nozzle with cavitation would help understand the internal flow field structure giving details about the vapor phase distribution closer to the nozzle exit. The solutions generated by the optimal design of the interior nozzle flow activities are taken as an input to simulate the exterior spray formation. In a parallel fashion, numerical simulations in the nozzle exterior domain with an assumed liquid flow rate and modulation characteristics are performed to characterize the breakup behavior of liquid jets subjected to different perturbation conditions. The information obtained from the Volume of Fluid (VOF) based numerical simulations are looped back into the interior nozzle flow simulations to modify the atomizer design for obtaining required breakup behavior.

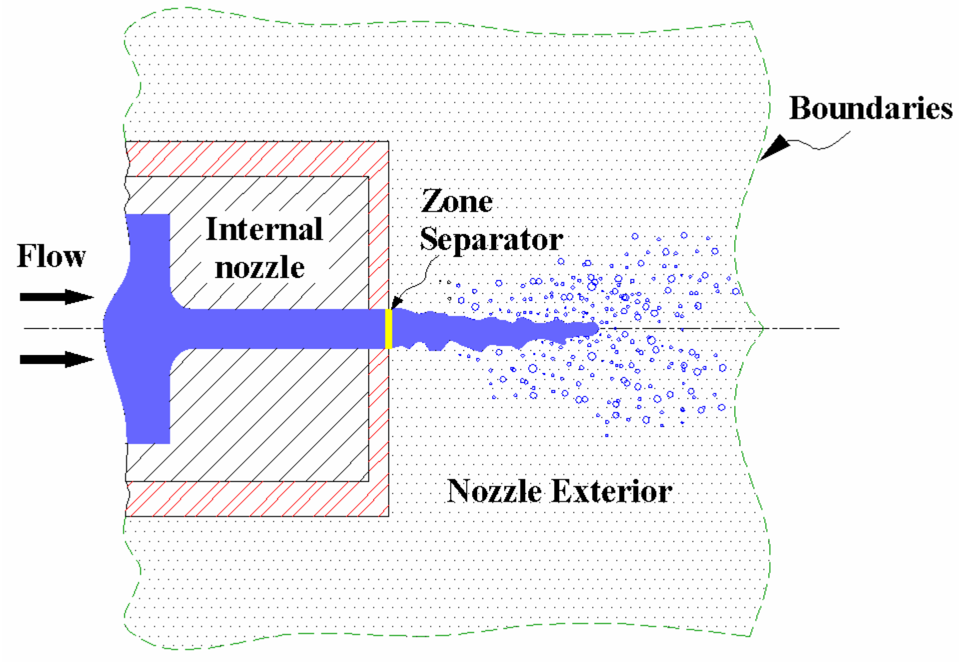

Figure 1.3: Discrete two-zone approach to solve a full disintegration behavior of atomizer flows

The two zone procedure, described in Fig. (1.3), provides continuity to two discrete simulation events. However, details like supercavitation, vorticity, swirl effects and associated phenomena may well have to be compromised [35]. It is, however, required that the supercavitation phenomena be restricted, since the traveling cavitation bubbles may further extend downstream within the ligaments and rupture on impinging on the surfaces in the vicinity leading to material damage.

Performing these simulations, the importance of modeling the transport of the internal nozzle fluctuations such as vorticity, velocity profile relaxations etc across the nozzle exit section are distinctly detected. In order to convincingly treat the coupled calculations, new cavitation models are developed: first, within a compressible flow framework, and then extended to work within an incompressible flow assumption. These newly developed cavitation detection algorithms are then combined with a Volume-of-Fluid (VOF) based methodology to include the cavitation effects in performing a coupled internal-external nozzle flow computation on the proposed design of the atomizer.

1.7 Overview of the thesis

The remainder of the dissertation is as follows.

Chapter 2 presents the literature review with emphasis of liquid jet instabilities and various atomization processes. Details of the breakup modes and of influencing mechanisms are stressed.

Chapter 3 provides an elaborate description on the numerical methods used in tracking disintegration of liquid jets. The models are validated against experimental conditions and, further, applied to simulate modulated liquid jets. Owing to the modulation effects, several liquid structures are generated. Utilizing the numerical approach, a detail assessment concerning the influence of modulation amplitude, frequency and mean jet velocity on the breakup process is carried out. In particular, the scaling parameters that govern the breakup behavior of such modulated jets are examined.

Chapter 4 is devoted to the study of internal nozzle cavitating flows. The atomizer design proposed in Chapter 1 involves ultrasonic oscillations of the horn structure immersed in a liquid medium. This invokes requirement of numerical simulations using a dynamic meshing procedure. A two-equation turbulence model based on RANS approximation is used to model the Reynolds stresses occurring in such highly strained flows. Characterization of cavitation dynamics generated by the horn oscillation is performed by performing a parametric study involving effects of horn stroke length, frequency, the horn position inside the nozzle, nozzle design and the flow rate. The critical nature of nozzle design in obtaining the required flow field set up for efficient spray generation is conceived.

Chapter 5 discusses development of new cavitation models developed during this study. This encompasses the newly formulated cavitation prediction algorithm based on a compressible framework by supplementing a homogeneous equilibrium model with a pressure correction equation. Extending this work, a new methodology for tracking the cavitation regimes within an incompressible liquid flow is derived and validated against experimental conditions. The methodology is extended to a two-phase liquid jet disintegration process to identify its capability to be coupled with multiphase systems.

Chapter 6 unveils coupled calculation utilizing a two-zone approach for simulating spray formation from the newly proposed spray applicator. Extending the two-zone approach, coupled internal-external nozzle computations with cavitation effects are carried out to assess the disintegration process generated by the novel atomizer design. Design and development of the newly proposed spray applicator is discussed and some flow field concerns are elaborated.

Chapter 7 provides concluding remarks and future directions of the current work.

1.8 Objectives of this thesis

There are four main objectives in this thesis study

1. To gain a good understanding of the factors influencing vibration cavitation mechanism. To compare the effects of oscillation frequency, amplitude on the cavitation generation process. Test different nozzle geometry design on the cavitation characteristics
2. To carry out detailed optimization procedures within the nozzle interior to obtain efficient cavitation and turbulence characteristics to enhance liquid jet disintegration
3. To develop models for simulating disintegration of round liquid jets supplemented with modulation parameters: amplitude and frequency. To examine the modulation and frequency effects on the drop formation and resulting flow structures

4. To develop new cavitation prediction models to identify the influence of cavitation on the jet breakup structures and to address the design and development of a new spray applicator design.

Chapter 2

Literature Review

Multitude of processes such as spray combustion, spray drying, spray cooling, spray deposition, aerosols etc require distinct droplet characteristics specific to the operating condition. Typically, droplets are generated from different flow configurations concerning liquids such as from round or planar liquid jets. The distribution of drop sizes and their spatial distribution characteristics, such as spray width, coverage area, types of cones, hollow or full cone, planar sheets etc., demand detailed probing to match the process requirements [1, 36, 37]. It is hence, of critical importance, to identify the best disintegration configuration required to suit specific system needs. One of the most common liquid flow configurations which are used for generating droplets is the round jet mode very frequently found in spray generation processes [1, 10]. Variation in drop sizes are achieved by carefully modulating the characteristics of the emanating liquid jet into ambience and/or can also be achieved by altering the properties of the system such as the ambient density, viscosity etc. [2]. A review on the breakup characteristics of round liquid jets and different parameters affecting the process is presented in this section.

2.1 Review of liquid-jet breakup

The stability and disintegration behavior of liquid jets have been investigated extensively both theoretically and experimentally over many years in various fields utilizing such jets. These studies have established that the breakup properties of the liquid jet are influenced by a myriad of parameters. The first researcher to analyze this phenomenon was Plateau [38]. He observed that surface energy of a uniform circular cylindrical liquid jet is not the minimum attainable for a given volume of jet and henceforth, argued that, jet tends to breakup into segments of equal length, each of which is 2π times longer than the jet radius. He proposed that this configuration was preferred by the liquid jet, since the spherical drops formed from these segments give the minimum surface energy. Later, Rayleigh [39] emphasized the mechanism of fundamental hydrodynamic instability influencing the jet breakup. Neglecting the ambient fluid, the viscosity of the jet liquid and the gravity effects, he demonstrated that a low velocity circular cylindrical jet is unstable with respect to disturbance of wavelengths larger than the jet circumference. His study identified the strong influence of liquid surface tension on the behavior of low-speed, inviscid liquid jets. He showed that a liquid jet disintegrates with respect to any axi-symmetric varicose surface instability whose wavelength is larger than the undisturbed jet circumference. Amongst all unstable disturbances, the jet is most susceptible to disturbance with wavelengths 143.7% of its circumference.

Extending his case to a viscous liquid in an inviscid gas, he proved that the most dangerous wavelength for disturbance amplification was infinite and that with an inviscid liquid in an inviscid gas, the most amplified wavelength value reaches 206.5% of the jet circumference. Chandrasekhar [40] took into account the liquid viscosity and the liquid density, and showed mathematically that the viscosity tends to reduce the breakup rate and increase the drop size. During this development, he proposed the mechanism of capillary pinching as responsible for the breakup of liquid jet in a vacuum. Further, Weber [41] identified the crucial influence of ambient gas density in addition to the liquid viscous effects. Later, Ohnesorge [42] addressed the influence of viscosity on the breakup process. Taylor [43] stressed on the profound influence of the gas density on the breakup process and insisted that, for a large gas-inertia force, a strong function of the density, relative to the surface tension force per unit of interfacial area, the liquid jet would breakup into drops of sizes several orders of magnitude smaller than the jet diameter. This Taylor mode of jet breakup is the so-called atomization that leads to fine droplets.

In discussing liquid jet disintegration, researchers adopted several dimensionless numbers to characterize the system under investigation [1, 2]. They correspond to the Reynolds number, Weber number and Ohnesorge number. The Weber number representing the ratio of inertial to surface forces is given by

$$We_i = \frac{\rho_i U_l^2 D}{\sigma},\ i = l, g \tag{2.1}$$

In the discussions, the nozzle exit diameter (D) and liquid injection velocity U_l are used as the characteristic length and velocity scale for deriving these dimensionless numbers. In the definition of Weber number, authors prefer gas-based Weber number, by using ρ_g, to reflect on the effect of ambient gas on the disintegration behaviour of liquid jets. The Ohnesorge (Oh) number represents a ratio of the viscous to surface tension forces in the liquid and is defined as

$$Oh = \frac{\sqrt{We_l}}{\mathrm{Re}_l} = \frac{\mu_l}{\sqrt{\rho_l \sigma D}} \tag{2.2}$$

where Re_l, the Reynolds number is given by

$$\mathrm{Re}_l = \frac{\rho_l U_l D}{\mu_l} \tag{2.3}$$

for a liquid jet into an gaseous flow.

2.2 Classification of breakup modes

The variation in the operating conditions under which the liquid jet is injected has been observed to reflect on the nature of the jet appearance downstream. The action of single or multiple dominant forces acting on the jet and henceforth influencing its breakup, are required to explain the different regimes encountered as a function of the operation parameters [44]. Four main breakup regimes have been identified that correspond to different combinations of liquid inertia, surface tension, and aerodynamic forces acting on the jet [1-4].

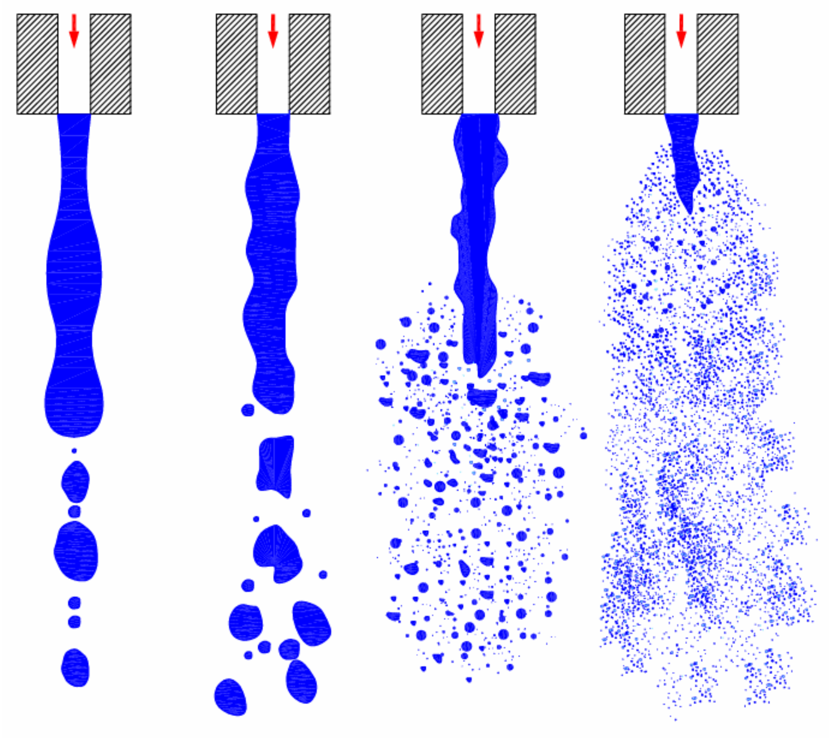

(a) (b) (c) (d)

Figure 2.1: Schematic of different regimes of liquid jet disintegration [3] (a) Rayleigh (b) First wind induced (c) Second wind induced (d) Atomization regime.

These correspond to the Rayleigh regime, the first wind-induced regime, the second wind-induced regime, and the atomization regime (Fig. (2.1)). Dimensionless numbers derived in Section 2.1 can be used to map different breakup regimes of the liquid jet, Figs. (2.2) and (2.3(a)). Reitz [3] classified the liquid jet breakup modes on Oh vs Re_l chart while Faeth et al. [45] depict the breakup regimes on a chart plotting Oh vs We_g for constant liquid properties such as viscosity and surface tension. Hence, for a constant Oh number, increase in the Weber number or the Reynolds number results in enhanced atomization characteristics of the turbulent liquid jet.

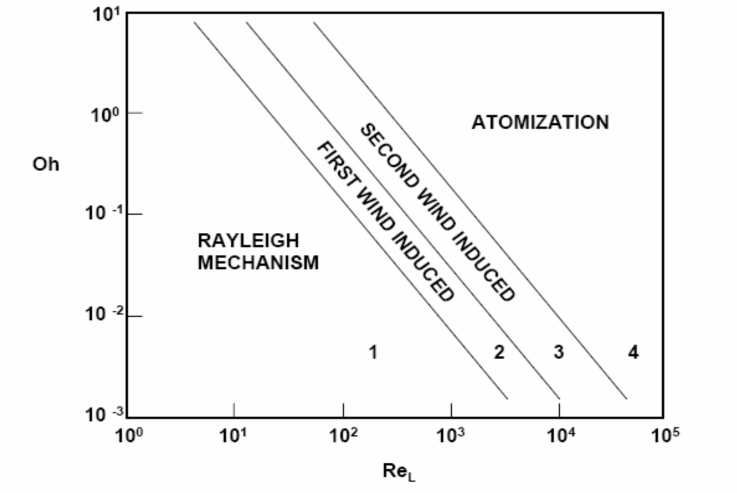

Figure 2.2: Different breakup regimes based on Reynolds number [1, 2]

Farago et al. [11] characterized different breakup behavior displayed by round liquid jets in a co-axial environment as described in Fig. (2.3(b)).

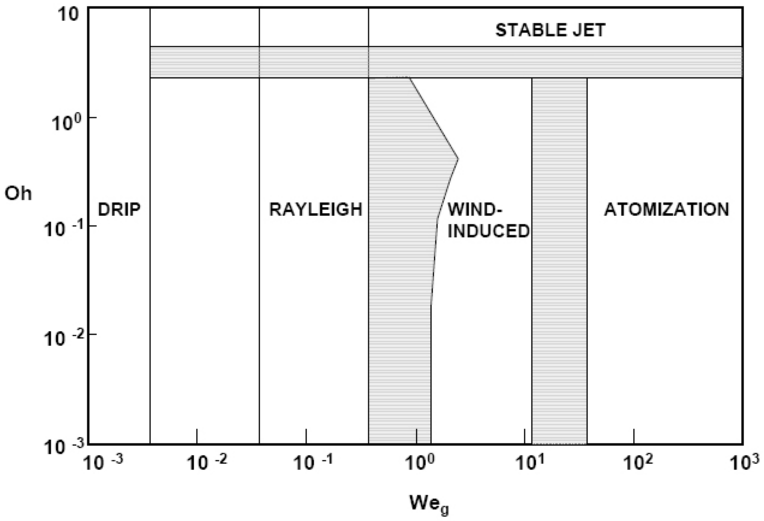

(a)

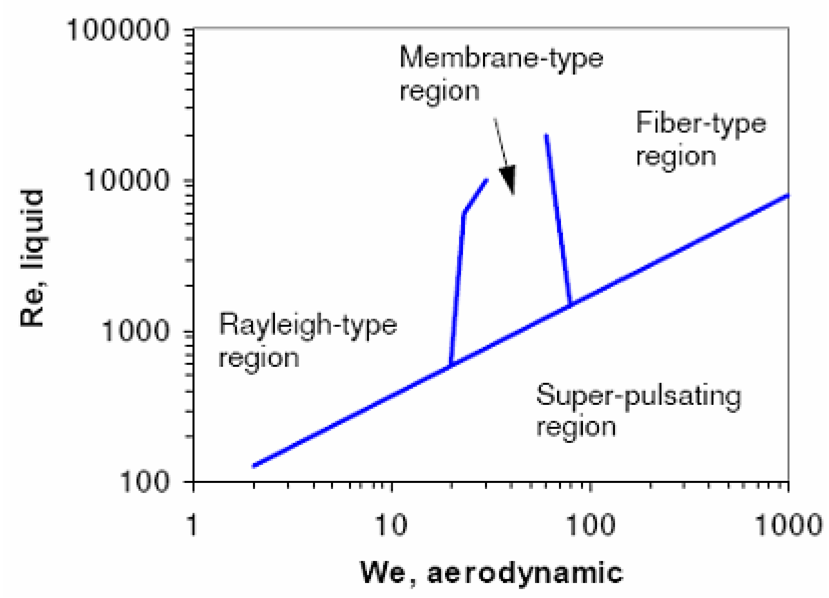

Figure 2.3: (a) Mapping Oh vs Weg : Faeth et al. [45] (b) Morphological characterization of the breakup behavior of round liquid jets [11]

The Rayleigh regime concerns the characteristics of low velocity liquid jets, where the growth of long-wavelength in combination with small-amplitude disturbances on the liquid surface promoted by the interaction between the liquid and ambient gas is believed to initiate the liquid breakup process [3]. The capillary forces are deemed responsible for the drop generation process [46]. With increase in liquid velocity, unstable growth of short-wavelength waves begins to appear. At this juncture, the generated drop sizes are of the order of the jet diameter representing the first wind induced regime. Further increase in injection velocity leads to the second wind induced regime and subsequently to the atomization regime. The drop sizes arising from the second-wind induced regime and the atomization regimes are several orders of magnitude smaller than the jet diameter. Based on the gas Weber number and the Ohnesorge number, Reitz and Bracco [5] mapped the different regimes as listed in Table (2.1) while Farago et al. [11] mapped the disruption modes of round liquid jets based on aerodynamic effects (gas Weber number).

Table 2.1.a Breakup modes of liquid jets

Rayleigh breakup	$We_g < 0.4$
First Wind Induced Regime	$0.4 < We_g < 1.2+3.4\ Oh^{0.9}$
Second Wind Induced Regime	$1.2+3.4\ Oh^{0.9} < We_g < 40.4$
Atomization	$40.4 < We_g$

Table 2.1.b Disruption modes of round jets

Breakup Type	**Limits**
Axisymmetric Rayleigh	$We_g < 15$
Nonaxisymmetric Rayleigh	$15 < We_g < 25$
Membrane breakup	$25 < We_g < 70$
Fiber-type breakup	$70 < We_g$
Superpulsating	$Re/We_g^{1/2} < 100$

2.3 Breakup length based characterization

In order to categorize the breakup regimes in a comfortable fashion, the length of the coherent portion of the liquid jet or its unbroken length, L, as a function of the jet exit velocity, U was utilized (Fig. (2.4)) [47, 48].

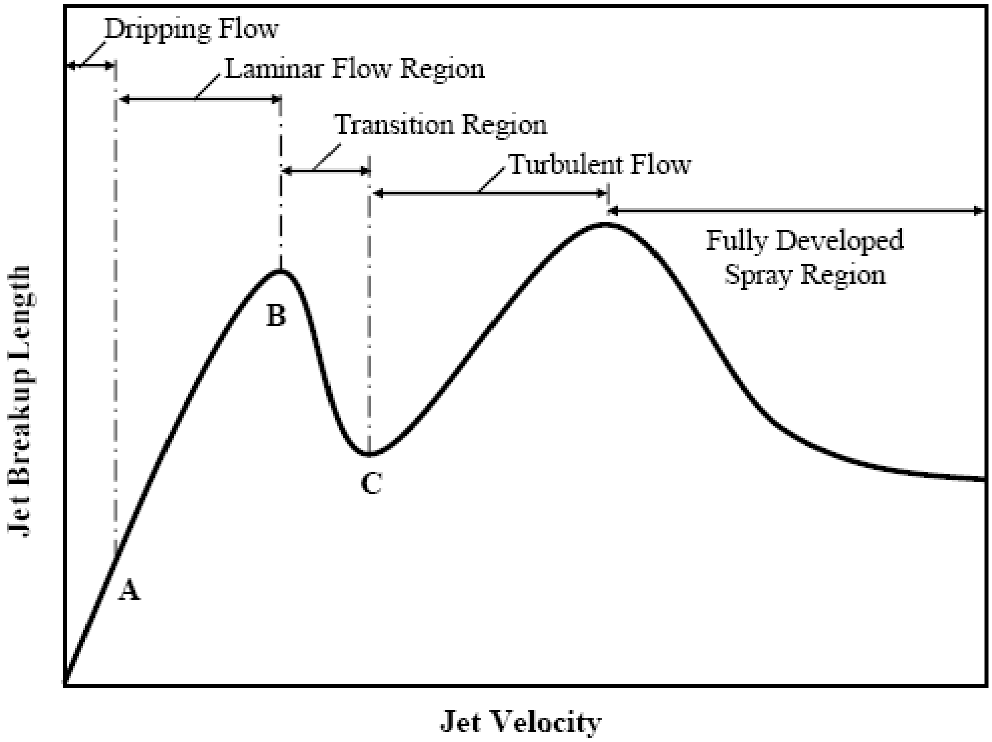

Figure 2.4: Categorizing the breakup modes using a comparison of jet breakup length as a function of jet velocity [47, 48].

Observe from Fig. (2.4) that beyond the dripping flow regime, the breakup length increases linearly with increasing jet velocity and after reaching a maximum starts declining (regions A and B). Drops are pinched off from the end of the jet, with diameters comparable to that of the jet [2]. These first two breakup regimes, which are reasonably well understood, correspond to the Rayleigh and first wind-induced breakup regimes. Beyond the first wind-induced breakup regime (region B, Fig. (2.4)) multiple theories have been established on the breakup-length trends [49]. While, Haenlein [50] reported that the jet breakup length increases again with increasing jet velocity (region C), and then abruptly reduces to zero (region D), McCarthy & Malloy [51] reported that the breakup length continually increases. According to Haenlein [50], Point B on the curve corresponds to the change in the breakup mechanism from varicose to sinuous breakup due to aerodynamic loading. Littaye [52] reported that the aerodynamic loading is not the only responsible factor for this point. Other authors attributed this point to the onset of the liquid turbulence. Both mechanisms were held responsible in expediting the jet breakup. Based on this assumption, the point B indicates the turn of the flow from laminar to turbulent flow. The jet breakup length decreases with increasing jet velocity (or corresponding Reynolds number) [2-5, 47-49].

The region beyond point C extending till the peak of the curve represent complete turbulent flow region where interfacial forces in the jet vicinity are considered more significant in comparison to the turbulence on the liquid-gas interface. In this zone, the breakup length of the liquid jet together with the internal flow turbulence increases with increasing jet velocity [2, 53-58]. With increase in jet velocity beyond point C uncertainity in the shape of the stability curve is still persistent. Even though the presence of a spray regime is evident, different explanations about the breakup trend of the liquid jet with increasing Reynolds number in this region exists. However, Newman [60] and McCarthy and Malloy [51] showed that a continuous portion of the liquid jet exists in this region even if its velocity is very high.

More recently, Hiroyasu et al. [57] discovered discontinuous elongations and shortenings of the jet with changes in the jet velocity. These apparent anomalies are associated with changes in the nozzle internal flow patterns caused by separation and cavitation phenomena, which also exhibited hysteresis effects. Jets from cavitating nozzles were found to have very short breakup lengths while detached flow jets resulted in long breakup lengths. These phenomena may help explain the previous discrepancies in measurements of breakup lengths in the spray literature to which, only recently have investigators paid any attention to nozzle flow and geometry effects.

The details of the unstable growth of short-wavelength waves on the surface of the liquid jet near the nozzle exit are obscured by the dense spray that surrounds the jet. However, it is generally believed that the jet consists of an unbroken inner liquid core in the vicinity of the nozzle exit, and droplets are stripped from the core by the action of aerodynamic forces at the liquid-gas interface [2, 3]. Attempts have been made to measure the length of the core region by using intrusive techniques such as electrical conductivity measurements [61], and laser sheet visualization [62]. The core length depends on the liquid/gas density ratio and only weakly on the fluid properties and the jet velocity. These trends can be demonstrated by using Taylor's [63] analysis of high-speed liquid jet breakup. Taylor considered the rate of mass loss per unit length of the jet caused by droplet erosion from the liquid surface resulting from the unstable growth of short-wavelength surface waves and showed that the breakup length of a high-speed jet is given by

$$B.L = Ca\sqrt{\frac{\rho_l}{\rho_g}} / f\left(T\right) \tag{2.4}$$

where *f(T)* is the spray angle parameter on Taylor's number

$$T = \frac{\rho_l}{\rho_g}\left(\frac{\mathrm{Re}_l}{We_l}\right)^2 \tag{2.5}$$

Note that for low liquid-gas density ratio, short breakup lengths are achieved by enhanced stripping of the liquid jet by the gas shear effects [3, 45].

2.4 Studies on disintegration mechanisms

Searching for the mechanisms impacting the generation of different breakup regimes several authors proposed influence of turbulence, cavitation, aerodynamic forces, velocity profile relaxation effects etc. Castleman [64, 65] postulated that the jet breakup is due to aerodynamic interaction between the liquid and gas phases and argued that the interaction of aerodynamic forces within the liquid phase lead to the formation of ligaments, with experimental results sought from Sauter [66]. He proposed that the formation of the ligaments, and hence their lifetimes, decreases and that smaller droplets are produced with greater gas phase velocity contribution. Ranz [67] analysed the forces involved in the breakup and energy expended in the ligament mode. He came up with a conclusion that the ligament diameters and thus the drop sizes were related to the wavelengths of unstable aerodynamically induced surface waves growing on the core of the liquid jet. However, various authors questioned the model, since, they reasoned that aerodynamically induced wave growth takes finite time to develop and thus the model cannot explain the experimental results which showed jet break up in the immediate exit of a jet into a chamber against the postulates of Ranz [67]. In search of explanation, DeJuhasz [68] proposed that the jet break up process possibly occurs within the nozzle itself, with some experimental evidences. He suggested that liquid turbulence may have an important role in the jet breakup process. Schweitzer [69] noted the existence of a radial component of velocity in turbulent pipe flows and argued that this radial flow could cause the disruption of the jet surface as soon as the jet emerged from the nozzle. In general the breakup mechanisms occurring in the atomization regime are thought to consist of two consecutive steps: primary and secondary breakup.

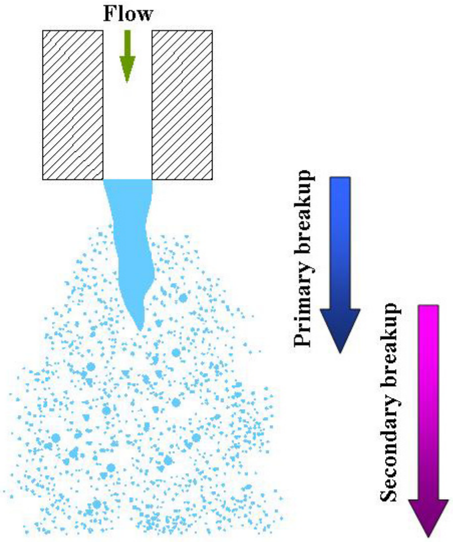

Figure 2.5: Primary and secondary breakup mechanisms in the higher gas-Weber number regimes

2.4.1 On the Primary Breakup of Round Liquid Jets

A great number of studies have been devoted to identify the fundamental mechanisms influencing the primary breakup process [2, 3, 5, 64-69]. While the studies by DeJuhaz et al. [68] and Lee et al. [70, 71] indicated the influence of liquid turbulence in expediting the liquid disintegration, Bergwerk [72] identified the effect of cavitation disturbances within the nozzle as a dominant factor. Further studies by Grant and Middleman [73] and McCarthy and Malloy [51] fortified the hypothesis concerning turbulence effects on the primary breakup process. In addition, Rupe [74] observed the contribution of the velocity profile relaxation mechanism of the liquid jet as it leaves the nozzle into a free shear domain. The energy associated with internal profile rearrangement, he argued, led to ramification of hydrodynamic instabilities, thereby hastening the jet breakup process [75]. The critical nature of ambient gas properties was investigated by Reitz [2] and Reitz et al. [3]. They observed the dominance of aerodynamic forces with decreasing liquid-gas density ratio and described the contribution of the shear stress arising from denser gas in initiating early breakup. Wu et al. [76] measured increased droplet sizes when the same liquid was injected into ambience with increased gas density. Many of the liquid jet disintegration theories formulated emanate from the classic Kelvin-Helmholtz instability associated with the aerodynamic interactions existing between the liquid and gas streams [2, 77, 78]. The contribution of aerodynamic forces in enhancing liquid jet hydrodynamic instability thereby leading to ligament and drop formation was emphasized by Castleman [64] and later Sallam et al. [79]. At large Reynolds numbers, Hoyt and Taylor [80] reported liquid surface stripping process due to a short-wavelength shear instability. In discussing the contribution of aerodynamic forces, various authors investigated the effect of co-flowing gas stream on the primary breakup process [81-85]. A wide range of experiments indicated that, based on the gas-liquid relative velocity, the magnitude of the initial disturbance potentially increases and augments the shear and normal stresses at the liquid interface further downstream [85-89].

The presence of liquid and gas streams co-existing in the same domain cast reciprocal influence on one another. This effect was identified and characterized by Shavit [81]. Using his experiments, consisting of an unstable liquid jet with a surrounding gas stream, he showed that the lateral and longitudinal motion of the liquid jet induces appreciable changes in the surrounding gas turbulence. Further, the motion of the jet was observed to be governed by their initial interaction with the gas phase and some inherent instabilities present within the liquid stream. The interaction of turbulence, surface forces etc with the growing instability of the liquid-gas interface is depicted in Fig. (2.6(a)). Different breakup modes generated by the non-linear interaction of forces is shown in Fig. (2.6(b)).

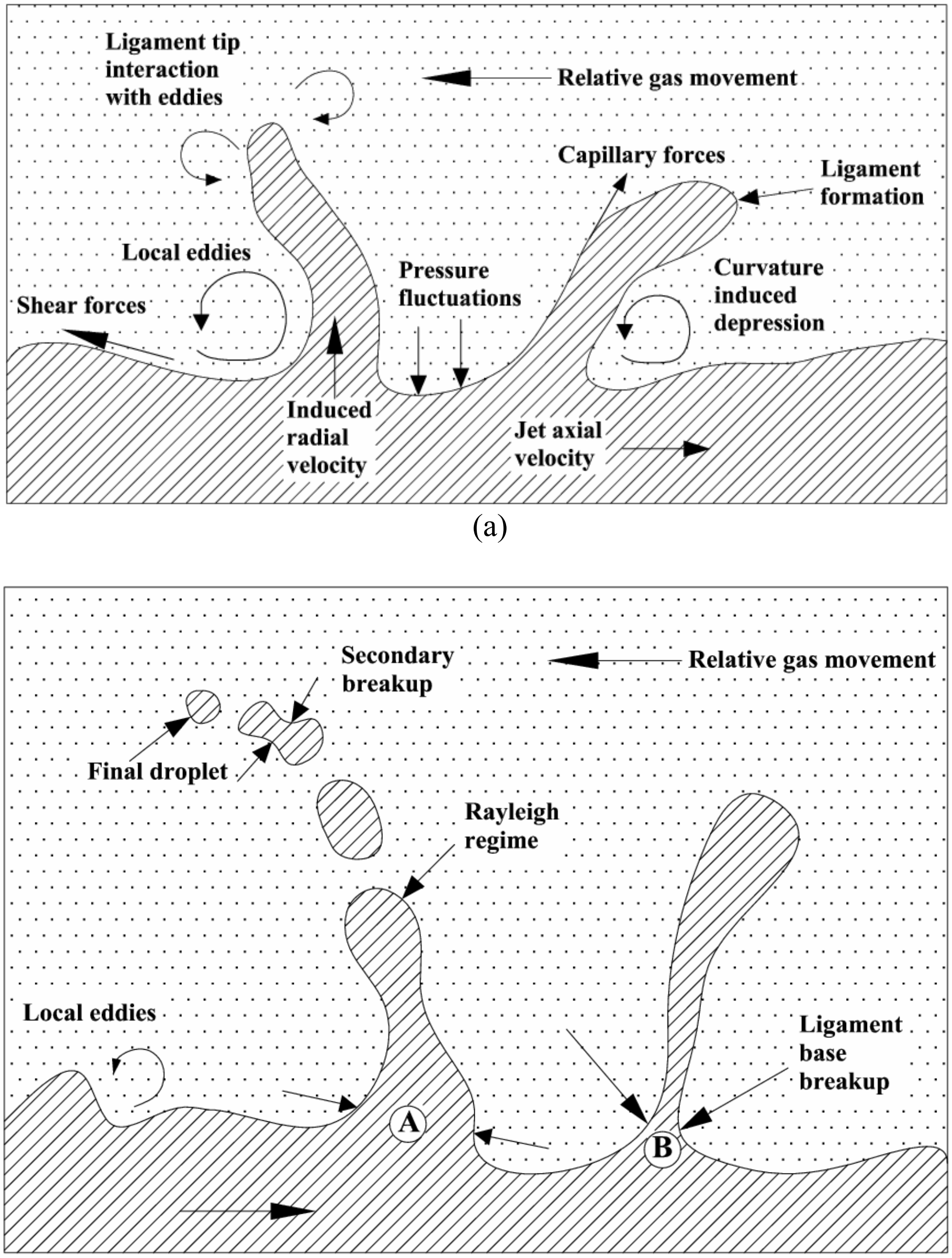

(a)

Figure 2.6 (a) Interaction of various forces during ligament formation (b) Classification of ligament base breakup and ligament tip breakup modes

2.4.2 Effect of cavitation in the breakup process

Various authors hinted at the influence of cavitation appearing as turbulent quantities enhancing the jet breakup, which led to a series of experiments on the influence of cavitation on jet breakup and atomization. As mentioned before, Bergwerk [72] paid attention to the liquid flow field within the nozzle and its influence on the jet breakup process coupled with turbulent interactions. He observed the presence of liquid cavitation regions within the tested nozzles tested and subsequently suspected that the liquid cavitation phenomena may play a crucial role in the jet atomization mechanism. He noticed that nozzles with short length-diameter ratios and sharp edged inlet sections allowed complete detachment of the liquid flow from the nozzle walls under certain operating conditions and showed no tendency to disintegrate. In the case of attached flows, his experiments revealed local cavitation regions within the nozzles. The emerging jet into atmospheric air then had a ruffled appearance and as a result, he proposed that the creation of large amplitude turbulent disturbances due to cavitation mechanism were the cause for enhanced jet atomization. This behavior was noted by Nurick [90] and Northrup [91]. Bergwerk [72] surmised that the reattachment of the flow beyond the cavitation zone created large amplitude turbulent disturbances which were responsible for the waviness of the jet surface seen in the vicinity of the nozzle exit. Sadek [92] hypothesized that cavitation bubbles which are formed in the cavitation region and swept along with the flow may influence the jet break up process.

Experiments of Wu et al. [76] highlighted the influence of cavitation on atomized spray cone angle, while the studies conducted by Chaves et al. [93] indicated the development of elongated vapor clusters along the walls of the orifice reaching the nozzle exit leading to events of supercavitation. Using the measurements on spray cone angle at different pressure drops along the injector, the combined influence of supercavitation and turbulence on jet atomization was assessed. Several other measurements identified turbulence amplification due to cavitation and their effect on primary breakup of jets [2, 3]. Quantitative prediction of the vapor formation and collapse using experimental techniques have been so far precluded due to the small time and length scales involved in cavitation phenomena [1, 2]. In particular, Arcoumanis et al. [94]

observed appreciable difference in cavitation characteristics between his scaled up and real size experiments.

Reitz and Bracco [3] studied various atomization mechanisms with the inclusion of cavitation phenomena. They observed wider spray cone angle with the nozzle cavitating. They were also able to observe hydraulic flips, when the liquid flow detaches itself from the wall and hence cavitation occurrence is wiped out. Fujimoto et al. [95] performed experiments on modeling of atomization and vaporization process in flash boiling sprays where he considered the effect of vapor bubble nucleation to enhance atomization. Tamaki et al. [96] worked on the effects of cavitation and internal flow on the atomization of a liquid jet. They found out that when cavitation takes place in a nozzle, a considerable reduction in the break up length of the jet is discerned. They associated the spray distribution primarily to the disturbance created due to cavitation. Perturbation effect due to cavitation inside nozzles was stressed upon by the experiments of Ruiz et al. [97], Ong et al. [98], Nishida et al. [99] and Soteriou et al. [100]. Real size nozzle cavitation effects were reported by Badock et al. [101]. Tomita et al. [102] predicted the impulse pressure accompanying the collapse of an isolated cavitation bubble which indicated that its strength decaying inversely over the radial distance. Hence, for smaller jet diameters, the pressure pulse due to the cavitation bubble collapse can trigger a growth wave leading to rapid atomization.

The instability analysis performed by Shkadov [103] showed that velocity profile relaxation can generate surface waves of growing amplitude, and their growth rate increases as the velocity gradient below the liquid surface increases. Research conducted by Leroux et al. [47] on the stability of Newtonian jets supplemented with experimental data confirms that the jet atomization is strongly influenced by the fastest growing wavelength in the radial direction. Figure (2.7) briefly summarizes the cavitation effects on the liquid jet breakup phenomena.

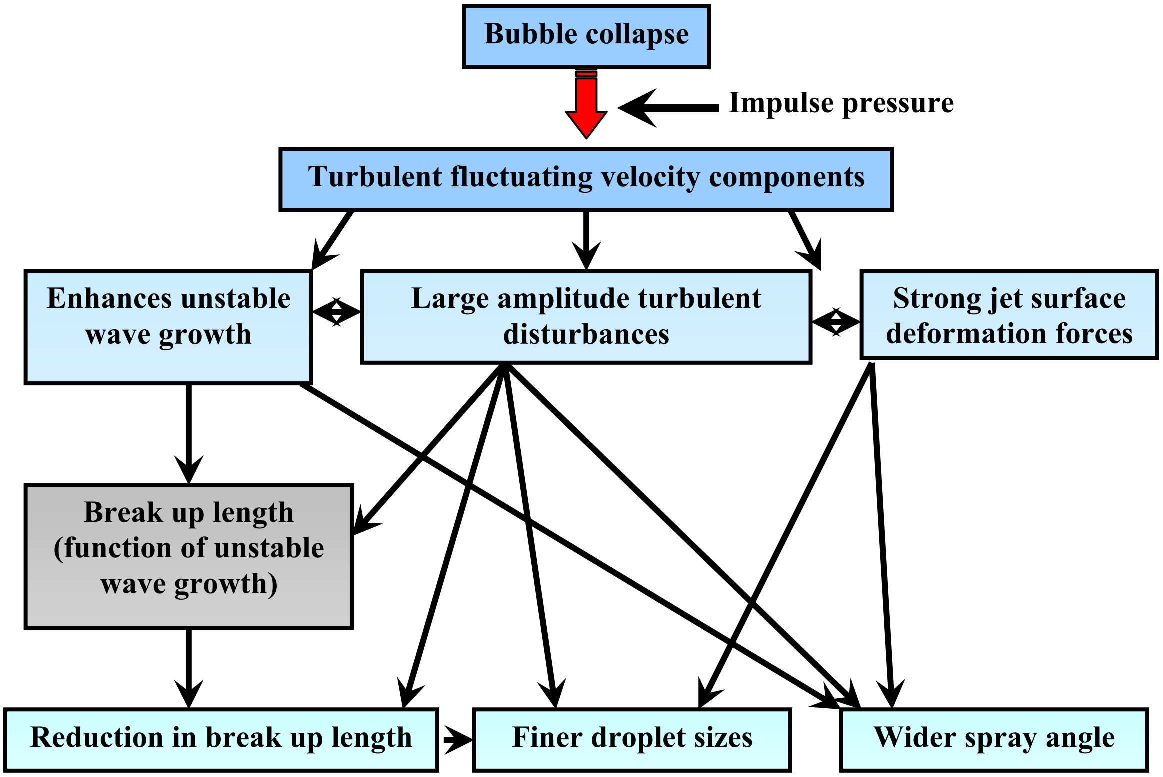

Figure 2.7: Cavitation induced mechanisms summarized from various studies

2.4.3. Effect of Veloity Profile and flow Turbulence

The nature of the exiting liquid jet, laminar, semi or fully turbulent, has been observed to have a profound influence on the liquid jet disintegration process. Schweitzer [69] and McCarthy et al. [51] suggested that in the event the exiting flow is laminar, a very slight velocity difference between the jet outer layer and the ambient air exist since the velocity at the outer layer is zero. They speculated that the strong radial fluctuations created by the turbulent components in the liquid resulted in hastened realignment of the liquid-gas interface and subsequently, rapid breakup process. In this case, even if the jet is injected into a vacuum, it will disintegrate under the influence of its own turbulence without the need of aerodynamic forces [70]. With a semi turbulent jet emanating from an orifice, the laminar sheet surrounding the turbulent core tends to prevent the turbulent liquid particles in the core reaching and disrupting the jet surface. Since the relative velocity between the jet surface and the surrounding air is minimum, the interfacial forces will not immediately lead to the break up close to the nozzle exit. However, farther downstream, the turbulent core dominates the laminar sheet and a momentum transfer takes place between the laminar and radial velocity components of the flow resulting in flattened jet velocity profile. As a result of this energy redistribution within the jet, the radial velocity components disrupt the jet at the surface leading to the breakup [74]. As soon as the jet leaves the nozzle, the constraint of the nozzle wall is removed. A rearrangement in the cross-sectional velocity profile takes place ascribed to a momentum transfer between transverse layers within the jet. The redistribution of the kinetic energy leads to relaxation from parabolic velocity profile of the laminar flow into a flat profile at the same average velocity, giving rise to turbulent radial velocity components [75]. This change in the velocity profile is called velocity profile relaxation and can contribute significantly to the irregular nature of the liquid jet irrespective of whether the flow within the nozzle is laminar or turbulent. In turbulent jets profile relaxation effects are minimal since they have flat exit velocity profiles. Therefore, along with relative motion of the jet induced by surface tension forces, this additional internal (relative) motion forces associated with profile relaxation contribute substantially to the irregular nature of the jet surface [51, 69, 75]. As a brief summary, it can be concluded that the drag action of ambient air is the primary reason for the disintegration although the internal forces (liquid turbulence, inertial or those resulting from velocity profile relaxation and surface tension) are also important factors. Internal forces cause the jet to possess a highly irregular surface, thereby making it susceptible to the drag action of the ambient air. These forces lead to the jet disintegration especially under conditions where aerodynamic forces are relatively small [2]. On the other hand, even if these internal forces are not significant, the liquid jet will break up at some distance downstream of the nozzle under the influence of air friction especially at high ambient pressures. The nature of the flow at the exit only determines the amount of time required by the ambient air to distort it [13, 26]. As may be imagined, a jet with more surface disturbances like turbulent jet will break up readily compared to a laminar jet.

Alternative mechanisms for the disintegration of the liquid jet have been proposed by a various number of authors. For example, Schweitzer [69] suggested that the jet breakup process starts within the nozzle and it is strongly influenced by the turbulence generated in preceding pipe flow. It is suggested that the liquid supply pressure vibrations may have an effect on the jet disintegration. Reitz [2] identified liquid supply pressure vibrations, cavitation inside the nozzle, liquid turbulence, non-uniform liquid jet exit velocity profile and viscous boundary layer adjustment (the viscous layer transforms from a wall layer to a free layer after it exits the nozzle) as possible responsible mechanisms for the jet breakup. Reitz et al. [3] emphasized that no single mechanism is responsible for jet breakup; in all cases, a combination of factors is involved including the importance of nozzle geometry effects. They suggested that the nozzle geometry such as details of the entrance of the nozzle, nozzle design and nozzle imperfections, could be the reasons to supply different initial disturbance to the flow drawing attention to the nozzle geometry effects [2].

Based on the discussions above, it can be concluded that these various proposed jet disintegration theories show that aerodynamic effects, instabilities present at the nozzle exit due to liquid turbulence, jet velocity profile rearrangement effects and liquid supply pressure vibrations cannot alone explain the breakup mechanism of the jet [2]. However, a mechanism that combines liquid-air aerodynamic interaction with nozzle geometry effects is believed to help better understanding of the disintegration phenomena of the nozzle jet.

2.4.4 Effect of nozzle diameter and L/D ratio on the breakup length

The effect of the nozzle diameter and the length-to-diameter (aspect ratio) has been investigated by various authors. Recently, Reitz and Bracco [3] reported that under the same operating conditions, when the internal geometry of the nozzles having the same exit diameter differs, the jet breakup length behavior changes revealing the fact that the details of the flow field within the nozzle greatly influences the jet breakup process.

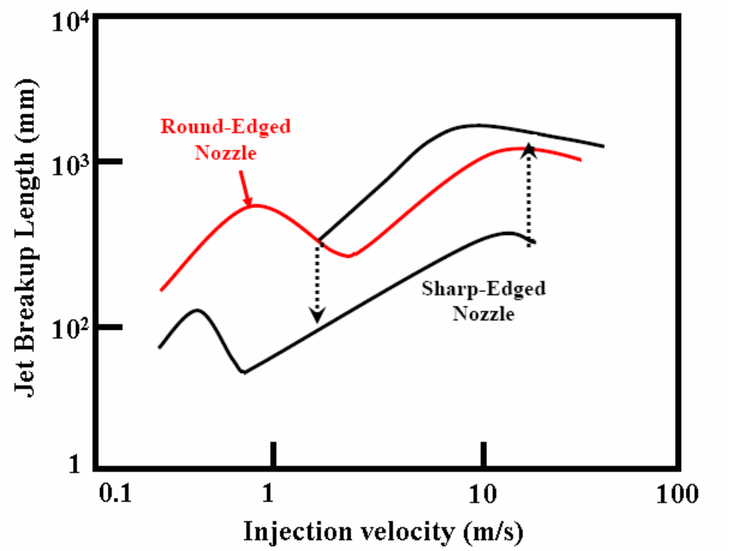

Figure 2.8: Breakup length vs Injection velocity curve [57]

Arai et al. [55, 56] and Hiroyasu et al. [57, 58] investigated the breakup length behavior of the liquid jet for different sharp-edged nozzle diameters and *L/D* ratios under the same operating conditions in atmospheric environment. As seen in Fig. (2.8), the breakup length versus injection velocity curve shows the same trend for different nozzle diameters in that the breakup length increases with increasing jet velocity in the turbulent region up to a maximum value and then decreases with increasing velocity until it reaches certain velocity where the discontinuous elongation of the breakup length takes place.

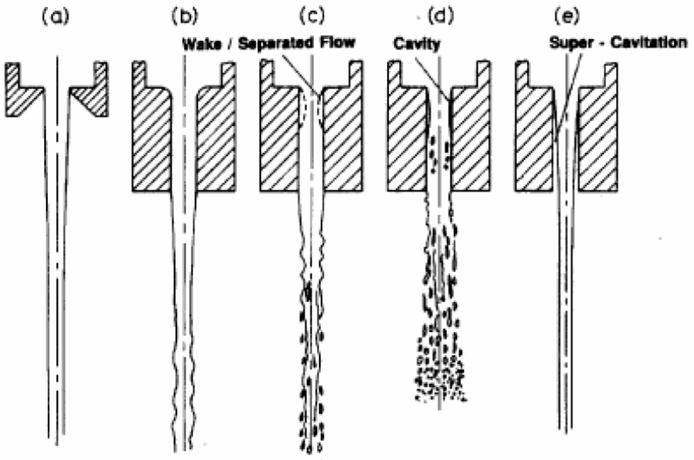

Figure 2.9: Appearance of liquid jet [57]

It is accepted that the breakup lengths produced by the nozzles with bigger *L/D* value is shorter than those produced by the nozzles with relatively small *L/D* values [57]. This is attributed to the reason that when the nozzle length is very long, the separation of the flow has enough nozzle length to recover and thus the flow reattaches to the nozzle wall. Thus additional disturbance caused by the frictional forces between the liquid jet and the nozzle inner walls acts on the internal flow promoting its disintegration. With small *L/D* ratios, the reattachment does not usually occur after contraction since the nozzle wall length after constriction is very short and thus the flow does not experience disturbances due to wall friction [59].

However, the breakup length produced from the nozzle with *L/D* ratio=50 is longer than that of the nozzles with smaller aspect ratios in the spray region (see Fig. (2.8)). This discrepancy was attributed to differences in the nature of the flow and shape of its velocity profile at the nozzle exit. It was considered that, when the aspect ratio is very large, the strong turbulence in the liquid jet caused by the separated flow and cavitation at the nozzle entrance may be reduced thus changing the nature of the flow at the nozzle exit to more stable in nature [59]. On the contrary, when the nozzle length is short, turbulence in the internal nozzle flow is not completely developed resulting in unstable flow in nature at the nozzle exit with a shorter breakup length [59, 96]. As a conclusion, the length-to-diameter ratio of the nozzle and the Reynolds number of the flow control the intensity of the wall friction after reattachment of the detached flow [59].

2.4.5 Effect of cavitation and nozzle entrance on the breakup length

Most of the engineering applications utilizing nozzle flows encounter sharp cornered entrance regions, typically when the flow enters from a large fluid reservoir into the nozzle sac. Presence of these sharp nozzle entrance regions enforce abrupt change in flow direction leading to very high shear rates. The variance in flow structure, brought about by the local pressure gradients, has been observed to initiate appreciable cavitation effects in these nozzles. A schematic of the cavitation inception region as the flow direction changes abruptly is described in Fig. (2.10).

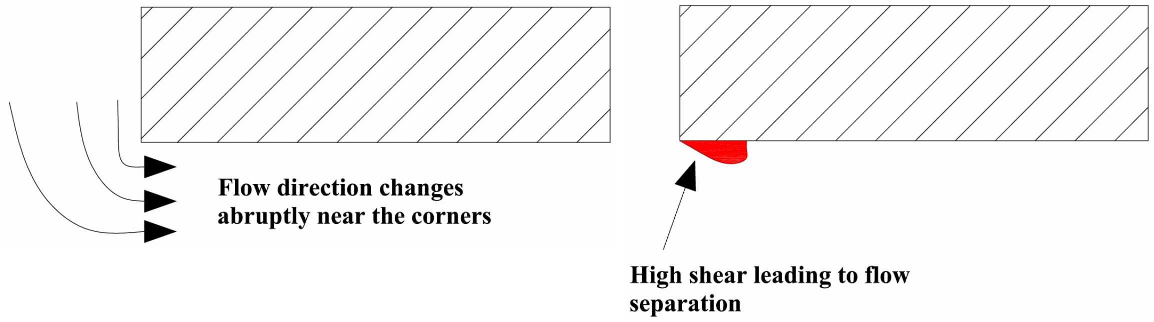

(a) (b)

Figure 2.10: Sharp cornered nozzles and cavitation regions

As the flow enters the sac, Fig. (2.10(a)), swift acceleration near the throat section is enforced due to sudden change in the flow area. The flow hustle occurs as a direct resultant of mass continuity constraint and brings along heightened pressure gradients near the nozzle entrance. As the liquid squeezes into small sac entrance, flow separation occurs just around the corner. Owing to the flow separation, vena contracta prevails. The effective flow area further reduces increasing the average fluid speed as a function of the thickness of the vena contracta. Schematic of vena-contracta formation and the flow structure alteration leading to ramification of shear effects near the nozzle entrance region is depicted in Fig. (2.11).

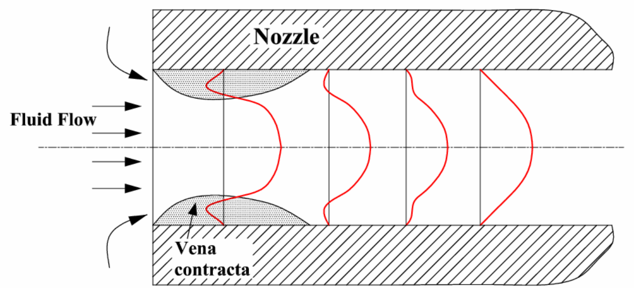

Figure 2.11: Formation of vena contracta as the flow passes the sharp corner. Notice the velocity profile modulation due to the strong pressure gradients near the sac entrance.

Regions of intense recirculation prevail in the vena-contracta zone leading to modification of the flow velocity profile. As the fluid surpasses the constricted passage created by vena-contracta, a velocity profile relaxation type mechanism follows subsequently to match the shear stresses in the near wall regions. Depending upon the pressure gradients existing in the near-sac entrance region, the absolute pressure of the liquid flow may fall below the vaporization pressure of the liquid triggering cavitation events. The flow separation zones, containing recirculating fluid regions, act as a reservoir of low pressure supplementing the growth of cavitation bubble clusters. The acceleration of the bubble growth process depends on the strength of the low pressure region existing near the nozzle corners. This is one of the primary reasons why a rounded nozzle does not exhibit intense cavitation as compared to its sharp cornered counterpart [59]. Several researchers have addressed the nozzle geometry issue while explaining the cavitation characteristics. A schematic detailing the geometry effect on the cavitation probability is described in Fig. (2.12).

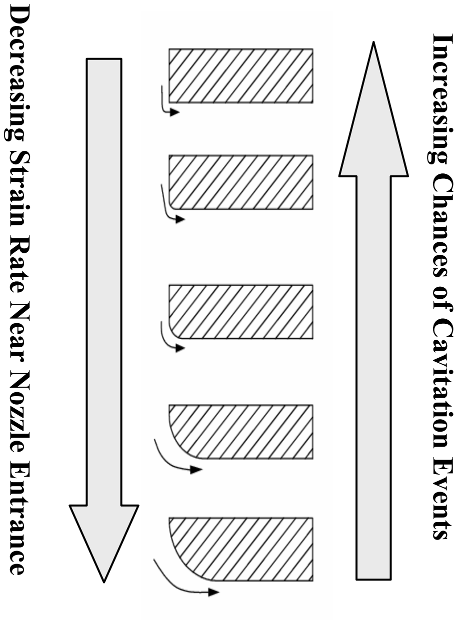

Figure 2.12: Tendency to cavitate as a function of the corner radius of the nozzle

In round nozzles, the pressure gradients are much lower than their sharp counterparts resulting in negation of any low pressure zones and subsequent liquid rupturing process. In addition, recirculation zones are avoided based on the curvature of the rounded nozzles. Once the cavitation clusters are formed near the corners, their growth, transport and collapse processes are dependent on the flow conditions existing in the domain. Based on pressure gradients across the injector different cavitation mechanisms are observed. The effect of pressure difference existing across the injector, also identified by the Cavitation number, is crucial in defining disparate cavitating flow characteristics in flow passages. A schematic of the pressure drop influence on cavitation dynamic is depicted in Fig. (2.13).

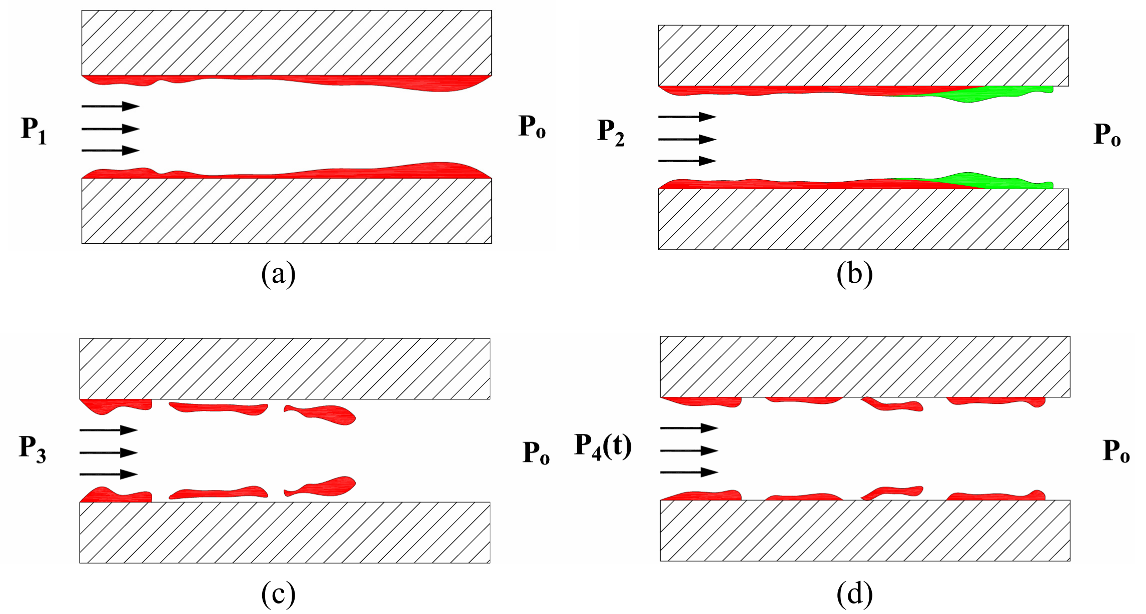

Figure 2.13: Effect of pressure difference across a sharp nozzle injector on the cavitation cluster behavior. $P_1 > P_2 > P_3$. $P_4(t)$ fluctuates between $P_1 - P_3$ as a function of time.

For very high pressure difference across the injector, Fig. (2.13(a)), the cavitation clusters that are formed near the nozzle sac entrance extend all the way towards the nozzle exit where they collapse due to their encounter with high pressure ambience. This event termed as 'supercavitation' often plays a critical role in determining the breakup lengths of liquid jets. In some occasions, supercavitating nozzles lead to very small breakup lengths. However, if the nozzle is improperly designed, air from the nozzle exterior can enter into the nozzle through the low pressure cavitating zones formed by cavitation giving rise to increased breakup lengths. This phenomenon also known as the 'hydraulic flip' is of paramount importance in industrial nozzles [2, 3, 100]. Flipped nozzles are hard to atomizer and give very poor performance. The supercavitation process is detailed in Fig. (2.13(a)). With reduced pressure drop or conveniently for reduced cavitation number, Fig. (2.13(b)), the cavitation clusters exhibit switching of long and short cavity length type mechanism. Rather than extending all the way to the exit they collapse just before the exit or even shorter. The cavitation cluster length along the nozzle walls fluctuate owing to the non-linearities associated with bubble dynamics. The strong fluid flow – cavitation coupling results in frequent shifting of reattaching cavitation zone lengths. These fluctuating behaviors contribute to increased turbulent fluctuations on the exiting jets which thereby influence the jet disintegration process [1, 3]. The nature of cavitation seen in the cases Fig. (2.13(a) and (b)) can be related to a sheet cavitation mechanism [33, 105]. As the pressure difference across the injector is further decreased, shorter cavity lengths are obtained. Several reports concerning cavitation dynamics of this type have been reported [34, 106]. As a consequence of the unsteadiness prevailing in the flow, cavitation clusters are often observed to be pinched-off from their parent cluster residing in the near-entrance region of the nozzle.

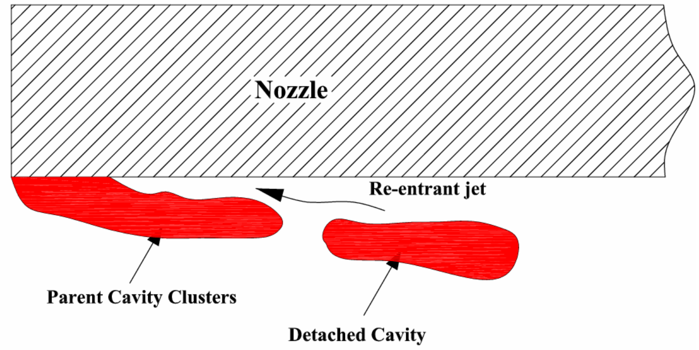

Figure 2.14: A schematic of vapor formation and detachment mechanism near the sharp corners of a nozzle

The pinch-off process has been hypothesized to occur due to re-entrant jet type mechanism [106]. After the detachment from the parent cluster, the vapor regions are convected by the liquid bulk where they mix with the core flow. Due to pressure fluctuations arising from turbulence and several other perturbations within the flow, the vapor clusters experience collapse events. The cluster detachment, agglomeration, diffusion and coalescence are often observed in experiments as “cloud structure” and hence the name cloud cavitation [33]. If the time scale of the core flow is smaller than the time scale required for the bubble collapse, the cavitation clouds reach the nozzle exit and collapse outside the nozzle. If the pressure gradient is not strong enough to carry them past the nozzle exit, their collapse occurs internally and lead to strong pressure fluctuations. This is attributed to the fact that the cavitation collapse is a compressive shock event and its implosion sends radial pressure pulse into the surrounding liquid. The strength of the pressure pulse attenuates in a fashion inversely proportional to the distance it has propagated [102]. The collapse energy generated by the cavitation bubble is strong enough to expedite chemical reactions, in generating sonoluminescence phenomenon [34], creating very high turbulent intensities and causing potential damage to the nozzle [33]. In several occasions, strong vorticity generation mechanisms within the nozzles have been reported as a consequence of cluster collapse [33, 34, 107].

2.4.6. Effect of flow fluctuations on cavitation dynamics

A strong pulsation to the incoming flow to the nozzle entrance can show any of the three characteristics described in Fig. (2.13(a),(b)&(c)). Imposing pulsations into the flow across the injector leads to a time varying pressure gradient across the nozzle. If the supercavitation mode is favored by the pressure drop along the injector at time *t*, this mode is subjected to change once the pulsation reaches its lowest value; at this point the pressure drop would be lowered considerably and might favor short bursts of cloud cavitation or cavity-length switching mechanisms [106-108]. Modulation of cavitation cluster features viz., their formation, growth, propagation and finally collapse, can, hence, be achieved by mutating the incoming fluid flow characteristics.

If cavitation bubbles collapse on nozzle surface, they may cause locally high stress on nozzle surface that may be three to four times higher than the jet pressure causing severe erosion of the nozzle surface [34].

2.5 On modulated liquid jets

When a liquid jet emerges from a nozzle into ambience, the deformation of its liquid-gas interface and subsequent breakup processes are governed by a wide range of parameters discussed in Section (2.4). Many of the distortions and peculiar shapes of the liquid elements of the jet can be explained by a time and space development of weak initial distortions of momentum in traveling waves during propagation. Studies performed on instability of jets use a known disturbance field, in the initialization procedure, often assumed as a function of exiting jet conditions [2]. This method is suitable only to assess the growth of this instability temporally and spatially along the jet surfaces. In real scenarios, it is not easy to quantify the finite value of the perturbation that is initiated near the nozzle. Most often, these disturbances are caused due to several internal nozzle phenomena such as swirl, separation, flow cavitation and turbulence [2, 3]. It might occur that most of them are highly stochastic in nature and hence, the prediction of liquid jet disintegration characteristics based on these quantities are highly non-deterministic.

In a different strategy, finite induced perturbations are imposed on liquid jets in the form of velocity modulations to study the resulting disintegration behavior. These forced liquid jets would carry with them, a well defined modulation amplitude and frequency. This approach was first reported by Crane et al. [109]. They experimented with the effect of modulations on the breakup of cylindrical water jets in air. His first account reported the break-up of liquid-jets due to an inertial type mechanism induced by high amplitude, high frequency mechanical vibration of an orifice. The results clearly indicated that under high frequency vibrations, inertial effects dominate the surface tension induced displacements. Extending the work of Crane et al. [109], McCormack et al. [110] carried out further experimental and theoretical analysis on velocity modulated jets. In their experiments, velocity modulation was realized by pressure variation upstream of the injector. They concluded that the application of mechanical vibration in the appropriate frequency range and at small vibration acceleration values can induce minute pressure fluctuations and trigger a capillary instability. With higher acceleration values, appreciable "bunching" effect in the liquid jet was observed. The term "bunching" denotes the radial velocity of liquid due to the relative velocity of adjacent particles in the jet. Formation of discs due to strong liquid bunching was evident [109]. However, no details of the aerodynamic interaction and the resulting spreading mechanism were discussed. Mass concentration appeared with definite periodicity equal in comparison to the imposed wavelength of modulation.

A modulated liquid jet issuing from a nozzle goes from a state of high shear inside the nozzle to a state of free shear in the ambience. A schematic of a modulated liquid jet interacting with the various force components is shown in Fig. (2.15).

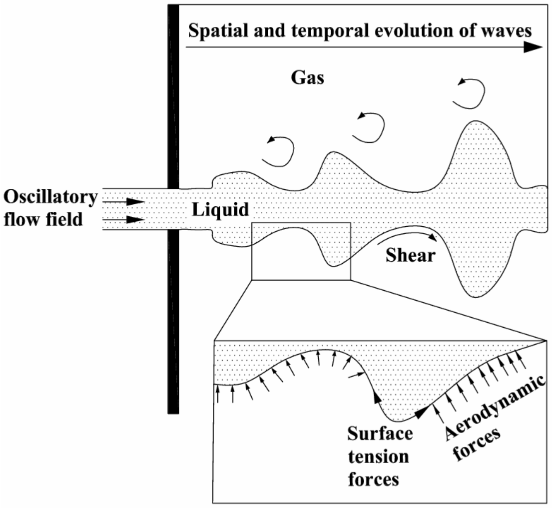

Figure 2.15: Schematic representation of various interacting forces in oscillatory free surface flows.

The liquid bulk in the exterior domain of the nozzle is subjected to the aerodynamic forces which interact with the surface forces leading to a liquid-gas interfacial instability. As the liquid jet enters the gas domain, shear layers are generated due to the velocity difference between the liquid and gas phases. The viscous interaction of the two fluids, in addition to the shear layer instability, contributes to the enhancement of the liquid surface wave instabilities. In the case of modulated liquid jets, local mass accumulation occurs at finite periodicity due to the transient variation in liquid velocity and as a result of momentum conservation, which was analyzed by Meier et al. [111].

Meier et al. [111] in their study of unsteady liquid jets showed that the conservation of initial momentum is one of the governing effects in jet instability and decomposition. They formulated the mass distribution along the axis of a modulated liquid jet without the effect of liquid properties such as surface tension and liquid viscosity. For large amplitudes and low frequencies of modulation, the jets are decomposed in very peculiar shapes, which can be very simply explained by the collision of packets of concentrated mass on the axis of the jet motion. Meier et al. [111] worked on large diameter and high velocity jets neglecting the effect of surface tension forces. However, it is well known that liquid properties such as surface tension and viscosity are crucial in deciding the magnification/suppression of the initial disturbances [2]. In different experiments with water jets, they demonstrated breakup of very low velocity liquid jets with the effects of modulations. Formation of disc like water-films were observed when a liquid jet was imposed with large amplitude distortions and concluded the existence of bowl shaped films. The instabilities occurring in such a system were seen reproducible. More recently, fundamental research on the disintegration of a sinusoidally forced liquid jet was performed by Chaves et al. [112, 113]. Their experimental setup assured less effects of turbulence, swirl or any related effects inside the nozzle so that an unperturbed jet is made available for investigation in the nozzle exterior. In their investigation, a wide gamut of jet morphology was obtained by varying the modulation characteristics, amplitude and frequency, along with the mean jet velocity and liquid-gas density ratios. Classification of the disintegration of harmonically excited round liquid jets revealed surface waves, upstream directed bells, discs, downstream directed bells, multiple chains of droplets and phase jump phenomena. When turbulent conditions existed inside the nozzle, stochastic atomization process was observed. Extending the work of Chaves et al., Geschner et al. [114, 115] created a non-dimensional map for the appearance of spray structures of a periodically excited round liquid jet. The influence of modulation parameters on the detection of variety of highly reproducible structures ranging from discs to droplet chain indicate that spray formation can be controlled as a deterministic process. The experimental investigations on the modulated jets provide us with a global understanding of the phenomena. In order to identify and comprehend the basic underlying mechanism, details on the non-linear interaction between various forces involved in free shear flows of round liquid jets needs further clarification.

2.5.1 Liquid bunching and modulation effects

Modulated free jets discharge has the particular property that the slow and fast stream portions of each discharge cycle tend to flow together or bunch in the free stream. Seno et al. [112] used same fluid jet to address the coherent structures generated by controlled stimulation of axi-symmetric jets. They observed formation of vortex rings and their coalescence in a reproducible fashion and identified the influence of modulation parameters on these structure formations. By modulating a liquid stream, structure formation is forced into the liquid phase which then results in gas phase structures due to interfacial matching conditions. The free stream thus becomes a train of bunches of water which eventually separate depending on the inlet conditions and aerodynamic interactions. Bunch diameter increases with downstream distance until the axial velocity becomes uniform with each bunch.

An issuing modulated liquid jet is always under the influence of aerodynamic forces present in the surroundings. These aerodynamic effects promote the growth of modulation bunching because gas (air) pressure deficiency or suction is produced at any jet surface protuberance, such as bunch edges, whereas increased pressure is obtained in surface depressions between bunches. This effect depends in relatively complex manner on aerodynamic pressure, air acoustic speed, and surface disturbance size and shape. In general, however, the aerodynamic pressures should help produce percussive jets. On the other hand, gas (air) drag acts to dissipate jets. The interaction of surface tension of the liquid and the aerodynamic forces result in droplet formation. This mechanism of droplet formation by modulated jets has been reported to be of deterministic nature [113-115]. The droplet sizes have been observed to be consistent and the entire process, repetitive. This mechanism indicated that a truly deterministic process of spray formation with controllable droplet size distribution is achievable.

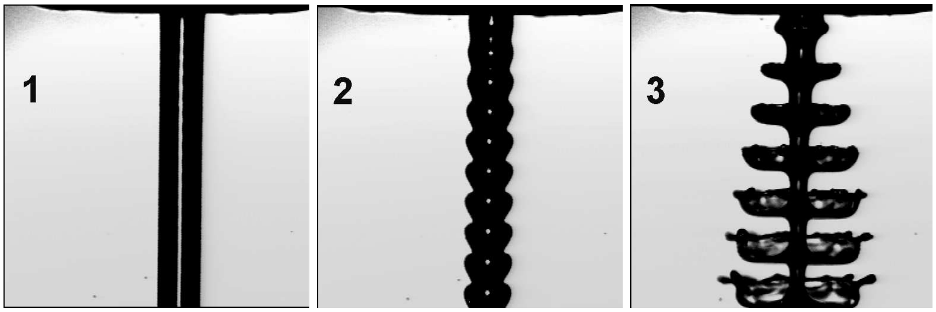

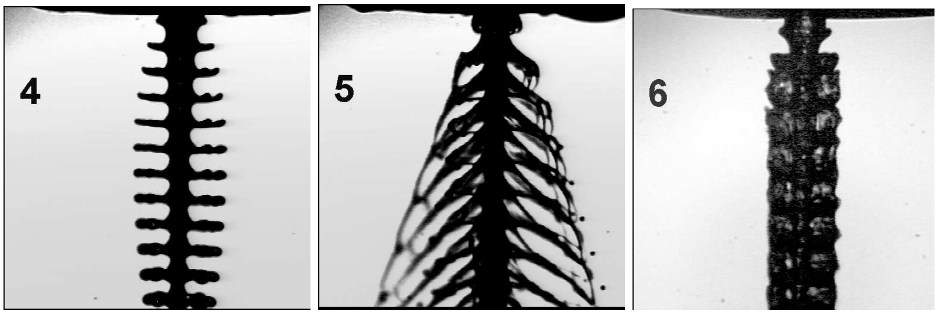

Figure 2.16: Classification of modulated jets under the influence of varying modulation amplitude under constant modulation frequency. Experimental liquid (ethanol) injected into an atmosphere of varying density from a 0.21 mm nozzle [115].

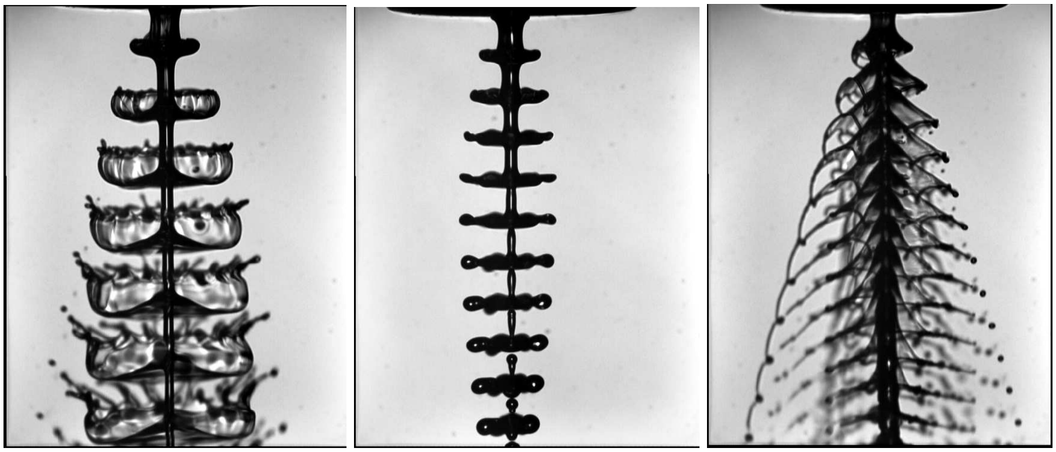

Figure 2.17: Transition between various structures for increased amplitude. No turbulence and influence of cavitation has been reported in these cases. Liquid jets are laminar in nature [115].

Besides the liquid, gas properties and jet parameters such as velocity and diameter, the analysis of modulated liquid jets includes additional variables in the form of modulation frequency (f) and amplitude (ε). Applying Buckingham π-theorem, the following set of dimensionless parameters is derived. The definition of Re^* and We^* are not the usual definitions as given by equations (2.1) and (2.3), since f, D and ρ_l have been used as the fundamental flow quantities by which all the other standard ones have been non-dimensionalized [113, 114].

$$Sr = \frac{\pi D f}{\bar{U}}, We^* = \frac{\rho_l D^3 f^2}{\sigma}, \; Re^* = \frac{D^2 f}{\nu} \tag{2.6}$$

$$\varepsilon = \frac{\Delta u}{\bar{U}}, \; \rho^* = \frac{\rho_g}{\rho_l}$$

Adding to the available set of non-dimensional numbers represented in equation (2.1) and (2.3), a modified weber number We_w is obtained by dividing the Weber number (*We*) by the Strouhal number (*Sr*).

$$We_w = \frac{\rho \bar{U}^3}{f \sigma} \tag{2.7}$$

This definition given by equation (2.6), has been used [113, 114] to provide a clearer map of the regions of appearance of structures in liquid jets than the standard definition given in eqns. (2.1) and (2.3).

In the experiments performed by Chaves et al. [113,114], they identified different possible jet structures such as waves, discs, upstream directed bells, downstream directed bells, touching bells, droplet chains, stochastic disintegration, and a phase jump based on the *Sr*, We_w and ε parameters. Geschner [115] observed that the basic parameter is the modulation amplitude which is representative of the structures that are formed. The Strouhal number by its definition directs to Rayleigh's theory of magnification of perturbation amplitudes. Identify Strouhal number as,

$$Sr = \frac{\pi D f}{\bar{U}} \Rightarrow Sr.\left(\frac{\bar{U}}{f}\right) = \pi D \tag{2.8}$$

If λ is the representative wavelength, $\lambda = \bar{U} / f$, and a finite modulation amplitude be applied , *Sr* indicates if the wavelength of the imposed perturbation exceeds the circumference of the liquid jet. If the amplitude is too small, no structures can be generated. Rayleigh's theory [39] predicts that in the range *Sr* > 1, where the wavelength is shorter than the circumference of the jet, perturbations are damped. Linear theories predict bunching of the liquid under certain modulation amplitudes [113]. However, the linear theories cannot be held valid for $\varepsilon > 0.003$. From the experiments of Chaves et al.[113] and Geschner et al.[114, 115], it was observed that prominent structures were produced with $\varepsilon = 0.07$ and above. A non-dimensional map created from the experiments of Geschner et al.[115] constructed using dimensionless numbers, ε, *Sr*, We_w, is shown in Figs. (2.18) and (2.19). These graphs are used to compare our numerical results with actual experimental results in a qualitative sense.

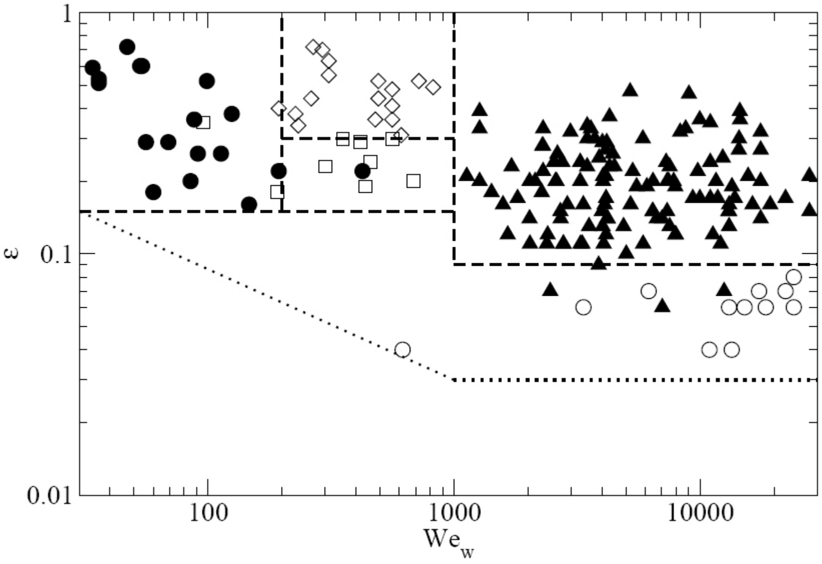

Figure 2.18: Variety of structures observed from the experiments of Geschner et al. [115] presented in the ε-We_w plane for comparing with our numerical simulations: ○ waves, ▲upstream directed bells, □ discs, ◊ downstream directed bells, ● droplet chains.

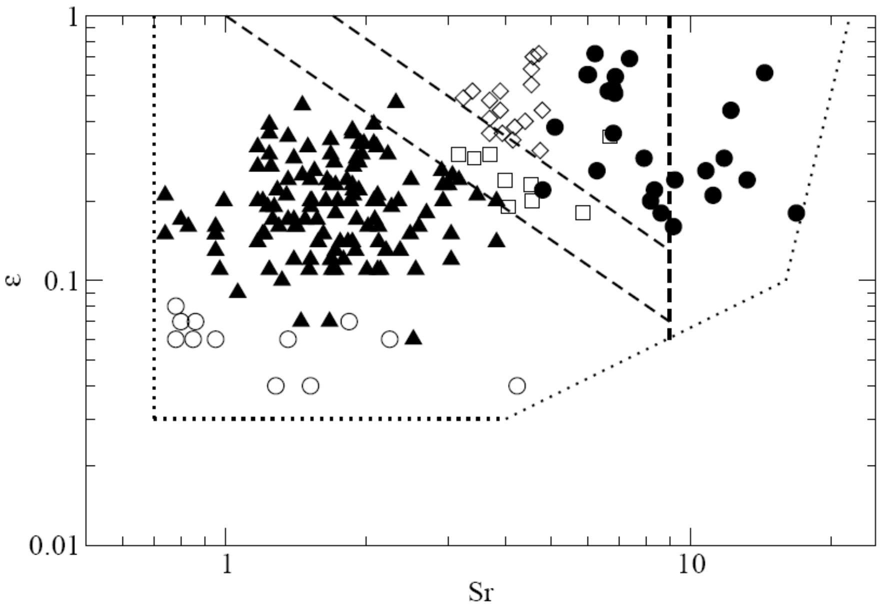

Figure 2.19: Variety of structures observed from the experiments of Geschner et al. [115] presented in the ε-*Sr* plane for comparing with our numerical simulations: ○ waves, ▲upstream directed bells, □ discs, ◊ downstream directed bells, ● droplet chains.

From the experiments, however, it was observed that, although liquid streams were separated from the central liquid core due to bunching process, the diameter of the axial liquid stream remained intact for a long distance before breaking up. In order to create a spray distribution with less statistical deviation of their mean diameter, it is required that a complete breakup of the liquid jet along the axial direction is crucial. This would require an extra term in the energy budget of atomization. In the present study, the extra energy would be supplied by the cavitation cluster collapse energy.

2.5.2 Note on Strouhal number definition

Strouhal number defines the ratio of structural deformation forces to the inertia forces. In this concern, a single or multiple frequency scales may co-exist within the system. Identification of these individual frequency contributions into the overall system involves highly complex mathematical concepts of bifurcation etc. In the discussions presented in this thesis, the inlet perturbation frequency has been chosen provide a representative Strouhal number indicating the deformation characteristics of the modulated liquid jet resistive to the inertial jet flow emanating from the nozzle.

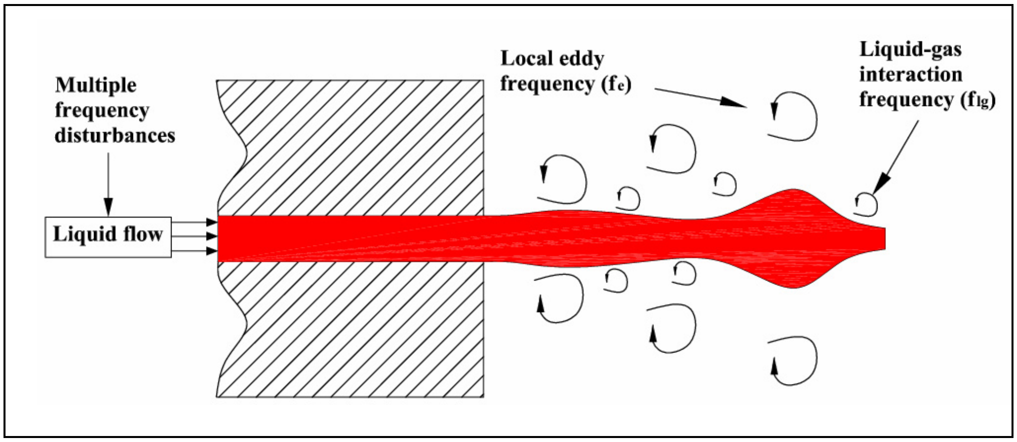

Figure 2.20: Existence of a multi-frequency domain in a free shear flow

By using the frequency of the perturbation to construct Strouhal number, the dominant effect of the modulation frequency is clarified. The order of the system frequency generated by the shear flow, local eddies etc is not well identifiable. Moreover, the interaction of a wide range of frequencies with the liquid structures generated by forced liquid jets requires further investigation and is beyond the scope of this study.

2.6 Closure

We have reviewed the fundamental forces influencing the liquid jet disintegration process. As concluded by several authors, no singled out mechanisms can be held responsible to affect the breakup process. On the other hand, single or multiple forces dependent on the operating condition of the liquid jet system would contribute to the droplet formation. Among several factors listed in this literature review, of particular interest in the current study, are the cavitation and pressure perturbation mechanisms which reveal substantial potential to generate fine droplet size distribution in a controllable fashion. The pressure perturbations realized by finite velocity fluctuations have been observed to produce reproducible structures while the cavitation mechanism generated by flow or geometry effects can critically transform the droplet characteristics such as its size and distribution in the spray domain. These two essential processes are united in a single nozzle by the use of ultrasonic oscillations of a solid horn placed inside the nozzle. In addition to the generation of these perturbation mechanisms, nozzle design and flow rates are critical in amplifying the destabilization forces caused by cavitation and modulation effects. Additional sources of perturbations such as turbulence, swirl etc requires careful attention to heighten their impact on accelerating the jet instabilities for enhanced drop formation.

Chapter 3

Numerical Simulation of Modulated Liquid Jets

This chapter is devoted to the analysis of modulated liquid jets using analytical and numerical methods. First, the governing equations of forced liquid jets and their characteristics are reviewed. A simple one-dimensional model is derived from first principles and an analytical expression for radius of a forced jet is deduced based on low modulation assumptions. Following this, numerical simulation of liquid jet disintegration using a Volume-of-Fluid (VOF) interface tracking method is detailed. A brief review of the interface-capturing scheme employed in the present study is provided. The capability of the interface tracking model is validated by investigating the disintegration of round turbulent liquid jets. Importance of turbulence modeling in simulating breakup behavior is elaborated. Later, the VOF scheme is applied to high and low speed forced liquid jets. Various structures arising from imposed modulations on a freely issuing liquid jet in the nozzle exterior are reported. Some scaling parameters pertaining to these systems are discussed. Finally, parametric study on the influence of modulation frequency and amplitude on the disintegration of a Newtonian low viscosity liquid, water in the present case, is reported.

3.1 Governing equations in modulated liquid jets

Considerable literature is available on the characteristics of submerged jets such as water into water or air into air system [35]. However, much less is known about the flow of free jets such as water into air. Although the former, after an initial region of the flow development, is completely described by the local momentum conditions and thus amenable to simple mathematical modeling, the latter displays a total absence of self-similarity and is governed by parameters such as pressure, nozzle dimensions and configurations, density, viscosity and surface tension of the jet fluid as evaluated in Chapter 2.

The breaking up of free jets has nevertheless attracted a good deal of attention. In the 19th century, Lord Rayleigh made a linearized analysis of the capillary instability of an inviscid liquid jet [39] wherein he showed that an axisymmetric disturbance is stable or unstable depending on whether its wavelength is less or greater than the circumference of the jet and explained that asymmetric disturbances of all wavelengths are stable. Recently, Rayleigh's work has been extended by others [116-118] to include the effects of non-linearity. However, the analysis is still adequate in dealing with high-amplitude, high frequency modulations as well as aerodynamic drag and turbulence, which are ever-present, especially when the jet flow is at a high Reynolds number and the mechanism most responsible for the bunching and eventual breakup is inertial rather than the surface tension induced.

3.1.1 Definition of the problem

Consider a water jet issuing at time t from a nozzle of radius R with a velocity $U(0,t)$ that is uniform across the exit area but periodic about a mean value U and is expressed as

$$U(0,t) = U + \Delta U \sin\left(2\pi ft\right) \tag{3.1}$$

where U is the average exit velocity, and ΔU and f are the amplitude and frequency of the modulation respectively.

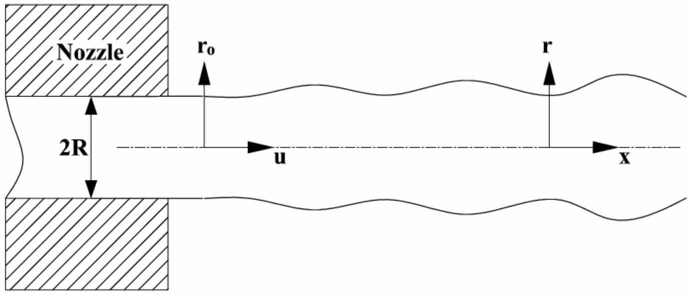

Figure 3.1: A one-dimensional cylindrical co-ordinate system for modulated jet analysis

Adopting a cylindrical polar co-ordinate system with *x* representing the downstream distance from the nozzle and *r* the radial co-ordinate, we can formulate the continuity equation and the equations of motion by considering an axi-symmetrical jet flow with no swirl, and by assuming the pressure and axial velocity profiles to be uniform across the jet. For the present study, the problem is to determine the surface configuration of the jet, $r_o(x,t)$, along the jet axis at any given instant.

3.1.2 Equations of motion

3.1.2.1 Continuity equation

Consider a control volume (*C.V*) bounded by the control surface (*C.S)* as shown in Fig. (3.2).

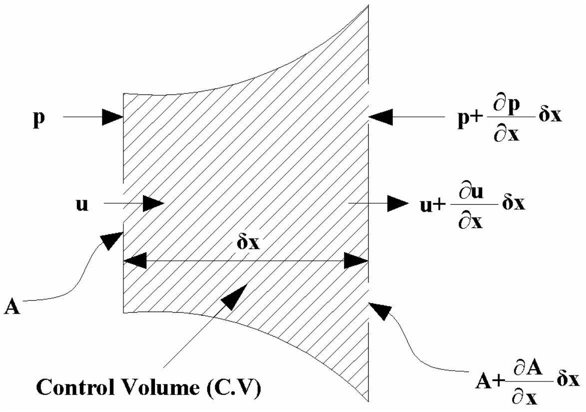

Figure 3.2: Control Volume

The integral form of the continuity equation for incompressible fluid can be expressed as:

$$\frac{\partial}{\partial t}\int_{C.V}\rho dV+\int_{C.S}\rho\vec{u}.\vec{n}dA=0 \tag{3.2}$$

where the control volume (*C.V*) is equal to (*A.dx*). For an incompressible fluid, equation (3.2) can be rewritten as

$$\frac{\partial}{\partial t}\left(A\delta x\right)-\int_{A}\vec{u}dA+\int_{A+\delta A}\left(u+\frac{\partial u}{\partial x}\delta x\right)\delta A=0 \tag{3.3}$$

For the round jet with a flat discharge velocity profile, the above expression (3.3) can be rearranged, expanded and after neglecting the higher order terms, reduce to

$$\frac{\partial r_o^{\,2}}{\partial t}+\frac{\partial\left(u r_o^{\,2}\right)}{\partial x}=0 \tag{3.4}$$

where $r_o(x,t)$ is the radius of the jet boundary given by $A=\pi r_o^{\,2}$. Expanding equation (3.4),we obtain the continuity equation in terms of r_o as

$$\frac{\partial r_o}{\partial t}+u\frac{\partial r_o}{\partial x}=-\frac{r_o}{2}\left(\frac{\partial u}{\partial x}\right) \tag{3.5}$$

3.1.2.2 Momentum equations

The Navier-Stokes equations representing momentum conservation for an axi-symmetrical jet flow with no swirl components, and after neglecting viscous and gravity effects with pressure and axial velocity profiles assumed uniform across the flow (*dp/dr* = 0, *du/dr* = 0), is given by

$$\frac{\partial u}{\partial t}+u\frac{\partial u}{\partial x}=-\frac{1}{\rho}\frac{\partial P}{\partial x}+\frac{\mu}{\rho}\frac{\partial^2 u}{\partial x^2} \tag{3.6}$$

and

$$\frac{\partial v}{\partial t}+u\frac{\partial v}{\partial x}+v\frac{\partial v}{\partial r}=-\frac{1}{\rho}\frac{\partial P}{\partial x}+\frac{\mu}{\rho}\frac{\partial^2 v}{\partial x^2}+\frac{\partial^2 v}{\partial r^2}+\frac{1}{r}\frac{\partial v}{\partial r}-\frac{v}{r^2} \tag{3.7}$$

The pressure term in equation (3.6) includes the effects of surface tension. If a hydrostatic pressure distribution across the jet is assumed, all components of the pressure other than surface tension can be ignored and the expression for the pressure written as

$$P=\frac{\sigma}{r_N}+\frac{\sigma}{r_T} \tag{3.8}$$

where r_N and r_T are the two orthogonal radii of curvatures and are expressed as

$$r_N = r_o\left[1+\left(\frac{\partial r_o}{\partial x}\right)^2\right]^{\frac{1}{2}} \tag{3.9}$$

and

$$r_T = r_o\frac{\left[1+\left(\frac{\partial r_o}{\partial x}\right)^2\right]^{\frac{3}{2}}}{\left(\frac{\partial^2 r_o}{\partial x^2}\right)} \tag{3.10}$$

Assuming small amplitude modulations, one can write $\frac{\partial r_o}{\partial x} \ll 1$ and upon simplification of the terms for r_N and r_T, we obtain

$$P = \frac{\sigma}{r_N}+\frac{\sigma}{r_T} = \sigma\left[\frac{1}{r_o}-\frac{\partial^2 r_o}{\partial x^2}\right] \tag{3.11}$$

Using the above approximation, we can write the momentum equation (3.6) as

$$\frac{\partial u}{\partial t}+u\frac{\partial u}{\partial x} = \frac{\sigma}{\rho}\left[\frac{1}{r_o^2}\frac{\partial r_o}{\partial x}+\frac{\partial^3 r_o}{\partial x^3}\right]+\frac{\mu}{\rho}\frac{\partial^2 u}{\partial x^2} \tag{3.12}$$

As stated before, the problem is to solve for $r_o(x,t)$. Since the radial component $v(r,t)$ of the velocity does not appear in either eqns. (3.5) or (3.6), the problem is reduced to the simultaneous solution of eqns. (3.5) and (3.6).

$$\frac{\partial r_o}{\partial t}+u\frac{\partial r_o}{\partial x} = -\frac{r_o}{2}\left(\frac{\partial u}{\partial x}\right) \tag{3.13}$$

$$\frac{\partial u}{\partial t}+u\frac{\partial u}{\partial x} = \frac{\sigma}{\rho}\left[\frac{1}{r_o^2}\frac{\partial r_o}{\partial x}+\frac{\partial^3 r_o}{\partial x^3}\right]+\frac{\mu}{\rho}\frac{\partial^2 u}{\partial x^2} \tag{3.14}$$

If the velocity u is now expressed in terms of a constant velocity U (unmodulated jet velocity) and a variation u' given as

$$U(x, t)= U+u'(x, t) \tag{3.15}$$

The eqns. (3.13) and (3.14) become

$$\frac{\partial r_o}{\partial t}+u\frac{\partial r_o}{\partial x}+u'\frac{\partial r_o}{\partial x}=-\frac{r_o}{2}\left(\frac{\partial u'}{\partial x}\right) \tag{3.16}$$

$$\frac{\partial u'}{\partial t}+U\frac{\partial u'}{\partial x}+u'\frac{\partial u'}{\partial x}=\frac{\sigma}{\rho}\left[\frac{1}{r_o^2}\frac{\partial r_o}{\partial x}+\frac{\partial^3 r_o}{\partial x^3}\right]+\frac{\mu}{\rho}\frac{\partial^2 u'}{\partial x^2} \tag{3.17}$$

Next, by translating the frame of reference at the unmodulated jet velocity *U*, the problem can be reduced to the study of a single wavelength of the stationary stream. We introduce a moving co-ordinate system represented by

$Z = x - Ut$, where $Z = Z(x, t)$ (3.18)

to study the amplification of the imposed perturbation wavelength along the liquid jet surface. After configuring various terms in eqns. (3.16) & (3.17) and modifying them using the new coordinate system presented in equation (3.18), we obtain

$$\frac{\partial r_o}{\partial t}+u'\frac{\partial r_o}{\partial z}=-\frac{r_o}{2}\left(\frac{\partial u'}{\partial z}\right) \tag{3.19}$$

$$\frac{\partial u'}{\partial t}++u'\frac{\partial u'}{\partial z}=\frac{\sigma}{\rho}\left[\frac{1}{r_o^2}\frac{\partial r_o}{\partial x}+\frac{\partial^3 r_o}{\partial x^3}\right]+\frac{\mu}{\rho}\frac{\partial^2 u'}{\partial z^2} \tag{3.20}$$

Equations (3.19) & (3.20) can be non-dimensionalized by the introduction of the following dimensionless parameters

$$\varsigma=\frac{r_o}{R} \tag{3.21}$$

$$\tilde{u}=\frac{u'}{U}$$

$$\eta=\frac{z}{\lambda}$$

$$\varpi_{1d}=\frac{tU}{\lambda}$$

$$\mathrm{Re} = \frac{\rho U R}{\mu}$$

$$We_{mo} = \frac{\sigma}{\rho R U^2}$$

$$St = \frac{R}{\lambda}$$

where, R is the nozzle radius (or the radius of the unmodulated jet), U the unperturbed jet velocity, λ and f are the wavelength and frequency of the modulation respectively. σ the surface tension of the liquid. The resulting expression in a non-dimensional form is expressed as

$$\frac{\partial \zeta}{\partial t} + \tilde{u}\frac{\partial \zeta}{\partial \eta} = -\frac{\zeta}{2}\left(\frac{\partial \tilde{u}}{\partial \eta}\right) \tag{3.22}$$

$$\frac{\partial \tilde{u}}{\partial \varpi_{1d}} + \tilde{u}\frac{\partial \tilde{u}}{\partial \eta} = -{We_{mo}}^2\left(\frac{1}{\varsigma^2}\frac{\partial \varsigma}{\partial \eta} + St^2\frac{\partial^3 \varsigma}{\partial \eta^3}\right) + \frac{St}{\mathrm{Re}}\frac{\partial^2 \tilde{u}}{\partial \eta^2} \tag{3.23}$$

In the case of high Re flows, the last term in the expression (3.23) can be neglected and one obtains

$$\frac{\partial \tilde{u}}{\partial \varpi_{1d}} + \tilde{u}\frac{\partial \tilde{u}}{\partial \eta} = -{We_{mo}}^2\left(\frac{1}{\varsigma^2}\frac{\partial \varsigma}{\partial \eta} + St^2\frac{\partial^3 \varsigma}{\partial \eta^3}\right) \tag{3.24}$$

Equations (3.22) and (3.24) can be solved simultaneously using simplified approximations to obtain analytical forms.

3.1.3 Analytical solutions to modulated jets

By assuming small amplitude modulation, ($\tilde{u} << 1$), one can neglect the second term of each equation (3.22) and (3.24). Further by assuming that surface tension plays a relatively small role as compared to that played by inertia, equations (3.22) and (3.24) reduce to

$$\frac{\partial \varsigma}{\partial \varpi_{1d}} = -\frac{\varsigma}{2}\left(\frac{\partial \tilde{u}}{\partial \eta}\right) \tag{3.25}$$

$$\frac{\partial \tilde{u}}{\partial \varpi_{1d}} = 0 \tag{3.26}$$

If the jet radius r_o is expressed, in terms of a constant radius R (the unmodulated liquid jet radius) and a variation r_o' given by

$$r_o = R + r_o' \tag{3.27}$$

the dimensionless parameter ζ becomes

$$\zeta' = r_o/R = 1 + r_o'/R = 1 + \zeta \tag{3.28}$$

Thus equation (3.25) can be written as

$$\frac{\partial \varsigma}{\partial \varpi_{1d}} = -\frac{(1+\varsigma')}{2}\left(\frac{\partial \tilde{u}}{\partial \eta}\right) \tag{3.29}$$

By assuming that ζ' << 1, this equation can be further simplified into the form

$$\left(\frac{\partial \tilde{u}}{\partial \eta}\right) = -2\frac{\partial \varsigma'}{\partial \tau} \tag{3.30}$$

A similar transformation and simplification can be applied to equation (3.24) resulting in

$$\frac{\partial \tilde{u}}{\partial \varpi_{1d}} = We_{mo}{}^{2}\left(\frac{\partial \varsigma'}{\partial \eta} + St^{2}\frac{\partial^{3}\varsigma'}{\partial \eta^{3}}\right) \tag{3.31}$$

Equations (3.29) and (3.31) can be cross-differentiated and reduced into

$$\frac{\partial^{2}\varsigma'}{\partial \varpi_{1d}{}^{2}} + We_{mo}{}^{2}\frac{\partial^{2}\varsigma'}{\partial \eta^{2}} + \frac{We^{2}}{2}St^{2}\frac{\partial^{4}\varsigma'}{\partial \eta^{4}} = 0 \tag{3.32}$$

When a solution of the type

$$\varsigma'(\eta,\varpi) = fn(\varpi_{1d}).\sin(K_o\eta) \tag{3.33}$$

where K_o is the dimensionless wave number ($2r/\lambda_o$) and λ_o the dimensionless wavelength is substituted into equation (3.30), after simplification, the Rayleigh criteria ($\lambda < 2\pi R$) for capillary instability. This solution has been reported by Lee et al. [120]. However, if one were to ignore the effects of surface tension on bunching phenomenon, equation (3.31) reduces to

$$\frac{\partial \tilde{u}}{\partial \varpi_{1d}} = 0 \tag{3.34}$$

Now the two equations (3.34) and (3.30) are solved simultaneously and the solution to the set of equations is given by

$$\varsigma' = -\pi M \varpi_{1d} \cos\left(2\pi\eta\right) \tag{3.35}$$

where M is the modulation amplitude. Expressing equation (3.35) in terms of the jet dimensionless outer radius,

$$\varsigma = 1 + \varsigma' = 1 - \pi M \varpi_{1d} \cos\left(2\pi\eta\right) \tag{3.36}$$

3.1.4 Computations - surface profile buildup

The formation of surface waves due to the modulation effect is demonstrated by using analytically modeled equation (3.36). For this purpose, a round liquid jet emanating from a 0.2 mm diameter hole with a mean velocity of 20 m/s is imposed with velocity fluctuations with an amplitude of 0.025 m/s and frequency = 20 KHz. The modulation amplitude, given by the ratio of the fluctuation magnitude to the mean velocity, measures 0.00125 which can be assumed to be much less than the mean velocity itself so that equation (3.25) is valid. Using equation (3.36), the behavior of the liquid jet due to the imposed perturbation at any given section of the jet is calculated. With the knowledge that the wavelength of the imposed perturbation, given by the ratio of velocity over the imposed frequency, approximates to 1e-03, a domain of four wavelengths along the flow direction is used in the simulation.

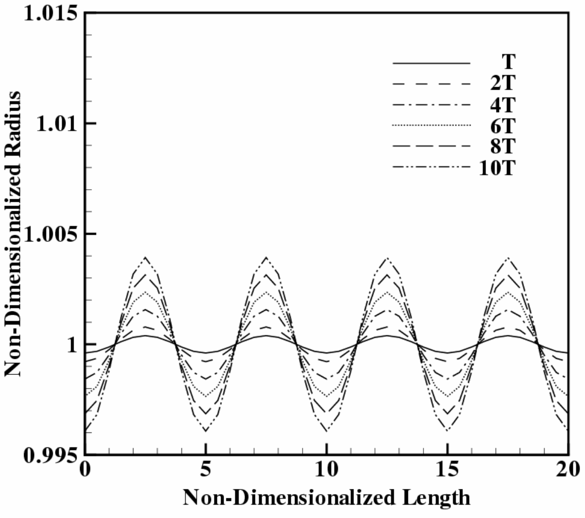

Figure 3.3: Buildup profile

Figure (3.3) shows the transient build up of liquid surface subjected to the imposed modulation parameters at different time intervals T, T representing time period of the imposed perturbations. The evolution of liquid jet emanating from the near nozzle exit cannot be treated in this fashion since it represents a boundary value problem while the analysis presented in Section (3.1) strictly deals with an initial value problem [119]. Further, as seen from Fig. (3.3), the amplification of the surface wave is distinct. Also notice that the wave profile build up results in very low curvatures between the successive fluid elements leading to the breakup of the liquid jet although no surface tension effects have been included in the model. Even with the inclusion of surface tension effects, analytical models have not been able to predict capillary pinching owing to the existence of singularity in the pinch-off event. Moreover, the one-dimensional solutions have been generated based on a low modulation assumption and can provide only a fundamental description of the impact of modulation on the jet behavior. The model fails to capture any detailed effect with modulation amplitude M = 0.003 and higher. As clearly distinct from the derivation process, the model does not account for any fluid dynamic interactions which might lead to proliferation of instabilities.

In general, the analytical methods fail to capture the complete description of the liquid jet due to their inability to accommodate a variety of non-linear interactions. Several researchers used numerical schemes to take into account several non-linear effects in the liquid phase such as surface tension, viscosity, density effects etc [120-122]. The one-dimensional methods were, however, able to predict liquid-gas interface fluctuations, but failed to obtain any details of drop formation. The problems in treating non-linearity inherent to the breakup process [123] is alleviated by using a full set of Navier-Stokes equations describing the liquid jet motion in combination with the dynamics of surrounding flow field.

Accurate treatment procedures are required to resolve the inter-phase dynamics engineered by the interaction of aerodynamic forces present in the ambience with the inherent forces present in the liquid, due to the surface tension, viscosity etc. Recently, numerical simulations of liquid jet disintegration have been performed using Marker and Cell (MAC) method [124], Volume of Fluid (VOF) method [125], cubic interpolated pseudo-particle method [126], level set methods [127], etc. These methodologies solve complete system of Navier-Stokes equations, defined by the continuity and momentum conservation equations (in the incompressible case), throughout the domain and use some special variables to quantify regions where different fluid activities are detected. Some vortex based interface tracking methodologies have also been recently reported [128]. Rather than tracking the interface explicitly several models consider averaged liquid-gas phase equations with inter-phase momentum exchange coupling mechanisms [129, 130]. Also, other computations involving dense sprays have been addressed using phase-average approximation between the phases [131].

The range of applications involving VOF is quite general and has been quite frequently used for the simulation of liquid droplet impact, jet and droplet breakup to cite a few [132-134]. In the VOF method, a scalar field is introduced in the discretized governing equations to describe the volume fraction of a fluid in each cell. The value of this field is zero when the cell does not contain any value of the scalar and one when the cell is entirely filled with it. Cells located at the interface are filled with several fluids, thus the scalar fields at these locations lie between zero and one. The VOF method, capable of modeling flows with complex free-surface geometries, including flows in which fluid volumes separate and reattach; yet remarkably economical in computational terms [124], is used in the current study. Details of the numerical methodology and governing equations used in this investigation are discussed in the following sections.

3.2 Numerical Modeling

3.2.1 Governing Equations

The present model treats the liquid-gas two-phase fields as a single incompressible continuum with an effective variable density ρ and an effective viscosity μ, which can be discontinuous across the liquid-gas interface. It is based on writing one set of conservation equations for the whole flow field where the material properties and the flow field are, in general, discontinuous across the boundary (or interface) between the fluids. The effect of surface tension is included in the governing equations by treating the phase boundary as an embedded interface and adding the appropriate source terms to the conservation laws. These source terms are delta functions localized at the interface and are selected to satisfy the correct matching conditions at the phase boundary. The effect of gravity is neglected in the current study. The effect of surface tension forces acting on the interfaces preserves the curvature.

Nevertheless, in a single-field formulation, the conservation equations have to account for both the differences of the material properties as well as the surface tension force acting at the interface. The governing mass and momentum conservation equations are the Navier-Stokes equations, which in the basic form can be represented in Cartesian form as:

$$\frac{\partial u_i}{\partial x_i} = 0 \tag{3.37}$$

$$\frac{\partial \rho u_i}{\partial t} + \frac{\partial \rho u_i u_i}{\partial t} = -\frac{\partial P}{\partial x_i} + \frac{\partial}{\partial x_j}\left(\nu \frac{\partial u_i}{\partial x_j} \right) + F_s \tag{3.38}$$

where u_i *(i=1,2,3)* represent the velocity components, *P* the pressure field and F_s is the force term arising due to surface tension. It can be expressed as,

$$F_s = \int_{S(t)} \sigma \kappa' n' \delta\left(x - x'\right) dS \tag{3.39}$$

which is computed based on the curvature of the interface denoted by κ' and the unit normal vector *n*' on the interface *S(t)*at *x'* representing the actual interface location. The surface tension term in the NS equations creates the most obvious difficulties, since it is a singular term. In several implementations of the method, these difficulties are manifest in both numerical instabilities and/or noise, and in poor accuracy of capillary effects.

The last term in equation (3.38), representing the source of momentum due to surface tension, acts only at the interface as indicated by the integral of a three-dimensional δ-function over a the entire surface of the interface S(t), i.e.$\int_{S(t)}$ δ(x-x') dS. The other variables in this term denote the surface tension coeffcient σ as well as the curvature κ and the normal vector *n* of the interface. Primed variables denote values at the interface.

An alternative, however equivalent, representation can be obtained by writing down the conservation equations separately for each fluid and matching them at the interface. It should be noted that equations (3.37) and (3.38) are valid for the whole flow field including the interface. The boundary conditions can be obtained by integrating the equations over a small volume enclosing the interface. Integrating the momentum equation (3.38) in normal direction to the interface yields the matching conditions that the normal stresses are balanced by surface tension. Integrating the tangential component shows continuity of the tangential stresses across the interface and integrating the mass continuity equation (3.37) shows that the normal velocities are also continuous. The Navier-Stokes equations have to be supplemented by an equation, which relates the deformations and the stresses within the fluids. The fluids investigated in this study obey the Newtonian law of viscosity and hence the viscosity of the fluids remains constant.

In this single-field representation, the fluids are identified by a step (Heavi-side) function *H*, which is 1 in one particular fluid and 0 elsewhere. Hence, the density as well as any other material property, can be written in terms of their constant values on either side of the interface and the Heaviside function:

$$\rho(x,t) = \rho_l H(x,t) + \rho_g \left(1 - H(x,t)\right) \qquad (3.40)$$

where t is the time, x is the position vector and ρ the effective density of the fluid. The interface itself is marked by a non-zero value of the gradient of the step function. The representation of inter-facial phenomena such as surface tension is achieved by adding the appropriate interface terms to the governing equations. Since these terms are concentrated at the interface, they are represented by three-dimensional δ functions. The three-dimensional δ-function is constructed by repeated multiplication of one-dimensional Dirac δ-functions:

$$\delta=\delta(x)\delta(y)\delta(z) \qquad (3.41)$$

As outlined before, the interface-capturing methodology employs the volume fraction as an indicator function to mark the different fluids. The interface is not defined as a sharp boundary and a transition region exist where the fluid is treated as some mixture of the two fluids on each side of the interface. In reality, this transition region is a discontinuous step. The location of the transient interface *S(t)* is determined by using a Volume of Fluid (VOF) surface capturing methodology employing the volume fraction indicator function equation. The volume fraction γ used in the VOF formulation is defined as:

$$\gamma = \begin{cases} 1 & \text{for a point inside the liquid} \\ 0 < \gamma < 1 & \text{for a point in the transition region} \\ 0 & \text{for a point completely outside the liquid} \end{cases} \tag{3.42}$$

It is associated with each fluid and is hence propagated with them as a Lagrangian invariant [124]. Therefore, it obeys a transport equation of the form:

$$\frac{\partial \gamma}{\partial t} + \frac{\partial}{\partial x_i}\left(u_i \gamma\right) = 0 \tag{3.43}$$

From the definitions of the phase indicator function γ as described above, the effective local density and viscosity of the fluid can be estimated as:

$$\rho = \gamma \rho_l + \left(1 - \gamma\right) \rho_g \tag{3.44}$$

$$\mu = \gamma \mu_l + \left(1 - \gamma\right) \mu_g \tag{3.45}$$

where the subscripts *l* and *g* represent the liquid and gas phase, respectively.

Since the interface is within the transitional zone, the exact shape and location are not explicitly known, and the surface integral in (3.39) cannot be evaluated directly. This problem is solved using the Continuum Surface Force (CSF) approach [135], which represents the surface tension forces as continuous volumetric force acting in the transition region. The interfacial surface phenomena are replaced by smoothly varying volumetric forces derived by integration of the surface tension forces over the interface. By means of the CSF approach, the surface tension force is transformed into a volumetric force yielding

$$\int_S \sigma\kappa' n' \delta\left(x - x'\right) dS \approx \sigma\kappa\nabla\gamma \tag{3.46}$$

where the curvature κ is given by:

$$\kappa = \nabla.\left(\frac{\nabla\gamma}{\left|\nabla\gamma\right|}\right) \tag{3.47}$$

The curvature is the divergence of the normal vector to an interface's surface element. The normal vectors are determined by the non-dimensional gradient of the volume fraction γ. The surface tension force acts on the interface between the two phases. It should be noted that the CSF model neglects the effects of a variable surface tension coefficient.

Also, the conservative nature of the surface force indicates that the total surface tension force over a closed surface equals to zero [135], i.e. .$\int_{S(t)} \sigma\kappa n \, dS = 0$. This property is important and errors result in an unphysical net force. However, it cannot be ensured in this technique since the surface is not defined as a sharp boundary in volume methods such as interface-capturing and surface integrals, equation (3.46), can therefore neither be evaluated accurately nor strictly obeyed. In fact, the above also applies to the closedness constraint, i.e. .$\int_{S(t)} n dS = 0$, which is not enforced in the current method. On the other hand, constraints based on the surface can be enforced in surface and moving mesh methods. However, as noted above, it is impossible to strictly conserve the volume of each fluid in surface methods. The strict, simultaneous assertion of both, conservation of volume and surface constraints, can only be achieved in some moving mesh methods.

3.2.2 Advection of scalar variable

Because the VOF scalar fields represent averaged volume fractions of fluids within each cell of the computational domain, information about interfaces is not readily available and as the fluids flow through the fixed grid, the fluid-fluid interfaces may cut through computational cells. In this case, extreme care should be taken in advecting the scalars so as to preserve the sharpness of the interfaces. Realizing this purpose, the discretization of the scalar equations in both the transient and spatial domains has to be accurate enough to prevent smearing associated with numerical diffusion. Standard convective schemes are not suitable for that purpose.

Various High Resolution (HR) schemes and compressive schemes have been tested for this purpose [136]. However, they were observed to be too diffusive, not guaranteeing the sharp resolution of the multi-fluid interfaces essential in free-surface flows or overly compressive leading to sharp interfaces stepped and distorted. Over the years, a number of advection schemes have been developed, which, for Eulerian meshes, can be classified under two categories: interface-tracking methods, interface-capturing methods. In interface-tracking methods the interface is explicitly reconstructed and used in the evaluation of the advection scheme, i.e., the advected scalar fluxes depends explicitly on the position of the interface within the individual computational cell. Hence the accuracy of the reconstructed interface plays a critical role in the performance of the advection scheme. Examples of interface-tracking methods include the well-known SLIC and PLIC algorithms and their many variations. The main drawback of these methods is the algorithmic complexity involved in the reconstruction the interface in a continuous manner across the computational domain, with this difficulty being compounded in three-dimensional problems.

In interface-capturing methods, the scalar value at a control-volume is formulated algebraically, without reconstructing the interface. Generally, in interface-capturing methods a compressive scheme is used to avoid smearing of the interface. However, this has been found to lead to stepping of the interface (i.e., loss of curvature) whenever the flow is not aligned with the computational grid. Workers [136, 137] have remedied this problem by adopting a switching strategy that toggles between a compressive and a non-compressive scheme depending on some criterion related to the VOF scalar. Many of these schemes base the switching criterion on a function of the angle formed between the interface normal direction, readily obtained using the gradient of the scalar field and the grid orientation. Generally the base scheme is the upwind scheme, but other higher-order schemes could also be used.

3.2.2.1 Blending strategy for interface capturing schemes

One way to address these two shortcomings is through a switching strategy that depends on the angle between the flow direction and the grid lines [139, 140]. The best approach is to have a continuous switching function whereby the values of a compressive and a HR advection scheme are blended together, with the blending factor depending on the angle between the flow direction and the grid lines. The angle can be determined using the grid orientation at the integration face and the gradient of the scalar field, whose unit vector represents the direction normal to the interface. This general approach has been followed in the derivation of CICSAM [136] scheme used in the present study.

From the above it is clear that an ‘‘interface-capturing’’ scheme based on the switching strategy should possess the following attributes:

1. It should be based on a combination of compressive and high-resolution schemes.

2. Its blending function should be based on the angle between the interface direction and the grid orientation, preferably in a continuous fashion.

3.2.2.2 Volume-of-Fluid: NVD Strategy

In general, the volume fraction indicator equation should be able to preserve sharp interface with negligible diffusion. However, some available classical VOF schemes have problems in maintaining the bounded nature of the volume fraction scalar. Due to numerical inaccuracy and grid refinement, discontinuity prevails over the reconstructed interface. VOF is an interface compression method which has been enhanced by Normalised Variable Diagram (NVD) based bounded compression schemes [138].

In the present study, interface capturing has been performed by using CICSAM (Compressive Interface Capturing Scheme for Arbitrary Meshes) [136], a fully conservative technique based on finite volume method. The CICSAM scheme based on Normalised Variable Diagram (NVD), switches between different high resolution differencing schemes depending on the orientation of the interface to the flow direction, to yield a bounded scalar field and preserve both the smoothness and sharpness of the interface. The derivation of the scheme is based on the recognition that no diffusion of the interface can occur. No explicit reconstruction of the interface is needed. This scheme is particularly applicable to sharp fluid interfaces. Further, the scheme does not need any operator splitting and is implicit with second-order temporal accuracy. The capability of the scheme in handling interface rupture and coalescence has been tested by Ubbink et al. [137].

The CICSAM scheme of Ubbink was formulated based on the idea of the donor-acceptor concept, i.e. as a scheme that varies as a function of the interface-cell face angle.

The discretization depends on the interface velocity direction and the angle it makes with the integration cell face. However, rather than choosing as base schemes the downwind and upwind schemes between the ULTIMATE QUICKEST scheme and Hyper-C scheme [139] are chosen, with Hyper-C scheme used when the cell face is perpendicular to the interface's normal vector and the ULTIMATE-QUICKEST scheme used when the cell face normal vector is aligned with the normal vector of the interface. A very brief mathematical description of the scheme is presented here. For detailed implementation, the readers are directed to Ubbink's thesis [136].

A schematic of control volume for derivation of CICSAM scheme is presented in Fig. (3.4).

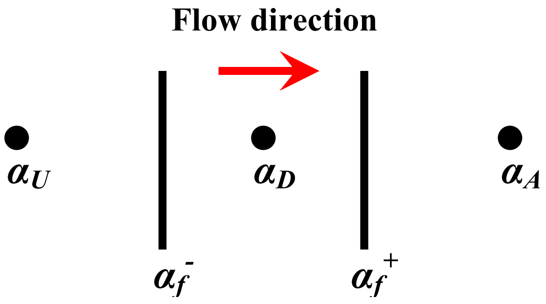

Figure 3.4: One-dimensional control volume

The most crucial element to generating a successful compressive scheme is to incorporate the downwind information in its formulation [141]. However, downwinding does not comply with the boundedness criteria and can give rise to non-physical volume fraction larger than unity or smaller than zero when applied to the scalar advection equation.

3.2.2.3 On the boundedness criteria

In the general CFD framework, it is normally expected that in the absence of any sources, the value of a flow property is the flow domain cannot take values higher or lower than prescribed in the boundaries of the flow domain [138]. For the purpose of volume fractions the the boundedness criteria are taken as the physical bounds zero and one. Local boundedness bounds a volume fraction value locally with its nearest neighbors.

3.2.2.4 Availability limits

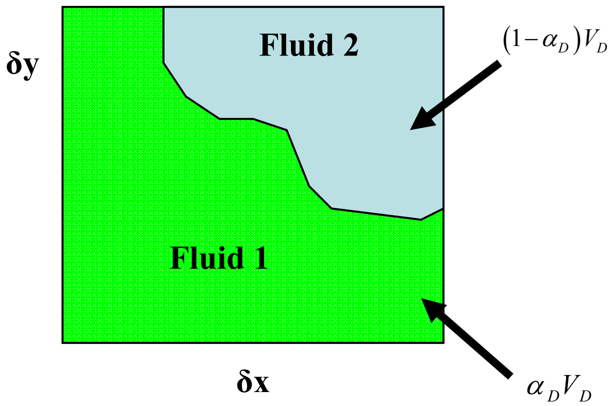

Figure 3.5: Fluid configuration in the donor cell

Figure (3.5) gives a schematic representation of a donor cell containing part of the interface. Given the volume of donor cell V_D and volume fraction α_D, the volume occupied by fluid 1 and 2 are given by $(1-\alpha_D)V_D$ and $\alpha_D V_D$ respectively. If $c_f = |u_f \delta t|/\delta x$ is the Courant number at the face and α_f be the volume fraction convected over the face in one time step, then $\alpha_f c_f V_D$ is the amount of fluid 1 convected over the face while amount of fluid 2 convected is given by $(1-\alpha_f)c_f V_D$. Availability criteria on fluid 1 dictates that the amount of fluid 1 convected over a face during a time step should be always less than or equal to the amount of available in the donor cell and similar statement given for fluid 2 provides

$$\alpha_f \leq \frac{\alpha_D}{c_f} \tag{3.48}$$

and

$$\alpha_f \geq \frac{\alpha_D}{c_f} - \frac{1-c_f}{c_f} \tag{3.49}$$

Ubbink et al. [135] formulated the controlled downwinding process as

$$\begin{aligned}\alpha_f &= \min\left\{\max\left\{\frac{\alpha_D}{c_f}-\frac{1-c_f}{c_f},\alpha_A\right\},\frac{\alpha_D}{c_f}\right\}\\ &=\min\left\{\alpha_A+\max\left\{\left(1-\alpha_A\right)-\frac{1-\alpha_D}{\alpha_D},0\right\},\frac{\alpha_D}{c_f}\right\}\end{aligned}\tag{3.50}$$

The normalized variable forms the basis of the high resolution schemes and is defined as

$$\tilde{\alpha}=\frac{\alpha-\alpha_U}{\alpha_A-\alpha_U}\tag{3.51}$$

which can be used to give expressions for $\tilde{\alpha}_D$ and α_f by replacing α in equation (3.51). The convection boundedness criteria uses the normalized variables and presents bounded value at the cell faces for which an implicit differencing scheme always preserves the local boundedness.

$$\begin{aligned}&\tilde{\alpha}_f=\tilde{\alpha}_D \quad \text{for } \tilde{\alpha}_D<0 \text{ or } \tilde{\alpha}_D>1\\ &\tilde{\alpha}_f\le\tilde{\alpha}_f\le 1 \quad \text{for } 0\le\tilde{\alpha}_D\le 1\end{aligned}\tag{3.52}$$

Using the normalized variable contribution, the normalized face value for each normalized donor cell value can be calculated as

$$\alpha_f=\tilde{\alpha}_f\alpha_A+\left(1-\tilde{\alpha}_f\right)\alpha_U\tag{3.53}$$

By using the normalized quantity $\tilde{\alpha}_D$, equation (3.53) gives

$$\alpha_U=\frac{\alpha_U-\tilde{\alpha}_D\alpha_A}{1-\tilde{\alpha}_D}\tag{3.54}$$

and hence, the expression for the face volume fraction value is obtained as

$$\begin{aligned}\alpha_f&=\left(1-\beta_f\right)\alpha_D+\beta_f\alpha_A\\ \beta_f&=\frac{\tilde{\alpha}_f-\tilde{\alpha}_D}{1-\tilde{\alpha}_D}\end{aligned}\tag{3.55}$$

The weighting factor β_f contains the upwind value information and gives an indication of the gradient α at the face. The computation of the normalized variable values for the face and donor cell for computing the weighting factor is provided in the preceding section. The VOF method of Hirt and Nichols [125], determines the slope of the interface and switches to upwinding differencing if the smallest angle between the interface and the face of the control volume is more than 45.

Leonard [139] compared several higher order differencing schemes with each other on the convection of a step profile, sine function and semi ellipse in a uniform flow field. The scheme which has performed the best regarding the convection of the sine and semi ellipse function is the ULTIMATE-QUICKEST (UQ) scheme, the one-dimensional explicit bounded version of QUICK.

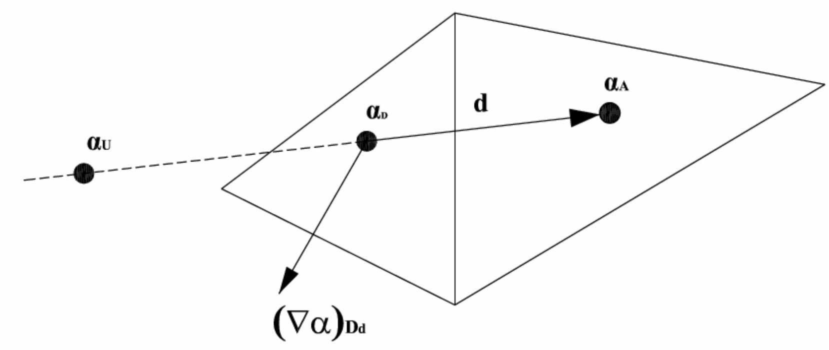

Figure 3.6: Arbitrary Cell arrangement for computation purpose

The upwind value required for the calculation of normalized variable $\widetilde{\alpha}_D$ is not available and hence Jasak et al. [143] proposed a new method to obtain this information by

$$\widetilde{\alpha}_D = 1 - \frac{(\nabla\alpha)_f \bullet d}{2(\nabla\alpha)_D \bullet d} \tag{3.56}$$

where *d* is the vector between cell donor and acceptor, *D* and *A*, respectively. Schematic of the two cell arbitrary arrangement is shown in Fig. (3.6). Expression for α^*_U is given by

$$\alpha_U^* = \alpha_A - 2\left(\nabla\alpha\right)_D \bullet d \tag{3.57}$$

Since the above expression does not guarantee bounded α^*_U, physical bounds 0 and 1 are applied using minimum and maximum operators.

In comparing various compressive differencing schemes, Ubbink [136] used Hyper-C as the most compressive scheme complying with local boundedness criteria. Using Hyper-C formulation, the normalized face value of the scalar variable is given by

$$\tilde{\alpha}_{f_{CBC}} = \begin{cases} \min\left\{1, \dfrac{\tilde{\alpha}_D}{c_f}\right\} & 0 \le \tilde{\alpha}_D \le 1 \\ \tilde{\alpha}_D & \tilde{\alpha}_D < 0,\ \tilde{\alpha}_D > 1 \end{cases} \tag{3.58}$$

Hyper-C is the most compressive differencing scheme which complies with the local boundedness criteria. Unfortunately, on its own it is not suitable for the modeling of interfacial flow, because it tends to wrinkle the interface [125, 142]. Numerical results demonstrating this behavior have been reported by Ubbink et al. [137]. This is because downwinding tends to compress any gradient into a step profile, even if the orientation of the interface is almost tangential to the flow direction. This incorrect or artificial steepening of the volume fraction gradients is shown by Leonard [139], who presents the results of the advection of one-dimensional semi-ellipse profile which becomes disfigured into a step profile by the scheme.

Furthermore, comparing several HR schemes, Leonard [139] concluded that ULTIMATE-QUICKEST (UQ), the one-dimensional explicit bounded version of QUICK, performed best regarding convection of step profile, sine and a semi-ellipse in a uniform flow field. The normalized face value of volume fraction used with UQ scheme is given by

$$\tilde{\alpha}_{f_{UQ}} = \begin{cases} \min\left\{ \frac{8c_f \tilde{\alpha}_D + (1-c_f)(6\tilde{\alpha}_D + 3)}{8}, \tilde{\alpha}_{f_{CBC}} \right\} & 0 \le \tilde{\alpha}_D \le 1 \\ \tilde{\alpha}_D & \tilde{\alpha}_D < 0, \tilde{\alpha}_D > 1 \end{cases} \tag{3.59}$$

By providing different HR schemes, one best utilized for boundedness while the other preserves the sharpness of the profile, Ubbink et al. [137] combined the two HR schemes to obtain the normalized volume fraction face value as

$$\tilde{\alpha}_f = \varphi_f \tilde{\alpha}_{f_{CBC}} + (1-\varphi_f)\tilde{\alpha}_{f_{UQ}} \tag{3.60}$$

The normalized variable diagram for the CICSAM scheme implies that the UQ scheme operates where the Hyper-C fails to preserve the gradient in the interface and Hyper-C operates where UQ fails to maintain the sharpness of the interface.

The derivation of the CICSAM scheme is completed by defining the weighting factor φ_f based on the cosine of the angle between the vector normal to the interface and the vector which connects the centres of the donor and acceptor cells.

$$\theta_f = \arccos\left| \frac{(\nabla\alpha)_D \bullet d_f}{\left|(\nabla\alpha)_D\right| \bullet \left|d_f\right|} \right| \tag{3.61}$$

$$\varphi_f = \min\left(\Omega_\gamma \frac{\cos(2\theta_f)+1}{2}, 1 \right) \tag{3.62}$$

Where $\Omega_\gamma \ge 0$ is a constant introduced to control the dominance of the different schemes. The recommended value is $\Omega_\gamma = 1$. For $\Omega_\gamma = 0$, equation (3.62) reduces to UQ and for a large Ω_γ it reduces to Hyper-C.

3.2.2.5 Summary

The normalized face value predicted using the CICSAM differencing scheme for explicit one-dimensional uniform flow is defined in Fig. (3.4). It can reformulated in the form needed for the finite volume discretization in using equations. The weighing factors β_f now carry all the information regarding the fluid distribution in the donor, acceptor, and upwind cells as well as the interface orientation relative to the direction of motion.

A predictor-corrector solution procedure for solving the face value of the volume fraction variable using CICSAM is adopted [136].

The predictor step is detailed as follows:

(1) Calculate the gradient $\left(\nabla\alpha\right)_D$ over the cell by using Gauss's theorem

$$\left(\nabla\alpha\right)_D = \frac{1}{V_D}\sum_{f=1}^{n} A_f \alpha_f \tag{3.63}$$

(2) Calculate the courant number for all the cells

$$c_D = \sum_{f=1}^{n} \max\left\{\frac{-F_f \Delta t}{V_D}, 0\right\} \tag{3.64}$$

(3) Determine the donor and acceptor cells

(4) Predict the upwind value α_U^* using equation (3.57) and bound it within the physical bounds zero and unity.

(5) Compute normalized variable for the donor cell $\widetilde{\alpha}_D$

(6) Compute $\widetilde{\alpha}_{f_{CBC}}$ using equation (3.58)

(7) Compute $\widetilde{\alpha}_{f_{UQ}}$ using equation (3.59)

(8) Determine Ω_f taking into account the interface orientation and flow direction

(9) Calculate normalized face value $\tilde{\alpha}_f$

(10) Compute β_f

(11) Solve discretized α equation for the new volume fraction distribution

The predictor step of Ubbink et al.[137] described above is followed by a corrector step in the event any non-physical volume fractions arise. For explicit split operator, face values are adjusted by utilizing the degree of unboundedness while for an implicit operation, the weighting factor β_f is corrected. The details of the correction procedure can be obtained from Ubbink [136].

3.2.3 Computational Framework

The numerical simulations were performed within the framework of OpenFoam [144] C++ libraries available for continuum mechanics. A finite volume method for arbitrary cell-shapes in combination with a segregated approach is used to discretize the equations. Finite volume based computations are performed with non-overlapping cells in the domain. These equations are iterated over time using a multi-step method. To reconstruct the fluxes from variables of adjacent cells interpolation of convective fluxes and difference approximations for inner derivates are required [146]. The convective fluxes are determined by Gamma scheme [145] which guarantees a bounded solution minimizing the numerical diffusion of sharp changes in the gradient of the variable. The gamma scheme is a high resolution second order convection-diffusion differencing scheme based on Normalized Variable Diagram (NVD) [139, 140] specially developed for multi-dimensional unstructured meshes. The discretization of diffusive fluxes present in equation (3.38) is carried out using a decomposition method to minimize the non-orthogonality errors. For this reason, the viscous fluxes are decomposed in orthogonal and non-orthogonal parts based on the cell configuration. Central difference approximations are applied to the orthogonal parts while the face interpolation of the gradients of the dependent variables is used for the non-orthogonal parts. Details of this decomposition procedure have been elaborated by Jasak [147].

The pressure velocity coupling is handled with a Pressure Implicit Splitting of Operators (PISO) procedure [148] based on a modified Rhie-Chow interpolation [149] for cell centered data storage. Pressure velocity coupling using PISO algorithm provides more accurate adjustment of the face mass flux correction according to the normal pressure correction gradient in transient simulations [150]. The equations are solved sequentially with iteration over the coupling terms with time marching using a first order backward euler implicit scheme.

Symmetric matrices arising from the discretization of the governing equation using Finite Volume method were solved using Incomplete Cholesky Conjugate Gradient (ICCG) based iterative solvers while the asymmetric matrices were solved using Incomplete-Cholesky preconditioned biconjugate gradient methods (BICCG) [146]. The code was assembled using C++ class libraries available for computational continuum mechanics in openFoam [144].

3.3 Numerical Model Validation

The Volume-of-Fluid based interface capturing method of Ubbink [136] outlined in Section (3.2) is utilized in simulating disintegration behavior of round liquid jets. On first account of these implementations, numerical studies concerning turbulent round liquid jets are discussed here, to identify the ability of the VOF model, combined with turbulent regimes, in predicting free surface dynamics. For modeling the turbulence phenomena to account for the turbulent viscosity and stress components, an Large Eddy Simulation model is incorporated, details of which are presented next.

3.3.1 Turbulence Modeling

The free surface of the injected liquid interacts with the ambient gas in dynamic fashion covering a wide spectrum of turbulent scales [151]. Accurate representation of these scales is required to simulate the disintegration mechanism to the closest detail. Literature review of the mechanism of drop formation indicate the forcing influence of fluctuating velocities components on liquid surface distortion leading to discs, rings and hence droplet formation [45, 79]. It is well established that turbulence near the interfaces separating the immiscible fluids is a very complex phenomenon associated with moving boundaries, topological transitions, vortex interactions, surface oscillations etc., to name a few [151]. Although several models have been developed to accurately track the liquid-gas interface for breakup predictions in laminar regimes, inclusion of a good model to include turbulence effects has been missing. Due to the strong non-linearity contents immersed in a turbulent free-surface flow, use of the interface tracking schemes, typically used for laminar flows, to simulate turbulent free-surface flow regimes can lead to unrealisitic solutions. Some Direct Numerical Simulations in combination with interface tracking have been performed using two-dimensional assumptions [132, 133]. However, the computations were restricted to low Reynolds numbers due to high computational requirements required by the DNS strategy [152]. Few free-surface computations using RANS based turbulence models have been reported recently [154-156]. From their computations using a two-equation eddy viscosity model with a interface tracking scheme, Banerjee [154] underscored the influence of shear rates near the liquid-gas interface on the development of turbulence structure. Later, Hong and Walker [156], based on their RANS equations for free surface flows, showed that in high-froude number turbulent flows, free-surface fluctuations provide significant contributions in enhancing surface currents. However, implementation of RANS based methodologies for estimating turbulence can lead to erroneous treatment of the local free-surface transients due to its fundamental time averaged strategy [152]. Adding, greater care is required in estimating turbulent viscosity, since its over-prediction can lead to poor description and artificial smoothening of the interface. In this paper, a Large Eddy Simulation strategy is adopted to include turbulence effects [152]. The LES methodology invokes a detailed prediction of geometry dependent large scale motions while the sub-grid scale effects are modeled to accurately represent the local transients. In the concern of simulating unsteady flows, LES offers several advantages over RANS and DNS [153]. Most of the transport of mass, momentum and energy, accounting for more than 90% of the total transport is carried out by the large eddies. In the concern of multiphase regime, the mathematical challenges arise from the presence of deformable interfaces between the fluids. The interaction of turbulence with these interfaces incorporates a large class of important and unsolved problems, including the generation, growth and breaking of nonlinear waves, and topological changes in the interfacial structure, leading to entrainment of droplets and associated dynamics of one phase into the other [151]. The scales of interactions occurring at different scales are seen to be fundamentally important. The primary role of the smaller eddies occurring in the system is to dissipate the fluctuations caused in the large scales [152]. Hence, it should be recognized that these larger eddies interact directly with the mean flow. The smaller eddies are less dependent on the boundary conditions and flow type, unlike the large eddies. Thus, the modeling developed for small eddies should be more generally applicable than models developed for the entire range of turbulence scales. With grid refinement, the solutions of Large Eddy Simulations (LES) converge to the solution obtained from Direct Numerical Simulations (DNS). We conclude that the use of Large Eddy Simulation is an attractive option combining accuracy with computational costs (grid requirement).

Applying filtering procedure to the instantaneous conservation equations for mass and momentum represented in equation (3.37) and (3.38) yields a sub-grid scale tensor that cannot be resolved in the flow and requires to be modeled. Note that the filtering operation results in additional perturbations terms arising due to the surface tension force. Presently, the effect of these fluctuating quantities are the sub-grid level are neglected since the local turbulence length and time scales generated by inertial forces are higher than the capillary length and time scales. The filtering method used for LES procedures employ spatial averaging as against ensemble averaging used in RANS techniques. LES resolves the transients that are missed with ensemble averaged models making it better suited for highly unsteady flows. The resolved component is directly determined by solving the filtered equations for mass, momentum and other scalars. The filtered LES momentum equation is given as follows:

$$\frac{\partial \rho \overline{u}_i}{\partial t} + \frac{\partial \rho \overline{u}_i \overline{u}_i}{\partial t} = -\frac{\partial \overline{P}}{\partial x_i} + \frac{\partial}{\partial x_j}\left(\nu \frac{\partial \overline{u}_i}{\partial x_j} - \tau_{ij} \right) \tag{3.65}$$

where the sub-grid stress tensor is expressed as,

$$\tau_{ij} = u_i u_i - \overline{u_i u_i} \tag{3.66}$$

Although several LES models are available for modeling the small scale motions, a good sub-grid scale (SGS) model is required to represent interaction with small scales. The SGS stresses act on the smallest resolved scales in the flow. When these are locally much smaller than the largest scales, their behavior can be expected to be relatively universal allowing simple SGS stress models to be used. The SGS stresses do, however, fluctuate in time and space with certain characteristic time and length scales. Besides the mean behavior, these fluctuating characteristics are expected to have an important effect on the flow. In addition, the most important feature of a SGS model is to provide adequate dissipation which represents transport of energy from the resolved grid scales to the unresolved grid scales; the rate of dissipation ε in this context is the flux of energy through the inertial sub-range. The dissipation rate must depend on the large scales of the flow rather than being imposed arbitrarily by the model. Importantly, the SGS model must depend on the large-scale statistics and must be sufficiently flexible to adjust to changes in these statistics. In energy conserving codes such as LES, the only way for turbulent kinetic energy to leave the resolved modes is by the dissipation provided by the SGS model [152]. Overall, the primary goal of an SGS model is to obtain correct statistics of the energy containing scales of motion.

In the current study, the one equation eddy viscosity model of Yoshizawa et al. [157] which utilizes an additional transport equation for the sub-grid scale turbulent kinetic energy. Solving an extra sub-grid scale kinetic energy equation allows better estimation of the velocity scale for the SGS fluctuations. The energy flows back and forth between the resolved and sub-grid scales while their sum decays monotonically due to viscous effects in the absence of external input of energy. Since the contribution of turbulence in mixing is very dominant, the present model is thought to closely approximate the real scale statistics present in the flow.

Modeling the sub-grid stress term is performed using a gradient approximation.

$$\tau_{ij} = \nu_t \overline{S}_{ij} + \frac{1}{3}\delta_{ij}\tau_{kk} \tag{3.67}$$

where δ_{ij} is kroneckar delta and the filtered rate of strain tensor is defined as

$$\overline{S}_{ij} = \frac{1}{2}\left(\frac{\partial \overline{u}_i}{\partial x_j} + \frac{\partial \overline{u}_j}{\partial x_i}\right) \tag{3.68}$$

Construction of the one equation eddy viscosity type model used in the current simulation is briefly explained. The sub-grid scale kinetic energy equation is written as,

$$\frac{\partial k_{sgs}}{\partial t}+\overline{u}_i\frac{\partial k_{sgs}}{\partial x_i}=\overline{u}_i\frac{\partial \overline{P}}{\partial x_i}-u_i\frac{\partial P}{\partial x_i}-\frac{\partial}{\partial x_j}\left(\frac{1}{2}\tau_e-\overline{u}_i\tau_{ij}\right)+\frac{\partial}{\partial x_i}\left(\nu\frac{\partial k_{sgs}}{\partial x_i}\right)-\tau_{ij}\frac{\partial \overline{u}_i}{\partial x_j}-eps_{sgs} \tag{3.69}$$

where the sub-grid kinetic energy k_{sgs} is defined by,

$$k_{sgs}=\frac{1}{2}\left(u_iu_i-\overline{u_iu_i}\right) \tag{3.70}$$

$$\tau_e=u_iu_iu_j-\overline{u_iu_iu_j} \tag{3.71}$$

and the dissipation rate defined by

$$eps_{sgs}=\nu\left(\frac{\partial u_i}{\partial x_j}\frac{\partial u_i}{\partial x_j}-\overline{\frac{\partial u_i}{\partial x_j}\frac{\partial u_i}{\partial x_j}}\right) \tag{3.72}$$

In order to close equation (3.69), four terms: sub-grid stress tensor, triple correlation term, sub-grid dissipation, and the pressure velocity term required to be modeled.

The dissipation of the sub-grid scale kinetic energy is modeled using the following expression:

$$eps_{sgs}=C_{eps}\frac{k_{sgs}^{3/2}}{\Delta} \tag{3.73}$$

and the sub-grid scale stress tensor, is modeled as:

$$\tau_{ij}=-2\nu_t\overline{S}_{ij}+\frac{2}{3}k_{sgs}\delta_{ij} \tag{3.74}$$

The sub-grid scale eddy viscosity is determined as:

$$\nu_t=C_kk_{sgs}^{1/2}\Delta \tag{3.75}$$

The pressure velocity and triple correlation term are modeled by adding the viscosity to the sub-grid kinetic energy equation. Substituting the modeled terms the sub-grid scale kinetic energy equation (3.69) is rewritten as

$$\frac{\partial k_{sgs}}{\partial t}+\overline{u}_i\frac{\partial k_{sgs}}{\partial x_i}=\frac{\partial}{\partial x_i}\left(\left(\nu+\nu_t\right)\frac{\partial k_{sgs}}{\partial x_i}\right)+\left(2\nu_t\overline{S}_{ij}+\frac{2}{3}k_{sgs}\delta_{ij}\right)\frac{\partial\overline{u_i}}{\partial x_j}-eps_{sgs} \tag{3.76}$$

The exact k_{sgs} equation represents the influence of turbulent diffusion, production term, dissipation, and viscous diffusion which forms the essence of equation (3.76). As with the case of other sub-grid scale models, the eddy viscosity approaches zero as the grid is refined such that all the momentum scales are captured. Δ is the SGS length scale which is taken proportional to the nominal cell dimension. The coefficients C_k and C_{eps} are specified as 0.07 and 1.05 respectively. In the current formulation,

$$\Delta=\min\left\{\Delta x,\Delta y,\Delta z\right\} \tag{3.77}$$

3.3.2 Turbulent disintegration – Validation test cases

The combined LES/VOF methodology discussed in the previous section is used in investigating the disintegration characteristics of a turbulent liquid jet emanating from an atomizer configuration previously experimented by Mayer et al. [158]. The setup consists of a two-fluid coaxial atomizer injecting liquid ethanol into gaseous nitrogen with gaseous nitrogen as the co-flowing gas. A schematic of the physical and computational domain for the simulations are shown in Fig. (3.7). Axi-symmetric grids used in openFoam can be generated only internally within the openFoam framework. Alternatively, 2D and 3D grids generated in Fluent can be imported into openFoam. Currently, openFoam does not support import of axi-symmetric meshes from other grid generation softwares; rather the grids have to be manually created within the *blockmesh* tool available in openFoam.

The inner diameter of the liquid (ethanol) injector is D_l = 2.2 mm with a 0.3 mm thick wall surrounded by the outer coaxial gas (Nitrogen) injector, D_g = 10 mm in diameter.

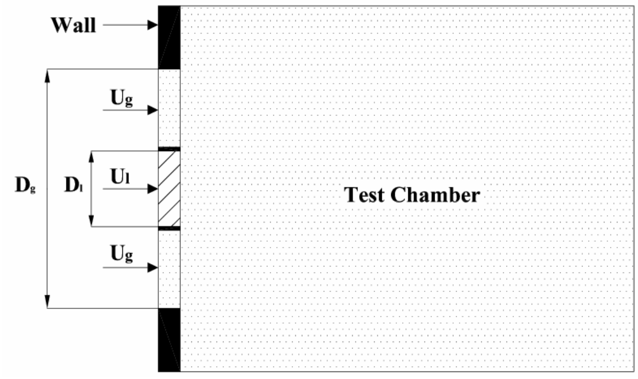

(a)

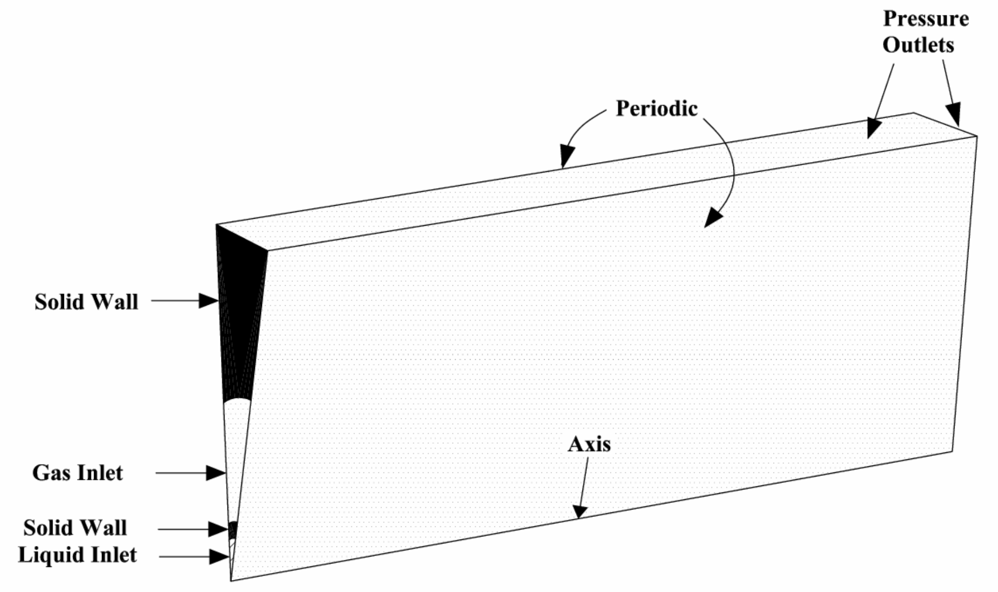

(b)

Figure 3.7: Experimental setup and computational domain

Wall and pressure outlet (atmosphere) conditions are being imposed surrounding the injection domain, as shown. The effect of gravity is neglected in our computations. Random white noise perturbations are imposed at the liquid inlet for turbulent computations. The injection velocity profile is assumed to be turbulent using a power law assumption. The present computation domain is treated axi-symmetric with a one cell extension in the azimuthal direction providing three-dimensional information for computations. The domain extends 10 mm in the radial direction and 20 mm along the axial flow direction which can help capture the primary breakup regime. Figure (3.8) represents the structured hexahedral grid frontal view used in the computation.

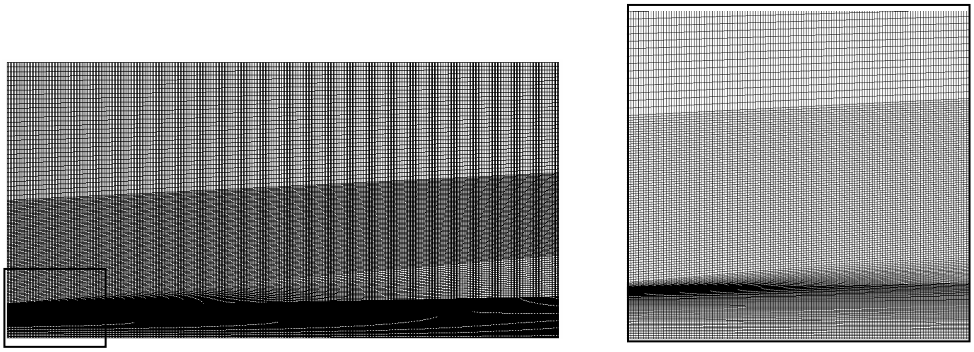

(a) (b)

Figure 3.8: (a) Structured hexahedral meshes frontal view (b) Fine grids near the inlet

Gaseous nitrogen, used in the computation as the gas phase, is assumed to behave as an ideal gas and hence its density change can be correlated to the change in chamber pressure using the ideal gas law. All fluid properties in the simulation domain were taken at $298^{o}K$. For our simulation purposes, the surface tension of ethanol was kept constant at σ=0.02 N/m. Structured hexahedral meshes, generated using *blockmesh* utility in openFoam [144], were used for simulation purposes in order to increase the accuracy of the simulation. The lowest mesh size of 2 μm was made available in the simulation domain in the vicinity of nozzle exit and upto 10 diameters downstream. Due to very fine mesh size, the time stepping requirement was reduced < 10^{-8} sec.

3.3.3 Simulation Platform

All the simulations presented using openFoam C++ libraries for continuum mechanics are performing using a Dual core AMD Opteron processor 265 with a processing memory of 2 GB. The model is a dual core – dual processor, totaling 4 processors with a SUSE v10.0 operating system. The hard-drive capacity of the system is 400 GB convenient for data storage and post processing purposes.

3.4 Results and Discussions

Experiments of Mayer et al. [158] included three discrete chamber pressures 0.1 MPa, 1 MPa and 6 MPa with varied injection velocities of liquid ethanol and gaseous nitrogen to observe the atomization characteristics of round turbulent liquid jets. However, enhanced droplet formation was observed only with tests involving 6 MPa chamber pressure due to reduced liquid-gas density ratio effect [3, 76, 158]. In this study, we address issues on relative velocity effect (between liquid and gas streams) and internal liquid turbulence (as a function of liquid injection velocity) for which a constant chamber pressure of 6 MPa is assumed in all our simulations, unless otherwise stated. Since we are concerned with axi-symmetric simulations with detailed breakup modeling, no test cases exhibiting helical wave instabilities or any asymmetry are chosen. Instead, from the available experimental observation with axi-symmetric propagation of instabilities which are prone to disintegration due to increased gas pressure or turbulence are considered. In this spirit, three numerical computations reported as tabulated in Table (3.1).

Table 3.1 List of test cases for validating the LES/VOF modeling approach

Liquid Velocity (m/s)	**Gas Velocity (m/s)**	**Relative velocity (m/s)**	**Reynolds number (Re)**	**Gas-Weber number (We_g)**
20	*0*	*20*	*30000*	*268*
20	*20*	*0*	*30000*	*268*
5	*0*	*5*	*7500*	*16.8*

3.4.1 Interpretation of results

Various mechanisms have been proposed to explain drop formation from a freely issuing liquid jet in still or moving gases [11, 158-160]. In the co-axial flow regime, low gas velocities give rise to flapping of liquid jet leading to bag-type breakup mechanism [11, 159]. At higher relative velocity ratios, a stripping mechanism occurs on the surface of the liquid jet and drop formation occurs via a series of instabilities. Hoyt and Taylor [80] noticed that similar stripping phenomenonlogy occurs even when a liquid jet is moving in still atmosphere. The drop sizes, on both occasions, were observed to decrease with the increase in velocity ratio between the two phases. The primary wavelength set by the shear instability has been identified to play a key role in deciding the nature of disintegration [11, 80]. Specifically, Marmottant et al. [159] identified that following the onset of primary, shear instabilities liquid surface protrusions are accelerated in two stages viz., a primary transverse modulation and an azimuthal modulation, the later resulting in elongated ligaments protruding into the gas medium. This criterion was achieved by increasing the relative velocity between the gas and liquid phases. With lower relative velocities leading to wavelengths comparable to that of the jet diameter, only axisymmetric wave formation was observed. From their experiment, they concluded that the formation of azimuthal ligaments indeed occurred when the wavelength of primary instability was lower than the jet diameter. The shear-wave Kelvin-Helmholtz instabilities generated by the conditions generated by three cases proposed, are calculated according to the equation

$$\lambda_{KH} = \frac{2\pi\sigma\left(\rho_l + \rho_g\right)}{\rho_l \rho_g \left(U_g - U_l\right)^2} \tag{3.78}$$

With no-coflowing gas components, $U_g = 0$, the primary wavelength generated by the liquid jet at $U_l = 20$ m/s and 5 m/s correspond approximately to $6.5e^{-06}$ m and $1.0e^{-4}$m respectively. In the case of co-flowing gas stream with equal magnitude as that of the liquid velocity, the primary shear-instability is calculated based on vorticity-layer thickness (Ψ_g) in the gas stream, as well as the density ratio between the liquid and gas phase as

$$\lambda_1 = \varphi\left(\frac{\rho_l}{\rho_g}\right)^{\frac{1}{2}}\left(\psi_g\right) \tag{3.79}$$

where φ is a constant = 1.2 based on experiments of Marmottant et al. [159]. The vorticity thickness scales as ratio of $(\upsilon_g / U_g)^{1/2}$ and given a turbulent profile for the gas jet emanating from the nozzle, the vorticity thickness is calculated at the gas inlet as

$$\psi_g = \frac{U_{\max} - U_{\min}}{\left.\frac{dU}{dy}\right|_{\max}} \tag{3.80}$$

Using the relations above, we compute the primary instability generated by the co-flowing gas stream as $\lambda_1 \sim 1e^{-06}$m. In all the three occasions, the primary instability wavelength is lower than the inlet liquid jet diameter. Since, our present formulation is axi-symmetric, this computation serves as a verification to see if indeed ligament formation occurs with the current set of parameters. In the event that the current parameters do not comply with the low wavelength criterion in comparison with the jet diameter, the observations would then highlight wave protrusion rather than any ligament formation process. Adding, the experimental observation by Mayer et al. [158] indicated that with the current set of parameters fiber breakup mode was obtained. Interestingly, even a low Reynolds number liquid jet under sufficiently high Weber numbers can undergo disintegration by fiber-stripping mechanisms [11, 158]. The process of ligament and drop formation has been identified to occur due to the amplification of surface waves on the surface of round turbulent liquid jets [79, 80, 159, 160]. Researchers concluded that a growing surface wave, a disc in three-dimensional sense, is associated with Rayleigh-Taylor type instability and that the ligament formation occurs from the radially expanding sheets. Furthermore, the ligament generation process was observed to possess a directional preference [159]. Although the true three-dimensionality of unstable liquid jet disintegration has been discussed by several authors, we limit our current study to an axi-symmetric configuration, taking into account the computational cost estimates for performing a full three-dimensional simulation.

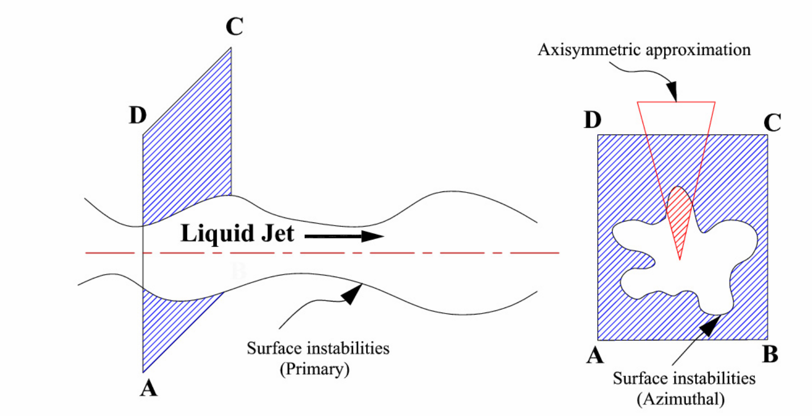

Figure 3.9: Primary and azimuthal perturbations. The axi-symmetric assumption can model only instabilities along the primary direction while rotational instabilities are compromised

Hence, our results can predict ligament formation in an averaged sense considering the axi-symmetric approximation but cannot predict the three dimensional wave growth leading to rim expansion with inherent Rayleigh-Taylor instabilities and subsequent breakup of droplets. This effect is illustrated in Fig. (3.9).

3.4.2 Results

For discussion and post-processing, simulation results were exported from openFoam framework into Fieldview software using *foamToFieldview9* tool available in openFoam [144].

The transient evolution of the turbulent liquid jets discharging into gas chamber under the different conditions proposed is shown in Fig. (3.10). With a relative velocity of 20 m/s, short wavelength shear wave instabilities are well captured as shown in Fig. (3.10(a)). Observe from Fig. (3.10(a)), that the presence of wrinkle like features on the jet surface helps promoting the expulsion of large liquid elements thereby enhancing liquid-jet surface instability [45]. From the numerical simulations, two major types of breakup mechanisms similar to the observations of Sallam et al. [160] are concluded: ligament tip breakup and ligament base breakup. Conforming to the current parameters, the former mechanism was predominant. Whenever, this mode was observed, it resulted due to a sequence of ligament growth, stretching and destabilization processes. The later mechanism, ligament base breakup, was observed less frequently.

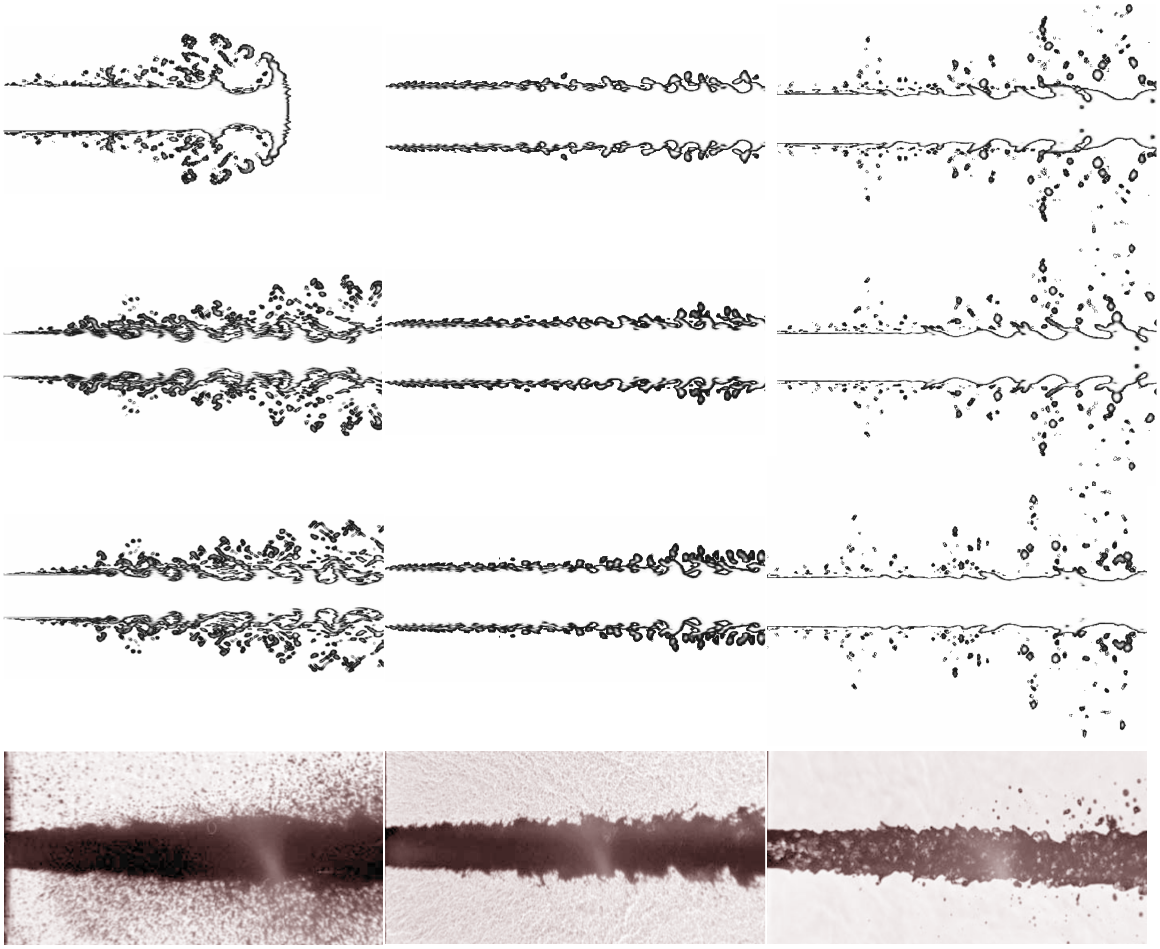

(a) (b) (c)

Figure 3.10: Transient disintegration process of liquid ethanol with (a) inlet velocity of 20 m/s into a stagnant nitrogen medium (b) inlet velocity = 20 m/s and a co-flowing nitrogen gas at 20 m/s (c) Inlet velocity = 5 m/s into a still gas medium. In all the three cases, the chamber pressure is maintained at 6 MPa. (Flow is from left to right)

With a relative velocity of 20 m/s, Fig. (3.10-a), different types of eddy interaction with the detached liquid fragments in the vicinity of the liquid-gas interface were observed. Figure (3.11) depicts the local flow structure interaction with the detached fragments.

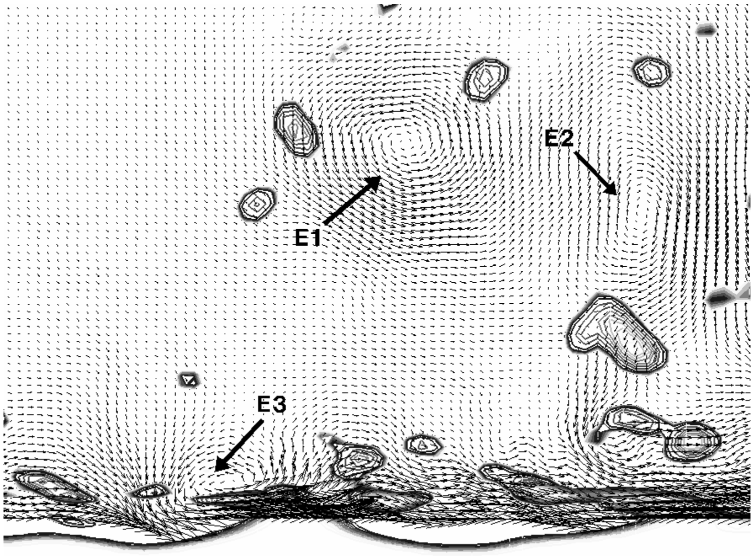

Figure 3.11: Capturing eddies in the vicinity of liquid-gas interface reveals highly complicated interaction phenomena between the disintegrated ligaments and the local flow field.

Observe from Fig. (3.11) that eddies formed in the close vicinity of the interface (E3) are entrained into the low pressure zones generated by ligament detachment process. The continued influence of the vortex propagation can be seen as E1 in Fig. (3.11). Simulation also indicated reattachment of several disintegrated ligaments on to the main core due to the localized pressure depression.

Introducing a parallel co-flowing gas stream of equal magnitude resulted in the suppression of liquid jet disintegration as seen in Fig. (3.10(b)). As the gas jet expands downstream, it penetrates into the liquid surface. The free expansion of the gas jet is inhibited by the presence of liquid jet and similarly the expansion of the liquid jet is arrested by the presence of a co-flowing gas stream [11, 158, 159]. The minimal activity of the radial expansion process of the liquid jet results in low radial-velocity gradients near the liquid-gas interface, subsequently suppressing shear instabilities.

With a low velocity jet emanating into still gas medium, as shown in Fig. (3.10-c), long-wavelength instabilities are detected. Decreasing the average velocity of the liquid jet leads to a decrease in shear rates near the liquid-gas interface which in turn reflects on the transport rate of the vortices away from the liquid core. The ligament distortion effects owing to their interaction with the localized eddy dynamics are distinctly visible in Fig. (3.10-c). Figure (3.12) shows interaction of local eddies with the stretching ligaments leading to drop formation [132, 165].

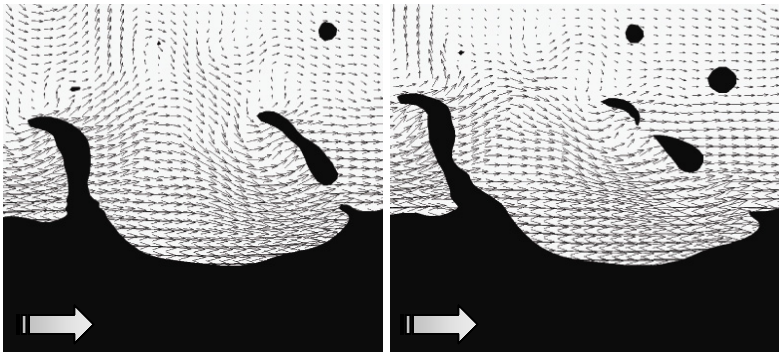

(a) (b)

Figure 3.12: Proximity analysis of the ligament dynamics for the low velocity liquid jet. Ligaments are stretched and undergo destabilization leading to disintegration from the primary liquid core. Note the varying drop size arising from the ligament due to capillary forces. Figure (a) and (b) are taken at 4μs separating them.

Interplay of aerodynamic and turbulent forces generate a diverse distribution of droplet sizes which are further modified by the surface forces of the droplets often referred as the secondary breakup mode. The droplet breakup modes and size distribution in the computational domain is visualized in Fig. (3.13).

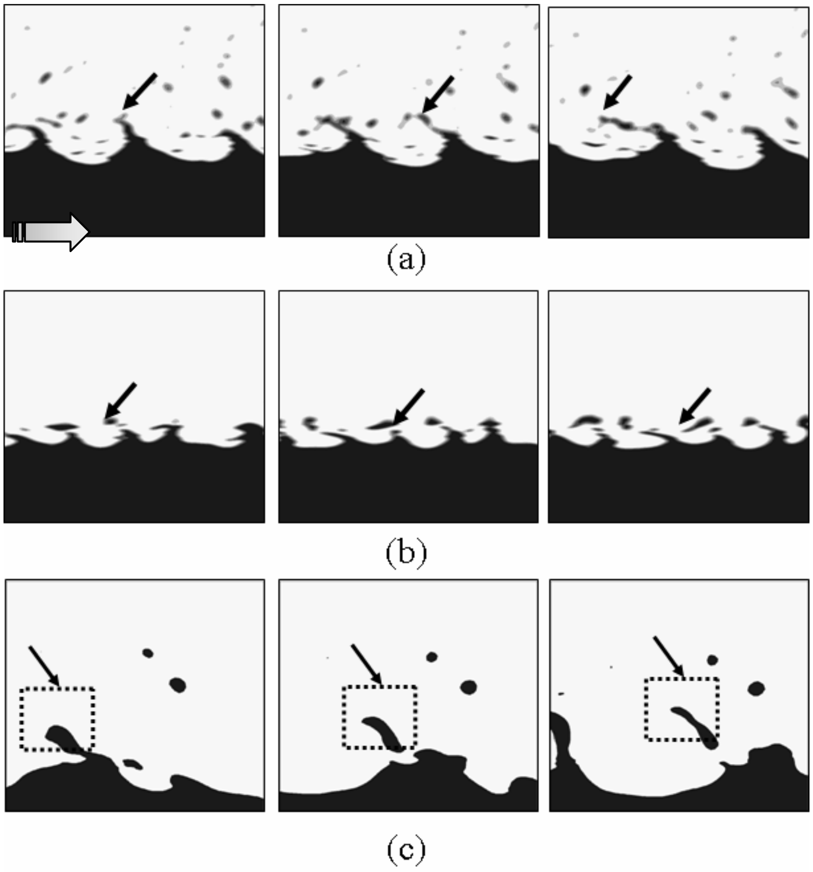

Figure 3.13: Droplet dynamics in 3 different injection conditions ($U_{rel} = U_l - U_g$) (a) With U_{rel} = 20 m/s, presence of slender ligaments with distinct tip breakup (b)U_{rel} = 0 m/s suppression of disintegration clearly visible (c) U_{rel} = 5 m/s: formation of large droplets and their deformation observed. As indicated, flow is from left to right.

From the detailed investigation of the disintegration process, a schematic of the drop generation process by the action of aerodynamic, surface, pressure and turbulent forces is constructed (Fig. (3.14)). As detailed in the figure, the action of surface tension and gas pressure forces dictate the nature of breakup and the drop size distribution [160, 161, 165].

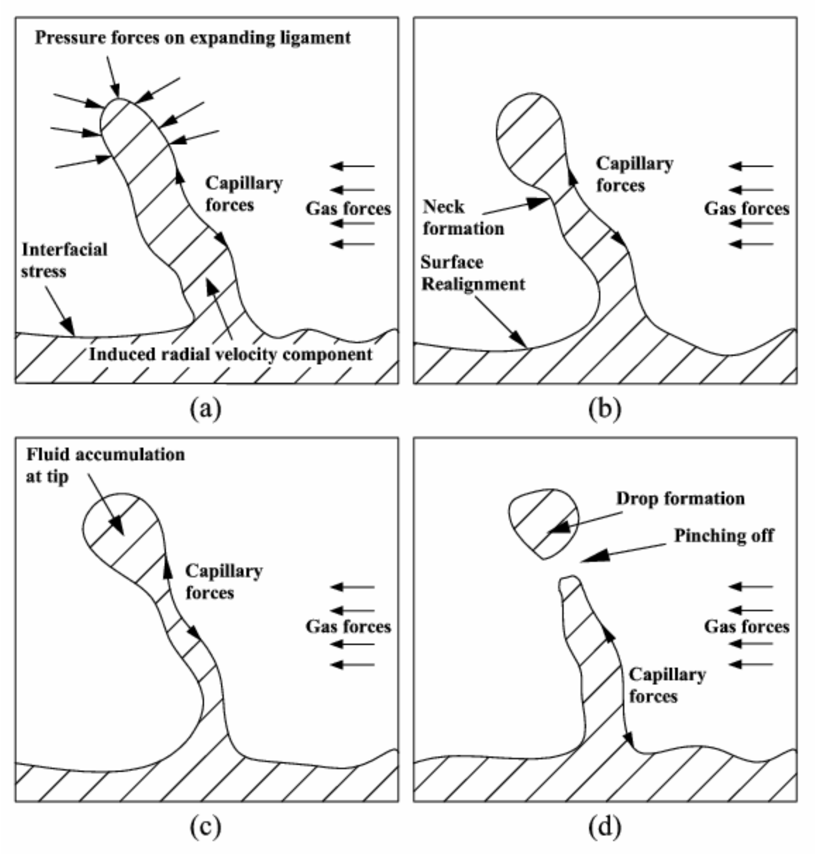

Figure 3.14: Drop formation from an expanding ligament structure

A comparison of the surface wave instabilities as a function of relative velocity of the liquid jet is shown in Fig. (3.15). Formation of short wavelength instabilities at higher relative velocities to longer wave features in low injection (relative to gas) velocity can clearly be distinguished from Fig. (3.16) [88, 163, 164].

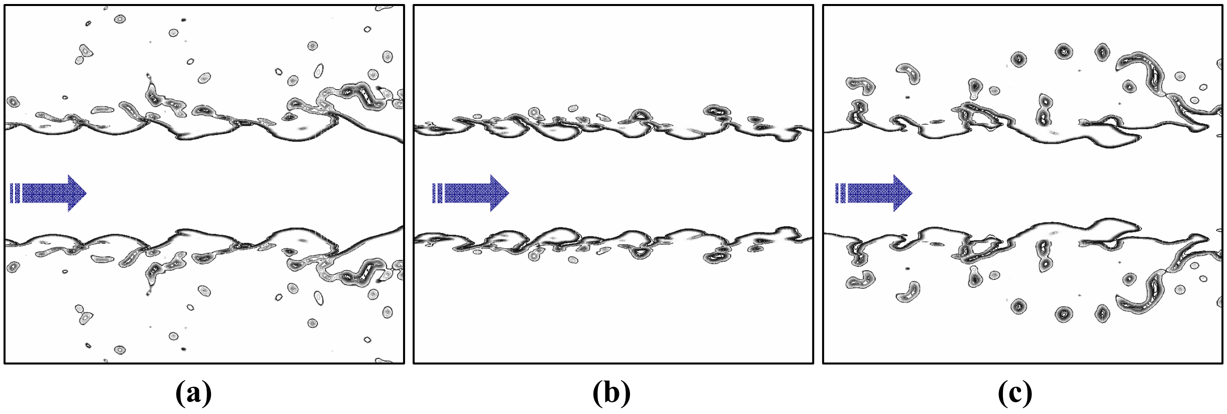

Figure 3.15: (a) U_l = 20 m/s, U_g = 0 m/s - Depiction of short wavelengths in the atomization regime (b) U_l = 20 m/s, U_g = 20 m/s: Smaller shear instability waves generated with co-flowing turbulent gas streams. Note the suppression of ligament growth when gas stream of equal magnitude is supplied parallel to the liquid bulk flow. (c) U_l = 5 m/s, U_g = 0 m/s: Presence of long wavelength instability.

For assessing the influence of injection parameters on the disintegration process, statistics of ligament thickness, their inclination with the parent liquid core are presented. Figure (3.16(a)) shows the relevant ligament parameters used in the discussion, while Fig. (3.16(b)) shows the variation in ligament orientation distribution in the three cases discussed previously.

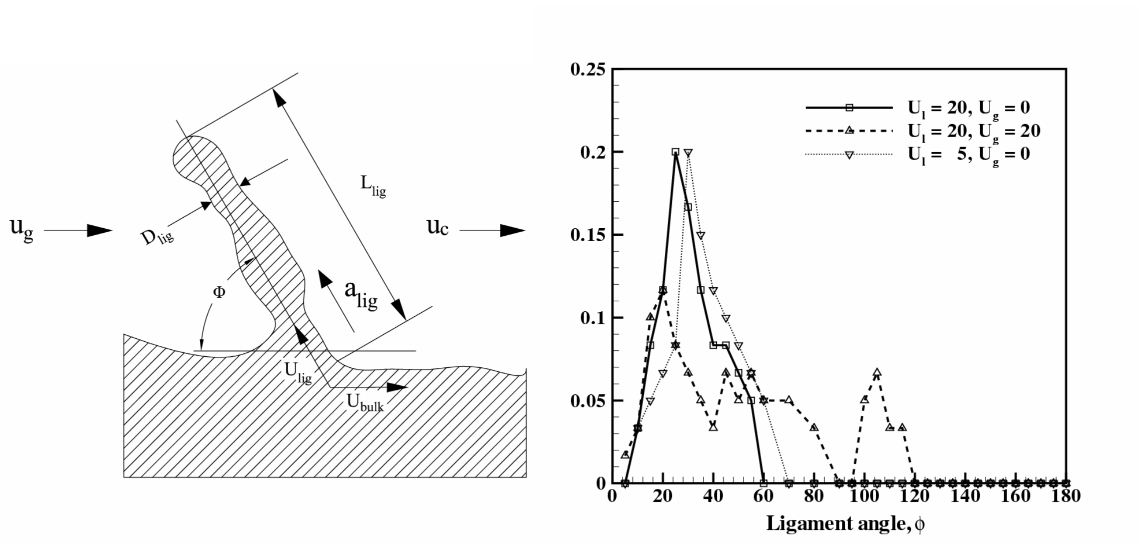

(a) (b)

Figure 3.16: (a) Ligament development characteristics (b) Probability density function plot of ligament size distribution in the domain for different relative velocity between liquid and gas streams

The power energy spectrum taken from the flow field generated by the LES model shows the matching of the Kolmogorov -5/3 spectrum at higher wave numbers [152, 153] (Fig. (3.17(a-b))).

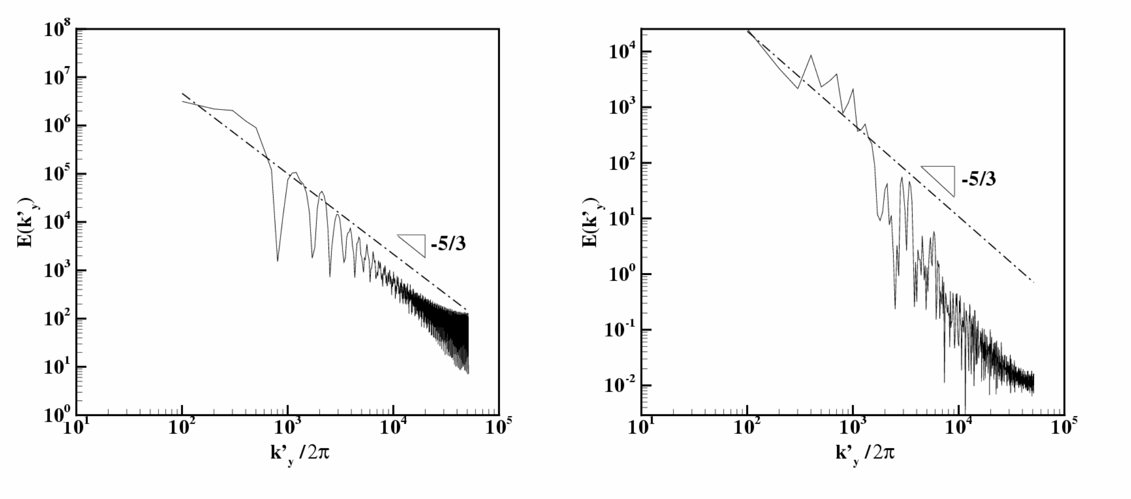

(a) (b)

Figure 3.17: Energy spectrum distribution at location X/D = 5 along the radial-direction taken for (a) first component of velocity (b) second component of velocity generated by liquid and gas injection at same velocity. Kolmogorov -5/3rd slope is shown in the panels.

3.4.3 Effect of turbulence models

The presence of turbulent effects adds a new dimension of complexity to the existing confusion in free-surface flow modeling [152, 153]. Certainly, inclusion of turbulence effects requires elaborate computational effort [152]. In order to compromise for accuracy and simulation expense, the necessity for including the turbulence effects needs to be addressed. In this section, one of the test cases simulated above in Section (3.4.2) is recomputed under three different scenarios. First, the present LES model implementation described in Section (3.4.2) is retained. Following this, a laminar assumption devoid of any turbulence modeling is processed. In the third case, a two-equation eddy viscosity type turbulence modeling is carried out [152]. The grids for all the cases are kept constant. From literature, it is easy to recognize that the computational effort decreases from LES > RANS > Laminar assumptions. The results obtained from the simulated three cases are detailed in Fig. (3.18).

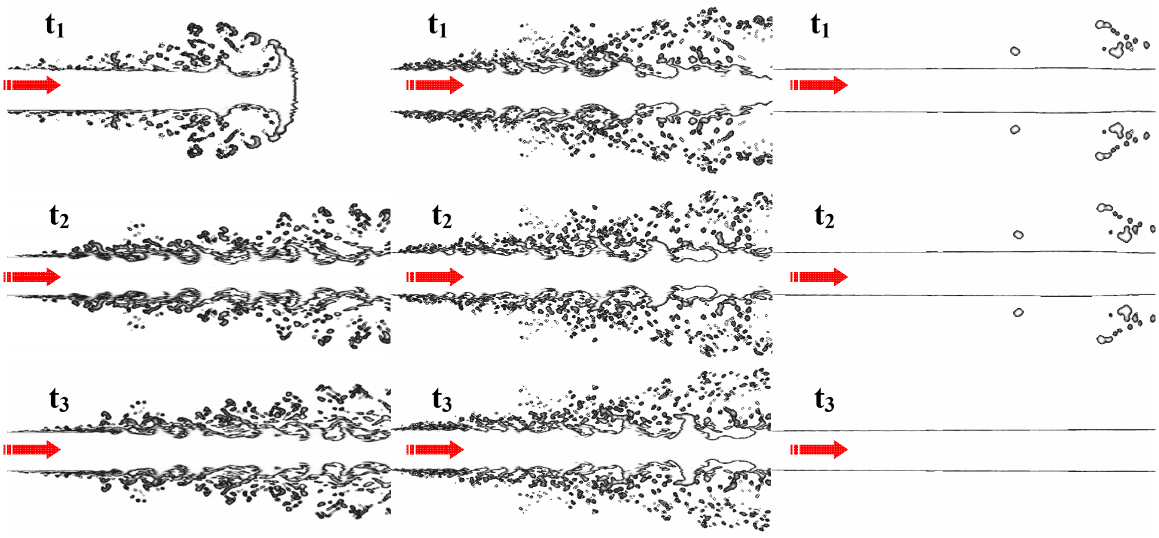

(a) (b) (c)

Figure 3.18: Breakup visualization at different instants t1, t2 and t3 with (a) LES turbulence model (b) Laminar breakup model (c) RANS turbulence. Flow is from left to right.

Comparing Fig. (3.18(a)) and Fig. (3.18(b)), the effect of turbulence model is evident. The stripping up of liquid fragments is delayed with the inclusion of dissipative turbulence effects while drop formation occurs immediately near the nozzle exit using laminar mode. In the absence of any turbulent viscosity, the laminar model over-predicts breakup as compared to the LES driven model. The case with RANS based framework offers a completely different perspective. The eddy viscosity generated by the model suppresses any liquid-gas surface instabilities and as a result suppresses drop formation. Although, some non-linearities in the surface exist, they were dissipated as the simulation progressed. Flow structure prevailing in a laminar and LES - turbulence based modeling is shown in Fig. (3.19(a)) and (3.19(b)).

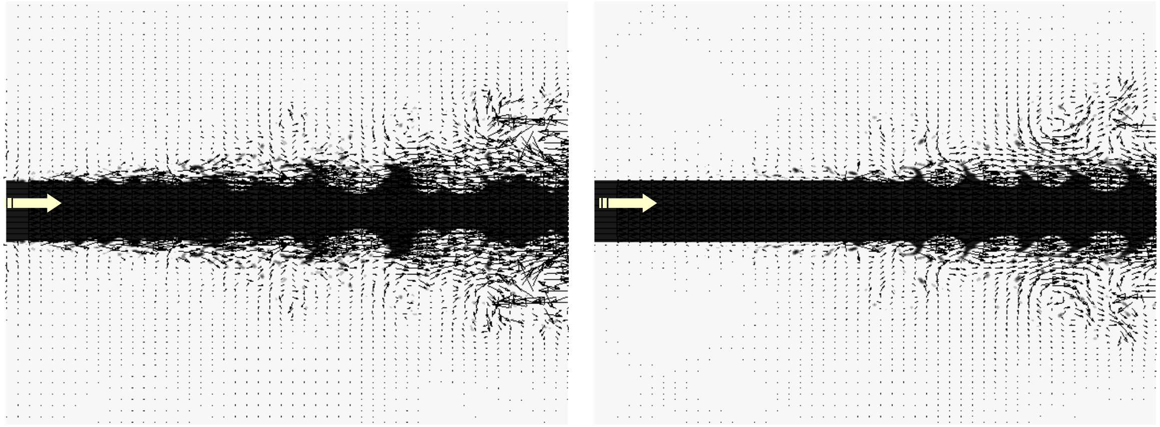
(a) (b)

Figure 3.19: Flow structure development in a (a) laminar breakup model (b) Turbulent breakup model with LES turbulence assumptions

The flow structure is represented by contours of the liquid fraction on which the velocity vectors are superimposed. Simulations taken at the same instant displayed in Fig. (3.19), reveal vital statistics of the flow features generated by neglecting turbulence effects and later by modeling the sub-grid scale viscous effects. The flow structure is more distorted in the case of the laminar flow while dissipative effects blatantly dominate the first few diameters in the disintegration of liquid jet breakup. The simulation clearly indicates that the influence of turbulence is decisive in predicting the breakup behavior of liquid jets [166]. Use of LES models are expensive yet yield decent results based on the mesh configuration. Laminar models over predict breakup in the absence of turbulence effects and hence can be used in systems with lesser turbulent effect composition [152]. The RANS model was observed to deliver the most dissipative effects on free-surface liquid jet disintegration, Fig. (3.18(c)). With the knowledge of implementing a Volume-of-Fluid based methodology for simulating breakup behavior of liquid jets, the preceding section is devoted to numerical studies concerning the breakup of modulated liquid jets.

3.5 Numerical simulation of modulated liquid jets

The results detailed in Section (3.4) provides a good measure of confidence in using a CICSAM based interface capturing method for simulating the disintegration behavior of liquid jets. Following the numerical description of round turbulent liquid jets disintegration, the breakup of forced liquid jets in the primary breakup region is addressed here.

3.5.1 Boundary Conditions

The computational domain with relevant boundary conditions used in the numerical simulation is shown in Fig. (3.20). Since the primary interest lies in observing the liquid jet behavior in the nozzle exterior, no internal portion of the nozzle domain is included. However, it is to be reminded that the nozzle interior regions play an important role in determining the disturbance levels of exiting jets [2, 3, 48, 88, 53]. The simulation domain extends 2.4 mm × 1.6 mm in the X (axial) and Y (radial) directions respectively. The diameter of the liquid inlet orifice is 0.2 mm. The simulations are performed in an axi-symmetric fashion with one cell thickness extending in the azimuthal direction. Periodic boundary conditions are assumed on either side of the faces. Pressure outlets representing the free stream conditions are imposed at the top and downstream boundary faces. The reference pressure in the system is set to 1 bar, standard pressure value at sea level. No-slip conditions are imposed on the wall boundaries. Velocity inlet conditions indicating the issuing liquid jet bounded by wall conditions are assumed.

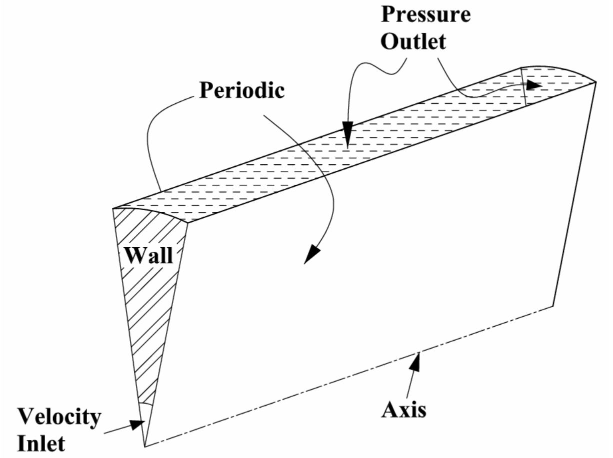

Figure 3.20: Schematic of the computational domain used in the simulation with relevant boundary conditions.

3.5.2 Simulation parameters

In the present computations, the relevant perturbation parameters viz., modulation amplitude and frequency, are applied at the velocity inlet in addition to the specification of mean jet velocity. In specifying the liquid jet velocity, an parabolic velocity profile distribution is assumed since, in reality, a finite boundary layer exists and results in a parabolic velocity profile distribution in case of a laminar regime. Several studies [2, 3, 48, 88] indicate that the velocity profile distribution affects the radial spread of the liquid jet downstream and hence its disintegration characteristics. This fact is supplemented by the fact that the dynamics of induced vorticity layers changes appreciably when the liquid emerges into a state of free shear. The injection velocity of the liquid jet at the inlet is held constant at $\overline{U}$ = 20 m/s throughout the simulation unless otherwise stated. The liquid jet properties used in the current study match ethanol properties, while the ambience is assumed to be filled with air. Standard density and viscosity properties of ethanol and air at STP have been assumed in the current simulation. The surface tension of ethanol in air is assumed to be 0.0225 N/m. Notice that the Reynolds number (Re) for the issuing jet corresponds to a value ~ 2600 which is just above the Laminar regime (< 2300) [1, 2]. The importance of resolving the turbulent fluctuations was earlier established in Section (3.4.3). Since the flow Reynolds number describes a transition regime, turbulence effects are ignored. Comparing the present regime Re = 2600 and gas Weber number $We_g = 1.1$ with Table (2.1), clearly indicates that the liquid jet is clearly in the Rayleigh regime of disrtuption with axi-symmetric growth and evolution.

3.5.3 Results and Discussions

3.5.3.1 Verification of scaling laws in modulated jets

As experimentally observed [113, 114], use of scaling parameters such as the Strouhal number and modified Weber number in combination with the modulation amplitude gives a strong indication on the nature of observed liquid jet morphology. Since, a numerical methodology for simulating the jet behavior is employed, to obtain faith in the numerical studies verification of scaling laws using a numerical approach is carried out in the following section. Different liquids with different material properties are sprayed under a given scaling parameter and we observe the regimes of liquid structure development. A computation table indicating the selected parameters and associated scaling parameters is provided in Table (3.2).

In the present study, two discrete frequency values (f = 50 KHz, 100 KHz) in the given range of modulation amplitudes (ε = 0.1, 0.2, 0.3) have been chosen to study their effect on the disintegration of round liquid jets. In the high frequency range, a value of ε = 0.4 has been tested. The wavelength of the modulations imposed on the liquid jet are computed as 0.0004 m, while the computational domain extending 0.0024 m is sufficient enough to take into account 6 cycles and more (with higher frequency) of oscillatory effect. In doing so, any non-linear effects that propagate with the oscillations are provided sufficient spatial and temporal resolution to mutually interact within the domain and any consequence can still be modeled. The following section details the results of numerical simulations and arguments concerning the formation of structures and the associated interface dynamics are discussed.

Table 3.2 Table of parameters used in the scale testing of modulated jets

Liquid	**Modulation amplitude (ε)**	**Modulation frequency (KHz)**	***Sr***	***We_w***
Ethanol	*0.1, 0.2, 0.3*	*50*	*1.57*	*5612*
		100	*3.14*	*2806*
Water	*0.1, 0.2*	*50*	*1.57*	*2222*
		100	*3.14*	*1111*

The first numerical test case presented here illustrates the transient evolution of liquid jet ethanol injected for a $Sr = 1.57$, $We_w = 5612$ and different $\varepsilon = 0.1, 0.2, 0.3$. These values depict a system with a Strouhal number, $Sr = 1.57$. The applied velocity perturbation creates fast and slow sections along the axis of each liquid shell [109, 110]. This results in accumulation of mass at finite spacing as defined by the wavelength of the superimposed perturbation. Computations with $\varepsilon = 0.1$, Fig. (3.21), shows generation of surface waves and bulging of the liquid jet with finite periodicity. Experimental observations [115] under this regime confirm our test results.

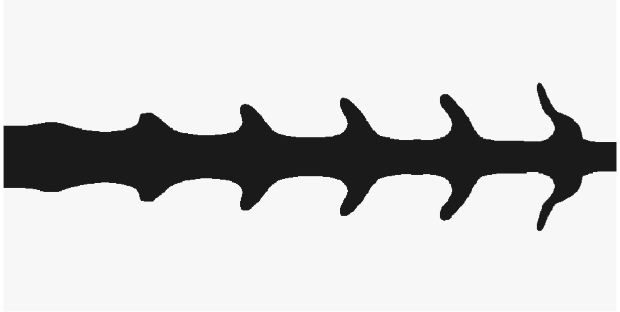

Figure 3.21: Plot of Volume fraction of liquid ethanol injected into air: $Sr = 1.57$, $We_w=5612$, $\varepsilon = 0.1$.

From Fig. (3.21), it is clear that the evolved discs are bent backwards due to the drag forces of the medium. The growth of the discs from the surface of the liquid jet is a strong function of the Reynolds number and the fluctuation amplitude [113, 115].

The transient variation in axial velocity components as the jet proceeds downstream induce radial velocity components which intrude into the gaseous medium. At this juncture, the interaction of aerodynamic forces with the capillary forces is crucial in deciding the fate of the protrusions [132, 133]. With increase in fluctuations to $\varepsilon = 0.2$, Fig. (3.22(b)), formation of ligament due to radial expulsion results in drop formation. The process intensifies with further increase in ε to 0.3 as seen in Fig. (3.22(c)). The liquid jet core narrows due to mass conservation effect [75] and a bell like structure is obtained. In all the three cases, however, the discs, and bell formation are directed upstream.

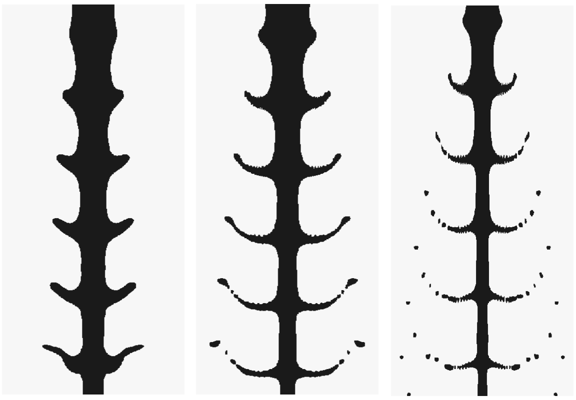

(a) (b) (c)

Figure 3.22: Numerical simulations with Sr = 1.57, We_w = 5612 (Test liquid ethanol) (a) ε = 0.1 (b) ε = 0.2 (c) ε = 0.3 (Flow is from top to bottom)

The transient process of stretching and thinning of ligament like structures and their interaction with shear vortices leading to drop formation is shown in Fig. (3.23(a)). The tip of these liquid sheets extends into the gas domain inducing vorticity components as clearly seen in Fig. (3.23(a-i)). The continuing interaction of eddies with the liquid tip results in instability similar to the Rayleigh-Taylor type [79, 160]. The instability propagates along the sheet and at this juncture, the aerodynamic forces overcome the surface energy of the liquid disc [165]. The detachment of liquid drops from the parent ligament, as observed in Fig. (3.23 (a-iii, a-iv)), is enhanced by surface tension.

As seen from Fig. (3.22), the instability of the liquid discs is enhanced by the increased modulation effect, moving from Fig. (3.22(a)-(c)). The disc thickness is reduced due to increased radial fluctuations. Another striking feature that demands attention is the alignment of the disc with respect to the flow direction. The liquid bulk forming thick sheets, extending into the gas interface, are not bent backwards. Rather, the alignment is almost orthogonal to the liquid flow direction. This feature is not seen in the immediate vicinity near the injector rather traversing a few nozzle diameters downstream.

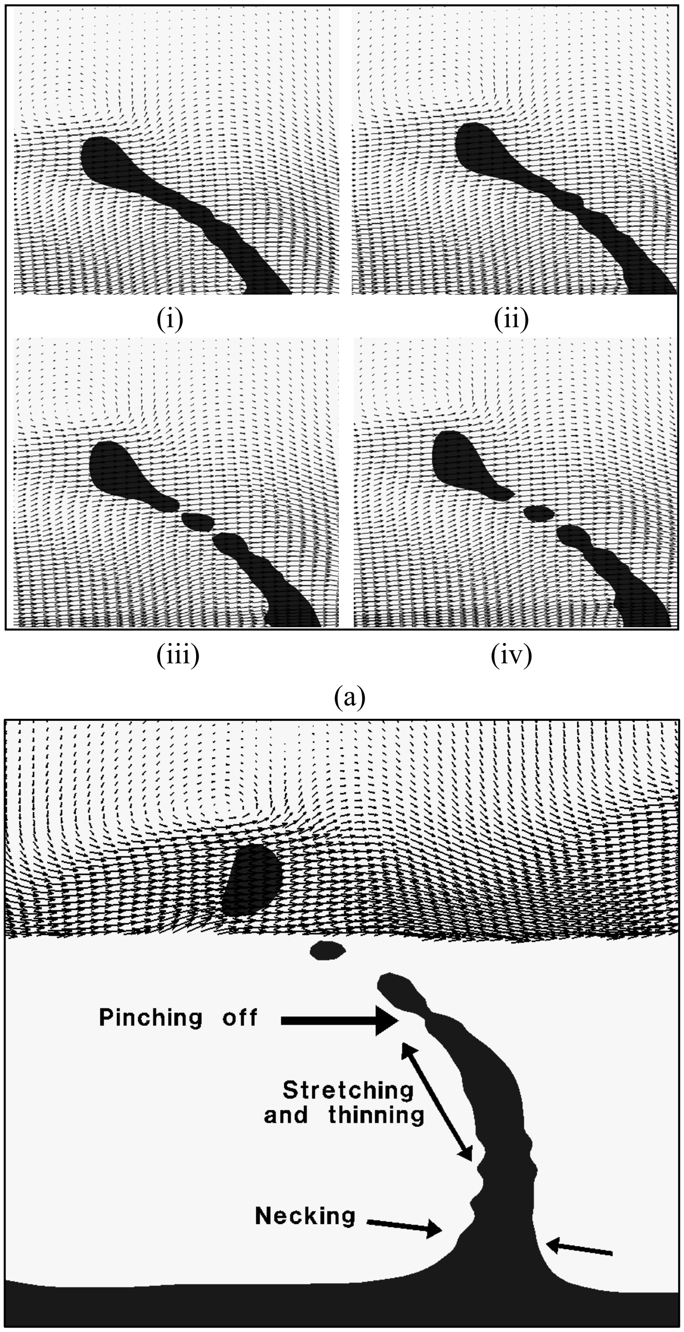

(i) (ii)

(iii) (iv)

(a)

(b)

Figure 3.23: (a) Transient ligament and drop formation with *Sr* = 1.57, We_w= 5612, ε = 0.2 using ethanol (b) Capturing pinch off mechanism at the edge of the disc occurring resulting in an overall upstream directed bell structure.

The mechanism of drop formation from a radially expanding finger like liquid structure is shown in Fig. (3.23(b)). Due to the effect of surface tension, the liquid surface tends to pull back the extending ligament leading to accumulation of fluid near the tip of the liquid filament [133, 165, 167]. Thinning of the cross wise extending ligament occurs due to drag forces which pull the ligament away from the jet surface to which it is attached, while the surface tension force acts to stabilize this surface instability [132, 133, 165, 166]. The interaction of surface forces with the aerodynamic forces is captured well by the numerical model. The effect of grid resolution plays a major role in reducing numerical diffusion and retaining sharp curvatures [166].

The present study is based on a single fluid model with interface construction performed only in regions where a liquid-gas interface exists. Plotting the overall flow field existing in the domain would help us resolve the magnitude of flow field variation induced by the high density liquid flow in a low density gas medium. In essence, we present a contour plot of axial-velocity component in the fluid domain, Fig. (3.24).

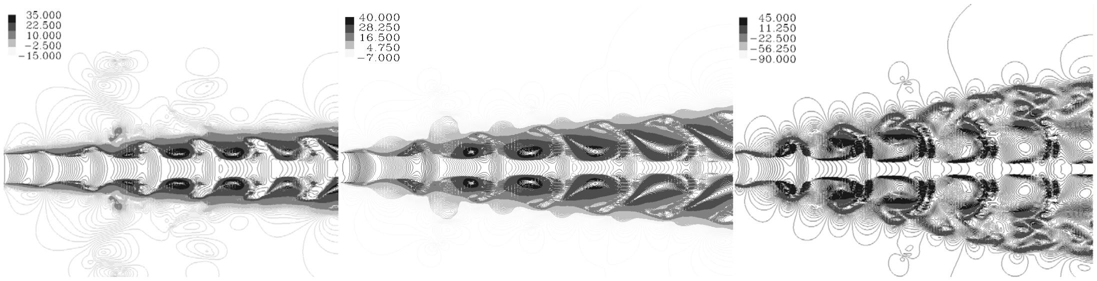

(a) (b) (c)

Figure 3.24: Contour plot of axial components of velocity for *Sr* = 1.57, We_w= 5612 (liquid: ethanol) (a) ε = 0.1 (b) ε = 0.2 (c) ε = 0.3. (Flow is from left to right)

When the liquid jets expand in phase with the shear vortices, the ligaments are trapped in the vortex cores, leading to their separation from the expanding liquid sheet. Flow structure generated by the modulated liquid jet is shown in Fig. (3.25) for a given *Sr* and We_w. Observe from Fig. (3.25(a-c)) that the characteristics of coherent structures are modified palpably by changing the Strouhal number, which characterizes the spacing of vortex structures, while the modulation amplitude controls the radial expansion of the structures.

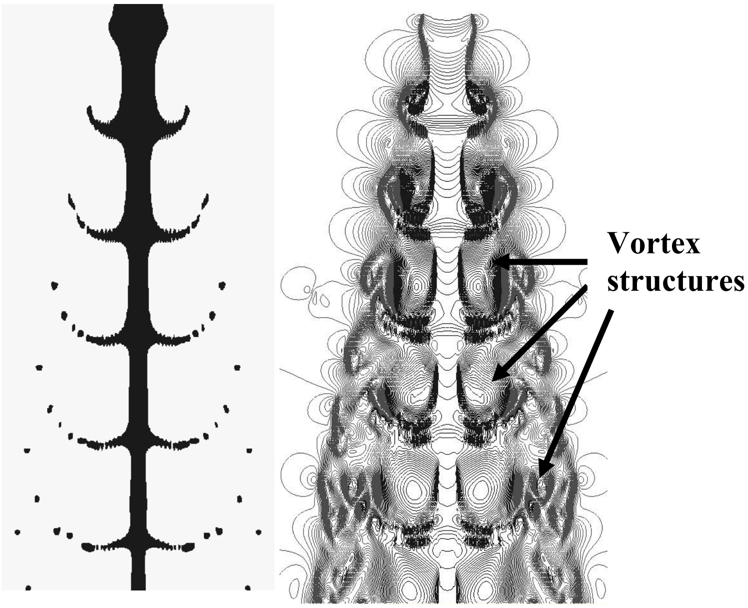

Figure 3.25: Flow structure generated by radially expanding and disintegrating liquid jets, $Sr = 1.57$, $We_w = 5612$, $\varepsilon = 0.3$. (Flow is from top to bottom)

Observe from Fig. (3.25), region of strong recirculation near the cusps formed by the modulated liquid jet. The axial velocity components are good representation of the existing local flow fields and the behavior of the liquid-gas interface. In the event that a strong recirculation zone is identified from the plot, we can conclude that this region can lead to increased pressure disturbances on the liquid bulk and based on its magnitude a breakup event can be closely monitored. Also, clearly note the localized region of highly transient flow field close to the liquid-gas interface. This is attributed to the fact that the given set of modulation parameters do not contribute to intensified radial spread and hence lesser influence on the gas entrainment dynamics.

Increased vorticity components prevail near the tip of the sheets which can be identified from the recirculating regimes in Fig. (3.25). Notice that as we proceed downstream, the plot indicates presence of vorticity components (recirculation zones) away from the central liquid core. These represent the shed-off vortices from the tip of the liquid sheet rim. They travel downstream, convected by the induced flow, and interact in a non-linear fashion with evolving recirculation regions. The identification of these vortex pairs is crucial in order to establish the path of low diameter droplets which get caught in these low pressure vortical structures. These shed-off gas vortices, on interacting with translating bigger droplets, induce stretching and destabilization due to shear, leading to secondary breakup phenomena [160, 165, 166].

We now double the modulation frequency, which effects in doubled Strouhal and halved modified Weber number. With $\varepsilon = 0.1$, very closely spaced liquid discs are observed in Fig. (3.26). The liquid disc like features are thicker as compared to those obtained with half the frequency.

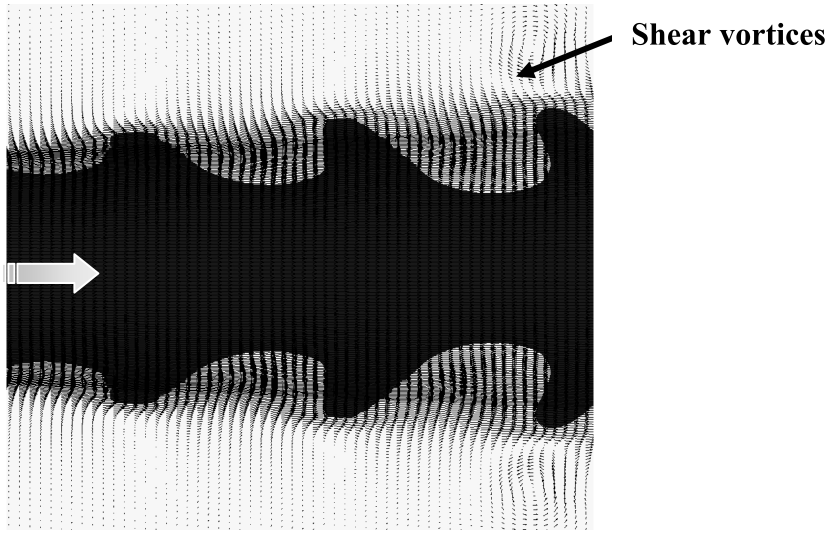

Figure 3.26: Velocity vectors near the growing liquid jet. Notice the small scale vortices near the rim of the disc due to shear generated by the liquid element intrusion into the gaseous medium. (Flow is from left to right)

The high frequency modulation results in bulging of liquid streams in close vicinity due to reduced imposed wavelengths. The surface wave amplification due to velocity modulation creates radial velocity components with less relaxation time for their spread. This shortened time period greatly helps the surface tension effects in distorting any radial propagation of instability [88, 159, 160]. The presence of a thicker rim as the jet proceeds downstream is due to the accumulation of liquid by the action of capillary forces. In the current simulation domain, no breakup of the liquid jet along the core or in the periphery was observed for the chosen set of parameters. However, moving into $\varepsilon = 0.2$, we notice in Fig. (3.27), a dramatic increase in drop formation behavior. Bell structure formation and strong liquid accumulation can be observed near the disc tips.

A detailed look in the vicinity of rim-mode breakup of the liquid sheet can be viewed in Fig. (3.27). Necking phenomenon [165] just before the event of pinch off can clearly be visualized in Fig. (3.27).

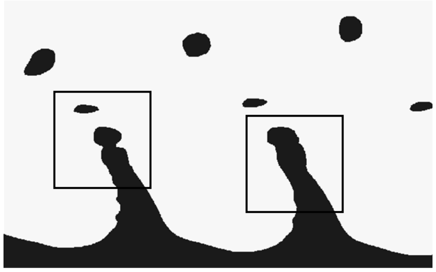

Figure 3.27: Disintegration at the tip of the disc for $Sr = 3.14$, $We_w = 2806$. (Flow is from left to right)

With ε = 0.3 (Fig. 3.28(c)), the modulation amplitude results in a dense drop formation process due to increased radial velocity contribution. Interestingly, at this amplitude the outer layer propagate much faster than the inner liquid core resulting in downstream directed bells. Evolution of spray morphology as a function of ε (constant *Sr* and We_w) is shown in Fig. (3.28).

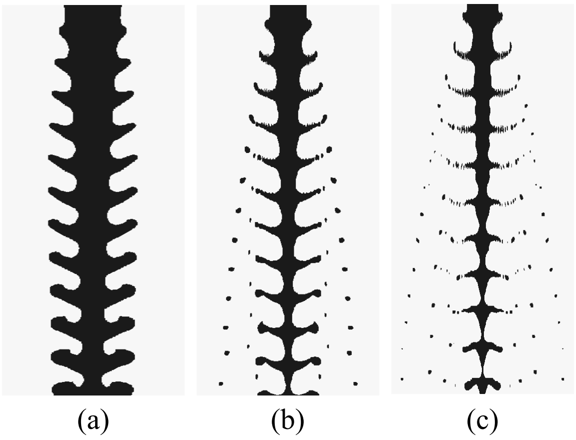
(a) (b) (c)

Figure 3.28. Generation of discs (ε = 0.1) and upstream directed bells (ε = 0.2), downstream directed bells (ε = 0.3) for *Sr* = 3.14, We_w = 2806 (ethanol). (Flow is from top to bottom)

The scaling parameters also dictate the formation of gas coherent structures which in turn dictate the nature of liquid structure generated by the modulated jet. The plot of axial-velocity components clearly indicates complicated flow structures as the liquid jet interacts with the surrounding gas domain downstream. As already discussed, there is a change in the orientation of the radially expanding liquid sheets and increased thinning of the liquid core along the axis [75]. Note that, the currently simulated parameters with increased modulation amplitude moves towards regions where downstream directed bells are formed (Figs. (3.24) and (3.28)). This is similar to the previous case where structures aligning towards downstream were observed. However, in the current scenario, the inclination of the liquid discs downstream is more predominant.

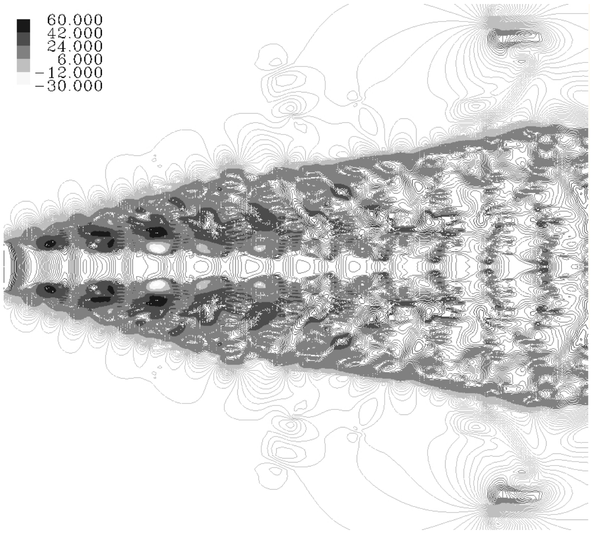

Figure 3.29: Contour plot of axial velocity components for high amplitude, high frequency regime corresponding to Fig. (3.28(c)). (Flow is from left to right)

The parameters opted for testing the current configuration penetrates into the downstream directed bell regime.

As the liquid jet traverses downstream, a redistribution of the internal energy of the liquid jet takes place depending on the extent to which the velocity profile of the liquid jet varies from the uniform velocity at the central core [75]. This redistribution process may create rigorous radial components by itself in addition to the superimposed modulation. In this concern, the viscosity of the liquid jet and the gas plays a vital role in determining the relaxation parameters [4, 88, 166].

A plot of velocity components along the central liquid jet axis is shown in Fig. (3.30). Increase in centerline velocity and the decrease in velocity around the edges is largely the result of the non-uniform aerodynamic pressure forces on the jet surface [165]. Classical aerodynamic theories of breakup are based on the concept that flow velocities in the radial direction are increased for the disc emerging from the liquid surface due to the acceleration of the gas over the tip of the liquid sheet [163, 164]. This results in a radial pressure drop across the sheet which causes an increase in the radial velocities near the liquid-gas interface. Over the depression present in the interface, a localized increase in pressure, combined with increased effects of surface tension, results in the necking experienced by the jet [165]. The laws of conservation of momentum result in an increased axial components due to thinning of liquid core between the extruded sheets resulting in low radial velocities. The non-linear interaction and uneven distribution of the pressure forces on the interface results in core breakup due to the action of surface tension which tends to minimize the surface energy of the liquid bulk [161].

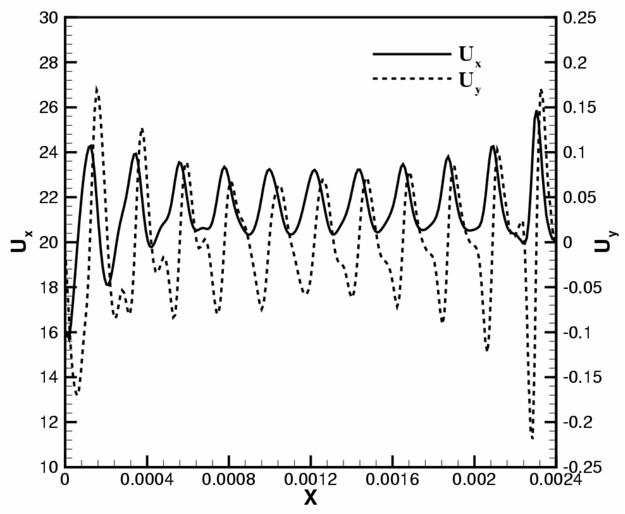

Figure 3.30: Plot of axial and radial velocity components along the central axis of the jet. Notice that for high thinning rates of the liquid jet at the center, the axial velocity increases rapidly as the jet interacts with uneven aerodynamic forces. *Sr* = 3.14, We_w = 2806, ε = 0.4.

To validate the scaling principles to obtain reproducible liquid structures using different liquids, a different liquid (water) is tested to under the same scaling parameters. Figure (3.31) shows the numerical results for water with comparison with ethanol under same scaling parameter (Sr).

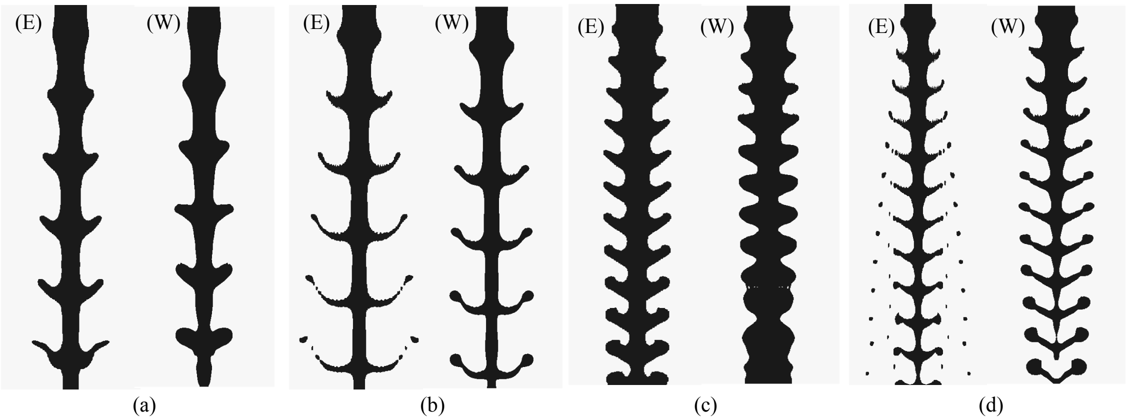

(a) (b) (c) (d)

Figure 3.31: Numerical simulations with same Strouhal number and same modulation amplitude produces similar reproducible structure using different liquids (E) ethanol and (W) water. (a) *Sr* = 1.57, $\varepsilon = 0.1$ (b) *Sr* = 1.57, $\varepsilon = 0.2$, (c) *Sr* = 3.14, $\varepsilon = 0.2$, (d) *Sr* = 3.14, $\varepsilon = 0.2$. (Flow is from top to bottom)

The effect of Strouhal number preserves the overall fluid structure while the modified Weber number (We_w) contributes to variation in disintegration characteristics among different liquids. Formation of discs is thicker with increased surface tension (of water) and this reflects in thicker ligaments during any occurrence of liquid jet disintegration [165]. Having performed a variety of simulation, we plot our simulated results against a non-dimensional map generated by Geschner [115].

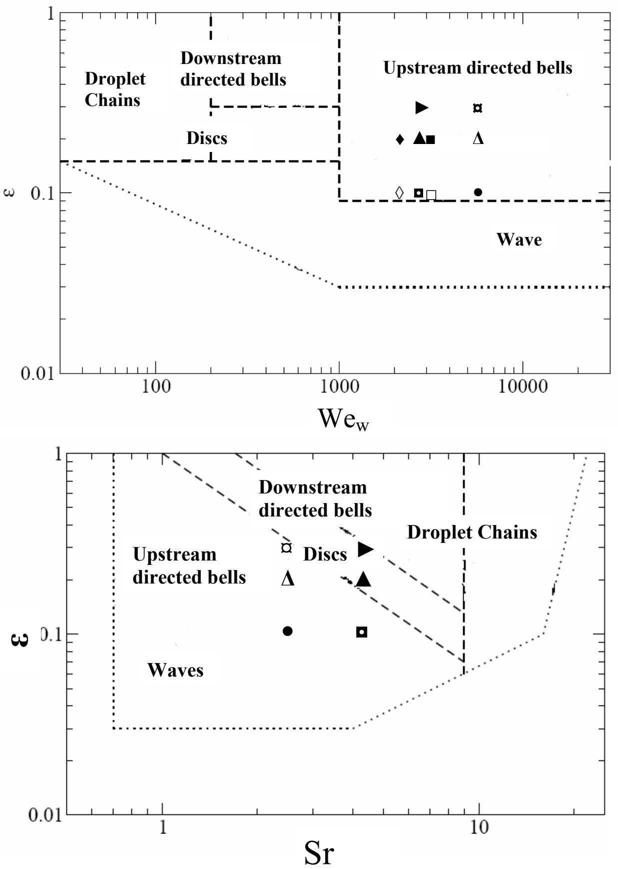

(a) (b)

Figure 3.32: Comparing our numerical simulations with the non-dimensional map [6]. Legend: Ethanol (●, Δ , ¤ , ◘, ▲, ►) Water (□, ■, ◊, ♦). Strouhal number for both liquids remain the same and hence no water symbol has been plotted over ethanol in (b).

Notice from Fig. (3.32) that most of our results are easily identifiable from the map below. Some inter-penetrating regions observed in the experiments relate well with our numerical results.

As simulated before, a variety of structure transitions are observed as the modulation amplitudes are increased under constant Strouhal and modified Weber numbers. The contours of liquid volume fraction presented in Figs. (3.24) and (3.28) indicates the influence of frequency in determining the spread of the jets. High frequency and high amplitude jets clearly result in higher disintegrated jet spreading. Maintaining specified modulation amplitude and reducing the frequency creates a smaller reduction in spread angle and more importantly affects the spacing of the protruding sheets. However, the modulation amplitude has a more profound effect on the jet disintegration as it affects the overall disintegration characteristics. Higher frequency perturbations lead to high non-linearity in the disintegration mechanism and potentially increases mixing between the gas and liquid phases.

3.6 Numerical Simulation of high-speed modulated liquid jets

From the literature review on the disintegration behavior of liquid jets, it is quite agreeable that large Weber number liquid jets have increased tendency to under go turbulent atomization. The modulation effect on large Weber number turbulent liquid jets has been previously utilized in obtaining percussive jets for corrosion removal from metal surface [29-31]. However, the jets emanating from such a scenario typically have high jet diameter so that a thick modulated liquid core, upon hitting the target surface, would enhance removal of metallic coatings. To reduce the jet core diameter and expedite the disintegration process, the jet diameter is reduced to 0.2 mm while maintaining a high speed injection of the liquid jet. The following numerical simulations of modulated high-velocity liquid jets reported in the preceding section were carried out to determine its potential in creating finely atomized sprays.

Three test cases are reported here are listed in Table (3.3) with relevant modulation parameters. For all the simulated cases, water is used as the simulation liquid with a surface tension of σ = 0.072 N/m. Further, the nozzle inlet diameter is assumed to be D = 0.2 mm and the ambient conditions involve air properties taken at STP.

Table 3.3 Test cases for simulating high speed modulated liquid jets

Case	**Mean Jet Velocity (m/s)**	**Modulation Amplitude**	**Modulation Frequency (KHz)**	**Strouhal Number**	**Modified Weber Number X 10^3**
1	*60*	*0.0833*	*15*	*0.15707*	*200*
2	*60*	*0.166*	*15*	*0.15707*	*200*
3	*80*	*0.5*	*15*	*0.1178*	*200*

With an inlet length scale of 0.2 mm and a mean liquid (water) jet velocity of 60 & 80 m/s, the Reynolds number is computed as 12000 and 16000 respectively. The gas based Weber number is of the order of 12.04 and 21.04 respectively. From the breakup map discussed in Chapter 2 and taking viscosity of water to compute the Ohnesorge number, these two liquid jets with the specified average velocity fall under the atomization regime [1, 2]. However, no clear description of the breakup length is available. Since turbulence effects are very critical in deciding the breakup behavior, Large Eddy Simulation turbulence modeling is utilized for providing the necessary dissipative effects. Details of the implemented LES model has already been presented in Section (3.3.1).

3.6.1 Boundary Conditions

The computational domain used in the current computation along with the boundary conditions is described in Fig. (3.33).

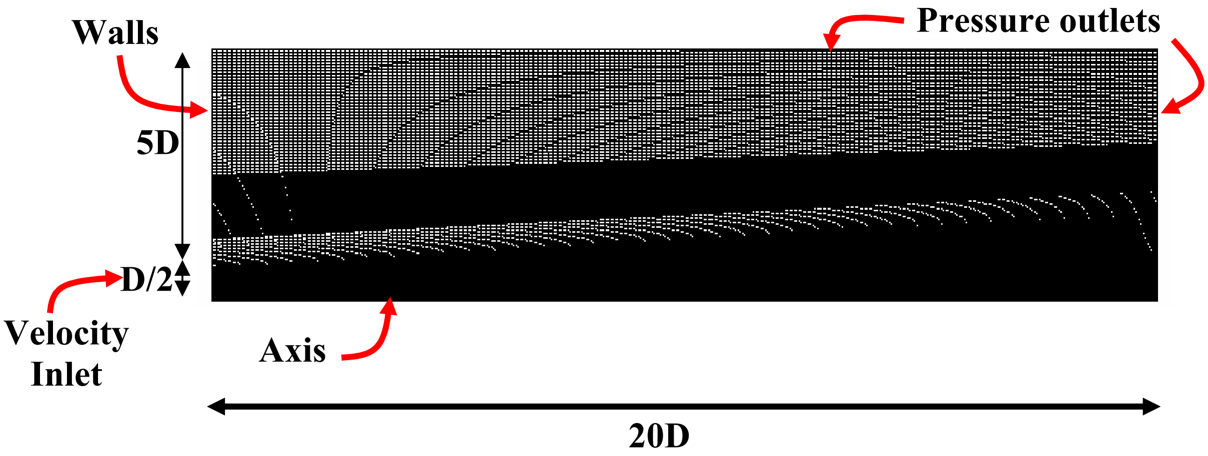

Figure 3.33: Axi-symmetric computational domain used for simulating high velocity modulated jets. Relevant boundary conditions are specified

A turbulent velocity profile at the injector inlet is assumed, constructed on the mean velocity [152] provided in Table (3.3), and the gravity effects are neglected. In the cases discussed, axi-symmetric simulations held valid since the range of Weber numbers discussed here, $We = 12 - 20$, are within the stripping mode of liquid jet disintegration. In this regime, the axi-symmetric behavior of the freely issuing liquid jet is retained while the ligaments and droplets are continuously stripped off from the liquid jet surface [11].

3.6.2 Simulations of high velocity jets

To identify the effect of modulations on high Reynolds number jets, a test case with no modulation is presented here. The inlet mean velocity is taken as 60 m/s and the scenario represents Newtonian liquid (Water) issuing into air at STP. The simulations are performed with a domain length of 15 nozzle diameters (3 mm downstream).

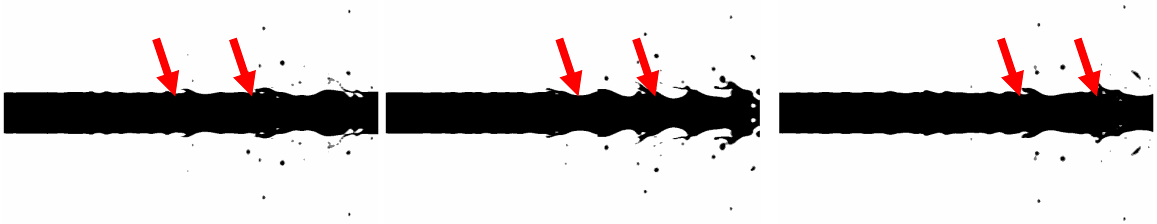
(a) (b) (c)

Figure 3.34: Evolution of a 60 m/s water jet into still air. Flow is from left to right

Observe from Fig. (3.34), the formations of short-wavelength shear instabilities formed at approximately 6 nozzle diameters downstream. However, as the simulation progressed, the amplitude of these instabilities was slightly suppressed due to the turbulence dissipation. Very limited drop formation events are encountered.

Following the numerical simulations obtained with no modulation effect, we now turn on the fluctuating parameters as listed in Table (3.3). Liquid jet with an average bulk velocity of 60 m/s and imposed frequency of 15 KHz, carries a superimposed perturbation wavelength of 0.004 m. Due to computational demand imposed by the breakup model, only three-quarters of the wavelength is taken into consideration and as a result, only the relevant dynamics observed within the computational domain is discussed. With an inlet velocity of 80 m/s, a longer domain length along the axial direction is considered (since the wavelength of the superimposed perturbation is considerably stretched).

Observe from Fig. (3.35), the low Strouhal number effect is clearly evident. Presence of low Strouhal number and low modulation amplitude results in bulging of the liquid jet [113, 114] and no breakup within the simulation domain is achieved. With increase in modulation amplitude, the bulging of the liquid jet is visible. The imposed perturbations travel along the liquid core and radial-component, generated by the modulation effect, acting to disintegrate the liquid jet is suppressed by the surface tension forces. The amplified surface waves are separated by length equal to the ratio of the imposed mean velocity over the modulation frequency.

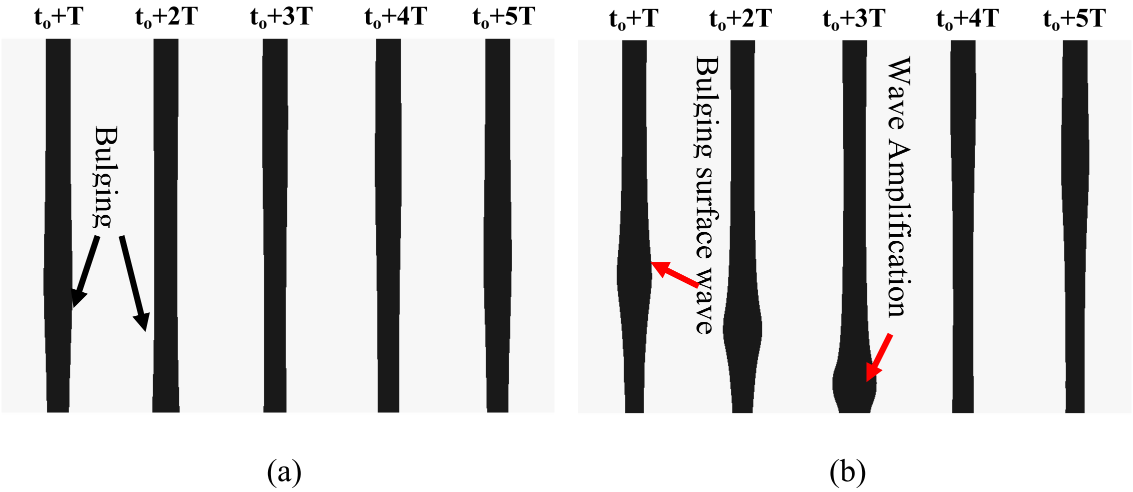

Figure 3.35: Evolution of low modulation high speed water jets in still air (a) Case 1 (b) Case 2. (Liquid jet direction is from top to bottom)

With increase in the inlet velocity, and retaining the same imposed frequency, the perturbation wavelength is expected to be even longer (approximated 0.00533 m) and cannot be sufficiently captured within the computational domain. For this reason, the simulation domain is extended further to 25 nozzle diameters (= 0.005 m) which can accommodate approximately one wavelength of the perturbation. The major problem in extending the domain is to carefully increase the count of computational cells to preserve accuracy. Since the simulations involve Volume-of-Fluid based computation in an Eulerian framework, irregular cell topology can be detrimental in providing breakup details [166]. Simulation result for the third case, Table (3.3), is shown in Fig. (3.36).

Notice that with increase in the modulation amplitude i.e., very high velocity fluctuations over a single perturbation cycle, ligament and later droplet formation is encountered. As explained before, only one single wavelength can be accommodated due to the effect of low frequency. Growth of surface waves resulting in droplet formation is clearly evident [114].

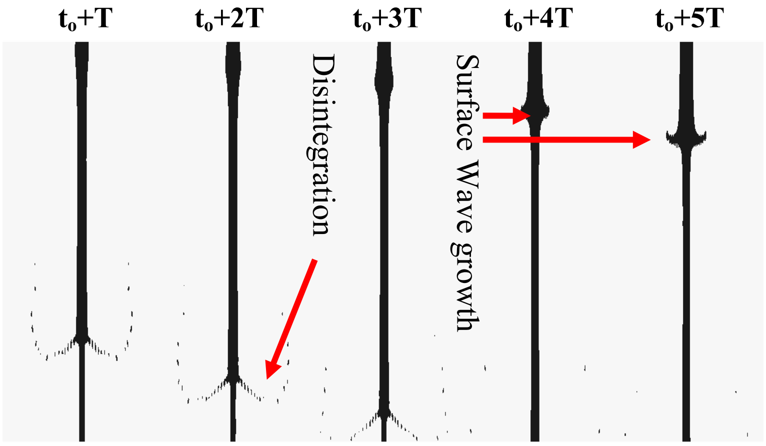

Figure 3.36: Breakup of high-modulation high-velocity water jets in still air (Flow is from top to bottom)

A closer observation of the near surface wave dynamics reveal presence of strong axial and radial components responsible for the ramification of the surface instabilities. Figure (3.37(a) and (b)) details the axial and radial velocity distribution respectively. From Fig. (3.37 (a)), visualize the presence of strong axial velocity components near the base of the surface waves. At the same location, Fig. (3.37(b)) indicates growing radial-velocity components expelling ligaments from the liquid jet surface.

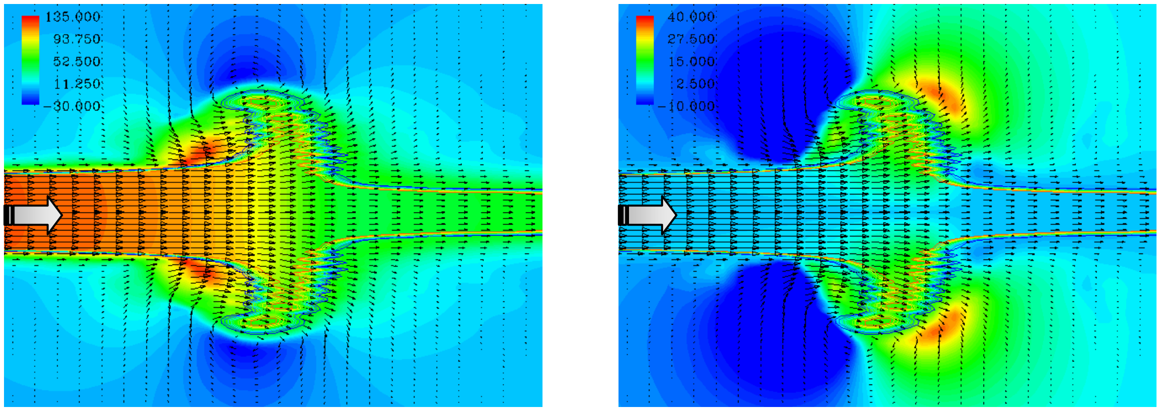

(a) (b)

Figure 3.37: (a) axial-velocity distribution near the bulging and disintegrating jet section (b) Corresponding radial-velocity distribution

As the liquid jet issues into the free shear region, shear vortices are generated due to the mismatch of the velocity component between the phases. The interaction of vortices with a growing surface wave and with disintegrated droplet regions are clearly indicated in Fig. (3.38(a)) and (3.38(b)) respectively.

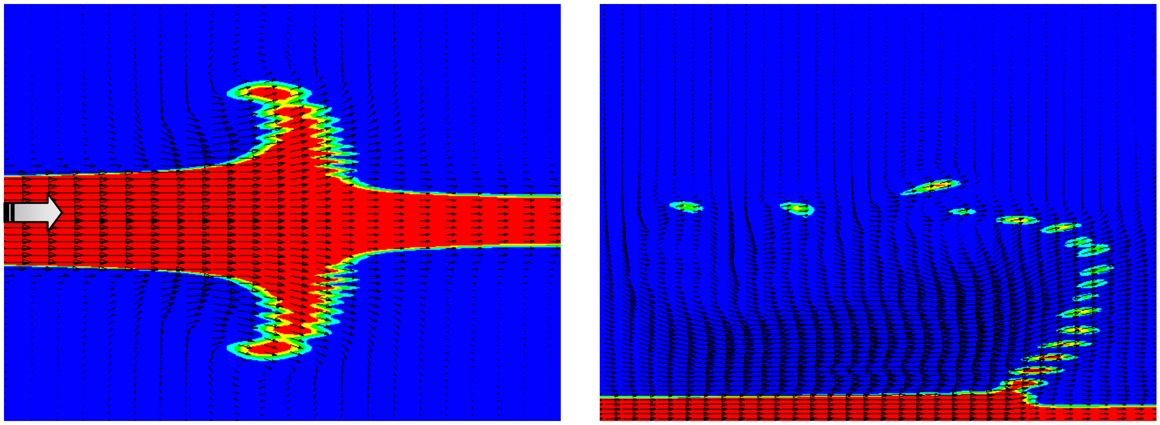

(a) (b)

Figure 3.38: Interaction of shear vortices in two locations (a) Initial bulging of the liquid jet (b) disintegration of elongated ligaments arising from the surface of the liquid jet

It is clear from our present simulation that use of low frequency modulation consumes longer downstream distances to initiate breakup (a measure of the imposed wavelength). Further, the large Reynolds number liquid jets do not respond well to the modulation effect since the inertial forces dominate the jet evolution [2]. To impose such high modulation amplitude upon a high speed jet in an increased frequency range dictates severe constraint on the nozzle design involved in the process. In this concern, it can be concluded that to obtain enhanced breakup features, use of low-velocity jets with increased frequencies of perturbation and higher modulation amplitude is favored.

3.7 Modulating low-viscosity Newtonian Liquid Jets

The current section is dedicated to provide extensive simulations concerning the disintegration behavior of low-velocity Newtonian liquid jets subjected to varied modulation effects. The liquid under consideration is water and its properties at STP are utilized in the computation while air is assumed as the ambient gas at STP. A table of parameters tested for design of the proposed spray applicator is provided in Table (3.4). In addition to the values of modulation amplitude provided in Table (3.4) some simulations with higher value of $\varepsilon = 0.5$ are tested to clarify effects of very high amplitudes on the breakup behavior. However, these tests are conducted only with 20 and 30 m/s liquid jets at specified frequencies. Further, in order to identify the effect of orifice exit diameter subjected to modulation effects three different diameters are tested ($D = 0.15$ mm, 0.2 mm and 0.25 mm). In all the simulations reported henceforth, a uniform parabolic velocity profile is assumed at the injector exit. The range of Reynolds numbers constructed based on the injector exit diameter (= 200 μm) and with a mean inlet velocity of 20 and 30 m/s is 4000 and 6000 respectively. The corresponding gas based Weber number lies between 1.33 – 3.0125. The magnitude of Reynolds number lies in the transitional laminar-turbulent regime [2] (2000<Re<4000).

Table 3.4 List of Modulation parameters

Mean Injection Velocity (m/s)	**Modulation Amplitude**	**Modulation Frequency (KHz)**	**Strouhal Number**	**Modified Weber Number**
20	***0.2***	***40***	***1.2566***	***2777.77***
	0.3	***80***	***2.5132***	***1388.88***
	0.4	***120***	***3.7699***	***925.92***
30	***0.2***	***40***	***0.8377***	***9375***
	0.3	***80***	***1.6755***	***4687.5***
	0.4	***120***	***2.5132***	***3125***

Inclusion of turbulence effects is not taken into account since it necessitates increased computational requirement. It is well known that the nature of turbulence is to dissipate the growth of surface waves in free shear liquid flow phenomena such as the present one. Testing of different turbulence models such as LES and a two-equation *k-ε* model against a simple laminar model yielded interesting results. The breakup predicted by models decreased from laminar to LES and finally to RANS based models. In particular, the dissipation provided by the RANS model diffused the surface growth and predominantly resisted the liquid jet breakup. However, much difference between the LES and laminar model was not observed. Hence, the results presented in this section are devoid of any turbulence assumptions in the domain. The only viscosity affecting the breakup process is provided by the viscous nature of the liquid and gas alone. The simulation assumes isothermal conditions with uniform liquid and gas properties. The liquid, water, is injected into a quiescent atmosphere, air, carrying with them imposed finite modulation effects and their disintegration behavior is reported.

3.7.1 Testing with no imposed fluctuating frequencies

In order to distinguish the effects of modulation from the un-modulated ones, results obtained from the numerical model for inlet velocities of U_{in} = 15, 20 and 30 m/s with no modulation are presented in Fig. (3.39). The corresponding Reynolds number is computed as 3000, 4000 and 6000 respectively. Observe from Fig. (3.39(a)), surface instabilities are distinct and are seen to evolve spatially and temporally. With increase in Reynolds number, however, suppression of the wave instabilities are predominant. In the case of higher velocity liquid jet injection, the wavelength of the surface protrusions is decreased along with the amplitude of the perturbations arising from the liquid jet surface [45, 160].

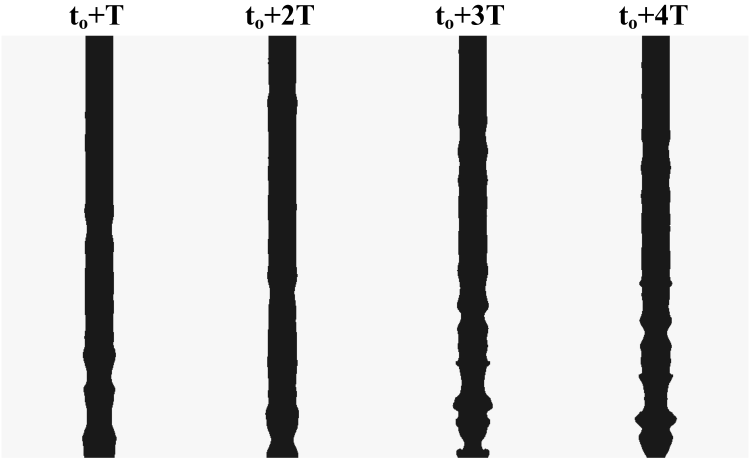

(a)

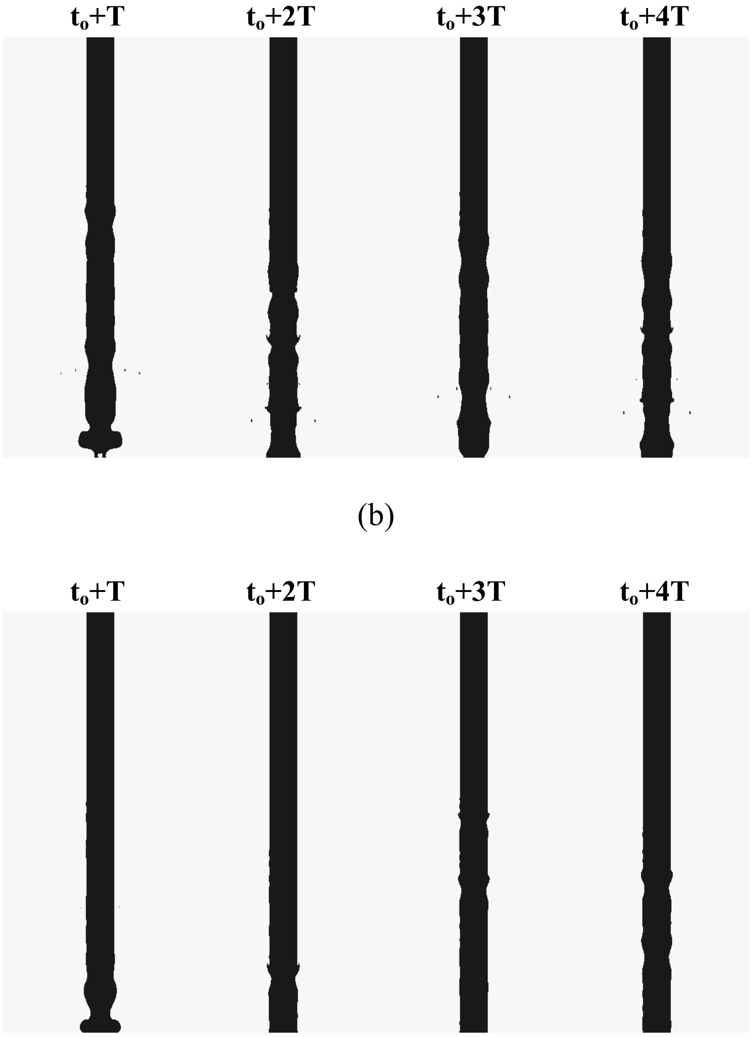

(b)

(c)

Figure 3.39: Transient evolution of non-modulated free shear liquid jets with an inlet velocity (a) U_{in} = 15 m/s (b) U_{in} = 20 m/s (c) U_{in} = 30 m/s. Results are presented with time step difference of $4e^{-06}$ seconds. (All flow directions are from top to bottom)

Recall that, with increase in the Reynolds number, the inertial force become very dominant and transition in wave instabilities occur. Various instability theories suggest that the wavelength of the surface shear wave instabilities decrease with increase in relative velocity between the liquid and ambient gas streams [2, 3, 11, 160]. Another important feature that requires considerable attention is the breakup mode itself. The current jet velocity injection variation, under constant nozzle diameter, surface tension and gas density, result in gas Weber numbers 0.75, 1.338, 3.0125 for U_{in} = 15, 20 and 30 m/s. For the Weber number under consideration, experiments suggest strong presence of axi-symmetric instabilities (varicose type) [2, 11] and hence, the axi-symmetric assumption is valid.

3.7.2 Results and Discussions

The plots are computed at 5 different time instants t_o+T through t_o+5T, where t_o represents the initial time while T the time step size. The initial time t_o is taken as 0.001 sec is assumed with a time step value of $T = 4\times10^{-06}$ s. This methodology alleviates any unsteady structures that might prevail during initial disintegration process. Given the domain length of L = 3 mm, a jet of 20 m/s would exit the domain in about 0.15 milliseconds and a 30 m/s liquid jet in 0.1 milliseconds. By assuming 1 millisecond time length before which the data is collected for discussion, any disturbance generated by the numerical model has sufficient time to be dissipated and a quasi-steady state disintegration behavior can be achieved.

3.7.2.1 Results

The first set of cases computed with Sr = 1.2566, We_w = 2777.7, for varying modulation amplitude of ε = 0.2, 0.3 and 0.4 are shown in Fig. (3.40). From Fig (3.40(a)) observe that modulation amplitude of 0.2 results in a cup like structure indicating highly amplified surface wave behavior. This feature compares well with the experimentally generated non-dimensional map of Geschner et al. [115]. No drop formation is observed. The surface waves are seen bent backwards as a consequence of gas drag. With further increase in amplitude to 0.3, drop formation is captured within 7 nozzle diameters downstream. In addition to drop formation from the ligament tip, breakup of the entire ligament is encountered further downstream. This mechanism of breakup at the base of a growing ligament gives rise to large droplet sizes [45, 160]. Extending the computations to $\varepsilon = 0.4$, droplets are observed within 4 nozzle diameters. The accelerated disintegration process is primarily due to augmented expulsion of liquid fragments from the liquid surface harvested by enhanced radial-velocity components. The outcome of higher modulation effects is clear: slender and longer sheet like structures, in a three-dimensional sense, are generated. Increased slender ligament protrusion into the gas domain increases the aerodynamic interactions effecting in expedited droplet generation.

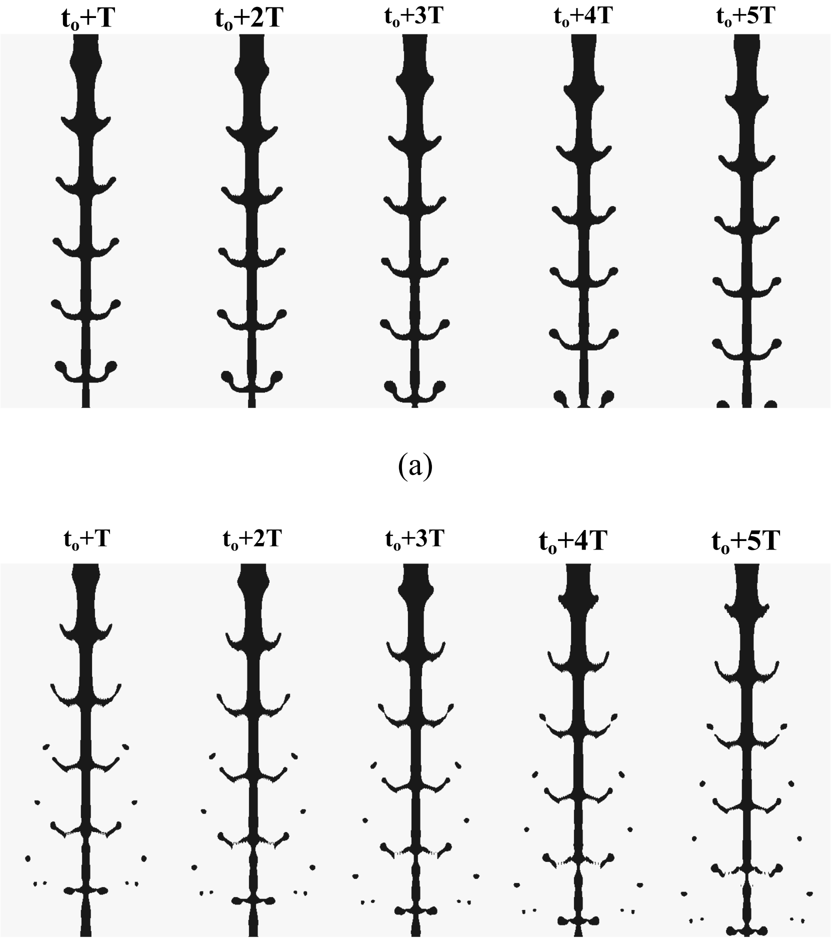

(a)

(b)

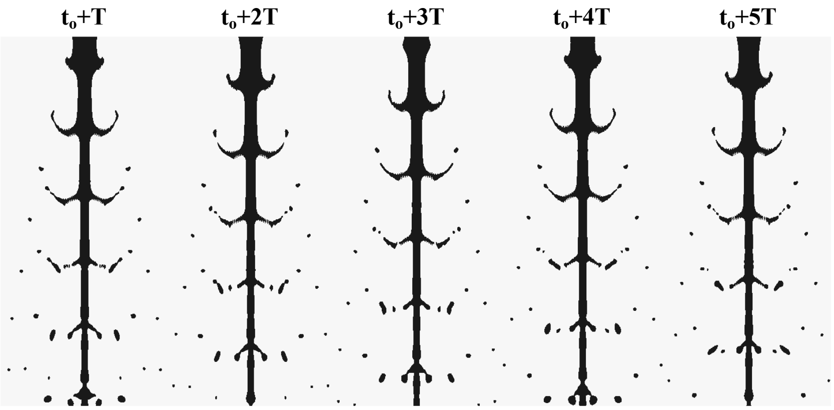

(c)

Figure 3.40: Numerical simulation of modulated jets with $Sr = 1.25$, $We_w = 2777.7$

(a) $\varepsilon = 0.2$ (b) $\varepsilon = 0.3$ (c) $\varepsilon = 0.4$ (Flow is from top to bottom)

Preceding the above computation, the Strouhal number is doubled retaining the injection velocity of 20 m/s. This directly indicates the doubling of imposed perturbation frequency (=80 KHz). Increase in the frequency reflects in shortened spacing between the liquid structures. For low modulation amplitudes such as $\varepsilon = 0.2$, thicker sheets are observed (Fig. (3.42)). Notice from Fig. (3.42), with $\varepsilon = 0.3$, drop formation occurs closer to the nozzle exit as compared to the results presented with a reduced modulation frequency (Fig. (3.40)). Progressing 10 nozzle diameters downstream, breakup of the central liquid core is observed. Furthermore, pulsating detached liquid jet streams with cup like features are detected giving rise to large size blobs in the central jet axis. Imposing higher amplification, Fig (3.42(c)), results in reduced drop sizes but does not prevent formation of concentrated blobs at the jet axis oscillating due to the effect of surface forces. Some coalescence effects of bigger blobs over smaller ones traveling along the same axis are also observed from Fig (3.42(c)). This effect can be attributed to the increased inertial content of the larger blob structure which moves faster as compared to smaller blobs and in the process, engulfs them.

Besides the presence of some intricate non-linearities, breakup of the central liquid core region is observed with increase in Strouhal number. Figure (3.41) shows the breakup length nomenclature used in describing the results henceforth. *B.L* refers to the breakup length, i.e., unbroken length of the liquid jet as it penetrates into ambience.

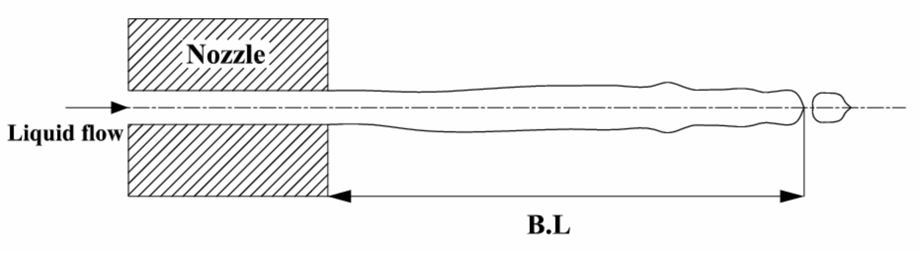

Figure 3.41: Breakup length of liquid jets emanating from a nozzle

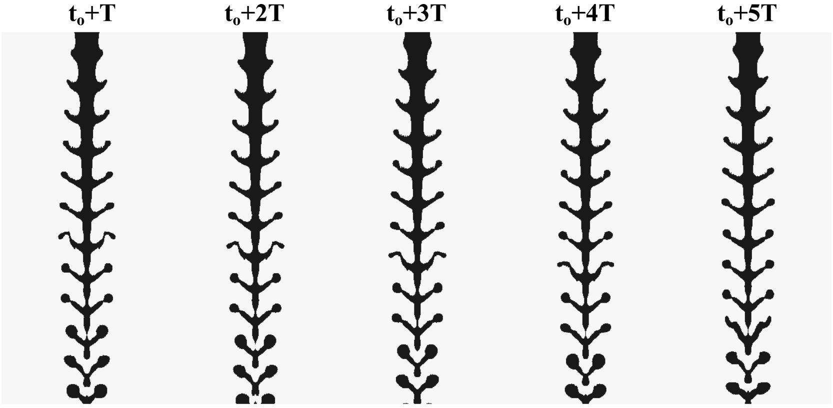

(a)

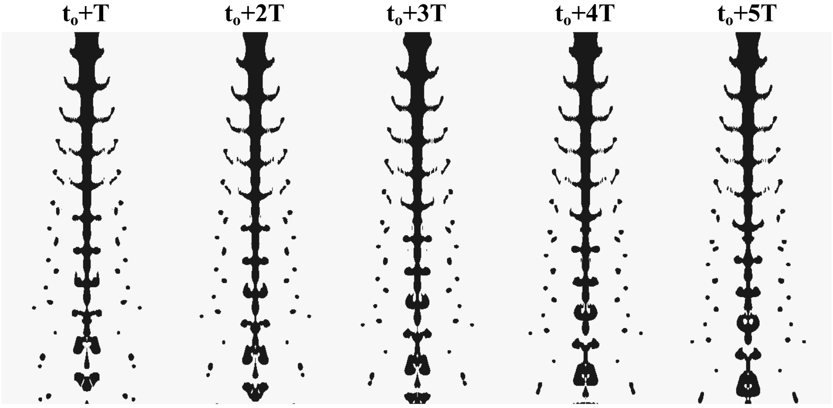

(b)

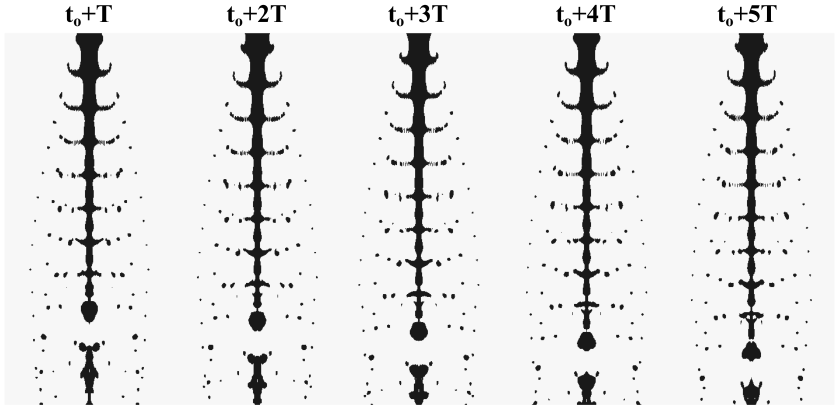

(c)

Figure 3.42: Numerical simulation of modulated jets with *Sr* = 2.5132 , We_w = 1388.88. (a) ε = 0.2 (b) ε =0.3 (c) ε = 0.4 (Flow is from top to bottom)

Breakup of the liquid jets under the given operating frequency and mean jet velocity were obtained at *12.4D*, *11.61D* and *11.44D*. Clearly, this trend indicates that with increase in modulation amplitude increased stripping from the liquid jet surface results in thinning of the central liquid jet bulk. Surface tension, at this juncture, interacts with the gas forces and plays a major role in breaking the slender jet. Thinning of the liquid jet axis initiates strong pressure gradients in the regions surrounding it owing to the Young's Laplace equation. Not able to withstand the high pressure gradients, the jet is disrupted and this process is further enhanced by the disturbances produced by local fluctuating gas force components.

With a fixed frame of reference, the evolution of liquid-gas interface and droplet deformation cum coalescence characteristics is captured in Fig. (3.43(a)). Figure ((3.43)a) shows two different size droplets moving close to each other after detachment from the parent liquid bulk. Both droplets experience the action of eddy interactions which influence their deformation. The drops were observed to deform due to their simultaneous rotation and translation motion within the flow field. In the case of larger drop sizes, this deformation was very profound while the mechanism is less clear in the small drops due to the action of capillary effects imposed in the model. The bigger drop size deformation is seen in Fig. (3.43(b)). As the drops move alongside each other, the local pressure depression generated due to the motion of the larger drop attracts the small size drops and the process of coalescence begins to accelerate [165]. This process is identified in Fig. (3.43(c)). As the coalescence process initiates, it starts so by forming a necking region due to the action of surface forces as indicated in Fig. (3.43(c)). Due to fine mesh sizes imposed in the simulations, the necking phenomenon is captured very well [166]. Figure (3.43(d)) shows enhanced coalescence leading to change in the total drop size. The coalescence process by itself induces addition rotation and inertia depending on the inclination at which the merger occurs.

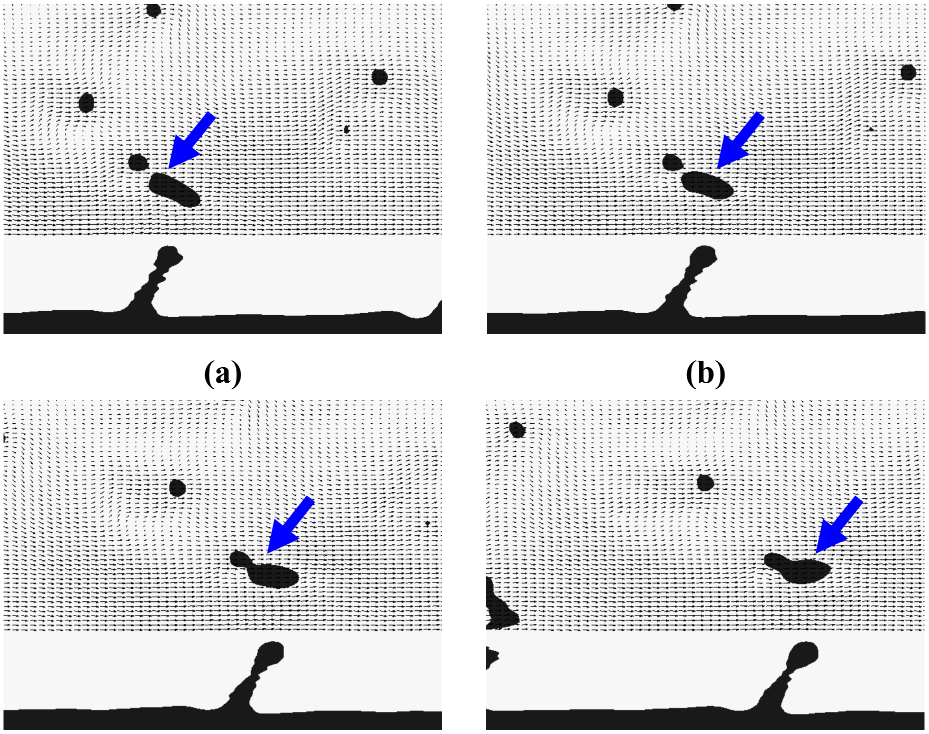

(a) **(b)**

(c) **(d)**

Figure 3.43: Droplets coalescence and deformation characteristics due to simultaneous rotation and translation. (Flow direction is from left to right)

In addition to describing the coalescence, the deformation motion of large fragments detached from the liquid surface is shown in Fig. (3.44). Again, with a fixed reference frame, the fragments are closely followed and monitored for any re-alignment and/or deformation that the liquid ligament might encounter. The realignment of a large droplet undergoing shearing action in addition to translation effects is distinctly perceivable from Fig. (3.44(a), 3.44(b) and 3.44(c)). In the same instant, clear-cut visualization of the ligament breakup process is noticeable from Fig. (3.44(d)).

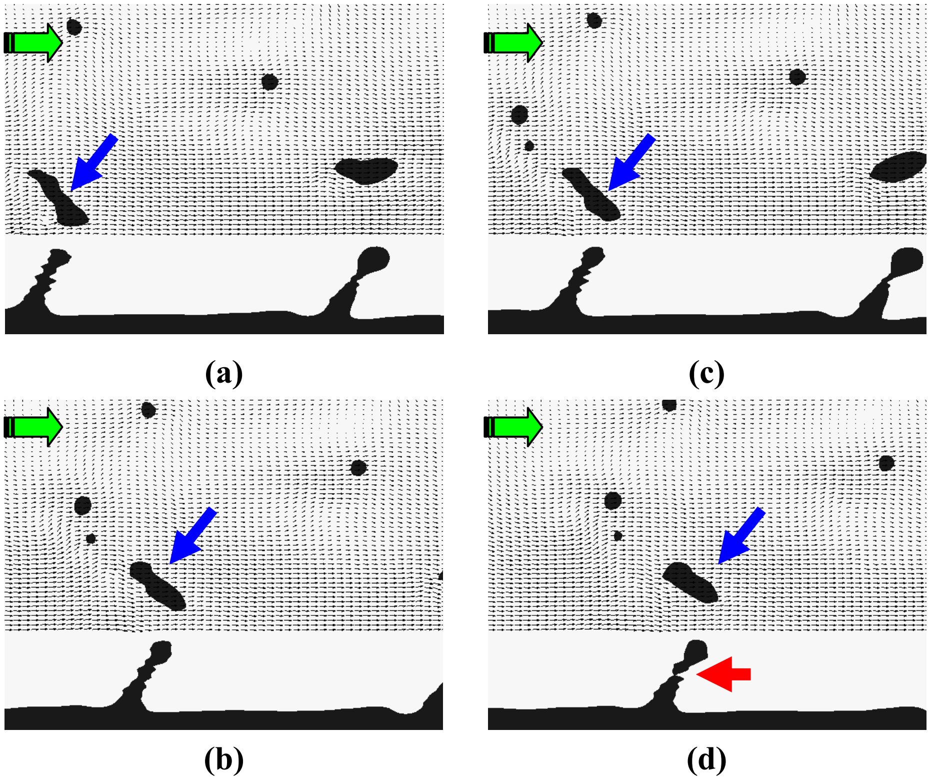
(a) **(c)**
(b) **(d)**

Figure 3.44: Droplet deformation and detachment process visualization

In order to understand the nature of pressure distribution existing at the time of droplet detachment from the amplified ligament like structure from the parent liquid bulk, a contour plot of pressure distribution at 10 nozzle diameters downstream is shown in Fig. (3.45). As seen from Fig. (3.45(a)), curvature of the liquid jet surface and its subsequent realignment induces strong pressure gradients [165]. A closer view of the detachment process is displayed in Fig. (3.45(b)), taken with a time delay of 4e^{-06} seconds after Fig. (3.45(a)). Note that at the pinch-off instant, very sharp variations in the local pressure distribution exist and induces local flow structure alteration.

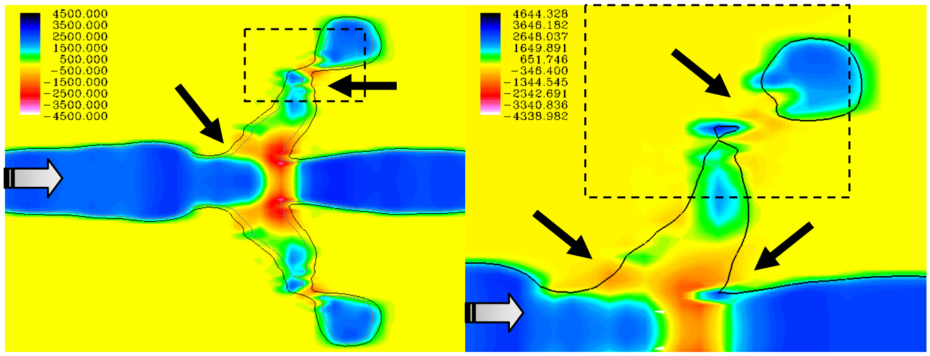

(a) (b)

Figure 3.45: Pressure contours near bulging liquid central core

Similar to the pressure distribution variation near a radially expanding ligament section shown in Fig. (3.45), a pressure distribution plot along the jet axis at a distance of 10 nozzle diameters for the case where strong oscillatory effects of jet were obtained is shown in Fig. (3.46). Notice the necking phenomenon along the central axis in Fig. (3.46(a)). Stretching of the necking liquid jet element and the subsequent re-organization of the liquid element downstream is shown in Fig. (3.46(b)). Finally, the surface tension forces contribute to the pinching and at this juncture strong pressure variation exist [165]. The strong coupling existing between the volume fraction model and the pressure fluctuation is a key element in capturing the fluctuation effects in a more elaborate manner. Fig. (3.46(c)) shows the pressure contours after a pinch-off had just occurred.

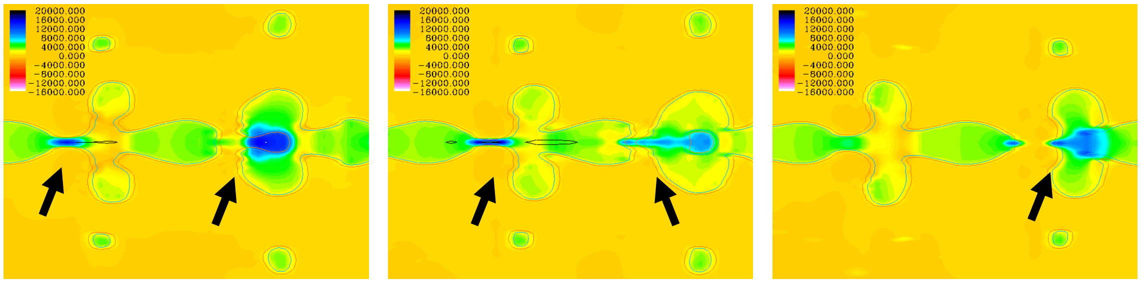

(a) (b) (c)

Figure 3.46: Pressure distribution variation along the central axis (Flow direction is from left to right)

The oscillatory fragment regime along the central axis of the liquid jet explained previously based on Fig. (3.47) is elaborated here using plots of liquid volume fraction. Mechanisms of liquid blob deformation, realignment, necking and detachment are shown in Fig. (3.47(a-d)).

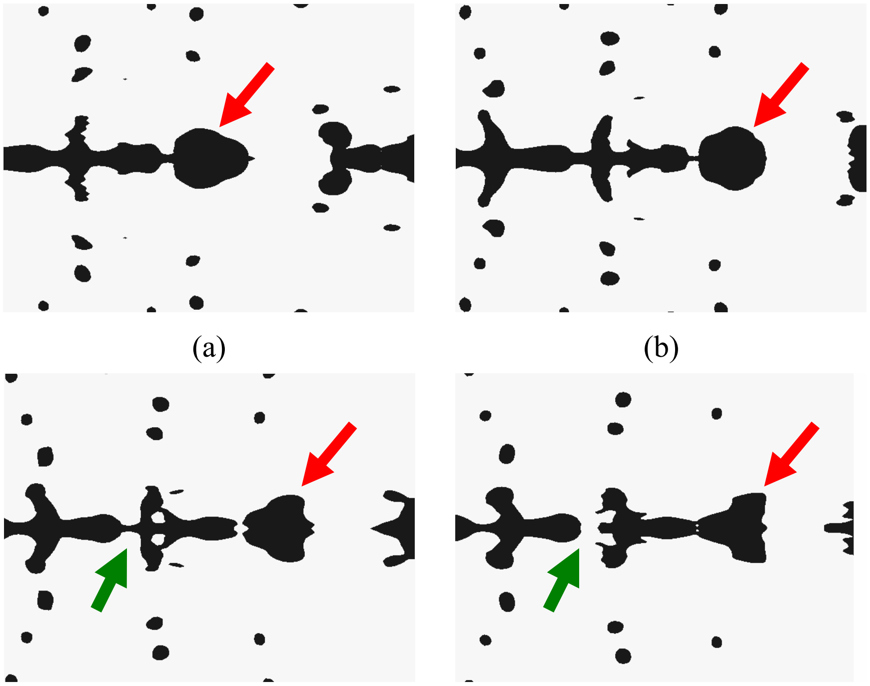

(a) (b)

(c) (d)

Figure 3.47: Thinning and bulging of liquid elements along the jet axis with $Sr = 2.5132$, $We_w = 1388.88$, $\varepsilon = 0.3$ (Flow direction is from left to right)

In this connection, the flow structure existing between the fragments at the pinch-off zone is portrayed in Fig. (3.48). Notice that strong recirculation regions are induced due to strong pressure gradients. As the pinch off occurs, the ligament stretches and increases the pressure within the liquid while a low pressure region is generated in the immediate vicinity which then accounts for the local flow reversal. Discussing the pinching off phenomena, it is to be reminded that mesh sizes are critical in determining the local flow transients [166]. One other numerical phenomena independent of the mesh size is the evolution of parasitic currents. Several authors [142] have identified the existence of parasitic currents that are artificially induced by the models than actually predicted in experiments. These currents are induced due to the local volume fraction calculation. The complexity arises in estimating the coupling between the volume fraction scalar, a Lagrangian invariant, and the local flow field. Lafaurie et al. [142] predicted that the order of magnitude of these currents scales as the ratio of surface tension over viscosity of the liquid. The use of interface-capturing technique such as the present one reduces the presence of these unwanted phenomena [142]: schemes such as PLIC generate higher parasitic currents [142].

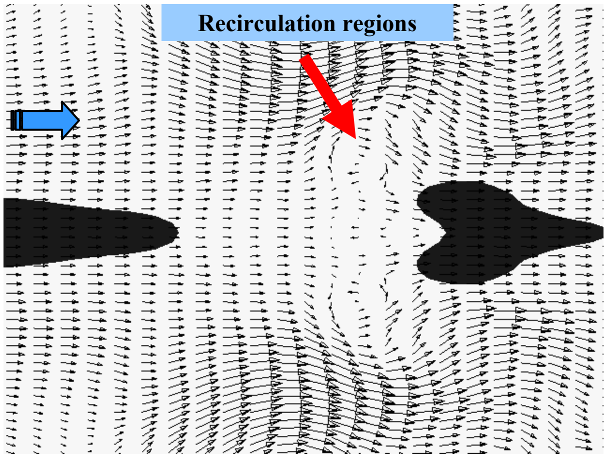

Figure 3.48: Presence of recirculation near pinch off event (Sr = 2.5132, We_w = 1388.88, ε = 0.4)

The existence of "bumps" along the central jet core in an intermediate location between the spots where typical bunching like phenomena is encountered is distinctly appealing. These bumps have been spotted to exist due to a local phase jump phenomena associated with the appearance of suppressed frequencies along the liquid jet. Due to the fine mesh sizes, higher wave numbers are well accommodated by our current model. This implies that the filter operation implicitly performed by the grid size to cut off frequencies lie in the high frequency ranges. Hence, these intermediate bumps characterized by twice the frequency of the imposed perturbation wavelength are detected by the current model.

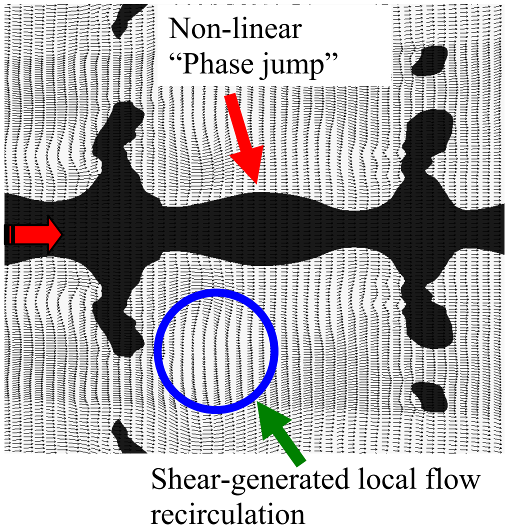

Figure 3.49: Portraying the evolution of multiple frequency zone within the modulated jet (Sr = 2.5132, We_w = 1388.88, ε = 0.3)

Motivated by the decrease in drop sizes and increased disintegration results obtained by doubling the frequency to 80 KHz, an imposed frequency of 120 KHz is explored to potentially envision an expedited breakup process. The results obtained from the numerical simulations for Sr = 3.7699, We_w = 925.92 is shown in Fig. (3.50). Increased Strouhal number at this juncture contributes to increased non-linearities in the breakup process. The reproducible structures associated with modulated jets are not recovered. For low modulation at $\varepsilon = 0.2$, two distinct behavior is noted. First, disintegration starts in about 5 nozzle diameters and continues until the jet stays intact after 10 diameters. The central liquid core now performs a pulsating motion moving back and forth with respect to its initial position, maintaining its trajectory along the center. As soon as the pulsation amplitude increases rapidly after just about 10 diameters, a second disintegration process is initiated. Similar phenomena is observed with $\varepsilon = 0.2$ and 0.3. In all three occasions, a discrete set of equally spaced reproducible droplet streams are created and move in the trajectory set by the radial components dictated by the modulation parameters. Comparing the simulation parameters to the non-dimensional map, it is revealed that indeed the following regime corresponds to a droplet chain regime in the map. However, in observing droplet chains in their experiments, Geschner and Chaves [115] did not observe occasional breakup from the central core. The numerical scheme presented in this study encompasses a compressive scheme to retain numerical sharpness in the Volume fraction scalar [136]. This methodology is strongly dependent on the mesh attributes and hence some unidentified pulsation and wiggles in the scalar function can be regarded as a manifest of numerical instability inherent in the model.

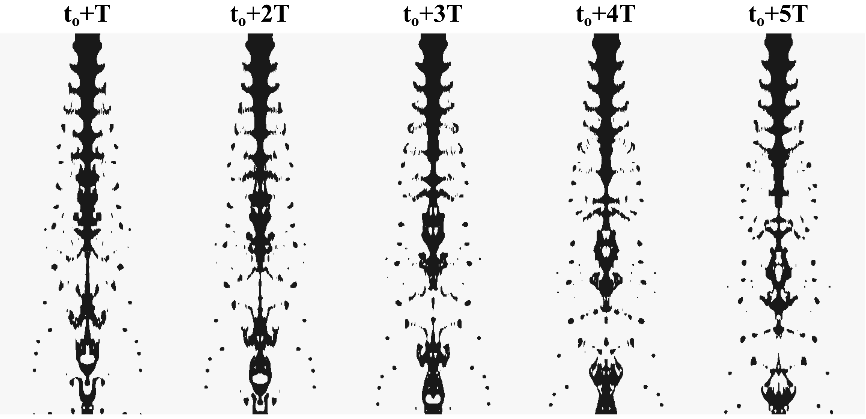

(a)

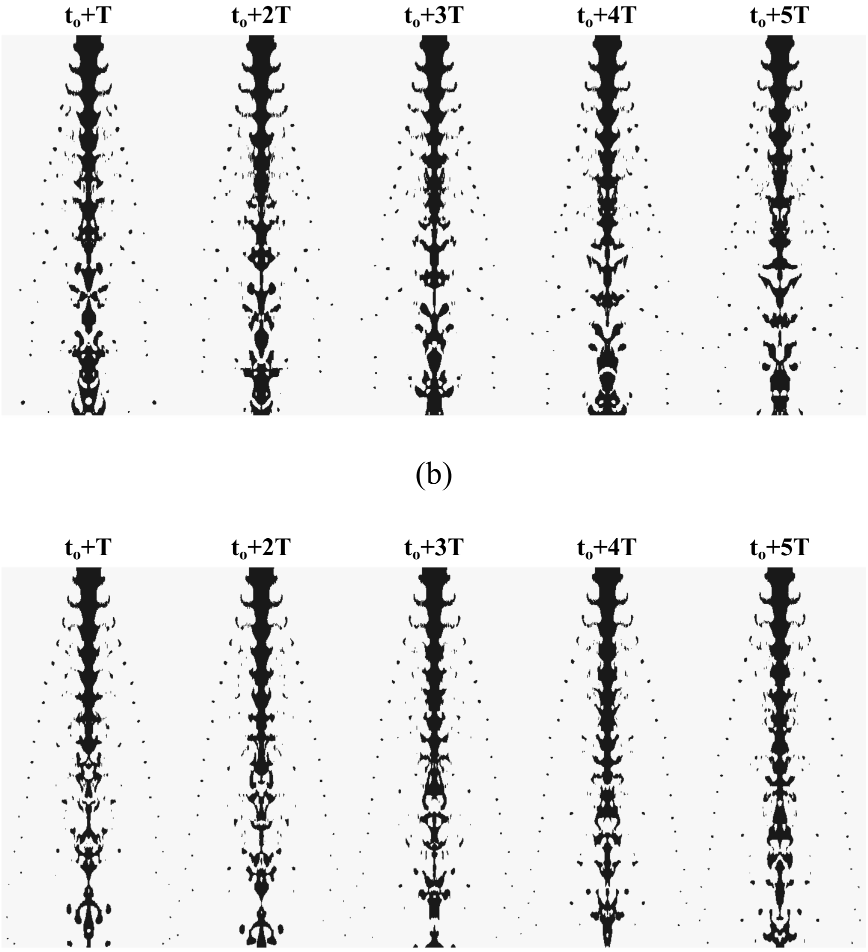

(b)

(c)

Figure 3.50: Numerical simulation of modulated jets with $Sr = 3.7699$, $We_w = 925.92$. (a) $\varepsilon = 0.2$ (b) $\varepsilon = 0.3$ (c) $\varepsilon = 0.4$ (Flow is from top to bottom)

The breakup length of the liquid jets were computed as 8.55D, 10.88D, 10.25D for $\varepsilon = 0.2$, 0.3 and 0.4 respectively. A contour plot of axial velocities and radial velocities existing in the system with $Sr = 3.7699$, $We_w = 925.92$ under modulation amplitudes $\varepsilon = 0.2$ and 0.3 are shown in Fig. (3.51) and Fig. (3.52) respectively.

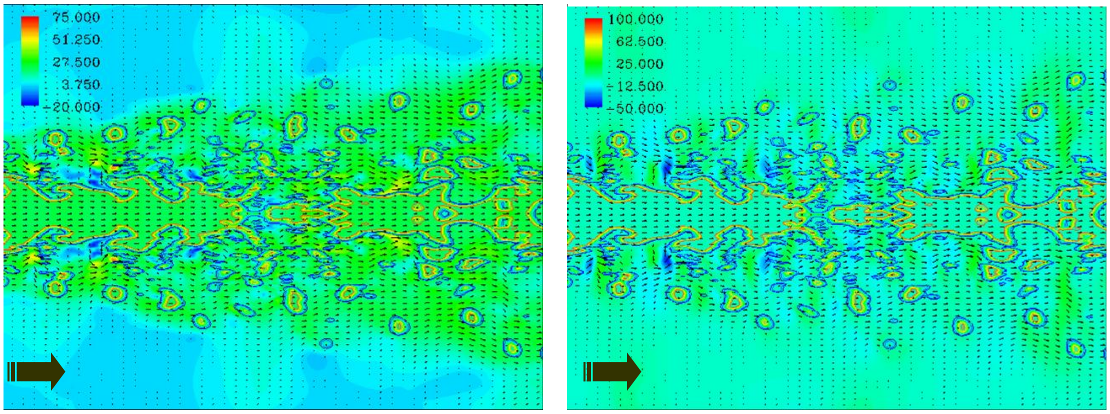

(a) (b)

Figure 3.51: Contours of (a) axial-velocity (b) radial velocity with Sr = 3.769, We_w = 925.92 and ε = 0.2 (Flow is from left to right)

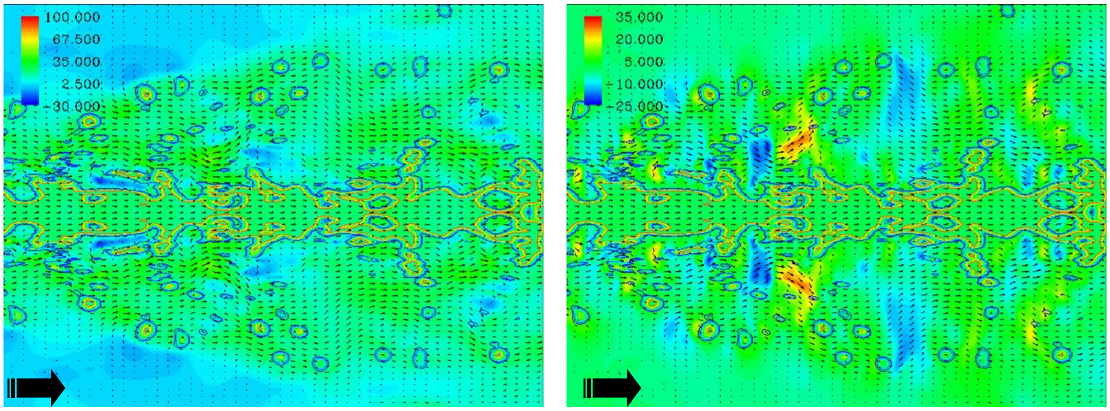

(a) (b)

Figure 3.52: Contours of (a) axial-velocity (b) radial velocity with Sr = 3.769, We_w = 925.92 and ε = 0.3 (Flow is from left to right)

From Figs. (3.51) and (3.52), notice the increase in the axial and radial velocity magnitude scale difference. With increase in modulation amplitude, aggravated axial and radial velocities are enforced into the domain.

A plot of the cone angle variation as a function of modulation amplitude, for a liquid jet injected with a mean velocity of U_{in} = 20 m/s is shown in Fig. (3.53).

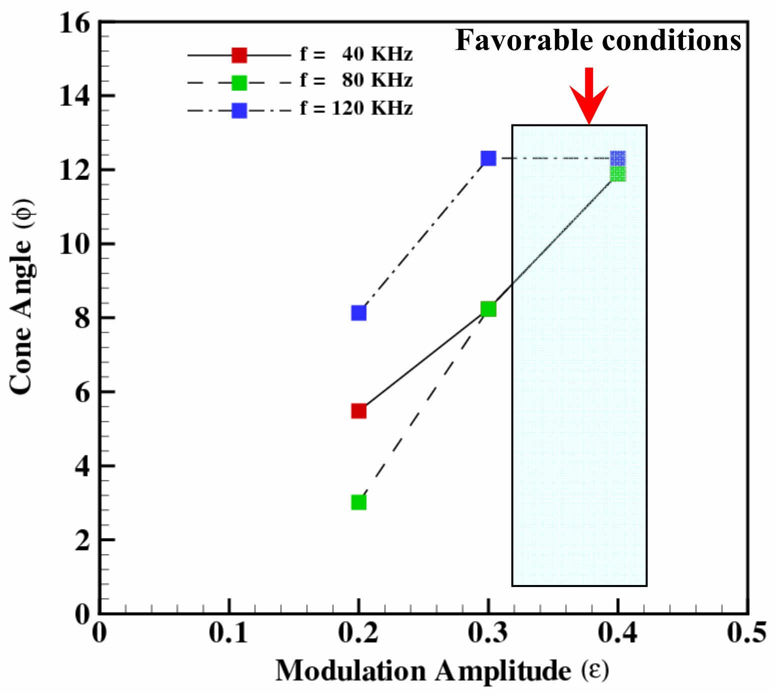

Figure 3.53: Plot of spray cone angle vs modulation amplitude at various frequencies tested under a constant inlet mean velocity of 20 m/s

Observe that strong variation in the spray cone angles occur only at low modulation amplitudes. As the amplitude increases, jets modulated at frequency of 40 KHz and 80 KHz show similar cone angle trends. Only at higher frequencies an increased cone angle at lower modulation is obtained. An important conclusion pertains to the cone angle trend indicated by high frequency modulations on the liquid jet. For ε = 0.3 and 0.4 the variation of cone angle in the case of perturbation frequency of 120 KHz is almost null. This indicates the limit of disintegration by downstream or upstream directed bell modes. The jets no more disintegrate under the frequency influence at higher Strouhal numbers, rather directly start forming droplet chains. This observation is similar to the observation trends obtained from the non-dimensional map of Geschner et al. [115].

The critical nature of the nozzle exit liquid jet velocity is analyzed by increasing the inlet mean velocity to 30 m/s. First, the modulation amplitude is varied with a Strouhal number *Sr* = 0.8377 and We_w = 9375. Figure ((3.54)(a)) shows formation of ligament breakup into drop formation near the exit of the simulation domain. This scenario is opposite to the results presented in Fig. (3.40)(a) with a Strouhal number of 1.2562 (U_{in} = 20 m/s). As occurred in previous computations, a slender liquid core exists although event of ligament and further drop formation occur as a result of simultaneous droplet stripping process from the liquid surface. Finer drops are obtained by increasing the amplitude ε to 0.3 and later, 0.4. As reported earlier, the central jet axis is still unatomized and hence can lead to potentially large drop sizes. Identify from Fig.(3.54), the orientation of the disc like structure emanating from the liquid bulk. The alignment is downstream oriented in the case of cases with ε = 0.3 and 0.4 indicating the shift in liquid structure regime towards a downstream directed bell regime.

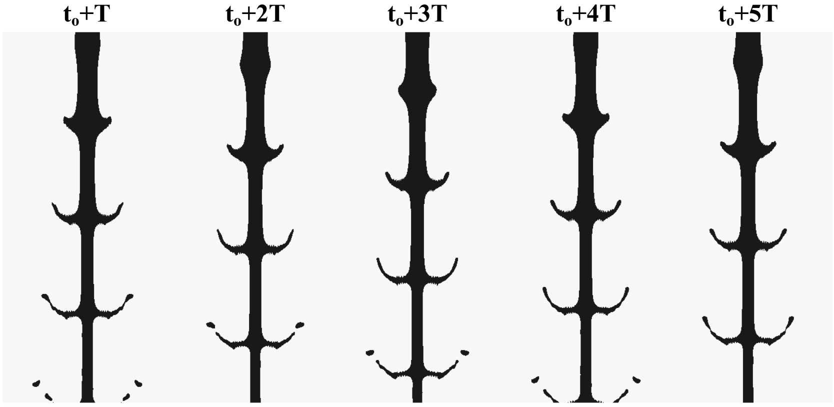

(a)

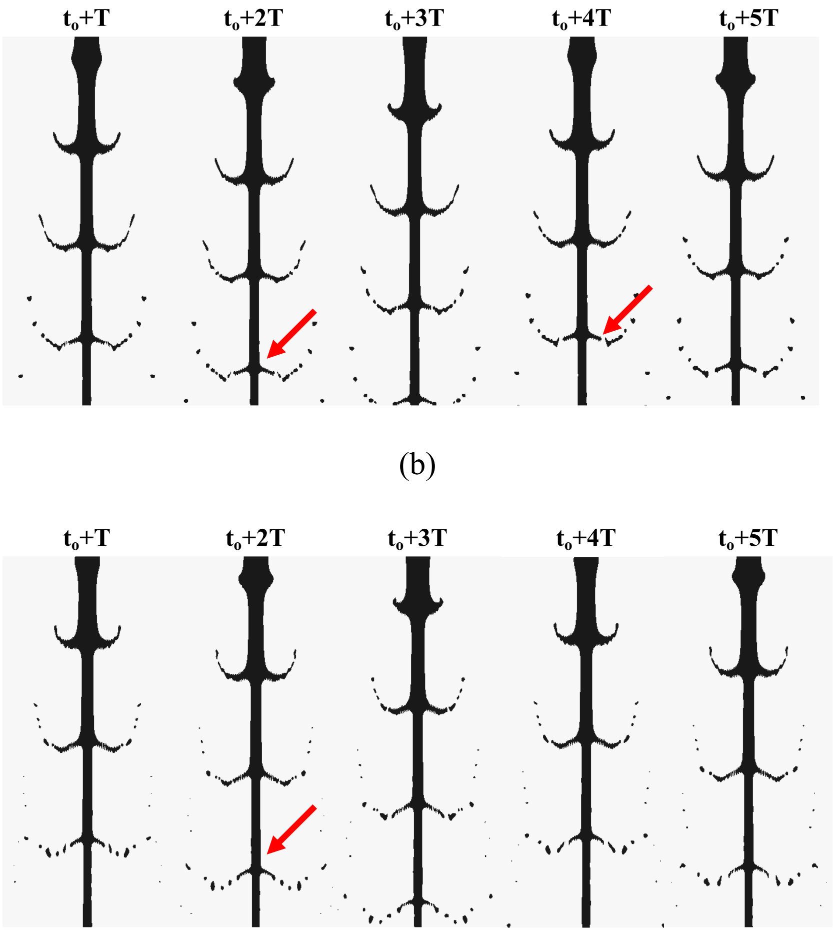

(b)

(c)

Figure 3.54: Numerical simulation of modulated jets with $Sr = 0.8377$, $We_w = 9375$ with (a) $\varepsilon = 0.2$ (b) $\varepsilon = 0.3$ (c) $\varepsilon = 0.4$ (Flow is from top to bottom)

The frequency of perturbations are increased to 80 KHz leading to a $Sr = 1.6755$ and $We_w = 4687.5$. With increase in frequency, similar observations to those observed in Fig. (3.54) are obtained. The increased jet velocity in this occasion only contributes to the fixed spacing between the bunching elements. With higher Wew, increased drop formation at lower modulation is observed. Moving into higher amplitude of $\varepsilon = 0.3$ leads to finer drop sizes and less coalescence between detached droplet streams. Progressing further into $\varepsilon = 0.4$ mode, drop sizes become even smaller but a flapping motion of the expanding liquid sheets along the liquid jet axis is detected. The motion of the liquid sheet is suspected to be due to the non-linear interaction of the gas forces and the confining forces of surface tension and viscosity. Owing to this interaction, the orientations of the discs perform an upstream/downstream flapping motion as they leave the computational domain. The boundary effect generated by the model cannot be ruled out which might cause some non-linear behavior due to the local numerical instabilities near the domain exit. In all the three cases investigated in the current frequency range, a slender liquid jet core exists and is not disrupted by the modulation effect.

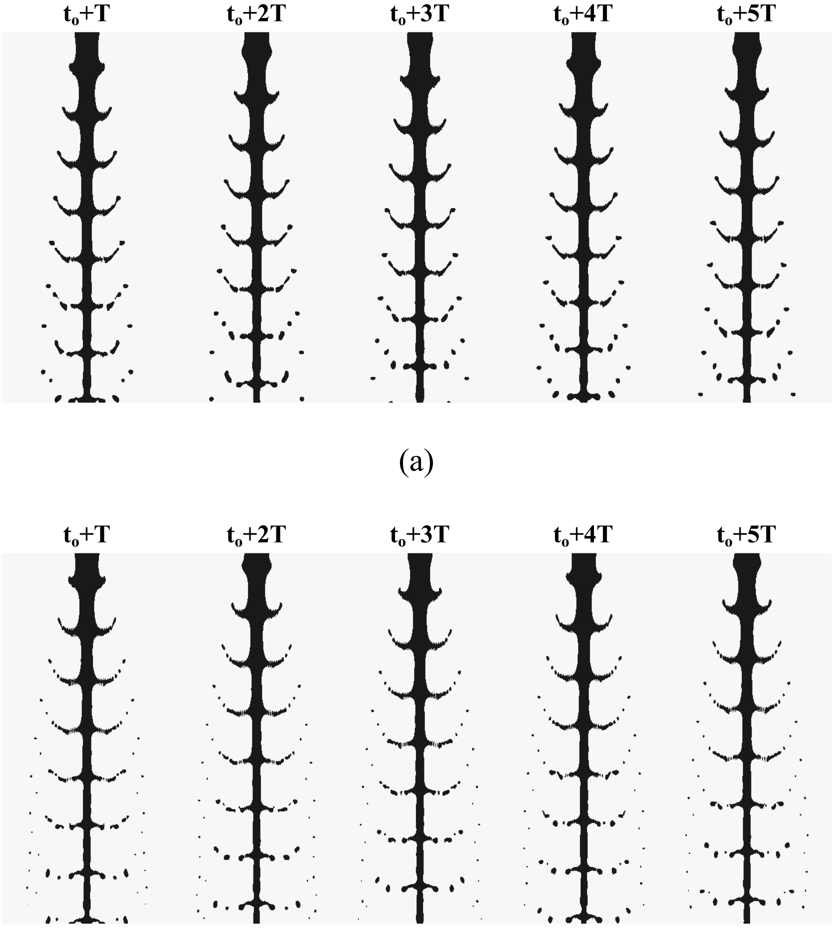

(a)

(b)

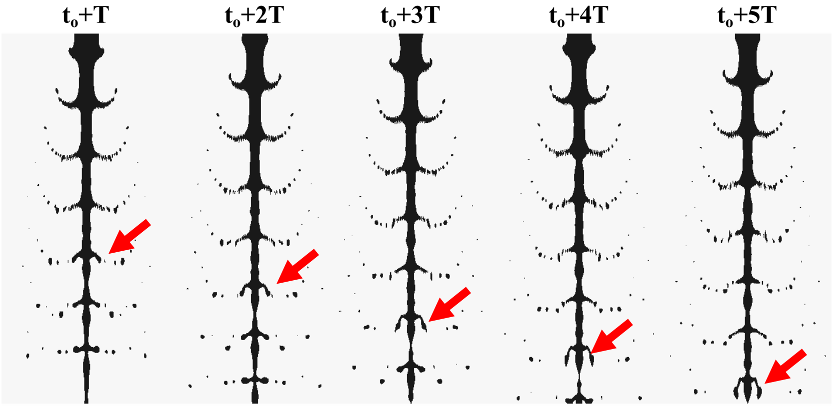

(c)

Figure 3.55: Numerical simulation of modulated jets with $Sr = 1.6755$, $We_w = 4687.5$ with (a) $\varepsilon = 0.2$ (b) $\varepsilon = 0.3$ (c) $\varepsilon = 0.4$ (Flow is from top to bottom)

With a 30 m/s mean velocity liquid jet, no breakup length within *15D* computational domain is observed. The influence of modulation amplitude on the jet spread is shown in Fig. (3.56). With increase in modulation, increased surface area of the slender ligaments, expelled radially from the liquid jet, is exposed to the gas forces resulting in enhanced breakup.


(a) (b) (c)

Figure 3.56: (a) $\varepsilon = 0.2$ (b) $\varepsilon = 0.3$ (c) $\varepsilon = 0.4$ at a frequency of 40 KHz and inlet mean liquid jet velocity = 30 m/s ($Sr = 0.8377$, $We_w = 9375$) (Flow is from top to bottom)

A shift from an upstream directed ligament orientation to a downstream direction is distinct traversing from Fig. (3.56(a) – (c)). With frequency increase to 80 KHz, as stated before, enhanced disintegration is obtained, however, with a slender liquid core. Figure (3.57) depicts the influence of modulation amplitude on the drop formation and spread angle.

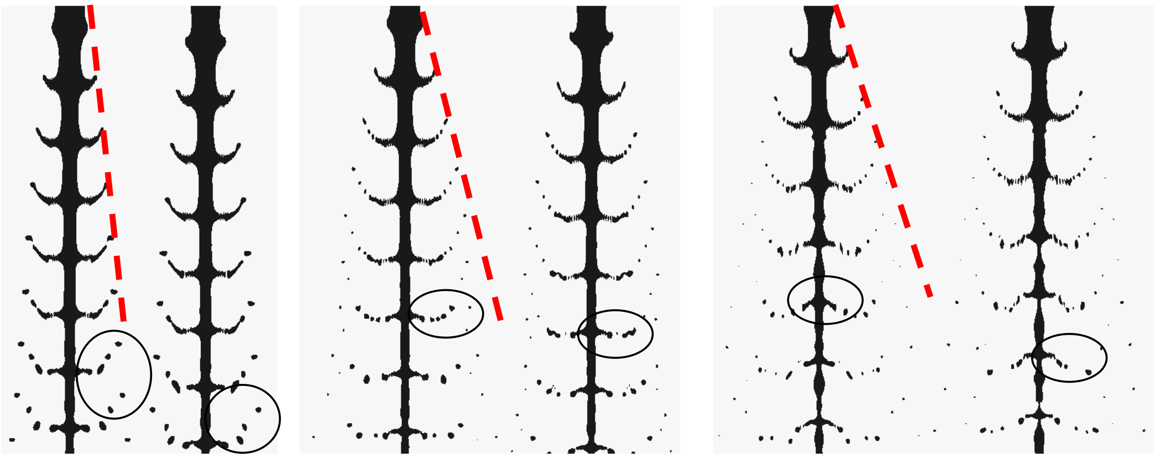
(a) (b) (c)

Figure 3.57: Contours of liquid fraction (black) in air (white) modulated with (a) $\varepsilon = 0.2$ (b) $\varepsilon = 0.3$ (c) $\varepsilon = 0.4$ at a frequency of 80 KHz, mean velocity = 30 m/s. ($Sr = 1.675$, $We_w = 4687.5$) Flow direction is top to bottom.

Motivated by the contribution of increased frequency modulation towards droplet generation, the perturbation frequency is further raised to 120 KHz retaining the same inlet flow velocity of U_{in} = 30 m/s. Since, the computations presented in Fig. (3.57) showed no appreciable disintegration for modulation amplitudes less than $\varepsilon = 0.3$, only modulation amplitudes of $\varepsilon = 0.3$ and above are considered. Results pertaining to $\varepsilon = 0.4$ and 0.5 are presented in Fig. (3.58) for discussion purposes.

With increase in amplitude to 0.4, Fig. (3.58(a)) shows a corresponding increase in droplet disintegration. The breakup mode is enhanced as compared to Fig. (3.57(c)) but with a reduced spray angle. This is attributed to the fact that the locally disintegrated fragments do not have sufficient time to radially propagate due to the high frequency axial propagation. Indeed, the increase in frequency provides less time for droplet spreading and modulation effects, which dictate the radial spread of the droplets. From the simulations the overshadowing effect of frequency over modulation can be satisfactorily concluded. With an increase in modulation to 0.5, no major change is observed in drop formation and spray angle. The only major modification that is observed with increased modulation concerns the increased liquid fragment pulsation along the central core and decreased breakup length.

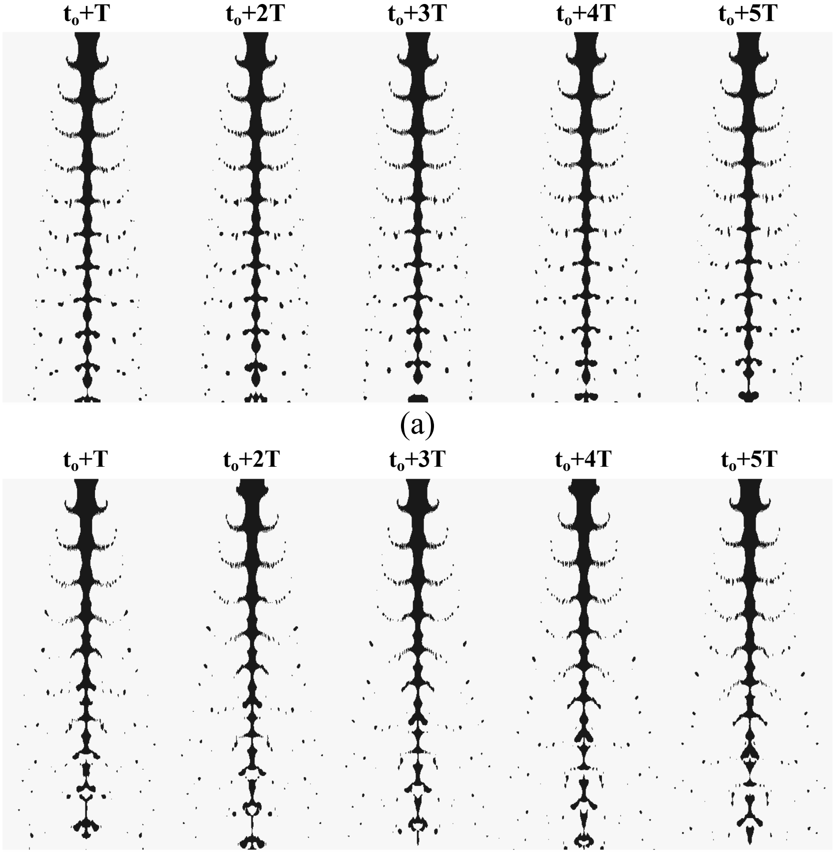

(a)

(b)

Figure 3.58: Numerical simulation of modulated jets with *Sr* = 2.5132 , We_w = 3125 with (a) ε = 0.4 (b) ε =0.5 (Flow is from top to bottom)

A comparative description of the simulation presented in Fig. (3.58) is reproduced for further clarification. Figure (3.59(a)) clearly shows presence of secondary phase existence as the jet evolves downstream. Bulging of the jet along the core is clearly visualized. Improving the modulation amplitude, detachment of larger liquid blobs, affected by multiple frequencies immersed in the flow, result in large droplets. Strong non-linearities in the central jet axis are represented in Fig. (3.59(b)).

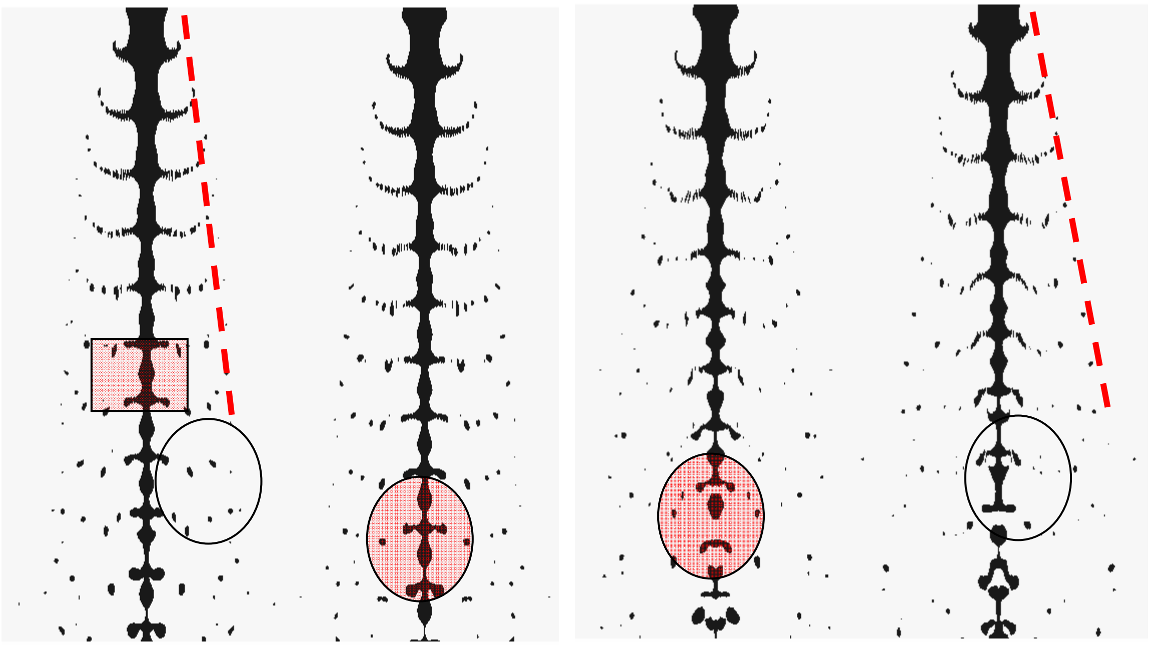

(a) (b)

Figure 3.59 Comparison of the numerical simulation results obtained by discharge of pulsed liquid jets with a mean velocity of 30 m/s and modulated with (a) $\varepsilon = 0.4$ (b) $\varepsilon = 0.5$ at a frequency of 120 KHz

Increase in fluctuation frequency does not expedite breakup rather the non-linear interaction results in increased coalescence and increased droplet sizes due to fluid structures generated by the modulated jet. A plot of the cone angle fluctuation as a function of modulation amplitude, in Fig. (3.60), shows higher spreading of the modulated jet as compared to the results obtained with a mean inlet velocity of 20 m/s. However, this disagreement exists only at frequencies 40 and 80 KHz. At higher frequencies, a trend similar to those obtained with U_{in} = 20 m/s is retained. This indicates the strong frequency influence on masking the amplitude effect. The higher angle contribution of the liquid jets with U_{in} = 30 m/s is attributed to the increased radial components generated by a faster moving liquid jet when imposed with a given modulation amplitude.

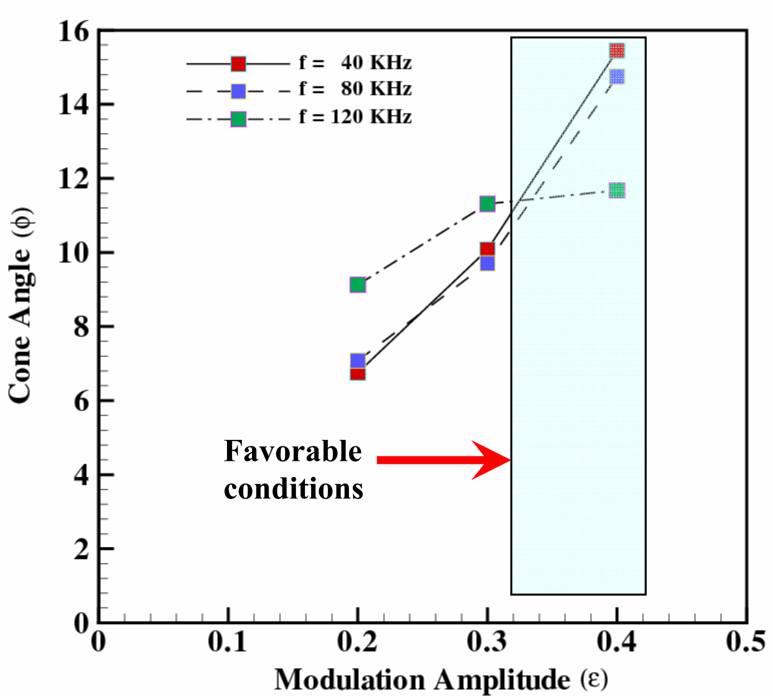

Figure 3.60: Plot of spray cone angle vs the modulation amplitude for different values of frequencies with an inlet velocity of 30 m/s.

A computation with reduced inlet velocity of 20 m/s with modulation amplitude of 0.5 at 120 KHz are carried out to compare the velocity effect (or the wavelength effect of the imposed perturbation) on the disintegration characteristics. Interestingly, with decrease in velocity but with a high frequency and high modulation, disintegration is reduced appreciably. Various non-linearly expanding and contracting fragments along the jet axis are observed in Fig. (3.61), with reduced droplet distribution.

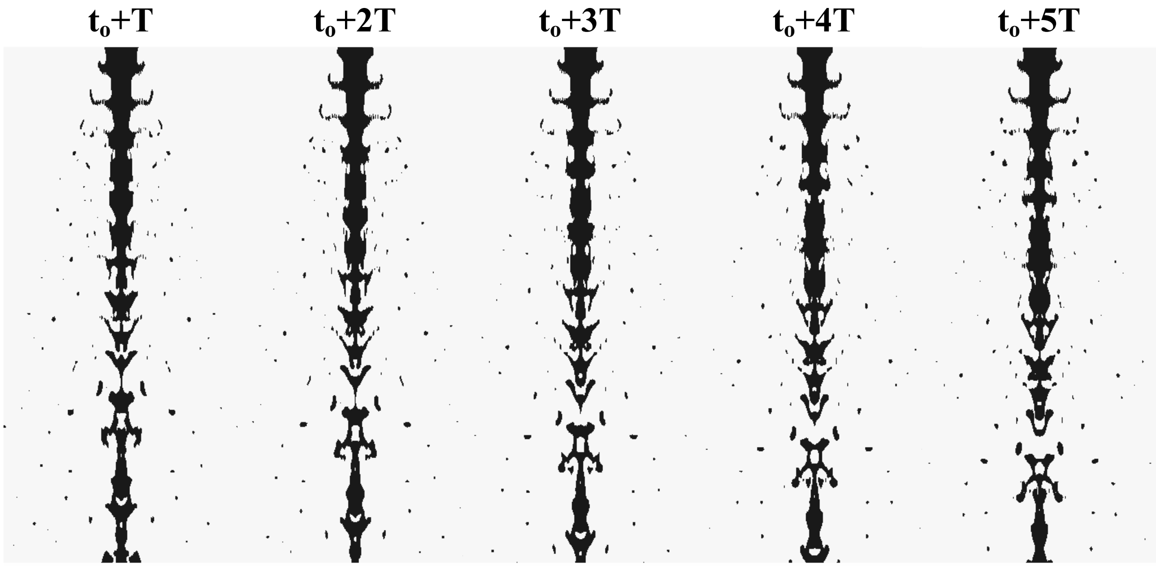

(a)

Figure 3.61: Numerical simulation of a modulated jet with $Sr = 3.7699$, $We_w = 925.92$ with (a) $\varepsilon = 0.5$ (Flow is from top to bottom). Presence of strong non-linear effects are distinct.

For a constant disturbance frequency of 120 KHz, description of the cone angle deviation as a function of modulation amplitude is presented in Fig. (3.62). Low velocity liquid jet cone angles peak between $\varepsilon = 0.3$ and 0.4, while the steepness of the higher velocity jet is still monotonically increasing. With a modulation amplitude of $\varepsilon = 0.5$, the spray width generated by a low velocity jet (U_{in} = 20 m/s) starts to shrink. In a similar fashion, the spray width generated by increased inertial (velocity) content of the liquid jet portrays strong radial expansion in the amplitudes considered. However, with higher amplitude this effect would diminish and spray width shrinking is expected (creation of droplet chains [115]). This is attributed to the interplay of Strouhal and modulation effect: Based on the magnitude of the Reynolds number, domination of either effect is decided. Recall that the terms on the right-hand side of the one-dimensional model described in equation (3.23) incorporates this inter-coupled mechanism. For low velocity jets, the frequency masking of the modulation amplitudes is observed to occur at small amplitudes; but with decreased Strouhal number, the amplitude required for generating this effect is considerably higher.

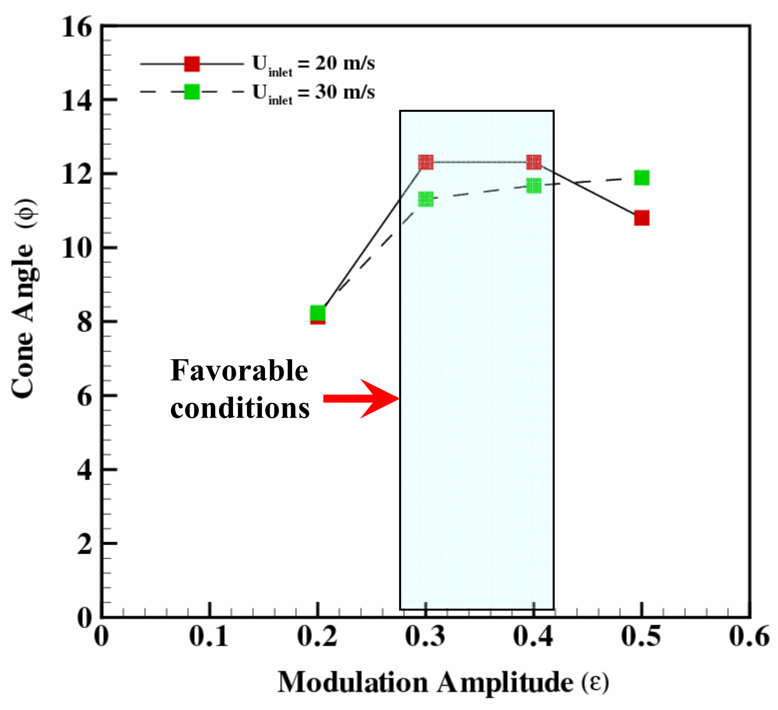

Figure 3.62: Plot of spray cone angle vs modulation amplitude at 2 different inlet velocity conditions with a perturbation frequency= 120 KHz

3.7.3 Effect of inlet diameter on disintegration characteristics

One other effect that requires careful analysis is the effect of inlet diameter given the modulation parameters viz., amplitude and frequency and the mean liquid velocity magnitude. An increase in inlet liquid jet diameter, all other properties such a liquid surface tension, gas density, liquid density and inlet velocity remaining constant, leads to an increased Weber number [2]. This in turn reflects on the ease at which a liquid jet would undergo disintegration [2, 3, 11]. Applying modulation to the jets can modify the disintegration properties considerably due to the growth of imposed perturbation with well defined amplitude and frequencies in addition to the disturbances induced by the system. Simulations are performed for three different diameters 0.15 mm, 0.2 mm and 0.25 mm under a constant inlet velocity. The modulation amplitudes in all the three cases are maintained constant at $\varepsilon = 0.3$ with a constant frequency of 120 KHz. This frequency is chosen since, no non-linear pulsating effects in the case of a 0.2 mm liquid jet were observed under the set of frequencies tested. Hence, the objective is to test without any severe non-linear effects generated by the high frequencies. Contour plots of liquid volume fraction obtained from the computations are shown in Fig. (3.63).

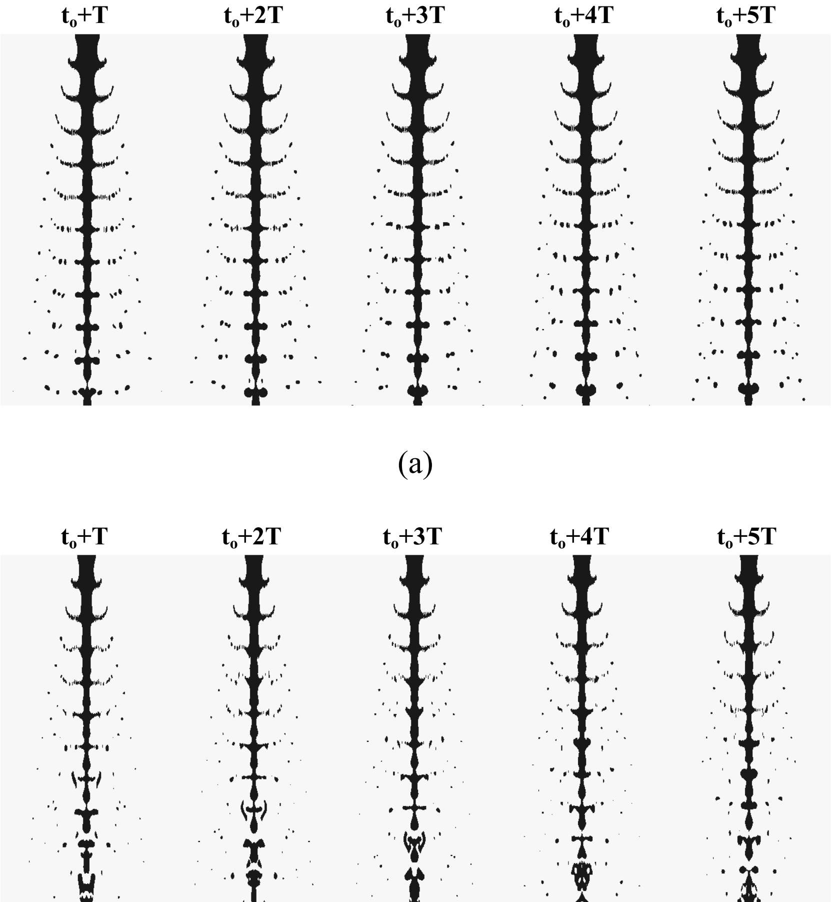

(a)

(b)

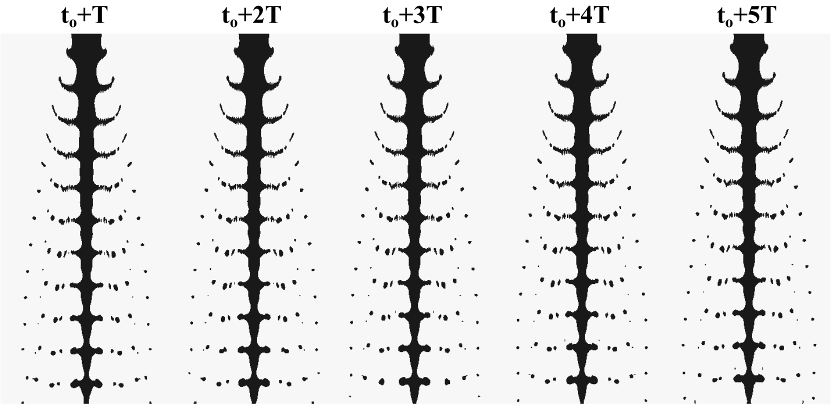

(c)

Figure 3.63: Numerical simulation of modulated jets with (a) *Sr* = 1.8849 (b) *Sr* = 2.5132 (c) *Sr* = 3.14 under a constant We_w = 9375 (typically representing inlet diameters (a) 0.15 mm, (b) 0.2 mm (c) 0.25 mm) (Flow is from top to bottom)

A trend line of the spray cone angle generated from the study above is shown in Fig. (3.64). As expected increase in diameter of the liquid jet leads to reduce cone angle, since a liquid jet with a higher diameter carries more inertial content as compared to surface forces and the Weber number effect dominates.

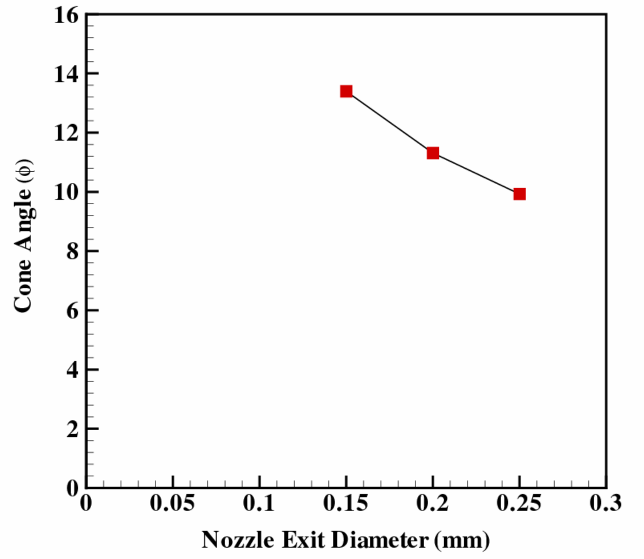

Figure 3.64: Influence of exit nozzle diameter on the droplet spread angle

The effect of frequency on the forced liquid jets is clear. With increasing frequency under constant amplitude, the disintegration or the amplitude effect is masked and only droplet chains are generated. Based on the simulation results from Section (3.7.2) and (3.7.3) increased spread angle and disintegration is obtained for an imposed frequency of 80 KHz. Lower frequencies contribute to larger intervals between breakup lengths while higher frequencies result in reduced stripping process. For observing the effect of injected velocity on the disintegration behavior, the system under a constant modulation amplitude and frequency of 0.3 and 80 KHz is retained. Figure (3.65) shows the variation in the cone angle spread as a function of inlet mean velocity ranging from 15-30 m/s.

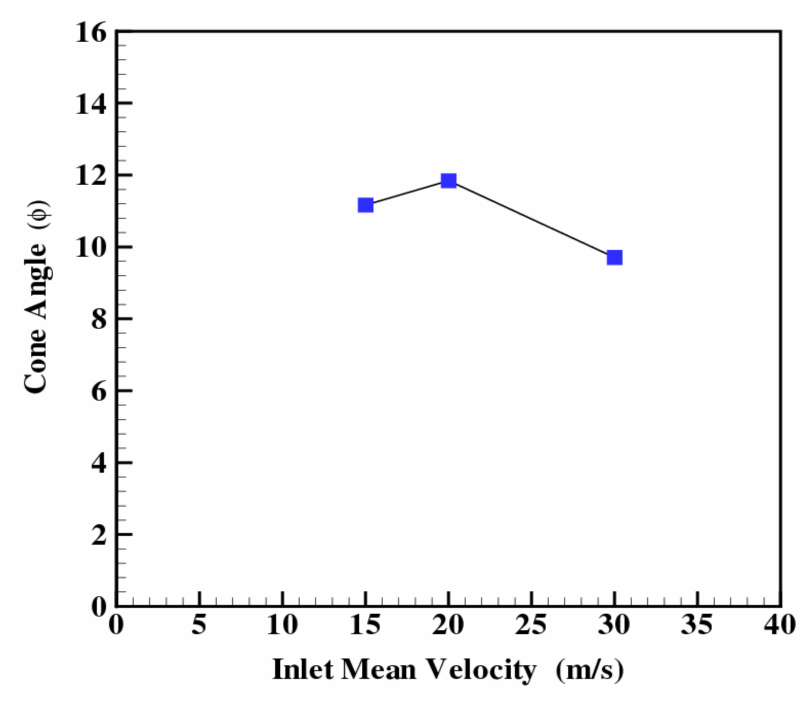

Figure 3.65: Variation in cone angle as a function of inlet mean liquid jet velocity at an imposed frequency of 80 KHz and amplitude of 0.3.

Observe that maximum spreading and hence, increased probability to encounter the gas forces and result in droplet generation, is obtained at U_{in} = 20 m/s. Adding to the injection mean velocity effect, the effect of modulation amplitude on the given liquid jet system parameterized by Strouhal number and a modified Weber number is shown in Fig. (3.66). Since increased disintegration is obtained around U_{in} = 20 m/s, this value is retained to study the frequency and amplitude effect. Figure (3.65(a)) shows the cone angle variation with increase in frequency for a liquid jet with a mean inlet velocity of 20 m/s. In all the three occasions presented, modulation amplitudes 0.2, 0.3 and 0.4, the cone angle increases as the Strouhal number increases. At higher amplitudes, the increase is less pronounced and an almost equal cone angle of magnitude 12.1^{o} is obtained.

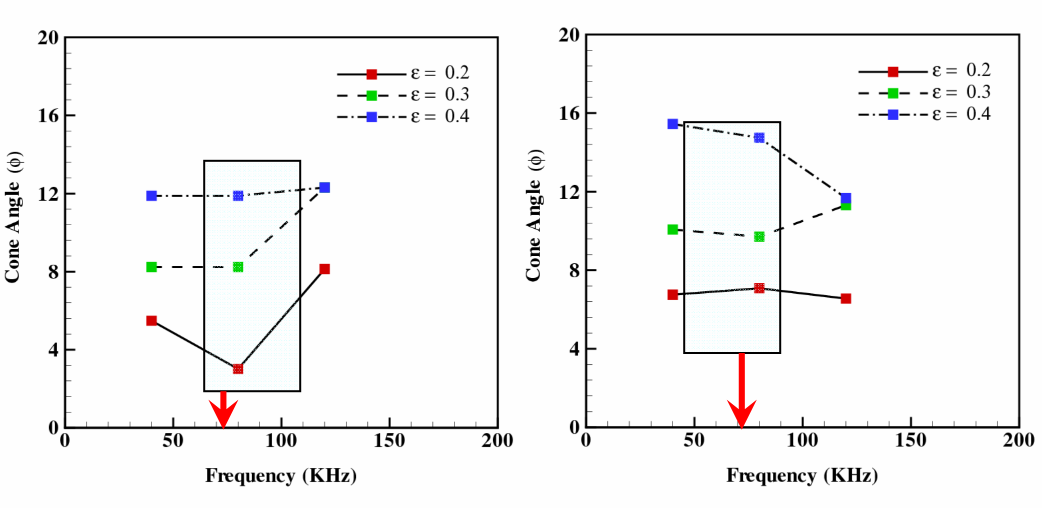

(a) (b)

Figure 3.66: Plots of cone angle variation with frequencies for different modulation amplitudes on a liquid jet discharging with an inlet mean velocity of (a) U_{in} = 20 m/s (b) U_{in} = 30 m/s.

Simulations with inlet mean velocity of U_{in} =30 m/s reveal a different scenario. With increase in Strouhal number (or frequency increase under constant mean velocity), the spray cone angle shows increasing trend only with a modulation amplitude of ε = 0.3. For higher modulation, the spray reduces its radial width considerably and a sharp reduction at a frequency of f = 120 KHz is obtained. This phenomenon is termed as the amplitude masking effect where the frequency effects are felt stronger compared to the amplitude effects. Although, the primary objective of the amplitude is to enhance dispersion of the liquid jets in a radial fashion, frequency response plays a critical role in suppressing the liquid jet expansion by accelerating surface tension enhanced coalescence effects.

This effect can be understood using the one-dimensional non-linear Navier-Stokes equation with the inclusion of surface tension and diffusion terms, equation (3.23). We rewrite the equation for reader's convenience here

$$\frac{\partial \tilde{u}}{\partial \varpi_{1d}} + \tilde{u}\frac{\partial \tilde{u}}{\partial \eta} = -{We_{mo}}^{2}\left(\frac{1}{\varsigma^{2}}\frac{\partial \varsigma}{\partial \eta} + St^{2}\frac{\partial^{3}\varsigma}{\partial \eta^{3}}\right) + \frac{St}{\mathrm{Re}}\frac{\partial^{2}\tilde{u}}{\partial \eta^{2}} \tag{3.81}$$

Notice from equation (3.81), that the first term in RHS contains the surface tension dominated components, We_m, while the second term contains the effect of inertial component, namely the Reynolds number. Note that for a given Strouhal number, an increase in Reynolds number leads to a surface tension dominated phenomena, the amplitude effect, while its decrease results in a Strouhal number dictated process, the frequency effect. The interplay between the two competing forces decides the outcome of the breakup process. For the present case, a low Reynolds number effect would considerably assist the modulation amplitude effect which is further enhanced by the surface tension dynamics.

3.8 Closure

In this chapter, first, governing equations of a modulated liquid jet in cylindrical co-ordinates was presented. Using low modulation assumptions, analytical model to predict modulation effects independent of the fluid properties were obtained. However, these analytical predictions were not able to accommodate high modulations and did not account for any non-linearities inherent to the fluid flow. To overcome this problem, numerical simulations of the fluid motion governing equations, the Navier-Stokes equations, were discussed. To track the events of liquid evolution into a gas domain, Volume-of-Fluid based interface capturing scheme was considered. For this purpose, the Compressive Interface Capturing Scheme for Arbitrary Meshes scheme of Ubbink et al. [135] was reviewed. All the simulations reported in this chapter were carried out within the OpenFoam framework available for simulating continuum mechanics in a finite volume framework. The VOF method employing CICSAM scheme was validated using a turbulent round liquid jet disintegration test case. To account for turbulence effects in the single-fluid domain, various models viz., LES, RANS were considered against the simple laminar assumptions. Laminar models over-predicted the breakup while LES models compared well with the experimental observations. RANS based turbulence models performed very poorly dissipating all the instabilities thereby completely suppressing the breakup process. Following this validation, the VOF scheme was applied to high and later, low speed modulated liquid jets. Scaling parameters affecting the liquid structure formation were carefully studied. Later, a series of computations to identify the modulation frequency and amplitude effect on the jet disintegration process was performed. Under low frequencies, the modulation amplitude dictated the disintegration; however, with increasing frequency under the same amplitude, frequency masking of the amplitude effect was discovered.

For high velocities, increased modulation resulted in lower disintegration and hence low spray cone angle, while for lower inlet velocities (~20 m/s) no change in spray angle with increase in frequency for higher modulation amplitude was established. Performing a wide range of computations, it became evident that to achieve good disintegration, the range of velocities exiting the nozzles should lie in the range of 25-30 m/s with amplitude of 0.3-0.4 modulated at frequencies close to 80 KHz. Copyright © Vedanth Srinivasan 2006.

Chapter 4

Numerical study of cavitating atomizer

A liquid at constant temperature could be subjected to a locally decreasing pressure, *p*, which falls below the saturated vapor pressure, p_V. The value of $(p_V - p)$ is called the tension, Δp, and the magnitude at which rupture occurs is the tensile strength of the liquid, Δp_C. The process of rupturing a liquid by decrease in pressure at roughly constant liquid temperature is termed as cavitation [33]. A schematic describing the process is shown in Fig. (4.1).

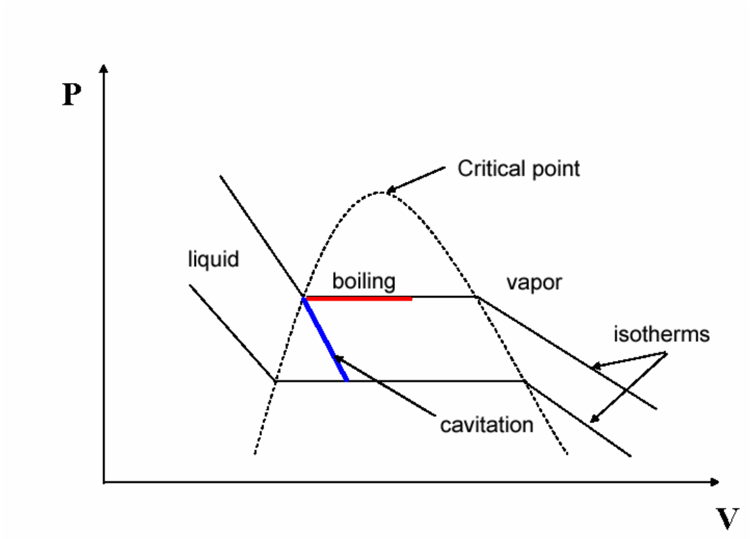

Figure 4.1: Description of cavitation phenomenon

The stage is therefore set to consider what happens in a given flow when either the overall pressure is decreased or the flow velocity is increased so that the pressure at some point in the flow approaches the vapor pressure, p_V, of the liquid at the reference temperature, T_∞. In order to characterize this relationship, it is conventional to define the *cavitation number* based on constant liquid density ρ_L and flow velocity U_∞. The cavitation number σ_c is given as

$$\sigma_c = \frac{p_\infty - p_V(T_\infty)}{\frac{1}{2}\rho_L U_\infty^{\ 2}} \tag{4.1}$$

Any flow, whether cavitating or not, has some value of σ_c. For large values of σ_c, obtained by large $p_\infty >> p_V(T_\infty)$ or for very small values of U_∞, single-phase liquid flow is established. With reduction in σ_c, first occurrence of nucleations is incepted at some particular value of σ_c called the incipient cavitation number (σ_i). Further reduction in σ_c below σ_i causes an increase in the cavitation number and extent of vapor bubbles (typically number density). Different types of cavitation are observed depending on the flow conditions and geometry [33, 168, 169]. Each type of cavitation has distinct characteristics. Some major types of cavitation are described briefly.

1) Traveling cavitation is a type of cavitation in which individual transient cavities or bubbles form in the liquid and move with it as they expand or shrink during their life cycles [33, 34]. It is typically observed in geometries with suddenly expanding or contracting sections. The geometries of the bubbles formed are highly dependent on the amount of nuclei present in the incoming flow [34]. In visualization, traveling cavitation may appear as sheet cavitation [105]. Individual transient spherical bubbles can be distinguished by advanced visualization procedures.

2) Cloud cavitation is caused by vorticity shed into the flow field resulting in strong vibration, noise and erosion [33, 34, 169, 170]. The shedding of cloud cavitation has been identified to be periodic and a re-entrant jet type mechanism is believed to trigger cloud cavitation [170, 172-174].

3) Sheet cavitation is also known as fixed, attached, cavity or pocket cavitation. Sheet cavitation is stable in a quasi-steady sense [170, 171, 175]. The interface between the liquid and the vapor

can be smooth and transparent or it can have the shape of a highly turbulent boiling surface [33]. The liquid vapor interface becomes wavy and breaks down in the closure region of the cavity. Downstream flow, which contains large scale eddies, is dominated by bubble clusters [105, 107].

4) Vortex cavitation occurring on the tips of rotating blades is known as tip vortex cavitation [21]. Cavities form in the cores of vortices, representing regions of high shear. These type of cavitations are not restricted to rotary frames and have also been known to occur in the separation zones of bluff bodies [33, 34].

4.1 Inception of cavitation and turbulence effects

Most of the flows in realistic situations are not only turbulent but also highly unsteady. Vortices occur not only because they are inherent in turbulence but also because of both free and forced shedding of vortices [35]. This has important consequences for cavitation inception because the pressure in the center of a vortex may be significantly lower than the mean pressure in the flow [33, 34]. Although cavitation number indicates the effect point at which cavitation nuclei is expected to appear, in real circumstances the actual cavitation number might vary from the calculated cavitation number due to various factors [171]. In sum, there are a number of reasons for σ_i *(calculated)* to be different from the value of σ_c *(actual)* that might be calculated from knowledge of the pressures in the single-phase liquid flow: while existence of tensile strength, residence time effects, presence of contaminant gas and viscous effect in the flow result in reduction of the incipient cavitation number, the turbulence effects, characterized by highly random flow velocity components, augments the incipient cavitation number index. Unfortunately, these effects can cause large departures from the criterion, σ_i=-σ_c, with important engineering consequences in many applications. Furthermore, the above discussion identifies the parameters that must be controlled or at least measured in systematic experiments on cavitation inception [34]:

1. The cavitation number, σ_c.
2. The Reynolds number, Re.
3. The liquid temperature, T_∞
4. The liquid quality – details of free stream nuclei available, dissolved gas component etc.
5. The quality of the solid surfaces such as its roughness, pit population, porosity etc contributes to variation in cavitation inception.

Since this is a tall order, and many of the effects such as the interaction of turbulence and cavitation inception have only recently been identified [33, 34], it is not surprising that the individual effects are not readily isolated from many of the experiments performed in the past. Nevertheless, some discussion of these experiments is important for practical implementations in many fluidic devices. With this fundamental background on cavitation, details concerning characteristics of gas/vapor bubbles in a flow field are presented next.

4.2 Bubble growth and collapse behavior

The growth and collapse of gas/vapor bubbles in a flow manifest a host of phenomena predominantly influencing technological processes [33, 34]. The current section is dedicated to understand the fundamental behavior of a growing/collapsing bubble in an infinite domain of liquid at rest far from the bubble. In the discussions, spherical symmetry is assumed although this assumption is violated in a majority of the processes [33].

4.2.1 Rayleigh - Plesset Equation

Consider a spherical bubble of radius *R(t)* in an infinite medium of liquid whose temperature and pressure far from the bubble are T_∞ and P_∞. A constant temperature surrounding the bubble is assumed and hence any temperature gradients are neglected [34]. The pressure, $P_\infty(t)$, however, is assumed to be available as a control input to monitor the growth or collapse of the bubble.

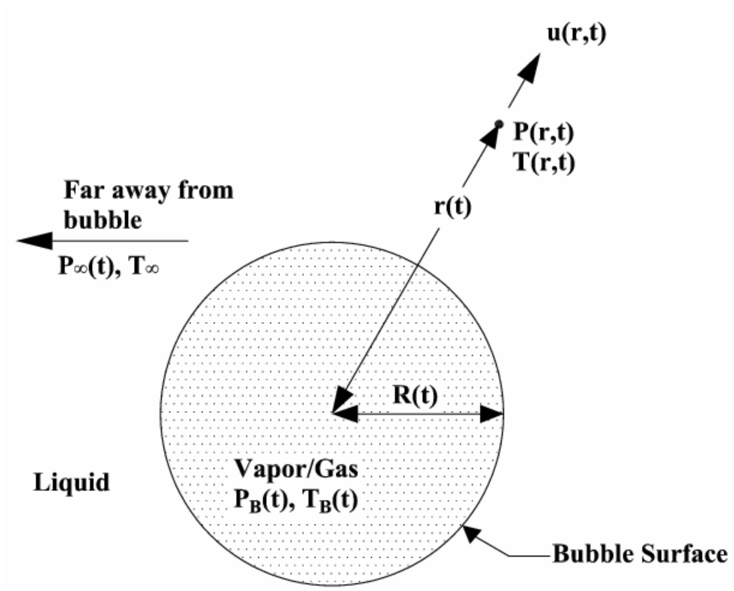

Figure 4.2: Schematic of bubble under consideration

Further, the liquid compressibility is assumed to be a constant, although it can important in the context of bubble collapse [34, 178, 179]. Similar assumptions are made based for the liquid viscosity. Furthermore, the contents of the bubble are assumed homogeneous and that the temperature, $T_B(t)$ and pressure, $p_B(t)$, within the bubble are considered to be uniformly distributed. Having the parameters of the bubble setup, the growth of the bubble, its radius, is monitored as a function of these parameters. As indicated in Fig. (4.2), the radial position within the liquid is denoted by *r* from the center of the bubble where the pressure is *p(r, t),* the radial outward velocity being *u(r,t)* and temperature *T(r,t)*. By conservation of mass we have,

$$u(r,t) = \frac{\phi(t)}{r^2} \tag{4.2}$$

where $\phi(t)$ is the potential function and is related to $R(t)$ by a kinematic boundary condition at the bubble surface. In the idealized case of zero mass transport across the liquid-gas interface, $u(R,t) = dR/dt$ and hence we can write,

$$\phi(t) = R^2 \frac{dR}{dt} \tag{4.3}$$

This is a good approximation taking into account the process of evaporation and condensation at the interface provided that the vapor density is much smaller than the liquid density, a true scenario in case of liquid water [34]. Assuming a Newtonian liquid, the Navier-Stokes equation for motion in spherical co-ordinates gives

$$-\frac{1}{\rho_L}\frac{\partial P}{\partial r} = \frac{\partial u}{\partial t} + u\frac{\partial u}{\partial r} - \nu_L\left(\frac{1}{r^2}\frac{\partial}{\partial r}\left(r^2\frac{\partial u}{\partial r}\right) - \frac{2u}{r^2}\right) \tag{4.4}$$

Substituting for u in terms of ϕ,

$$-\frac{1}{\rho_L}\frac{\partial P}{\partial r} = \frac{1}{r^2}\frac{d\phi}{dt} - \frac{2\phi^2}{r^5} \tag{4.5}$$

The viscous terms are eliminated during the substitution process. Equation (4.5) can be integrated and applying the condition as $r \to \infty$, $p \to p\infty$ resulting in

$$\frac{p - p\infty}{\rho_L} = \frac{1}{r}\frac{d\phi}{dt} - \frac{1}{2}\frac{\phi^2}{r^4} \tag{4.6}$$

A dynamic boundary condition on the bubble surface is utilized in addition to expressing $\phi = R^2 dR/dt$ to obtain the final form of Rayleigh-Plesset (R-P) equation for bubble dynamics as

$$\frac{p_B(t) - p_\infty(t)}{\rho_L} = R\frac{d^2R}{dt^2} + \frac{3}{2}\left(\frac{dR}{dt}\right)^2 + \frac{4\nu_L}{R}\frac{dR}{dt} + \frac{2\sigma}{\rho_L R} \tag{4.7}$$

Given $p_\infty(t)$, equation (4.7) can be solved to find $R(t)$ provided the bubble pressure $p_B(t)$ is known. Rayleigh [180] used the expression without the surface tension and viscous terms. Later, Plesset [181] used the R-P equation to solve problems concerning traveling cavitation bubbles. The effects of viscosity on the bubble dynamics was addressed by Poritsky [182].

4.2.2 Note on Bubble contents

In order to completely clarify the total bubble dynamics in any given system considerations of the bubble contents are crucial. It is assumed that the bubble contains some finite amount of non-condensable gases whose partial pressure is p_{Go} at some reference size, R_o, and temperature $T\infty$ [33, 34]. Neglecting any contribution of appreciable mass transfer of gas to or from the liquid, the bubble pressure is given as

$$p_B(t) = p_V(T_B) + p_{Go}\left(\frac{T_B}{T_\infty}\right)\left(\frac{R_o}{R}\right)^3 \qquad (4.8)$$

In deriving equation (4.8) isothermal bubble expansion is assumed. In some accounts, this assumption is not justified and it then requires solving a mass transport problem for the liquid [183]. Clearly, the temperature difference between $T_B(t)$ and $T\infty$ is important since it leads to different vapor pressure $p_V(T_B)$. As a result, the bubble dynamics is modified palpably. To demonstrate this effect, a general Rayleigh-Plesset equation incorporating the thermal effects, thus, leads to

$$\frac{p_v(T_\infty) - p_\infty(t)}{\rho_L} + \frac{p_v(T_B) - p_v(T_\infty)}{\rho_L} + \frac{p_{go}}{\rho_L}\left(\frac{T_B}{T_\infty}\right)\left(\frac{R_o}{R}\right)^3 = R\frac{d^2R}{dt^2} + \frac{3}{2}\left(\frac{dR}{dt}\right)^2 + \frac{4\nu_L}{R}\frac{dR}{dt} + \frac{2\sigma}{\rho_L R} \qquad (4.9)$$

Observe that the first term represents the instantaneous tension or driving term determined by conditions far from the bubble while th second term, the thermal inertia term, varies according to the magnitude of the former. However, the solution to such a problem with variation in thermal energy content involves a multi-step process to compute the difference between the bubble and surrounding liquid temperature and hence evaluate the bubble behavior. This process invokes solution of a heat diffusion in the liquid domain. Following this, a heat balance equation across the interface is used to calculate the growth rate of the bubble wall radius which when coupled with the temperature gradient across the interface with the R-P equation generates as integro-differential equation for the bubble radius, $R(t)$. Existence of considerable non-linearities in the heat diffusion equation and non-existence of any analytical solution for the governing equation makes the thermal computation very difficult [34, 184]. Some approximations have been dealt with simplifying assumptions based on boundary layers have been performed by Plesset et al. [183].

Some fundamental difference between cavitation and boiling phenomenon requires clarification. While the boiling mechanism is inhibited by limitations on heat transfer at the interface, the bubble growth and collapse occurring during the cavitation process is limited only by the inertial effects in the surrounding liquid. Cavitation, therefore, is considered as an explosive process and is far more violent than corresponding bubble dynamics of boiling. In the case of cavitation, where pressure fluctuations, relating to the inertial content of the surrounding liquid, regulate the growth and collapse of vapor bubbles, neglecting the thermal content of the bubble can be considered a good approximation [34, 185].

4.2.3 Influence of oscillating pressure fields

Frequently, vapor/gas bubbles are found immersed in a fluid flow environment. The translatory motion of the bubble affects its response to the local pressure fluctuations by either increasing the energy content or by draining it. Various other parameters associated with flow field characterization such as vorticity and gradients impose severe constraints on the bubble dynamics [33, 34]. The effect of translation on the bubble dynamics with gravity effects was reported by Chakraborty et al. [186].

Although several studies deal with the dynamics of bubbles under constant pressure field [34, 185, 187], investigating the effect of gas/vapor bubble dynamics in the presence of fluctuating pressure fields has caught the notice of few researchers. In practice, interaction of varying pressure fields with gas and vapor bubbles are observed in a wide gamut of systems, such as those occurring in pressure waves across boiling channels, acoustically enhanced heat transfer systems etc [185, 188]. Plesset & Prosperetti [184] pointed out that the bubble response to a time-periodic pressure field can be chaotic, even when the bubble is assumed spherical. A preliminary study of bubble dynamics in oscillating pressure fields based on linearized theory was performed by Plesset et al. [188]. Due to the nonlinearities in the governing equations, particularly the Rayleigh-Plesset equation, the response of the gas or vapor bubble to the fluctuating pressure fields may be greatly amplified based on the amplitude and frequency of these perturbed fields. With an oscillating pressure field surrounding the gas or vapor bubble, the stable oscillations that exist with a constant pressure ambience encompassing the bubble, can be modified appreciably [189].

The early experiments of Blake [190] were concerned with the behavior of a gas bubble in oscillating pressure fields. Willard [191] carried out experiments extending the work of Blake[190] and his theory of inception of cavitation in an oscillating pressure field encouraged the discussions on the influence of modulated pressure fields on bubble behavior. Willard [191] stated that as a gas bubble enters the pressure field, it alternately expands and contracts. It grows in average size because of the rectified diffusion effect of the pressure cycle, i.e., the surface of the bubble is larger during the negative half of the pressure cycle than during the positive half.

Hence more gas or vapor enters the bubble during the negative half. He assumed that this process continues as a forced oscillation for a large number of cycles until the volume reaches such a size that its natural frequency of oscillation is in resonance with the imposed frequency of the pressure field. At this point the bubble size increases with great rapidity, as evidenced by the burst seen in his experiments. It can be inferred from Willard's experiments that a bubble of a given size under a low frequency pressure field has a very much longer time to reach resonance and produce a finite size. Lauterborn [192] investigated the non-linear oscillations of gas bubbles in liquids subjected to forced oscillations. He concluded that a gas bubble could be driven to high amplitudes in its oscillation at harmonics of the resonance frequency of the bubble. Further, all resonances lean towards lower frequencies and show jump phenomena depending on the direction of the frequency alteration. Importantly, he observed that sub-harmonic and ultra-harmonic oscillations occur only beyond a critical threshold value of the driving pressure amplitude. It was also indicated that if the pressure amplitude is raised from a low value to a higher value, the resonance curve as a whole alters its appearance. Recently, the effect of oscillating pressure fields on bubbles filled with gas and vapor mixtures have been reported [185]. To validate asymptotic-theory predictions such as the existence of resonant radii and limit size for given acoustic amplitude and frequency [194], the behavior of vapor bubbles under the influence of acoustic pressure fields was studied numerically. The study revealed that a vapor bubble in appropriate acoustic frequency and amplitude range grew quickly to resonance and at a slower rate indefinitely thereafter. Resonance phenomena were identified as playing a major role for a few cycles but in order to reach a limit size, higher cycles were required. Further work on rectified heat transfer into pulsating vapor bubbles with added effect of translation was carried out by Hao et al. [193, 194]. The influence of translation and ensuing convective process on enhancement of heat transfer in vapor bubbles was identified. In their computations, the bubble was assumed to translate with different fixed rectilinear velocities. Recently, Srinivasan et al. [195] addressed the influence of oscillating pressure field with bubble translation effects on the bubble dynamics. They identified the critical nature of pressure perturbation amplitude and frequency on the collapse behavior and growth rates.

The characteristics of the bubble dynamics fluctuate in a profound manner as a strong function of the imposed pressure fluctuation magnitudes. For very small pressure amplitudes the response is linear. As explained earlier, the nonlinearities in the governing equations (4.7) contribute to the stability of the oscillating bubble. Nevertheless the bubble may continue to oscillate stably. Such circumstances are referred to as ‘stable acoustic cavitation’. Several different nonlinear phenomena such as production of subharmonics, the phenomenon of rectified diffusion, and the generation of Bjerknes forces [34] can affect stable acoustic cavitation in important ways. Under other circumstances the change in bubble size during a single cycle of oscillation can become so large that the bubble undergoes a cycle of explosive cavitation growth and violent collapse. Such a response is termed ``transient acoustic cavitation" and is distinguished from stable acoustic cavitation by the fact that the bubble radius changes by several orders of magnitude during each cycle. Neppiras et al. [196] examined the effect of ultrasonic pressure oscillations in the vicinity of a cavitation bubble on its growth and collapse behavior. Noltingk et al. [197] later described the critical radius beyond which the bubble starts to grow rapidly. For their analysis, Neppiras et al. [197] assumed an incompressible liquid and that the gas content of the cavitation bubble is assumed to be a constant over its life cycle. The external fluid pressure at infinity, *p(t)*, was modified to carry an added ultrasonic pressure wave such that

$$p_\infty(t) = p_a - p_o \sin\left(\omega_b t\right) \qquad (4.10)$$

where p_o is the amplitude of ultrasonic pressure wave with a frequency of $\omega_b/2\pi$ superimposed on a pressure field p_a. Furthermore, it is assumed that the applied ultrasonic pressure wave is sinusoidal, although the very changes in the volume of the bubble under consideration must distort the pressure wave to some extent in its vicinity. Adding, the diameter of the bubble is assumed to be much smaller than the wavelength of the incoming pressure wave.

The cavitation bubble is given an arbitrary initial equilibrium radius R_o, and its evolution as a function of the pressure and frequency field is monitored. For brevity, two computations performed by Neppiras et al. [196] are presented here with imposed angular frequencies (ω_b) of $3x10^7$ and $9x10^7$. The mean pressure, p_a, is taken as 10^5 Pa while an initial bubble size of 0.8μm is assumed. The liquid under investigation concerns water at STP and hence, standard properties are taken for computation purpose. Neppiras et al. [196] did not account for the viscous effects in their computation and hence the preceding results do not accommodate any effects of liquid viscosity. With these conditions, the Rayleigh-Plesset equation described in equation (4.7) is solved, using IV order Runge-Kutta integration method, for variation in Radius of the bubble. The results obtained by Neppiras et al. [196] are reproduced here as shown in Fig. (4.3(a)). Following this computation, the code is used to compute the influence of bubble initial radius on its dynamics. For this purpose, the frequency of imposed oscillation is maintained constant along with other liquid and vapor parameters. Since, no collapse was observed with a frequency of $\omega_b = 9x10^7$, this frequency value is assumed while the initial bubble radius is varied as $R_o = 8$ and 10 μm. The calculated results are shown in Fig. (4.3(b)). Notice from Fig. (4.3(b)), a small change in the initial radius of the bubble results in out of phase peaking of the bubble radius. This portrays the complex behavior of bubbly mixtures wherein a wide range of bubble sizes exist and mutually affect one another.

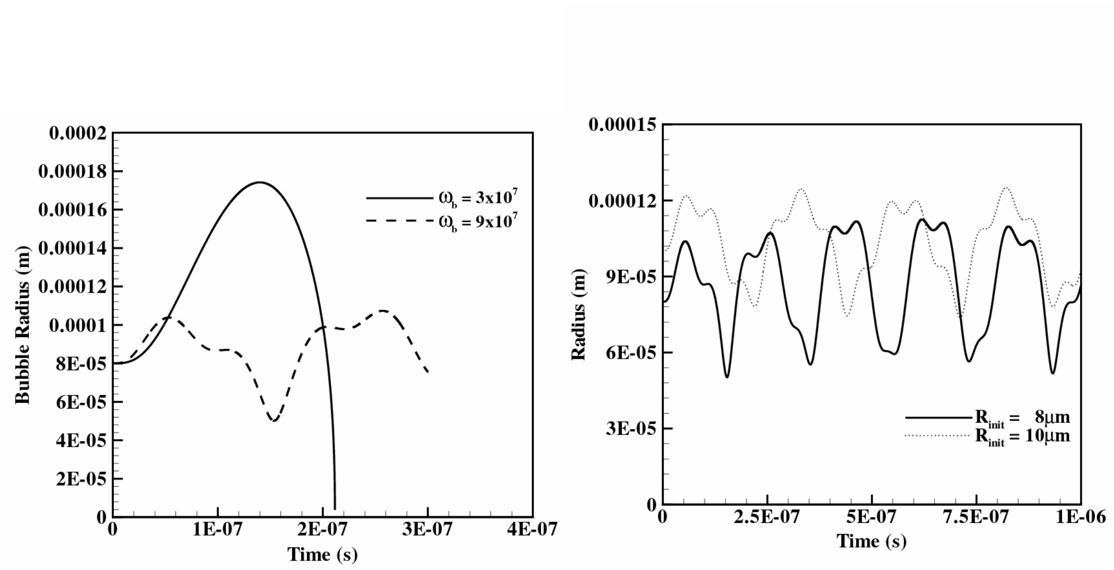

(a) (b)

Figure 4.3: Radius history curves (a) Influence of imposed perturbation frequency (b) Influence of initial bubble radius on the vapor bubble dynamics

For a frequency of 3x10^7 in Fig. (4.3(a)), events of collapse occur within 0.2 μs while with increase in the frequency of the pressure wave, the collapse is averted and a non-linear bubble evolution behavior is obtained. Neppiras et al. [196] inferred that for each impressed frequency on the pressure wave there exists a maximum bubble size that can give rise to cavitation. As the frequency is raised, they concluded, this limit becomes smaller and smaller. As a result of this, by sufficiently increasing the ultrasonic frequency, with other parameters remaining the same, the expected intensity of cavitation can be reduced to vanishing point [34]. For the imposed pressure wave frequency $p_o << p_a$, Neppiras et al. derived the resonant frequency of the bubble as

$$\left(2\pi f_{res}\right)^2 = \frac{3w\left(p_a + {}^{2\sigma}\!/_{R_o}\right)}{\rho R_o^{\,2}} \tag{4.11}$$

where w is the polytropic constant. With a wide range of computations performed using different bubble equilibrium radius and pressure wave parameters, Neppiras et al. [196] concluded that the pressure field, p, is fundamentally governed by the ultrasonic amplitude, $p_{o,}$ and the pressure of gas inside the bubble at its maximum radius, $p_{g,}$ for a constant maximum radius on the initial bubble radius R_o. They showed that the maximum bubble radius reached during the evolution of the cavitation bubble is inversely proportional to the imposed angular frequency ω_b. Following this, all cavitation effects will be expected to fall off with increasing frequency, and disappear completely in the range

$$\omega_b = \frac{1}{2\pi R_E}\left(3w\left(p_a + \frac{2\sigma}{R_o}\right)\right)^{\frac{1}{2}} \tag{4.12}$$

4.2.4 Frequencies of oscillating bubbles

The response of the vapor/gas bubbles to perturbations in the surrounding pressure fields vary as a function of the magnitude of such fluctuations. Due to the nonlinearities in the governing equations, particularly the Rayleigh-Plesset Equation (4.7), the response of a bubble will begin to be affected by these nonlinearities as the amplitude of oscillation is increased [185]. For a given set of operating parameters such as the pressure difference across the bubble, the equilibrium radius, the properties of the liquid and vapor such as surface tension, viscosity etc determines the frequency ranges in which the bubble response would be critical [196]. Considering the viscous effects, the peak frequency is calculated as

$$\omega_P = \left[\frac{3w\left(p_\infty - p_v\right)}{\rho_L {R_o}^2} + \frac{2\left(3w-1\right)\sigma}{\rho_L {R_o}^3} - \frac{8\upsilon_L}{{R_o}^4}\right]^{\frac{1}{2}} \tag{4.13}$$

where R_o is the bubble equilibrium radius [34]. The bubble peak frequency is an important quantity in any bubble dynamic problem. From equation (4.13), it is clear for larger bubbles the viscous terms become negligible and the peak frequencies are driven by the pressure difference term. Typical peak frequencies for a water bubble, under varying equilibrium radius, are plotted in Fig. (4.4).

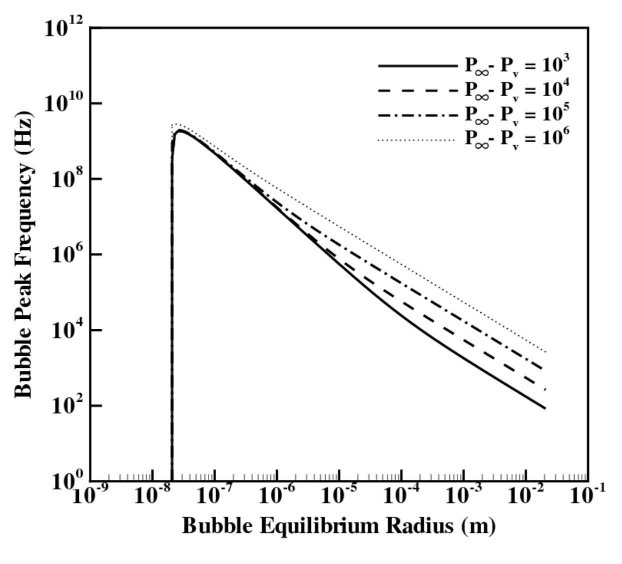

Figure 4.4: Bubble resonant frequency in water at 300K.

For no damping, neglecting viscous effects, the natural angular frequency of oscillations of the bubbles is given by

$$\omega_n = \left\{ \frac{1}{\rho_L R_o^{\ 2}} \left(3w\left(p_\infty - p_V\right) + 2\left(3w-1\right)\frac{\sigma}{R_o} \right) \right\}^{\frac{1}{2}} \tag{4.14}$$

In the range of typical nuclei found in water (1-100μm) the natural frequencies are of the order, 5-25 KHz. The range of natural frequencies has serious implications in several applications [34, 185, 189, 190]. Example, if a given sample of water requires cavitation using an imposed acoustic pressure field, then the frequencies that will be most effective in producing a substantial concentration of large cavitation bubbles will be in this frequency range. It should be noted that the oscillation of the nuclei produced in this way will be highly non-linear and therefore peak response frequencies will be significantly lower than those computed numerically.

The effect of imposed frequency on the cavitation bubbles is reported to be of paramount importance in assessing the transient cavitation characteristics. For example, if the imposed frequency $\omega >> \omega_n$ then the liquid inertia is unimportant and the response of the bubble is observed to be quasi-static. However, if the frequency of the imposed oscillation is much greater than ω_n, inertial content of the surrounding environment controls the size of the perturbations and hence the bubble size. Details of this bubble dynamics as a function of frequency fluctuation has been addressed by Flynn [198] and some guidelines provided by Apfel [199].

4.2.5 Growth and collapse characteristics of cavitation bubbles

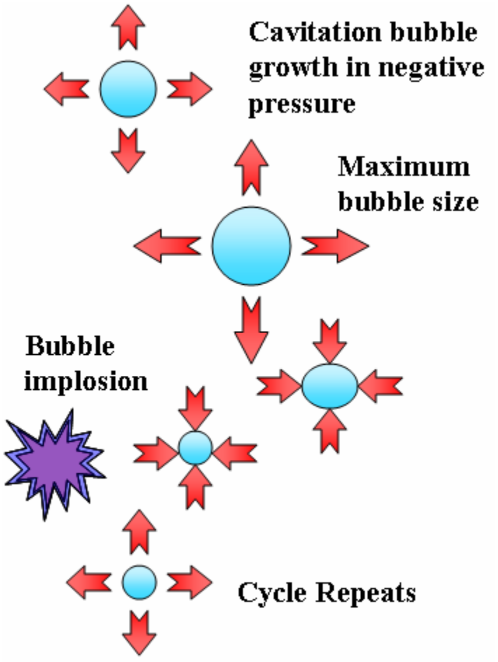

Figure 4.5: Growth and collapse characteristics of cavitation bubble

It has been observed that as amplitude of pressure fluctuations increase, the magnitude of the negative pressure in the areas of rarefaction eventually becomes sufficient to cause the liquid to ‘fracture’ because of the negative pressure. Bubbles are created at sites of rarefaction as the liquid fractures or tears because of the negative pressure region in the liquid [200, 201]. The "bubbles" oscillate under the influence of positive pressure, eventually growing to an unstable size. Finally, the violent collapse of the cavitation "bubbles" results in implosions, which cause shock waves to be radiated from the sites of the collapse [33, 34, 201-207].

4.3 Vibration cavitation

Inception of cavitation event can be realized by several methodologies such as flow geometry effects or as a direct consequence of flow field itself (vortex cavitation etc.). The underlying fundamental mechanism that contributes to the initiation of cavitation events are the non-linear pressure perturbations imposed on the flow field. As discussed earlier, the response of the vapor bubbles to pulsating pressure fields can be quite catastrophic. The process of vibratory cavitation [202-206] utilizes the oscillatory motion of a solid structure immersed in a liquid field to proliferate cavitation phenomena. Typically, ultrasonic vibrations of a moving structure are utilized to cause rupturing of the liquid medium, or in other words, initiate cavitation. The presence of a vibrating structure induces oscillatory pressure fields in the liquid medium. As amplitude of vibration increases, the magnitude of the negative pressure in the areas of rarefaction eventually becomes sufficient to cause the liquid to fracture because of the negative pressure [33, 34, 191, 199-207].

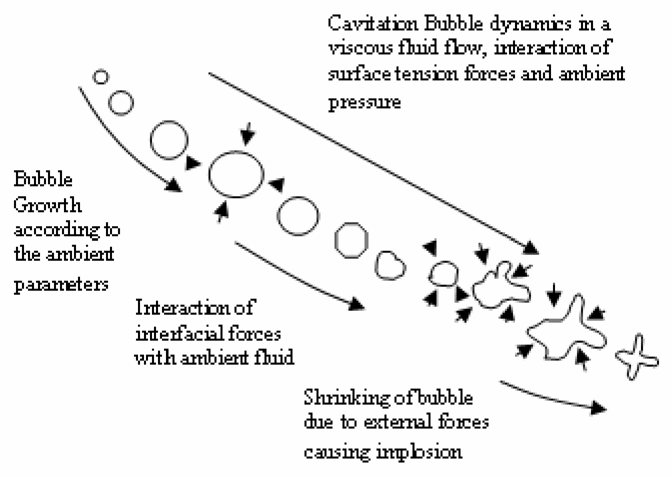

Figure 4.6: Influence of pressure fields on cavitation bubbles

A schematic of the vibratory cavitation process is shown in Fig. (4.7). Vibratory cavitation equipment, used for surface erosion purposes, consists of an ultrasonic transducer, which drives an amplification horn beneath which a stationary specimen can be placed. The vibration frequency of such equipment can be ultrasonic [29-31, 203-206] to intensify cavitation.

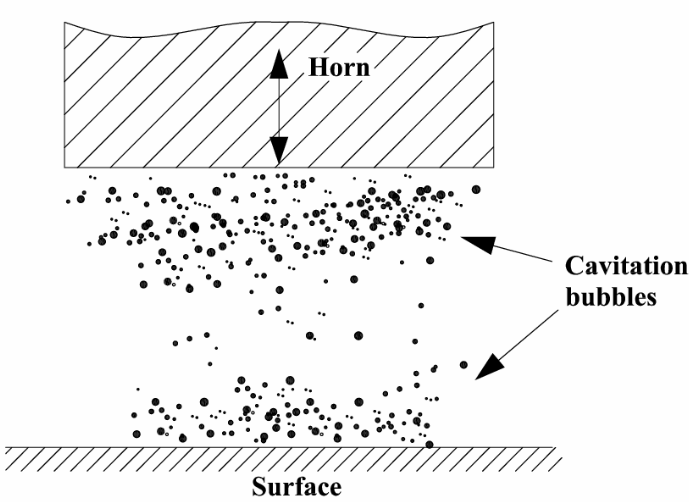

Figure 4.7: Vibration cavitation process

The effects of collapse of a cluster of bubbles in close proximity to each other have been investigated by Knapp [33]. Brennen [207] used a vibrating wall of high amplitude to produce cavitation bubble clusters. With increased vibration amplitude, he noticed that cavitation bubbles experience larger and larger growth and their subsequent collapse becomes more violent.

4.3.1 Modeling vibration cavitation

Hansson et al. [206] formulated a numerical model based on the vibratory cavitation system to track the collapse process of a cavitation bubble, given its initial radius and void fraction. In their work, a simple one-dimensional model was created to observe the propagation of pressure waves emanating from the oscillating horn surface influencing the growth and collapse of cavitation bubble on solid surface and near the horn surface. Their model assumes a constant vapor fraction of gas dissolved in the system. A simple approximation using a differential formulation leads to analytical expressions for pressure. The pressure equation encompasses the horn characteristics such as oscillation amplitude, frequency and distance of separation between the solid surface and the horn position.

Free gas nuclei are always present in real liquids as bubbles of very small radii and with very low void fractions. Their sizes and concentration distribution are too small to influence any kind of compression wave in the liquids [33]. However, when a rarefaction wave is introduced into the medium containing these nuclei, the bubbles undergo expansion and lead to events of cavitation [34, 192, 195]. The wave profile becomes significantly distorted due to the absorption of energy by the small dissolved nuclei. Since these events can lead to massive nucleation, more nuclei crossing the energy barrier supplementing their growth, two phase models need to be investigated including the tensile stresses in the system. However, model of Hansson et al. [206] and Kedrinskii et al. [205] contains no detail of the nucleation process involved in studying the collapse of cavitation bubbles. Instead, growth and collapse of a single bubble, independent of the distorted pressure field due to nucleation, is carried out. In order to communicate the influence of nucleation phenomena on the characteristics of a cavitation bubble, a new vibratory cavitation collapse model based on nucleation theories is derived. Based on the formulation, the effect of parameters such as separation distance between the horn and surface, horn oscillation amplitude is studied under a constant frequency of oscillation. Schematic of the parameters used in representing the vibration cavitation process is shown in Fig. (4.8).

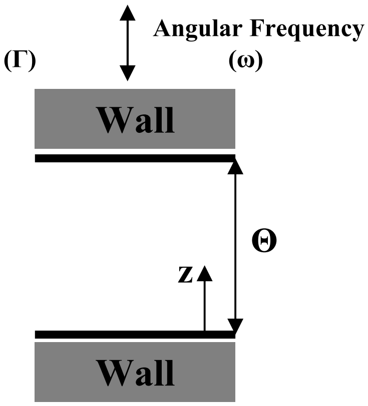

Figure 4.8: Vibration Cavitation modeling parameters

4.3.2 Cavitation cluster modeling using nucleation theories

A two-phase, one dimensional system is used in conjunction with revised classical homogeneous nucleation theories to predict the pressure profile and cavity dynamics developed between a stationary wall and an oscillating horn representing a vibratory cavitation system. The effect of operating horn frequency and its amplitude on the cavity dynamics is numerically simulated. The results indicate that for increased amplitude, under constant horn oscillation frequency, the collapse of the bubble is delayed. The homogeneous nucleation theories predict the nucleation rates and their occurrence during the compression-rarefaction cycle.

4.3.2.1. Introduction to nucleation theories

The classical nucleation theory of cavitation parallels that of condensation. The critical bubble is a void of radius R (if the coexisting gas pressure is low, the bubble will be almost empty). Once again a free energy per unit volume favors the formation of the new (gaseous) phase and surface tension disfavors it. Based on the free energy barrier ΔΩE* bubbles with radii larger than the critical radius R^* will tend to grow, and those that are smaller will shrink.

To consider the nucleation process occurring in the space between the oscillating horn and target surface, we use the revised classical theory formulation of Delale et al. [208]. Their formulation constructs the minimum (reversible) work of formation of a bubble of critical size in a phenomenological way convenient for comparison with experiments. The model is a consequence of second law of thermodynamics that the minimum work of formation has to be carried out in a reversible path, the latter most probably not achieved in cavitation experiments. The minimum work W_{min} required to form a vapor bubble of volume V from the homogenous liquid phase at constant temperature T is given by

$$W_{\min} = \sigma A - \left(p_v - p_L\right)V + i\left(\mu c_v - \mu c_L\right) \tag{4.15}$$

Where σ is the surface tension, A is the surface area of the bubble, p_v is the gas pressure within the bubble, p_L is the pressure in the bulk liquid, V is the volume of the bubble, i is the number of molecules inside the bubble and μc_v and μc_L are, respectively, the chemical potentials of the gaseous and liquid phases. Note that the first term in the right hand side of equation (4.15) characterizes the surface energy needed to create the surface of a vapor free cavity and the second and third terms characterize the reversible work that the 'i' molecules vaporizing into the cavity can provide. For a spherical vapor bubble of radius 'r', equation (4.15) can be written as

$$W_{\min} = 4\pi r^2 \sigma - \frac{4}{3}\pi r^3 \left(p_v - p_L\right)_{rev} + i\left(\mu c_v - \mu c_L\right)_{rev} \tag{4.16}$$

4.3.2.2 Numerical formulation

Adopting a cylindrical co-ordinate system, the one-dimensional assumption leads to the following system of equations incorporating the two phase model [206].

$$\frac{\partial \rho}{\partial t}+\rho\frac{\partial u}{\partial z}=0 \tag{4.17}$$

$$\frac{\partial u}{\partial t}+\frac{1}{\rho}\frac{\partial p}{\partial z}=0 \tag{4.18}$$

$$\rho=\left(1-b\right)\rho_0 \tag{4.19}$$

$$b=\frac{4}{3}\pi R^3.N \tag{4.20}$$

In the previous work reported by Hansson et al. [206], the bubble number density, *N*, was assumed to be a constant in the working incompressible liquid. In the present work, we assume a nucleation mechanism based on free energy barrier phenomena, to dictate the variation in bubble number density. As detailed earlier, inclusion of bubble nucleation is critical in deciding the dynamics of the cavitation bubble, due to the latter's tight coupling with the surrounding pressure field. The Rayleigh-Plesset equation (4.7) concerning the dynamics of an individual vapor bubble, neglecting effects of viscosity and surface tension, can be written as,

$$R.\frac{d^2R}{dt^2}+\frac{3}{2}\left(\frac{dR}{dt}\right)^2=\frac{1}{\rho_0}\left(p_o\left(\frac{R_0}{R}\right)^{3w}-p\right) \tag{4.21}$$

Combining equations (4.17)-(4.20), the resulting equation for spatial variation in pressure field reduces to

$$\frac{d^2p}{dz^2}=-\rho_0 b_0.\frac{d^2b}{dt^2} \tag{4.22}$$

The rate of change of bubble number density can be represented as,

$$\dot{N}=\frac{dN}{dt}=J \tag{4.23}$$

Now combining (4.20) and (4.23) we have,

$$\frac{d}{dt}\left(\frac{3b}{4\pi R^3}\right)=J \qquad (4.24)$$

Expanding equation (4.24) leads to

$$\frac{db}{dt}-\frac{b}{R}\frac{dR}{dt}-\frac{4}{3}\pi R^3 J=0 \qquad (4.25)$$

Equation (4.25) can be integrated analytically to give

$$b(t)=-\frac{\frac{4}{3}\pi R^3 J}{\frac{1}{R}\frac{dR}{dt}}+e^{\left(\frac{1}{R}\frac{dR}{dt}.t\right)}.C_3 \qquad (4.26)$$

Where constant C_3 can be obtained from the initial conditions available for *b* at t=0. The numerical evaluation of the bubble radius *R* and its wall velocity *dR/dt* together with the nucleation rate *J* can be used to evaluate the void fraction value *b* at any instant of time. Clearly, the transient change in void fraction of the dispersed phase in the primary liquid is related to the nucleation process.

The steady state nucleation rate is given by the phenomenological nucleation rate derived by Delale et al. [208] as

$$J=J_o\,\mathrm{e}^{(-Gb)}=Z_v\left(\frac{3\sigma\rho_L{}^2}{\pi m_1{}^3}\right)^{\frac{1}{2}}\exp\left(-\frac{4\pi r^{*2}\,\sigma}{3.kb.T_L}\left(1-2fi\right)\right) \qquad (4.27)$$

where m_1 is the molecular mass of the liquid, Z_v the compressibility, ρ_L is the density of the liquid, *kb* the boltzmann constant, T_L the temperature of the liquid and *fi* the fiddle factor. For our simulations, we use *fi* = 0.499999925 close to 0.5 as suggested by Delale et al. [208].

Minimum work required to form a spherical bubble of radius *r** in the classical theory can be constructed in a phenomenological manner using the pressure difference achieved in the experiments as

$$W^{*}_{\min} = 4\pi r^{*2} - 4\pi r^{*3}\left(P_v - P_L\right)_{\exp} - FL^{*}\left(T_L, P_L\right) \tag{4.28}$$

where $FL^{*}\left(T_L, P_L\right) \geq 0$ is introduced to denote the phenomenological correction to the free energy for the formation of a vapor bubble of critical size *r** with vapor pressure *(P_V*)exp* at temperature T_L and liquid pressure P_L. With the correction factor, *FL** marching towards zero, the dissipative effects in the experiments are assumed to vanish and reversibility be achieved. This is possible in case of experiments concerning cloud chambers, shock tubes, nozzles etc where isentropic situations are possible unlike in the formation of a vapor bubble where the phenomenological correction is required.

$$J = J_o\, \mathrm{e}^{(-Gb)} = Z_v \left(\frac{3\sigma \rho_L{}^2}{\pi m_1{}^3}\right)^{\frac{1}{2}} \exp\left(-\frac{4\pi r^{*2}\sigma}{3.kb.T_L} + \frac{F^{*}\left(T_L, P_L\right)}{kb.T_L}\right) \tag{4.29}$$

For our simulations, equation (4.27) constructed from equation (4.29) replacing the correction factor by the phenomenological correction factor (1-2*fi*) is used.

Defining the void fraction *y* as the ratio of *b*/*b*

$$\ddot{y} - \frac{\dot{y}^2}{6y} + \frac{11}{6}\left(\frac{\dot{N}}{N}\right)^2 y - \frac{5}{3}\dot{N}\dot{y} = -\frac{3}{\rho_o R_o{}^2}(y)^{1/3}\left(\frac{N}{N_o}\right)^{-2/3}\left[p_o\left(\frac{N}{N_o}\right)^{w} y^{-w} - p\right] \tag{4.30}$$

$$\begin{aligned}\frac{1}{\rho_o \beta_o}\frac{\partial^2 p}{\partial z^2} = &-\frac{3}{\rho_o R_o{}^2}(y)^{1/3}\left(\frac{N}{N_o}\right)^{-2/3}(y)^{-w}\left(\frac{N}{N_o}\right)^{w} p_o + \frac{3}{\rho_o R_o{}^2}(y)^{1/3}\left(\frac{N}{N_o}\right)^{-2/3} p \\ &+\frac{\dot{y}^2}{6k} + \frac{11}{6}\left(\frac{\dot{N}}{N}\right)^2 y - \frac{5}{3N}\dot{N}.\dot{y}\end{aligned} \tag{4.31}$$

$$\begin{aligned}\frac{\partial^2 p}{\partial z^2} = &-\frac{3b_o}{R_o{}^2}(y)^{1/3}\left(\frac{N}{N_o}\right)^{-2/3}(y)^{-w}\left(\frac{N}{N_o}\right)^{w} p_o + \frac{3b_o}{R_o{}^2}(y)^{1/3}\left(\frac{N}{N_o}\right)^{-2/3} p \\ &+\frac{\rho_o b_o \dot{y}^2}{6k} + \frac{11\rho_o b_o}{6}\left(\frac{\dot{N}}{N}\right)^2 y - \frac{5\rho_o b_o}{3N}\dot{N}.\dot{y}\end{aligned} \tag{4.32}$$

Equation (4.32) is a Helmholtz type equation governing the propagation of variable *p* and can be represented as

$$\frac{\partial^2 p}{\partial z^2} = -A + B.p + B - C + D - E \tag{4.33}$$

Where,

$$A = \frac{3b_o}{R_o^{\,2}} (y)^{1/3} \left(\frac{N}{N_o} \right)^{-2/3} (y)^{-w} \left(\frac{N}{N_o} \right)^{w} p_o$$

$$B = \frac{3b_o}{R_o^{\,2}} (y)^{1/3} \left(\frac{N}{N_o} \right)^{-2/3}$$

$$C = \frac{\rho_o b_o}{6k} \dot{y}^2 \tag{4.34}$$

$$D = \frac{11}{6} \rho_o b_o \left(\frac{\dot{N}}{N} \right)^2 y$$

$$E = \frac{5\rho_o b_o}{3N} \dot{N}.\dot{y}$$

The solution to equation (4.33) is given by,

$$p(z) = C_1 e^{\sqrt{B}z} + C_2 e^{-\sqrt{B}z} + \frac{A + C - D + E}{B} \tag{4.35}$$

where C_1, C_2 are constants.

The above equation requires two boundary conditions to evaluate the constants C_1 and C_2.

Note that for a constant bubble density *N*, the above equation reduces to the analytical model developed by Hansson et al. [206]. Equation (4.35) does not neglect the effect of nucleation and the rate of change of volume gas concentration as previously assumed [205, 206]. The co-efficients A, B and C can be evaluated solving the void fraction equation (4.30) after obtaining the values of *b*.

Typically, $\frac{\dot{N}}{N}$ can be expressed in terms of *R* and *b* as

$$\frac{\dot{N}}{N} = \left[\frac{1}{b}\frac{db}{dt} - \frac{3}{R}\frac{dR}{dt} \right]. \tag{4.36}$$

4.3.2.3 Numerical methodology

The combined equation for void fraction (4.30) is solved using IV order Runge Kutta integration method previously tested in simulating the effect of oscillating pressure fields on bubble dynamics with translatory motion [195]. The computed scalar y is used in calculating the pressure distribution $p(z)$ using equation (4.35). Using the computed value of y, the radius of the bubble under the influence of pressure fluctuation and also the nucleation process is plotted for different parameters tested.

4.3.2.4 Test Cases

In the first set of simulations reported, numerical simulation parameters such as the horn frequency, oscillation amplitude and distance of separation between the horn and the target surface etc are taken from the experiments of Hansson et al. [203]. In their experiments, the horn motion is described by a sinusoidal wave form with a constant frequency of 20 KHz. The distance between the horn and the solid surface is 2mm. The polytropic constant w is assumed to be 1.4. With these conditions, two different horn amplitudes were tested: 2.5 µm and 3.5 µm. An initial void fraction of $b_o = 10^{-7}$ is assumed in our computations which is a realistic value frequently found in normal liquids [33, 203-206]. The behavior of bubble radius near the solid surface under such oscillating pressure fields are plotted in Fig. (4.9(a)). Simultaneous pressure and nucleation history are provided in Fig. (4.9(b)-(c)). Notice that strong nucleation effects are seen during the initial phase of the bubble growth when the pressure at the surface falls well below the vaporization pressure. The pressure modulation imposed on the system is sinusoidal in time and hence, the initial phase represents retracting motion of the horn inducing low pressure regions near the horn surface.

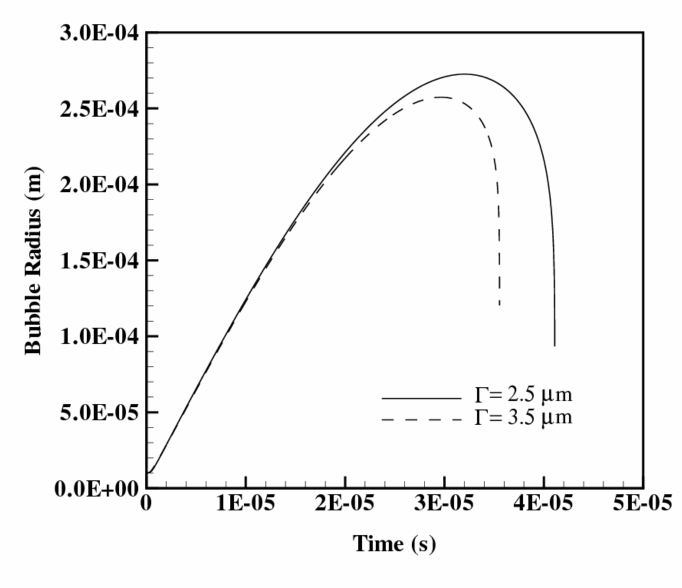

Figure 4.9: Numerical simulations of bubble dynamics with a constant forcing frequency of 20 KHz. Distance between the horn and solid surface is maintained at 2mm.

In a different test case, experimented previously by Hansson et al. [204], the horn frequency and amplitude were kept constant at 20 KHz and 2.5 μm respectively, while different separation distances Θ = 200 and 220 μm were experimented. Computations of the resulting bubble dynamics are presented in Fig. (4.10(I)). Although, the pressure oscillation period is 50 microseconds, collapse occurs within half the time period for the higher proximity case. However, the bubble growth is extended farther beyond the ½ cycle time in the lower proximity test case (approximately 35 μm) indicating the strong influence of nucleation and pressure fluctuation characteristics. The nucleation rates and pressure history are detailed in Figs. (4.10II(a) and (b)) respectively. As observed from the numerical simulations, the coupled process of bubble nucleation, growth and collapse characteristics exhibit very high degree of non-linearity. The above results presented for a single cavitation bubble behavior gives an indication of the true nature of complexity inherent to a cluster of cavitation bubbles.

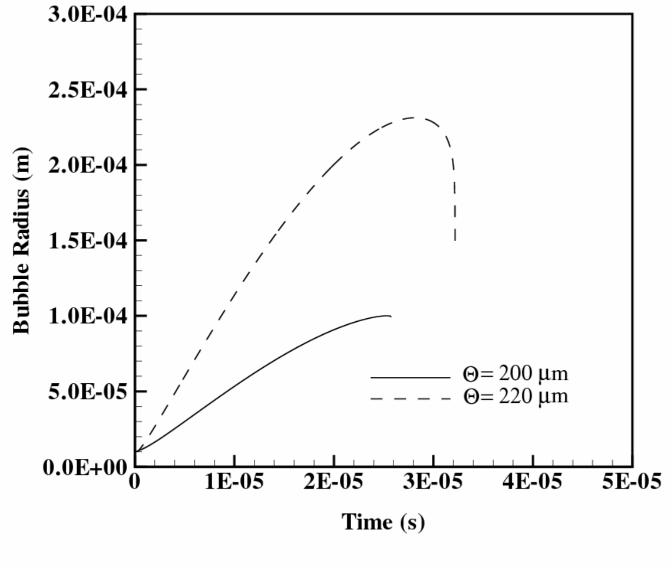
Bubble Radius (m)
3.0E-04
2.5E-04
2.0E-04
1.5E-04
1.0E-04
5.0E-05
0.0E+00
0
1E-05
2E-05
3E-05
4E-05
5E-05
Time (s)
Θ= 200 μm
Θ= 220 μm

(I)

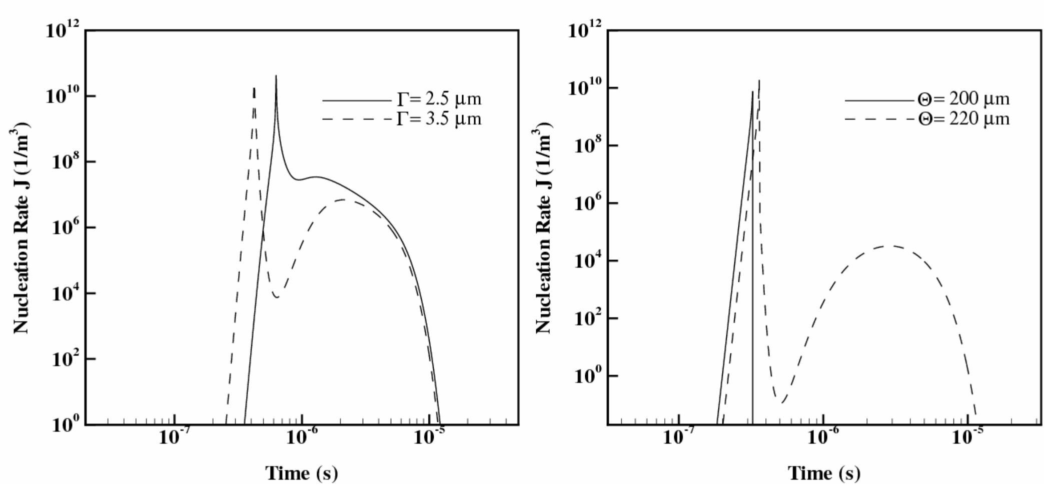
Nucleation Rate J (1/m^3)
10^{12}
10^{10}
10^8
10^6
10^4
10^2
10^0
10^{-7}
10^{-6}
10^{-5}
Time (s)
Γ= 2.5 μm
Γ= 3.5 μm
Nucleation Rate J (1/m^3)
10^{12}
10^{10}
10^8
10^6
10^4
10^2
10^0
10^{-7}
10^{-6}
10^{-5}
Time (s)
Θ= 200 μm
Θ= 220 μm

(i) (ii)

II (a)

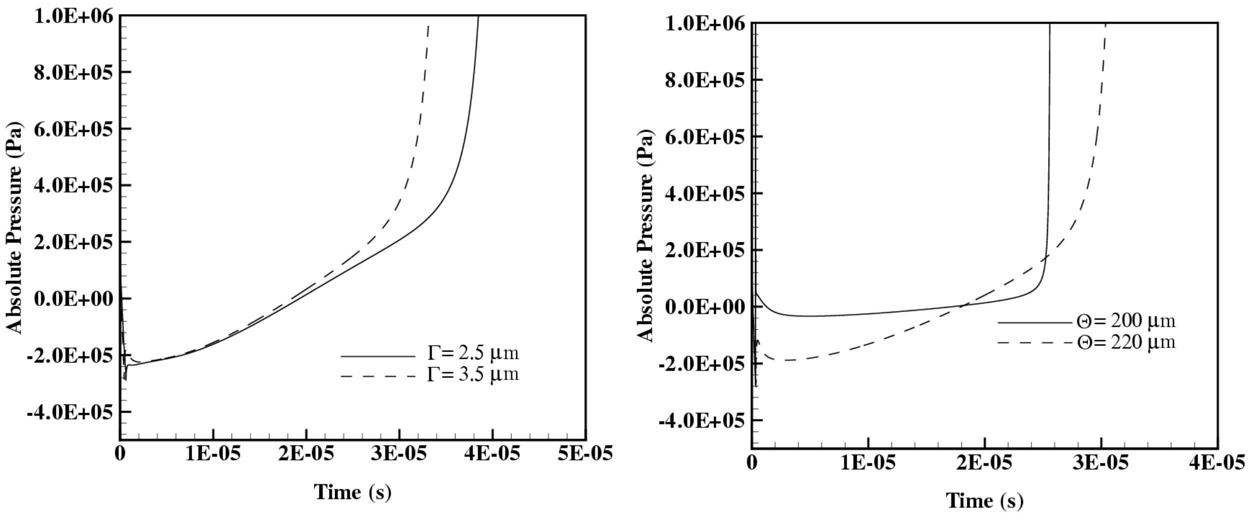

(i) (ii)

II (b)

Figure 4.10(I) Numerical simulation of bubble dynamics in a vibratory cavitation system under forcing amplitude of 2.5 μm at 20 KHz. (II) (a) Nucleation plots and (b) pressure history for system under a (i) a constant forcing frequency of 20 KHz. Distance between the horn and solid surface is maintained at 2mm. (ii) forcing amplitude of 2.5 μm at 20 KHz.

The new numerical model, comprising of the nucleation mechanism, is able to well resolve the bubble dynamics phenomenon encountered in vibratory cavitation process. The results match well with the experimental observations of Hansson et al. [203, 204]. Having validated the numerical model with experimental observations, we use the current model to observe the effects of frequency over a given horn amplitude and system geometry (horn-surface distance).

4.3.2.5 Effect of frequency on cavitation bubble dynamics

The effect of oscillation frequency in vibration cavitation system is considerable significance in determining the nucleation rates. This is attributed to that fact that the development of pressure profile varies as square of the angular frequency of the imposed perturbations. As detailed in Section (4.2.3), a given bubble dynamics system has a discrete resonant frequency associated with it. Increasing the perturbation frequency close to matching the resonant frequency of the system can potentially result in uncontrolled growth of the bubbles leading to severe non-linearities. To examine this effect, four different frequencies are imposed on a condition previously tested by Hansson et al. [203]. The separation distance between the horn and the surface is 2 mm while amplitude of 6 μm is maintained by the oscillator. Although, Kedrinskii [205] tested an applied frequency of 20 KHz, computations with frequencies 10 and 15 KHz lower than the standard 20 KHz and a higher frequency of 25 KHz is carried out to obtain the radius characteristics.

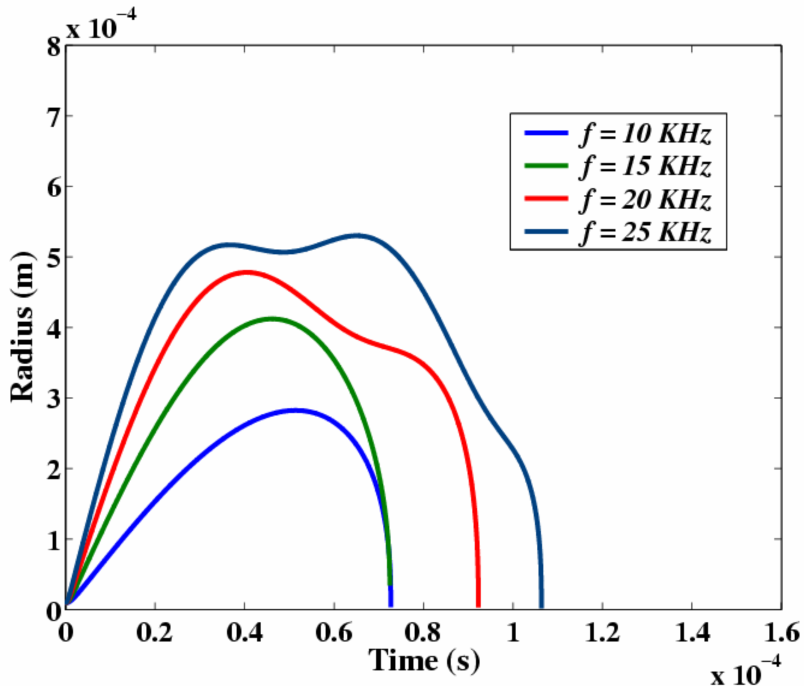

Figure 4.11: Effect of frequency on the bubble dynamics under nucleation conditions

Observe from Fig. (4.11), with standard frequency of 20 KHz, the standard result obtained by Kedrinskii et al. [205], increased bubble growth and collapse time period, is reproduced. With lowered frequency of 10 KHz, a quick collapse of the order of its imposed time period is obtained. For an intermediate frequency of 15 KHz, slightly increased growth is concluded.

Interestingly, for very high frequencies subjected to similar conditions tested before, non-linear growth of the bubble is predicted. This is explained by the non-linear bubble nucleation process influencing the overall pressure field distribution. Also, with increased frequency perturbation, the rate at which the bubble grows is far higher than the rate at which the surface forces, pressure difference fluctuation, act to reduce the growth rate.

The current discussions provided here are based on a one-dimensional assumption along the axial direction (directed from the horn to the surface) as shown in Fig. (4.8). Different types of cavity cluster collapse behavior have been reported [34, 209]. Major ones include an axial, cylindrical or spherical type. Schematic of the cavity cluster collapse configuration for each mode is shown in Fig. (4.12). Although the numerical study presented in Section (4.3.1) is based on an axial-type collapse mode, existence of cylindrical type cavity dynamics have been strongly supported by other researchers [33, 205, 209].

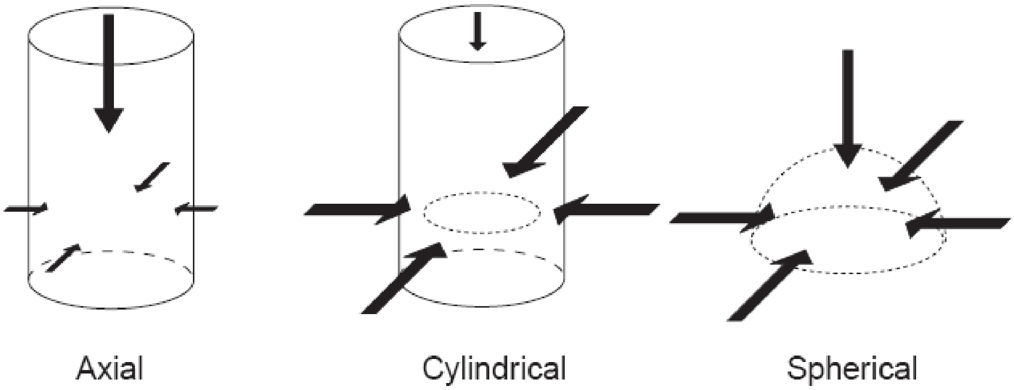

Figure 4.12: Different types of collapse structure [209]

For modeling a dynamic system configuration comprising of cylindrical collapse process, the cavitation bubbles are assumed to be placed in a cylindrical fashion separated by a distance comparable to that of the bubble radius [209]. A typical cylindrical collapse configuration is shown in Fig. (4.13)

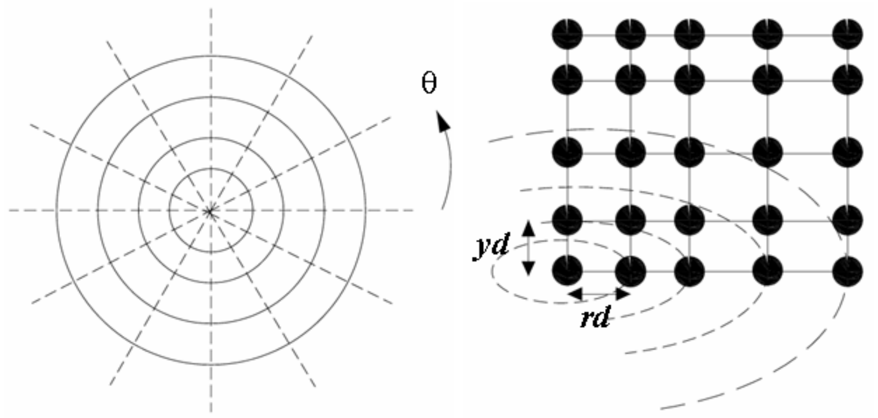

Figure 4.13: Placement of bubbles in a cylindrical fashion mimicking a cylinder collapse [209]

The Rayleigh-Plesset equation (4.9) can be extended to include an array of bubble system incorporating the mutual interaction effects and time delay between the communication of characteristics from one bubble to another within the system. Konno et al. [209] computed the growth and collapse of multiple bubble placed in a cylindrical configuration using a highly non-linear coupled R-P equation as described in equation (4.37). In deriving the equation the following assumptions are made:

1. Bubbles consist of both vapor and non-condensation gas. While vapor pressure is constant, the non-condensation gas obeys polytropic change.
2. Gas density is very small in comparison to liquid density and hence can be neglected.
3. Liquid is compressible and hence, mutual bubble fluctuations transmits at the speed of sound.
4. Far field velocity field of the bubbles is zero.
5. Viscosity of surrounding liquid is ignored, but retained for the motion of bubble wall.
6. Bubble sphericity is assumed.
7. No transitional motion of bubbles is considered and as a result expansion/shrinkage of the size of the bubble cluster cannot be simulated in the current context.

The modified bubble dynamics equation taking into account the mutual interactions within the bubbles and their enthalpy exchange with the surrounding fluid is given by

$$\begin{aligned}
&\left\{1-\left(\Xi+1\right)\frac{\dot{R}_{IO}(t)}{a_{\infty}}\right\}R_{IO}(t)\ddot{R}_{IO}(t)+\frac{3}{2}\left\{1-\left(\Xi+\frac{1}{3}\right)\frac{\dot{R}_{IO}(t)}{a_{\infty}}\right\}\dot{R}_{IO}^{2}(t)\\
&+\sum_{j=1,\,j\neq i}^{N}\frac{\dot{R}_{IO}(\varsigma_{JI})}{L_{IJ}}\left\{R_{IO}(\varsigma k_{JI})\ddot{R}_{IO}(\varsigma k_{JI})+2\dot{R}_{IO}^{2}(\varsigma k_{JI})\right\} \qquad (4.37)\\
&=\left\{1+\left(1+\Xi\right)\frac{\dot{R}_{IO}(t)}{a_{\infty}}\right\}\left\{h_{iw}(t)+\dot{\phi}(t)\right\}+\frac{R_{IO}(t)}{a_{\infty}}\left\{\dot{h}_{iw}(t)+\ddot{\phi}(t)\right\}
\end{aligned}$$

The I and J represent bubble indices, R_{IO} the bubble radius, a_{∞} the speed of sound, L_{IJ} separation distance between bubble I and J, h_{iw} – enthalpy at bubble wall, ϕ the velocity potential of the far field and Ξ is an arbitrary parameter $0 < \Xi < 1$. In the current study, we assume $\Xi = 0.5$. Of particular interest is the variable ζk_{IJ} given by

$$\varsigma k_{IJ} = t - \left\{L_{JI} - R_{JO}\left(\varsigma_{JI}\right)\right\}/a_{\infty} \qquad (4.38)$$

Equation (4.38) represents the duration of pressure propagation from bubble J to I. The pressure propagation phenomena included in the study details the mutual interaction between bubbles distributed within the same domain and affected by the same pressure field. In the present case, a linear mutual interaction process is assumed [209]. First term in the left hand side of the equation represents surface acceleration, while the second term governs the surface collapse rate. The critical term in the governing equation is the three term in the left hand side which denotes the interference between different radii characteristics in the system. The interference term presented here has an information delay parameter implicit in it. The terms in the left hand side of equation (4.37) are equated against the heat and mass transfer term at the bubble cluster boundary [34, 195]. For comprehending the behavior of such a system, numerical simulations using an IV order Runge Kutta method is employed. The cylindrical configuration tested in the present study is shown in Fig. (4.14(a)). The pressure is assumed atmospheric and water is assumed as the simulation liquid. The bubbles placed along the axis, $R_1 - R_{21}$ measure 0.3 mm while the rest of the bubbles are taken to be of equal diameter = 0.2mm. The distances between the bubbles in all the directions equal *rd* = *yd* = 0.2 mm. The pressure in the system is initially atmopsheric and the gas pressures in the bubbles evaluated by a simple Young's laplace equation across the boundary.

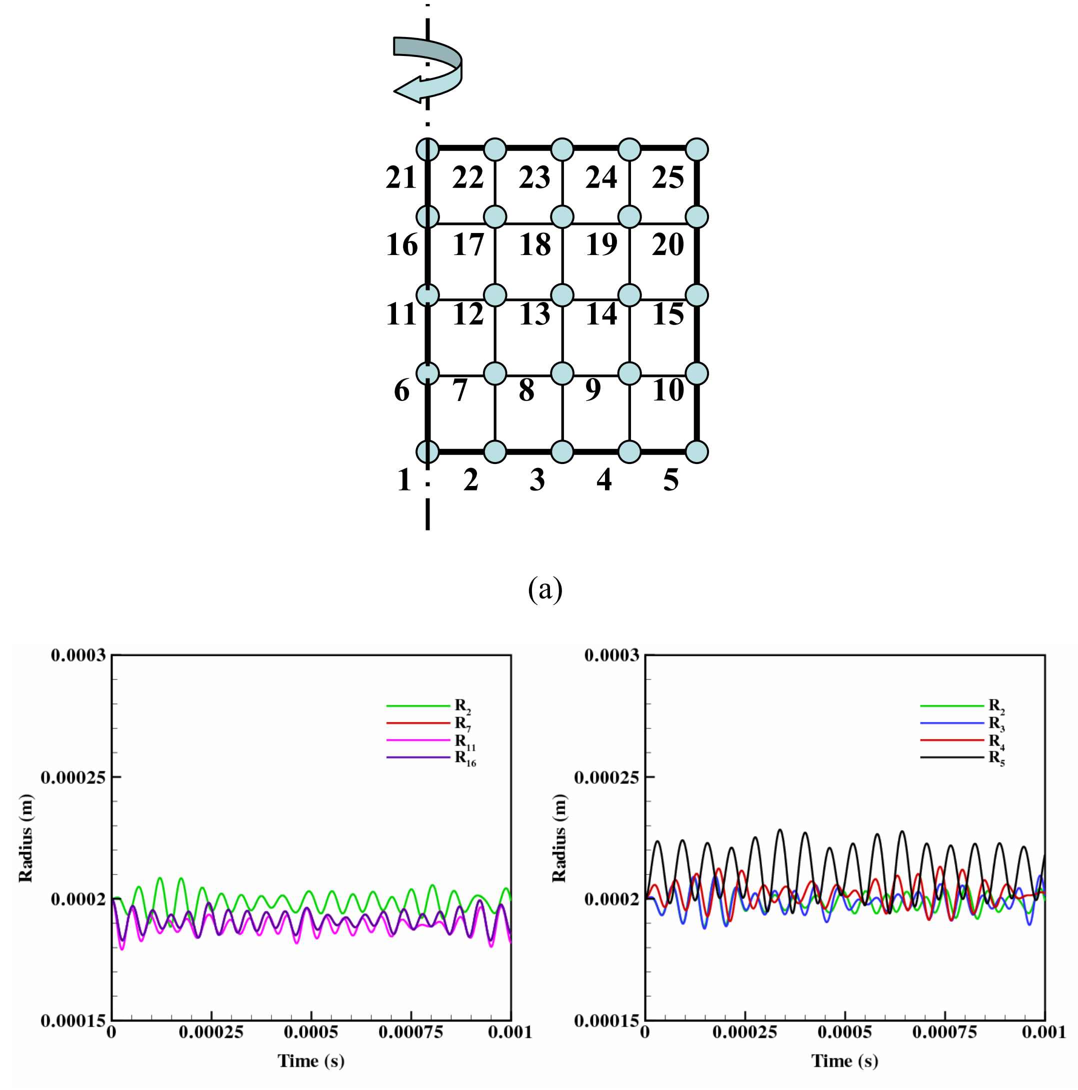

(a)

(i)

(ii)

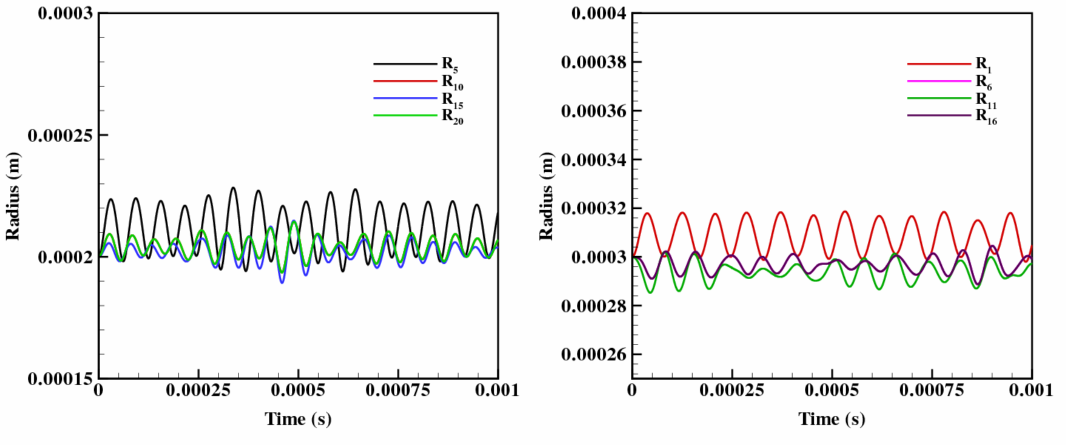

(iii) (iv)

(b)

Figure 4.14: (a) Bubble placement configuration (b)Radius history for bubbles in different positions placed according to configuration shown in (a)

Results presented in 4.14(b) for the bubble history at different location within the cylindrical configuration indicate the highly interlinked non-linearity in the system. Each and every bubble when presented with a constant pressure difference across the bubble-liquid interface produce a ringing structure with collapse and rebound which decays to zero in the presence of viscous effects [34, 195]. The plot, Fig. 4.14(b), shows deviation in the bubble characteristics at different locations due to the presence of another bubble. Presence of another bubble is communicated by the non-linear third term on the right hand side of equation (4.37). This also indicates that, a bubble collapse triggered at the cylindrical configuration boundary can severely impact the dynamics of the bubble placed at the center of the configuration. We reduce the computational configuration involving 25 bubbles in an array to a simple two-spherical bubble system but with radius, an order of magnitude smaller than our previous investigation. Two vapor bubbles each of radius 8 and 10 μm respectively are placed in a liquid (water) medium and their dynamics based on mutual interaction and enthalpy exchane across their bubble walls is monitored.

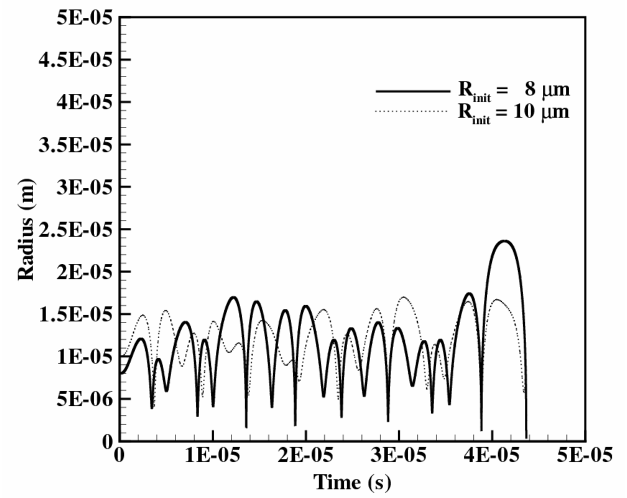

Figure: 4.15 Monitoring a two spherical bubble dynamics using equation (4.37) reveals strong departure from their ringing structure [34, 210]

Observe from Fig. (4.15), with the inclusion of a mutual interference term into the Rayleigh-Plesset equation, the dynamics of the bubbles are modified appreciably. Further, the bubble sizes investigated in the present scenario are typically found in many fluidic applications [33]. The numerical simulations presented here describes the complexity in the dynamics of simple bubble configurations which when extended to multiple bubble scenario would only worsen the stability of the system. In addition, Smereka et al. [211] reported dynamics of periodically driven bubble clouds using compressibility effects within the Rayleigh-Plesset equation. Deviation from spherical behavior of the cavitation bubbles was discussed by Fujikawa et al. [212] while Park et al. [213] used molecular dynamics simulation including nucleation effects in their recent study. Details of the non-linear bubble dynamics investigated presented in Section (4.3) are detailed in Fig. (4.16).

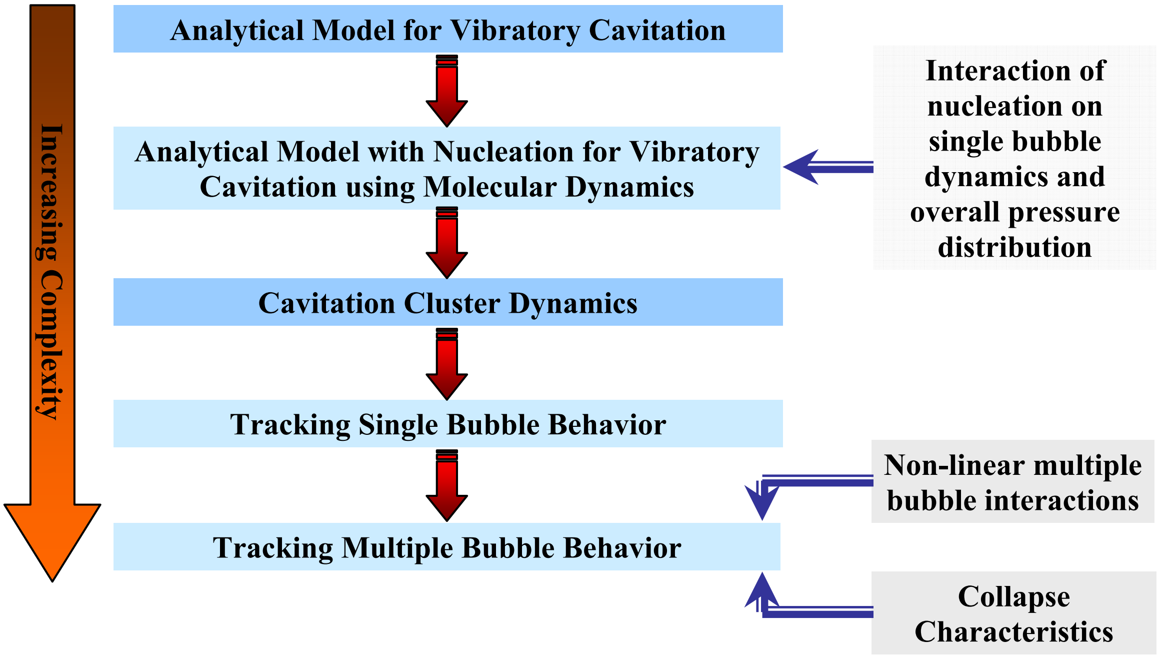

Figure 4.16: Bubble dynamics studies presented in the current research

The discussions on the newly developed bubble dynamics model based on nucleation theories, the cylindrical collapse model and steady-state models for bubbly flows provide a detailed description of the complexity involved in treating cavitating flow mixture. For example, the treatment of a single bubble behavior using molecular dynamics assumption portrayed very high non-linearity. Typical time step sizes of the order of 10^{-9} seconds and lower were required to stabilize the computations. Extending such a model to multiple-bubble environment would invoke a step-by-step process demanding tremendous amount of computational cost and time. Further, the parity existing between the length and time scales of the systems constructed on molecular dynamics basis are far lower than the influential macroscopic scales required to simulate a large scale bubble dynamics phenomena [33, 34]. Furthermore, no influence of the flow field is accounted in computing the variation in pressure fields surrounding the bubble and the phenomenon is reduced to an ideal one-dimensional case which is far from realistic. Three-dimensional effects are very crucial and can impose a myriad of non-linearities on their own such as vortex phenomena, dissipative effects etc [33, 179]. Mixing all these parameters into the fundamental equations governing bubble dynamics and coupling the derived equations to a large bubble density environment would give rise to systems with several hundred dependent variables. Depending upon the size of the flow domain and related entities, it would require quantum effort to solve every aspect of the system behavior. In order to circumvent this situation, models providing an ensemble effect of the cavitating mixture flow variables began to be applied.

4.4 Modeling of cavitating flows

Cavitating flows entail phase changes and hence include very high pressure and density gradients in the regions where cavitation inception is likely to occur, regions of low pressure in the liquid medium. They are very sensitive to the formation and transport of vapor bubbles, the turbulent fluctuations of pressure and velocity and the magnitude of non-condensable gases which are dissolved or ingested in the operating liquid. One of the simplest multiphase flow configurations representing bubbly flow of mixtures is the one-dimensional bubbly liquid flows in ducts and nozzles. Several investigations based on this problem have been studied in the context of cavitation bubble interactions. The nozzle flow is a useful model for simulating any cavitating flow in which a low pressure region causes the flow to accelerate, for example, the cavitating flow on the suction surface of a hydrofoil or a sharp cornered nozzle. In this essence, study of the one-dimensional accelerating flow with bubble cavitation effects certainly show valuable potential in building up fully non-linear solutions for more practical large-scale three-dimensional mixture flows. Non-linear continuum bubbly mixture model coupled with the Rayleigh-Plesset equation for the bubble dynamics was first proposed by Wijngaarden [214].

Ishii et al. [215] proposed a bubbly flow model and used it to study steady flows through a converging – diverging nozzle assuming that the gas pressure inside the bubbles are equal to the ambient fluid pressure. They neglected the bubble radial dynamics which are dominant in cavitating flow. Wang and Brennen [216] presented effect of bubble dynamics on the flow structure using steady state assumptions. Fundamental one-dimensional cavitating flow studies indicated the critical nature of geometry, initial cavitating vapor bubble radius and the bubble volume fraction. Researchers concluded that geometric models seeking considerable pressure reduction in throat can substantially increase the bubble cluster density leading to choking conditions [216-218]. However, these models are simplistic in the sense that, although coupled with the Navier-Stokes equations for obtaining information pertaining to the fluid motion, they cannot account for other fluid flow mechanisms such as vortex interactions, shear based perturbations inherent in the flow and several other unsteady phenomena which have been critically observed to impact bubble dynamics. In this concern, modeling of the cavitation process retaining a complete description of the flow field is essential. Studies dealing with cavitation modeling through the computation of the Navier-Stokes (N-S) equations have emerged in the last decade. These studies can be put into two categories, namely interface tracking methods and homogeneous equilibrium flow models. In the first category the cavity region is assumed to have a constant pressure equal to the vapor pressure of the corresponding liquid and the computations are done only for the liquid phase. The second category can be termed the homogeneous equilibrium flow models in which the single-fluid modeling approach is employed for both phases. Differences between the various models in this category mostly come from the relation that defines the variable density field.

The Interface tracking methods [219, 220] used in simulating cavitation dynamics employ separate treatment of the phases for their hydrodynamic behavior with the added complexity of resolving the liquid-vapor interface using higher order surface reconstruction schemes, while Continuum methods consider the flow as a homogeneous mixture employing a void fraction variable to quantify the regions where the fluid has changed its properties, typically density. The smearing of liquid-vapor interface occurs at the sub-cell level and the mixture density reflects the fraction of vapor and liquid in a given cell. Since no interface tracking is employed, surface tension forces are often neglected. Continuum methods have been used in various forms: computations with vapor production terms [221], bubble dynamics [222] and barotropic equation of state [223, 224]. Computations with vapor production terms encountered several stability problems at low void fractions which made them less attractive for cavitating flow computations, while the barotropic model computations were restricted by density ratios [222]. We briefly discuss various models available in the literature and indicate the relevance of using the current model cavitation simulations.

Delannoy and Kueny [223] utilized an arbitrary barotropic equation of state to compute the density field, while Chen and Heister [224] derived a time and pressure dependent differential equation for density. Ventikos and Tzabiras [225], in their model, introduce water-vapor state laws to model the cavitation dynamics, and consider the whole domain, including both vapor and liquid phases, as a compressible fluid. Considering the isothermal character of cavitating flows in many applications, utilizing a temperature or enthalpy equation and assuming the whole flow field as compressible may not be the most effective approach. Kubota et al. [222] coupled the Rayleigh-Plesset equation to the flow solver and compute the void fraction based on the bubble radius. Following the computation, the density is calculated using the void fraction formalism.

Due to the time dependent nature of the Rayleigh-Plesset equation [34], the model is restricted to unsteady cloud cavitation. The authors have also reported that this method is prone to instability because of high pressure-density dependence, and could not reach the convergence levels of non-cavitating flow simulations. Recently, cavitating flow simulations using a number density approach was addressed by Yuan et al. [226, 227], while Sauer et al. [228] used similar methodology for assessing the modeling requirement for cavitation and condensation process. An elaborate cavitation event capturing method based on gas/vapor bubble dynamics within the liquid bulk with drag effects was addressed by Tamura et al. [229]. Many authors used a compressible framework invoking Homogeneous Equilibrium assumptions [230] for time-dependent cavitating flow computations [231-233] but were restricted to high flow speed due to preconditioning requirement to match eigenvalues between the flow and acoustic speeds [234, 236]. To account for the cavitation dynamics in a more flexible manner, recently, a cavitation vapor transport equation model has been developed [237]. In this approach, volume or mass fraction of liquid (and vapor) phase is transported along the bulk flow. Singhal et al. [237, 238], Merkle et al. [239], and Kunz et al. [240] have employed similar models based on this concept with differences in the source terms. One apparent advantage of this model comes from the convective character of the equation, which allows modeling of the impact of inertial forces on cavities like elongation, detachment and drift of bubbles. Cavitation model developed by Singhal et al. [237], which accounts for the source terms arising from evaporation and condensation of liquids, is used as the primary numerical method in our current study. This method is incorporated in the software Fluent [241] which is used for simulation purposes. It is convenient and realistic to note that this model considers the liquid to be incompressible and the vapor phase may be considered compressible if there are high temperature effects acting on the system [242].

4.4.1 Numerical Modeling Approach

The numerical model of Singhal et al. [237] is represented as a 'Reduced Bubble Dynamic Formulation'. The model accounts for all first order effects such as the bubble dynamics and the phase change process with turbulent pressure fluctuations. The model assumes an interpenetrating assumption between the two phases and accounts for the slip between the vapor and liquid phases [243]. Cavitation process is modeled using rate of bubble formation (evaporation) and rate of collapse (condensation) considerations without any temperature dependence of the involved quantities. The working fluid is assumed to be a mixture of liquid, vapor and non-condensable gases which is the real situation in major industrial flow systems [33, 34]. Standard governing equations in the mixture model and the mixture turbulence model describe the flow and account for the effects of turbulence [242]. To obtain an expression of the net phase change rate, the two phase continuity equations are as follows:

Liquid Phase Equation:

$$\frac{\partial}{\partial t}\left[(1-\alpha)\rho_l\right]+\nabla.\left[(1-\alpha)\rho_l\vec{U}\right]=-Rp \tag{4.39}$$

Vapor phase continuity equation:

$$\frac{\partial}{\partial t}(\alpha\rho_V)+\nabla.\left(\alpha\rho_V\vec{U}\right)=Rp \tag{4.40}$$

For the complete mixture:

$$\frac{\partial}{\partial t}(\rho)+\nabla.\left(\rho\vec{U}\right)=0 \tag{4.41}$$

where Rp is the net phase change rate (= Re-Rc) and ρ is the mixture density. Also, the volume fraction of vapor 'α' can be related to bubble density 'N' and radius of bubble (R_B at equilibrium) as

$$\alpha = N\frac{4}{3}\pi {R_B}^3 \tag{4.42}$$

The Rayleigh-Plesset equation provides a physical approach to introduce the effects of bubble dynamics into the cavitation model [34, 237, 238]. It can be considered to be an equation for void propagation and mixture density. Using the R-P equation, neglecting the effects of viscous damping and surface tension, and combining it with equation (4.42), the bubble radius can be deduced to

$$R = \left(N4\pi\right)^{1/3}\left(3\alpha\right)^{2/3}\frac{\rho_v\rho_l}{\rho}\left[\frac{2}{3}\left(\frac{P_B - P}{P_l}\right) - \frac{2}{3}R_B\frac{D^2R_B}{Dt^2}\right]^{\frac{1}{2}} \tag{4.43}$$

Using equation (4.40) and (4.43), the vapor transport equation assumes the form

$$\frac{\partial}{\partial t}\left(\rho q\right) + \nabla.\left(\rho q U\right) = \left(N4\pi\right)^{1/3}\left(3\alpha\right)^{2/3}\frac{\rho_V\rho_l}{\rho}\left[\frac{2}{3}\left(\frac{P_B - P}{\rho_l}\right)\right]^{1/2} \tag{4.44}$$

where the right hand side of the equation represents the vapor generation or evaporation rate and *q*, the vapor mass fraction. The working fluid is assumed to be a mixture of liquid, vapor and non-condensable gases. Standard governing equations in the mixture model and the mixture turbulence model describe the flow and account for the effects of turbulence. A vapor transport equation governs the vapor mass fraction, given by

$$\frac{\partial}{\partial t}\left(\rho q\right) + \nabla\left(\rho \vec{U}_v q\right) = \nabla\left(E\nabla q\right) + \mathrm{Re} - Rc \tag{4.45}$$

where ρ is the mixture density, $\overrightarrow{U_v}$ is the velocity of the vapor phase, *E* is the effective exchange coefficient and Re and Rc are the vapor generation and condensation rate terms (or phase change rates). The rate expressions are derived from Rayleigh-Plesset equations and limiting bubble size considerations (interface surface area per unit volume of vapor). These rate functions of the instantaneous, local static pressure are given by:

If $p < p_{sat}$

$$\mathrm{Re} = Ce\frac{U_{ch}}{\sigma}\rho_l\rho_v\sqrt{\frac{2(p_{sat}-p)}{3\rho_l}}(1-q) \tag{4.46}$$

if $p > p_{sat}$

$$\mathrm{Re} = Cc\frac{U_{ch}}{\sigma}\rho_l\rho_l\sqrt{\frac{2(p-p_{sat})}{3\rho_l}}q \tag{4.47}$$

where suffixes l and v denote liquid and vapor phases. U_{ch} is the characteristic velocity, which is approximated by the local turbulence intensity, $U_{ch} = \sqrt{k}$, σ is the surface tension of the liquid, p_{sat} is the liquid saturation vapor pressure at the given temperature, and *Cc* and *Ce* are empirical constants. The default values are *Ce*=0.02 and *Cc*=0.01.

It should be reminded that the bubble wall velocity approximation includes only first order effects and additional effects of surface tension, viscosity and the wall stress terms are neglected in comparison with the pressure forces. Adding, the transfer rate of pressure information, surrounding the cluster, is proportional to square root of the turbulent kinetic energy magnitude. Any liquid compressibility effects on the vapor collapse are neglected and are implicitly realized by the magnitude of pressure field in the vicinity of the cavitation clusters. Effects of drift fluxes arising from the difference in velocity between the vapor and liquid phases are taken into account to compute drag coefficient [243, 245] required for computing the coalescence and local relaxation mechanisms.

4.4.2 Turbulence Modeling for Cavitating Flows

Multitude of experiments suggests the profound influence of turbulence structure on the cavitation phenomena [33, 246, 247]. This is supplemented by the fact that cavitation process is highly sensitive to pressure perturbations, which are tightly coupled to the turbulence dynamics. Furthermore, occurrence of cavitation clusters and their dynamics within the flow domain are greatly enhanced by production or disruption of shear rates [33] and nuclei effects [248]. In this essence, use of appropriate turbulence model, can be very critical in monitoring events of cavitation [249]. For example, use of a simple two-equation *k-ε* model in highly strained flow can lead to poor resolution of the strain rates [150] and hence can provide unrealistic results concerning the cavitating flow regime. However, since the mixture flow phenomenon is complex, use of sophisticated turbulence tools can destabilize the system owing to their intricate coupling with the cluster dynamics. After a careful study on the available turbulence models, such as two-equation models, *k-ε*, RNG *k-ε,* realizable *k-ε, k-ω*, *SST* models and computationally intensive LES models, an RNG *k-ε* model [244] is chosen to simulate turbulence effects due to its ability to effectively incorporate both high and low Reynolds number regimes with transitional effects. It is, however, important to highlight that both RNG *k-ε* and realizable k-ε models show substantial improvement over the standard k-ε model in regions where the flow encounters strong streamline curvatures, vortices and rotation. Realizable *k-ε* model satisfies mathematical constraints on the Reynolds stresses which are not accounted in the RNG k-ε model and hence, show significant improvement in simulating separated flows and flows with complex secondary flow structures [244]. However, an important limitation of the realizable model rests in the creation of non-physical turbulent viscosities in computational domains with both stationary and rotating fluid zones. Since the present study requires a moving structure implementation within the stationary fluid zone, a RNG *k-ε* model is preferred. The RNG-based *k-ε* turbulence model is derived from the instantaneous Navier-Stokes equations, using rigorous statistical technique called renormalization group theory. The RNG model has an additional term in its *ε* equation that significantly improves the accuracy for rapidly strained flows. Further, the RNG model incorporates effect of swirl on the turbulence structure enhancing accuracy of the model when a swirling flow is encountered. Specifically, the RNG theory provides an analytical formula for turbulent Prandtl numbers, while the standard k-ε model uses user-specified, constant values.

The standard k-ε model is a high-Reynolds-number model and considers no special treatment of the low-Reynolds number effects while the RNG theory provides an analytically-derived differential formula for effective viscosity that accounts for low-Reynolds-number transitions. Effective use of this feature does, however, depend on an appropriate treatment of the near-wall region. These features make the RNG *k-ε* model more accurate and reliable for a wider class of flows than the standard *k-ε* model. A more comprehensive description of RNG theory and its application to turbulence can be found in [244]. Brief details of the turbulence transport process are described in the following section.

4.4.2.1 Turbulent Transport equations

The RNG *k-ε* model solves transport equation for the turbulent kinetic energy and the dissipation rate (*eps*). The turbulent kinetic energy (*k*) transport equation is given by

$$\frac{\partial(\rho k)}{\partial t}+\frac{\partial(\rho k u_i)}{\partial x_i}=\frac{\partial\left(W_k \mu_{eff}\frac{\partial k}{\partial x_j}\right)}{\partial x_j}+G_k+G_b-\rho(eps)-Y_M+So_k \qquad (4.48)$$

and the turbulent dissipation (*eps*) rate equation is given by

$$\frac{\partial(\rho.eps)}{\partial t}+\frac{\partial(\rho.eps.u_i)}{\partial x_i}=\frac{\partial\left(W_{eps}\mu_{eff}\frac{\partial(eps)}{\partial x_j}\right)}{\partial x_j}+ \quad (4.49)$$

$$C_{1\varepsilon}\frac{(eps)}{k}\left(G_k+C_{3eps}G_b\right)-C_{2eps}\rho\frac{(eps)^2}{k}-(reps)+So_{eps}$$

G_k represents the turbulent kinetic energy generation term due to mean velocity gradients and is calculated as

$$G_k=-\rho\overline{u_i'u_j'}\frac{\partial u_j}{\partial x_i} \quad (4.50)$$

G_b is the generation of turbulent kinetic energy term due to buoyancy effects, which in the present study is neglected due to isothermal system approximation. The term Y_M represents the contribution of the fluctuating dilatation in compressible turbulence to the overall dissipation rate. This effect can be safely ignored in simulating incompressible flow limits. The quantities W_K and W_{eps} are the inverse effective Prandtl numbers for *k* and *eps* while So_k and So_{eps} are the respective source terms caused by other effects in the respective *k* and *eps* equations.

The term *reps*, providing the critical difference between the standard *k-ε* and the RNG based turbulence two-equation model, is given by

$$reps=\frac{C_\mu\rho\Upsilon^3\left(1-\frac{\Upsilon}{\Upsilon_o}\right)}{1+C_\beta\Upsilon^3}\frac{(eps)^2}{k} \quad (4.51)$$

where $\Upsilon=Sk/eps$ and $\Upsilon_o=4.38$, $C_\beta=0.012$.

In regions where $\Upsilon<\Upsilon_o$ the *reps* term makes a positive contribution and elsewhere, resulting from high strain rates, the term *reps* provides a negative effect. Due to this feature, the smaller destruction of dissipation rate *(eps)* augments *reps* thereby reducing *k* and eventually, the effective viscosity. Owing to this modification, the RNG model yields low turbulent viscosity than the standard *k*-*ε* model in rapidly strained flows [244]. The superior response of the RNG model to rapidly strained flows makes them suitable for simulating cavitating flows since the latter are associated with large strain regions and intense shear rates. Also, modeling cavitation requires fine grids to capture steep pressure gradients accompanied by highly fluctuating vapor formation and collapse regions in addition to the effective implementation of the relevant turbulence models [249, 250]. The cavitation model discussed in Section (4.4.1) is used in conjunction with the RNG *k*-*ε* model, whose impact was discussed in Section (4.4.2.1), in simulating cavitating flows within the commercial code Fluent's framework.

4.4.3 Solver controls

In the computation of cavitating flows careful attention is required in choosing the pressure-velocity coupling due to the variety of face flux correction methodologies built within the schemes. In reality, the cavitation phenomenon is a highly unsteady process although it might exhibit quasi-steady state in some applications [250]. An extensive comparison study on various iterative schemes, such as SIMPLE, SIMPLEC and PISO, available within the Fluent [241] framework suggests the use of SIMPLEC methodology in simulating cavitating flows. This is attributed to the fact that SIMPLEC offers accelerated convergence rates with good stability with turbulence models as compared to SIMPLE schemes. Use of PISO scheme is limited due to increased computational expense associated with the iterative loops involving large time steps and mesh-skewness corrections. Further, the use of SIMPLEC is advocated due to its reduced sensitivity to the selection of under-relaxation factors as well as fewer requirements for under-relaxation. Linear pressure interpolation, which computes the face pressure as the average of the pressure in the adjacent cells, is used in conjuction with SIMPLEC owing to its stable performance. First order upwinding is used for momentum, volume fraction equations and turbulence transport equations since they offer high stability and decreased computation time as against increased effort and instability occurrence using higher order discretization methods [150, 146].

The internal cavitating nozzle flow modeling carried out in the present study has an additional complexity of a moving solid structure domain in the stationary fluid zone. The presence of the solid structure manifests in a multitude of flow dynamics such as vortex shedding, pressure pulsation, turbulence and shear effects. Modeling of a moving boundary zone in association with a stationary zone is carried out using the Fluent's dynamic remeshing procedure.

4.4.4 Description of dynamic meshing procedure

The dynamic mesh model in Fluent [241] can be used to model flows where the shape of the domain is changing with time due to motion on the domain boundaries. The structure motion is prescribed based on specified linear and angular velocities about the center of gravity of a solid body with time or an unprescribed motion where the subsequent motion is determined based on the solution at the current time. The update of the volume mesh is handled automatically by Fluent at each time step based on the new positions of the boundaries. To use the dynamic mesh model, a starting volume mesh and the description of the motion of any moving zones in the model is provided. In the present study, User Defined Functions (UDFs) are used to describe the motion of the solid boundary on the face zone for 2D computations or in a cell zone for 3D computations. Furthermore, regions that are deforming due to motion on their adjacent regions must also be grouped into separate zones in the starting volume mesh. Fluent offeres three mesh motion methods to update the volume mesh in the deforming regions subject to the motion defined at the boundaries:

- Spring-based smoothing

- Dynamic layering
- Local remeshing

After careful review of the different mesh adaption procedure, the local remeshing procedure is adopted. The other methods show fundamental incompatibility with the generated grids and simulation assumptions such as axi-symmetric fashion, periodic boundaries etc. Local remeshing method can be used only in cell zones that contain tetrahedral or triangular cells which is relevant to the present case. Due to the nature of the sharp boundaries (horn surface and internal nozzle shape), we perform computations using unstructured grids (triangular cells in the axi-symmetric case). The moving zone in the current model is the horn tip which is defined as a rigid body performing oscillatory motion. The face of the moving zone is imposed with a time varying velocity profile. If deforming face zones are defined in the model, local remeshing in the adjacent cell zone can be used. Also, the faces on the deforming face zone can be remeshed only if they are triangular (or linear in 2D), are all adjacent to moving loops (i.e., moving nodes), are on the same face zone, and form an annular (i.e., closed loop) and not be part of a symmetry or conformal periodic boundary.

For the remeshing procedure, obtaining optimized results lies in the treatment of skewness and cell volume (in 2D the cell area). Inputs in the form of maximum and minimum cell area using are crucial. In order to create grids of small skewness and uniform shapes, the difference between the maximum and minimum cell volume and /or area should be minimum as possible. However, too much decrease in this difference quantity would lead to introduction of too many cells in one part of the domain at some instant while at a different instant the cell density might be completely different. This can be overcome by carefully manipulating the cell density change in the generated mesh manually. For our 3D simulations, a mesh skewness of 0.7 was acceptable while for 2D axi-symmtric computations discussed, the mesh skewness was reduced to 0.4 with sufficient iterations to smoothen out the variation in remeshing procedure. All the grid generation process used in conjunction with Fluent has been carried out using GAMBIT [241]. All the CFD computations utilizing Fluent are run in the superdome HP cluster at the University of Kentucky. The superdome clusters run on Itanium-2 (Madison) processors rated at 1.25 TF sustained / 1.6 TF peak with an HPUX 11iv2 (11.23) operating system. Each processor has 2 GB of memory per and the total disk space of 7 TB is available. A total of 256 total processors (64 procs per host/node) is available in the supercomputing facility.

4.5 Numerical simulation of interior nozzle flow with moving horn structure

4.5.1. Factors Influencing Nozzle Design

The development of a optimized spray applicator design rests on the following crucial parameters.

1. Nozzle internal shape factor
2. Frequency of the oscillating horn
3. Amplitude of the horn motion
4. Fluid parameters
5. Shape of the horn

4.5.1.1 Nozzle Internal Shape factor

The shape of the nozzle dictates the pressure gradient close to the horn surface and further towards the exit [29]. It is required that minimal pressure is maintained near the horn surface so that lesser energy is required to create the cavitation clusters. Adding, the nozzle shape leading to the favorable pressure gradient helps to convect the cavitation clusters created near the horn surface.

4.5.1.2 Frequency of oscillating horn

The frequency of the transformer is very critical in controlling the bubble population and in achieving the necessary perturbation to be imposed on the liquid jet. The magnitude of the frequency summarizes the amount of energy that is being supplied to the liquid to create the cavitation regions. Increasing the frequency directly relates to increase in the energy applied to overcome the cohesive liquid forces leading to cavitation bubble cluster [203-206]. The Navier-stokes equation neglecting the non linear terms compared to the transient velocity term and the pressure gradient can be written as

$$\frac{\partial u}{\partial t} = -\frac{1}{\rho}\frac{\partial P}{\partial x} \qquad (4.52)$$

If the motion of the horn is sinusoidal, the pressure gradient relates to the angular frequency as,

$$\rho\frac{\partial P}{\partial x} = -ap_h = \Gamma\omega^2 \sin(\omega t) \qquad (4.53)$$

Where ρ is the density, ap_h is the horn acceleration, Γ is the amplitude, $\omega = 2\pi f$, f is the frequency of the oscillating horn. Numerical simulation of bubble dynamics in oscillating pressure fields indicate that the behavior of bubbles under different imposed pressure fluctuation frequencies varies appreciably. Further, the frequency of the transformer closely indicates the fluctuation frequency in the exiting modulated liquid jets (neglecting the viscous effects, cavitation interaction and other geometry effects).

4.5.1.3 Shape of the horn surface

According to the discussions on the cavitation generation techniques, the bubble population is substantially enhanced if the energy of the oscillations is well focused in a given area. This is achieved by use of concave surface at the tip of the oscillating horn. Horn surface concavity increases the power density of the bubble formation [31] and enhances high frequency pulsing to the liquid downstream. The curvature of the tip is a function of the horn tip width, based on which the calculations are performed.

4.5.1.4 Amplitude of the horn motion

Another critical parameter in the present design is the horn amplitude which directly dictates the amplitude of transient pressure field, the bubble population and hence the droplet size distribution. From equation (4.53), note that the pressure gradient is governed in a linear fashion by the horn amplitude. Increased amplitude results in formation of extended vapor region and consequent convection downstream. Amplitude in conjunction with the frequency is decisive in designing the horn tip to enhance cavitation. Designs with high amplitude of oscillation can lead to intensified cavitation regions [204, 205]. But without the proper adjustment of the forcing frequency, this might hinder the horn operation itself.

4.5.1.5 Liquid parameters

The basic spray generation is dependent on the liquid parameters such as its viscosity, surface tension, compressibility effects (high speed sprays). In this discussion, it is to be noted that simulations are performed for a single component low viscosity liquid (water in the present study). Also, the flow field inside the nozzle is designed to eliminate any choking of the flow, with added constraint of the liquid flow rate.

4.5.1.6 Shape of the horn

Various horn shapes such as exponential, catenoidal, rectangular, cylindrical etc. have been experimented by researchers and based on their ability to less influence the flow field, catenoidal and exponential shaped horns have been considered for such designs [31]. It is important to see that, motion of structures such as a rectangle horn can induce circulation regions with high shear in the domain, which can negate the effect of cavitation cluster inception.

4.5.2 Preliminary nozzle design

Several preliminary nozzle designs were tested varying the horn diameter, horn shape, nozzle exit diameter for different horn motion characteristics. In the event that the flow exiting the nozzle is a mixture of liquid and vapor, sufficient flow area must be provided in order to prevent any occurrence of choking phenomena.

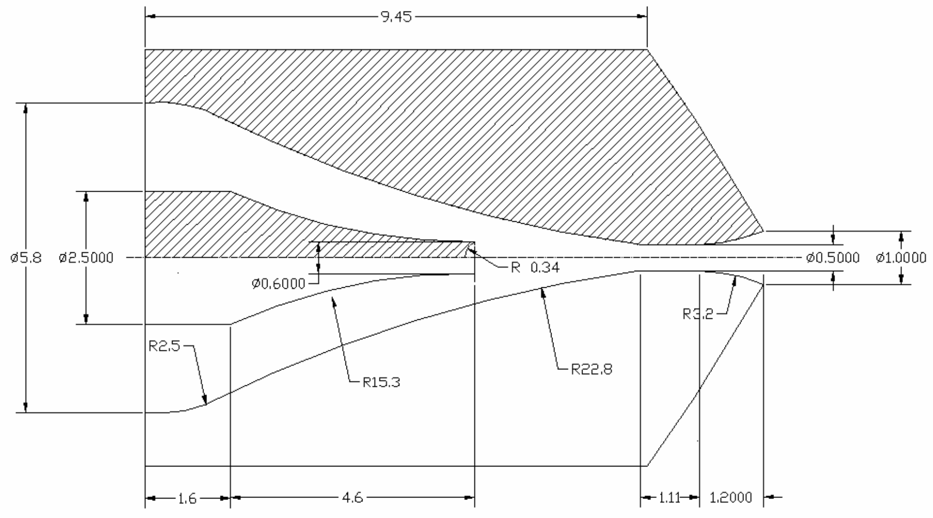

All Dimensions are in mm

Figure 4.17: Preliminary nozzle design

With these considerations, the first design of a cavitating atomizer is obtained. Dimensioned nozzle configuration is detailed in Fig. (4.17). Computational modeling using the design shown in Fig. (4.17) is carried out within the Fluent framework using unstructured grids with a total of 30,000 cells in the computational domain.

4.5.3 Horn operation parameters

After carrying out some initial assessment for the appropriate horn parameters and the delivery flow rate, the following list of horn operating parameters was obtained

- Horn frequency: 10,000 Hz - 20,000 Hz (Use of Piezoelectric Transducer)
- Horn stroke length: 0.2mm – 0.3 mm
- Liquid flow rate: 300 cc/min

The nozzle exit diameter proposed here takes into account, high mixture flow velocities generated by high vapor volume fraction exiting the nozzle. In the following section, we address the influence of horn surface design on the cavitation characteristics.

4.5.4. Effect of curved surfaces

In order to understand the effect of horn frontal profile on the cavitation characteristics, three types of horn tip design were tested using axi-symmetric flow assumptions. The three type of frontal shapes tested include (a) Concave horn surface (b) Convex horn surface (c) Flat horn surface. It is important to understand these effects since their influence is critical in discussing their manufacturability. Adding curvature to surface during the machining process induces its own level of complexity and numerical testing is carried out to inquire if providing a curvature to the frontal surface would provide any additional cavitation effects. The results from the numerical testing have been elaborated in Section (4.5.4.1).

4.5.4.1 Concave horn frontal surface

As seen from the simulations, Fig. (4.18), the concave region creates a region of localized low pressure where the cavitation regions are incepted. Due to the curvature effect and the pressure gradients in the vicinity, a stretching phenomenon during the oscillatory motion of the horn is observed. The amplitude of the motion, in our case, was larger than the stretching limit of the cavitation cluster and hence, detachment from the parent cluster accumulated near the horn surface is observed.

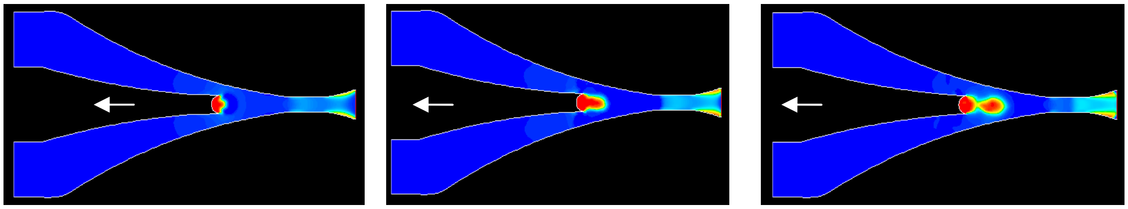

1(a). Creation of clusters, near horn surface

1(b). Stretching of clusters

1(c). Detachment of clusters

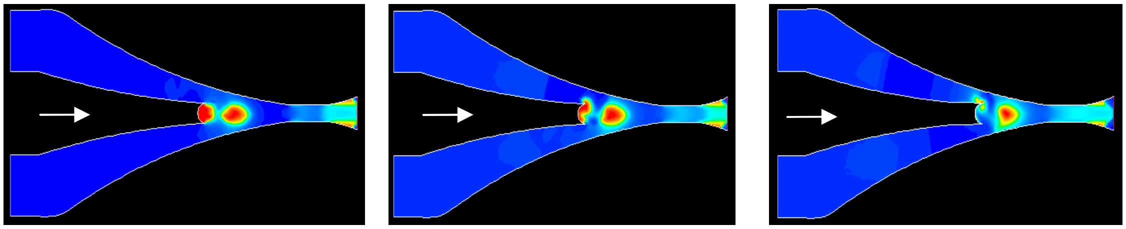

1(d). Cluster detachment from horn surface completed, translation of clusters visualized

1(e). Cluster propagation

1(f). Shrinkage of clusters due to flow parameters

Figure 4.18: Effect of curved surface on cavitation dynamics: Contour plot of vapor volume fraction generated using concave frontal horn surface. (Blue – water, Red- Vapor)

After their inception, the cavitation clusters detect the presence of fluid flow in the neighborhood and as a result get transported downstream along the flow. Since this is an accelerated flow towards the nozzle exit, pressure depression occurs. This pressure depression helps in maintaining the cluster size and intensity until the flow faces the divergent portion of the duct where the fluid pressure increases. An increase in the local pressure has an immediate effect on the cavitation cluster [34]. The Rayleigh-Plesset equation indicates that for an increase in the local liquid pressure would result in an immediate collapse of the liquid [33, 34]. The immediate collapse in this concern depicts the time scale of collapse which is far less than the flow time scale. Hence, this collapse can be identified as an instantaneous phenomenon. For the design of the atomizer, this instantaneous collapse feature is required close or very near the nozzle exit so that no event of super cavitation occurs, wherein the cavitating bubbles exit the nozzle orifice with the exiting liquid and enter into the external domain [2, 48, 57]. If the intensity of the supercavitating clusters is comparatively smaller, they are expected to collapse within few diameters downstream of the nozzle, posing no problem for the surfaces to be sprayed upon.

4.5.4.2 Convex horn frontal surface

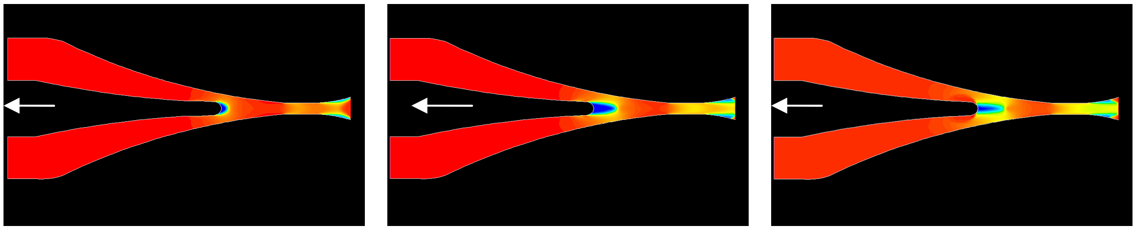

(a) Creation of Clusters, near horn surface and nozzle exit

(b) Stretching Clusters near horn surface due to horn motion

(c) Cluster shrinkage due to curvature effect of horn profile

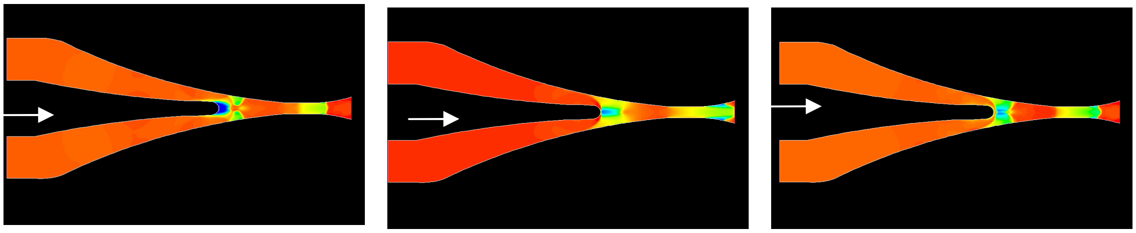

(d) Forward motion creates elongated membrane type clusters

(e) Cluster collapse near horn due to unfavorable pressure gradient

(f) Cluster propagation – growth and collapse not favored by convex surfaces

Figure 4.19: Effect of curved surface on cavitation dynamics: Contour plots of vapor volume fraction generated using a convex frontal horn surface (Red – Water, Blue – Vapor)

The horn convex surface replacing the concave horns have a radius of curvature equal to the radius of the oscillating horn tip. Numerical simulations visualized in Fig. (4.19) show the formation of cavitation clusters near the tip due to the retracting motion of the horn. However, due to negating gradient effects, these clusters are short lived and hence no detailed cavitation cluster mechanisms such as stretching, convection are appreciably noted. Hence, it could be expected that decreasing the amplitude and frequency levels of horn vibration can lead to zero cavitation levels even though a concave surface may still be able to provide appreciable amount of cavitation levels.

4.5.4.3 Flat horn frontal surface

One of the easiest configurations that could possibly be machined is essentially a flat horn profile. Due to sharp corners of the flat horn and infinite radius of curvature, the interaction between the vortex and the cavitation is noticeably different.

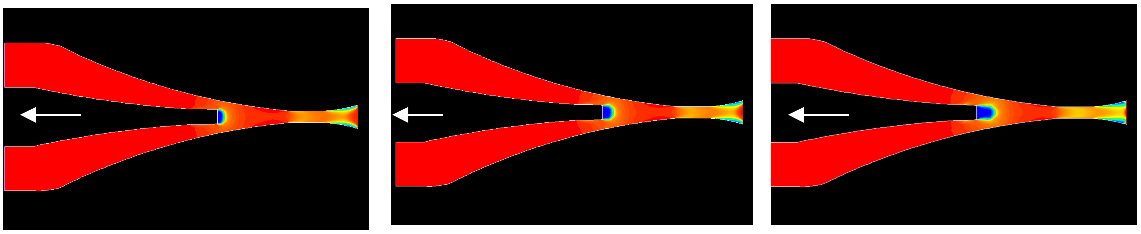

(a) Creation of clusters, near flat horn surface

(b) Growth of clusters near horn and nozzle exit

(c) Cavitation Cluster Stretching

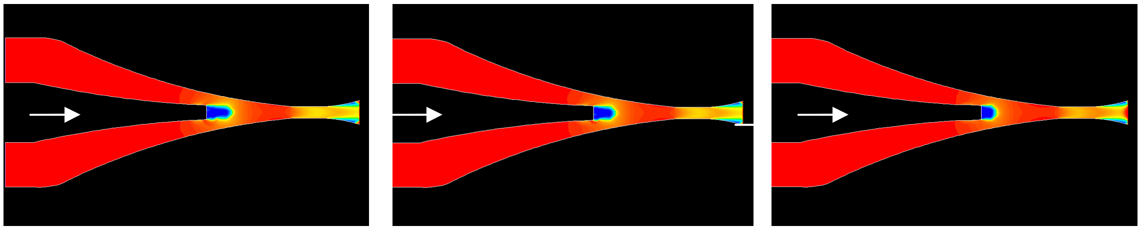

(d) Prolonged Cluster formation

(e) Decay of Clusters due to horn motion

(f) Formation of high vapor stagnant 'hanging' regions near oscillating surface

Figure 4.20: Effect of curved surfaces: Flat horn frontal surface (Red – Water, Blue – Vapor)

In the case of a concave surface, the dented regions served as an accumulation region of the local reversed flow while in the flat surface case, these reversal flows are opposed and dissipated as quickly as possible. Visualizations of the cavitation dynamics process is depicted as a series of images in Fig. (4.20). Note that the arrow mark indicates the direction of motion of the horn at that instant. As seen from the simulations presented in Figs. (4.18), (4.19) and (4.20), the curved concave horn tip surface is seen as a constant source of cavitation bubble clusters, which is seen to propagate and collapse, that can potentially enhance spray formation. The horn tip with convex surface does not create detached clusters which can propagate to the nozzle exit. Further the convex shaped tip creates an unfavorable pressure field distribution for the growth/propagation of the cavitation bubble clusters due to its curvature. It is also seen that the flat horn surface can create ‘hanging’ clusters. However, for given energy input, a curved surface can intensify the bubble nucleation compare to a flat tipped horn. Our computations indicate that the intensity of cavitation levels lie between the upper bound reached by concave frontal horn surface and the lower bound of convex shaped horn frontal surface. From our preliminary testing using various operating parameters, some crucial factors were identified as parameters of primary importance in the nozzle interior design. They include

(a) Ratio of the tip diameter to the stroke length

(b) Position of the horn in the flow field.

(c) Pressure distribution in the regions close to exit

4.5.5 Nozzle Design Parameters

4.5.5.1 Ratio of Tip Diameter to stroke length:

The variation of diameter of the oscillating horn tip to the amount of displacement it performs during the operation has a profound influence not only on the cavitation dynamics, but also on the flow structure. For a given displacement magnitude at any instant of time by the horn tip, the volume of liquid displaced per unit time goes as the square of the frontal horn surface times the displacement. In the perspective of designing an atomizer, with a very low throat diameter section, this fluctuation in flow rate is very crucial in computing the flow turbulence and velocity relaxation at the nozzle exit. With further complication in the form of cavitation, the behavior of the two-phase flow mixture becomes highly stochastic [34]. Hence, an optimization procedure for fixing the tip diameter to stroke length in the form of parametric study was performed to find out its implications on the internal flow dynamics.

From our varied numerical testing it was clear that when the stroke length is less than half the tip diameter, the cavitation cluster cannot be propelled due their "adhesion" to the concave surface.

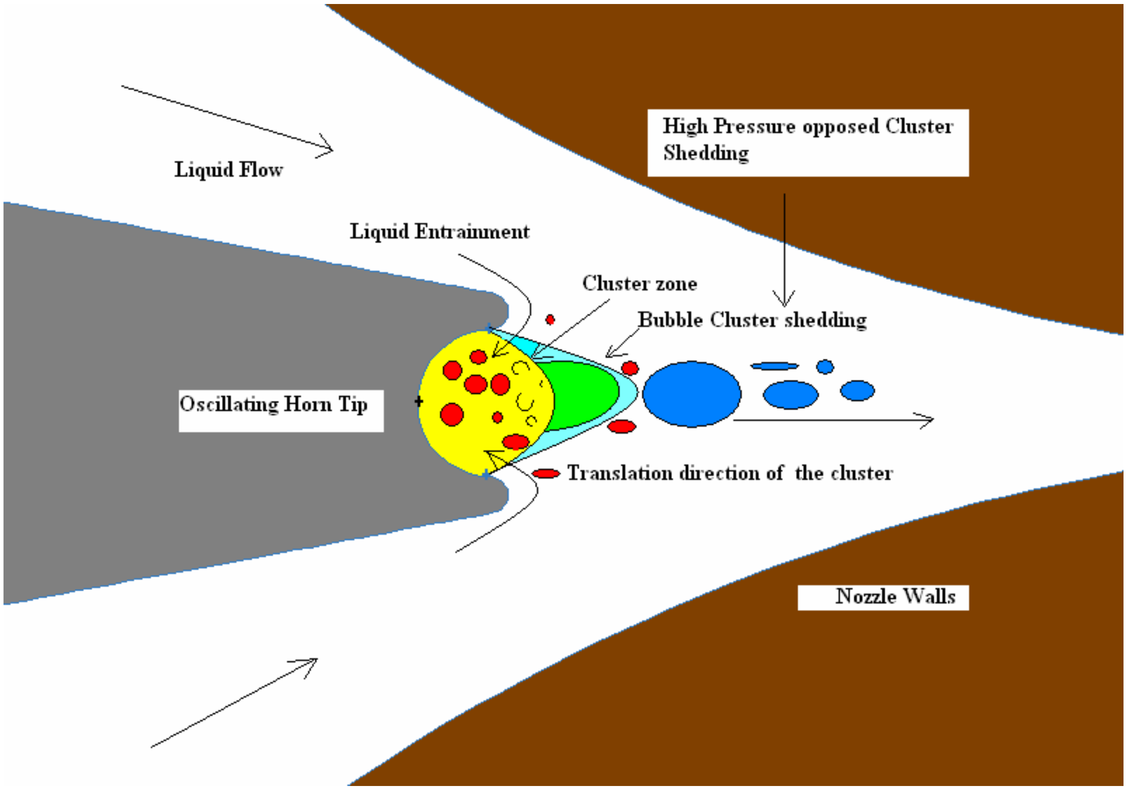

Figure 4.21: Effect of Ratio of Horn Tip Diameter to Stroke.

4.5.5.2 Position of the horn relative to the nozzle exit

It can be inferred from the simulations presented in Section (4.5.4.1-4.5.4.3) that the location of the horn has a dominating influence on the translation of cavitation bubble clusters. Besides altering the cavitation dynamics, the relative position of the horn also carries with itself the ability to control the pressure pulse propagation superimposed on the fluid flow pressure [204, 205]. Simply put, the closer movement of the horn position towards the nozzle exit will have a greater domination on the jet modulation as compared to moving it farther away due to the dissipation process. It is to be reminded that the presence of horn in the flow region inside the nozzle acts as a constriction to the free flowing liquid.

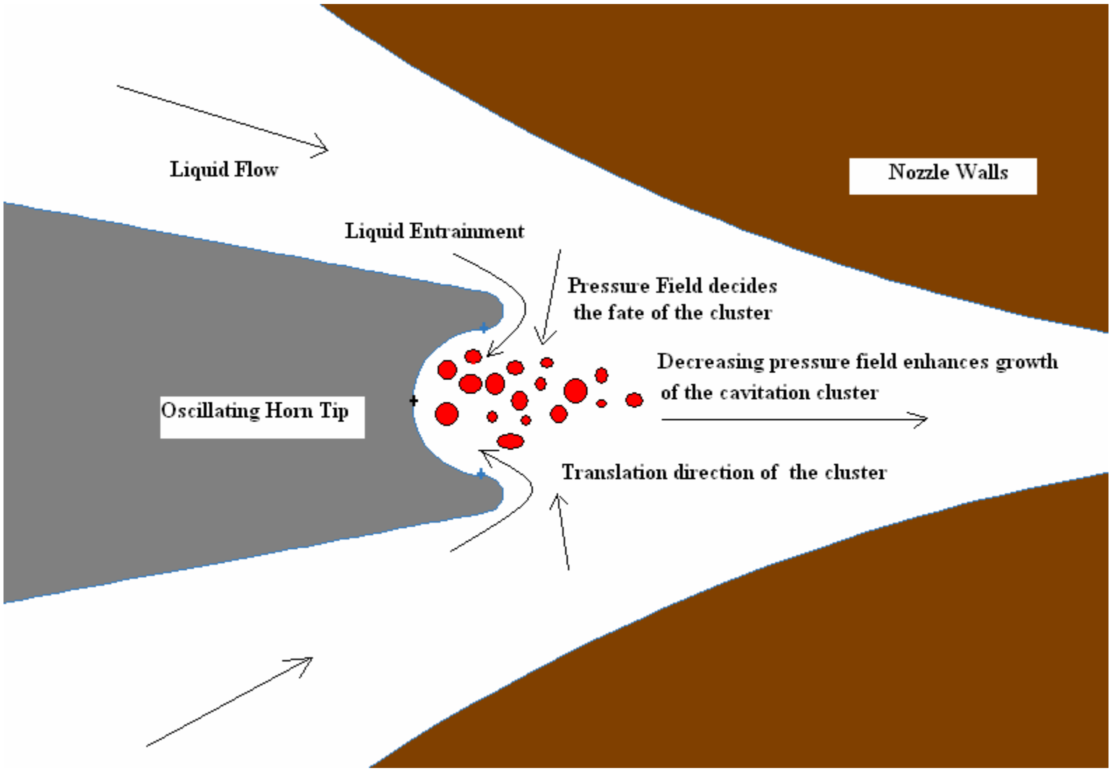

Figure 4.22: Position of the Horn in the Flow Field

Moving the horn closer to the nozzle exit will decrease the effective area of cross section available for the flow to reach the exit and hence severe vortex structures may be triggered in addition to high velocities accompanied by rapidly changing flow rate due to horn motion. This effective change in flow structure changes the pressure fields which is tightly coupled to the cavitation dynamics.

4.5.5.3 Pressure distribution in the flow field

As well understood from the flow physics and cavitation dynamics [33, 34], pressure distribution is a very critical parameter which enhances or opposes the growth of the cavitation cluster [105, 170]. To lower pressure near the growing clusters, accelerative flow mechanisms are required and may be supplemented with low pressure inducing geometry effects such as recirculation zones, vortex inducers etc.

4.5.6 Modified prototype design

The previous design presented in Section (4.5.5) has an exit diameter of 1 mm. Numerical simulations presented in Chapter 3 on the effect of inlet liquid jet diameter on the disintegration characteristics suggest that increase in the jet diameter results in un-atomized central liquid core structure. Theories stemming from breakup studies also indicate the increased effect of inertia over surface tension in the case of large diameter liquid jets [2].

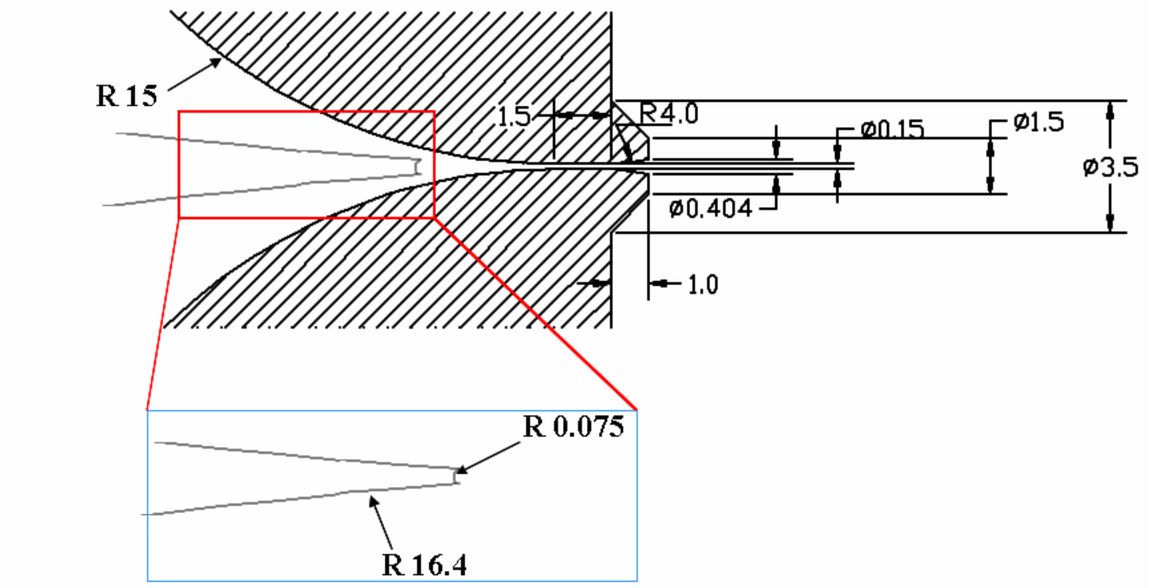

Figure 4.23: Modified prototype design with nozzle exit diameter = 0.4 mm, nozzle throat diameter = 150µm.

The same horn operating frequency of frequency 15,000 Hz with a horn tip diameter = 150 µm and horn stroke length (2 X amplitude) =150µm are utilized for the numerical study. In order to clarify the cavitating flow dynamics, preliminary simulations suggests that a stroke length equal to the horn diameter would help create a cavitation region that would not shrink under the motion of the horn itself. For providing favorable cavitation cluster generation the oscillating tip is placed at a position wherein, the horn surface takes approximately 1/3rd of the flow cross section area. Since the nozzle geometry is cylindrical, axi-symmetric approximations can be made for carrying out transient and steady state computations.

4.5.7 Numerical simulations of proposed cavitating nozzle

As stated earlier, several design parameters such as horn stroke length, its operation frequency etc critically influence the operation of the nozzle. In order to quantify these effects, parametric study using CFD methods are carried out on the proposed nozzle design shown in Fig. (4.23). List of characteristic parameters is detailed in Table (4.1).

Table 4.1 Parametric study to identify the influence of horn operation and nozzle design parameters

Investigated Parameter	**Stroke Length (µm)**	**Frequency *f* (KHz)**	**Horn Tip Diameter(µm)**	**Nozzle Throat Diameter (µm)**	**Flow Rate(cc/min)**
Baseline Case	*150*	*15*	*150*	*150*	*50*
Effect of Stroke	*100*	*15*	*150*	*150*	*50*
	200	*15*	*150*	*150*	*50*
Effect of Frequency	*150*	*10*	*150*	*150*	*50*
	150	*20*	*150*	*150*	*50*
Effect of flow rate	*150*	*15*	*150*	*150*	*100*
	150	*15*	*150*	*150*	*150*
Effect of Horn tip position					
1/3rd total area	*150*	*15*	*150*	*150*	*50*
1/4th total area	*150*	*15*	*150*	*150*	*50*
Scaling atomizer Geometry (1/2)	*75*	*15*	*75*	*75*	*50*

4.5.7.1 Modified UCA design

The use of an axi-symmetric assumption is favored due to the nature of the atomizer design. More importantly, the current Fluent's dynamic meshing procedure does not allow any periodic boundaries to be part of the procedure. As a result, numerical simulations with the moving mesh procedure can be carried out only using an axi-symmetric assumption or performing a complete three-dimensional simulation. Since we have opted to carry out axi-symmetric computations, a full three-dimensional computation is carried out on the modified prototype (Fig. (4.23)) and is compared with axi-symmetric calculations.

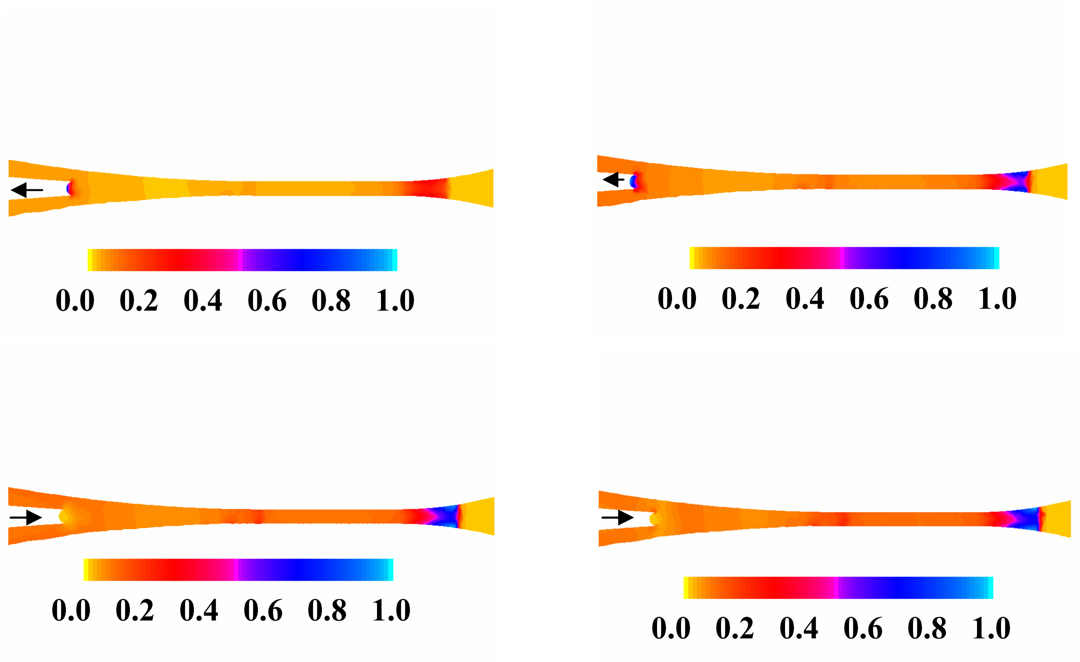

Figure 4.24: Contour plot of vapor volume fraction from a full three dimensional simulation on the proposed design.

In order to reduce the computational effort and associated tasks, axisymmetric simulations of the proposed design are carried out for comparison with the complete three dimensional simulations and verify its applicability in future numerical simulations.

4.5.7.2 Results and Discussions

Computational domain for axi-symmetric computations is detailed in Fig. (4.25). At the liquid inlet, velocities are specified based on flow rate requirement. The exit of the nozzle is treated as a pressure outlet with ambient pressure conditions. Walls are treated as no-slip boundary conditions and the oscillating horn is treated as a moving structure with specified user-defined movement specification. In the current simulation, a sinusoidal movement of the horn is specified at its boundaries. A total of 40,000 unstructured cells are used in the present computations.

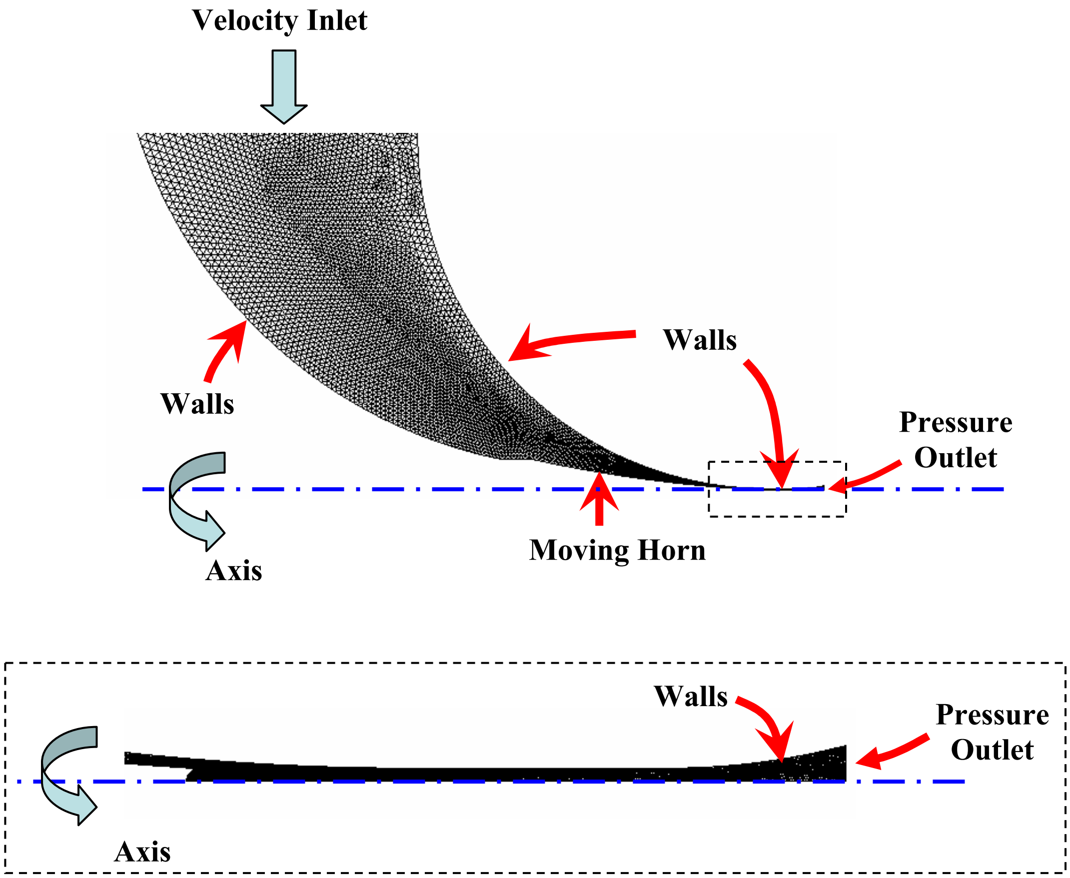

Figure 4.25: Computational domain and grids used in the axi-symmetric simulations

Computational results obtained from axi-symmetric simulations of the proposed design shown in Fig. (4.23) with *LS* = 150μm and a frequency of 15 KHz is shown in Fig. (4.26). The liquid flow rate at the nozzle inlet is maintained at 50 cc/min. The standard atmospheric conditions at the pressure outlets are assumed.

Axi-symmetric simulation of the proposed design reveals cavitation generation near the horn surface, its subsequent detachment and convection within the flow and formation of a strong vapor front near the nozzle exit due to the interaction with the local pressure gradients. It was observed that the residence time of the cavitation bubble region near the nozzle exit is very short. A collapse event occurred for every return motion of the horn. Based on this observation, it can be concluded that the collapse frequency of the clusters matched closely with that of the horn oscillation frequency.

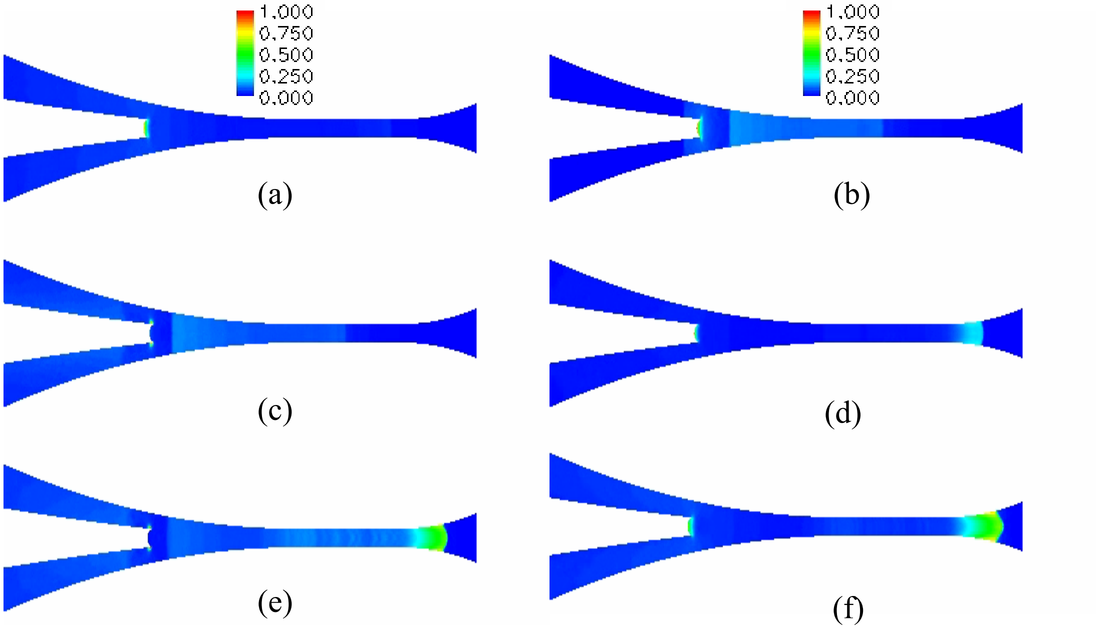

(a) (b)

(c) (d)

(e) (f)

Figure 4.26: Contour plot of vapor volume fraction: plots (a) – (f) represents the transient nature of cavitation dynamics inside the nozzle.

This indicates that a proper design of the nozzle interior can contribute to the enhancement of the domination of deterministic nature exhibited by the collapsing clusters. The formation of vapor fronts near the nozzle exit and their interaction with the local flow field is described in Fig. (4.27).

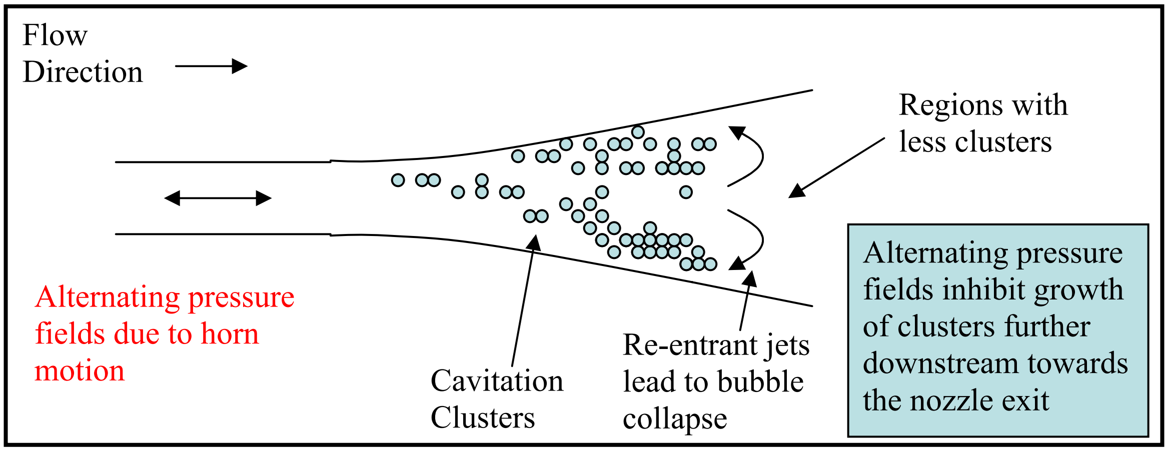

Figure 4.27: Schematic of cavitation cluster interaction with the flow structure

The presence of diverging section of the atomizer results in a cavitation growth inhibition due to adverse pressure gradients leading to flow reversals along the nozzle walls [108, 170]. In addition to the effect of nozzle shape, the superimposed pulsating pressure fields also considerably influences the collapse behavior. In the absence of pulsating fields, the cavitating clusters exit the nozzle and lead to events of supercavitation, an effect not explicitly reported here. In the presence of oscillating fields, the collapse behavior become much localized and is largely influenced by the flow structure. As noted from the simulations, both the 3D and axi-symmetric configuration provide similar details of the cavitation dynamics embedded in the flow structure. Hence, all the simulations presented in this Chapter are carried out using an axi-symmetric approximation, unless stated otherwise. The use of axi-symmetric models significantly reduces computational time and effort at the expense of losing three dimensional phenomena such as vortex structures and related instabilities [35].

4.5.8. Effect of horn stroke length

Numerical simulations using nucleation theories imposed on a one-dimensional model presented in Section (4.3) highlighted the importance of horn amplitude on the bubble dynamics. In this section, similar effect, the horn stroke length on the cavitation dynamics, is treated more elaborate by solving the complete set of Navier-Stokes equations. It is to be reminded that the pulsation of the horn inside the nozzle directly relates to the modulations imposed on the liquid jet. Extending the current design to analyze the effect of stroke length of the vibrating tip, CFD simulations are carried out with stroke lengths smaller and larger than the proposed stroke length of LS_{pro} = 150 μm. This analysis would help identify the influence of stroke length on cluster formation and propagation, which has been investigated to have a strong influence on the spray characteristics (Chapter 3).

- Stroke lengths chosen for this study include:
    (a) $LS1$: 100μm ($LS1 < LS_{pro}$)
    (b) $LS2$: 200μm ($LS2 > LS_{\mathrm{pro}}$)

The frequency of the oscillating horn has been kept constant at f = 15 KHz. The effect of stroke length on the cavitation dynamics inside the nozzle is shown in Fig. (4.28). With lower stroke length values, Fig. (4.28(i)(a–e)) , no dense vapor regions close to the horn surface are encountered although strong vapor regions are formed consistently near the diverging portion of the nozzle. The residence of vapor regions close to the nozzle exit is prolonged compared to the proposed design, Fig (4.28(ii) (a-e)). However, the extent of vapor regions near the nozzle exit is lesser compared to the vapor domain visualized in the proposed design. The formation and collapse of the clusters in the flow domain are observed to bear a one-to-one relationship with the oscillation frequency.

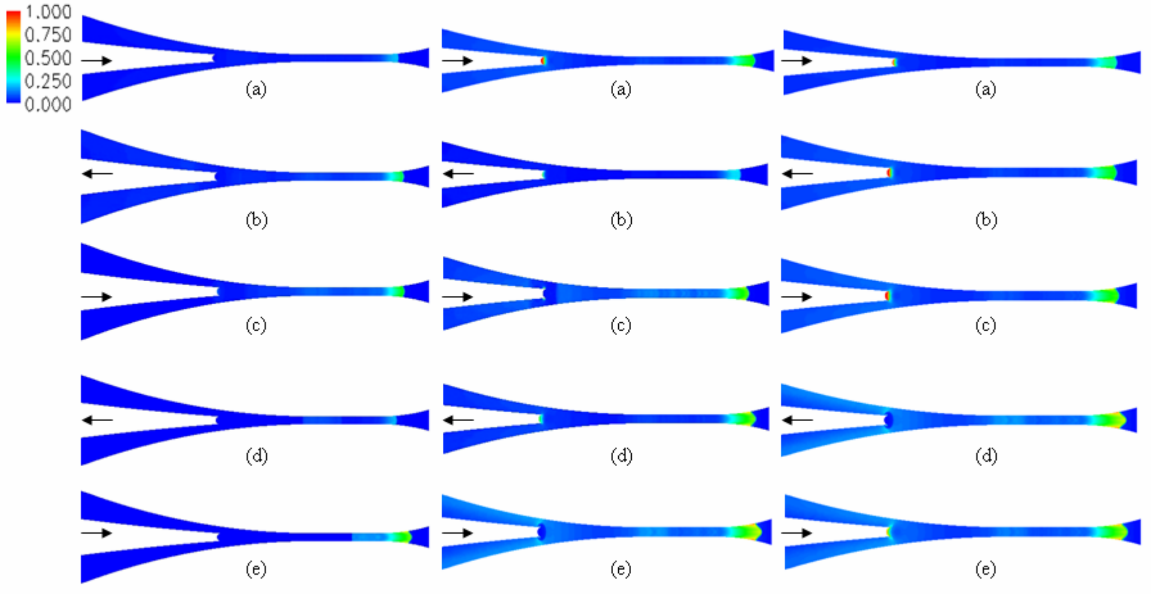

(i) (ii) (iii)

Figure 4.28: Influence of stroke length on cavitation cluster dynamics (i) $LS1$ = 100 μm (ii) LS_{pro} = 150 μm (baseline study) (iii) $LS2$ = 200 μm.

Retaining the same flow configuration and horn frequency, the stroke length of the proposed horn is increased to 200 μm resulting in very peculiar cavitation cluster behavior near the horn surface. The process is illustrated with time frames obtained from the numerical simulations in comparison to our baseline case, Fig (4.28 (iii)(a3-e3)). Observe from Fig. (4.28(iii)), the creation of very high dense cavitation clusters region in the vicinity of the horn surface. Clusters formation and their detachment are observed to increase with increase in the stroke length. The vapor cluster interacts with re-entrant jets during backward stroke of horn leading to their separation process from the horn surface. This process results in a complicated flow structure near the horn surface. The complexity in flow structure is also attributed to the flow area fluctuation between the horn surface and nozzle walls. Presence of fluctuating transient area profile in combination with a cavitating mixture flow results in distorted fluid flow motion. This hints that the position of horn surface relative to the nozzle exit is critical in deciding the cluster detachment mechanism. By increasing the stroke to 200µm, creation of elongated vapor structures that are detached and propagated downstream towards the exit of the nozzle, are detected. The clusters created by increasing the stroke (at a constant frequency of 15 KHz) are more frequent compared to the base case with a stroke length of 150µm at 15 KHz oscillation frequency. This can be explained due to the increased energy input in the same time duration which delays collapse (condensation process). The extent of cavitating clusters reaching the nozzle exit is higher compared to other stroke length designs. The fundamental alteration in cavitation dynamics can be attributed to the fact that, higher stroke length results in increased pressure pulse magnitude across the length of the nozzle.

A closer view of the cavitation dynamics generated by increased stroke length is portrayed in Fig. (4.29). From equation (4.53), identify that the energy input per unit time increases linearly with horn amplitude. In combination with the local flow structure, a variation in stroke length to 200 µm leads to intensified cavity formation near the horn. One other parameter that is of considerable importance is the shear generated between the horn structure and the surrounding liquid stream. Heightening the stroke length correspondingly increases the shear rates and in the intensification of the magnitude of absolute pressure near the curved horn surface. The time required for fluid entrainment into the concave surface of the horn is increased and hence, rupturing of the liquid is favored.

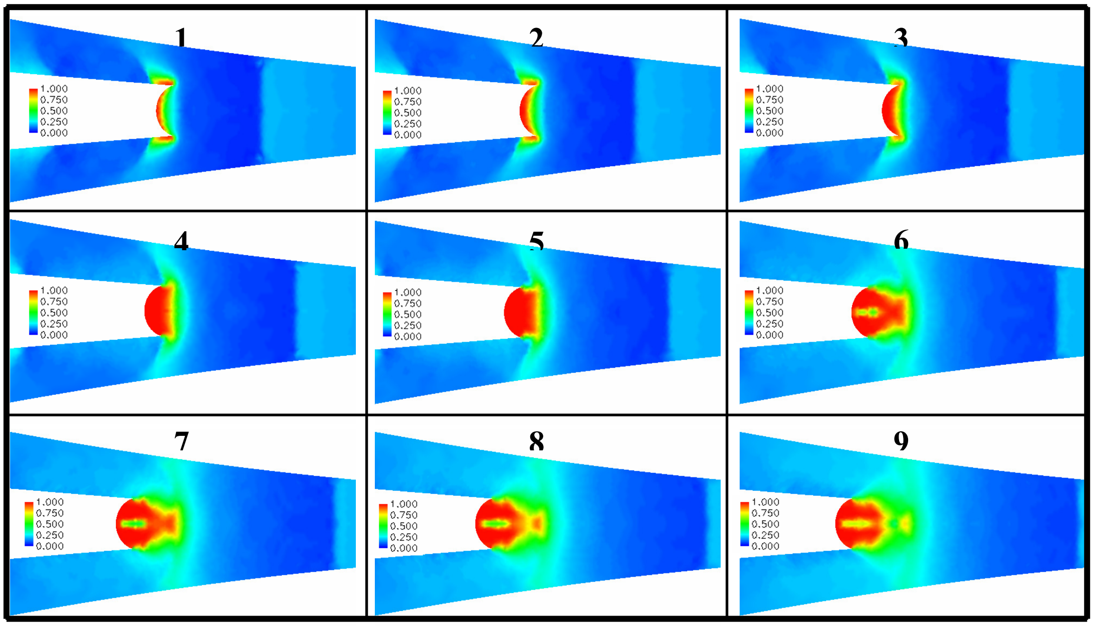

Figure 4.29: Characteristics of cavitation clusters near the horn surface with increased stroke length of 200 μm at a frequency of 15 KHz.

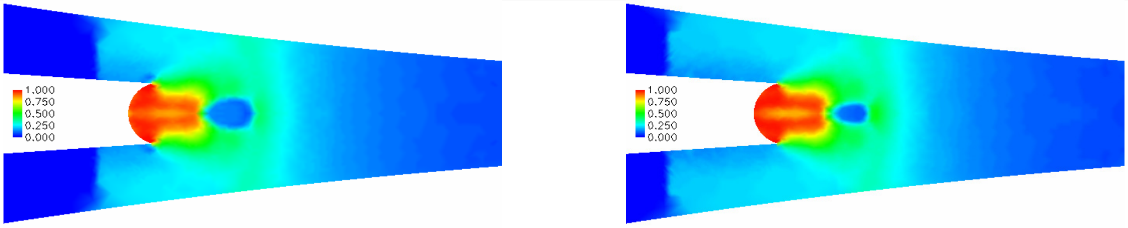

Cluster elongation near horn surface **10**

Detaching vapor clouds **11**

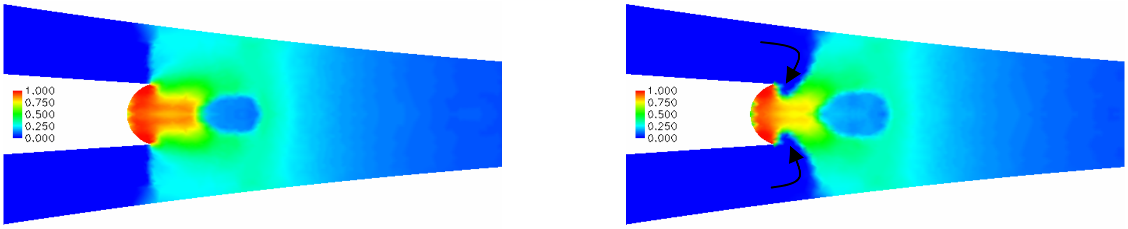

Vapor cloud interaction with flowing liquid **12**

Flow entrainment influencing the cluster growth **13**

Figure 4.30: Close up illustration depicting the flow physics near an oscillating surface with cavitating zones.

Following the investigation on the stroke length effect on cavitation dynamics, the effect of the horn oscillation frequency is addressed under a constant stroke length magnitude.

4.5.9. Effect of oscillating horn frequency

With a detailed description available on the effect of stroke length on cavitation process, the effect of horn oscillation frequency on the latter is discussed here. From our understanding on the dynamics of bubbles under pulsating fields, increasing the frequency of the oscillating pressure fields contributes to the bubble growth since the mass transfer rate by diffusion process takes places at a faster rate than the reverse condensation process across the bubble walls in a cavitation bubble [34]. The vapor bubbles under high frequencies would thus start growing due to a rectified diffusion effect. The current cavitation model, however, treats only the first order effects where the radius of the bubble grows proportional to the time scale and the pressure difference existing across the bubble and the surrounding fluid [237, 238]. In the testing process, two different frequency values are chosen

(a) Frequency = 10 KHz (< base case value = 15 KHz)

(b) Frequency = 20 KHz (> base case value = 15 KHz)

Simulations are performed under a constant stroke length = 150 μm and a flow rate of 50 cc/min.

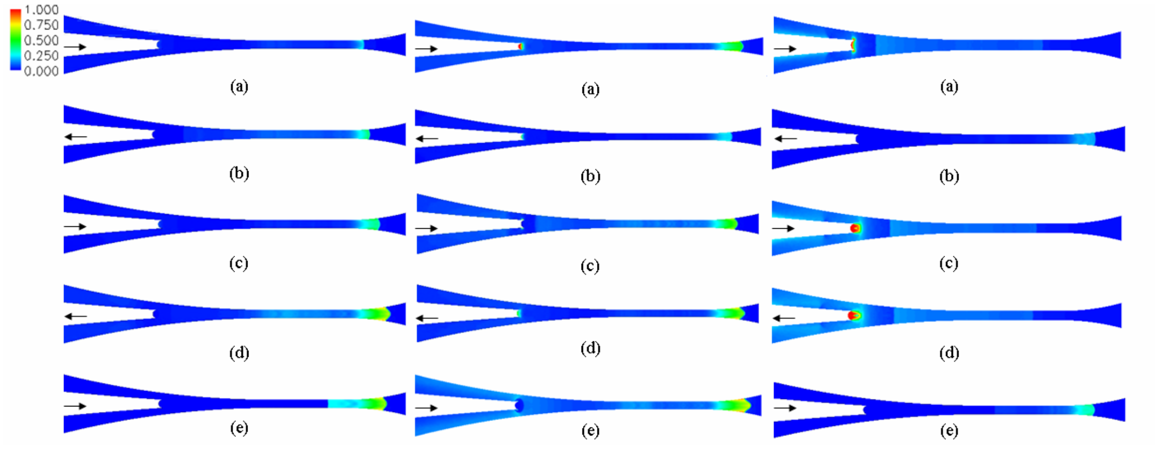

(i) (ii) (iii)

Figure 4.31: Numerical simulation of cavitating atomizer under different horn frequency perturbations (i) 10 KHz (ii) 15 KHz (iii) 20 KHz at a constant stroke length $LS = 150$ µm

For an oscillation frequency of 10 KHz, no appreciable cavitation cluster zone is created near the horn surface (Fig. (4.31(i))). The absence of cavitation cluster near the horn surface can be attributed to the fact that energy supplied by the oscillating horn tip is not favorable enough to produce the required pressure gradients for cavitation inception. Further, if the gradients created by the horn tip is not strong enough, or even at the verge of creating cavitating zones, the fluid flow entrainment negates these low intense gradients. This is also the reason why creating cavitation in a static no flow zone is far different than cavitation inception in a flow field [33, 34]. The later has fluid flow interaction changing the local features of the flow while in the former, any such interaction is absent. In the above case, however, the pulsating pressure field induces cavitation zone formation along the walls of the nozzle near the entrance into the throat section. Due to reduced pressure created by the accelerated flow, the cavitation clusters grow until the diverging section interacts leading to vapor collapse. A vapor front during the collapse is clearly visible in the contour plot shown in Fig. (4.31(i)). With increased horn oscillation frequency, f = 20 KHz, increased intensity of vapor creation is encountered, Fig. (4.31(iii)), similar to the effect obtained by using a high stroke length horn motion, Fig. (4.28(iii)). The imposed frequency of the horn motion provides two effects: owing to high perturbation effects imposed on the flow cavitation clusters do not have sufficient time to travel towards the nozzle exit. Their convection downstream is overtaken by the traveling pressure wave created by the next oscillation cycle resulting in quicker collapse. Second, the increased frequency content near the horn implies increased pressure gradients, directly dictated by equation (4.53). Hence, improvement in cavitation cluster density near the horn is expected. The former effect indicates that sufficient increase in the nozzle length would then give rise to a different collapse structure. However, another alternative is to increase the flow speed and match the pressure wave propagation velocity downstream.

4.5.10. Effect of flow rate

The previous simulations, assessing the effect of stroke and frequency, clearly indicate that besides the horn parameters, the accelerated fluid flow inside the nozzle is very crucial in deciding the overall behavior of the cavitation characteristics [217, 218] and finally the atomizer performance. Evaluating the critical nature of flow rate is essential for a wide range of reasons. First of all, the flow rate relates to the volume of liquid exiting the nozzle per unit time, to be sprayed onto the surface. Further, defining the flow rate fixes the liquid velocity at the nozzle exit (for a constant diameter of the orifice with no imposed pulsation). Having the liquid velocity fixed at the nozzle exit clearly maps the liquid jet behavior, using widely available instability theories, to the modes of their disintegration. This disintegration mechanism can be extrapolated to the nature of primary and secondary jet breakup processes which then dictate the spray size distribution [2, 3]. With this background, we proceed to evaluate the effect of increased flow rate on the cavitation and flow structure inside the nozzle. In this concern, 2 different flow rates (a) 100 cc/min (b) 150 cc/min maintaining the same stroke length (150μm) and frequency of (15 KHz), are reported. Figure (4.32) presents transient axi-symmetric simulation performed for the configuration (a) with 100 cc/min and is compared with the (ii) baseline case of 50 cc/min.

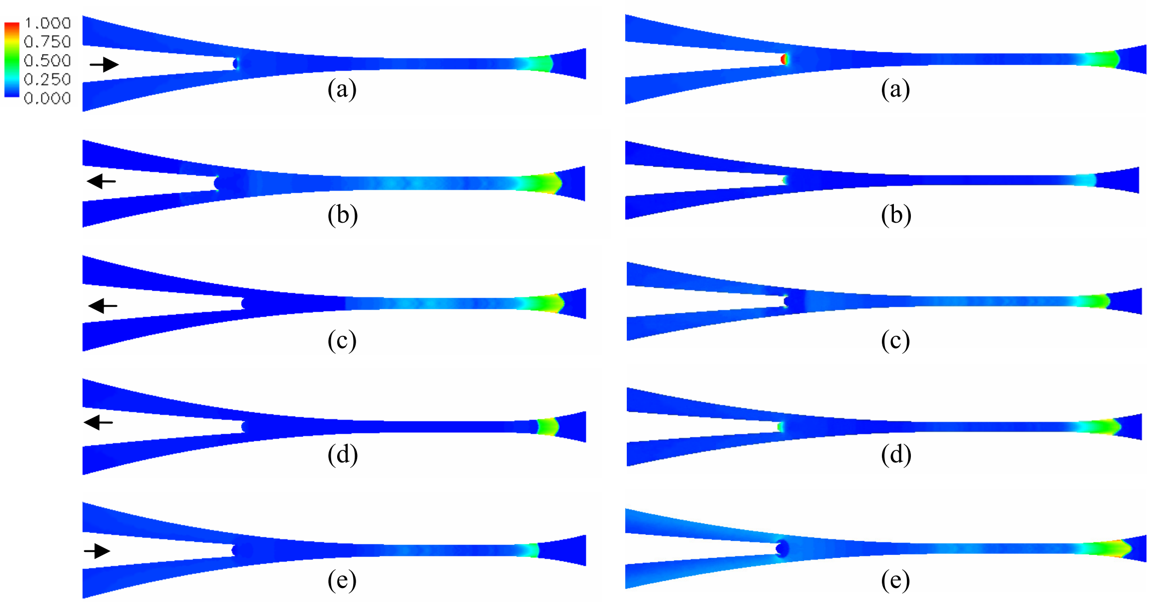

Figure 4.32: Contour plots of vapor volume fraction for flow rate (i) 100 cc/min (ii) 50 cc/min with horn stroke length of 150μm at a frequency of 15 KHz.

With doubled flow rate no major cavitation cluster characteristics alteration is observed. In fact, with a lower flow rate of 50 cc/min, cluster length near the nozzle exit region is seen pronounced. Although, it is expected that increase in flow rate would directly reflect on the increased velocity and hence the shear rate, would produce more cavitation effects, the pressure pulsation is observed to play a predominant role in masking the shear effects. Observable effects include growth of vapor regions towards the nozzle exit although collapse occurs within the nozzle interior domain. The increased cavitation cluster as compared to the base case with a flow rate of 50 cc/min is attributed to the lowered local pressure field or an increase in mixture velocity along the nozzle section due to increased flow rate. The combined effect of liquid flow velocity, shape of nozzle diverging portion and vapor distribution results in condensation (collapse) of the cavity clusters.

Unlike what is observed with 100 cc/min, the cluster intensity near the horn surface is virtually eliminated with a flow rate of 150 cc/min (Fig. (4.33)). Further increase in flow rate to 150 cc/min results in supercavitation regime [2, 48, 54]. A strong vapor region persists near the nozzle exit although a consistent interaction with the re-entry jets is noticeable. The intensity of the clusters near the nozzle exit is clearly seen increased. This simulation reiterates the fact that increased velocity leads to lowered local pressure and hence increased cavitation rates [34, 218]. As expected, regions close to the horn are less prone to cavitation since high flow rate results in faster entrainment and diffuses the pressure gradients induced by the oscillating horn.

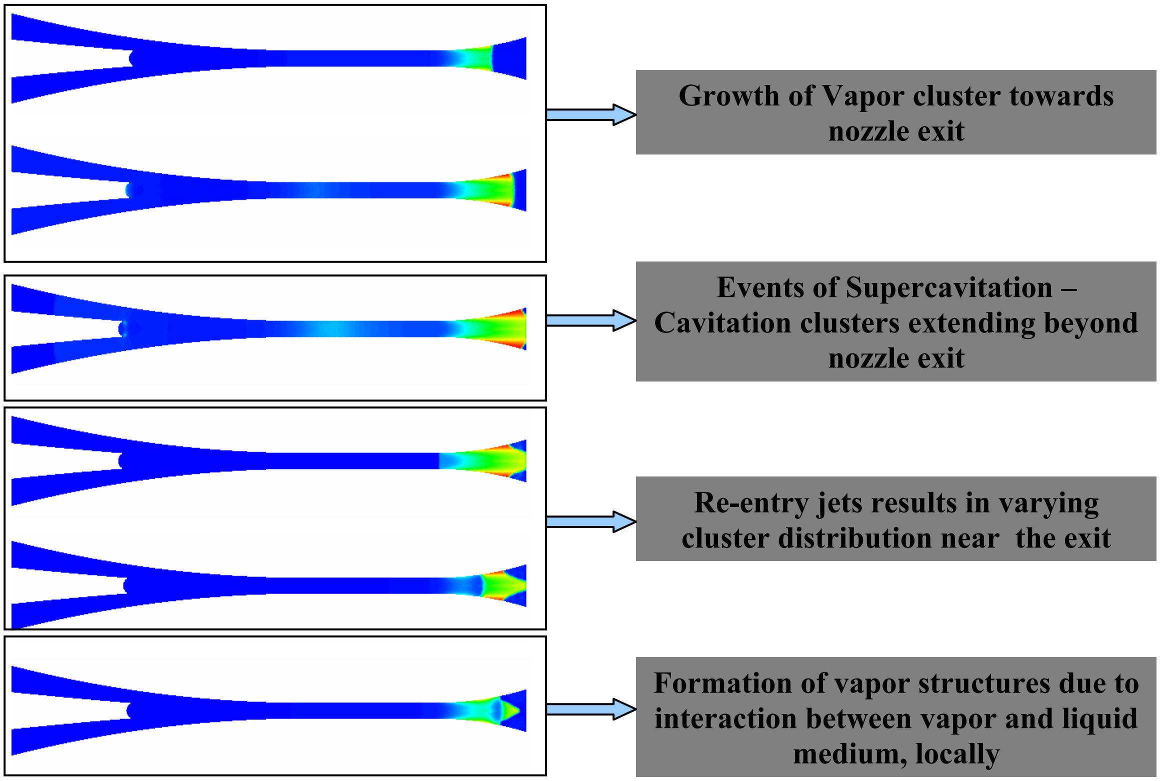

Growth of Vapor cluster towards nozzle exit

Events of Supercavitation – Cavitation clusters extending beyond nozzle exit

Re-entry jets results in varying cluster distribution near the exit

Formation of vapor structures due to interaction between vapor and liquid medium, locally

Figure 4.33: Contour plot of vapor volume fraction showing events of super-cavitation. Flow rate = 150 cc/min. Stroke length = 150µm, horn frequency = 15 KHz.

An increase in flow rate to 150 cc/min resulted in very high velocities at the throat and increased cluster density near nozzle exit. Unsteady operations prevailed due to very high non-linearity shown by the bubble dynamics. To overcome high non-linearity due to cavitation dynamics and to accommodate higher flow rate, it is advised to either increase the throat diameter to allow higher mixture flow towards nozzle exit or use multiple nozzle heads for spray applications. Increased flow rate has its own drawbacks, since an increase in the flow near the constricted passage between the horn surface and the walls can lead to extensive cavitation on the horn surface. The energy utilized for the horn motion (force required to move horn by the amplifier has to be reevaluated). At this juncture, it is required that the liquid velocity at nozzle exit be maintained in the atomization regime to obtain well defined spray patterns. To obtain a “good” collapse inside the nozzle, testing the position of the horn inside the nozzle is required, while maintaining a required flow rate.

In the numerical simulations, it has been quite frequently observed that collapse of cavitation clusters occurs near the diverging section of the nozzle due to the shear generated by the moving liquid against the wall [170]. The shear effect can be enhanced by altering the nature of the nozzle geometry. In the following section, chief reasons for the formation of collapsing vapor front and the implications of the nozzle shape on spray dynamics is described.

4.5.11. Effect of nozzle shape

The cavitating flow simulations presented in previous sections clearly revealed that the flow through the convergent-divergent nozzle design is complicated by the condensation (collapse) process near the nozzle exit, particularly near the diverging section of the nozzle. In the current design encompassing accelerated nozzle flows, pressure wave propagation at any given instant of time ensures that the cavitation and flow dynamics near the nozzle exit are bound to be influenced by the flow variable (pressure-velocity) history. This effects the mixing of the two phase flow and in the development of a complete turbulent regime. The mixing of multiphase mixture has varying length and time scales resulting in highly sensitive flow development. The velocity profile, which is crucial in inducing relaxation effects on the outgoing liquid jets, experiences considerable amount of variation in a very brief instant of time, approximated to the inverse of imposed oscillatory frequency. This developing flow structure and its effect on external jet behavior are depicted by the schematic as shown below.

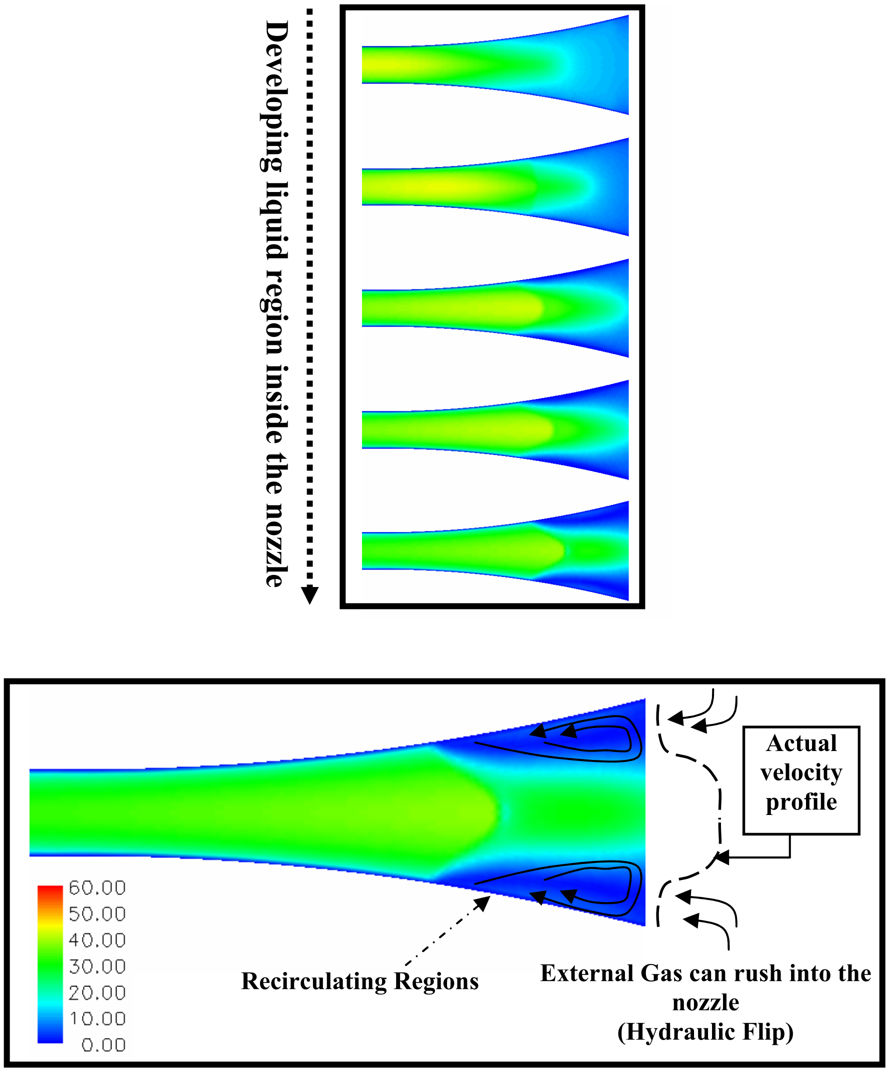

Figure 4.34: Contour plot of liquid-vapor mixture velocity near the nozzle exit.

As clearly indicated in the Fig. (4.34), entry of gas from ambience into nozzle – hydraulic flip can easily occur. It has been experimentally observed that the hydraulic flips results in mixing of external air with the interior flow, preventing the occurrence of any cavitation events. The jet surface becomes smoother as a result of hydraulic flip [54, 57, 59], where the cavitation instabilities are negated by the air interaction entrained into the nozzle, and results in increased breakup length. This has serious implications on the jet break up characteristics and hence the final droplet characteristics. Also, observe that the recirculation zones near the exit results in smaller liquid jet diameter exiting the orifice, detached from nozzle surface. In discussing gas entrainment into nozzle, the volume entering the nozzle depends on the recirculation region length. Several studies have identified the influence of Reynolds number in modulating the recirculation zones when a sudden enlargement in the flow section is intercepted. In the present study, variation in the flow velocity due to modulation parameters such as operating horn frequency and amplitude, alongside the horn position and flow rate, can lead to intensified recirculation zones capable of enhancing hydraulic flip.

Having discussed the flow rate impact on the cluster dynamics, a similar effect could be brought about by changing the effective flow area. This effect can be implemented by changing the relative position of the oscillating horn with respect to the nozzle exit.

4.5.12. Effect of horn tip position

The simulations characterizing the effects of stroke length, frequency and flow rate on the cavitation dynamics detected strong association of the vaporization process with the horn tip dynamics. In this concern, numerical simulations presented here are devoted to comprehend the impact of horn tip positioning on the liquid-vapor mixture flow. To realize this purpose, axi-symmetric simulations of the proposed design shown in Fig. (4.23) are carried out by modifying the horn position. In the proposed design, the horn tip occupies 1/8th the total flow area. The ratio of horn tip area to flow area in the relevant cross-section is modified so that the ratios read (a)

0.25 (tip occupying 1/4th total flow area) and (b) 0.33 (1/3rd area coverage by the horn tip). The modification is achieved by translating the horn tip to different locations within the nozzle. This process restricts the flow passage and hence cavitation dynamics are expected to portray new features. The simulations performed here retain a constant horn tip diameter of 150 µm, a stroke length = 150µm and for a flow rate of 50 cc/min.

4.5.12.1 Effect of 1/4th flow area

Simulation results obtained by moving the horn tip to occupy 1/4th the total flow area, shown in Fig. (4.35), depict pronounced complexity of cavitation dynamics. Due to increased flow acceleration near the curved horn surface, some dense vapor clustering is observed. The results indicate increased cavitation cluster strength propagating towards the nozzle exit. However, they do not withstand the adverse pressure gradient prominent near the diverging section and it results in their collapse before reaching the exit. In this connection, it should be noted that the strength of the clusters formed are much stronger than the initially tested design (Fig. (4.26)).

The regions near the horn surface also experienced sufficient cavitation inception since the restricted flow resulted in faster flow velocities, which represents lowering of liquid pressure. CFD simulations suggest strong re-entry regions near nozzle exit affecting the overall liquid-vapor mixture flow field.

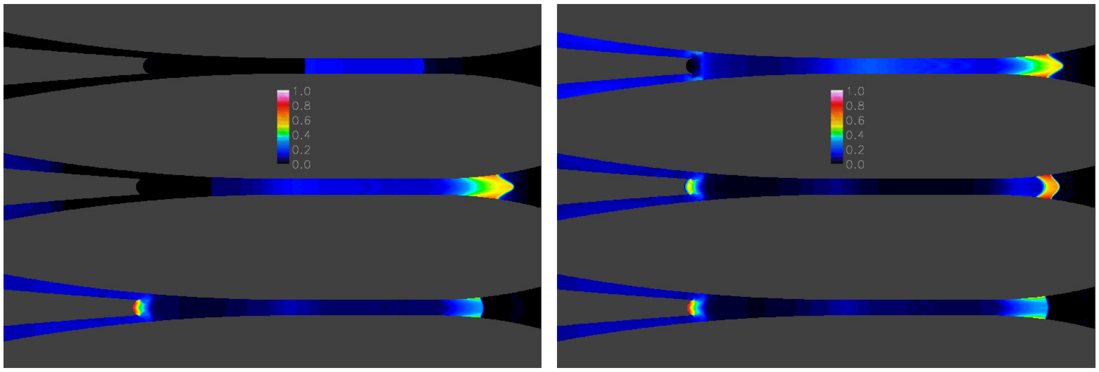

(i) (ii)

Figure 4.35: Contour plot of vapor volume fraction indicating the effect of change in horn tip position with respect to the nozzle exit.

4.5.12.2Horn tip occupying $1/3^{rd}$ *total flow area*

With increased penetration of the horn tip into the nozzle throat, very high cavitation rates were observed. The cavitation intensity near the horn surface and in the nozzle exit resulted in very high flow velocities. The tests reveal close matching with the one-dimensional steady-state tests of Wang and Brennen [217], when their convergent-divergent nozzle flows choked at the nozzle throat, when the inlet void fraction of the vapor was increased. In the current system, however, no steady state approximation has been used. Rather, the true nature of the cavitation bubble dynamics relating to the high non-linearity is numerically treated [237, 238].

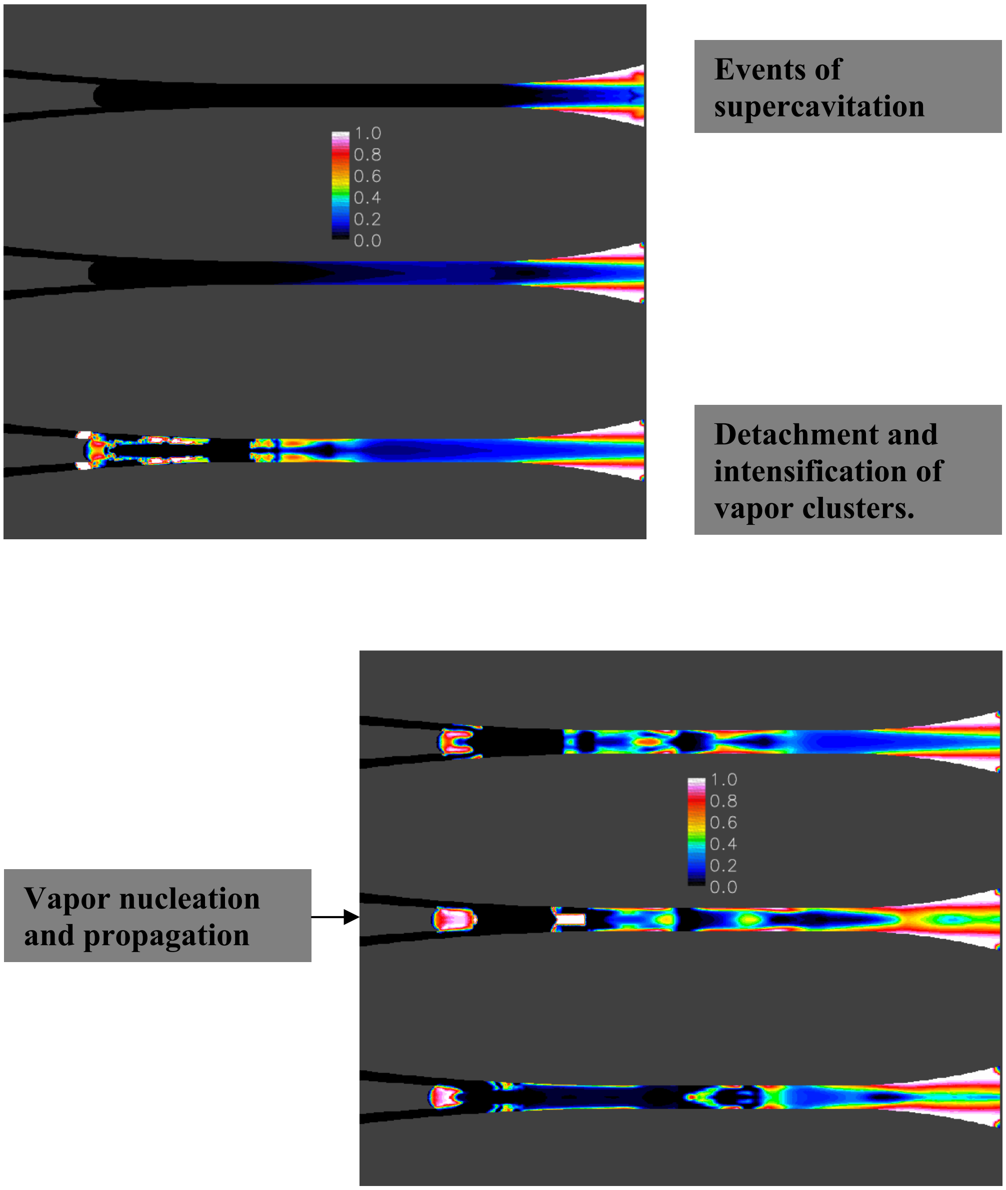

Figure 4.36: Contour plot of vapor volume fraction showing very highly stochastic nature of the flow with intense cavitation fields.

The simulation involving the displacement of the horn tip such that it occupies 1/3rd flow area portrayed:

(1) intense vapor nucleation near horn surface and subsequent detachment and propagation.

(2) very high cluster intensities which in turn increases the effective flow velocities.

(3) Supercavitation regimes near the nozzle exit.

The simulations strongly suggest that changing the position of the horn tip in the nozzle interior ramifies the cavitation intensity thereby perturbing the flow structure considerably. The above conclusions can effectively help design cavitating and modulated flows at lower stroke lengths, optimizing its position such that the vapor cluster formation, propagation and collapse are consistent. Plots of mixture velocity distribution at the nozzle exit for different horn-position cases tested are shown in Fig. (4.37). Note the dramatic increase in the exit jet velocity, by increasing the horn coverage area from 1/4th to 1/3rd. The spiking in the mixture velocity is attributed to the intense cavitation cluster initiated by increasing the horn coverage area.

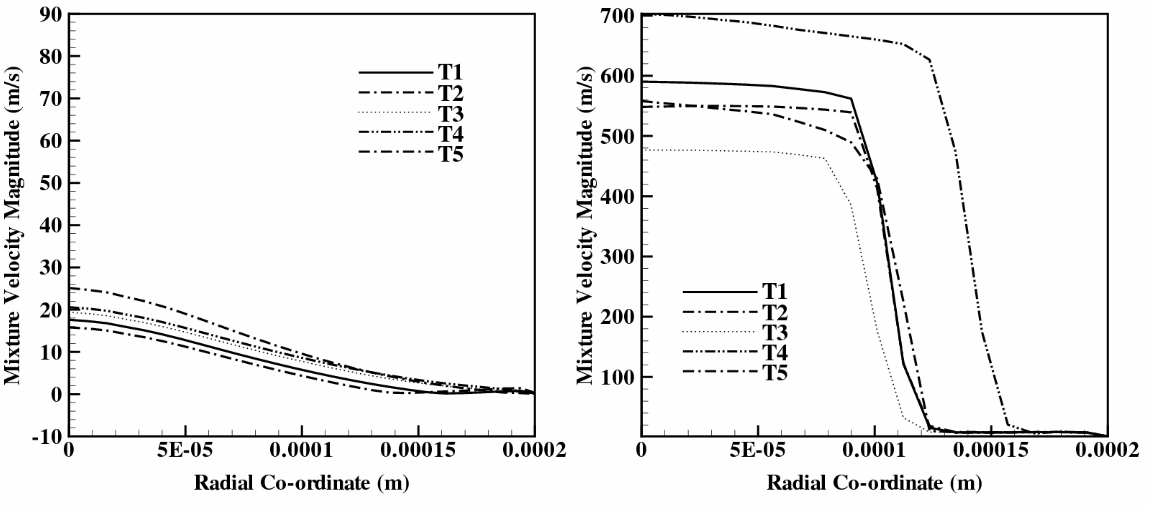

(a) (b)

Figure 4.37: Plots of mixture velocity magnitude at the nozzle exit section when the horn tip occupies (a)1/4th and (b)1/3rd the flow area in the horn tip section

It is, however, important to notice that with a cavitation intensifying tip position lower stroke length combination with appropriate flow rate can meet the cluster formation/collapse requirements. As seen from simulations it can be deduced that, tip position (b) can be used with much lower stroke lengths compared to position (a) maintaining the same flow rates. The effect of tip position on the velocity modulation at nozzle exit has to be considered before formulating the above combination.

4.5.13 On the influence of horn tip position

4.5.13.1 Near horn surface

In the near horn region, depending on the clearance existing between the nozzle walls and the horn surface, cavitation intensification due to increased shear opposing the flow direction (return stroke) is encountered. The formation and propagation of cavity clusters near the horn surface can, hence, be controlled by adjusting the shear rates required for the process. Monitoring the position of the horn provides one such approach to control the shear development process as a function of amplitude and frequency. A schematic of the dynamics exhibited near the oscillating horn tip surface is detailed in Fig. (4.38).

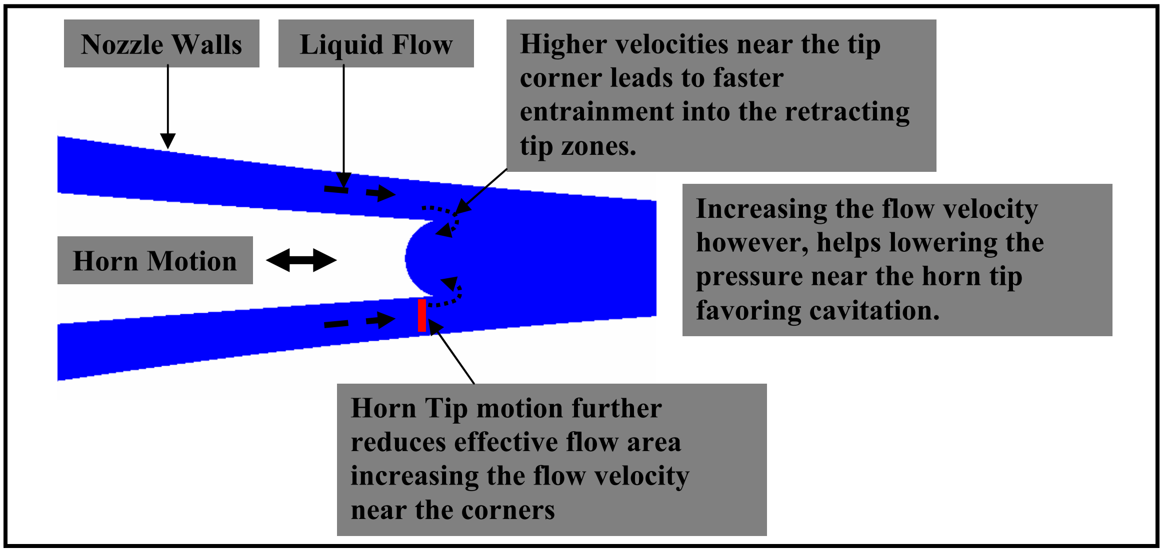

Figure 4.38: Influence of horn tip position near the horn surface

However, near the nozzle exit a multitude of mechanisms act to control the cavitation mechanism and pressure fluctuations.

4.5.13.2. Near Nozzle exit

From a variety of numerical simulations presented in this study, on a preliminary cavitating atomizer design, the critical influencing nature of the diverging (diffuser) section on the cavitation behavior is satisfactorily concluded. A schematic, describing impact of the diverging nozzle section, is shown in Fig. (4.39). The impact of the near horn dynamics is felt along the entire nozzle length till the fluid reaches the exit section. This is attributed to the disturbances created within the flow, in the form of cavitation, turbulence, vorticity components, by the oscillatory motion of the horn. Figure (4.39) illustrates the effects encountered in the near nozzle exit regions.

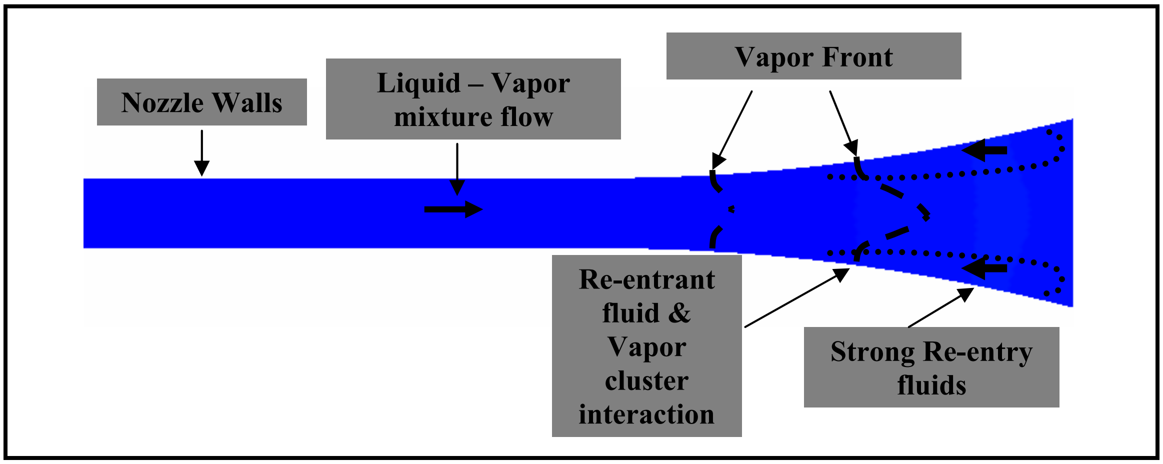

Figure 4.39: Influence of horn tip position variance on the cavity dynamics near the nozzle exit.

As explained in Fig. (4.39), the modulations provided by the oscillatory horn impose vital characteristics to the fluid flow and eventually control their behavior in the near exit regions. In this regard, an increased displacement of horn tip reflects on increased intensity of recirculation regions near the nozzle exit enforcing greater shear on the diverging nozzle section, an effect of increased horn stroke length. By moving the horn tip closer to the exit section, it is observed that the velocity profile (modulation) at the nozzle exit is influenced appreciably since the pressure waves emanating from the horn surface travel faster towards the nozzle exit (proximity). Based on the numerical simulations, we can conclude that the residence time of the vapor clusters is altered distinctly depending on a combination of operating parameters of the horn, the flow rate and the nozzle design. With various parametric study involving flow rate evaluation, horn stroke and frequency, the effect of recirculation near the nozzle exterior due to diverging section always created a vapor front and a collapse behavior, characteristic to the operating system. The following details should be noted in assessing the influence of nozzle design.

(1) Intensity of recirculation is dependent on the shear generated (coupled to flow rate, stroke and frequency) near the diverging nozzle section.

(2) The velocity profile (modulation) at the nozzle exit is influenced appreciably as a strong function of the modulated pressure signal. A frequency spectrum analysis shows that the peak frequency embedded in the flow is indeed the imposed horn frequency.

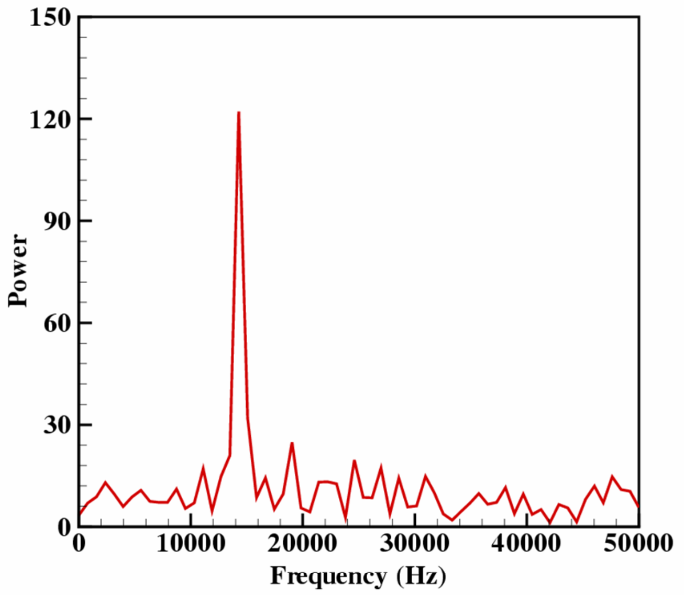

Figure: 4.40 FFT of the velocity signal at the nozzle exit taken from simulation results in Section (4.5.7.2) indicates a peak frequency equal to the imposed horn frequency of 15 KHz.

4.5.14. Modified Nozzle Design

Since the presence of recirculation regions can arguably flip the nozzles [2, 47, 48], a straightforward implementation to remove the regions of recirculation is carried out by removing the diverging nozzle section and replacing it with a constant diameter of section of magnitude equal to the throat diameter. The modification process is described in Fig. (4.41).

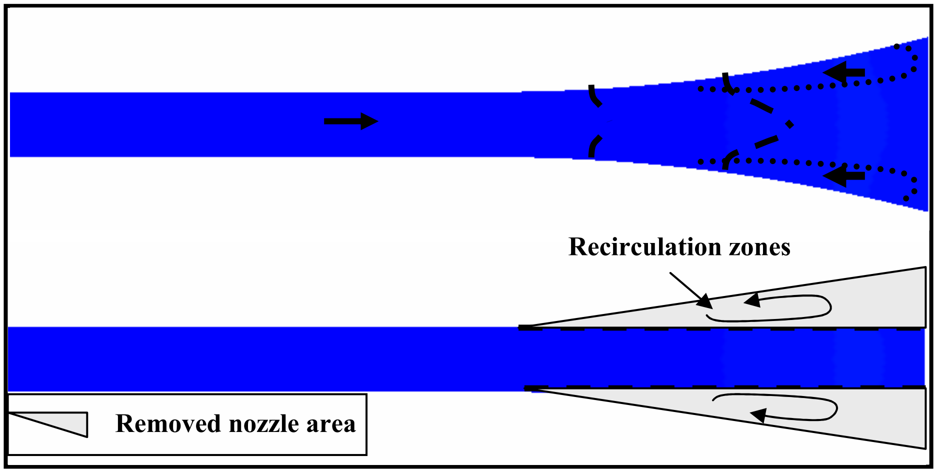

Figure 4.41: Schematic of nozzle design by removing the divergent portion in the proposed nozzle design and replacing it with an extended constant diameter section.

One possible outcome of this design alteration is a direct consequence of the diffuser effect, i.e., reduction in the residence time of the vapor clusters near the nozzle exit due to removal of flow deceleration mechanism. This nozzle design contributes to the formation of cavitation regions within the nozzle flow only due to the pressure modulation effect. Geometry based shear effects can no longer contribute in a major fashion to the inception and evolution of cavity clusters.

4.5.14.1. Effect of Nozzle Design

In this concern, the diverging section of the nozzle is replaced by a constant diameter cross-section zone with its diameter equaling the nozzle throat diameter. The simulation results presented in Fig. (4.42) are computed for a flow rate of 50 cc/min with horn oscillation stroke length = 150 µm at 15 KHz. The exit diameter in this case is 0.15 mm with a nozzle length to diameter ratio equal to 5.

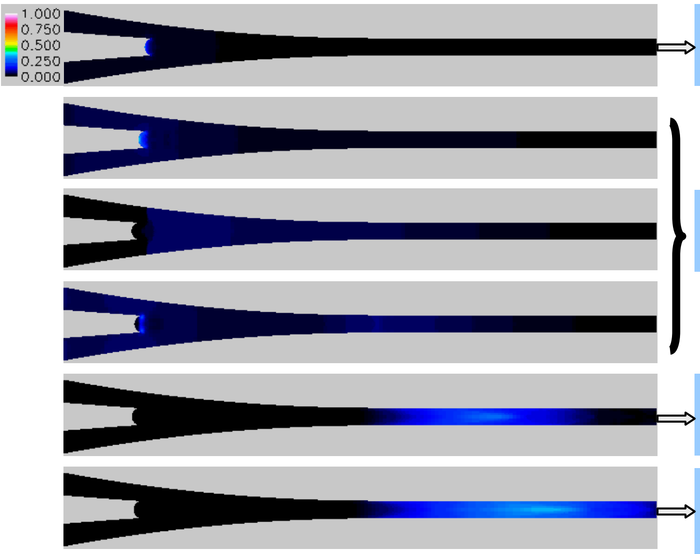

Formation of vapor pockets near the horn surface

Vapor clusters propagated downstream by horn motion

Maximum propagating vapor fraction intensity ~ 0.2

No re-circulating jet type mechanism seen due to nozzle shape (no presence of diverging section)

Figure 4.42: Contour plot of vapor volume fraction with the diverging section of the nozzle replaced by a constant diameter section.

Replacing the diverging section eliminates the occurrence of the vapor front near the nozzle exit. However, the intensity of the cavities near the nozzle exit is considerably reduced since there is not abrupt change in pressure near the nozzle exit on which the cavitation clusters used to survive. A plot of velocity magnitude and corresponding vapor volume fraction at the exit section is shown in Fig. (4.43).

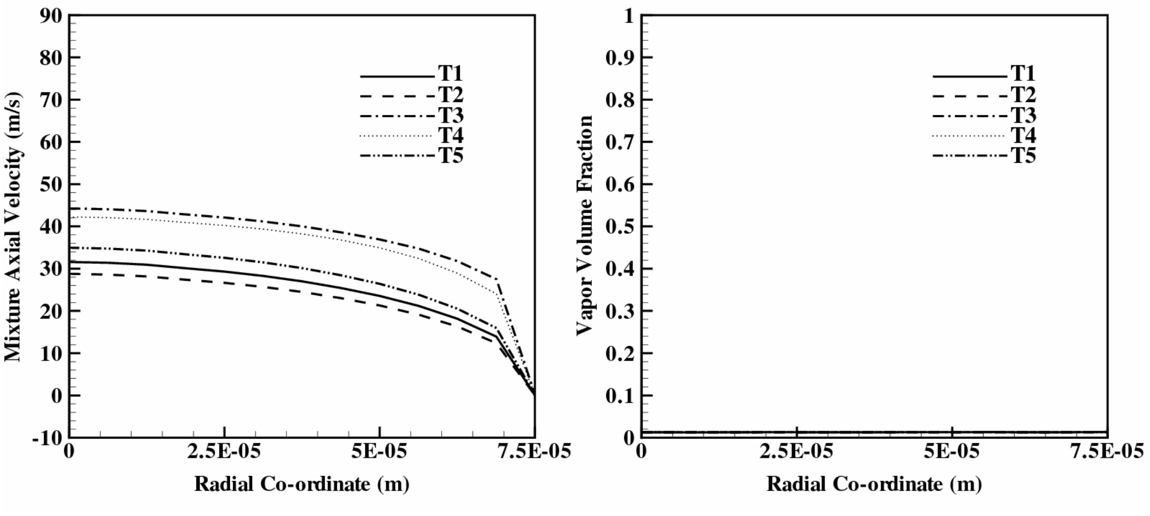

(i) (ii)

Figure 4.43: Plot of (i) Mixture axial velocity fluctuations over different time instants (T1-T5) (ii) Vapor volume fraction at same instants (T1-T5). T1-T5 separated by Δt = $5e^{-07}$. Nozzle L/D = 5 operating at 50 cc/min with horn stroke length of 150 μm at 15 KHz.

Notice that the maximum modulation effect of the outgoing liquid jet is about 0.3 with an average magnitude of 37 m/s. No major vapor volume fraction is reported at the exit section.

Following this computation, the exit diameter of the nozzle is increased to 0.3 mm while the other horn parameters are kept constant. This process is carried out by displacing the nozzle walls a distance 0.075 mm on either side of the horn. The horn tip in this scenario occupies 7% of the total flow area. Due to an increase in the exit diameter section, the exiting liquid jet velocity would be considerably lowered assuming the same flow rate of 50 cc/min. In order to achieve higher velocity-modulated liquid jets, the flow rate is increased to 100 cc/min. With increased exit diameter sufficient passage of liquid-vapor mixture can be accommodated quite satisfactorily and any event of choking is avoided. However, it is to be reminded that thicker jets are hard to atomize since the inertial forces are strong enough to resist any stripping mechanism along its surfaces [1, 2]. The study is carried out as a part of the parametric evaluation pertaining to the nozzle design influence on the cavitation characteristics.

With increase in the diameter of the exit section, the resulting pressure gradients are appreciably reduced reflecting in the generation of low intensity cavitation clusters. This effect is clearly spotted from Fig. (4.44(i)). Numerical simulation identified the inception of cavitation near the horn surface with vapor fractions close to 0.1. An increase in the throat diameter to 0.3 mm considerably moderates the shear transitions leading to negligible cavitation detection. The concentration of cavity clusters near nozzle exit is reduced thereby contributing less to atomization enhancement. Typical vapor cluster concentration observed at the nozzle exit is of the order ~ 0.1. At this point, it is reiterated that the cluster formation and related dynamics can be modified severely by nozzle design in addition to the flow rate and horn parameters.

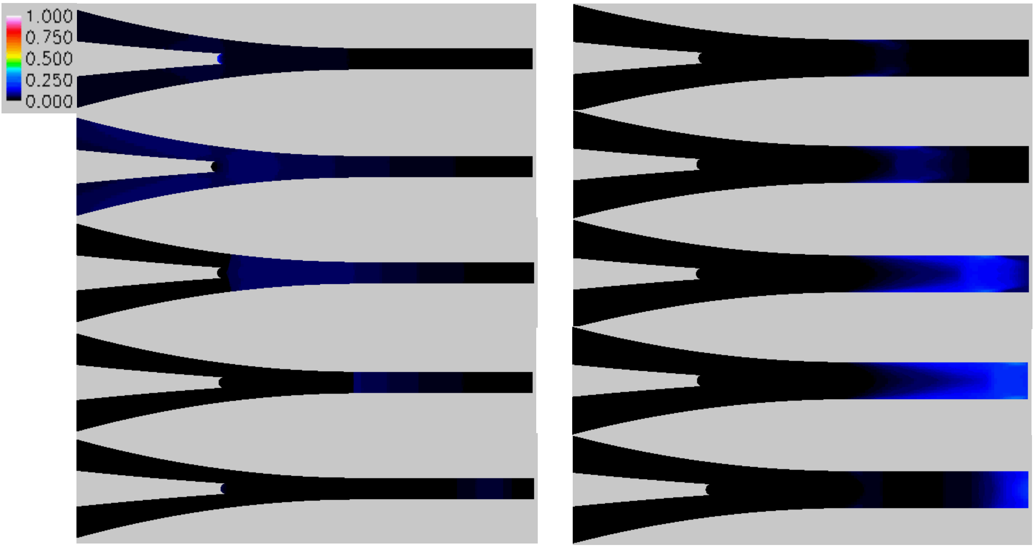

(i) (ii)

Figure 4.44: Contour plot of vapor volume fraction of vapor when (i) the throat diameter is increased (= 0.3 mm), twice the originally proposed value (ii) throat and exit diameter = 0.5 mm

Due to an increase in the overall system scale, the cavitation dynamics no longer prevail. Although the cavitation number of the system can be held constant, by maintaining the pressure drop across the nozzle and the free stream velocity, cavitation dynamics cannot be scaled, an effect previously reported by several authors [2, 93]. Similar tests are performed with a nozzle throat diameter of 0.5 mm with a flow rate of 200 cc/min. The horn tip diameter, the stroke length and frequency are maintained as 150 µm, 150µm and 20 KHz respectively. Although the increased throat diameter scales 3 times bigger than the horn tip diameter, the horn oscillation produces sufficient shear to induce cavitation near the entrance regions of the nozzle throat. The intensity of the clusters is of the order of ~ 0.2. Events of supercavitation are noticeable in Fig. (4.44(ii)) due to the low length to diameter ratios (the cavitation convection time scale is reduced due to small nozzle lengths). Plot of mixture axial velocities generated in the two cases discussed above is shown in Fig. (4.45). With a 0.3 mm diameter nozzle exit, velocities of the order of 100 m/s are obtained while considerably low velocity modulated jets are obtained in the case of a 0.5 mm diameter nozzle.

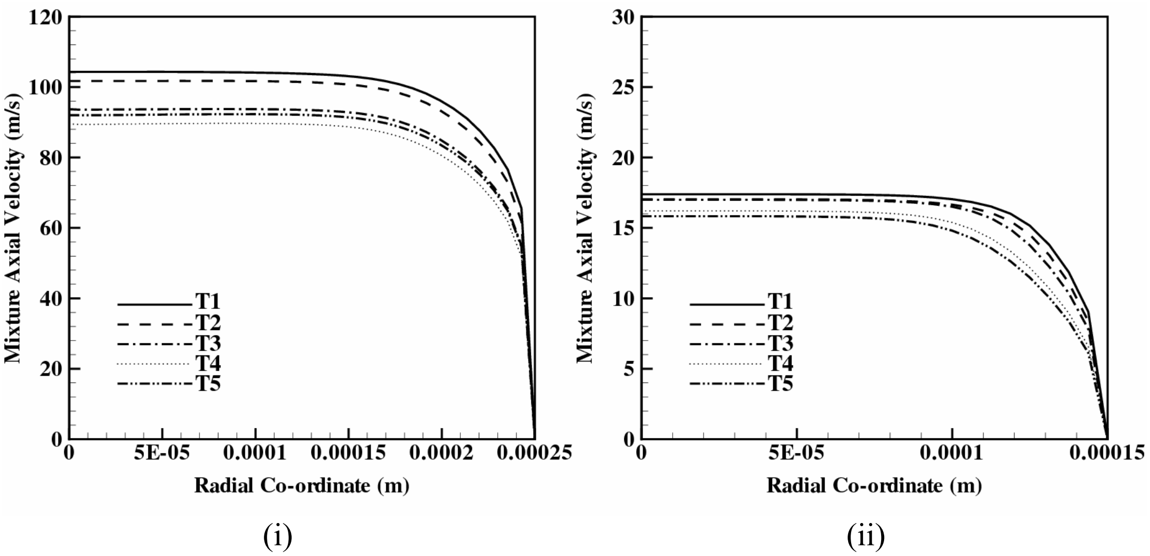

(i) (ii)

Figure 4.45: Plots of mixture axial velocity magnitude for horn operating with an exit diameter (i) Diameter = 0.3 mm with a flow rate of 100 cc/min (ii) Diameter = 0.5 mm with a flow rate of 200 cc/min. In both cases, horn stroke length = 150 µm, *f* = 15 KHz.

4.5.15. Effect of scaling atomizer geometry

An important requirement that demands careful attention is the scalability of the prototype. As mentioned before, cavitation effects are not scalable since they have their own time and length scales [2, 33, 34]. To demonstrate this effect, an overall scaling of the proposed atomizer geometry was carried out with a scaling factor of ½. Details of the geometry and horn parameters are listed in Table (4.1).

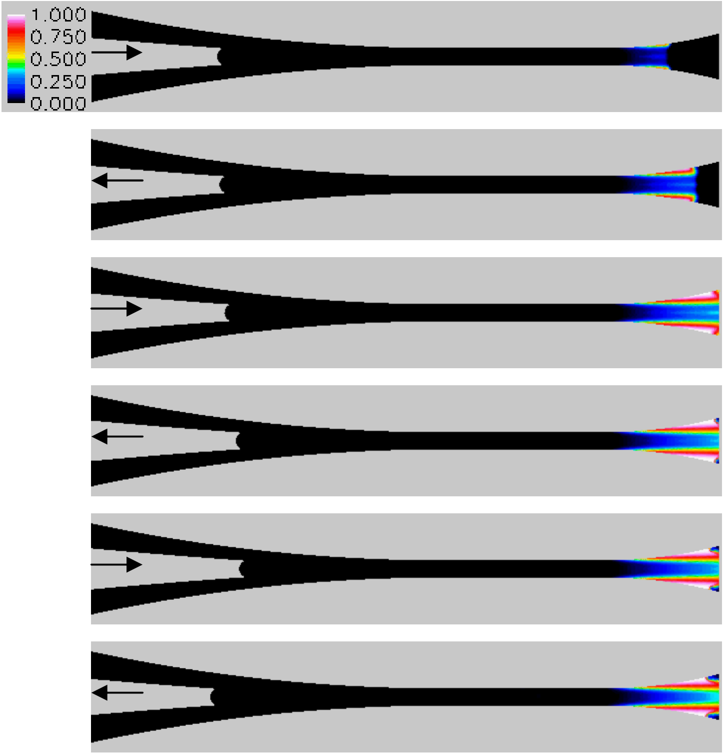

Figure 4.46: Contour plot of vapor volume fraction during the operation of a scaled atomizer geometry (scaled with respect to the original proposed design) maintaining the same flow rate of 50 cc/min and other horn operating parameters listed in Table (4.1).

Scaling the cavitating atomizer by ½ results in very strong vapor regions near the nozzle exit. Regions of high shear contributed to intense cavitation regions near the nozzle exit. However, no cavitation clusters formation or propagation near the horn surface could be identified from the

CFD calculations. The interaction of liquid flow near the horn surface disrupts the cavity growth and its propagation. Plot of mixture velocity magnitude at the exit along with vapor distribution is detailed in Fig. (4.47). Figure (4.47(a)) shows generation of very high velocity jets with a mean velocity of 190 m/s are obtained with low modulations (~ 0.1). The vapor distribution plot Fig. (4.47(b)) indicates presence of strong supercavitation regimes with more vapor clusters seen near the nozzle walls, a direct effect of enhanced shear rates.

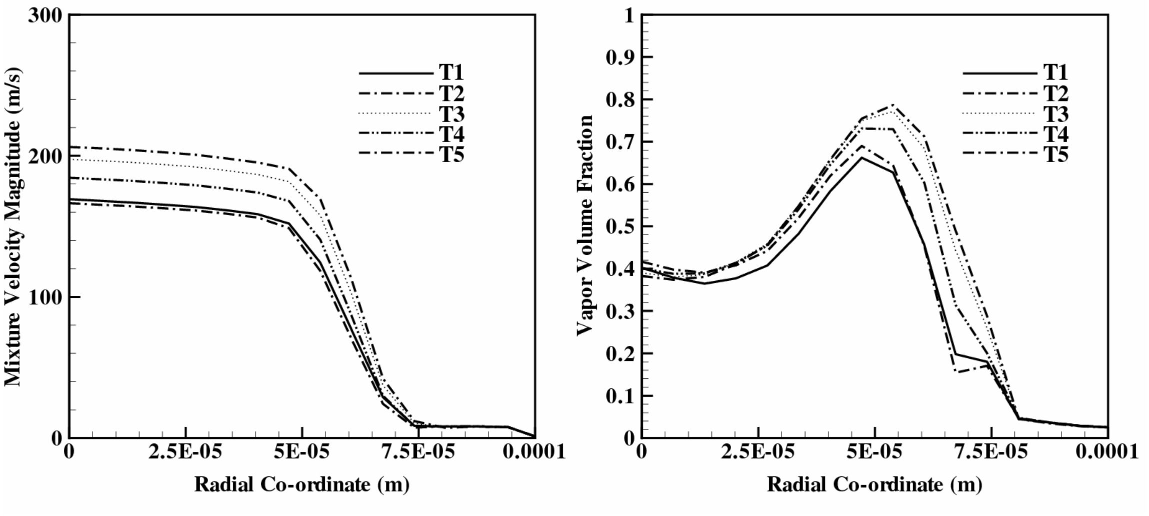

(a) (b)

Figure 4.47: Distribution of (a) mixture velocity magnitude (b) vapor fraction at the nozzle exit at different time instants T_1-T_5 in the scaled atomizer. Time instants separated by $5e^{-07}$ seconds.

4.5.16 Modifying Horn parameters: Stroke length and frequency

In the prototype development, use of a high frequency low power piezo-transducer is envisioned to actuate the horn motion. The atomizer configuration investigated so far assumed an operating stroke length of 150 μm at a frequency of 15 KHz. Brief discussions with Piezo manufacturers revealed that manufacturability of such horn due to the high amplitude requirement at given frequencies would require intense tuning with considerable cost and time. In this concern, the study required that an investigation with other horn operating parameters be performed. Complying to the constraint of product availability two main configurations were identified for the present application: Piezo-transducers operating at a stroke length of 20µm operating with a maximum frequency of 68 KHz and a stroke length of 40µm operating at 36 KHz. These two high frequency models are chosen based on the results obtained from Chapter 3 which indicates that the high frequency perturbations augment breakup and result in shorter breakup lengths. All the testing results presented henceforth shall be based on either of the two configurations stated above. Following this modification in the horn parameters, testing of three different configurations (Table (4.2)) on the modified nozzle design reported in Section (4.5.14) are presented here.

Table 4.2 Modified horn operation parameters

Type	**Horn frequency (KHz)**	**Stroke length (µm)**	**Nozzle Exit diameter (µm)**
Configuration 1	*68*	*20*	*400*
Configuration 2	*36*	*40*	*400*
Configuration 3	*36*	*40*	*150*

The original prototype design specifications, Section (4.5.6), are retained for addressing the modified frequency and amplitude effects. Figure (4.48) details a contour plot of vapor volume fraction obtained with the new set of frequency/amplitude combinations.

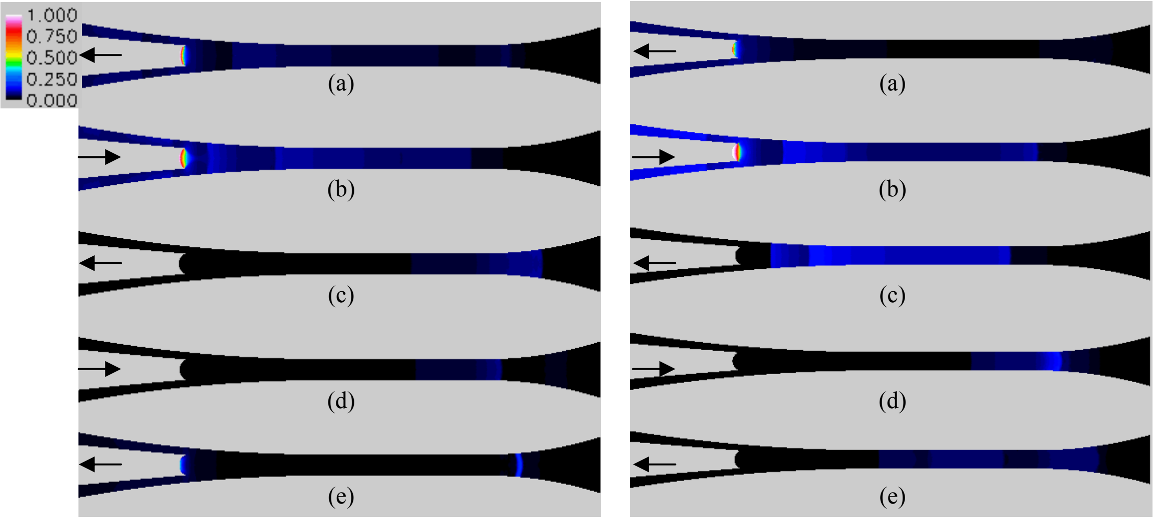

(i) (ii)

Figure 4.48: Contour plots of vapor volume fraction obtained from CFD simulations using (i) Configuration 1 (ii) Configuration 2

Probing into the near horn regions, formation of cavitation zones is evident in both the configurations tested. Notice that the evolution of clusters and their propagation is similar to those obtained with a smaller frequency and increased amplitude combination. Plots of axial-velocity magnitude of the mixture flow at the exit section are reported in Fig. (4.49). Concerning both the cases, configuration (1) and (2), little modulation affect in the low velocity range is discerned. A mean velocity of 15 m/s with a very low modulation of 0.1 is obtained. As noted from our numerical simulations concerning modulated liquid jets in Chapter 3 earlier, the current parameters indicate a surface wave regime and hence no breakup can be observed.

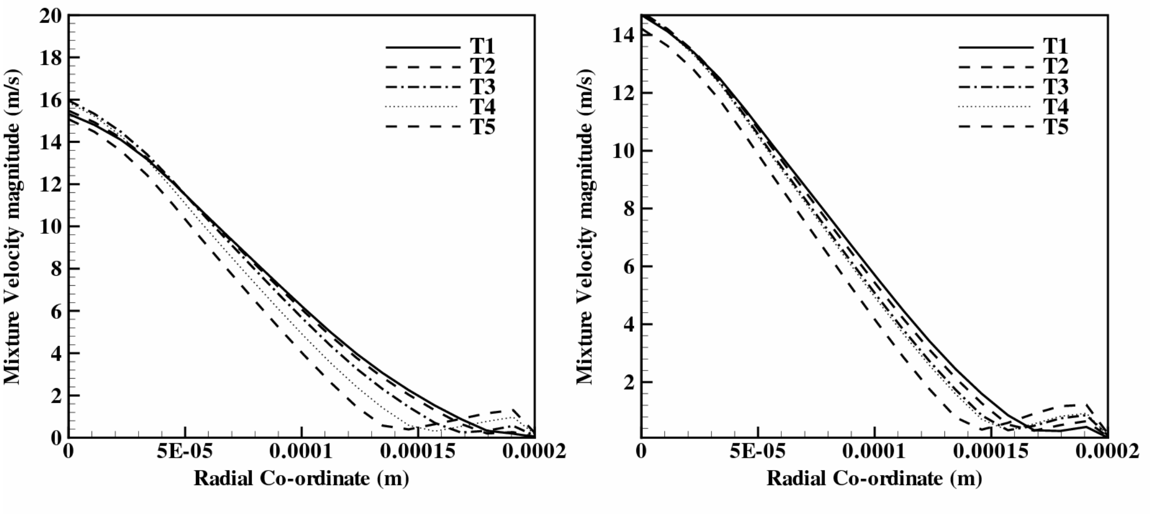

(a) (b)

Figure 4.49: Plots of mixture velocity magnitude at the nozzle exit for nozzle operating with (a) Configuration 1 (b) Configuration 2

Since the intensity of vapor fraction leaving the exit conforms to very low magnitudes, no description of their distribution is provided. Testing the new set of frequency and amplitude parameters with a modified nozzle design, Section (4.5.14.1), with removed diffuser section near the nozzle exit reveals similar cavitation characteristics to configuration-1 and 2 described above without any collapse front near the exit section.

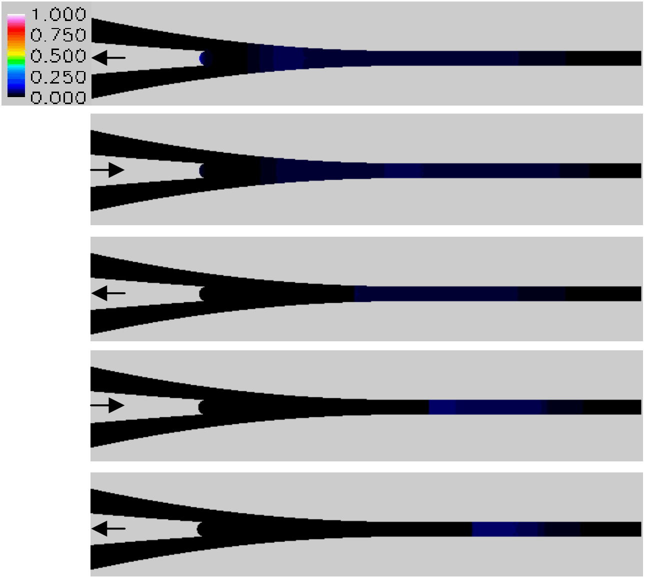

Figure 4.50: Contour plot of vapor volume fraction using Configuration (3). Absence of the diverging portion in the nozzle relieves any formation of vapor front. Further, the intensity of cavitation clusters near the nozzle exit is low (~ 0.25).

However, a plot of mixture velocity magnitude reveals impressive modulation effects at the nozzle exit. The velocities exiting the domain possess a mean velocity of 28 m/s with a modulation of 0.3. However, the cavitation characteristics are not yet satisfactory to be taken up for prototyping discussions.

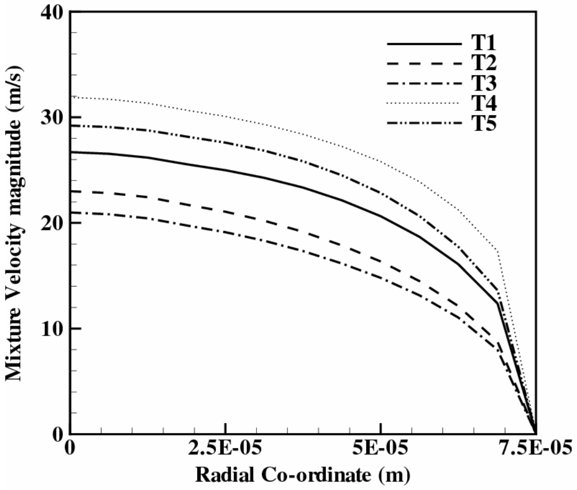

Figure 4.51: Plot of mixture axial-velocity magnitude at the nozzle exit obtained from the CFD simulations using Configuration (3) on the modified nozzle design, Section (4.5.14.1).

4.5.17. Effect of L/D ratio

One of the foremost important parameter affecting liquid jet disintegration is the length-to-diameter ratio of nozzles. Detailed analysis of the L/D effects on the breakup is provided in Chapter 2. In this section, combination of different frequency and stroke lengths, based on Configration (1) and (2) listed in Table (4.2), are tested with two different L/D ratios of 5 and 10. One important modification presented here pertains to the position of the oscillating horn. The vibrating tip placed closer to horn exit, occupying an 25% of the total flow area, to amplify cavitation effects. Configurations tested in the present study have a constant throat diameter of 150 μm equal to the vibrating tip diameter. Flow rate = 50 cc/min has been maintained in the current simulations. The effect of L/D ratio on the liquid jet breakup is shown in Fig. (4.52)

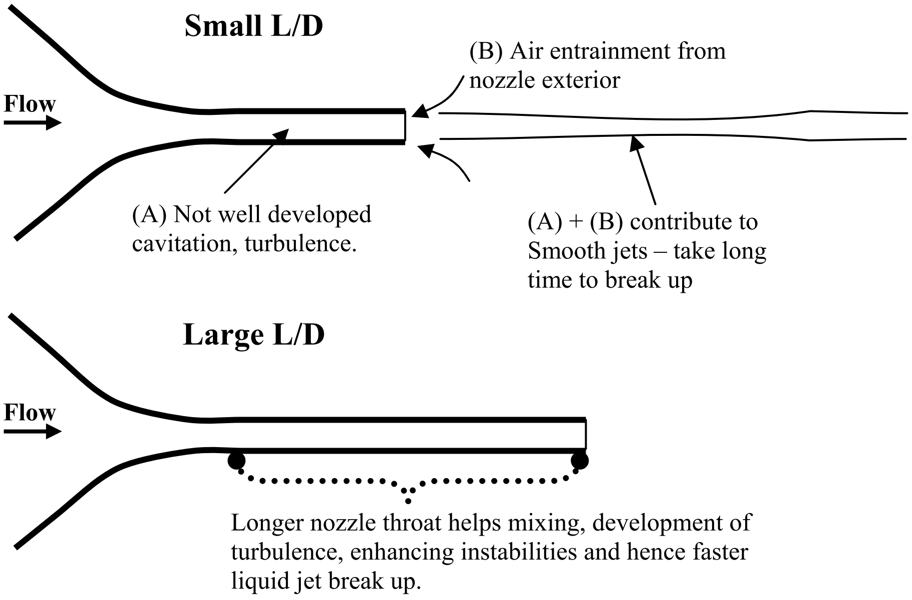

Figure 4.52: Effect of L/D ratio on the jet disintegration characteristics

4.5.17.1 Simulations with L/D =5

From our simulation results shown in Fig. (4.53), collapse of cavitation clusters outside the nozzle is evident.

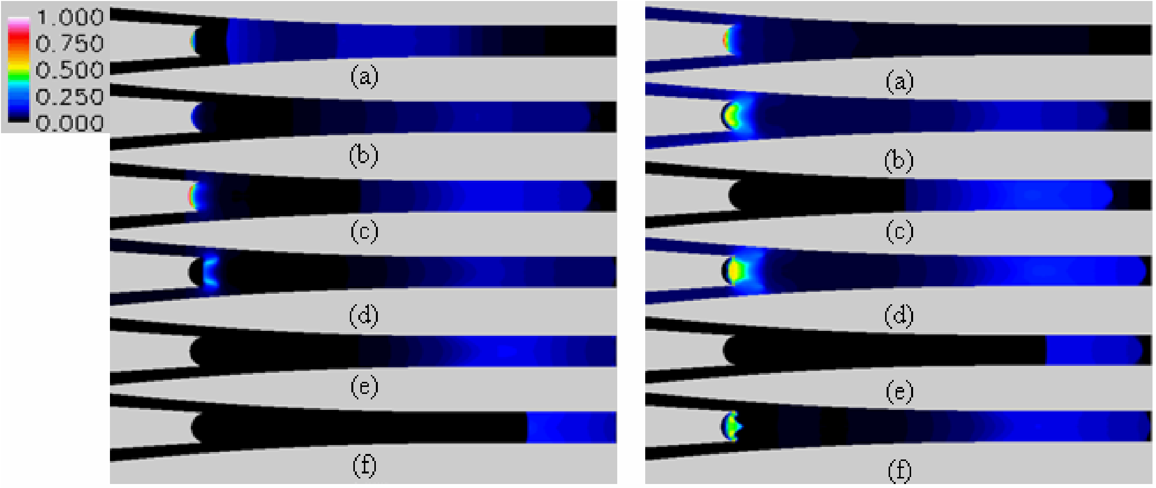

Figure 4.53: Contour plots of vapor fraction inside the nozzle with L/D = 5 operating with (i) *f* = 36 KHz, *LS* = 40 µm (ii) *f* = 68 KHz, *LS* = 20 µm

Depending on the frequency and amplitude, the cluster propagation characteristics are not easily tracked since the clusters do not have sufficient time to grow and collapse within the nozzle exit. For a horn oscillation frequency of 68 KHz (stroke length *LS* = 20µm), more clusters are formed near the surface and the 'cluster packet length' are observed to be smaller compared to our previous simulations with convergent divergent nozzles. Further, using Configuration (2), the cluster exiting the nozzles have a vapor volume fraction in the range varying from 0.2~ 0.4. Periodic cluster movements across the exit cannot be achieved. In the case of oscillations with 36 KHz (*LS* = 40 µm), some clusters of low intensity (vapor volume fraction: 0.2 ~ 0.3) were seen to exit the nozzle and the 'cluster packet length' were longer than the 68 KHz frequency case.

4.5.17.2 Simulations with L/D = 10

With increased L/D ratio to 10, cavitation collapse occurs inside the nozzle with horn operation being carried out with both Configuration (1) and Configuration (2).(Fig. (4.54))

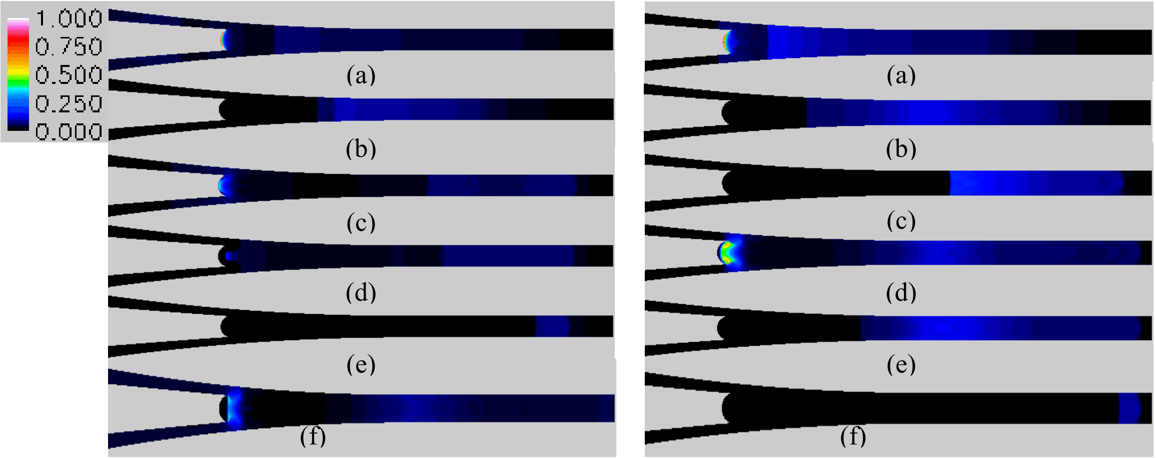

Figure 4.54: Contour plots of vapor volume fraction inside the nozzles with L/D = 10 operating with (i) *LS* = 40 μm, *f* = 36 KHz (ii) *LS* = 20 μm, *f* = 68 KHz

The growth and collapse of clusters can hence be controlled in appropriate frequency range. For a horn oscillation frequency of 68 KHz (*LS* = 20μm), more clusters are formed near the surface and collapse occurs confined to the nozzle. Although, in the case of oscillations with 36 KHz (*LS* = 40 μm), some clusters of low intensity (vapor volume fraction ~ 0.2) were seen to exit the nozzle. From the simulations, it is clear that small L/D nozzles have a region of cavitation clusters near the throat which creates region of low pressure and hence gas entrainment from the exterior ambience can destroy the cavitation effects. It is further important to notice that the collapse characteristics in small nozzles are not easily identifiable due to the cavitation dynamics in the presence of oscillating pressure fields, which does not guarantee sufficient time for the clusters to grow and collapse in a periodic fashion. With longer L/D nozzles, it is possible to create cavitation clusters and track their collapse characteristics as a function of the horn input (frequency and amplitude). In case more turbulent mixing is required, larger L/D nozzle can be opted to enhance atomization conditions near the nozzle exit. Present simulations have been modeled based on the proposed prototype design. It is interesting to see, how change in the chamber design under these characteristics would influence cavitation growth, propagation and collapse behavior. In addition, observe that the horn tip position is very crucial in determining the velocity and associated turbulence of liquid jet exiting the orifice. In the current case with flow rate = 50 cc/min, very high velocities were achieved due to the change in flow configuration induced by the presence of the moving horn inside the nozzle. Our design of the internal nozzle needs to be coupled with the exterior spray requirements so that proper adjustment can lead to controllable spray patterns.

4.6. Numerical simulation of sharp corners

Several studies addressed in Chapter 2 indicate that the flow cavitation process is strongly sensitive to any perturbations in the bulk flow, since they carry with them modulations capable of altering shear rates, mean velocity gradients and pressure fluctuations. Combination of different cluster dynamics can be utilized to effect enhancement of the jet breakup in the nozzle exterior by modulating their collapse behavior. To realize this perturbation effect, an oscillating horn, perturbing the flow field at a well-defined finite frequency and amplitude, is placed near the nozzle entrance region. The motion of the horn is viewed as a source of creating a pulsating flow regime into the nozzle sac. The motion of the horn near the nozzle entrance results in a variable area flow close to the corners as shown in Fig. (4.55).

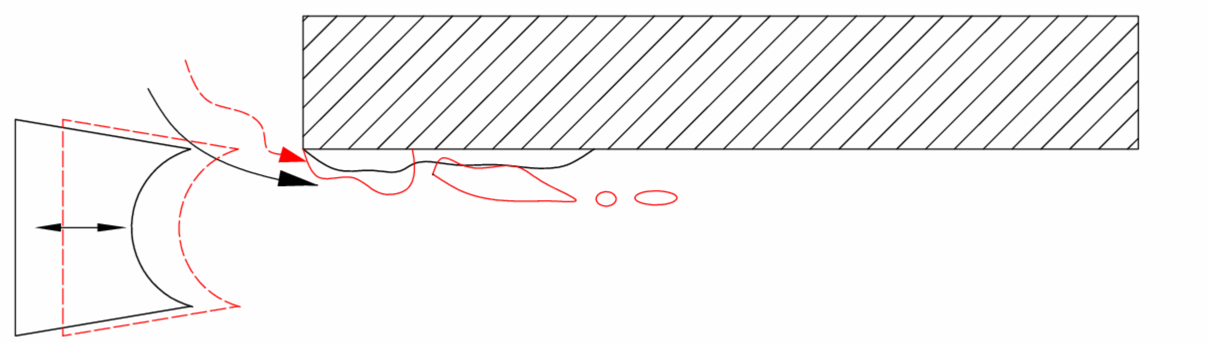

Figure 4.55: Placement of concave tip horn near the nozzle hole entrance results in distorted flow structure triggering strong cavitation collapse events

The fluctuating flow area in the vicinity of the horn surface reflects vehemently on the gradients of flow variables. As a result of intense fluid straining, a strong coupling is acquired between the cavitation dynamics and the local transient in flow structure. As shown in Fig. (4.56), the motion of the horn induces high pressure drop in the forward motion while retracting fluid against leaving the nozzle in its backward motion. As the recirculation zones near the sharp nozzle corners are formed, the shear generated by the local horn oscillations force their detachment from the nozzle surface. The process is carried out in a reproducible fashion distinct to the horn oscillation frequency.

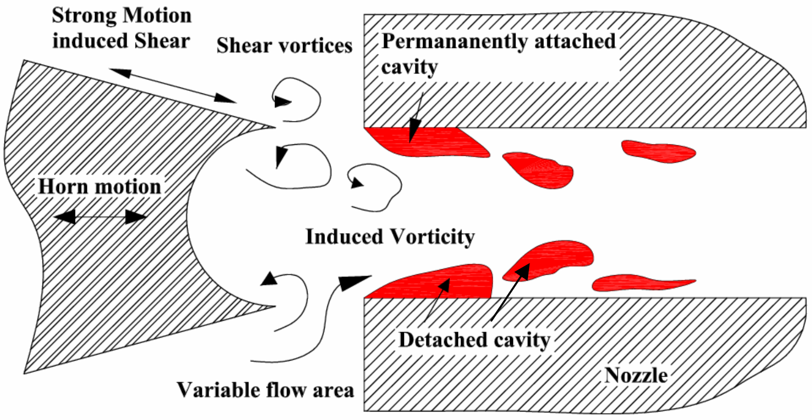

Figure 4.56: Schematic of the horn actuated cavity cluster detachment mechanism near the entrance of sharp cornered nozzles

Any cavitation regions formed near the horn surface or in the near-nozzle entrance zone are now altered at the same frequency matching the horn operating condition. Complexity of the process arises due to the interaction of the vorticity components with the vapor transport process [247, 249, 250]. The influence of vortex interaction with cavitation clusters has been demonstrated by several authors [34, 247, 249]. The possibility of obtaining repetitive cavitation cluster as a function of the horn parameters, as explored above, serves as a primary motivation for investigating these effects using numerical simulations. For the computations, different combination of the horn operating conditions and nozzle designs are carried out. A schematic of the representative variables used in the calculation is shown in Fig. (4.57). Length scales used in characterizing the nozzle system under investigation comprises of

(a) D_h – Diameter of the horn tip

(b) D_{en} – Diameter of the inlet nozzle entrance

(c) D_{ex} – Diameter of the exit nozzle entrance

(d) D_{he} – Distance between the nozzle entrance and horn tip center of curvature

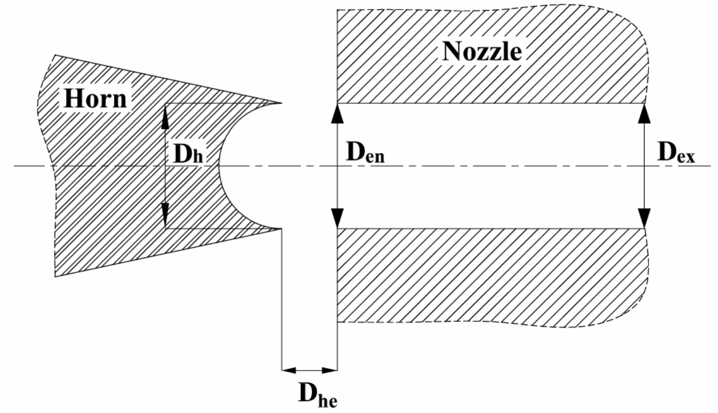

Figure 4.57: Representation of parameters used in CFD testing of sharp cornered nozzles

In addition to the various geometric factors specified in the above schematic, the horn parameters, stroke length and frequency, and the liquid flow rate are modified to observe the cavitation response of the system. The computational domain with relevant boundary conditions for the CFD testing is explained using Fig. (4.58).

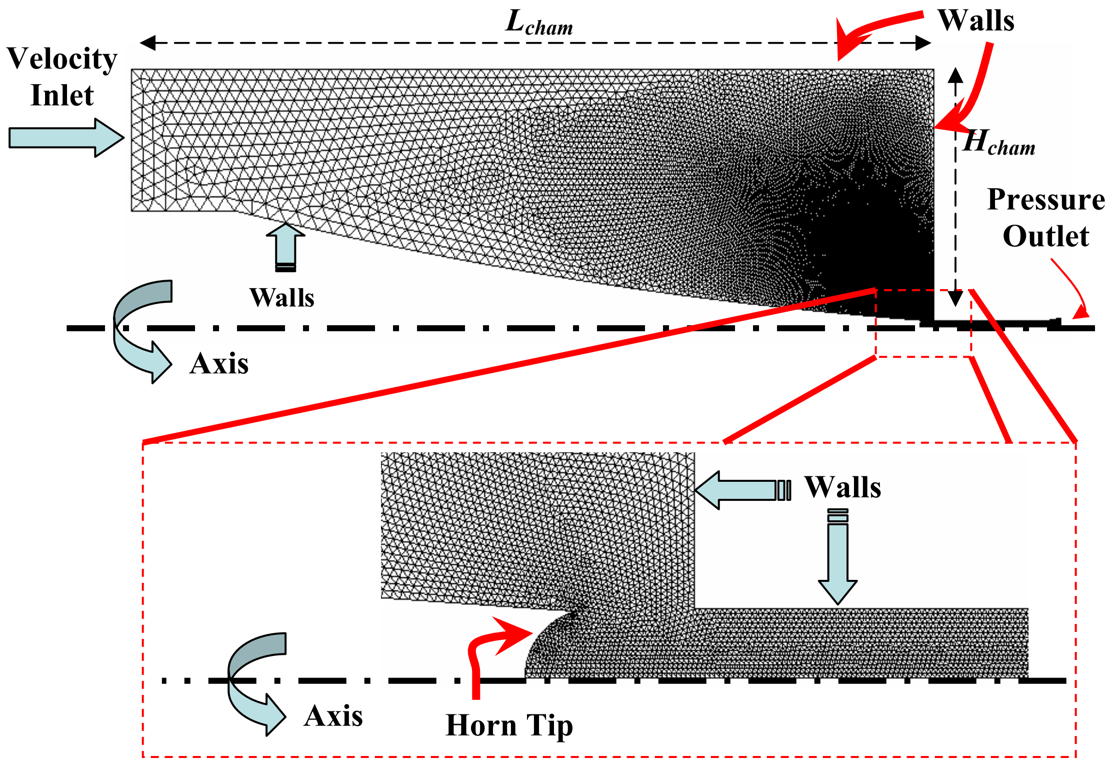

Figure 4.58: Computational domain and grid generation for numerical simulations

For simulation and prototyping, the length of the chamber (L_{cham}) and height of the chamber (H_{cham}) are taken as 5 mm and 2 mm respectively. This alleviates any boundary effect that may prevail near the oscillating horn motion. With the parameters specified above, the list of numerical experiments discussed in the current study is detailed in Table (4.3). Unstructured grids are favored over the regular quadrilateral meshes owing to the strong curvature prone regions in the flow.

Table 4.3 List of Compuations

Simulation configuration	D_{en} (µm)	D_{ex} (µm)	D_h (µm)	D_{he} (µm)	*LS* (µm)	L/D_{en}	*f* (KHz)	Flow rate (cc/min)
S_1	*150*	*150*	*150*	*150*	*40*	*10*	*36*	*50*
S_2	*150*	*200*	*150*	*150*	*40*	*10*	*36*	*50*
S_3	*150*	*150*	*150*	*150*	*10*	*10*	*68*	*50*
S_4	*150*	*150*	*150*	*150*	*20*	*10*	*68*	*50*
S_5	*200*	*200*	*150*	*75*	*40*	*10*	*36*	*50*
S_6	*200*	*200*	*150*	*75*	*40*	*4*	*36*	*50*
S_7	*200*	*150*	*300*	*75*	*40*	*2*	*36*	*50*

4.6.1 Case S_1:

4.6.1.1 Computations with no pulsation effect

The geometry and horn operating configuration presented in Table (4.3) is tested without any horn oscillation effect ($LS = 0, f = 0$) to distinguish the perturbation effect produced by the horn on the flow structure and cavitation dynamics. Although cavitation phenomena is an unsteady process, a steady state calculation is performed since no transient effect of horn motion is included. The geometry used in the simulation and the steady state results obtained for the current configuration is illustrated in Fig. (4.59).

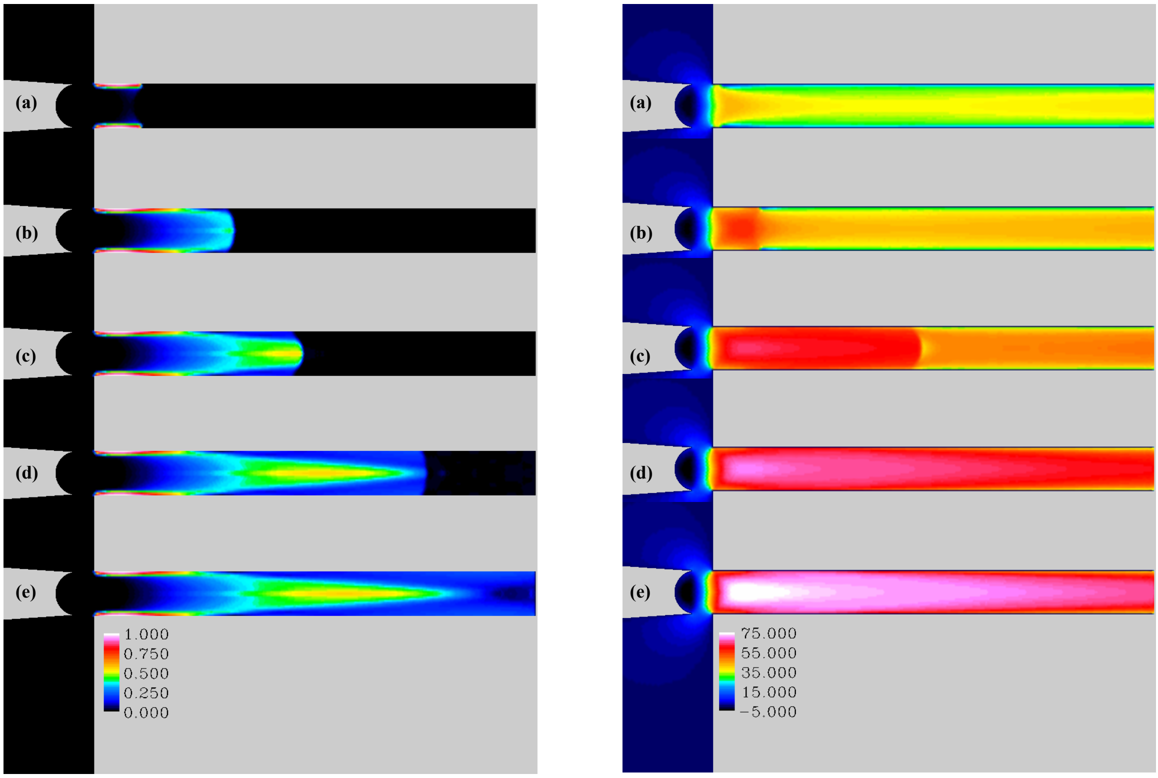

(i) (ii)

Figure 4.59: Contour plots of (i) vapor volume fraction (ii) mixture axial-velocity magnitude Flow rate = 50cc, $D_h = 150\mu m$, $D_{en} = 150\mu m$, $D_{ex} = 150\ \mu m$, $D_{he} = D_h/2$, L-D = 10. No horn oscillation is effected

Contour plots of vapor volume fraction and velocity magnitude of the exiting liquid jet is shown in Fig. (4.59). Observe that strong intense vapor regions exist only near the nozzle entrance regions while the strength of vapor fraction exiting the nozzle is of the order of 0.2. Steady state mean mixture velocities of 55 m/s are obtained at the orifice exit. The computations are modeled using a SIMPLEC pressure-velocity procedure with first order discretization for momentum and vapor scalars [146, 150]. Use of lower-order scheme certainly imposes artificial diffusion effects and does not capture highly transient cavitation formation, detachment and fluctuating transport process. However, the model provides an overall good understanding of the vapor distribution in the domain in combination with decent computational accuracy and cost effectiveness.

4.6.1.2 Case S_1: with pulsation effect

Following the steady-state computation, the horn oscillation effect is turned on with a stroke length of 40 μm at a frequency of 36 KHz. Contour plots of vapor volume fraction and the axial velocity magnitudes are shown in Fig. (4.60). Figure (4.60(i)(a)) shows formation of small vapor regions during the initial stages of horn oscillations. The expanding and contracting motion of the horn creates an intermittent cavity formation and collapse effect. Observe from Fig. (4.60(i)(b) and (c)), simultaneous cluster formation near the nozzle entrance corners and at the nozzle exit are detected. Also, the propagation of detached cavitation clusters sent as discrete streams indicating the strong influence of the pressure perturbation are distinct. As the flow evolves, the cavitation formation and propagation process intensifies. This effect can easily be verified from Fig. (4.60(i)(d) -(e)). Even under strong flow non-linearities, the pulsating cavitation flow regime is preserved. Corresponding velocity distribution in the nozzle domain is shown in Fig. (4.60(ii)) indicating the nature of velocity profile that exists during the pulsating flow. Axial velocity plots in Fig (4.60(ii)(b)-(c)) clearly show the advanced velocity front of the order of 50 m/s. In Fig. (4.60(ii)(e)), spot the presence of low velocity regions amidst high velocity regions on either side. This is due to the retracting motion of the horn motion which sends faster and slower flowing liquid streams alternatively.

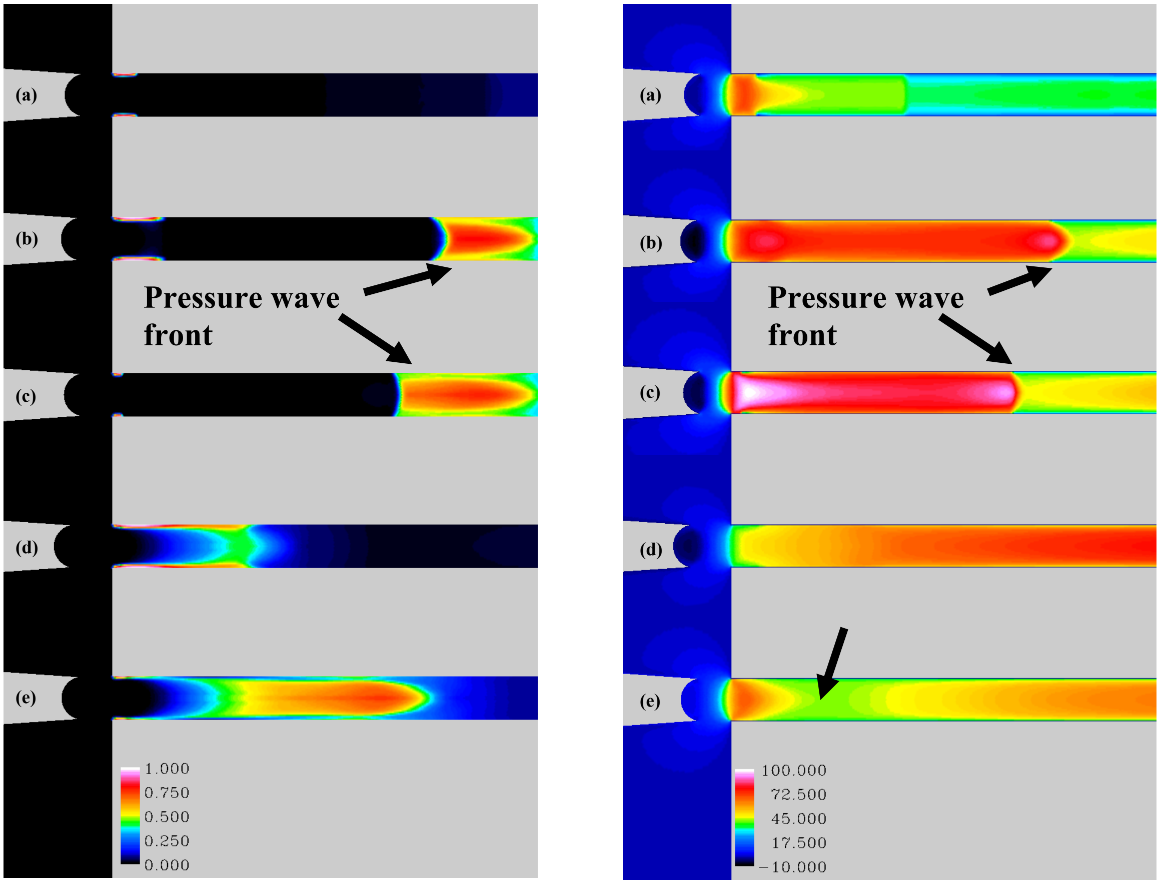

Figure 4.60: Contour plots of (i) vapor volume fraction (ii) mixture axial-velocity magnitude

Flow rate = 50cc/min, D_h = 150μm, D_{en} = 150μm, D_{ex} = 150 μm, D_{he} = D_h/2, L-D = 10

The distribution of mixture axial velocity and vapor volume fraction at the nozzle exit section is plotted in Fig. (4.61).

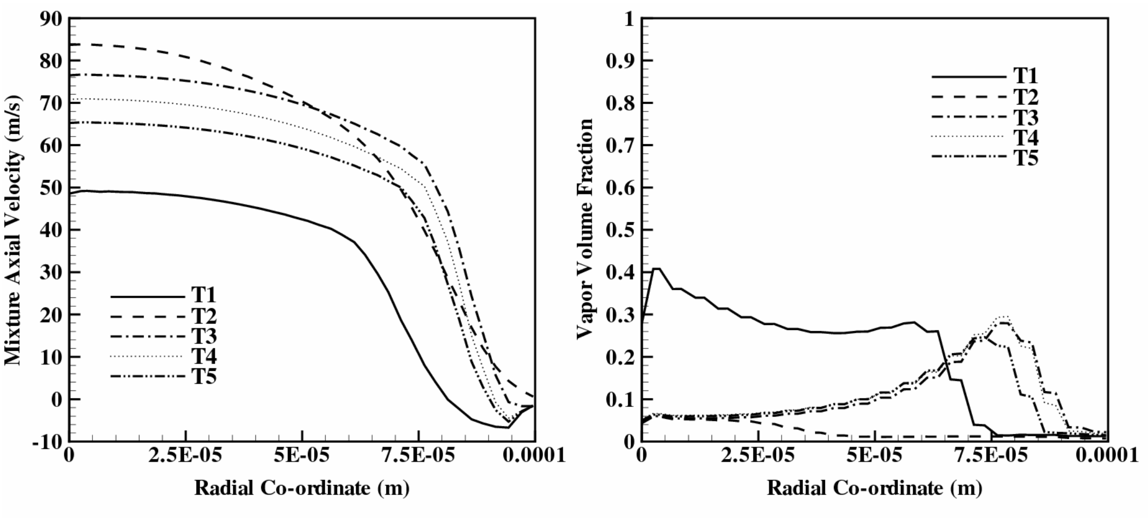

(a) (b)

Figure 4.61: Plots of (a) Axial velocity magnitude (ii) Vapor volume fraction at the nozzle exit for configuration S_1 at increasing time instants. $T_1<T_2<T_3<T_4<T_5$ separated by 0.5μs.

Note that the exiting liquid jet is modulated between 50 m/s – 85 m/s with a mean velocity of 65 m/s. Although, these fluctuations are very influential for obtaining forced liquid jets, the magnitude of mean liquid velocity is far too high to be influenced by the modulation effect. As observed from the modulated jet simulations in Section (3.6), increase in mean liquid jet velocity results in long breakup lengths. The wavelength of imposed perturbations increases proportionally and does not support shortened breakup lengths. The vapor volume fraction exiting the nozzle approximately equal 0.4 indicating a strong presence of cavitation clusters in the exiting jets.

4.6.2 Case S_2: Influence of exit section design

Extending the previous design presented in Section (4.6.1), the exit section is modified with a diverging flow section to diffuse the cavitation clusters and decrease the exit velocity of the liquid jets so that modulation effects can be improved.

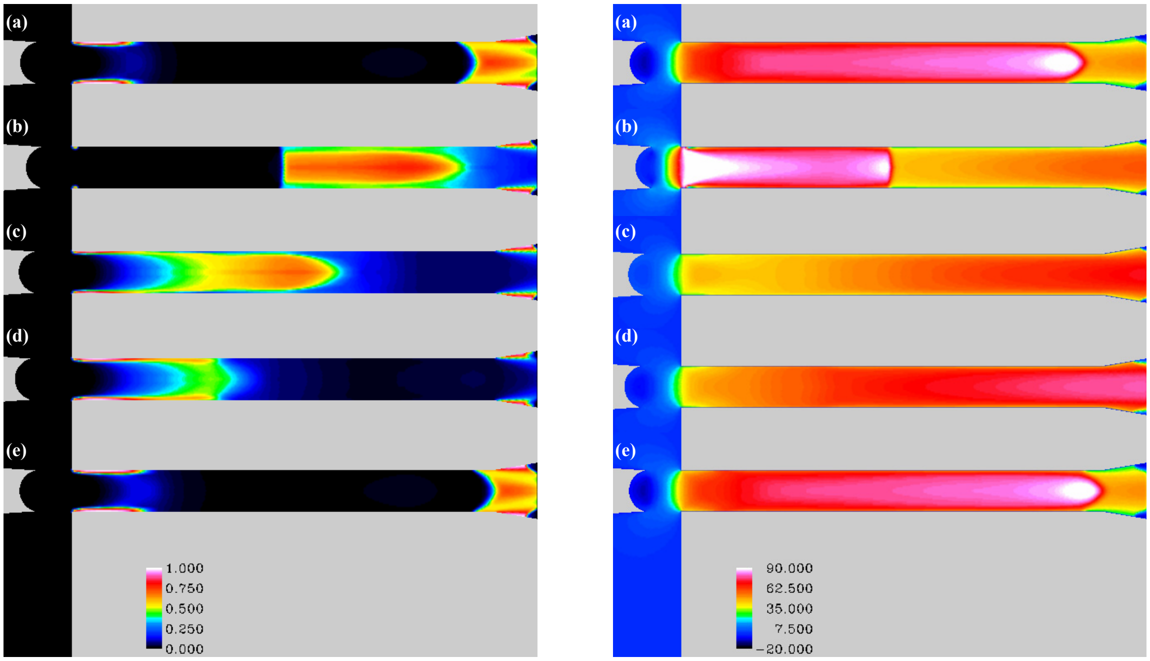

Figure 4.62 Contour plots of (i) vapor volume fraction (ii) mixture axial-velocity magnitude

Flow rate = 50cc/min, D_h = 150μm, D_{en} = 150μm, D_{ex} = 200 μm, D_{he} = D_h/2, L-D = 10.

Results from the computations are shown in Fig. (4.62). Presence of strong vapor residence near the divergent section in the orifice exit zone is distinct from Fig. (4.62(i)). Although, with increase in the exit diameter a corresponding decrease in average flow velocity is expected, the presence of strong vapor regions, Fig. (4.61(i)(b)), results in amplified velocity distribution as spotted in Fig. (4.60(ii)). However, unlike the previous case, Section (4.6.2), strong modulation effects at the nozzle exit are detected. Figure (4.61) presents the axial-velocity of the exiting liquid jets and the vapor fraction.

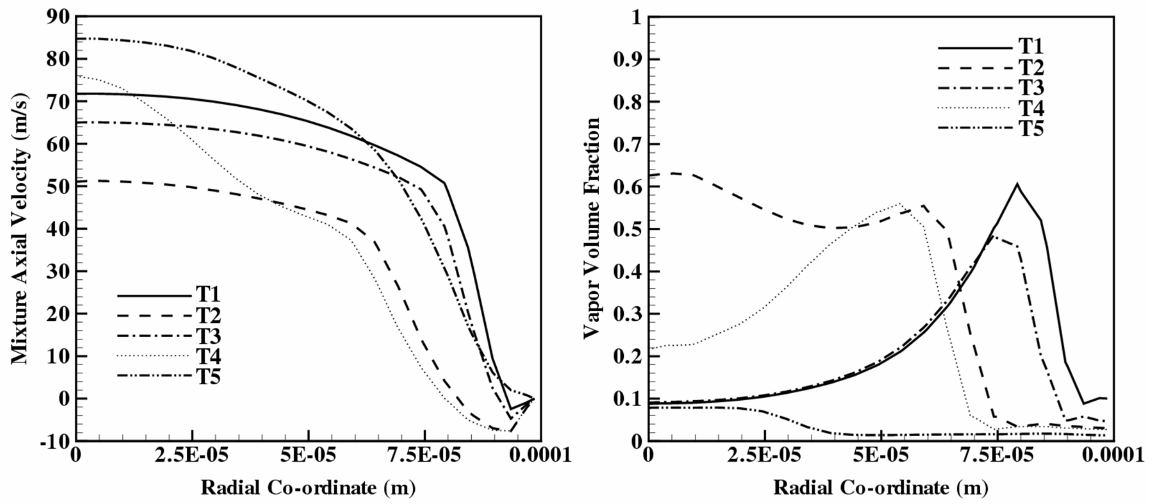

(a) (b)

Figure 4.63: Plots of (a) Axial velocity magnitude (ii) Vapor volume fraction at the nozzle exit for configuration S_2 at increasing time instants. $T_1<T_2<T_3<T_4<T_5$ separated by 0.5μs.

Clearly, very high modulation amplitudes (~0.4) with averaged velocities of 65 m/s result from the tested configuration with strong vapor presence. With high mean velocities, longer breakup lengths would be required to completely atomizer the liquid jet.

4.6.3 Case S_3: Influence of horn parameters

The geometry configuration presented in Section (4.6.1) is retained and the horn parameters are now modified to extract the influence of frequency and modulation on the cavitating flow behavior. The horn oscillation frequency is increased to 68 KHz while the stroke length is reduced to 10 μm. Since the piezo-transducer is calibrated to provide a maximum stroke length of 20 μm at an appropriate frequency ≤ 68 KHz, it can be surmised that the maximum amplitude need not occur during the simultaneous occurrence of the maximum frequency. The following computation is carried out to ensure that cavitation dynamics can be retained with reduced stroke lengths maintaining the same frequency limit. The impact of variation in horn operating condition is seen pronounced. Notice from Fig. (4.64(i)(a)), the separation distance between two cluster packets is reduced considerably as a direct consequence of increasing the horn modulation frequency. This effect can also be identified by the pulsating velocity front propagating at the same frequency as that of the horn oscillations.

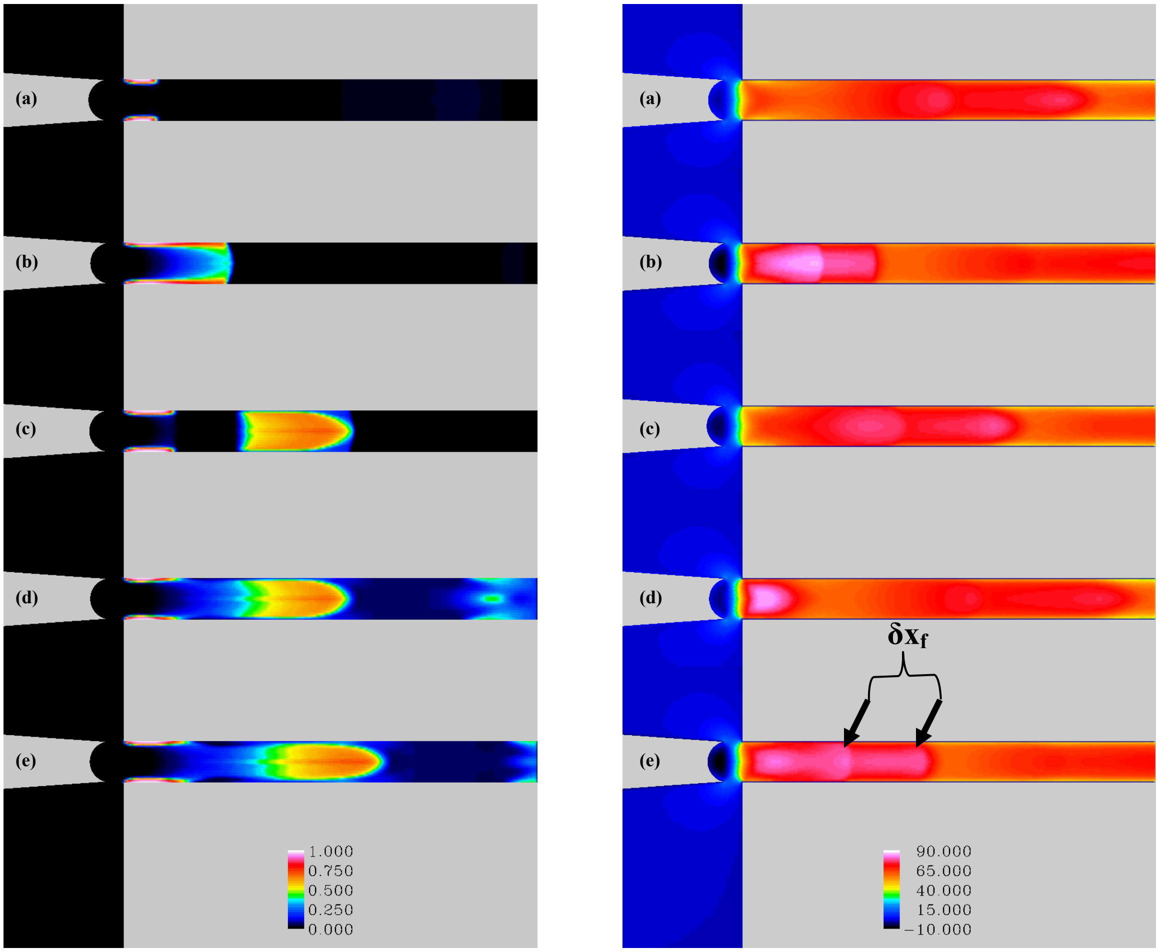

(i) (ii)

Figure 4.64: Contour plots of (i) vapor volume fraction (ii) mixture axial-velocity magnitude Flow rate = 50cc/min, D_h = 150μm, D_{en} = 150μm, D_{ex} = 150 μm, $D_{he} = D_h/2$, L-D = 10, *LS* =10μm, *f* = 68 KHz.

The convecting velocity fronts are captured in Fig. (4.64(ii)) distinctly and computing the distance between the front (δx_f) and the flow velocity, the separation frequency is determined. In this case, δx_f measures ~ 450μm and the velocity of the front ~ 80 m/s. This directly gives a time separation of 65 KHz which includes the viscous dissipation effects that decelerates the flow. The frequency effect is easily comprehended at the nozzle exit. From plots shown in Fig. (4.65), observe the reduced modulation with increased vapor fractions. The increase in vapor fraction transmittal across the section can be related to the coalescence or vapor diffusion effects within the nozzle flow. As explained before, the separation distance between the cluster packets decreases in a profound manner. Adding to the proximity of the clusters traveling behind each other in the flow, the flow viscous effects and action of transient pressure gradients enhance the coalescence phenomena [33, 34, 249, 250].

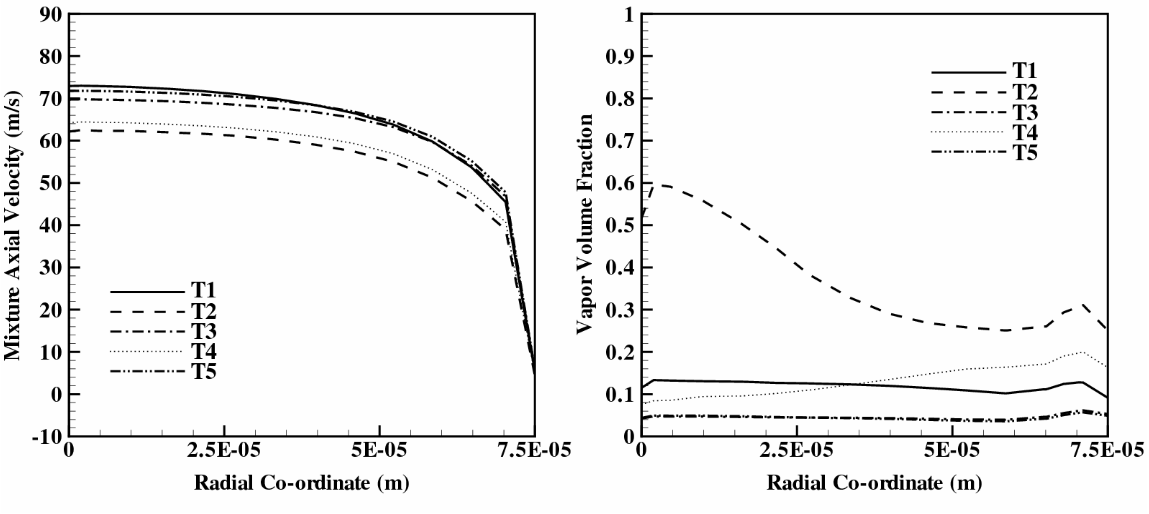

(a) (b)

Figure 4.65: Plots of (a) Axial velocity magnitude (ii) Vapor volume fraction at the nozzle exit for configuration S_3 at increasing time instants. $T_1<T_2<T_3<T_4<T_5$ separated by 1μs.

4.6.4 Case S_3: Horn stroke-length effect

The effect of horn stroke length is assessed by maintaining the same horn frequency and other flow and geometry parameters detailed in Section (4.6.3). The stroke length, however, is increased to 20 μm. A direct implication of increase in the stroke length magnitude leads to profound distribution of vapor region within the nozzle sac region as shown in Fig. (4.66(i)). The amplification of vapor distribution consequently leads to higher flow velocities due to the mass conservation effect.

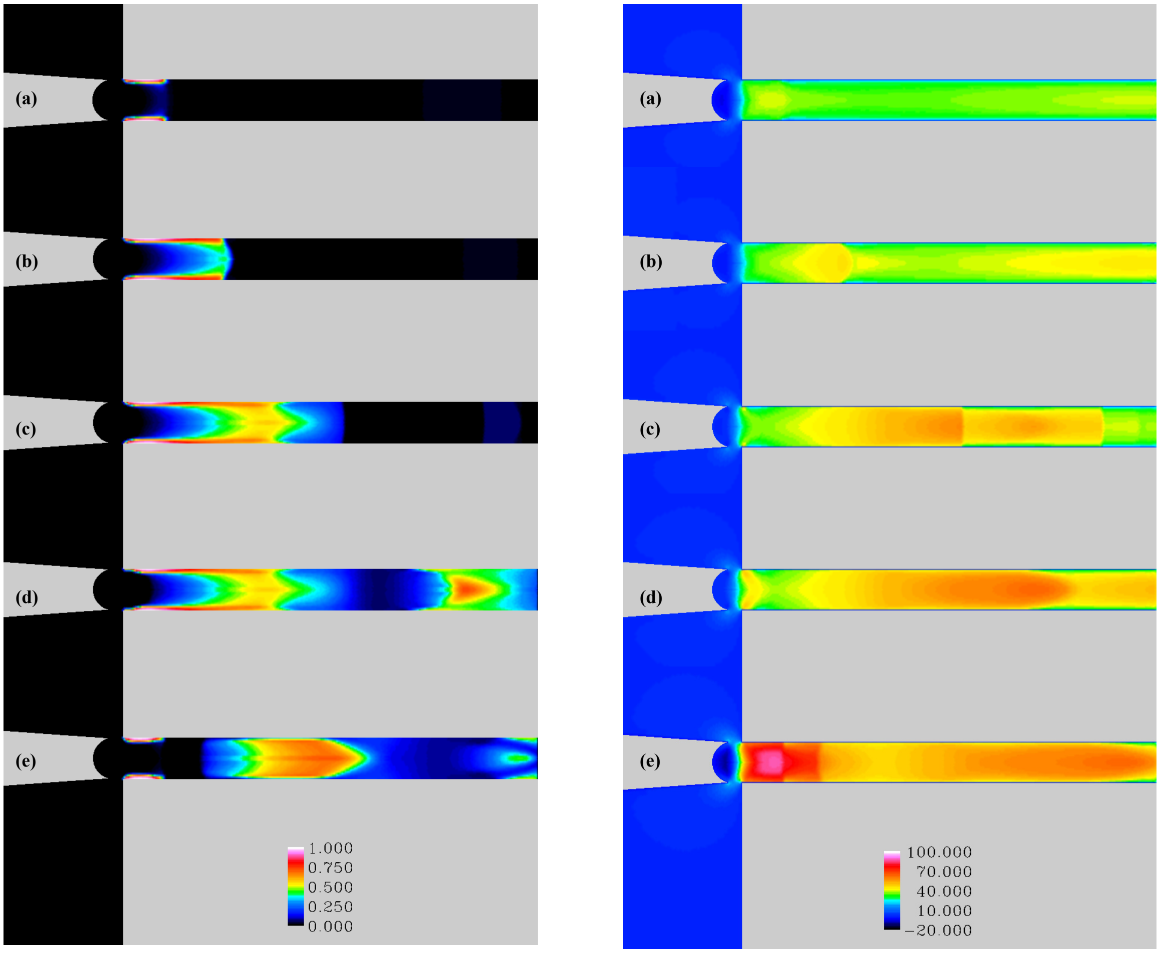

(i) (ii)

Figure 4.66: Contour plots of (i) vapor volume fraction (ii) mixture axial-velocity magnitude Flow rate = 50cc/min, D_h = 150µm, D_{en} = 150µm, D_{ex} = 150 µm, D_{he} = $D_h/2$, L-D = 10, *LS* = 20µm, *f* = 68 KHz.

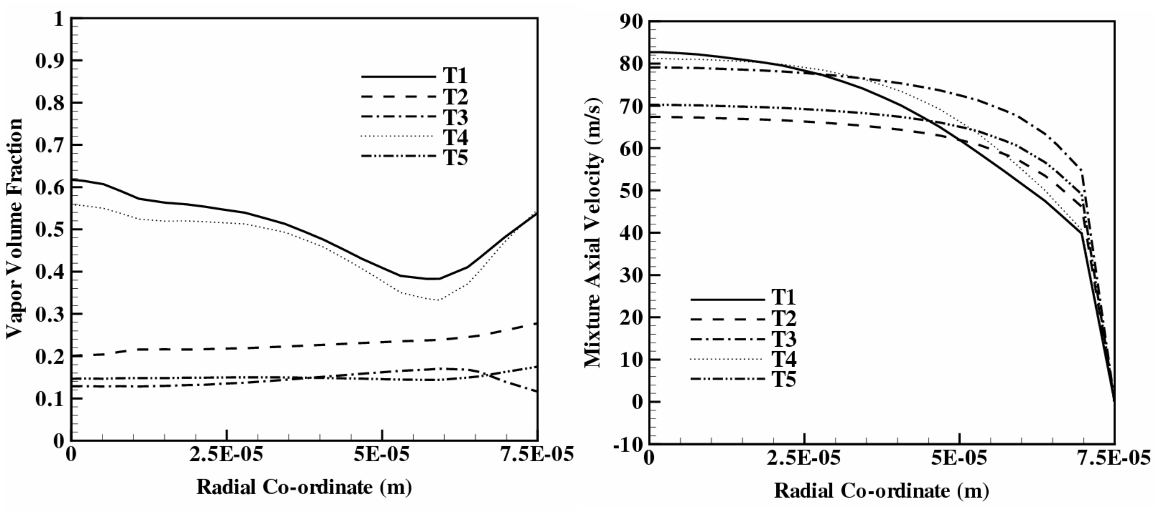

(a) (b)

Figure 4.67: Plots of (a) Axial velocity magnitude (ii) Vapor volume fraction at the nozzle exit for configuration S_4 at increasing time instants. $T_1<T_2<T_3<T_4<T_5$ separated by 1µs.

Plots of vapor fraction and axial velocity distribution are shown in Fig. (4.67 (a) and (b)) respectively. As compared to lower horn modulation, Section 4.6.3, the vapor fraction distribution is more proliferated and increased velocities at the nozzle exit are concluded. However, the modulation amplitude of the exiting liquid jets is still questionable, with a low value of 0.1 imposed on a 75 m/s mean velocity jet.

4.6.5 Case S_5 : Nozzle entrance effect

The previous cases presented in Section 4.6.1- 4.6.4 incorporated nozzle diameters equal to that of the tip. Considerable reduction in jet diameter, under increased modulation amplitude, can result in low Strouhal numbers and hence formation of drop chains. Furthermore, smaller diameter nozzles can clog or choke easily depending on the viscous nature of the flow and vapor fractions respectively. In this spirit, the nozzle sac diameter is increased while retaining the same horn tip diameter. The geometry and operation configurations are listed in Table (4.3). The background of the design is described schematically in Fig. (4.68).

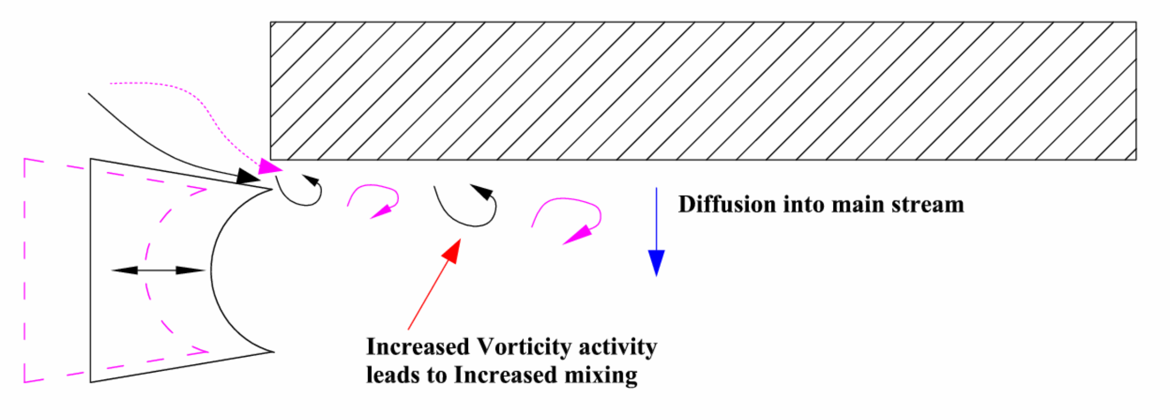

Figure 4.68: Schematic illustrating the effect of horn motion near the entrance of a sharp cornered nozzle as observed from numerical simulations

The shear action of the horn motion in combination with the highly strained flow structure is expected to enhance mixing as a direct consequence of the shear rate enhancement. Calculated results obtained by performing CFD computations on the proposed configuration are shown in Fig. 4.69. Figure (4.69(i-a)) shows detachment of clusters from the nozzle surface and prolonged elongation due to shearing action in Fig. (4.69 (i-d)). The distortion of flow structure due to strong straining can be observed in Fig. (4.69(ii-a)), while strong propagation flow fronts are captured in Fig. (4.69(ii-d)) and Fig. (4.69(ii-e)).

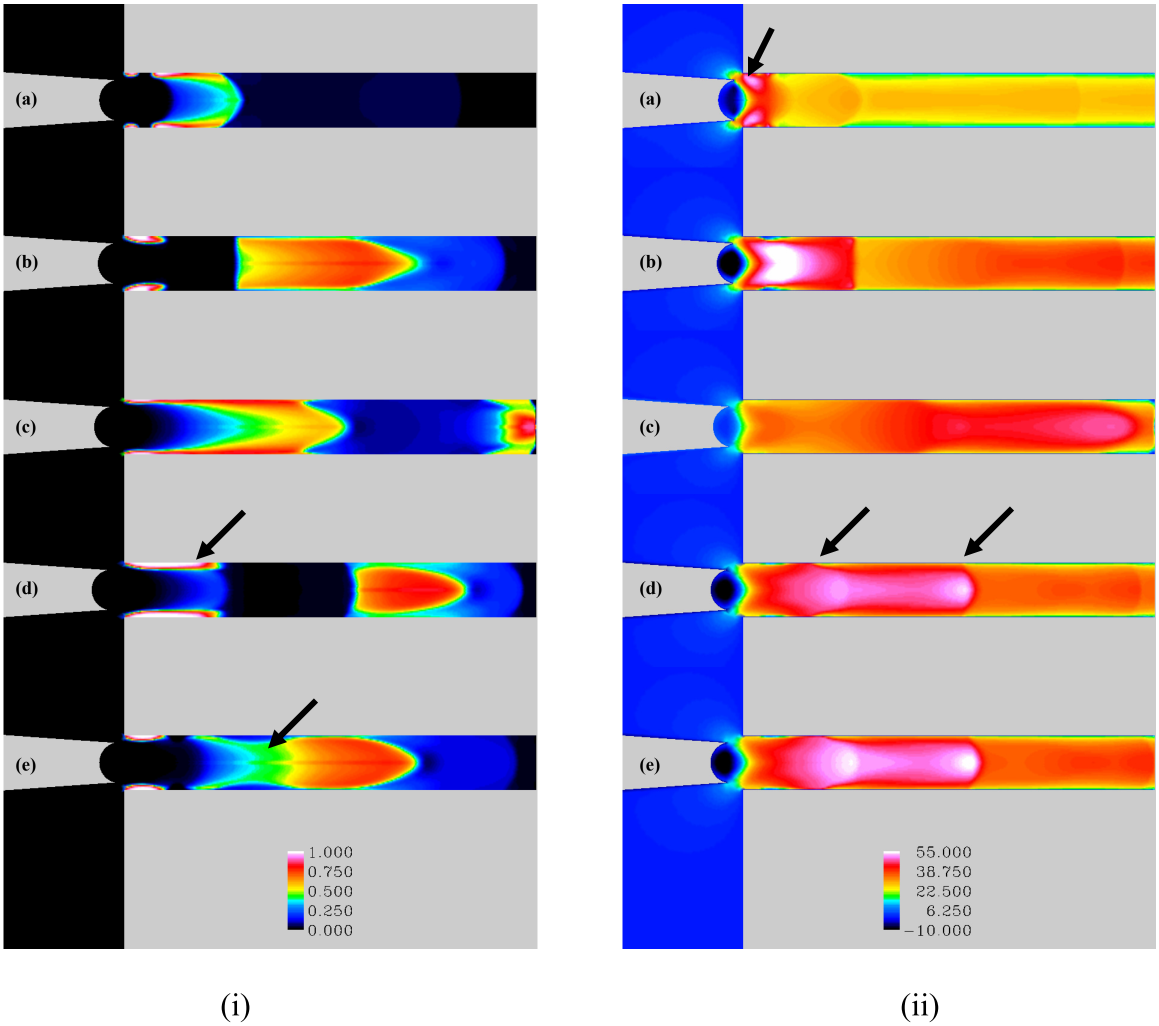

Figure 4.69: Contour plots of (i) vapor volume fraction (ii) mixture axial-velocity magnitude

Flow rate = 50cc/min, D_h = 150μm, D_{en} = 200μm, D_{ex} = 200 μm, D_{he} = D_h/2, L-D = 10

The axial-velocity distribution and vapor fluctuations over different time instants separated by ½ of the oscillation time period is displayed in Fig. (a' and b') in comparison with our previous calculation with D_{en} = D_{ex} = 150 μm indicated by flow variables in Fig. (4.70 (a & b)), all other factors remaining the same. Observe from Fig. (4.70), increased nozzle diameter for the same flow rate results in reduced mean velocities and reduced modulation effects in comparison with the results obtained with D_{ex} = D_{en} = 150μm. However, due to low frequency perturbations the vapor mixture has sufficient relaxation time to redistribute their profile in the axial and radial direction (comparing Fig (4.70(b-b'))).

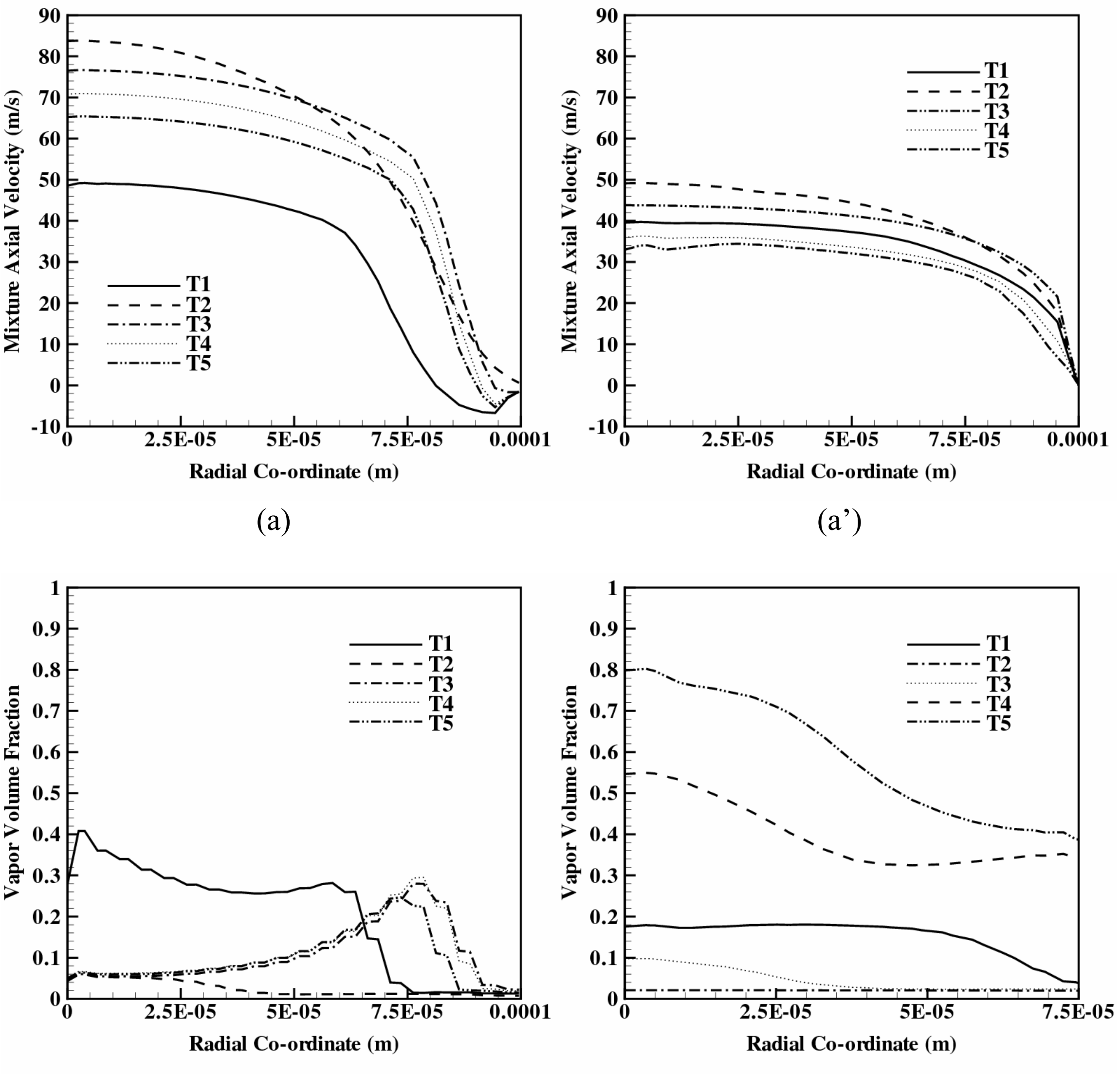

(a) (a')

(b) (b')

Figure 4.70: Plots of (a), (a') axial velocities for case S_5 and S_2 (b), (b') vapor fractions for case S_5 and S_2 at different time instants time instants. $T_1<T_2<T_3<T_4<T_5$ separated by 1µs.

4.6.6 Case S_6: L/D ratio effect

Preceding the computations presented in Section 4.6.5, the L/D ratio is the nozzle is decreased to 4 to observe the unsteady effect on the flow structure. The horn is placed at a distance equal to horn tip diameter from the nozzle corner. This unsteadiness can accelerate the jet disintegration at the nozzle exterior by a velocity profile relaxation mechanism hypothesized by Rupe et al. [74] Results from the simulations are presented in Fig. (4.71).Formation of cavity clusters near the nozzle entrance is clearly visible in Fig. (4.71(i-a)). They eventually grown and detach from the parent cluster in a controlled fashion as shown in Fig. (4.71(i-b)-(i-e)).

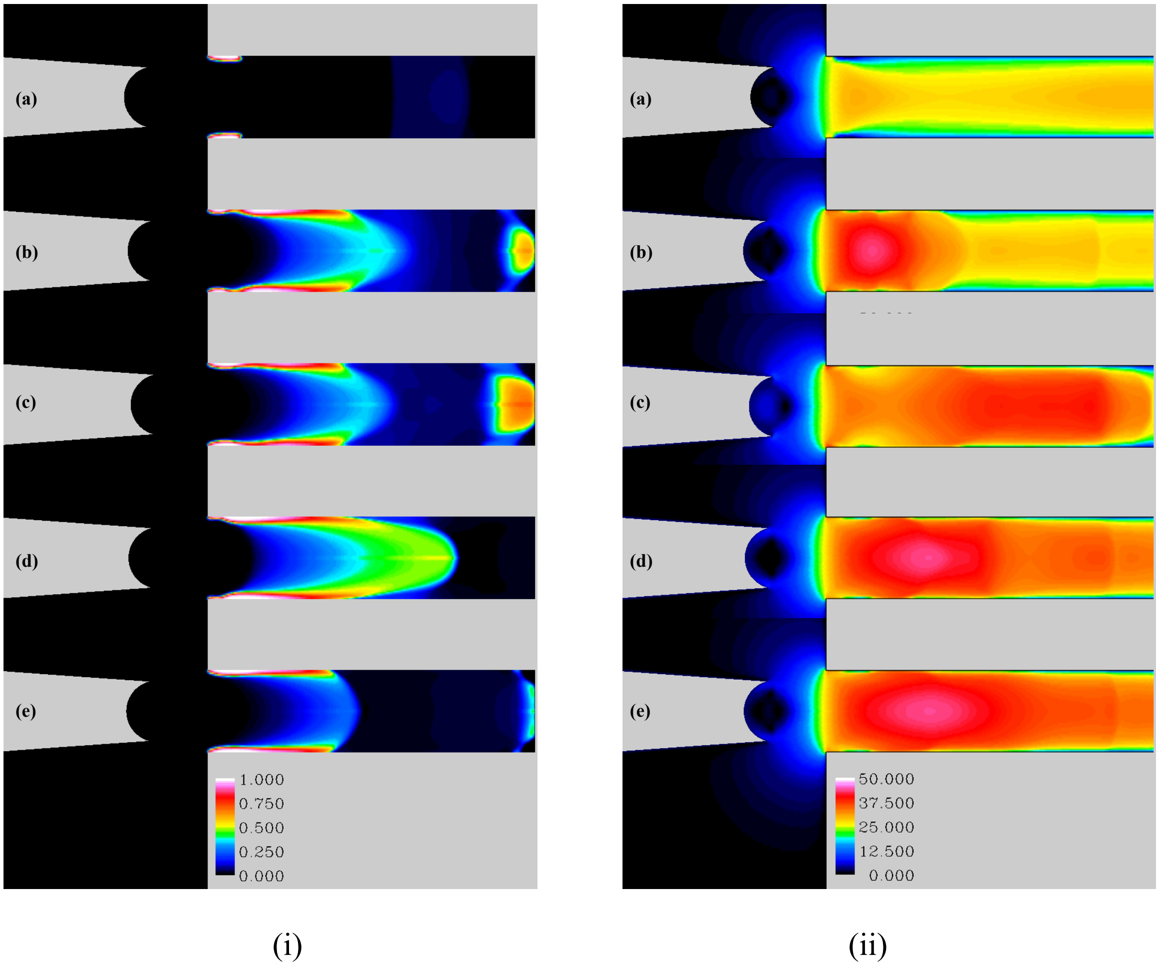

(i) (ii)

Figure 4.71: Contour plots of (i) vapor volume fraction (ii) mixture axial-velocity magnitude

Flow rate = 50cc/min, D_h = 150µm, D_{en} = 200µm, D_{ex} = 200 µm, $D_{he} = D_h/2$, L/D = 4

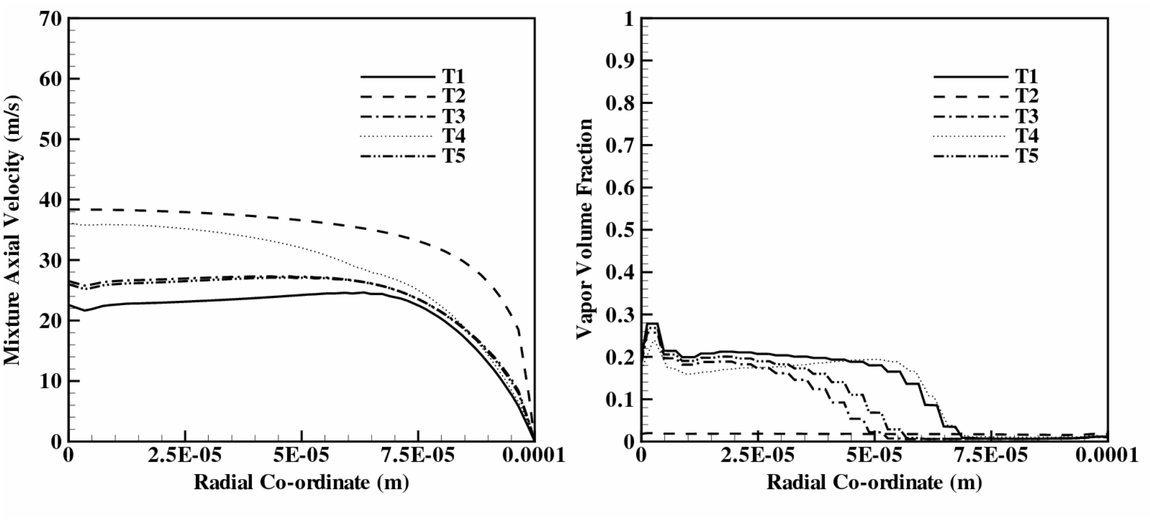

(a) (b)

Figure 4.72: Plots of (a) Axial velocity and (ii) vapor fraction distribution at the nozzle exit for configuration S_4 at increasing time instants. $T_1<T_2<T_3<T_4<T_5$ separated by 1μs.

Visualizing the predicted velocities in Fig. (4.71(ii-a)-(ii-e)), a mean velocity of 30 m/s with a modulation amplitude of 0.3 is imposed on the exiting liquid jets. This fluctuation is verified from the plots at the exit cross-section computing the axial velocity magnitude and the vapor volume fraction, Fig. (4.72 (a)–(b)). Some accumulative response of the exiting liquid jets is observed in the sense that between different time intervals variation in the velocity profile is not monotonic. The boundary effects, a pressure outlet in our simulation with Neumann conditions for velocity gradients, impose flow constraints near the exit section leading to local transients. The maximum vapor fraction exiting the liquid jets was of the order of 0.2-0.3 as shown in Fig. (4.72 (b)).

4.6.7 Case S_7: Horn geometry effect

The influence of horn geometry on the multiphase flow is evaluated by increasing the diameter of the horn tip such that $D_h = 1.5D_{en}$. The unsteadiness in exiting liquid jets is improved by reducing the nozzle length-to-diameter ratio to 2 [2, 74]. The center of the horn is positioned along the nozzle axis. The present design is carried out in such a fashion that the pulsation motion of the horn creates a stagnation zone at the center of the horn curvature which can then be propelled into the nozzle sac. This is intended to achieve both nozzle cavitation due to sharp corners provided by the shear of the accelerating flow into the sac in addition to the cavitation clusters that are formed by the vibratory cavitation produced by the horn itself. The nozzle diameter at the entrance is maintained at 200 µm while a converging portion at the nozzle exit is included to achiever smaller diameter jets with profound modulation effects.

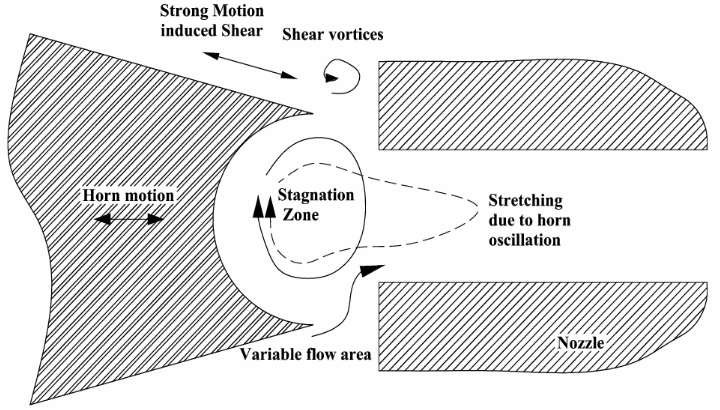

Figure 4.73: Influence of $D_h > D_{en}$ in the characterization of cavitating modulated nozzle flows

Computation with the current configuration yielded very interesting results as depicted in Fig. (4.74). As seen from Fig. (4.74(i-a)-(i-e)), formation of cavitation regions are restricted very close to the horn interior curved surfaces. Due to the large curvature oscillating wall surface, the flow entrapped within the curved zone does not convect the clusters out of the stagnation zone resulting in a local deposition (growth and collapse) of the cavity clusters. This effect is indicated in Fig. 4.74(i)(a). Very low intensity cavitation regions are generated near the nozzle entrance zone as observed from the contour plot of vapor volume fraction, Fig. (4.74(i-d)). Stagnation zones are easily visible from the contours of axial velocity magnitude Fig. (4.74(ii)(a-e)). The transmission of the pulsating effect of the horn motion can be detected from Fig. (4.74(ii)(d).

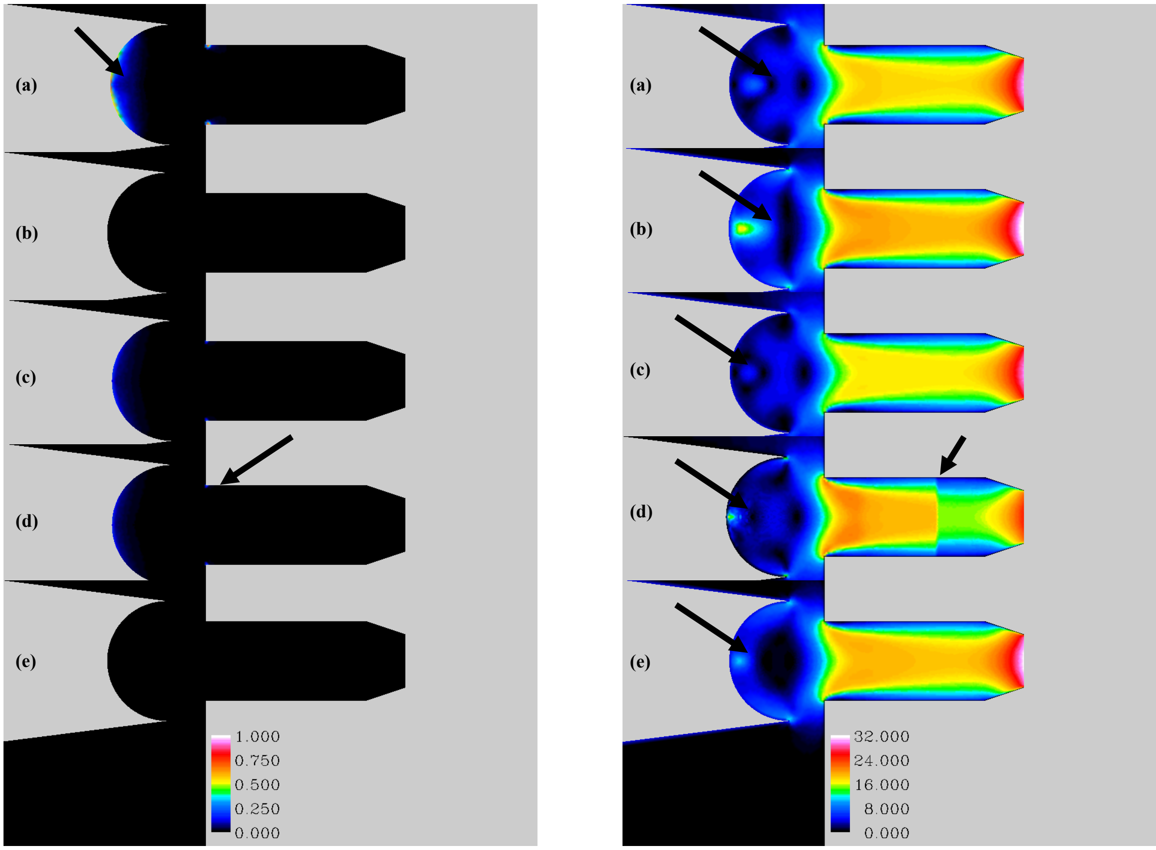

(i) (ii)

Figure 4.74: Contour plots of (i) vapor volume fraction (ii) mixture axial-velocity magnitude

Flow rate = 50cc/min, D_h = 150μm, D_{en} = 200μm, D_{ex} = 200 μm, $D_{he} = D_h/2$, L/D = 2

Plots of axial-velocity and vapor distribution at the exit section are shown in Fig. (4.75).

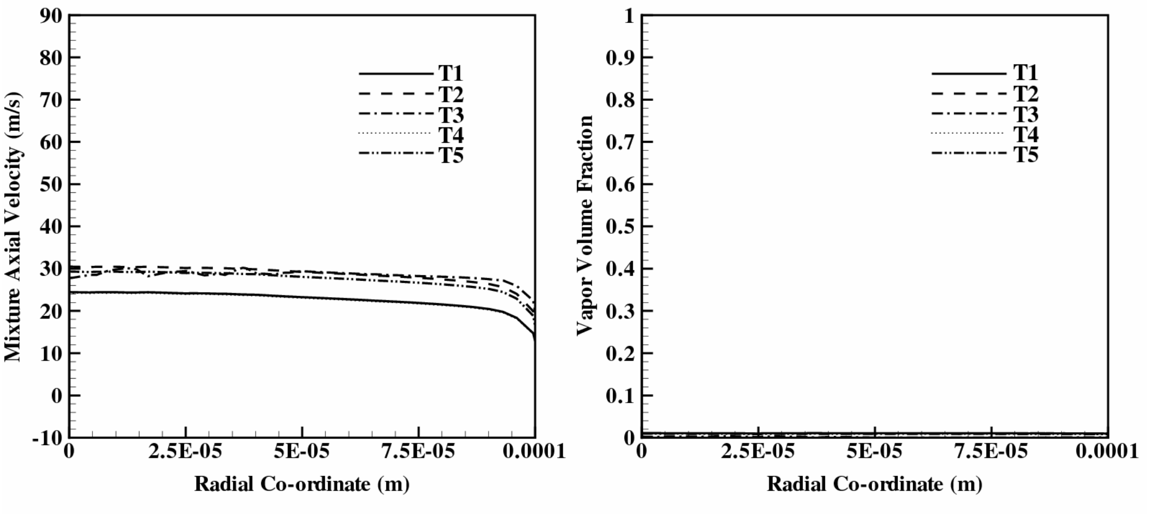

(a) (b)

Figure 4.75: Plots of (a) Axial velocity and (ii) vapor fraction distribution at the nozzle exit for configuration S_7 at increasing time instants. $T_1<T_2<T_3<T_4<T_5$ separated by 1μs.

As seen from the axial-velocity magnitude, little variation is obtained at the nozzle exit due to high frequency and shorter nozzle lengths. The mean velocity is of the order of 30 m/s. However, no cavitation effects are prevalent.

4.6.8. Conclusions from numerical simulation of sharp corners

From the numerical simulations of sharp cornered nozzlems very high activity of cavitation clusters are concluded. The cluster formation, detachment and propagation are satisfactorily accommodated in the current simulation. Flow rate in the simulations ~ 50 cc/min give rise to very high mean velocities ~ 70 m/s which are harder to atomize with modulation. As demonstrated earlier, modulation of high speed jets leads to increased breakup lengths, as a result of which, modulating a low speed jet is preferred.

4.7 The Backward facing step approach

The phenomena of flow separation and reattachment, widely found in many fluidic devices, are accompanied by appreciable energy losses, influencing the performance of fluid machinery and imposing severe limitations on their design and operation [35, 251-254]. The backward-facing step flow is a well-known test case for studying the influence of local streamline curvature. In this scenario, the flow separates at the step edge, forming a curved shear layer which bifurcates at the reattachment region; one branch flowing back creates a separation bubble behind the step, another branch creates a new boundary layer downstream [251]. The level of turbulence in the separated shear later aligned with the mean dividing streamline bordering the separation bubble is of decisive importance when controlling the reattachment length [251, 254]. Increased shear stress levels imply an enhancement of the fluid entrainment into the shear-layer leading to higher momentum transport and consequently a shortening of the recirculation zone. In addition to the strong mean flow gradient in the vertical direction, representing the main source of turbulence production, and a curvature-generated turbulence production, the turbulence can be further generated by introducing a high-velocity jet into the shear layer. The flow perturbation created in such a way causes an intensive flow stretching (mean flow deformation enhancement, especially with respect to the axial velocity component) leading consequently to an enhanced turbulence level. The presence of a separated flow, together with a reattaching flow, gives rise to increased unsteadiness, pressure fluctuations, structure vibrations and noise [251]. Also, they enhance heat and mass transfer and augment mixing.

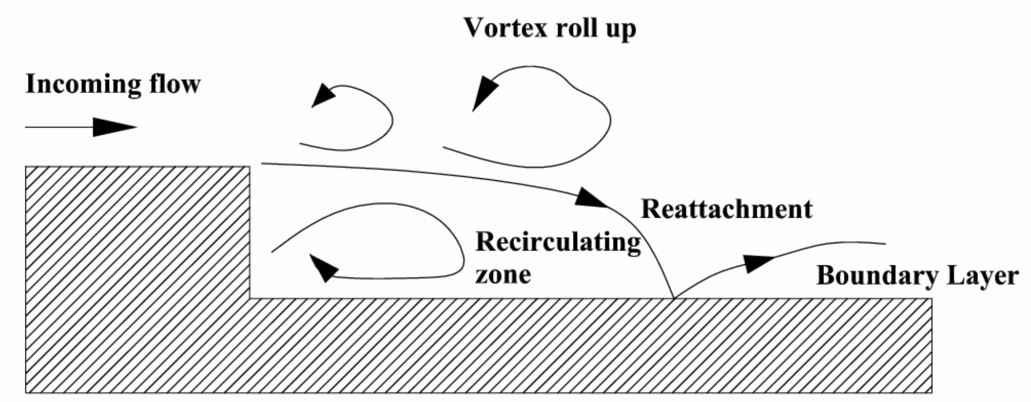

Figure 4.76: A backward facing step configuration.

A literature study reveals that there have been many attempts to control or lessen the unfavorable behavior associated with separated and reattaching flows. The method of an oscillating separation edge was applied by Nagib et al. [255] and Roos and Kegelman [256]. Use of sound waves to influence the reattachment process was examined by several researchers, and the relevant flow geometry, forcing method and effective reduced frequency. As a feasible technique, the introduction of a local forcing in the vicinity of the separation edge has been contemplated. These experimental efforts utilized a small-amplitude localized jet flow close to the separation edge. The jet flow contained a well-defined single-frequency pulsation. It was demonstrated that, by means of a small localized perturbation near the separation edge, the overall characteristics of the separated and reattaching flows were altered significantly. The effect of local forcing on the flow structure was scrutinized by altering the forcing frequency and amplitude. Chun and Sung [257, 258] clarified that the local forcing mechanism is effective for controlling the separated and reattaching flows. A small localized forcing near the separation edge enhanced the shear-layer growth rate and produced a large rolled-up vortex at the separation edge.

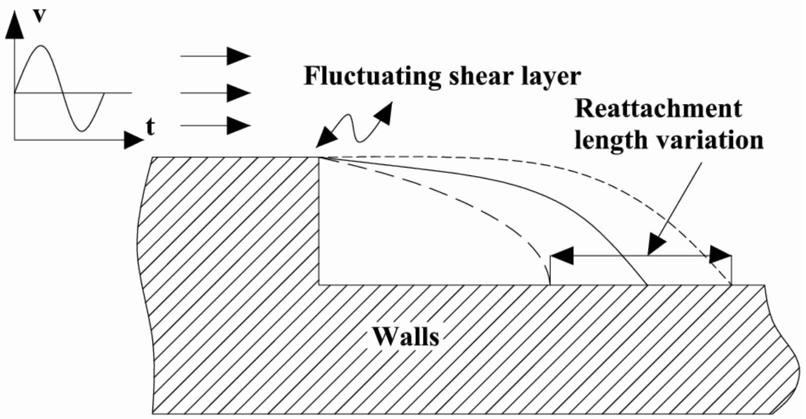

Figure 4.77: Variation in reattachment length obtained by modulating the incoming liquid jet

Saric et al. [259] using their numerical experiments concluded that imposing perturbation frequencies in an appropriate range result in appreciable alteration of the reattachment length. They concluded that the main effect of the oscillatory flow field on a separated shear layer is that it reattaches earlier due to momentum transfer enhancement caused by an increase in turbulence production. The increase in turbulence intensity in the shear layer and consequent shortening of the mean recirculation zone are clearly recognizable.

4.7.1. Notes on Shear-Cavitation

Cavitating shear flows occur in the closure region of attached cavities and are associated with the formation of strong vortices downstream of a partial cavity [107, 247, 260-263] The cavitating turbulent shear flow associated with attached cavitation plays an important role in the formation of cloud cavitation and in the processes that cause cavitation erosion [171, 172]. The vapor phase is often preferentially concentrated within the low-pressure cores of the strongest vortices, the sites of cavitation inception, and the presence of vapor in the shear layer can alter both the large-scale and small-scale flow processes.

4.8. Cavitation enhancing prototype models

As described in the Section (4.7) and (4.7.1), presence of a backward facing step augments mixing by shear rate enhancement while cavitation in shear layers show strong potential for increased turbulence activities. Combining both the effects, a new cavitation enhancement type model is proposed. The pulsating liquid flow generated by the horn is introduced into a backward facing step chamber and a modulation chamber (typically a convergent type flow accelerator) back into the main nozzle throat. The process of cavitation shear layer enhancement is offered to the liquid-vapor mixture flow to deliver increased level of turbulence intensities in addition to flow modulation by the converging section design. The preceding section is devoted to discussing various atomizer configurations utilizing the concept of residence and flow modulation chambers within the framework of Backward Facing Step configuration. A schematic of the configuration described in Fig. (4.78) details the variables used in the construction of test cases and the following discussions.

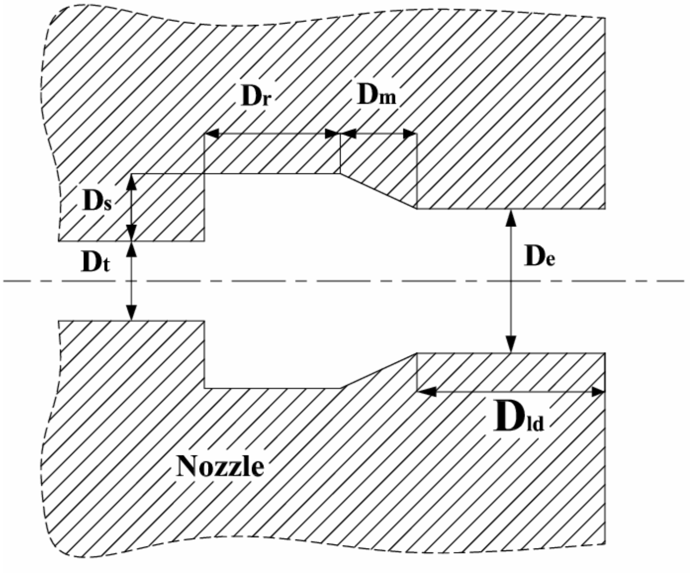

Figure 4.78: Schematic of parameters used in classifying residence chamber based cavitator

As stated before, the use of a backward-facing step in a pulsating environment shows increased potential for mixing and turbulence enhancement. In view of this favorable scenario, modification to the existing cavitating atomizer design is carried out by the procedure described in Fig. (4.75).

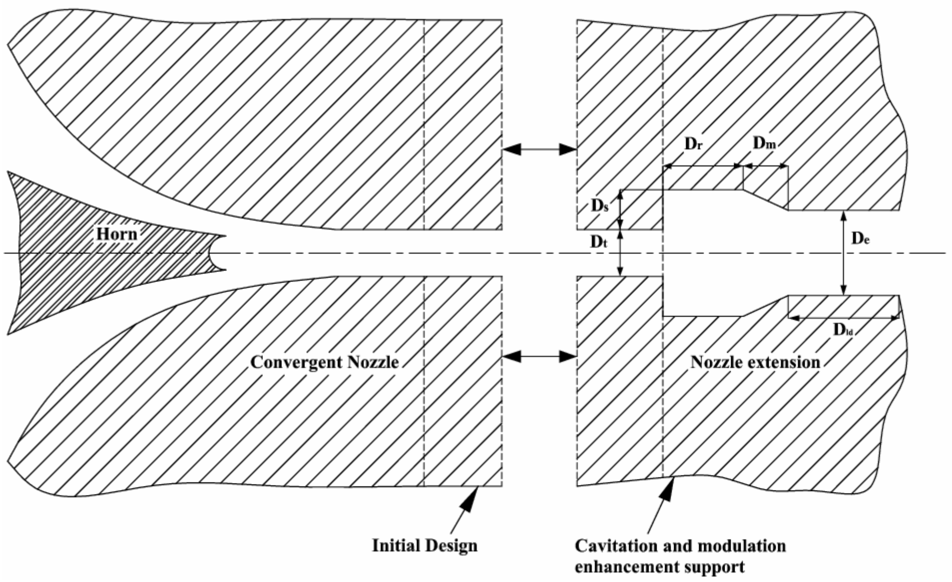

Figure 4.79: Modification process of the cavitating atomizer design

In order to comprehend the response of cavitating mixture flows over a backward facing step and to enhance the perturbations, a series of numerical simulation using the parameters listed in Table (4.5) is carried out. List of configurations tested based on the new cavitator design is tabulated as follows

Table 4.5 List of simulation parameters varied in the geometry construction

Configuration	D_t	D_s	D_r	D_m	D_e	D_{ld}	Flow rate
C_1*	D_t	$D_t/5$	$2D_t$	0	$1.33D_t$	0	50
C_2	D_t	$D_t/2$	D_t	$D_t/2$	$1.33D_t$	0	50
C_3	D_t	$D_t/2$	D_t	$D_t/2$	$1.33D_t$	$2.66D_t$	50
C_4	D_t	$D_t/2$	D_t	$D_t/2$	$1.33D_t$	$2.66D_t$	25
C_5	D_t	$D_t/2$	D_t	$D_t/2$	$1.33D_t$	$5.32D_t$	50
C_6	D_t	D_t	$2D_t$	$D_t/4$	$1.33D_t$	$2.66D_t$	50

$\mathbf{C_7}$	D_t	D_t	$2D_t$	$D_t/4$	$1.33D_t$	$2.66D_t$	*25*
$\mathbf{C_8}$	D_t	D_t	$2D_t$	D_t	$1.33D_t$	$2.66D_t$	*50*
$\mathbf{C_9}$	D_t	D_t	$2D_t$	D_t	$1.33D_t$	$2.66D_t$	*50*

* denote additional modifications to the designated geometry configurations

4.8.1. Configuration C_1: open-end type cavitator

With $D_{ld} = 0$, the modification results in an open-type cavitating atomizer design. The backward facing step profile attached at the rear end of the nozzle opens up to the exterior gas domain. Hence, any cavitation clusters generated in the shear layer region at the separation edge would collapse along the central nozzle axis creating impulse energy for efficient atomization. Application of open-end BFS procedure is not new to fluid dynamics enhancement studies. Several version of the BFS implementation for micro-combustor applications have been carried out to improve mixing efficiency [264-267]. The above configuration indicates no presence of a converging flow modulator section. Simulation results for the proposed design with an open-end backward facing step profile are presented in Fig. (4.80). Recognize from Fig. (4.80(a) – (e)) formation of intense cavity clusters due to the shear layer generation near the separation edge. The incoming flow Reynolds number is ~ 7500 with a superimposed fluctuation frequency of 68 KHz and a mean velocity of 30 m/s in a 150 μm nozzle diameter resulting in a fluid flow.

The cavitation cluster formation near the nozzle exit is clearly visible from Fig. (4.80(e)). The sudden enlargement of the nozzle sac leads to deceleration of the liquid-vapor mixture flow. However, the recirculation zones formed near the corners of the backward facing step profile create low pressure regions and act as a constant source of low pressure zones for vapor replenishment [34]. Cavitation clusters are also visible near the oscillating horn surface due to the effect similar to that of vibratory cavitation [29, 204]. Constant stretching of the cavitation cluster leading to super-cavitation events is noticeable from Fig. (4.80(i-b)-(i-e)). The forward motion of the horn enhances the shear layer formation increasing the turbulent production energy and hence increased cavitation rates [251]. During the forward motion, the cavitation clusters propagate towards the nozzle exit. However, before reaching the nozzle exit they are either consumed by the strong adverse pressure gradient generated by the expansion section or by the retracting motion of the horn. In this debate, it is important to identify the effect of downstream step profile length (D_r). The horn is positioned at a distance of approximately 9 nozzle exit diameters, to obtain a 3/8th flow area coverage, and hence any imposed flow oscillations consumes a convective time, determined by the product of length and flow velocity, equaling $9D/U_{mean}$ where U_{mean} is the mean liquid jet velocity predicted. Given the step profile length D_r and an incoming mean flow velocity of U_{mean}, the time taken for the cavitation cluster to leave the domain is approximately D_r/U_{mean}. The relationship between D_r and nozzle diameter D_t is known explicitly by the geometry definition. Clearly, the time taken by the perturbation signal to reach the cavitation cluster is far higher than the convection time of the clusters themselves. This indicates that the influence of pressure gradients generated by expanding section dominates the cavitation growth/collapse behavior near the exit. Contour plot of axial-velocity magnitude corresponding to the evolution of cavitation region is shown in Fig. (4.80(ii)). A strong variation in velocity magnitude ranging from 20 m/s – 34 m/s is obtained. Presence of strong velocity fronts, as a result of pressure modulation upstream, is evident from the plots. Since the cavitation model is strongly coupled to the pressure variation effects, a clear one-to-one correlation between the vapor formation and the pressure pulse propagation can be easily be identified from the plots, such as in Fig. (4.80(i-d)-(ii-d')). The shape of the cavitation vapor front is similar to the velocity front advancing towards the nozzle exit.

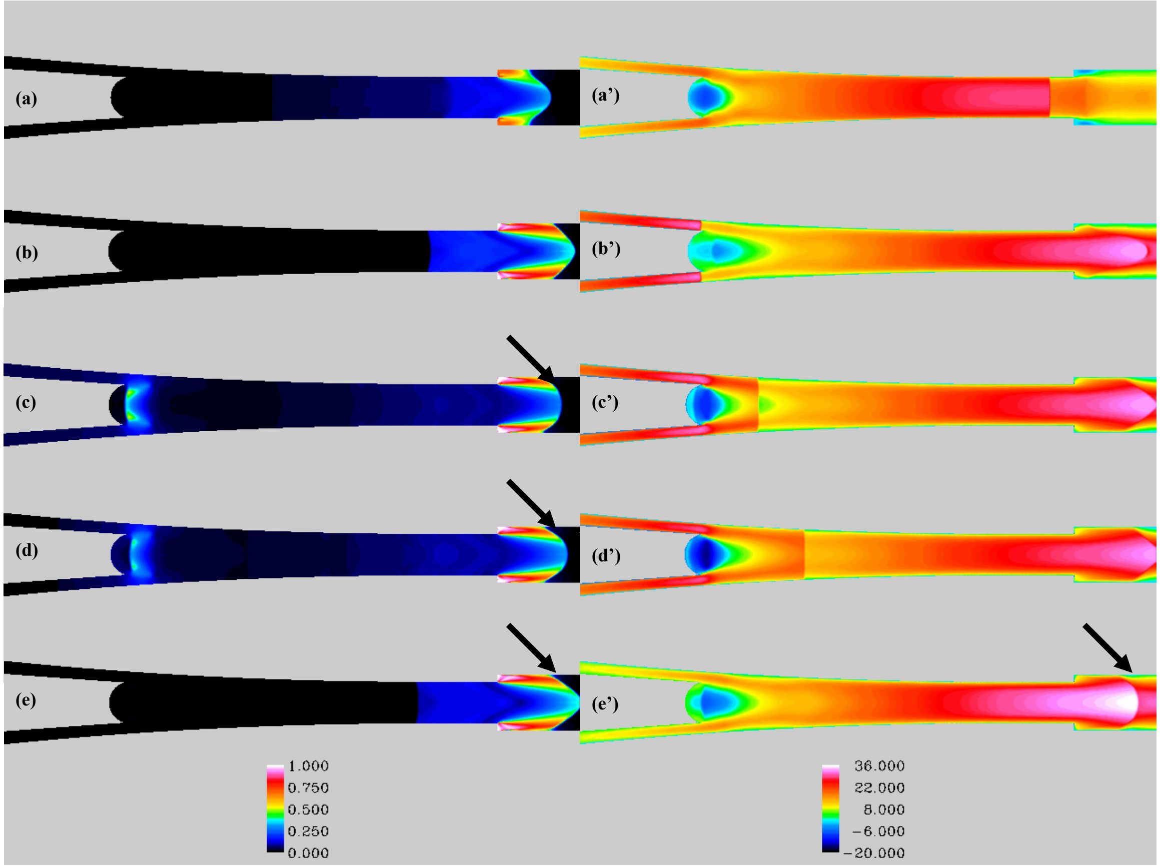

(i) (ii)

Figure 4.80: Contour plots of (i) Vapor volume fraction (ii) Axial-velocity magnitude using CFD computations on Configuration C_1- Open type cavitating atomizer

Axial velocity profile modulation at the exit of the open-end cavitator type shows low modulation effect (~0.2) with a mean jet velocity of 27 m/s. This configuration results in a Strouhal number = 1.584 with a modulation amplitude of 0.3. Such a configuration, discussed in Chapter 2, would result in downstream directed bells with appreciable big drop sizes [115].

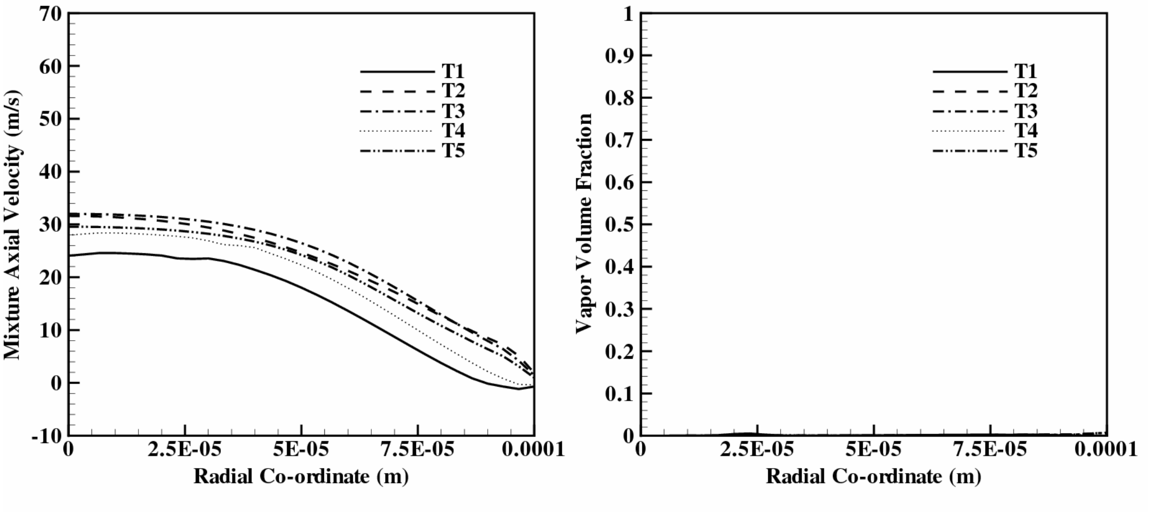

(i) (ii)

Figure 4.81: Plots of (a) Axial velocity and (ii) vapor fraction distribution at the nozzle exit for configuration C_1 at increasing time instants. $T_1<T_2<T_3<T_4<T_5$ separated by 1μs.

From a closer look at the results, considerable drawbacks were detected. The most influential being the fluctuating velocity profiles generated at the nozzle exit. Due to the presence of boundary layers in the flow any modulation generated in the mean flow gradient affects the gradients in the boundary layer as well. As a result, reverse flow regions were spotted near the nozzle exit domain. The consequence of such a region is very detrimental. Presence of re-circulating flow profile near the nozzle exit section can intensify the hydraulic flip mechanism. Following this, the outside gas can creep into the nozzle domain nullifying any cavitation effects. The hydraulic flip mechanism is known to result in smoothening of the exiting liquid jets thereby leading to long breakup lengths [2, 48, 54]. A schematic of the detected drawback of the current model is shown in Fig. (4.82).

4.8.1.1.Drawbacks of the open-type cavitator design

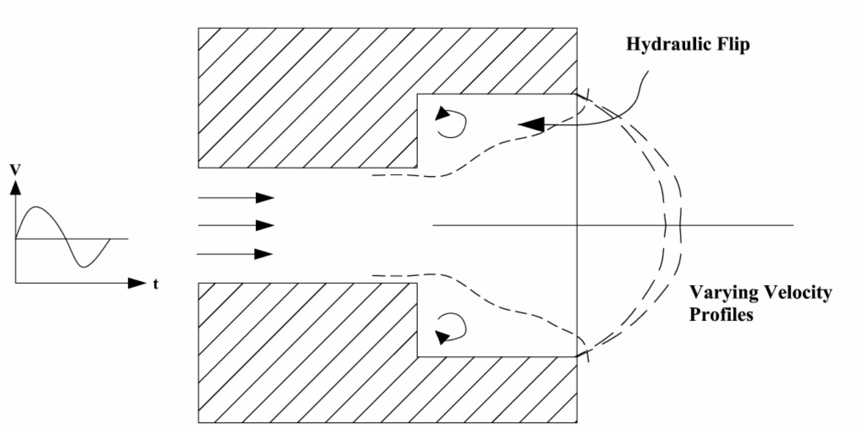

Figure 4.82: Open type cavitator. Influence of fluctuating velocity profiles lead to increased access of the outside gas to the nozzle interior.

Following this initial design, a modification to the atomizer design with an attached backward facing step profile section is proposed. Since the open-type cavitator design has known issues of creating hydraulic flips, the nozzle section following the open end of the cavitator described in Fig. (4.82) is replaced by a modulation chamber. This modulation chamber consists of a convergent nozzle followed by a constant area flow section. A schematic of the modification proposed here is displayed in Fig. (4.83).

4.8.1.2 The Residence-Modulation Chamber Design Modification

The expansion chamber is now seen to act as a residence chamber where cluster formation and their subsequent transient evolution are monitored. This residence chamber seeks to increase the cavitation cluster mixing with the bulk flow, a straightforward consequence of utilizing the backward facing step profile [251]. The increased turbulent production and increased shear layer contribution increases the perturbations within the liquid-vapor mixture flow which is then accelerated using a flow modulation inducer section.

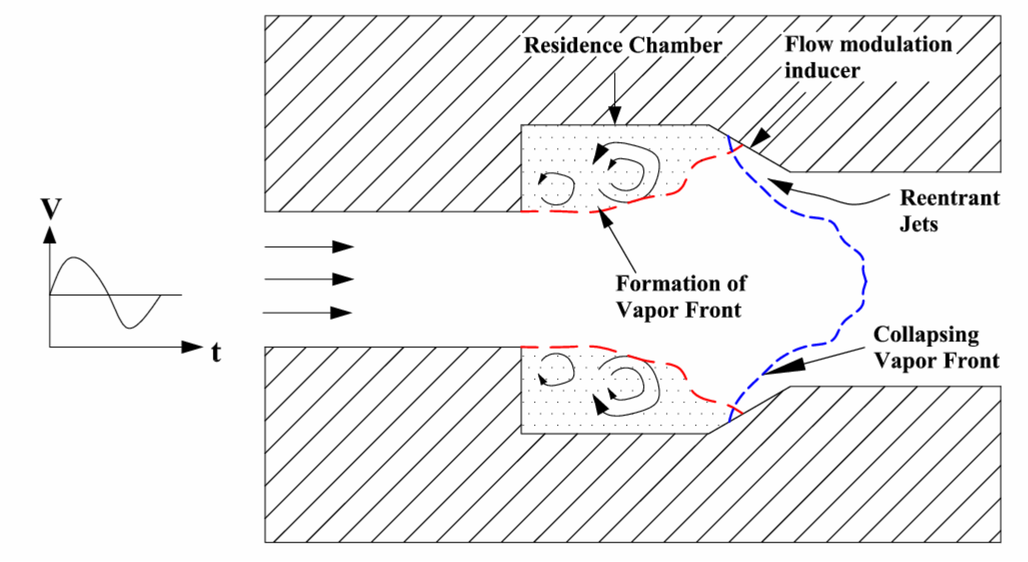

Figure 4.83: Concept of Residence chamber

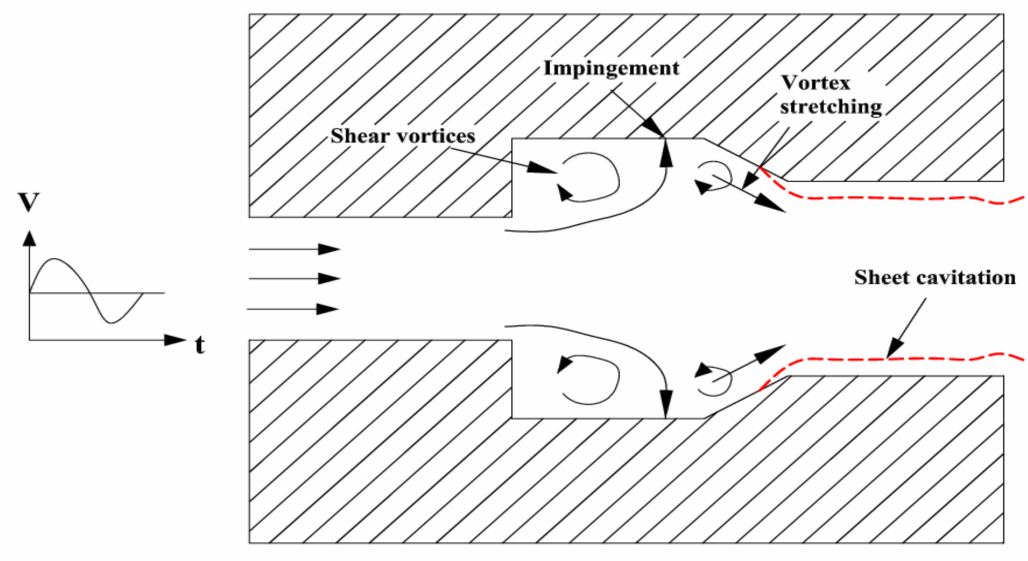

Figure 4.84: vortex interaction mechanisms

This design is a simple flow convergent nozzle type which by results in decreased pressure zones by accelerating the flow. There are two competing forces acting on the mixture flow near the entrance of the flow modulation inducer: the impingement of the cavitating liquid increases the stagnation pressure leading to the collapse of the vapor clusters and at the same instant, the flow modulation region act against this pressure increase by accelerating the fluid. As a result of both the dominating mechanism, some cavitation clusters survive the expansion section and propagate into the constant diameter section. Meanwhile, due to the geometry curvature, a strong reverse pressure gradient acts near the corners of the section joining the flow modulation inducer and the constant diameter chamber leading to the separation of cavitation clusters from the nozzle walls. Thus concentration of cavity cluster into the core of the bulk flow is achieved. Mechanisms of vortex stretching and rollup contribute to the mixing of the vapor phase with the main liquid flow leading to increased perturbation of the exiting liquid jets [251, 253].

The presence of cavitation within a turbulent shear flow can potentially alter the dynamics of the flow through both local and global mechanisms. The presence of developed cavitation can lead to overall flow changes through a reduction in mean flow density, an increase in the overall flow volume, or due to modification of the mean pressure field. Cavitation can also modify the vortical flow locally [247]. Belahadji et al. [268] have suggested that cavitation in the cores of vortices will affect the process of vortex stretching by the decoupling of the vortex strain and rotation rate. Gopalan and Katz [108] demonstrated that significant flow–vapor interactions exist in the cavitating shear flow downstream of a partial cavity. Furthermore, Laberteaux and Ceccio [262, 263] showed how the growth and collapse of disperse cavitation bubbles led to the production of small-scale turbulence in the wake of partial cavities.

4.8.1.2.1 On Cavitation Shear layers

Visual observations of the shear layer suggest that the overall formation, growth, and convection of the primary and secondary vortical structures in the shear layer are not significantly affected by the presence of cavitation [108, 247]. The average flow field downstream of the cavitating shear layer is not significantly altered both in terms of average velocities and mean pressure drop across the test section. The largest differences between the cavitation and the noncavitating flows were in the turbulent fluctuations examined downstream of the cavitating shear layer. The streamwise fluctuations increased by about 15% compared to the noncavitating case in the center of the shear flow. However, the maximum cross-stream fluctuations and Reynolds stresses decreased by about 30%. As bubbles collapse, an increase in turbulence levels is expected [262, 263]. The decrease in the cross-stream fluctuations and Reynolds stresses suggest that the cavitation within the cores of streamwise vortices has decreased the coupling between the streamwise and cross-stream velocity fluctuations. This is consistent with the hypothesis of Belahadji *et al.* [268] whereby cavitation in the cores of the streamwise vortices decoupled the stretching and rotation rate of these flow structures. The reduction in Reynolds stresses downstream of the shear layer is inconsistent with the scaling of the shear stress within the shear layer based on the shear layer growth rate, mean density, and the mean flow profiles [251].

4.8.2. Case C_2: Modification to the open BFS cavitating atomizer

Following the reverse flow solutions obtained with an open-end cavitator, a larger scale cavitator design with modified BFS cavitator is simulated. The design consists of engaging a converging nozzle (with large radius of curvature) with a forward facing step profile followed by a constant diameter section leading to a diffuser section (a backward facing step profile). The forward step length measures 1/4th the throat diameter section. The end of the backward facing step is made convergent to increase flow acceleration and modulation and further, resist any hydraulic flip. The exiting nozzle diameter is 0.2 mm while the diffuser section has a diameter of 0.4mm. The constant diameter region on the other hand is 0.15 mm to provide intermediate acceleration to the liquid-vapor mixture flow formed near the entrance to the nozzle sac passing the forward facing step. The results of the simulation are presented in Fig. (4.85). Axial-velocity fluctuations measure 55-75 m/s at the nozzle exit. The reason behind the high velocity regime generated by the present configuration is attributed to the nature of vapor distribution in the design. The cavitation regions generated near the forward facing step region due to high shear of the liquid bulk modify the flow profile appreciably leading to very high velocities (~80 m/s) which are then fed to the diffuser section. The high Reynolds number (~12500) jet results in increased turbulent production and a very low pressure zone past the backward facing step. This process immediately warrants cavitation generation. A strong dependency of the cavitation phenomena on the flow pressure necessitates rapid growth of the clusters and soon they fill up the residence chamber completely (Fig. (4.85(i))) [34]. Owing to the mass conservation constraint, increase in cavity clusters leads to flow acceleration rather than flow deceleration in the diffusion chamber. No fluctuating cavitation cluster behavior near the diffuser region is observed. However, some small perturbations in the expanding cavitation layers towards the nozzle exit are experienced due to flow modulation effects.

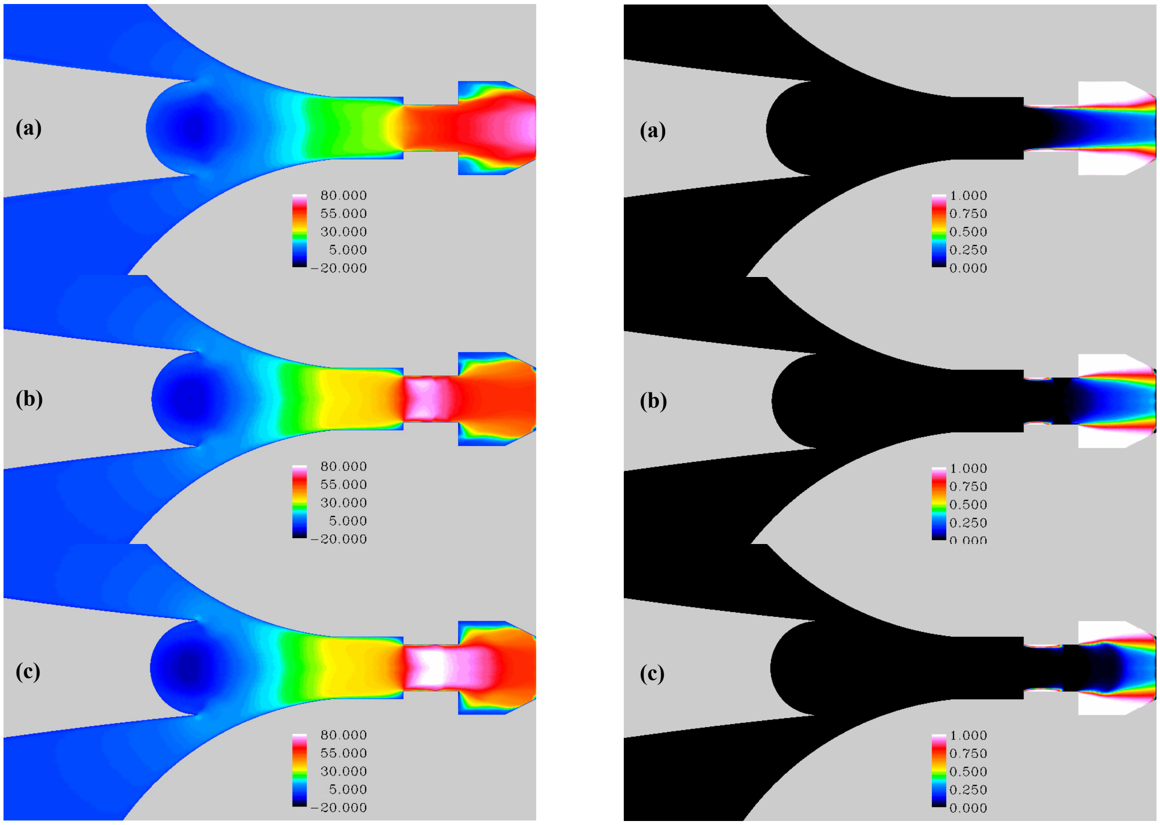

(i)

(ii)

Figure 4.85: Contour plots of (i) Vapor volume fraction (ii) Axial-velocity magnitude using CFD computations on Configuration C_2- Forward facing step profiled cavitating atomizer

As observed from plots Fig. 4.85 (i) and (ii), low modulation of exiting liquid velocities and cavitation vapor distribution are evident. Hence, no detailed representations of the flow variables at the exit section are presented.

4.8.3. Case C_3: Modified cavitator design

4.8.3.1Case C_3: with no pulsation effects

Observing the effect of forward step profile in Section (4.8.2), the sharp nozzle entrance regions are removed; the residence chamber region and the modulation chamber retained with an appropriate constant diameter section added to its rear portion. The final model configuration is listed in Table (4.5). Numerical simulations with no horn motion are carried out to identify the regions of cavitation inception without any oscillatory effect. The results obtained for such a configuration is presented in Fig. (4.86). With no pulsation effect, cavitation regions are formed in the residence zone and extend all the way towards the nozzle exit showing strong potentials for supercavitation.

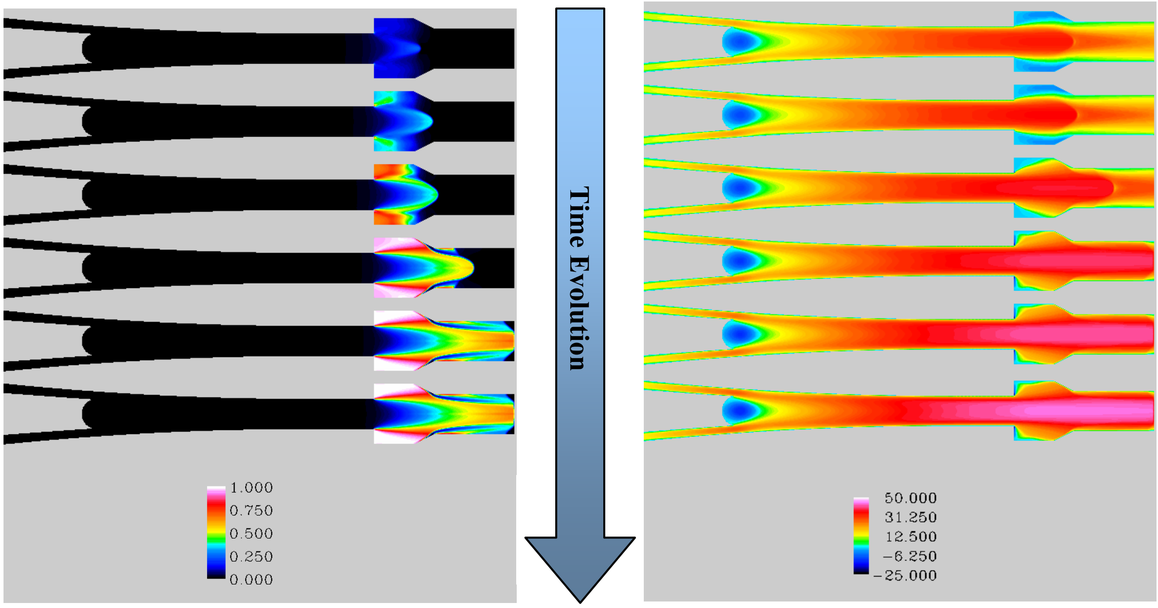

(a) (b)

Figure 4.86: Numerical simulations with no oscillatory horn effect in C_3 atomizer configuration (a) Contour plots (a) vapor volume fraction (b) mixture axial velocities. Cavitation regions are still evident and are concentrated at the nozzle axis core

A steady state vapor fraction intensity of 0.5 along the central nozzle axis is obtained with a mean mixture velocity of 45 m/s. Preceding this computation, pulsation effects are incorporated into the simulation domain.

4.8.3.2. Case C_3: modified BFS cavitator with pulsation effects

The steady state case presented in Section (4.8.3) is supplemented with horn oscillation effect, the frequency and stroke length being 68 KHz and 20 µm respectively. The simulation is carried out in a transient fashion. Transient vapor and flow velocity evolutions in the domain are presented in Fig. (4.87 (i)) and Fig. (4.87(ii)) respectively.

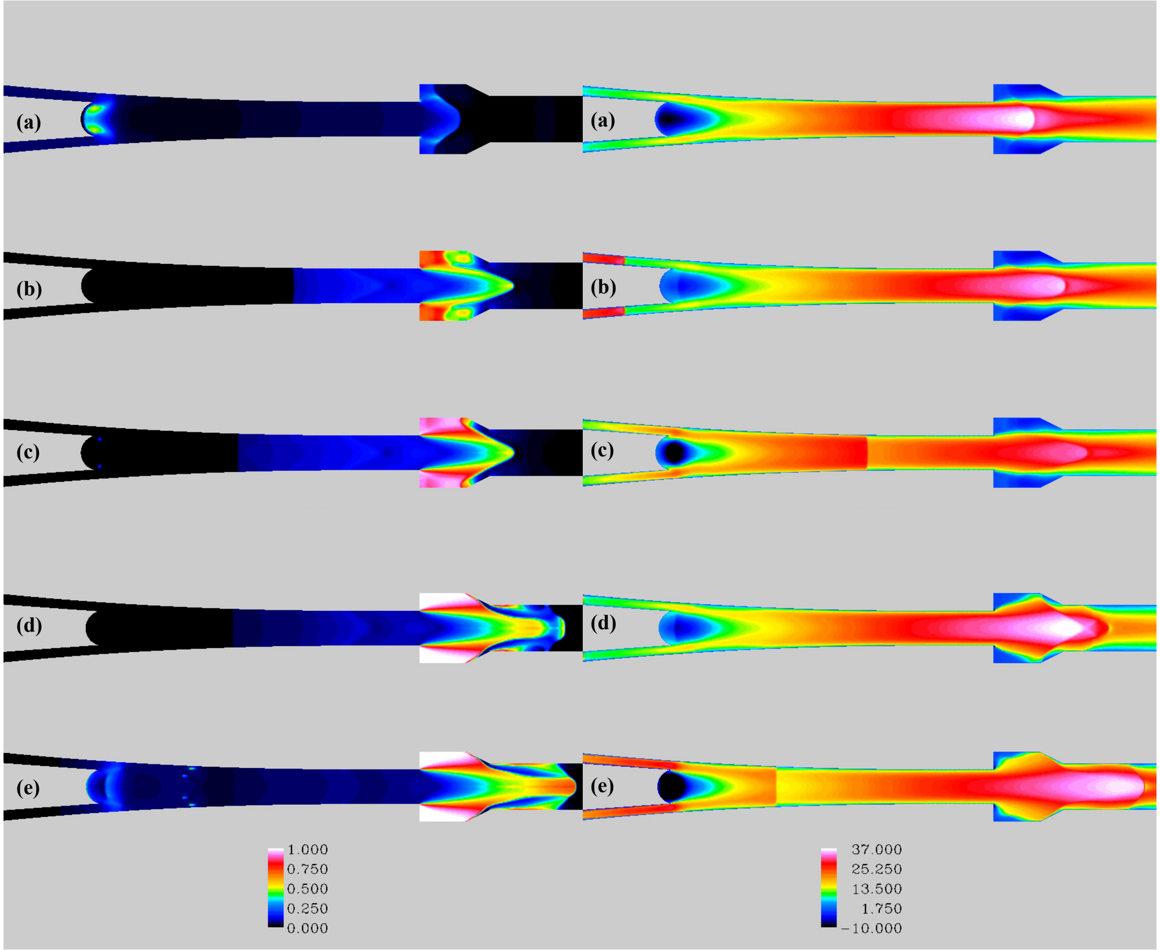

(i) (ii)

Figure 4.87: Contour plots of (i) Vapor volume fraction (ii) Axial-velocity magnitude using CFD computations on Configuration C_3- BFS type cavitating atomizer

Observe that in addition to high cavitation clusters formation near the nozzle exit, intense cavitation regions are spotted near the horn surface as well. As clearly seen from the axial velocity plot, Fig. (4.87(ii)(a-e)), the pulsation effects sends fluctuating velocity front towards the nozzle exit.

Events of supercavitation are still encountered. From the numerical simulations, the frequency of the collapse at the exit is determined as 70000 Hz which is close to the imposed perturbation frequency of 68 KHz. Also notice from Fig. (4.87(i)) strong regions of cavitation vapor are seen propagating along the nozzle axis towards the axis. This effect is particularly important, since it is necessary that the cavitation effects prevail along the exiting jet axis to act additionally on the liquid jet core, which under certain modulation conditions is unaffected by the liquid jet surface stripping process. Contour plots of axial-velocity, radial-velocity and the turbulent kinetic energy magnitudes prevailing in the domain are shown in Fig. (4.88(a)). The axial-velocities in the exit section approximately measure 25-35 m/s. Generation of strong turbulence effects near the BFS entrance regions can be singularized from Fig. (4.88(a)(iii)T1-T3). Correspondingly, high radial velocities are encountered in these regions (Fig. (4.88(a)(ii)T1-T3). Notice from Fig. (4.88(a)(iv)T1-T3) that a strong vapor cavitation region is present through the specified time intervals. A description of the velocity profile at the nozzle exit can be obtained from Fig. (4.88(b)). The velocity fluctuates between 16 m/s to as high as 37 m/s with a mean of 26 m/s implying a modulation amplitude of approximately 0.4. According to the studies presented in Chapter 3, this value lies in the closest recommended limits. When the liquid jet velocities reach minimum limits, the corresponding vapor fractions peak to their maximum, indicating the strong presence of cavitation clusters in the exiting liquid jets.

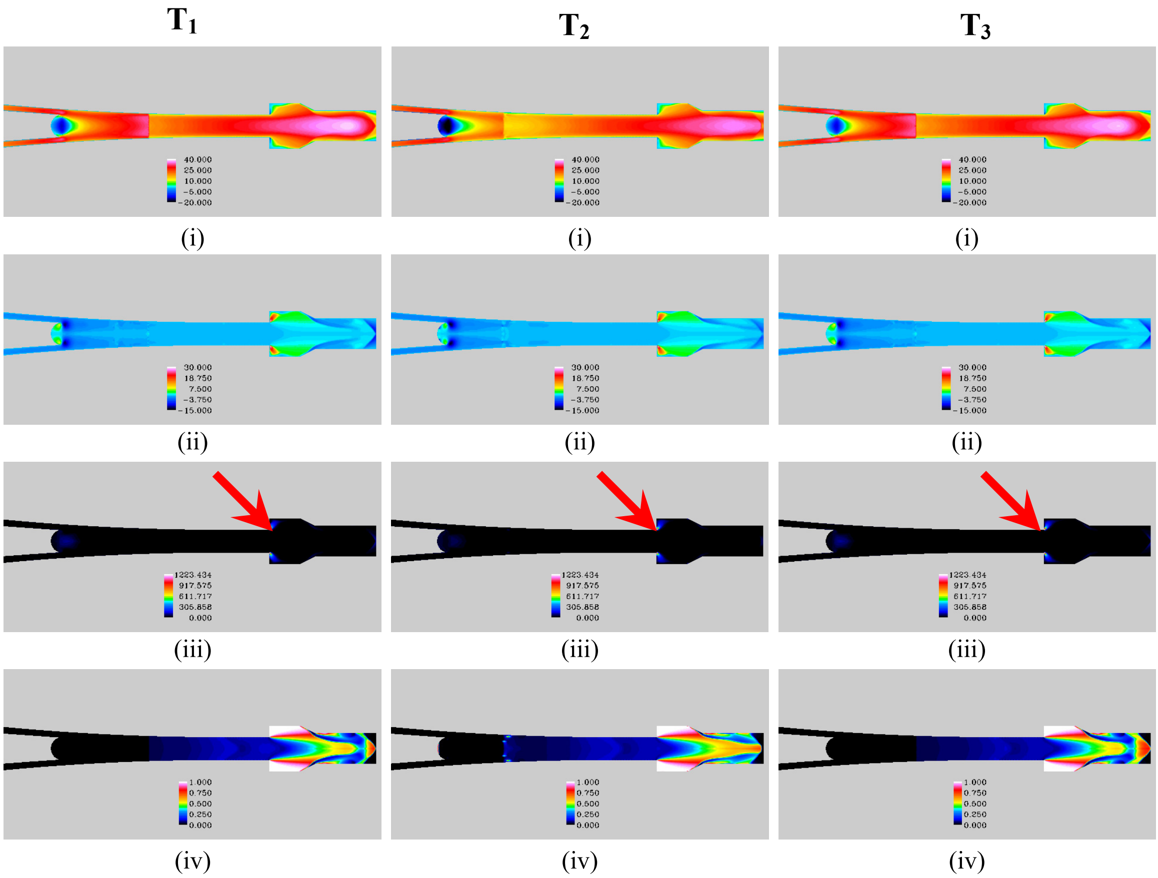
T1
T2
T3
40.000
25.000
10.000
-5.000
-20.000
(i)
30.000
18.750
7.500
-3.750
-15.000
(ii)
1223.434
917.575
611.717
305.858
0.000
(iii)
1.000
0.750
0.500
0.250
0.000
(iv)

(a)

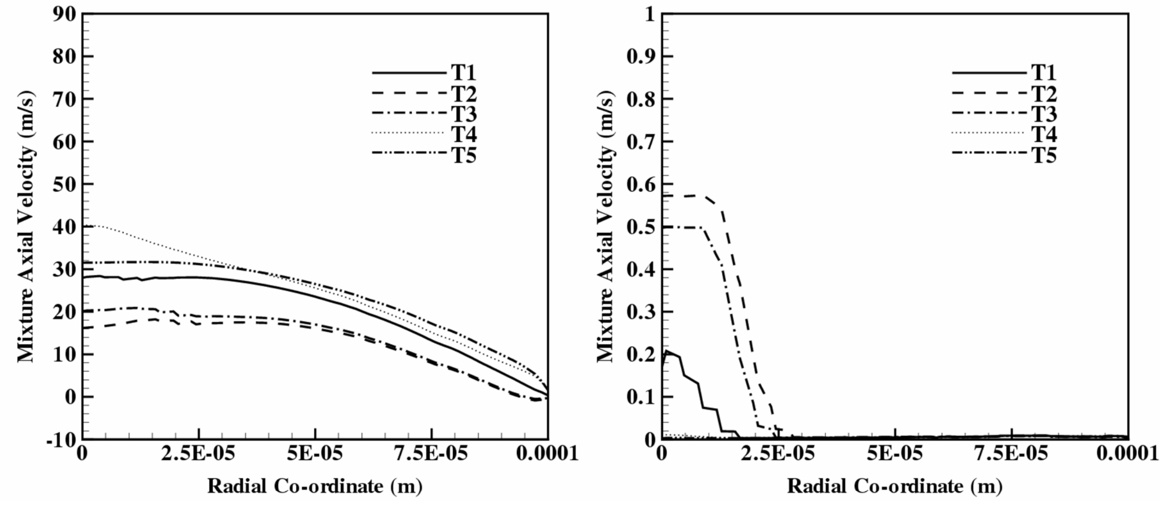
Mixture Axial Velocity (m/s)
Radial Co-ordinate (m)
T1
T2
T3
T4
T5
90
80
70
60
50
40
30
20
10
0
-10
0
2.5E-05
5E-05
7.5E-05
0.0001
1
0.9
0.8
0.7
0.6
0.5
0.4
0.3
0.2
0.1
0

(i) (ii)

(b)

Figure 4.88 : Contour plots of (a) (i) axial velocity (ii) radial-velocity (iii) turbulent kinetic energy (iv) vapor fraction distribution in the nozzle domain at different time instants T1<T2<T3. Plots of (b)(i)axial velocity magnitude and (ii) vapor fraction distribution at the nozzle exit for configuration C_3 at increasing time instants. T1<T2<T3<T4<T5 separated by 1μs.

4.8.4. Case C_4: Flow rate effects

Implementation of a modified BFS cavitator design in Section (4.8.3) yielded a modulated jet with a mean velocity of 27 m/s and modulation amplitude 0.4 with major cavitation collapse occurring just inside the nozzle. With the same nozzle design, the injected liquid flow rate is reduced to 25 cc/min, in order to address the flow rate effects.

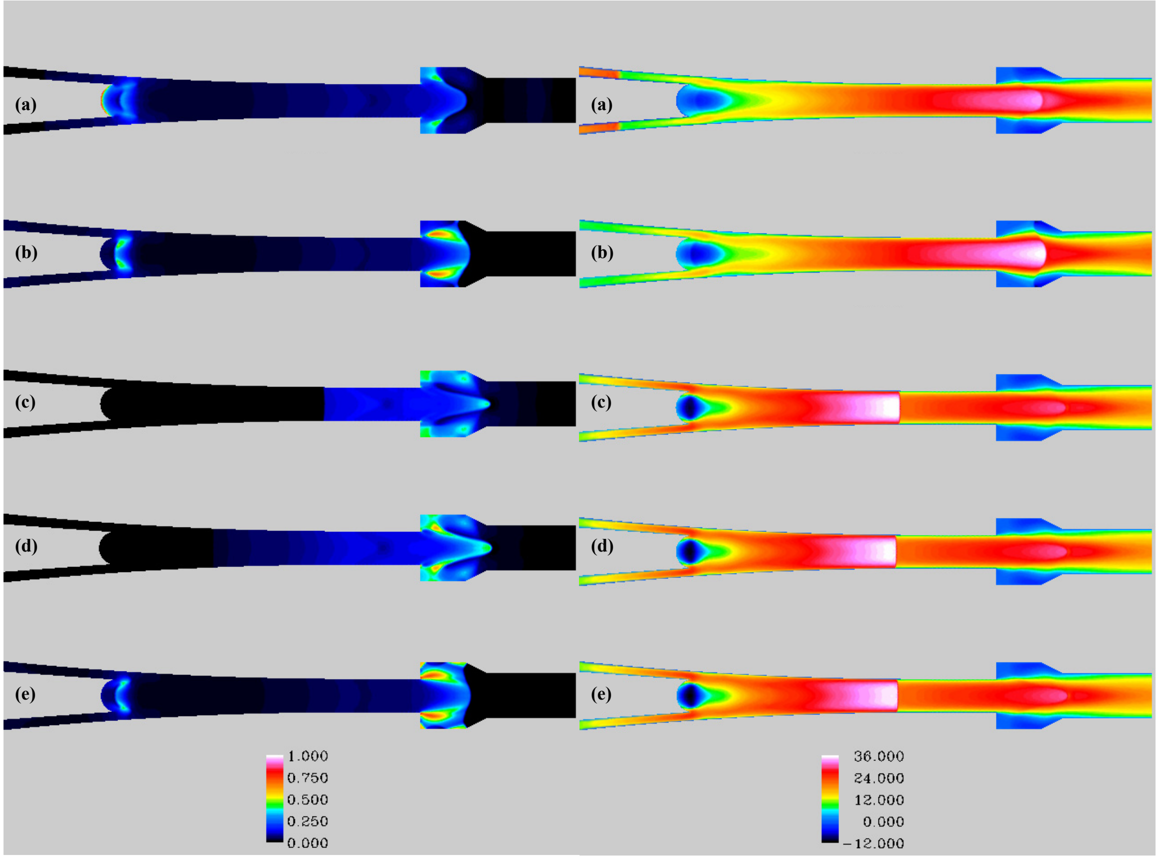

(i) (ii)

Figure 4.89: Contour plots of (i) Vapor volume fraction (ii) Axial-velocity magnitude using CFD computations on Configuration C_4- BFS type cavitating atomizer with low flow rate

Distributions of vapor and mixture axial velocities obtained from the computations are presented in Fig. (4.89 (i) & (ii)). As seen from the vapor distribution plots, the collapse of the cavitation clusters are predominantly restricted to the enlarged residence and modulation chamber. Reduction in flow rate reflects on low liquid velocities as seen in Fig. (4.89 (ii)). The velocity fluctuations at the nozzle exit shown in Fig. (4.90(a)) indicate very-low velocity jets with low modulation amplitude ~ 0.2. No vapor presence is detected at the nozzle exit section (Fig. 4.90 (b)).

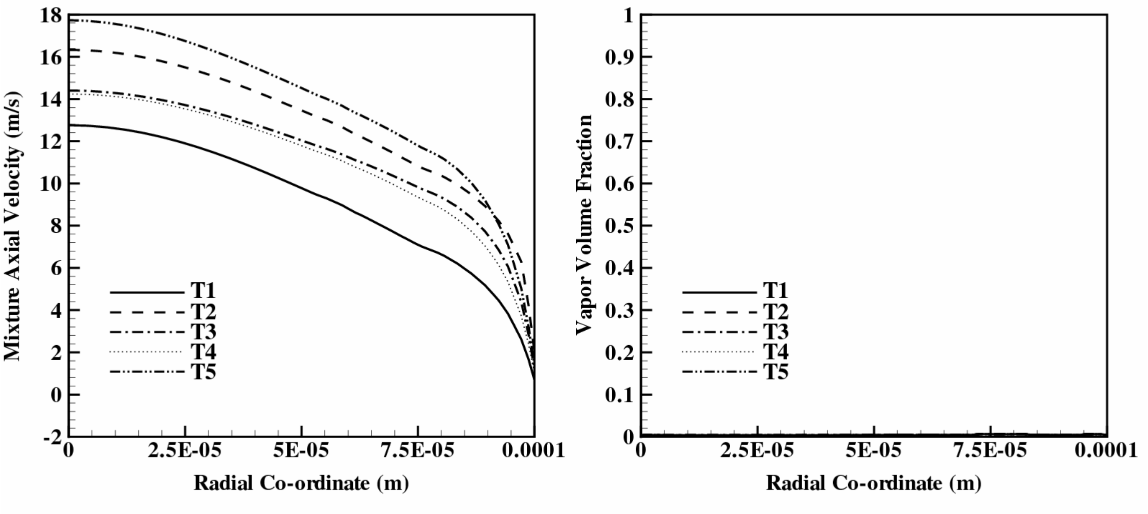

(a) (b)

Figure 4.90 : Plots of (a) Axial velocity and (ii) vapor fraction distribution at the nozzle exit. for configuration C_4 at increasing time instants. $T_1<T_2<T_3<T_4<T_5$ separated by 1μs.

4.8.5. Case C_5: Influence of L/D ratio

The influence of high length-to-diameter ratios in cavitating nozzles has been reported to have a profound influence on the jet breakup [2, 3, 48]. The primary objective of retaining high L-D ratios lies in the creation of fully developed turbulent flow profiles [2, 3, 5]. Extending the case simulated in the Section (4.8.2), an elongation to the constant diameter exit section is carried out. The L-D ratio is increased to 4 conforming to the same exit nozzle diameter of 200 µm. As seen from Fig. (4.91(i)), the volume fraction distributions are similar to those obtained with an L/D ratio = 2, Fig, (4.87(i)). However, pronounced elongation of the cavitation zone further downstream within the nozzle interior is predicted by the numerical model.

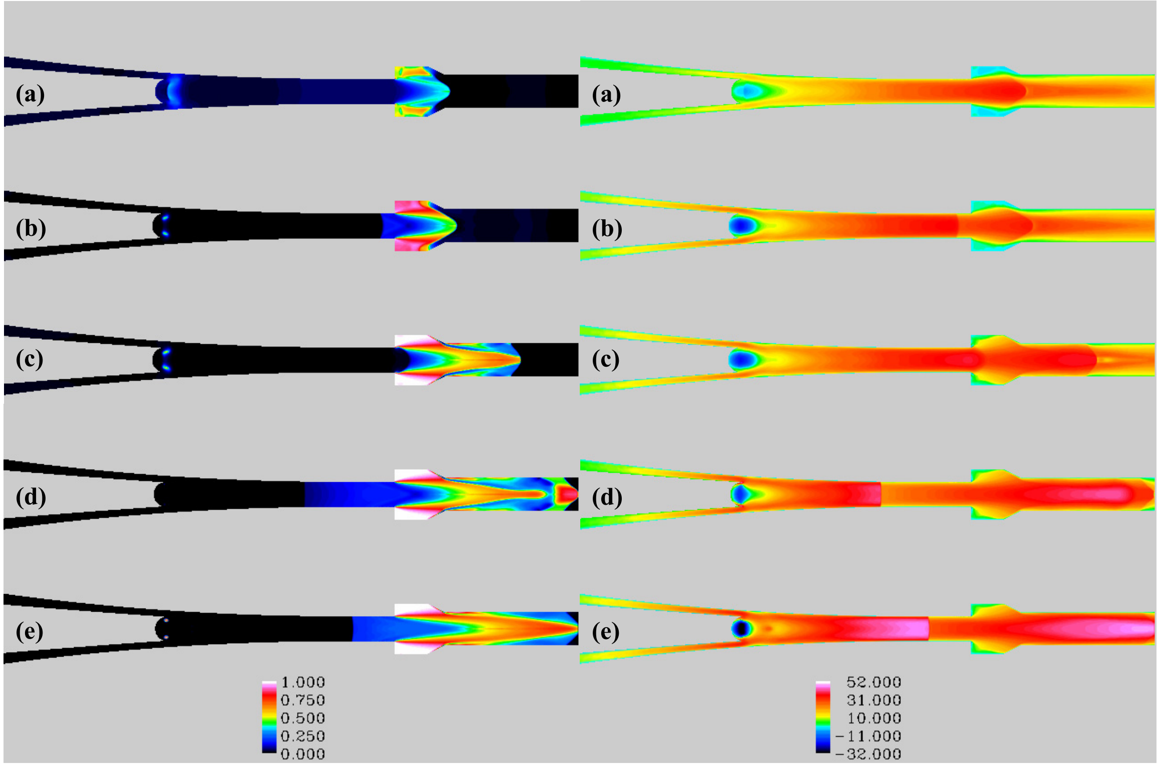

(i) (ii)

Figure 4.91: Contour plots of (i) Vapor volume fraction (ii) Axial-velocity magnitude using CFD computations on Configuration C_5- BFS type cavitating atomizer with increased L/D ratio

These results clearly indicate the boundary effects in flow profile development. Clearly experiencing a pressure outlet with an L/D ratio = 2 retards the growth of cavitation clusters since the flow has to locally adjust faster to the upcoming pressure boundary. With increase in the length of the constant diameter section, this constraint is removed and the flow relaxes slowly. The lowered flow relaxation rates have a profound impact on the cavitation rates due to the reduction in fluctuating quantities of velocity and pressure. The cavitation stretching is more enhanced, however, with reduced gradients along the mean flow. Since the cavitation zones extend longer, the effect of superimposed pressure perturbations using the horn motion results in uneven collapse of the cavity clusters near the nozzle exit. As the pressure wave passes along the diffuser section and towards the exit, its diffusion in the mixture is enhanced and hence its strength decays. This is clearly seen from the levels of turbulence achieved at the nozzle exit Fig (4.92(b)).

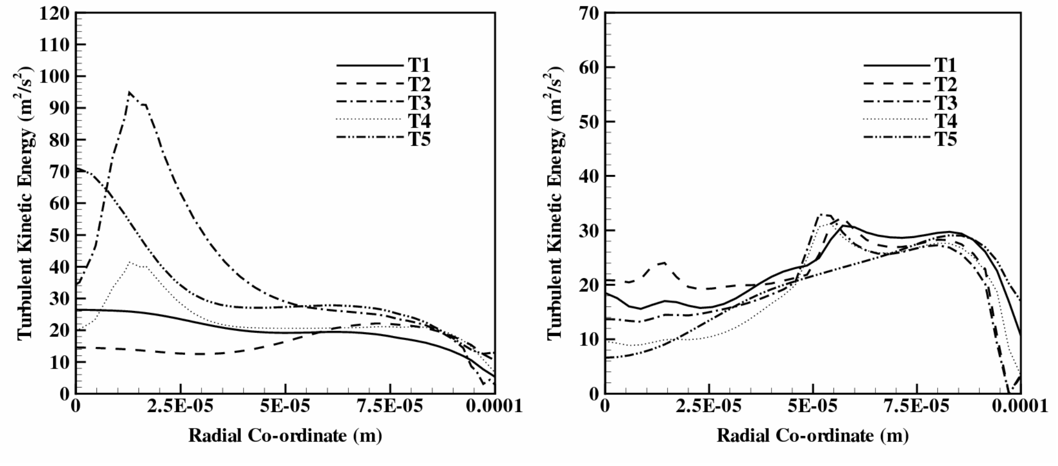

(a)

(b)

Figure 4.92: Plots of Turbulent Kinetic Energy distribution for (a) Configuration C_3 (b) Configuration C_5

In the present case, however, very strong modulation amplitudes (~0.5) with favorable mean velocities (~ 31 m/s) and vapor fraction distribution (~ 0.7) are obtained, suggesting strong potential for obtaining enhanced breakup at the nozzle exit.

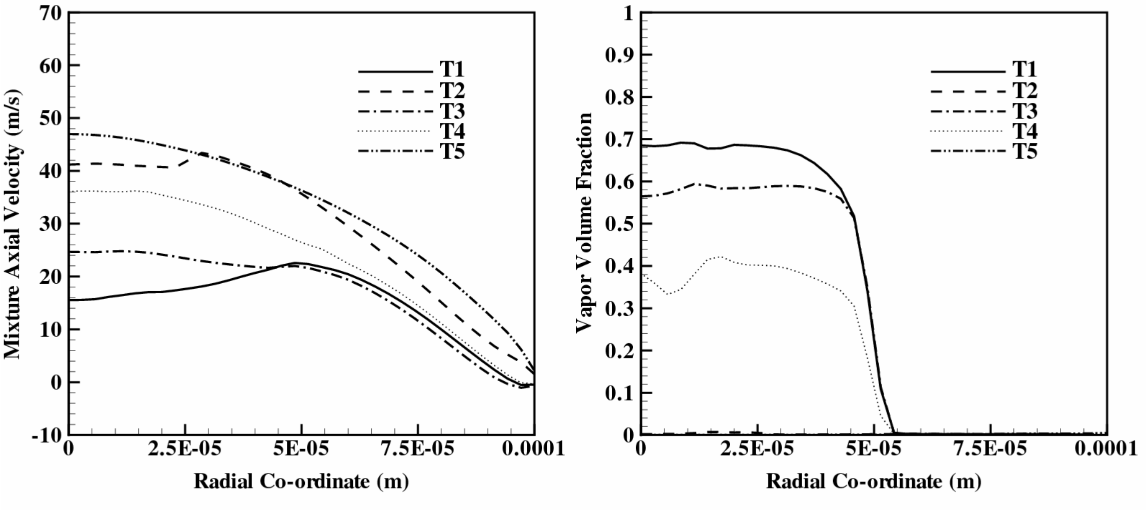

Figure 4.93: Plots of (a) Axial velocity and (ii) vapor fraction distribution at the nozzle exit for configuration C_5 at increasing time instants. $T_1<T_2<T_3<T_4<T_5$ separated by 1μs.

The comparison results between smaller and longer L/D nozzles shown in Fig. (4.92) favor the shorter L/D nozzle design tested in Section (4.8.3) due to the increased turbulent kinetic energy content available in the flow.

4.8.6. Case C_6: Diffuser chamber effect

In an attempt to increase the mixing process and enhance turbulence structure of the exiting jets, the effect of increased diffusion chamber length is addressed. Investigations reveal that cavitation clusters generated by shear layer phenomena tend to accumulate both in the large scale and small scale vortex structures [242, 247, 249]. Since the length of the residence chamber is increased, the vortical structures rolled up from the separation edge have sufficient time to be spaced within the diffuser region

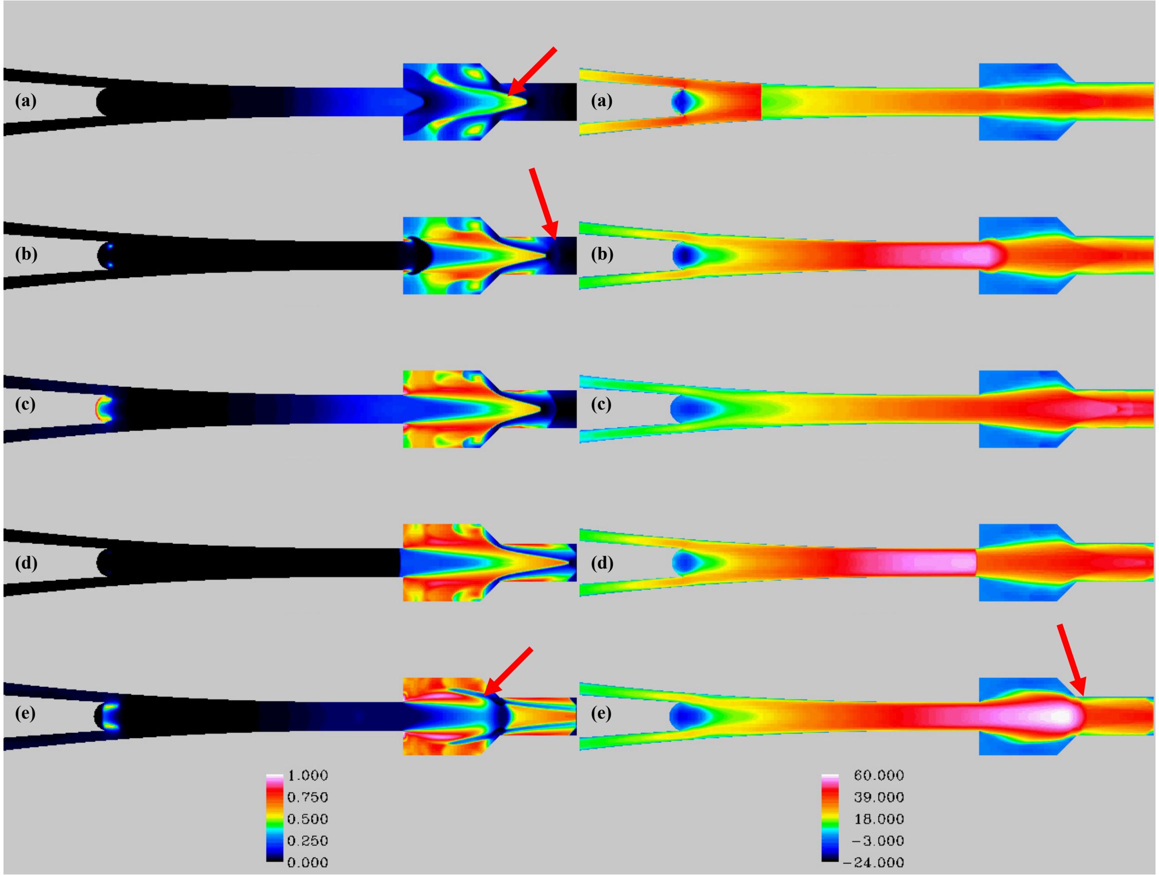

(i) (ii)

Figure 4.94: Contour plots of (i) Vapor volume fraction (ii) Axial-velocity magnitude using CFD computations on Configuration C_6- BFS type cavitating atomizer with diffusion chamber effect

During the initial simulation stages, approximately within 10 frequency cycles, cavitation regions mainly resided within the diffuser section showing little elongation into the constant diameter section Fig (4.94). However, as time progressed, cavity cluster elongations became pronounced and finally lead to events of supercavitation Fig. (4.94(i)). Clearly visible from Fig. (4.94 (i)) are the formation of cavitation clusters in the low pressure-recirculating zones present in the residence chamber. The interaction of cavities with the rolled up vortex structures result in the separation of cluster entities, Fig. (4.90(ii)). As indicated in Fig. (4.94 (i-a) & (i-b)), the collapse is concentrated towards the nozzle central core. Figure (4.94(i-e)) shows strong reversal flow effects on cavity collapse aided by accelerating velocity fronts as shown in Fig. (4.94 (ii-e)). Axial-velocity distribution at the nozzle exit portrayed in Fig. (4.95(a)) reveal increased mean velocities (~45 m/s) with a modulation ratio of 0.3. Certainly, supercavitation modes are obtained at the nozzle exit as plotted in Fig. (4.95 (b)).

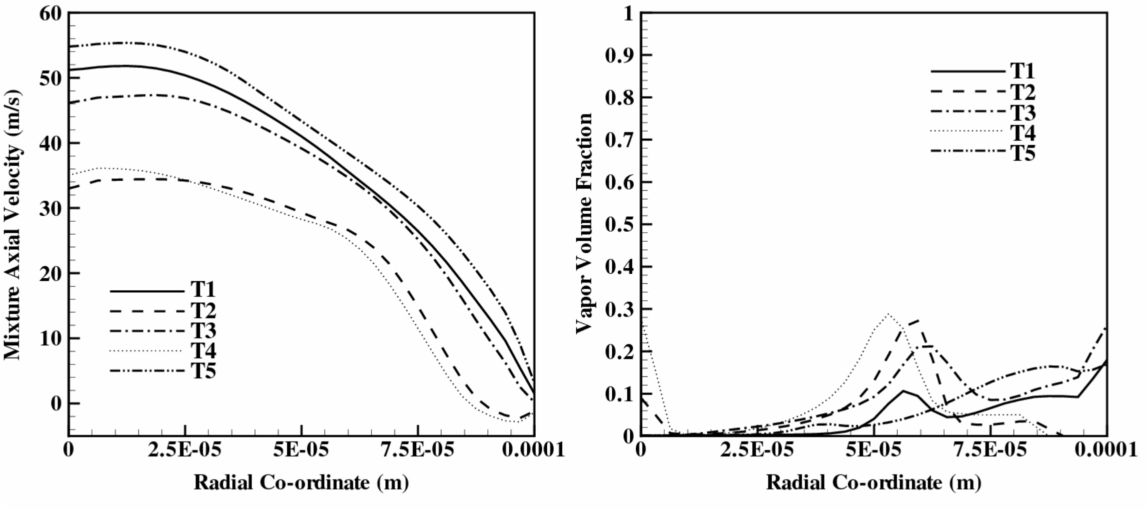

(a) (b)

Figure 4.95: Plots of (a) Axial velocity and (ii) vapor fraction distribution at the nozzle exit for configuration C_6 at increasing time instants. $T_1<T_2<T_3<T_4<T_5$ separated by 1μs.

From our knowledge of the modulation jets from Chapter 3, the velocities generated by this configuration are not favorable to create well modulated liquid jets and the high mean velocities can potentially result in long breakup lengths.

4.8.7. Case C_7: Flow rate modification

With application of reduced flow rates = 25 cc/min applied to the case discussed in Section 4.8.5, the extent of collapse of cavity clusters was controlled within the limits of the diffuser chamber zone. The flow rate effect on the vapor fraction distribution is identified in Fig. (4.96 (i)). Correspondingly, low velocity liquid jets are obtained with low modulation ratios.

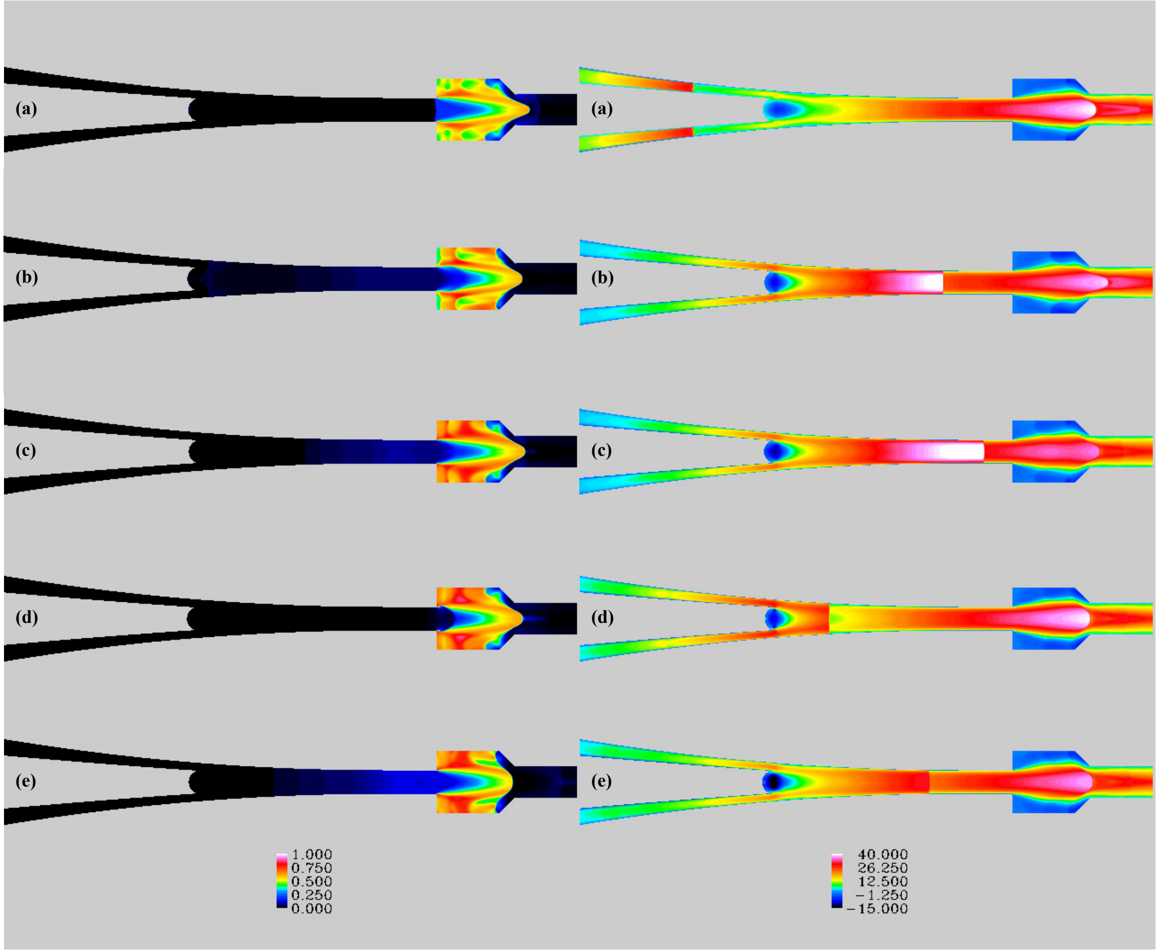

Figure 4.96: Contour plots of (i) Vapor volume fraction (ii) Axial-velocity magnitude using CFD computations on Configuration C_7- BFS type cavitating atomizer with expanded diffusion chamber and lowered flow rate

The velocity profile distribution at the nozzle exit is plotted in Fig. (4.97(a)) while Fig. (4.97(b)) describing vapor fraction exiting the nozzle shows no presence of mixture flow.

The velocity modulation obtained from the low flow rate model measured close to 0.2 with a mean velocity of 27 m/s, not sufficient enough to expedite liquid jet breakup.

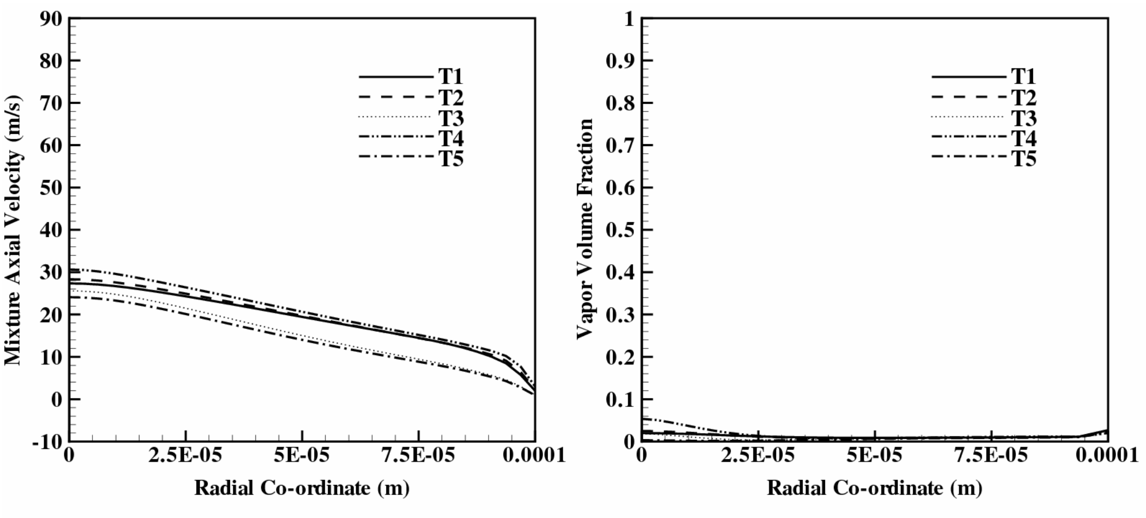

(a) (b)

Figure 4.97: Plots of (a) Axial velocity and (ii) vapor fraction distribution at the nozzle exit for configuration C_7 at increasing time instants. $T_1<T_2<T_3<T_4<T_5$ separated by 1μs.

4.8.8. Case C_8: Flow modulator design

In an another design modification, the length of the diffusion chamber is kept constant as in the case discussed in Section (4.8.5) and (4.8.6) while modifying the flow modulation inducer section. The convergence cone angle of the accelerating section is reduced to 22.5° to reduce the pressure gradient effect and thus enforcing a reduced momentum change rate. The results obtained from this alteration varied dramatically in comparison with the previous design detailed in Section (4.8.5). The volume fraction of vapor regions in the residence chamber increased to 1, indicating an intensified vapor production or an equivalent reduction in vapor collapse rates. Owing to the re-entrant jet type mechanism based on pressure gradient effects explained using Fig. (4.83), Fig. (4.98(i)) shows clear separation of the cavity layers from the walls and simultaneously resulting in a core-concentrated vapor distribution inside the nozzle.

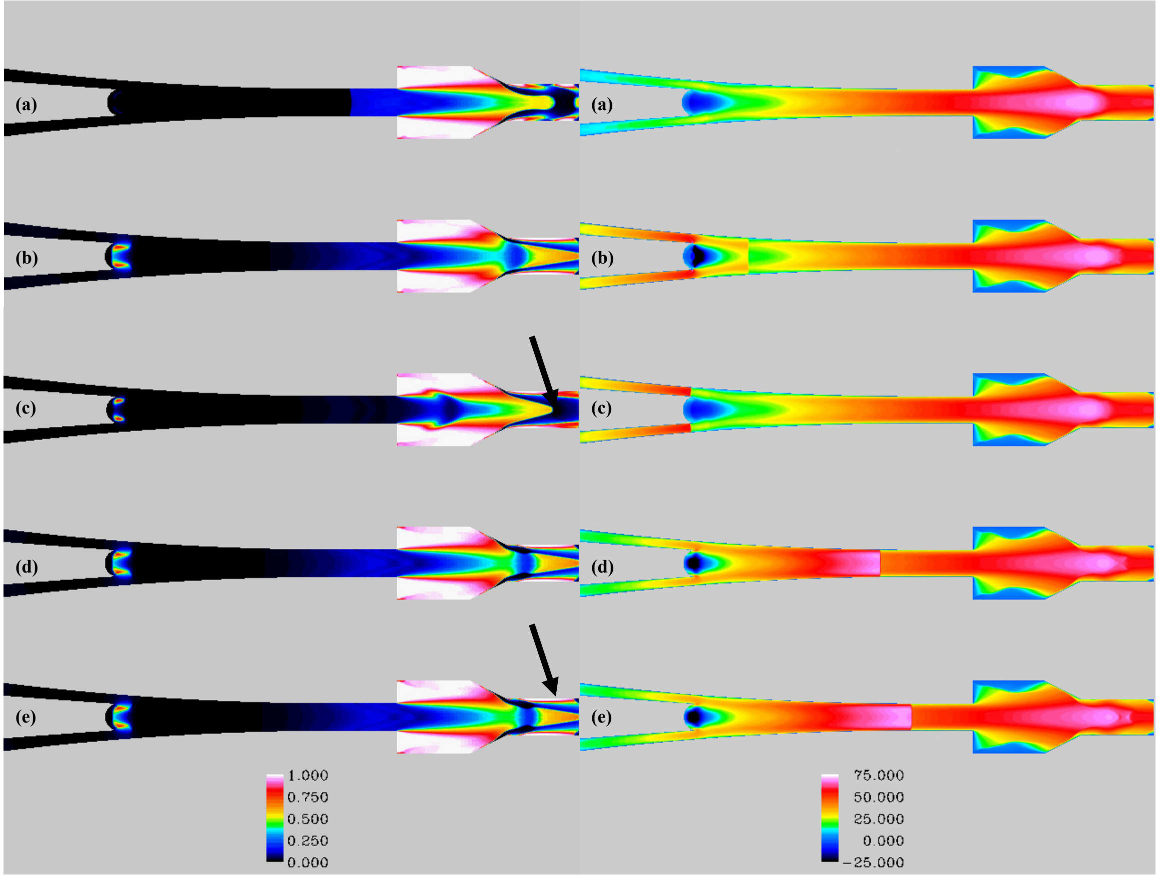

(i) (ii)

Figure 4.98: Contour plots of (i) Vapor volume fraction (ii) Axial-velocity magnitude using CFD computations on Configuration C_8- BFS type cavitating atomizer enhanced flow modulation

The increased vapor concentration in the diffuser section triggered increased mean velocities due to the mass conservation constraint. In addition, the increased flow speeds in the diffusion chamber is further intensified by the presence of flow modulation inducer section resulting in overall high velocity liquid jets exiting the nozzle domain. Owing to the elaborated effects, the liquid jet velocities at the nozzle exit were modified palpably as seen in Fig. (4.99(a)). Plots of vapor fraction distribution, Fig. (4.99(b)), at the nozzle exit detected strong presence of cavitating vapor regions along the nozzle walls.

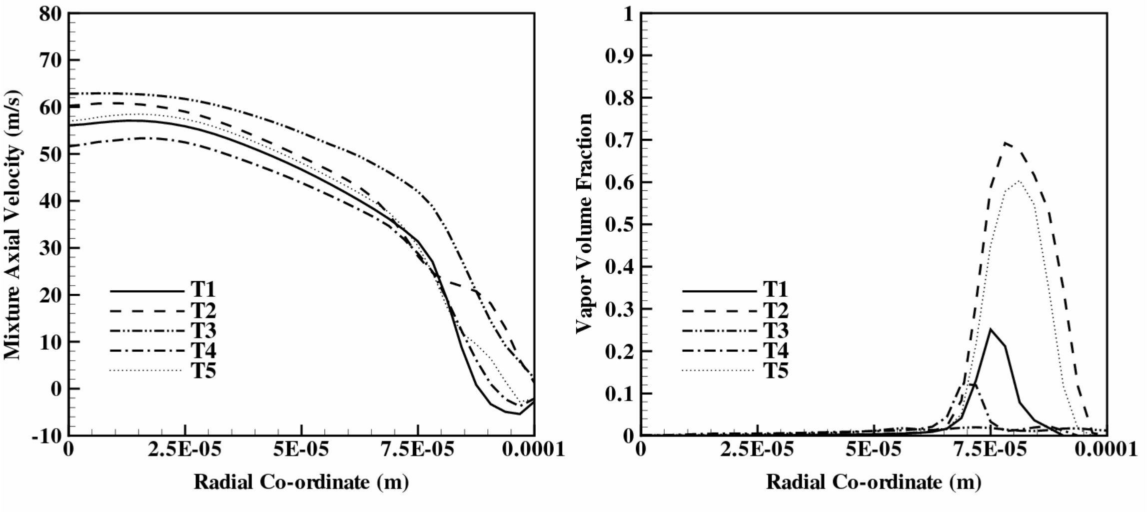

(a) (b)

Figure 4.99: Plots of (a) Axial velocity and (ii) vapor fraction distribution at the nozzle exit for configuration C_8 at increasing time instants. $T_1<T_2<T_3<T_4<T_5$ separated by 1μs.

Diverse simulations carried out, using a Backward facing step approach type cavitator, in Sections (4.8.1) through (4.8.7) indicated the strong influence of introducing pressure defects exploiting geometrical modifications. From the studies conducted, case C_3 portrayed promising results in terms of favorable exiting liquid jet variables, such as mean velocity, modulation amplitude and inherent kinetic energy, for prototyping purposes. The preceding studies are dedicated to advance testing of the atomizer design proposed in Configuration C_3.

An effect of horn position on the proposed atomizer design (C_3) is carried out to highlight the importance of horn placement in order to achieve desired cavitation and flow modulation characteristics. In this concern, five tests reported here are detailed in Table (4.6).

Table 4.6: Effect of horn position on Cavitation dynamics described by C_3 type atomizer

Configuration	**Basic Design Configuration**	**Modification proposed**	**Flow Rate**
C_9	C_3	*Horn placement such that horn tip covers 20 % of total flow area*	*50 cc/min*
C_{10}	C_3	*Horn placement such that horn tip covers 20 % of total flow area*	*25cc/min*
C_{11}	C_3 *modified with* $D_e = 1.66D_t$	*Horn placement such that horn tip covers 20 % of total flow area*	*25cc/min*
C_{12}	C_3	*Horn placement such that horn tip covers 30 % of total flow area*	*50 cc/min*
C_{13}	C_3	*Horn placement such that horn tip covers 30 % of total flow area*	*25 cc/min*

4.8.9. C_9 : Horn placement effect

The atomizer design presented earlier consists of the horn position placed in the flow such that it occupies 40% of the total flow area. For attaining 20% flow coverage area, the horn distance from the nozzle exit section is increased and its position results in a flow section where the mean liquid velocity is ½ the maximum speed of horn motion. Typically, it represents the position of the horn in a zone where the shear generated by the horn motion typically result in vortex motions away from the nozzle axis. This is attached to the fact that the surrounding liquid velocities are smaller in magnitude in comparison to the horn surface velocity. Hence, radial velocities emanate from the faster of the two fluid motions; here the velocity spreading starts from the shear layer generated by the horn and propagates away from the central axis. Distribution of vapor and axial velocity contours evolving in the domain are exposed in Fig. (4.96 (i) and (ii)) respectively.

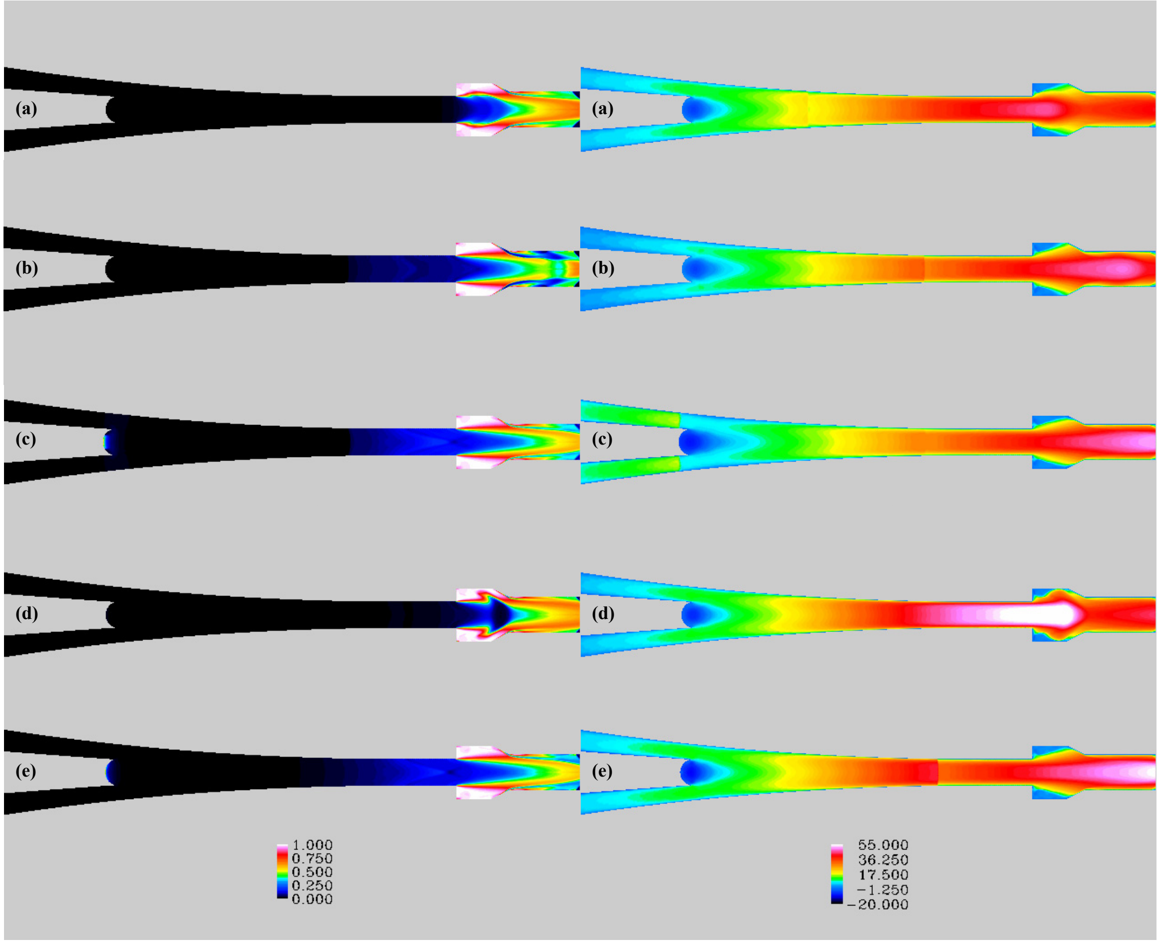

(i) (ii)

Figure 4.100: Contour plots of (i) Vapor volume fraction (ii) Axial-velocity magnitude using CFD computations on Configuration C_9- BFS type cavitating atomizer (Horn tip occupying 20% flow area)

Since, the pressure perturbation is now handled across larger cross-sectional area, the resulting modulation is enhanced, an effect arising from mass conservation. Since the product of area times the velocity across a section in a continuous fluid flow is a constant, fluctuating a larger area would result in increased modulation in a smaller area. As a resultant, shear layer enhancement is achieved near the separation edge resulting in intensification of the cavitation regions. As the pulsing effect in this scenario is stronger, events of supercavitation are easily achieved. Figure (4.101(a)) shows higher axial-velocity magnitudes at the nozzle exit using the same nozzle design from our baseline case, C_3 configuration, and by changing the position of the horn placement.

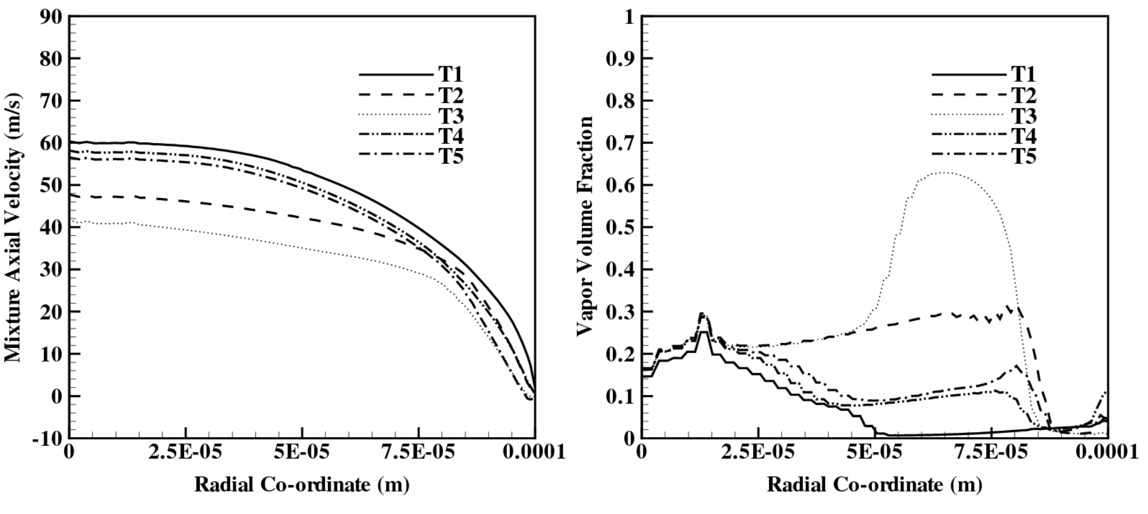

(a) (b)

Figure 4.101: : Plots of (a) Axial velocity and (ii) vapor fraction distribution at the nozzle exit. for configuration C_9 at increasing time instants. $T_1<T_2<T_3<T_4<T_5$ separated by 1μs.

One way to decrease the cavitation intensification in addition to combination of low velocity - high modulation is to decrease the flow rate into the system. This effect is tested by reducing the flow rate of the system to 25 cc/min as demonstrated in Section 4.8.9.

4.8.10. C_{10} Configuration: Effect of flow rate

Decreasing the flow rate dictates the net mass flow rate and in turn influences cavitation rates. The difference between the cavitation characteristics between Fig. (4.100(i)) and Fig. (4.102(i)) is self-evident. The cavity clusters in the present case are restricted to the diffuser section with reduced vapor fraction intensity. Strong collapse front, observed in Fig. (4.102 (ii-d)), indicate the effect of pressure reversal on the low flow rate (low inertial content) fluid flow. As a combined product of low fluid flow rate and reduced cavitation clusters occupying the flow passage, low velocity jets with low modulation effect are obtained.

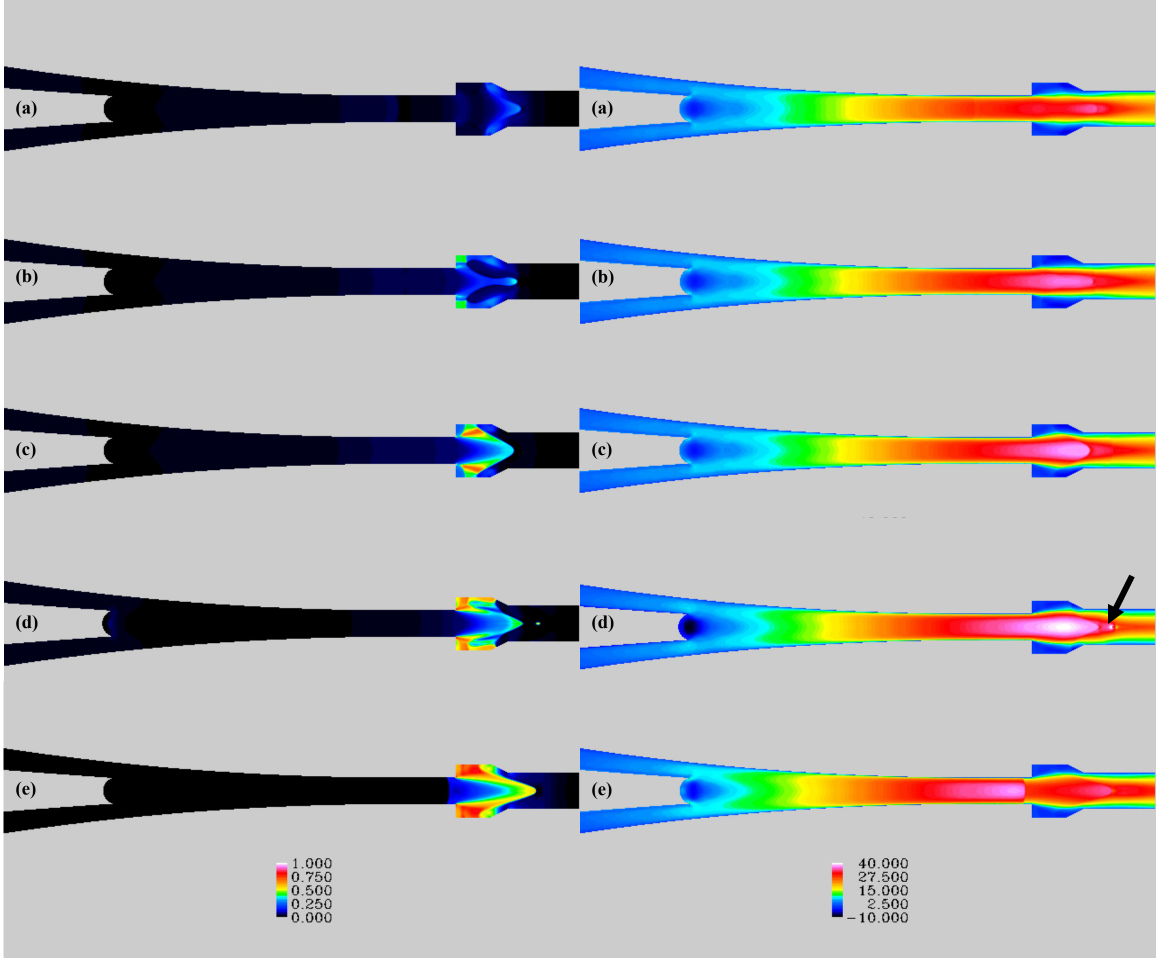

(i) (ii)

Figure 4.102: Contour plots of (i) Vapor volume fraction (ii) Axial-velocity magnitude using CFD computations on Configuration C_{10}- BFS type cavitating atomizer (Horn tip occupying 20% total flow area with low flow rate)

A plot of flow axial velocity distribution presented in Fig. (4.103(a)) fortifies this claim. A mean velocity of 27 m/s is obtained from the current configuration with modulation amplitude of 0.2. The modulated jet Strouhal number exiting the nozzle domain is evaluated as 1.5824. Heightened collapse effects deprive any events of vapor transport across the exit section, as elaborated in Fig. (4.103 (b)).

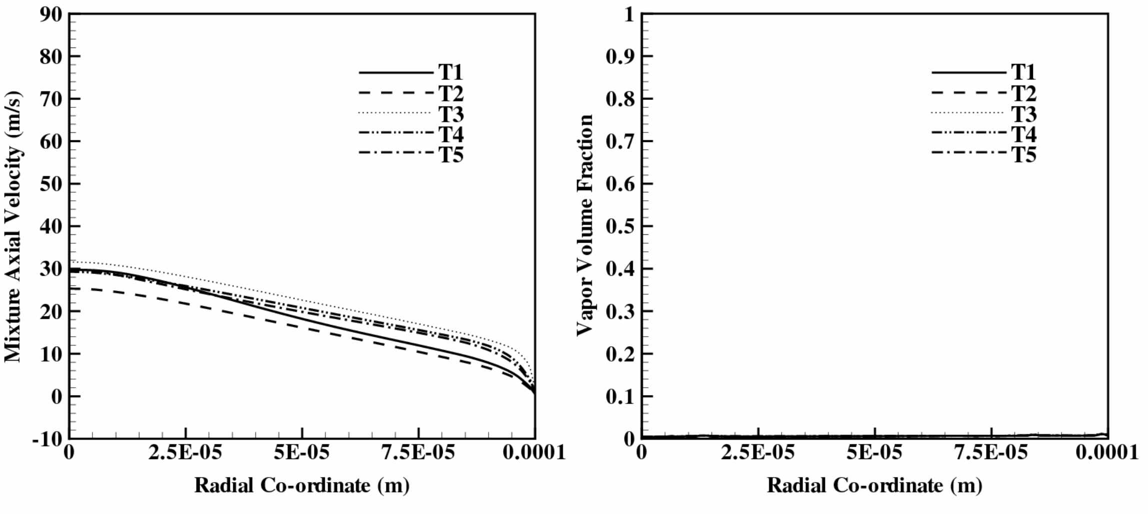

(a) (b)

Figure 4.103: Plots of (a) Axial velocity and (ii) vapor fraction distribution at the nozzle exit. for configuration C_{10} at increasing time instants. $T_1<T_2<T_3<T_4<T_5$ separated by 1μs.

4.8.11. Configuration C_{11}: Exit diameter effect

Modulating the flow exit velocity for a given mass flow rate can also be achieved by varying the exit nozzle diameter. The configuration presented here is a direct modification of the tested C_3 configuration with the exit diameter increased to 0.25 mm from 0.2 mm, while retaining all the other design parameters constant.

The results obtained for such a configuration is displayed in Fig. (4.104 (i) & (ii)). An observation similar to the one obtained with 0.2 mm exit diameter is predicted. Intense cavitation cluster regions are generated in the backward facing step profile zone. But with increase in the constant diameter cross sectional area, the collapse is accelerated. Further, the cavitation layer separation from the nozzle walls, due to the adverse pressure gradient near the corners of the flow modulation inducer section is seen diminished in an appreciable fashion. The cavitation clusters approach events of supercavitation.

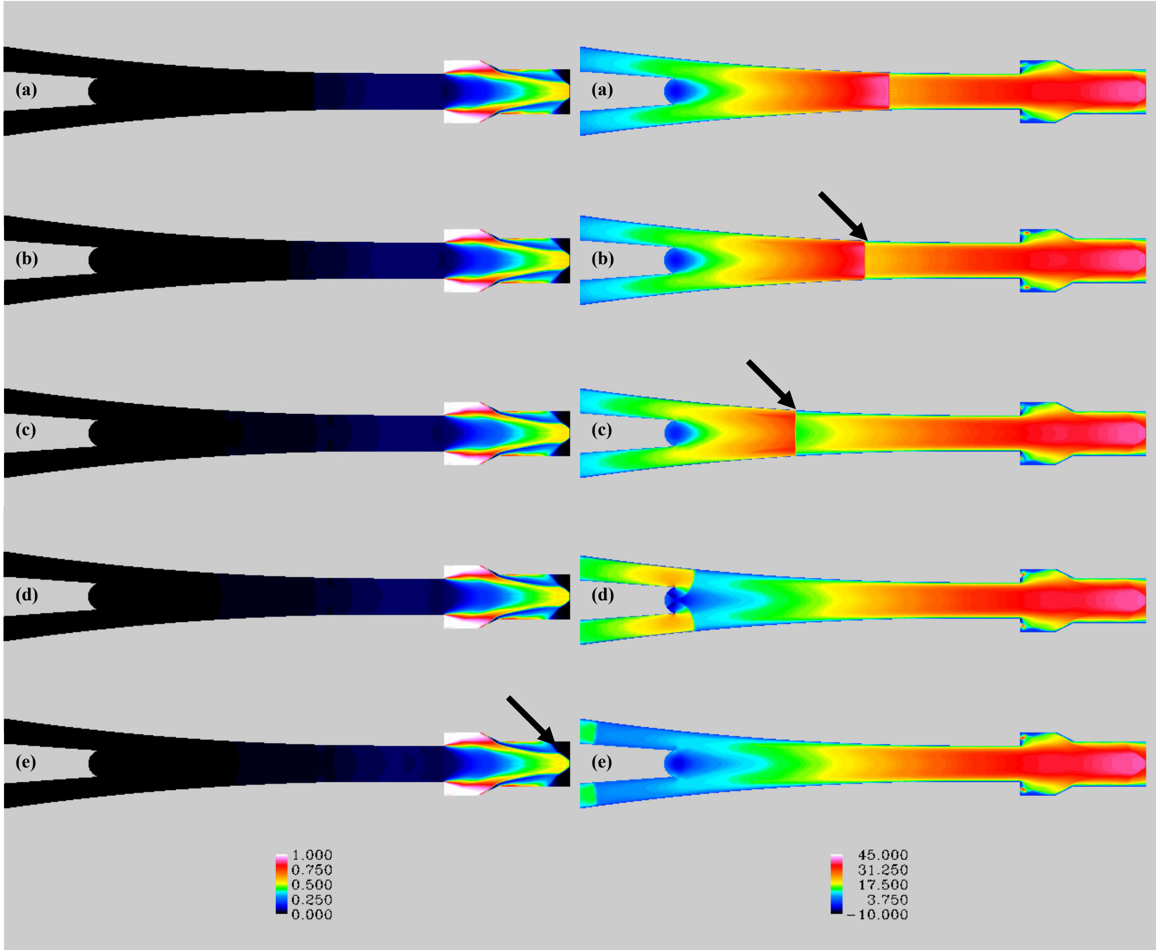

(i) (ii)

Figure 4.104: Contour plots of (i) Vapor volume fraction (ii) Axial-velocity magnitude using CFD computations on Configuration C_{11}- BFS type cavitating atomizer (Horn tip occupying 20% total flow area with low flow rate)

As the cavity cluster elongates into the main stream, the boundary layer in the constant diameter section enforce increased pressure gradients close to the nozzle walls leading to cavity sheets detachment from the nozzle surface. The volume fraction of vapor clusters exiting the nozzle is typically 0.5 with most of the vapor contents concentrated at the nozzle center. One important effect that requires special attention is the flow modulation produced by the design. Since, the flow modulation inducer section is considerably reduced in length due to a quicker introduction to constant diameter nozzle zone, the flow modulation achieved at the exit section compares very poorly against our previous test cases with a value of 0.15. The liquid jets emanate from the nozzle with modulation amplitude of 0.2 and a mean velocity of 33 m/s as observed from Fig. (105(a)). Concentration of vapor packets along the liquid central core is obtained, Fig. (105(b)). This is attributed to the effect of unfavorable pressure gradients and boundary layer effects in the near wall region along the nozzle surface.

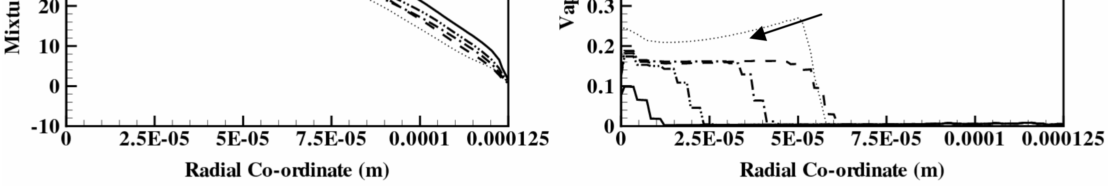

(a) (b)

Figure 4.105 : Plots of (a) Axial velocity and (ii) vapor fraction distribution at the nozzle exit for configuration C_{11} at increasing time instants. $T_1<T_2<T_3<T_4<T_5$ separated by 1μs.

4.8.12. Configuration C_{12}: Effect of horn position

The horn tip position is modified such that it occupies 30% of the overall flow area. Even with a 10% decrease in flow area modulated, the cavitation dynamics undergo magnified variations. The results pertaining to vapor fraction distribution in the nozzle domain look similar to the simulations results with the horn covering 20% of total flow area at 50 cc/min, Fig. (106 (i) & (ii)).

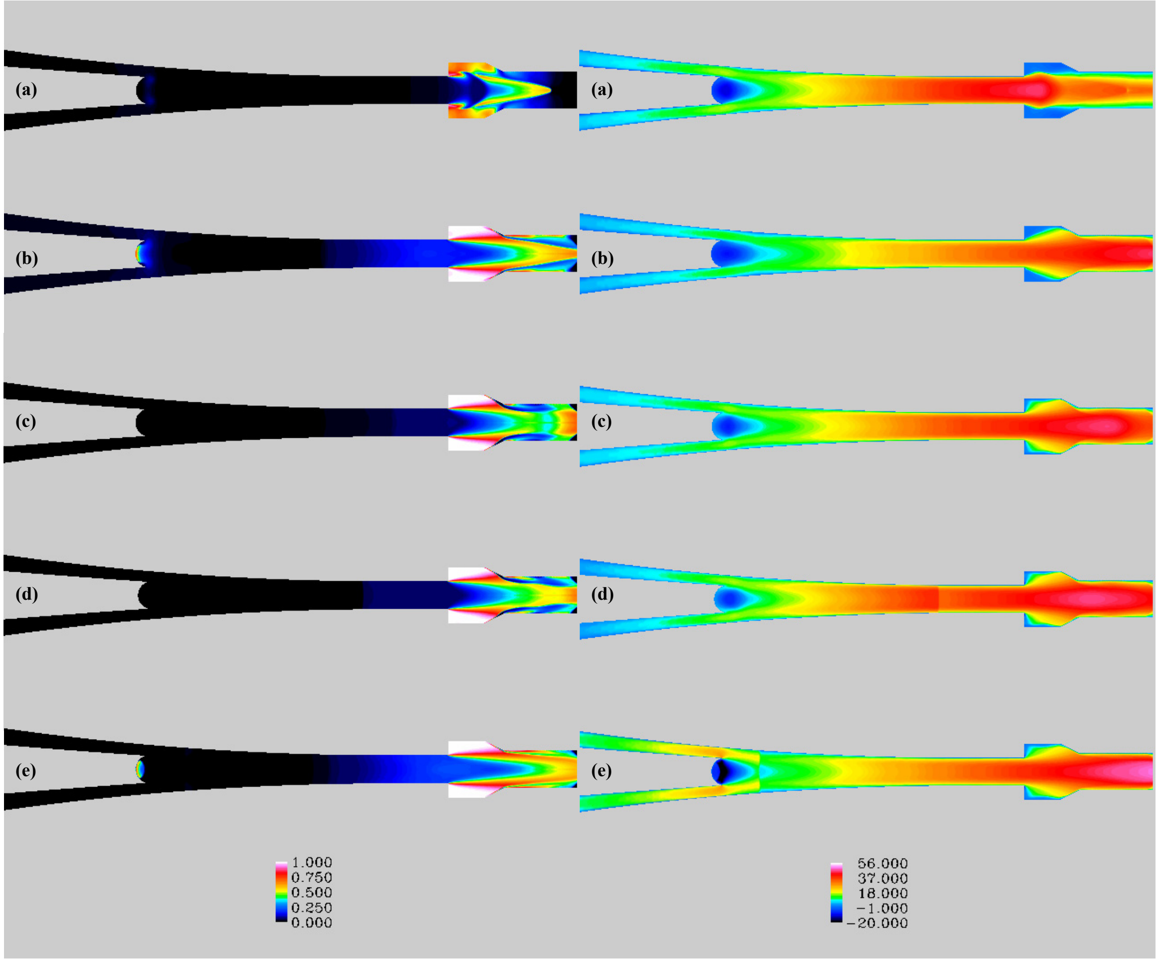

(i) (ii)

Figure 4.106: Contour plots of (i) Vapor volume fraction (ii) Axial-velocity magnitude using CFD computations on Configuration C_{12}- BFS type cavitating atomizer (Horn tip occupying 30% total flow area with low flow rate)

However, probing at the exit velocity profile of the liquid jet using Fig. (107(a)), a reduced modulation ratio of 0.3 with an average velocity of 47 m/s is concluded. This exit conditions result in a Strouhal number, *Sr* = 0.909 with a modulation amplitude of 0.3 indicating high probability of generating surface waves rather than promoting breakup. Observe from the plots of vapor fraction distribution at the nozzle exit, Fig. (107(b)), strong presence of cavitation clusters near the nozzle corners as compared to their existence near the central liquid core.

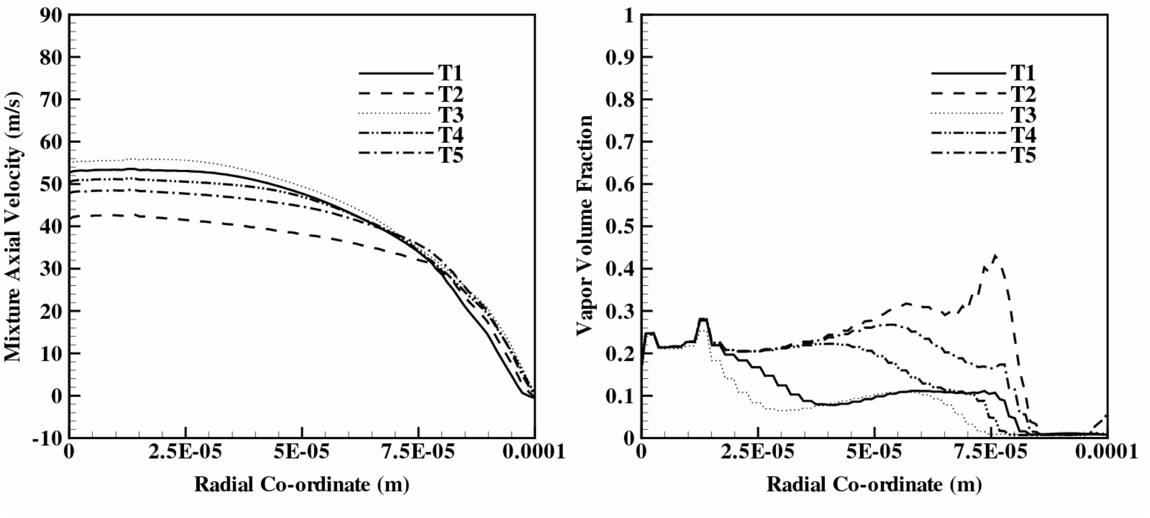

(a) (b)

Figure 4.107: Plots of (a) Axial velocity and (ii) vapor fraction distribution at the nozzle exit. for configuration C_{12} at increasing time instants. $T_1<T_2<T_3<T_4<T_5$ separated by 1μs.

4.8.13. Configuration C_{13}: Flow rate effects

CFD simulations are carried out by decreasing the flow rate of configuration C_{11} to 25 cc/min. Recognize from the contour plots presented in Fig. (4.108(i)), the cavity formation, growth and collapse transients are captured within the diffuser region. However, in striking contrast to the simulation performed with C_{10} configuration, horn occupying 20% flow area with a 25 cc/min flow rate, the intensities of the cavitation clusters are greatly reduced. The volume fraction achieved due to the shear layer formation and subsequent pressure fluctuation possesses a peak value of 0.6 only close to separation edge and flow modulation inducer corners. This is attributed to the combined effect of pressure oscillations and the horn placement effect on the strength of the shear layer induced in the separation edge of the backward facing step profile. Occasional coalescence owing to growing non-linearities in the system is observed such as in Fig. (4.108 (i-e)). Relaxed vortex interactions are achieved and slow down the collapse of the cavity clusters as they entrain into the constant diameter section of the nozzle. Reduced cavitation clusters are still incipient near the horn surface due to localized low pressure vaporization process resulting from the horn motion dynamics.

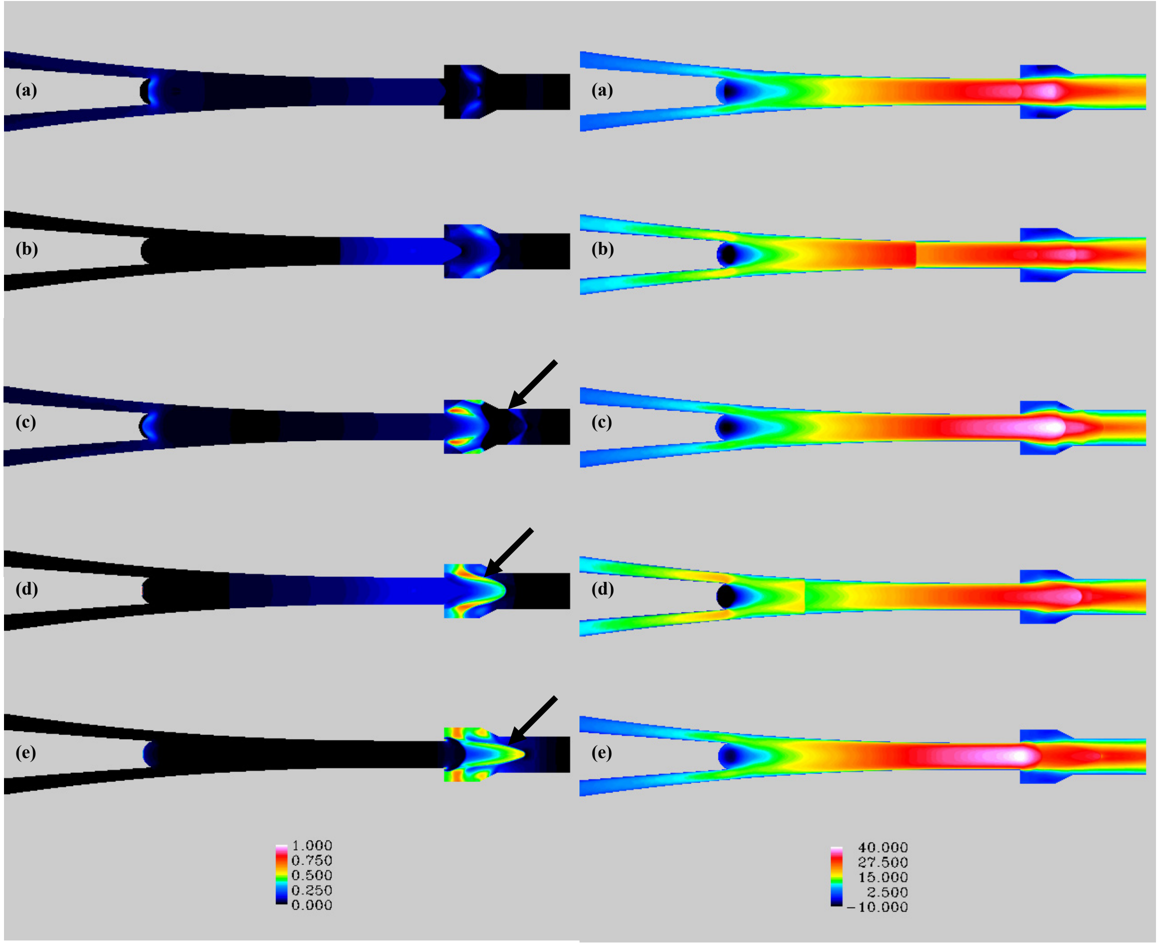

(i) (ii)

Figure 4.108: Contour plots of (i) Vapor volume fraction (ii) Axial-velocity magnitude using CFD computations on Configuration C_{13}- BFS type cavitating atomizer (Horn tip occupying 20% total flow area with low flow rate)

As revealed by exit section velocity profile plot in Fig. (4.109(a)), the velocity averages 30 m/s with modulation amplitude of 0.2. A strong boundary layer presence is acquired although no recirculation zones near the nozzle exit are detected. Vapor distribution plots at the exit section indicate no presence of cavitation clusters crossing the nozzle domain.

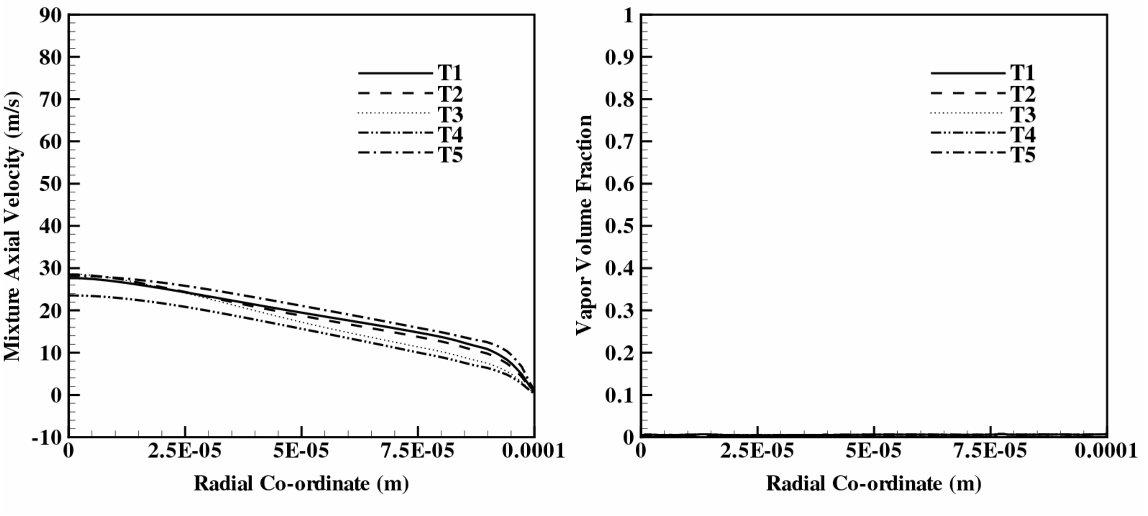

(a) (b)

Figure 4.109: Plots of (a) Axial velocity and (ii) vapor fraction distribution at the nozzle exit for configuration C_{13} at increasing time instants. $T_1<T_2<T_3<T_4<T_5$ separated by 1μs.

4.9 Closure

This chapter addressed the fundamental bubble dynamics issues and the major factors altering their behavior. It was observed from literature and carefully learnt that a cavitation bubble placed in a pulsating pressure field environment can lead to chaotic oscillations which might possible end in a collapse behavior resulting in rapid heat and mass transfer into the surroundings. Vibratory cavitation process utilize this mechanism as stated in Chapter 1 ; Since, the present atomizer model comprises of an oscillating horn placed within the nozzle boundaries, we studied the influence of horn parameters such as its frequency and amplitude on the fundamental cavitation bubble behavior by developing new models based on nucleation theories. The models were able to predict prolonged collapse behavior previously visualized in experiments. Extending the single bubble behavior based on nucleation theories to multiple bubble system, we identified the intricacies involved in treating a multi-bubble collapse configuration. Further, all these systems were treated in a much smaller domain; the domain size being the bubble size itself or the cylinder radius in the case of a cylindrical bubble array simulation. Since use of any such bubble dynamics model to simulate a more macroscopic industrial phenomenon would require enormous computational time and effort, we resort to the use large-scale cavitation models based on averaged bubble dynamics. In this concern, the reduced order bubble dynamic formualtion of Singhal et al. [237] was chosen due to its robust implementation in the commercial code Fluent. We use the commercial code for all the macro-scopic nozzle flow simulations presented in this chapter. The Fluent solver is used owing to its capability to handle dynamic meshes when the boundaries are varying with time. Concerning the atomizer design, various parameters such as horn tip profile, its stroke length, frequency and amplitude, flow rate and nozzle geometry effects are tested in a parametric fashion using a initial nozzle design. Extending further, numerical simulations are carried out using sharp cornered nozzles. Pulsation effects accelerate cavitation formation, detachment and propagation mechanism leading to a highly overall strained flow structure. The velocity modulation obtained with the sharp cornered nozzles resided in the range of 50 m/s and higher, which according to our numerical study in chapter 3, would take longer downstream distance to completely atomize.

Searching for a mechanism to improve turbulence, cavitation and the pulsation effects, implemention of a Backward Facing Step (BFS) profile configuration into the nozzle design was carried out. Since, the primary objective of the BFS profile is to enhance shear layer and improve turbulence, atomizer geometry based on different BFS configurations were constructed and numerically tested. The tests showed some interesting results and modulation behavior. Although the horn tip position was retained in the earlier part of the simulations, some modifications to the horn tip position within the nozzle interior was carried out in combination with modification to the flow rate. Among several atomizer design tested, we singled out configuration C_3, which was able to provide a mean velocity of 27 m/s with a modulation of 0.4 while generating some events of supercavitation. Using the numerical simulation results, the configuration also showed one-to-one correspondence in its collapse behavior with respect to the imposed oscillations. Moreover, the cavitation clusters generated within the nozzles were focused towards the nozzle central axis so that any events of hydraulic flip along the nozzle walls would be averted due to the presence of these low pressure cavitation zones near the exit region. In summary, the current chapter provided the required atomizer configuration for further testing to observe external spray formation.

Chapter 5

Coupled Computations of Free Surface Flows with Cavitation Effects

As noted from Chapter 2, a large number of experiments have been devoted to assess the influence of cavitation disturbances on the breakup of liquid jets. However, several complications associated with experimental techniques forced the scientific community to turn to numerical methods to investigate the dynamics of cavitation. In Chapter 4, numerical simulations of multiphase flows entailing cavitation was discussed in a predominantly incompressible framework. We noted that apart from interface tracking methods for simulating cavitation, continuum methods have been used in various forms. More recently, Schmidt et al. [231] performed numerical simulations on high speed cavitating injector flows using Homogeneous Equilibrium Model (HEM) in a compressible framework. His work incorporated a density based single-fluid compressible solver provided with an explicit analytical relation between pressure and density for closure of hydrodynamic equations. This method takes less computational time, since no pressure equation treatment is performed. However, the density based solvers suffer from instability and slow convergence at low Mach number limits [146, 236]. Further, use of discrete functional values in different zones can result in loss of transient characteristics inherent in the flow. Turkel et al. [235] noted that, in the low Mach number limit, the discretized solution of the compressible fluid flow fails to provide an accurate approximation to the incompressible equations. Several authors [234-236] have discussed the stiffness of the time dependent equations associated with the density based solver at low Mach number limit. The stiffness arises due to the mismatch of the acoustic speed and the fluid flow speed leading to slow convergence.

In this Chapter, a new solver procedure for predicting cavitating flows, treating liquid and vapor as a continuum has been constructed based on HEM. Compressible Navier-Stokes equations, decoupled from the energy equation, in combination with HEM are solved using pressure based methods on arbitrary unstructured meshes. Unlike the density based solvers previously used [231], this procedure built from first principles, solves pressure correction equations to compute the pressure variable. The resulting pressure correction equation automatically switches from hyperbolic behavior at high speeds to elliptic at low speeds [236]. The method has the advantage of simulating a wide gamut of Mach number flows without any preconditioning or asymptotic schemes [235, 236]. In this framework, pressure variation remains finite irrespective of the Mach number of the flow, offering computational capability throughout the entire spectrum of Mach numbers, an advantage over the density based methods. The pressure–coupling is achieved through PISO scheme [148], particularly suitable for simulating transient compressible flows. The requirement for volume fraction equation to update the mixture density is eliminated by the continuum assumption. The new methodology is used to qualitatively characterize the cavitation dynamics associated with high speed injector flows using a new pressure correction equation technique in conjunction with HEM. Varying pressure drop along the injector is used as a representative parameter in characterizing the cavitation dynamics. The flow is assumed to exit into a variable pressure chamber. The treatment of the boundary conditions is dealt with special interest, since reflective nature of boundary conditions, typically encountered in compressible flows can lead to erroneous calculations [234]. In the following section, a brief description of the governing equations and HEM assumptions are presented.

5.1 Mathematical description

5.1.1 Governing equations

In the homogeneous method, with the hypothesis of thermodynamic equilibrium, Navier Stokes equations in the compressible form are solved for a single phase flow. Because of the nature of the barotropic state relations, the energy equation is decoupled from the system [231]. This enables us to consider a reduced set of compressible flow equations involving only the mass and momentum conservation equations without the effect of gravity. The mass conservation equations, in tensorial form, can be expressed as

$$\frac{\partial \rho}{\partial t} + \nabla \bullet \left(\rho \mathbf{U} \right) = 0 \tag{5.1}$$

while the momentum conservation equations are given by

$$\frac{\partial \left(\rho \mathbf{U} \right)}{\partial t} + \nabla \bullet \left(\rho \mathbf{U} \mathbf{U} - \mathbf{T} \right) = 0 \tag{5.2}$$

where **T** is the total stress tensor defined as

$$\mathbf{T} = -\left(P + \frac{2}{3} \mu \nabla \mathbf{U} \right) I + 2 \mu \mathbf{D} \tag{5.3}$$

P in equation (5.3) is the pressure, *I* the unit tensor and **D** representing the rate of strain tensor. The strain rate tensor is elaborated as

$$\mathbf{D} = \frac{1}{2} \left(\nabla \mathbf{U} + \nabla \mathbf{U}^{T} \right) \tag{5.4}$$

The momentum equations are tightly coupled with density and viscosity relations. The density constitutive relations in the compressible scenario are given as functions of pressure:

$$\rho = \rho \left(P \right) \tag{5.5}$$

The effective viscosity of the mixture is given by,

$$\mu = \alpha \mu_{g} + \left(1 - \alpha \right) \mu_{l} \tag{5.6}$$

where μ_g and μ_l are viscosities of vapor and liquid phases respectively and α the volume fraction of vapor in the given computational cell. In the current simulation, no turbulence model has been included to effect any change in the viscosity of the mixture. The additional viscosity, turbulent viscosity due to the flow turbulence and dissipation, has been neglected. The dropping of the turbulent viscosity term can be attributed to the fact that the order of magnitude of turbulence generated by cavitation alone is far higher than that of the flow [97]. Although, several authors [178, 179] hinted at the influence of turbulence on the events of cavitation, implementation of turbulence models in the compressible framework would be the scope of future work. In sum, we solve for unsteady laminar compressible Navier Stokes equations in the flow domain using HEM assumptions for relating the mixture density to the variation in pressure fields.

5.1.2 Closure of hydrodynamic equations

The accuracy of numerical simulations on liquid flow with phase change rests on the modeling of the closure of hydrodynamic equations. The assumption of homogeneous equilibrium of different phases of the liquid in the flow leads to the conservation of energy statement with viscous dissipation terms. The pressure and enthalpy of mixture terms are several orders of magnitude higher than the conduction and viscous dissipation terms in the energy balance equations [231]. Using an isentropic assumption in the flow domain, and neglecting contributions of viscous dissipation and thermal conductivity, the energy statement can be reevaluated as

$$a^2 \frac{D\rho}{Dt} = \frac{DP}{Dt} \tag{5.7}$$

The above equation (5.7) can be considered as an isentropic model in a phase change process, where the speed of sound is given by the Homogeneous Equilibrium Model (HEM) [230] as

$$dP = a^2 d\rho \tag{5.8}$$

Where a, the speed of sound in the two phase mixture, is given by,

$$a = \sqrt{\frac{1}{\left(\alpha.\rho_g + (1-\alpha)\rho_l\right).\left(\frac{\alpha}{\rho_g.a_g^2} + \frac{(1-\alpha)}{\rho_l.a_l^2}\right)}} \tag{5.9}$$

The values of a_g and a_l being the speed of sound in pure gas and pure liquid phases respectively. ρ can be identified as the mixture density related to pure liquid and vapor densities as

$$\rho = \alpha\rho_g + (1-\alpha)\rho_l \tag{5.10}$$

From expression (5.10), void fraction α is obtained as

$$\alpha = \frac{\rho - \rho_l}{\rho_g - \rho_l} \tag{5.11}$$

The fluid in the current simulation is considered as single-phased, whose density varies from liquid to vapor according to the barotropic equation of state. The local vapor fraction predicted based on equation (5.11) is used in computing the speed of sound of the mixture using equation (5.9). The expression presented in equation (5.9) considers the fluid homogeneously mixed on the sub-grid scale [230] which forms the basis of HEM. The relative velocity between the phases can be neglected based on the homogeneous approximation leading to single phase equations with a mixture equation of state [231]. When the pressure of the mixture is either well above or below the vapor pressure the speed of sound is large but finite and the flow is considered weakly compressible. In the phase transition region, the speed of sound retains a small speed of sound. However in practical computations, the mach number of the flow would vary from 0.001 to as high as 30. Hence, for efficient computation of the multiphase mixture with the homogeneous assumption it is required that the time marching procedures are stable and accurate in the range of mach numbers specified.

5.1.3. Computational methodology

In simulating cavitating injector flows, Schmidt et al. [231] used analytically integrated expressions to explicitly solve for the pressure values in the cell as a function of density. Performing an accurate transient simulation of the cavitating flows with incompressible zones and highly supersonic (vapor-liquid mixture), requires dealing with the strong gradient discontinuities with radical changes of physical quantities near saturation regions. In the present scenario, the analytical expressions are replaced by a transient pressure-correction equation which implicitly incorporates various transition regions occurring in the multiphase mixture flow. The current simulations performed are based on finite volume discretization available in the openFoam framework [144], used for simulating continuum mechanics. Computations are performed over unstructured grids, with a collocated variable arrangement [138, 150]. Rhie and Chow [149] interpolation schemes are used for obtaining face values. The interpolation method works well on co-located meshes where pressure gradients are the major driving force, typical in the case of injector domains [149]. In the current methodology involving unsteady compressible flows, Pressure Implicit with Splitting of Operators (PISO) scheme has been utilized for pressure-velocity coupling. This pressure-velocity treatment proposed by Issa [148], originally developed for non-iterative computation of unsteady compressible flows. This pressure implicit method uses a predictor-corrector approach to advance the momentum equation while enforcing the continuity equation. In the compressible PISO formulation [148], the pressure–density coupling is introduced only through the time-dependent term of the continuity equation, which helps enforce a strong coupling between the density variation and the flow field. In the following sub-section, a brief description of the formulation of pressure correction equation and relevant numerical analysis is presented.

5.1.4 Discretization procedure

In order to accurately solve the constitutive governing equations to resolve the transient behavior of the compressible flows, the development of a pressure correction equation absorbing the effect of phase change is instrumental. In this section, we detail the discretization procedure of the governing equations, leading finally to the development of the pressure correction equation. Rewriting the momentum equation, we have

$$\frac{\partial(\rho\mathbf{U})}{\partial t}+\nabla\bullet(\rho\mathbf{U}\mathbf{U}-\mathbf{T})=0 \tag{5.12}$$

The accurate prediction of pressure-velocity coupling is very crucial in resolving the non-linearity present in the momentum equation. In the finite volume framework, the non-linear convection terms can be linearized [147] and written as

$$\begin{aligned}&\nabla\bullet(\rho\mathbf{U}\mathbf{U})=\sum_{face} Su\bullet(\rho\mathbf{U})_{face}(\mathbf{U})_{face}=\sum_{face} Fa(\mathbf{U})_{face}\\&\sum_{face} Fa(\mathbf{U})_{face}=aa_P\mathbf{U}_P+\sum_{Ne} aa_{Ne}\mathbf{U}_{Ne}\end{aligned} \tag{5.13}$$

Where *Fa*, the face flux and the coefficients aa_P, aa_{Ne} are functions of *U*. After standard discretization procedure [147], the semi-discretized form of momentum equations equation (5.2) can be written as

$$aa_P\mathbf{U}_P=HP(\mathbf{U})-\nabla P \tag{5.14}$$

Rewriting the discretization equation for velocity

$$\mathbf{U}_P=\frac{HP(\mathbf{U})}{aa_P}-\frac{\nabla P}{aa_P} \tag{5.15}$$

where

$$HP(U) = \sum_{Ne} aa_{Ne}\mathbf{U}_{Ne} \,. \tag{5.16}$$

5.1.5 Formulation of pressure equation

In evaluating compressible flows the fluid density can be related to the fluid compressibility factor as

$$\rho = \psi P \tag{5.17}$$

where Ψ is the compressibility of the mixture. Using the isentropic phase change considerations, the compressibility can be calculated as

$$\psi = \frac{1}{a^2} \tag{5.18}$$

Equation (5.18) helps in the closure of hydrodynamic equations by relating the density functional with the pressure variable using the compressibility factor. Combining equations (5.1), (5.15) and (5.18), we have

$$\frac{\partial \psi P}{\partial t} + \nabla \bullet \left(\frac{\rho HP(\mathbf{U})}{aa_P} \right) - \nabla \bullet \left(\frac{\rho \nabla P}{aa_P} \right) = 0 \tag{5.19}$$

Further, using equation (5.17) to represent density as a function of pressure and speed of sound in the liquid-vapor mixture, we have

$$\frac{\partial \psi P}{\partial t} + \nabla \bullet \left(\frac{\psi HP(\mathbf{U}) P}{aa_P} \right) - \nabla \bullet \left(\frac{\rho \nabla P}{aa_P} \right) = 0 \tag{5.20}$$

Equation (5.20) represents the characteristic pressure equation for compressible flows derived from continuity and momentum equations. The equation has the compressibility factor associated with the pressure in the unsteady time derivative and with the velocity in the convection terms. From a preliminary analysis of the characteristic pressure equation, we can deduce that improper numerical treatment can result in an unbounded nature of the individual terms and can propagate into unrealistic results in the domain [150]. For improving accuracy and obtaining boundedness criteria, a blending scheme (combined upwinding and central differencing) is used in the treatment of non-linear terms [146, 147, 150].

For steady flow computations, the nature of pressure-density coupling affects the convergence since the final solution becomes independent of the coupling due to the nature of pressure correction equations. However, in the unsteady formulations, the choice of pressure-density coupling is crucial, since it relates to the propagation of information from the cavitation region to the rest of the domain. Treatment of the divergence terms in an explicit manner leads to an elliptical solving procedure which enhances convergence as compared to hyperbolic systems. Note that in the event that the flow regimes tend toward very low Mach numbers, the equations would typically reduce to the familiar solenoidality condition pertaining to incompressible flow [138, 150]. The implicit implementation of the pressure equation helps in maintaining the computation convergence. Explicit first order time integration procedure with two corrector steps within the PISO procedure is carried out. The predictor corrector equations formulated using PISO and the density equations are solved using Incomplete-Cholesky Preconditioned Biconjugate gradient method (BICCG). The courant number for the simulation is maintained at 0.2 to improve accuracy of the simulation and improve convergence of the procedure.

5.1.6. Model Validation

The unsteady cavitating flow formulation presented in Section (5.1.3) is applied to a simple injector nozzle geometry used in the experiments of Roosen et al. [107]. In the present study, no interaction of cavitating flow with nozzle exterior is considered. The experimental set up consists of a rectangular shaped channel 0.2mm × 0.28mm × 1mm representing the width, height and length respectively. For validating the formulation, only two-dimensional calculations are considered (width neglected) in the current study. The end effects arising due to the constriction of the passage in the width-dimension may modify the flow structure by inducing three dimensional vorticity components. However, the effect of these interactions in the orthogonal sense to the bulk flow is neglected in the current study. Physical domain used for the simulation is shown in Fig. (5.1).

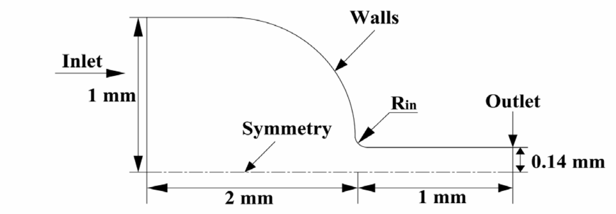

Figure 5.1 Physical domain of Roosen et al. [107] used for Cavitating flow computations

We use the same sac hole entrance curvature of R_{in} = 0.1×height as applied in the computations of Yuan et al. [226]. The simulation uses unstructured triangular meshes for finite volume discretization in the nozzle domain. Mesh clustering operation is performed near the contraction corners in the nozzle to capture high pressure and density gradients accompanying phase change (cavitation inception). The left inlet boundary, representing a reservoir, is specified with a total inlet pressure. The wall conditions with no-slip boundary conditions for velocity and zero gradient condition for pressure fields are imposed. The outlet is designated as a pressure outlet representing free stream conditions at the nozzle exit. In order to qualitatively compare our simulation results, we use water as the testing liquid as in the case of experiments. All properties of water and water-vapor have been taken at Standard Temperature and Pressure (STP). Variation of speed of sound in the water-vapor mixture is shown in Fig. (5.2).

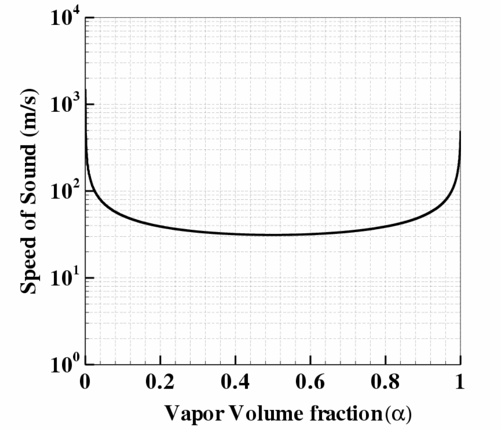

Figure 5.2: Speed of sound in water-vapor mixture estimated using equation (5.9).

5.1.7 Treatment of boundary conditions

The conditions prevailing at pressure outlet are very complicated due to the interaction of the boundary with the liquid-gas compressible mixture. In this context, it is essential to understand that the boundary conditions for subsonic outflows can be reflecting. Hence, the boundary condition must be able to accommodate two phase regimes and be able to allow acoustic waves generated by the two phase flows to pass through them. If the boundary conditions are reflective, they would back transmit perturbations affecting the upstream leading to totally non-physical behavior of the flow structure. In highly non linear cavitating flows, exit boundaries are often supersonic when the neighboring cells contain mixture of the phases although the exit conditions may be subsonic for the flow of pure liquid phase. This local supersonic regime is caused because the cell containing vapor phase has a low sonic speed. We use NSCBC (Navier-Stokes Characteristic Boundary Conditions) approach, expressing Navier-Stokes equations as characteristic equations at the boundary [269]. The conservative equations at the exit are written in terms of characteristic equations with characteristic wave amplitudes and propagation velocities of characteristic waves. Poinsot et al. [270] suggested incoming characteristic wave of the form

$$l_1 \propto \kappa ref\left(P_{exit} - P_2\right) \tag{5.21}$$

where l_1 is the incoming characteristic wave that transmits downstream pressure back into domain with P_{exit} being the current pressure value at the boundary between a cell and exit. P_2 represents the specified exit pressure. An approach to estimate this constant has been presented by Poinsot et al. [270]. With specified *κref* value, the boundary condition causes the downstream pressure to vary from the specified downstream pressure to allow structures such as waves and vapor regions to pass through without reflection. The construction of this constant is critical, since it shows the reflecting nature of the boundary condition. An increase in the *κref* value leads to a strong coupling with the specified downstream pressure, which implies that the boundary becomes more reflecting. When the cavitation regions extend to the domain exit, no relaxation over the exit pressure is made, such that the regions exit the domain without any numerical collapse. Hence, using NSCBC characteristic equation situations arising from subsonic inflow, supersonic inflow, subsonic outflow, supersonic outflow conditions at the nozzle exit are computed [269]. Further, current study prohibits any occurrence of hydraulic flip phenomena [2, 48, 54, 59, 100], where gases present in the downstream of nozzle can move into the nozzle and act to stabilize the liquid flow, typically occurring during events of supercavitation.

5.2. Test cases

Experimental studies have confirmed that the cavitation number (σ_c) and Reynolds number (Re) are the most important parameters to describe similarity of cavitating flows in nozzles [2, 33]:

$$\sigma_c = \frac{P_1 - P_2}{P_2 - P_v} \tag{5.22}$$

$$\mathrm{Re} = \frac{\rho_l U_l D_l}{\mu_l} \tag{5.23}$$

where p_1 and p_2 are pressures upstream and downstream of the nozzle, p_v is the vapor pressure, U_l is the average velocity of the flow, and D_l is the hydraulic diameter of the nozzle. We base our discussions on the cavitation number, although Re is critical in providing insight on the turbulence intensity present in the system. For validation purposes, the computations were performed with a constant inlet stagnation pressure of 80 bar and varying exit static pressures: (a) 16 bar (b) 19 bar. These numerical experiments help us analyze in detail the influence of the pressure drop, or equivalent cavitation number, on the transient nature of cavitating flows and related phenomena such as vapor shedding, collapse etc., A constant value of $\kappa ref = 0.01$ is used throughout the simulation unless otherwise stated.

5.2.1 Exit pressure: 16 bar

With $\sigma_c = 4.0$, our transient simulation revealed acceleration of the fluid near the entrance regions of the bore hole resulting in flow separation and formation of vena contracta. Since this separation zone serves the low pressure requirement for the inception of cavitation, the first occurrence of vapor pockets was spotted near the entrance region. The flow separates from the outer wall as the fluid enters the sac, but then reattaches near the nozzle entrance. Formation of circulation regions as well as their stretching mechanism and events of vapor formation are shown in Fig. (5.3).

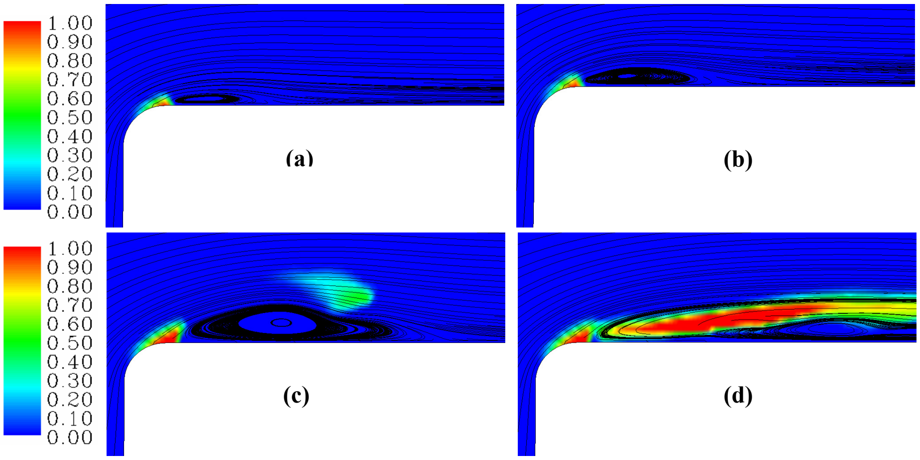

Figure 5.3: Separation near nozzle entrance region and stretching of circulation zones observed for flow with $\sigma_c = 4.0$. Separation zones occur at a small distance away from the entrance corners.

The formation of vena contracta reduces the effective flow area resulting in higher velocities, due to conservation of mass. Consequently, the conservation of momentum results in pressure depression due to accelerating liquid flow. This increase in liquid velocity supplies the vapor cavities with low pressure required for their growth [34]. As flow evolves, the reattachment zones restricting the cavity length tend to elongate. The low density vapor pockets that are initiated near the nozzle corners extend downstream to form a stable film. The vapor cavities thrive on the low pressure content zones close to the nozzle walls.

The formation of vapor cavities and subsequent events leading to a ‘stable’ supercavitation regime are presented in Figs. (5.4(a) – (e)). Some collapse features near the exit section of the nozzles may vary from actual experimental results [271] due to the very fact that we allow partial transmission (partially reflecting condition) of pressure waves across the boundary. In reality, several other mechanisms such as free surface interaction of the issuing jet with atmosphere, hydraulic flip etc., might influence the collapse characteristics of the cavitation clusters [2, 48, 54, 271].

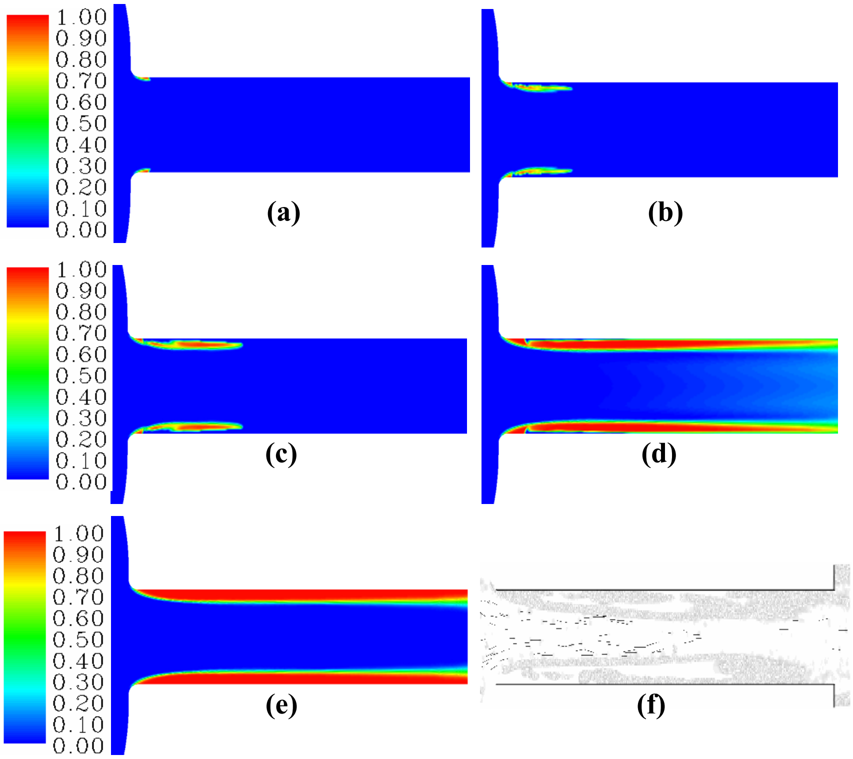

Figure 5.4: Computations with $\sigma_c = 4.0$ results in events of stable supercavitation (a) – (e). This behavior is observed to resemble the experimental results [107] shown in (f).

In the present formulation, since the density change is tightly coupled with the fluid velocity, the low density regions resulting from appearance of cavitation clusters, is well identified based on the local flow conditions. In this case, the pressure drop across the sac is strong enough to carry portions of vapor cluster past the nozzle exit against the re-entrant jets leading to stable vapor film. It has been experimentally shown that the cavitation number strongly influences the cavity length and events of supercavitation [2, 3, 47, 48, 56, 57].

The clusters formed at the corners are swept downstream by the accelerating fluid. The local density modeled using a transient compressible formulation in the current investigation reflects the pressure history encountered by the fluid in the regions prone to cavitation. The transient variation of vapor fraction and *x*-component of velocity at the nozzle exit is plotted in Fig. (5.5) to analyze the constancy of the cavitating system.

Our transient-pressure-based framework helps capture the temporal effects of the cavitation phenomenon in the entrance region and in the downstream region. In the current simulations, the initial cavity formation was highly transient with severely fluctuating vapor regions. However, as the simulation progressed, the cavity length was stabilized and a quasi-steady behavior of the vapor regime was obtained. Figure (5.5(a)) shows existence of a stable vapor film with a steady distribution at the nozzle exit. Pertaining to this vapor concentration, a steady exit velocity at the nozzle exit is achieved, Fig. (5.5(b)), with minor fluctuations near the nozzle walls.

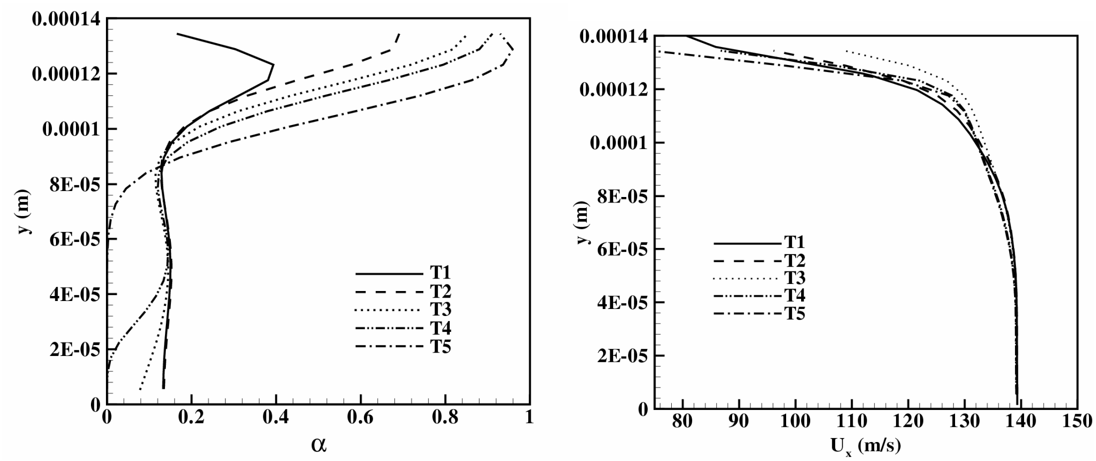

(a) (b)

Figure 5.5: Plot of (a) vapor volume fraction (b) and *x*-velocity component at the nozzle exit represented as time series (T1 – T5). Observe little fluctuations in vapor distribution and coupled velocity component profile near the nozzle walls at the exit section.

5.2.2 Exit Pressure: 19 bar

Following our previous computation, we increase the counter (exit) pressure to 19 bar (σ_c = 3.21) to observe its effect on cavitation dynamics. Unlike our previous computation, severe unsteadiness in vapor pocket stretching and elongation leading to pinch off from the parent cluster was observed. As flow evolved, events of supercavitation were detected. The vapor cluster fraction reaching the exit did not show a steady nature. The decrease in the cavitation number of the system resulted in a regime consisting of prominent shifting between a longer and shorter cavity length influencing the flow structure and the exiting supercavitation behavior. Figure (5.6) illustrates unsteady supercavitation and cavity length shifting phenomena.

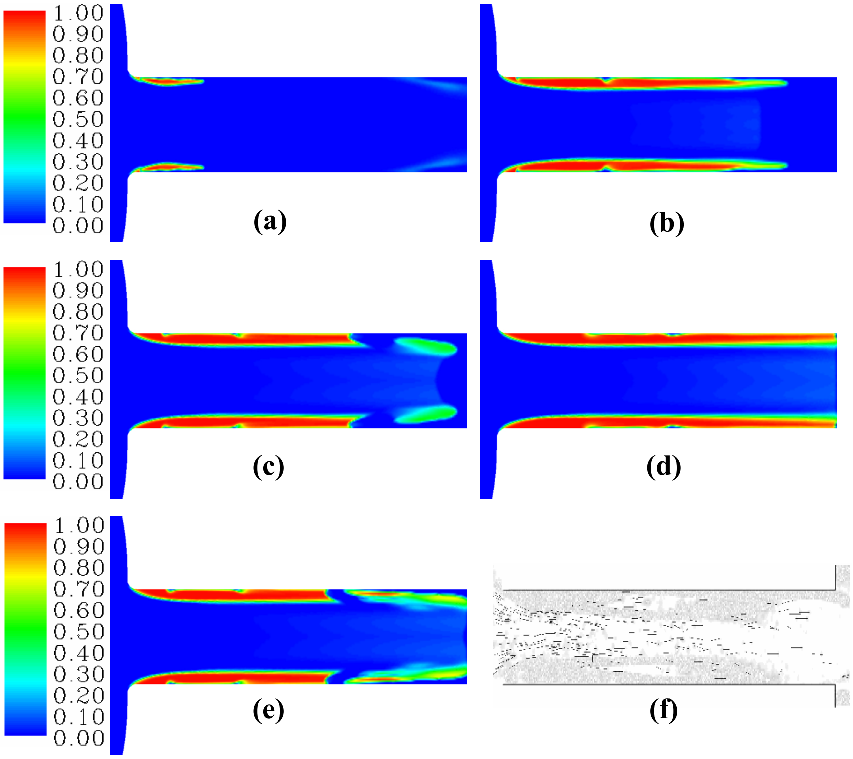

Figure 5.6: Computations with $\sigma_c = 3.2$ reveal transient cavitation characterisics as shown in (a) – (e). This fluctuating nature compares well with the experimental result [107] shown in (f).

Observe from Fig. (5.6), formation of highly transient vapor pockets formation and their subsequent shedding. This interaction creates a highly perturbed flow field which results in intensification of the turbulent nature of the exiting liquid jet. Radial disturbances due to localized pressure variation in the cavitating regime potentially describes the wrinkles on the jet surfaces [45, 72] exiting from cavitating nozzles and enhanced disintegration phenomena [2, 56].

The cavities formed at the corners entering the sac would periodically stretch to the exit and then collapse partially somewhere along the midsection of the orifice, generating strong pressure waves and vortices. This finite propagation of pressure waves can be satisfactorily accommodated in compressible formulations such as the present one. After collapse, bubble clusters would pinch off the main cavity and be swept downstream during the collapse process. Following this, another stretching of the vapor film would occur and this process repeats itself several times although no definite frequency was associated with this phenomenon. The flow structure looked highly distorted due to shifting cavity length mechanism. When the cavity gets shortened strong re-entrant jets finds their way back to stabilize the cavity. However, the local flow conditions prevailing in the flow aid the growth of clusters which works its way downstream against the re-entrant jets. Analogous to the cavity formation, stretching and collapse, the re-entrant jets appear at intervals corresponding to the presence of short cavity lengths. The stretching and collapse of the cavity induces very strong local recirculation regions depicted in Fig. (5.7).

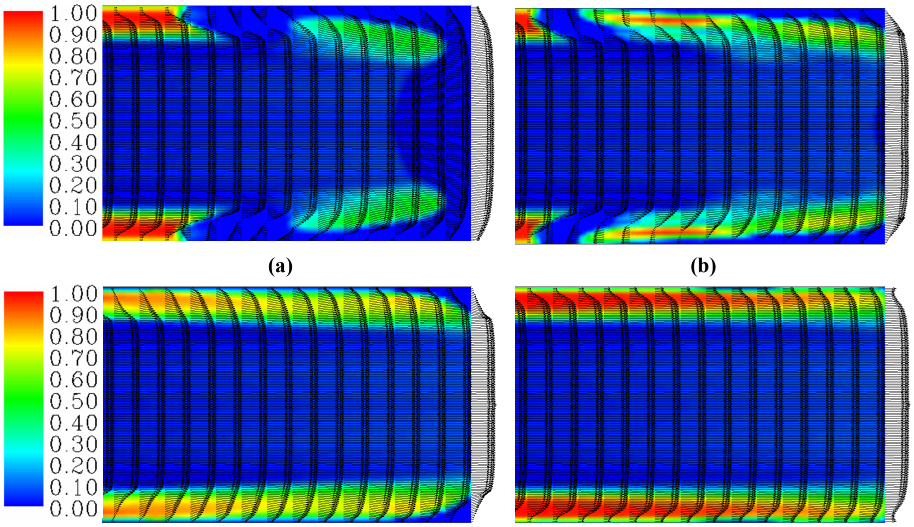

(a) **(b)**

(c) **(d)**

Figure 5.7: Highly transient vapor detachment mechanisms generate recirculation regions within the nozzle. Although very short lived, these strong circulations are clearly seen to affect the velocity profile relaxation at the nozzle exit.

Plot of vapor fraction at the nozzle exit shown in Fig. (5.8(a)) exhibits unsteady supercavitation behavior. Figure (5.8(b)) representing the x-component of velocity displays similar unsteady trends. Note that any fluctuating behavior in the x-component reflects on the *y*, *z* directional components due to the continuity constraint.

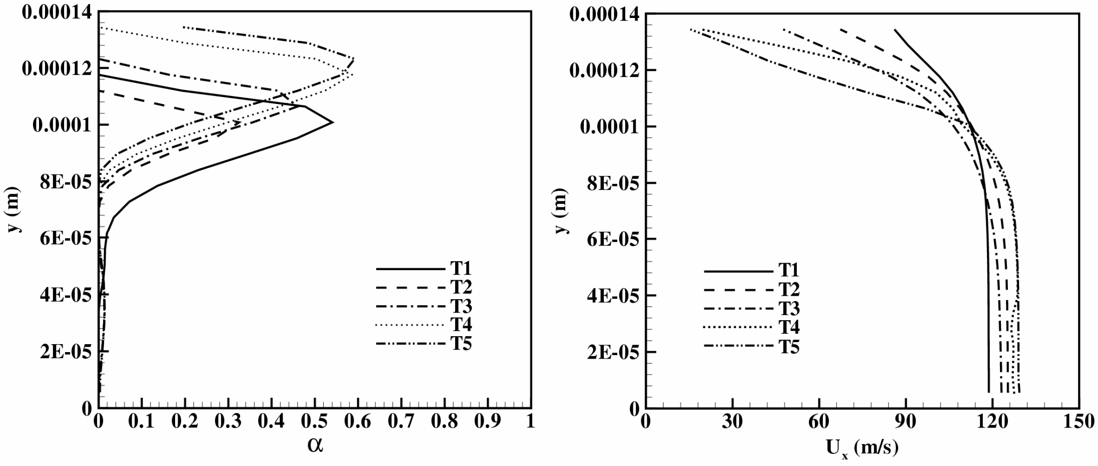

(a) (b)

Figure 5.8: Plot (a) vapor volume fraction (b) *x*-velocity component at the nozzle exit for σ_c = 3.2 with increasing simulation time (T1 – T5). Fluctuations in the vapor exit behavior appear simultaneously as fluctuations in the velocity distribution at the exit.

The induced orthogonal components near the nozzle exit tend to amplify due to aerodynamic interaction leading to shorter breakup length of the jets [2, 48, 49, 94, 96]. The distribution and intensity of exiting vapor pockets is highly transient and, as our simulation suggests, is a strong function of the cavitation number.

5.2.3 Concluding remarks

Numerical simulations using compressible formulations with HEM assumption have been utilized to capture cavitation dynamics in injector flows. Two different cases representing different modes of cavitation dynamics were tested using our new formulation and our results indicate events of supercavitation, cluster stretching and pinch-off compared well with the experimental results. The formulation helps validate the effect of the cavitation number on the cavitation dynamics. Increasing the cavitation number leads to intensified liquid-vapor mixture flows. The outlet velocity increases when cavitation appears. This can be explained as reduction in cross-section of the liquid phase in the outlet section of the hole due to vapor growth and the simultaneous collapse in mass flow. The modified velocity components arising from our coupled computations due to cavitation effects describe the enhanced disturbance levels in the exiting liquid jets leading to altered disintegration dynamics at the nozzle exterior. Velocity fluctuations upto 10-20% of mean velocity were observed when cavity shifting mechanisms took place. The current simulation is two-dimensional and hence some discrepancy in the cavitation sheet stabilization can be attributed to the true three dimensional nature of the cavitating flows. The effect of turbulence in a compressible framework with cavitation needs to be evaluated. Further, the effect of reflecting boundary conditions needs thorough investigation, since a wide range of cavitation behavior can be achieved by shifting from no-reflecting to fully-reflecting conditions. Also, the effect of grid size is very important since coarse gridding often results in smoothing the scalar function and hence in inaccurate description of the related dynamics. Since no accurate quantitative data description was available, we presently limit our computations to resolving the fundamental cavity dynamics. Overall, the code is able to capture the qualitative essence of cavitation dynamics in high speed injector flows which can help improve our understanding of the underlying mechanism behind spray enhancements.

5.3 The Cavitation-Induced-Momentum-Defect (CIMD) correction approach

The cavitation model presented in Section (5.2) is based on a compressible fluid flow framework applicable in ranges of flow Mach number > 0.05. However, cavitation mechanisms have been observed even in very low Mach number flows, $Ma < 0.001$, due to several factors such as geometry effects, turbulent quantities, density of cavitation nuclei etc. Compressible formulations help capture the transmission of pressure waves emanating from the liquid-vapor mixture regions while in incompressible fluid flow no such information can be accommodated. However, the application of compressible formulation in low speed flows typically encountered in industrial devices, where the flow Mach number varies from 0.001 to 0.2, result in poor convergence and erroneous calculations [234-236]. Although the predominantly pure liquid flow carries low Mach number characteristics, the cavitating zones comprising of vapor regions, on the other hand, can possess Mach numbers of the order of 10 or above due to low sound speed in vapor [234]. In this effect, the cavitation models need to account for the local liquid-vapor compressibility affecting the flow structure of a predominantly incompressible liquid. However, detailed treatment of compressibility effects in the cavitating region within the bulk flow demands increased computational expense. Adding to the complexity, several numerics have to be altered to improve convergence of such numerical simulations [235, 236]. In this concern, a new cavitation event tracking model is introduced where the dynamics of compressible liquid-vapor mixture are modeled using the bulk flow parameters and resulting effects are fed back into the core flow governing equations using a cavitation induced momentum source formulation.

The numerical model presented here is validated using the experimental observations of Sato et al. [272]. Planar nozzles were used in their experiments to observe the geometry effects on cloud cavitation phenomena. The planar nozzle geometry can be well represented using a two-dimensional flow assumption and, further, requires less computational effort than a complete three-dimensional simulation. Before delving into the numerical validation, some mechanisms involved in sheet and cloud cavitation processes are elaborated here.

5.3.1 Sheet and Cloud Cavitation

The studies concerning sheet and cloud cavitation phenomena are copious due to their frequent appearance in a wide gamut of hydraulic systems. The ensuing instabilities are known to procreate abnormal dynamic behaviors, noise, erosion and vibration among others [33, 34]. Different types of cavitation, emerging due to variation in geometry and flow characteristics, have been identified to effectuate distinct unsteady characteristics [33]. The mechanism of sheet cavitation has a quasi-steady character with notable unsteadiness localized in the closure region. With increase in intensity of perturbations at the rear end of the cavity, large vapor clusters are shedded into the flow downstream, a phenomena often termed as cloud cavitation. The cavitation cloud, unlike its parent source, exhibits very strong unsteadiness in the whole cavity [273, 274]. Several studies have identified the existence of a re-entrant jet that flows under the sheet cavity from its rear part to its upstream end, leading to generation of cloud cavitation [273-275]. Callenaere et al. [172], in their study on re-entrant jet mechanisms, discussed two major classes of instabilities: intrinsic and system instabilties. While the intrinsic type is thought to originate within the cavity, the latter is cerebrated to have been ingenerated from the interaction of cavities with the flow system components, such as flow lines, valves etc. They observed that an increase in adverse pressure gradient at the closure region of cavity has a direct impact on the development of re-entrant jets. Myriad of experiments [170-173, 175] on the re-entrant jet process indicated the following sequence: a sheet cavity stretching along the walls nears a critical size; owing to discrete instabilities at its rear end, violent periodical oscillations effects shedding of cloud cavities downstream at each oscillation cycle. Experiments revealed the profound influence of the adverse pressure gradients, existing near the reattachment zone of the separated cavitation bubbles, on the oscillation mechanisms [175]. In a separate study by Kawanami et al. [171], the role of re-entrant jet on the onset of cloud cavitation was confirmed. The motion of re-entrant cavity is believed to result in breaking up of developing partial cavities. The detached cavity is then convected by the main flow until it collapses. Development of flow reversal has been hypothesized to be due to collapse of previous vapor cloud [276] or due to a mechanism based on cavity growth [170, 175]. Using planar nozzles, Stutz et al. [175] highlighted the importance of reversed two-phase flows within the cavity. Following the cavity detachment, other researchers emphasized on the interaction of shedded vapor clouds with large-scale vortex structure in the downstream region [170, 172]. Also, experimental observations have revealed that the cavitation appearance relates closely to the viscous phenomena of the liquid-phase, such as boundary layer and vortex motion. It can be inferred from numerous accounts of cavitating flow studies that detailed experiments are crucial for obtaining an accurate description of underlying mechanisms and in order to predict the occurrence of such phase change events.

5.3.2 The CIMD strategy

The current section is devoted to the development of a novel technique for simulating unsteady cavitating flows, combining the compressible characteristics of the two-phase mixture in the cavitation region within a regnant incompressible flow. The events of cavitation, their inception, growth and transport process are described by supplementing the incompressible Navier-Stokes equation with an additional scalar transport equation. Homogeneous Equilibrium Model (HEM) assumptions are employed in constructing the source term in the vapor transport equation. The source term, evoking a barotopic formulation, essentially describes the compressible characteristics of the cavitating regions. Whenever the liquid flow pressure falls below the vaporization pressure of the liquid, the source terms are activated and the solver computes the local vapor fraction. It can be easily deduced that the formulation represents a local scale phenomenon obtaining information from the solution of the bulk Navier-Stokes (NS) equations. Thus the dynamics of the multiphase mixture is tightly coupled with the explicit solutions available from the NS equations. Convection and diffusion terms present in the vapor transport equation helps in the interaction of the vapor regions with the surrounding flow field. Using the transport scheme, the vapor clusters can be convected into the main flow from the regions of their inception. Since, the change in phase from liquid to vapor directly indicates a change in property of the liquid, density (in a compressible sense), we use a pseudo-momentum correction approach to mimic the density-change effect. In other words, whenever events of cavitation are encountered, the computed vapor fraction in the local neighborhood is used to compute the momentum loss/gain due to variation in cell density. The rate of change of momentum is supplied as a cavitation-induced momentum source to the Navier-Stokes equations. In this account, an inception event is considered as transient momentum loss event while, a collapse phenomenon is built to supply an additional source of momentum into the fluid.

5.3.3. Governing equations

The numerical model solves the unsteady Reynolds averaged Navier-Stokes equations, coupled with a localized vapor transport model for predicting cavitation. The fundamental equations governing the flow of an incompressible fluid are given by the continuity and momentum conservation equations. We rewrite the continuity equation as

$$\nabla \bullet \boldsymbol{U} = 0 \tag{5.24}$$

while the momentum equation with source terms can be written as

$$\frac{\partial(\rho \boldsymbol{U})}{\partial t} + \nabla \bullet (\rho \boldsymbol{U}\boldsymbol{U} - \boldsymbol{T}) = Fc \tag{5.25}$$

where $\boldsymbol{T}$ is the total stress tensor defined as

$$\boldsymbol{T} = -\left(P + \frac{2}{3}\mu \nabla \boldsymbol{U}\right) I + 2\mu \mathbf{D} \tag{5.26}$$

P in Eq. (5.26) is the pressure, I the unit tensor, μ the effective viscosity and $\mathbf{D}$ representing the rate of strain tensor. The effective viscosity of the mixture μ is given by

$$\mu = (1-\alpha)\mu_l + \alpha \mu_v \tag{5.27}$$

where α represents the vapor volume fraction in the fluid domain.

The strain rate tensor is expressed as

$$\boldsymbol{D} = \frac{1}{2}\left(\nabla \boldsymbol{U} + \nabla \boldsymbol{U}^T\right) \tag{5.28}$$

Fc in equation (5.25) represents momentum source terms resulting due to cavitation effects. The local cavitation induced force terms are activated when the flow pressure falls below the vaporization pressure of the liquid. During this event, the numerical schemes incite a vapor transport equation to be solved to mutate the flow structure due to the local phase change phenomena. Thus, the fluid is composed of pure liquid at the domain inlet, and transforms into a mixture of liquid and vapor in cavitation areas. Also, the stress terms present in the bulk N-S equations given by equation (5.25) are modified palpably due to the induction of viscosity gradients due to cavitation events. Methodologies involved in constructing the terms of the proposed vapor transport equation have been elaborated below.

5.3.3.1 Modeling vapor transport equation

The transport equation for the vapor scalar (α) is given by

$$\frac{\partial \rho_v \alpha}{\partial t} + \nabla \bullet \left(\rho_v U_v \alpha \right) - \nabla Di_\alpha \nabla \alpha = Sp_\alpha \tag{5.29}$$

where ρ_v, Di_α, U_v represents vapor density, effective mass exchange coefficient and the vapor phase velocity, respectively. Sp_α indicates the volumetric source term in the given computational cell. The mass exchange coefficient is an implicit function in vapor fraction representing inter-phase mass transfer within the computational cell. Details of its derivation are included in the source term evaluation. The vapor velocity U_v, to be derived later in the section, is modeled based on slip between phases arising due to a local vapor relaxation effect. The convection term assembled using the vapor fraction and bulk N-S flow properties, provide a strong implicit coupling with the governing momentum equation solved for the liquid region. The source term is deduced from fundamental assumptions of Homogeneous Equilibrium between the phases.

5.3.3.2 Modeling cavitation source terms

The source term in the vapor transport equation (5.29) is calculated by the simple relation generated from energy of bubble growth and collapse as

$$Sp_\alpha = \rho_v N.4\pi R^2 \dot{R} \tag{5.30}$$

N in equation (5.30) represents the bubble number density i.e., number of cavitation bubbles per m^3, R the bubble radius and $\dot{R}$ is the bubble wall velocity. The bubble radius is calculated from the vapor fraction scalar (α) in combination with the bubble number density as

$$R = \left(\frac{3\alpha}{4\pi N} \right)^{\frac{1}{3}} \tag{5.31}$$

The Rayleigh-Plesset equation representing the fundamental bubble dynamics is given by

$$R\ddot{R} + \frac{3}{2}\dot{R}^2 = \frac{P_{vap} - P}{\rho_l} - \frac{2\sigma}{\rho_l R} - \frac{4\mu \dot{R}}{\rho_l R} \tag{5.32}$$

The importance of bubble wall acceleration term has been recognized to be restricted to the initial growth phase period of the bubble [34]. The second order acceleration term is eventually taken over by the first order inertial term and which from then governs the bubble dynamics, competing against the pressure, surface tension and viscous forces. Hence, for obtaining a representative growth, we drop the non-linear acceleration term, the surface tension and viscous contribution terms from equation (5.32) to approximate the Rayleigh-Plesset bubble dynamics equation leading to

$$\dot{R} = sign\left(P_{vap} - P\right)\sqrt{\frac{2}{3}\left(\frac{P_{vap} - P}{\rho_l}\right)} \tag{5.33}$$

Equation (5.33) represents a simplified Rayleigh equation under the assumption that no thermal barrier affecting the bubble growth is expected. This model allows the fluids to be interpenetrating and hence mass transfer can occur between the phases. Of course the bubble grows if the mixture pressure is less than the vaporization pressure and collapse alternatively. The bubble collapse, as modeled by the Rayleigh second order differential equation, is much more rapid than the bubble growth [34]. However, the above equation (5.33) seems to make no such difference between growth and collapse. A positive bubble wall velocity represents the bubble growth, while a negative value indicates the bubble proceeding towards a collapse.

The effective mass exchange coefficient Di_α is defined as the diffusive mass flux of vapor penetrating across the cluster of an equivalent radius R_e into the surrounding fluid.

$$Di_{\alpha} = \left(\rho_v \dot{R}\right) R_e \tag{5.34}$$

where

$$\boldsymbol{R_e} = \left[\frac{3\alpha V_{cell}}{4\pi}\right]^{\frac{1}{3}} \tag{5.35}$$

Note that the effective mass exchange coefficient is a strong function of pressure gradient and acts over the cluster size taken as the length scale. A schematic representing the localized scalar computation is shown in Fig. (5.9). In order to obtain the vapor scalar as a function of the flow field variable, typically pressure, we invoke the Homogeneous Equilibrium assumption between phases.

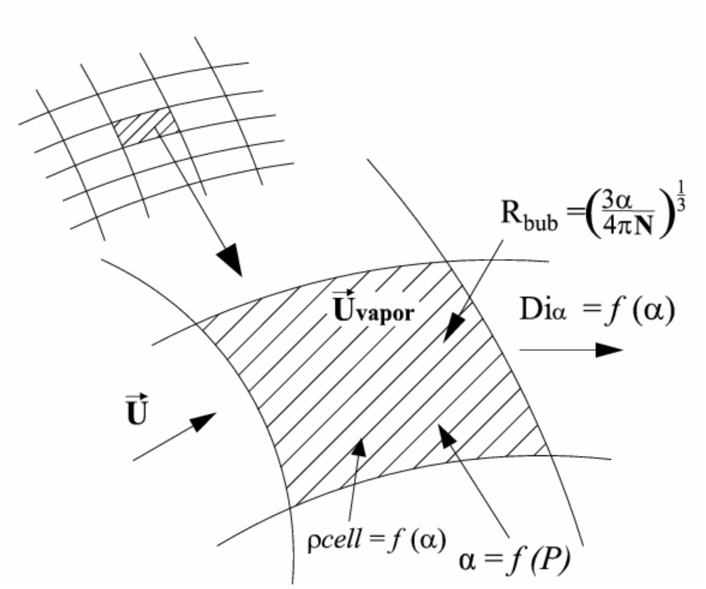

Figure 5.9: Computational Cell

5.3.3.3 Coupling Homogeneous Equilibrium Model and vapor transport process

An energy statement assuming homogeneous equilibrium of the liquid and vapor phases with viscous dissipation (φo) can be expressed as

$$\rho\frac{Dh}{Dt}=\frac{DP}{Dt}+\nabla tk\nabla T+\varphi o \tag{5.36}$$

where h represents enthalpy, tk the thermal conductivity, T the temperature. An order of magnitude analysis carried out by Schmidt et al. [231] suggests that the viscous terms and conduction terms can be neglected from the energy equation and with negligible irreversibilities, the equation (5.36) reduces to a simple energy equation representing reversible work given by equation (5.7) rewritten here

$$\rho\frac{Dh}{Dt}=\frac{DP}{Dt} \tag{5.37}$$

Replacing the energy equation by an isentropic relation model, we generate equation (5.38) as

$$a^2\frac{D\rho}{Dt}=\frac{DP}{Dt} \tag{5.38}$$

where a is the speed of sound. Equation (5.38) represents cavitation as an inertially dominated process with negligible thermodynamic effects. This assumption is valid since the heat transfer from a vapor bubble to surrounding is almost instantaneous [33, 34]. The isentropic model of the phase change process is given by the Homogeneous Equilibrium Model (HEM) as equation (5.9)

$$dP=a^2 d\rho \tag{5.39}$$

where the speed of sound of the mixture is calculated using the analysis of Wallis [231]

$$a=\left[\left(\alpha.\rho_v+(1-\alpha)\rho_l\right).\left(\frac{\alpha}{\rho_v.a_v^2}+\frac{(1-\alpha)}{\rho_l.a_l^2}\right)\right]^{-\frac{1}{2}} \tag{5.40}$$

The values of a_v and a_l in equation (5.40) are the speed of sound in pure vapor and liquid phases respectively. The variation of speed of sound in water-vapor mixture using equation (5.40) is shown in Fig. (5.2). The vapor fraction α is given by

$$\alpha = \frac{\rho_l - \rho}{\rho_l - \rho_v} \tag{5.41}$$

represents the density variation within the computational cell. By assuming constant speed of sound for the saturated vapor and liquid, Schmidt et al. [231] obtained analytical expressions for pressure as a function of void fraction as

$$\begin{aligned} P &= P_l^{sat} + P_{vl} \log\left[\frac{\rho_v a_v^2\left(\rho_l + \alpha\left(\rho_v - \rho_l\right)\right)}{\rho_l\left(\rho_v a_v^2 - \alpha\left(\rho_v a_v^2 - \rho_l a_l^2\right)\right)}\right] \\ P_{vl} &= \frac{\rho_v a_v^2 \rho_l a_l^2\left(\rho_v - \rho_l\right)}{\rho_v^2 a_v^2 - \rho_l^2 a_l^2} \end{aligned} \tag{5.42}$$

For the purpose of constructing the source term of the vapor transport model, we compute the vapor scalar as a function of pressure in the given computational cell, an inverse fashion of the above representation leading to

$$\begin{aligned} \alpha &= \frac{C_1 \rho_v a_v^2 - \rho_v}{\left(\left(\rho_v - \rho_l\right) + C_1\left(\rho_v a_v^2 - \rho_l a_l^2\right)\right)} \\ C_1 &= \frac{\rho_l e^{\left\{\frac{P - P_l^{sat}}{P_{vl}}\right\}}}{\rho_v a_v^2} \end{aligned} \tag{5.43}$$

The equation for vapor fraction involving explicitly calculated pressure from the bulk N-S equations is used to compute the scalar source terms in equation (5.29). The fluid in the current simulation is considered incompressible except in cavitating regions where its density varies from liquid to vapor according to the barotropic equation of state. The local vapor fraction predicted based on equation (5.41) is used to compute the speed of sound of the mixture in conjunction with equation (5.40). The expression presented in equation (5.40) considers the fluid homogeneously mixed on the sub-grid scale [230], which forms the basis of HEM. When the pressure of the mixture is either well above or below the vapor pressure, the speed of sound is large but finite and the flow in the cavity is considered weakly compressible. In the phase transition region, the speed of sound retains a small speed of sound. However in practical computations, the mach number of the flow would vary from 0.001 to as high as 30. Hence, for efficient computation of the multiphase mixture with the homogeneous assumption it is required that the time marching procedures are stable and accurate in the range of mach numbers specified. It should be noted that the bubble number density N has been held constant during the simulation procedure. In future a transport equation for the bubble number density would be dealt with. This procedure would increase the number of scalar equations solved in the cavitation region for which a good stability analysis is required.

5.3.3.4 Momentum-source formulation

Sections (5.3.3.1) – (5.3.3.3) elaborated the scalar transport equation for computing the cavitation inception and transport process. As suggested by works based on one-fluid model, cavitation regions can be characterized as regions where the fluid properties have been altered as a consequence of a local phase change process.

Consider a liquid element of density ρ_l and velocity U_l entering into a computational cell where cavitation events are present due to reduction in absolute liquid pressure of the incompressible fluid. If ρ_m and U_m are the density and velocity of the liquid-vapor mixture in the given cell, then the net momentum change is given by

$$\Delta\left(\rho U\right) = \rho_m U_m - \rho_l U_l \qquad (5.44)$$

The generation of a volumetric cavitation-induced-force term due to local variation in momentum is computed by simply deriving the rate of change of net momentum. Hence, the force induced by cavitation dynamics is given by

$$Fc = \frac{d}{dt}\left[\Delta\left(\rho U\right)\right] \tag{5.45}$$

The liquid-vapor mixture velocity in the computational cell obtained by mass-averaging results in

$$U_m = \sum_{k=1}^{n} \frac{\alpha_n U_n \rho_n}{\rho_m} \tag{5.46}$$

where $n = l$, v and ρ_m is the mixture density is given by

$$\rho_m = \left(1-\alpha\right)\rho_l + \alpha\rho_v \tag{5.47}$$

In other words when the liquid enters a cavitating region filled with vapor, it experiences a momentum loss. When condensation, the collapse of vapor bubbles, occurs, the model imparts added momentum into the liquid flow. This phenomenon is numerically represented by the contribution of equation (F_c) in the momentum equation and can be considered as a cavitation induced momentum defect correction methodology.

A relative velocity U_{rel} exist between the liquid and vapor phases due to viscous effects, and requires to be modeled. Although, the HEM model invokes sub-grid level mixing of the phases, presence of fluctuations due to mismatch of vapor and liquid phase velocities necessitates accurate numerical treatment to be finally incorporated into the momentum defect equation.

For computing the vapor phase velocity, we use a relaxation-effect analogy similar to the computation of droplet velocity in a fluid medium. A modified version of the algebraic slip formulation [243] is used for deducing the slip velocities between the phases. A local equilibrium between the phases is assumed to be reached over short spatial length scales as required by the model. In the present scenario, the cavitation clusters have an effective radius R_e taken to represent the volume of vapor occupied within the cell. The approximate effective cluster radius length scale is given by equation (5.35).

The relative velocity between the bubble clusters and the bulk liquid flow is then computed as

$$U_{rel} = \frac{2\left(\rho_v - \rho_m\right) R_e}{18 \mu_v fd_{drag}} Ax_c \tag{5.48}$$

where fd_{drag} is the drag function given by [245]

$$fd_{drag} = \begin{cases} 1 + 0.15\,\mathrm{Re}^{0.687} & \mathrm{Re} \le 1000 \\ 0.0183\,\mathrm{Re} & \mathrm{Re} > 1000 \end{cases} \tag{5.49}$$

and Ax_c, the acceleration term is defined as

$$Ax_c = \overline{g} - \left(U \bullet \nabla\right) U - \frac{\partial U}{\partial t} \tag{5.50}$$

where U represents the bulk liquid flow velocity. The relative velocity between the phases computed using equation (5.50) in combination with the explicitly solved liquid flow velocity from the conservation equations, the vapor velocity, U_v, is deduced. Obtaining the necessary information we build the cavitation-induced-momentum-defect source as

$$Fc = \left[U_v \rho_v - U_l \rho_l\right] \frac{d\alpha}{dt} + \alpha \left\{ \rho_v \frac{dU_v}{dt} - \rho_l \frac{dU_l}{dt} \right\} \tag{5.51}$$

The rate of change of density change is directly computed as a transient change in the vapor fraction. Observe from equation (5.51), that the nature of cavitation induced force is governed by a transient formalism and hence only unsteady calculations can be performed with this momentum correction approach. The essence of unsteadiness is crucial in tracking the true transient nature of the cavitation dynamics. Also, observe that in the limit that no vapor regions exist, the force term due to cavitation disappears and we retain the original form of Navier-Stokes equation for an incompressible fluid.

5.3.4. Numerical Methodology

The described model equations presented in Section (5.3.3) were solved in commercial code Fluent [242] by using appropriate User Defined Functions (UDF's) to represent the scalar transport variables. The mass, momentum and the scalar transport equations were solved in a segregated fashion iterated using a first order implicit time advancement procedure. Since our cavitation model, employing the vapor transport equation, has a strong coupling with the pressure and velocity variables within the flow, we use a Pressure Implicit Splitting of Operators (PISO) procedure for achieving pressure-velocity coupling [148]. This procedure is well suited for unsteady calculations and is based on the higher degree of approximate relation between the corrections for pressure and velocity. The pressure discretization is achieved using a Linear scheme. The vapor scalar transport equation involves accurate and stable computation of the gradients to achieve accurate description of the cavity dynamics. To realize this purpose, a second order upwinding scheme is used for discretizing both the scalar and momentum equations. Furthermore, by using a second order upwinding scheme the transport behavior of the flow variables can be capture more effectively due to the flux-direction-sensitive upwinding process [138, 146, 150]. Strict multigrid operations are applied to monitor stability and convergence. Cavitating flows are highly sensitive to turbulent fluctuations present in the flow [179, 251]. The following section describes the turbulence approximations and correction strategies employed in the current simulation.

5.3.5 Turbulence modeling

The effects of modeling turbulence quantities have an enormous impact on the cavitation dynamics and the overall flow structure. For example, application of standard two-equation model is known to dampen the cavitation behavior [179]. Recently, Yuan et al. [277] reported serious difficulties using a standard two-equation turbulence model for simulating cloud cavitation phenomena. The difficulty arose from the systematically overestimation of turbulence viscosity by the turbulence model, leading to a stable cavity at the rear end of the sheet. Re-entrant jet formation was averted and flow remained stable due to increased dissipation. Similar concerns need to be addressed when modeling a compressible two-phase region within an incompressible fluid due to prevalence of local turbulent characteristics. Coutier [178] have shown that taking into account the effects of compressibility on the turbulence structure by applying corrections to standard models can lead to a substantial improvement in the computation results.

For the present computations, we use a renormalized group k-ε model due to the presence of highly strained regions in the flow and their ability to accurately predict low Reynolds number regimes [244]. In the case of the k-ε RNG model, a modification for including the compressibility effects can be applied directly in the expression of the turbulent viscosity. The function $f(\rho)$ which is simply equal to ρ_l for a single phase flow, is turned to $fn(\rho) = \rho_v + \alpha n(\rho_v - \rho_l)$ in the case of cavitating flows, with $n = 10$. The function fn is then equal to ρ_v *or* ρ_l in the regions containing pure vapor or pure liquid, but it decreases rapidly toward ρ_v for intermediate void values. This modification, previously applied to several configurations, resulted in accurate estimation of unsteady flow properties. The use of mixture density for estimating the turbulent viscosity limits the kinetic energy and allows re-entrant jet formation and subsequent events of cloud cavitation. For modeling the flow close to the wall, standard wall function approach was used with enhanced wall functions approach applied in the near-wall region.

5.3.5.1 Modeling source terms due to cavitation-induced-turbulence

Cavitation induced turbulence effects cannot be neglected while solving the transport equations for kinetic energy and dissipation rate variables. This methodology improves the coupling between the scalar transport equation and its effect on the bulk mixture flow, while retaining the sensitive nature of the cavity dynamics based on turbulent fluctuations.

The velocity surrounding a vapor bubble at position R_L can be expressed as [34]

$$v(R_L) = \left(\frac{R}{R_L}\right)^2 \dot{R} \tag{5.52}$$

while the total kinetic energy [34] of the liquid around the bubble is deduced as

$$En_k = \frac{mv^2}{2} = \frac{1}{2}\int_{R_L=R}^{R_L=\infty}\left(\frac{R}{R_L}\right)^4 .\dot{R}^2.4.\pi.\rho_V {R_L}^2 dR_L = 2\pi\rho_V R^3\dot{R}^2 \tag{5.53}$$

Assuming that the disturbance caused by the vapor bubble evolution/collapse is proportional to the rate of change of kinetic energy, the cavitation induced turbulent kinetic energy (CITKE) can be written as

$$So_k = \frac{d\left(NEn_k\right)}{dt} \tag{5.54}$$

The turbulence length scales are represented by the bubble wall velocity, a strong function of the pressure difference across the bubble walls. The turbulent fluctuations induced by cavitation are, hence, assumed isotropic with propagation speeds equal to that of bubble wall velocity. The dissipation rate (So_{eps}) due to cavitation effects are derived by obtaining the transient fluctuation of the cavitation turbulent kinetic energy source as

$$So_{eps} = \frac{dSo_k}{dt} \tag{5.55}$$

The computed source terms for turbulent kinetic energy and turbulent dissipation rates are added to their respective transport equations.

5.3.6. Simulation set up and boundary conditions

The unsteady Navier-Stokes formulation with cavitation effects presented in Section 3 are implemented in a convergent-divergent planar nozzle flow [272] to demonstrate its ability to predict cloud cavitation and complex vortex interactions. The simulation domain with the boundary conditions is shown in Fig. (5.10).

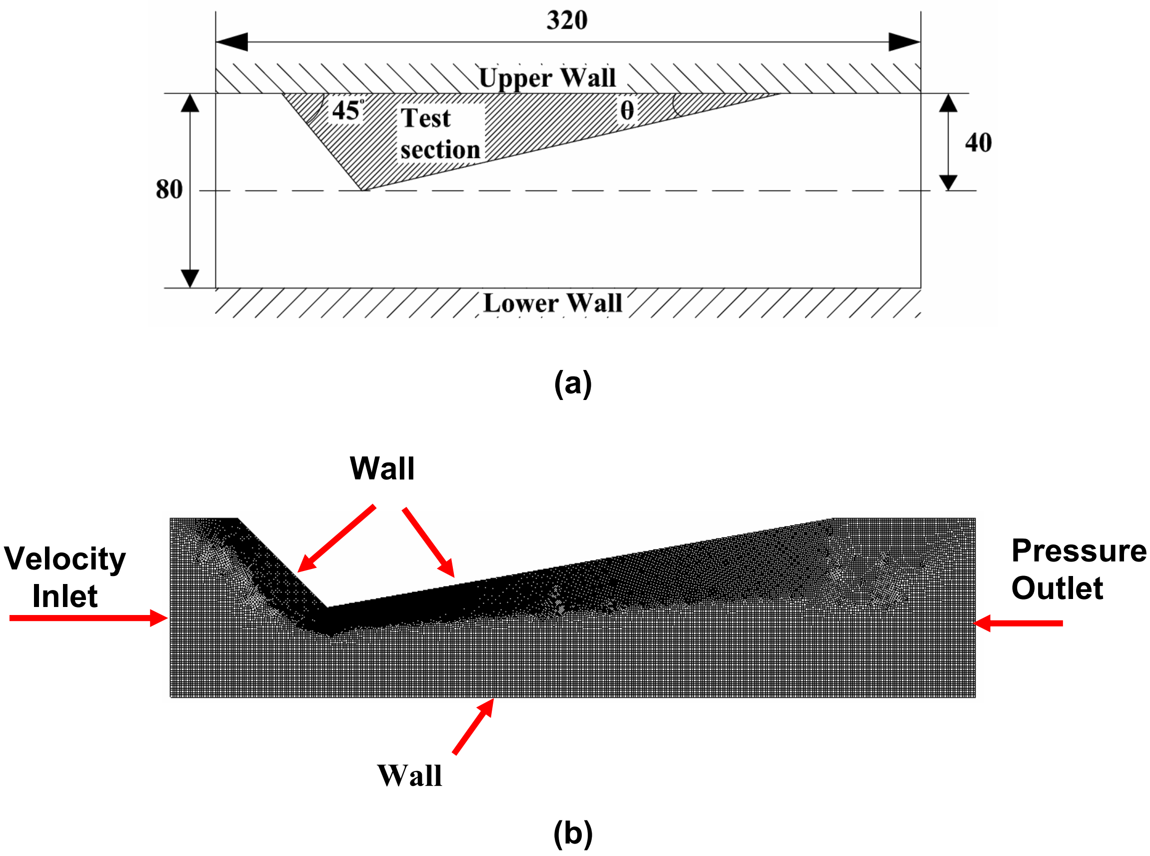

Mesh clustering near sharp corners

Figure 5.10: (a) Simulation domain. (b) Computational grids indicating boundary conditions. All dimensions are in mm

The cavitation tunnel section consists of a small closed-type rectangular test section of 80 mm height and 60 mm width. Three different nozzle types were used in the experiments. However, for numerical validation purposes we relate to tests run using nozzle-A and nozzle-B types with $\theta=18.4^{o}$ and 10^{o} divergent angles respectively. Both these nozzle types have a convergent angle of 45^{o} and a contraction ratio of 0.5. Details of the experimental setup and optics utilized can be obtained from Sato et al. [272]. For the computations, two dimensional flow is assumed to exist in the planar nozzle. However, it is to be noted that three dimensional effects play a major role in altering the cavitation dynamics such as sheet rollup and vortex interactions [105, 108, 247]. The simulation uses unstructured quadrilateral meshes for finite volume discretization in the nozzle domain. A total of 30,000 quadrilateral cells were used with mesh clustering operation performed near the contraction corners in the nozzle to capture high pressure and density gradients accompanying events of cavitation.

The boundary conditions required for the numerical simulations were taken from the experimental procedures of Sato et al. [272]. A velocity inlet was imposed at the flow entrance. The tunnel walls were treated as no-slip boundaries while the flow exit section was treated as a pressure outlet. By imposing a finite static pressure at the exit, the cavitation number of the system can be modified easily. The bubble number density was assumed to hold a constant value of 10^{14} /m^3 as previously used by researchers [277]. For simulation and validation purposes, we use water-vapor mixture. All properties of water and vapor have been taken at STP.

5.3.7. Results and Discussions

Experimental studies have confirmed that the cavitation number (σ_c) and Reynolds number (*Re*) are the most important criteria, which describe similarity of cavitating flows in nozzles [33, 34]. In the current discussions, the cavitation number is expressed as

$$\sigma_c = \frac{2\left(P_\infty - P_{vap}\right)}{\rho_l U_\infty^{\ 2}} \tag{5.56}$$

where P_∞, U_∞ are the static pressure and velocity of the liquid flow in free stream. The Reynolds number is defined as,

$$\mathrm{Re} = \frac{U_c He}{\nu_l} \tag{5.57}$$

where U_c and He represent mean velocity at nozzle throat and the height of nozzle throat respectively. ν_l is the kinematic viscosity of the investigated liquid (water). Computations are performed with a constant inlet velocity of U = 3.47 m/s in both the nozzle types A and B. However, the cavitation number of the system is varied as σ_c = 6.7 and 6.5 for nozzles A and B respectively. Reynolds number of the flow inside nozzles A and B is of the order of 2.89 X10^6 and 2.7 X10^6 respectively.

5.3.7.1 Computations with Nozzle-A

Instantaneous vapor volume fraction distributions at increasing time instants are shown in Fig. (5.11).

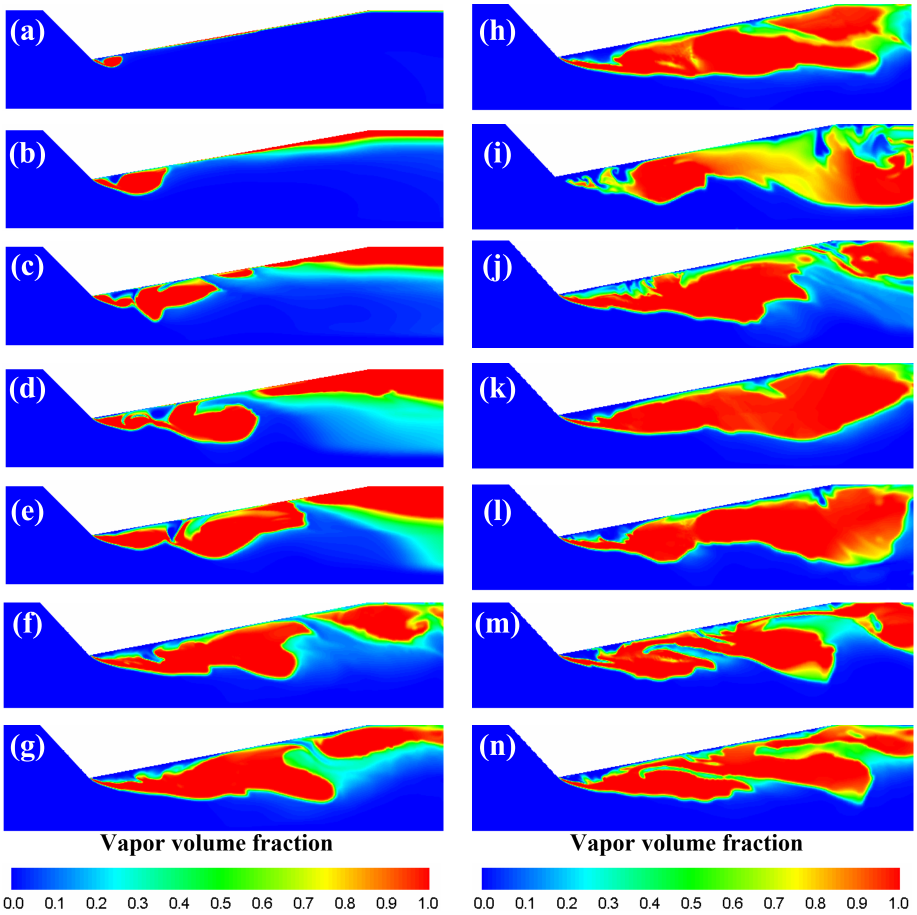

Figure 5.11: Transient evolution of cavitation vapor fractions for Re = $2.89\text{X}10^6$ and σ_c = 6.7.

As the fluid goes past the nozzle throat, it experiences sudden expansion leading to flow reversal and vortex shedding phenomena. The flow acceleration near the leading edge of the divergent section results in lowering of fluid pressure below the liquid vaporization critical activates the scalar transport model. Inception of cavitation computed by the model is shown in Fig. (5.11(a)). The cavitation clusters thrive on the low pressure core of the vortex regions that are shed by the upstream boundary layers due to sudden expansion in the throat downstream region. The scalar transport equations governing the cluster dynamics inclusive of their formation, convection and diffusion process have been modeled as strong functions of the flow field variables. This makes the transport model assume hyperbolic, elliptic or parabolic nature depending on the strength of the convective variables. In particular, the diffusion term represented by the effective mass exchange coefficient, dominates region of low inertia. On the otherhand, regions of strong convection suppress any diffusion of the vapor clusters. From Figs. (5.11(b) – (d)) strong interaction of the cavity clusters with the vorticity transport is evident. As the cavitation cluster grows close to the wall, Figs. (5.11(e) – (f)), a re-entrant motion of the liquid-vapor mixture finds it's away propagating upstream resulting in separation of vapor layer from the upper wall of the nozzle tunnel. The reverse flow propagates towards the leading edge of the divergent section along the walls causing the collapse of the developing sheet cavity. The collapsing sheet cavity is partially shed as detached cavity. Fig. (5.11(d)) suggests that the source of the reverse flow is the flow along the face side of the foil which normally detaches at the trailing edge. It is supposed that the change in the pressure distribution near the trailing edge due to the extension of the sheet cavity triggers this reverse flow [170, 171]. Since the source term in the transport model is strongly dependent on the flow pressure variable, the instabilities are well accommodated. The interaction of the re-entrant jet motion with the cavitation clusters results in detachment of cavity clouds from the main cavity. This is clearly seen in Fig. (5.11(e)) as the shedding mechanism separates the clusters. As the simulation progresses, cavitation layers grow close to the nozzle walls interacting with the vortical structures in a simultaneous fashion. Events of cluster coalescence are observed, Figs. (5.11(f) – (h)), as the cavities shedded from the parent cluster mix with each other. Presence of strong vortex pairing mechanism, while being in a diffusive environment due to flow expansion, dictates the cavity coalescence. As the coalesced cavity grows larger in size, smaller cavities are observed to exist in the rear end of the nozzle as seen in Figs. (5.11(h) – (j)). The cavity evolution and detachment near the leading edge follows a quasi-steady mechanism. However, we observe that the intensity of cavity cluster, the cavity volume shedded, is not repeated identically from one cycle to another.

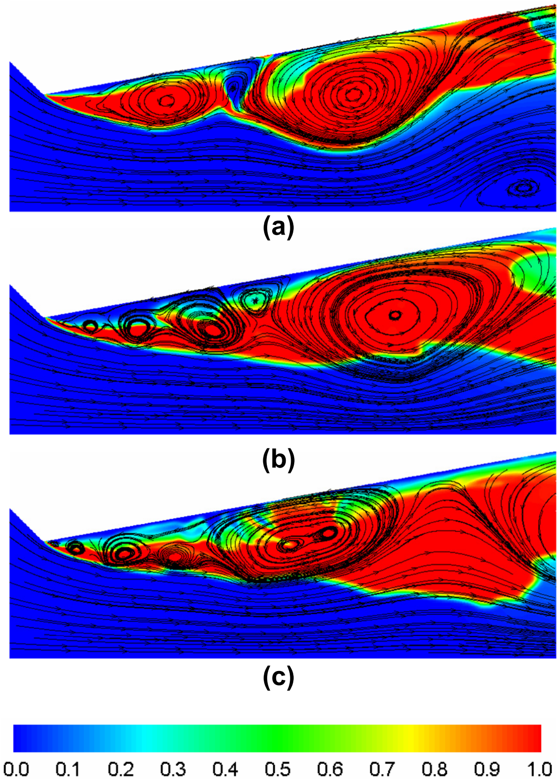

Figure 5.12: Streamlines indicating vorticity present in the flow domain. The colors indicate volume fraction of vapor. Capturing the vortex interaction with cavitation clusters. Growth of cavity clusters and their diffusion is observed to be a strong function of vorticity transport.

This observation can be attributed to the fact that the cavitation source terms are built on a sub-grid cell mixing and any non-linearity propagating within the scalar source construction can perturb the flow structure due to its strong implicit nature. Individual clusters branching out from the main cavity as they expand downstream under the influence of flow field is shown in Figs. (5.11(k)-(n)). Similar observation on the influence of local flow field on the cavity cluster penetration has been reported by Stutz et al. [175].

The role of large-scale vortex structures in modulating the nature of cloud cavitation mechanism has been identified by several researchers [170, 172]. Observe from Fig. (5.12) the presence of vortex structures within the cavitation clusters. As the re-entrant jet motion results in separation of cavitation clusters from the parent source, the detachment process results in a strong local recirculation region. Fig. (5.12(a)) shows presence of vortex structures sandwiched between two large scale vortices on its either sides. As the simulation progressed, the growth of this sandwiched vortex resulted in complete detachment of the cavitation clusters resulting in shedding of larger cavity downstream. Fig. (5.12(b)) shows the formation of multiple vortices and their mutual interaction within the cavitating region. An interesting observation is the presence of paired vortices as seen in Fig. (5.12(c)) which later coalesce to form a large vortical structure. Contours of vorticity, vapor fraction, X and Y velocity components magnitudes are plotted in Fig. (5.13) for the flow structure represented by Fig. (5.12(a)).

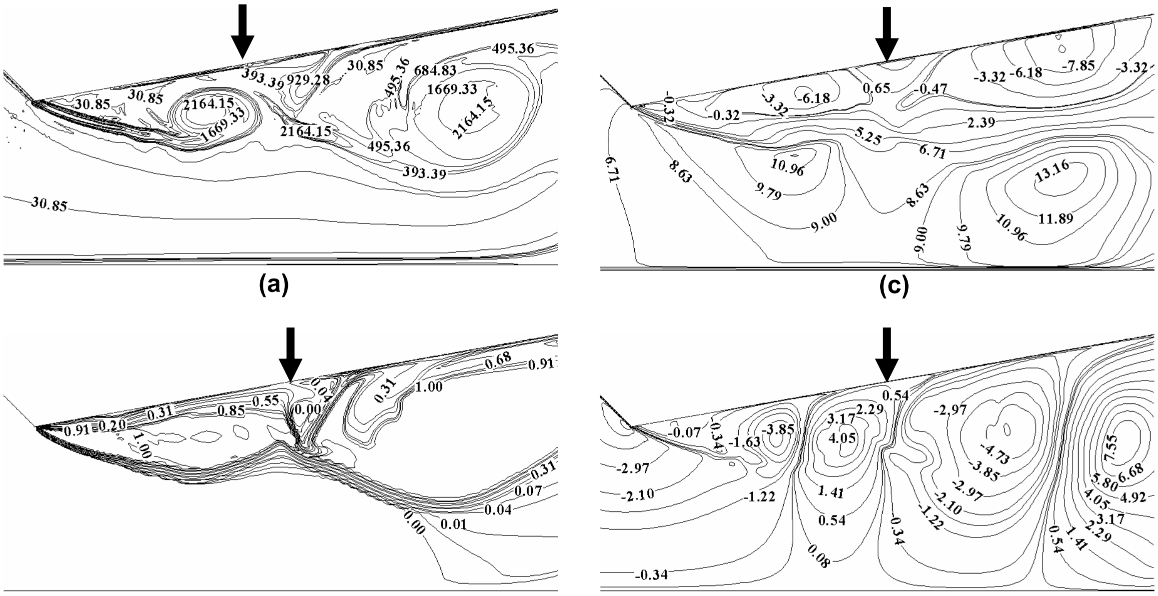

(a)

(c)

(b)

(d)

Figure 5.13: Contour plots of (a) vorticity (b) vapor volume fraction (c) x-velocity components and (d) y-velocity components during a breakup event of a cavity from a stretching vapor layer

attached to the leading edge. Arrow mark indicates region where breakup is typically encountered.

Observe from Fig. (5.13(c) and (d)) presence of low X-velocity components and high Y-velocity components at the stage of cavitation cluster separation (indicated by arrow head). Specially, recognize the re-entrant velocity magnitude from Fig. (5.13(c)) which equates to 75% of the bulk flow velocity. As the re-entrant jet moves along the wall upstream it results in a localized low pressure region in its trail. Due to the persisting local low pressure a stream of liquid gushes into this space impacting obliquely against the wall. This mechanism generated by the re-entrant jet makes the flow re-attach to the wall. Behavior of this kind has been previously reported by several authors [170, 173, 175]. The vortical structures separated by length scales approximately equal to the height of the throat section as seen in Fig. (5.13(a)) create strong pressure gradients which, then induces cavity separtion (Fig. 5.13(b)). The flow velocity in the vicinity of the cavitating structures strongly affects the vapor fraction distribution and their expansion [175].

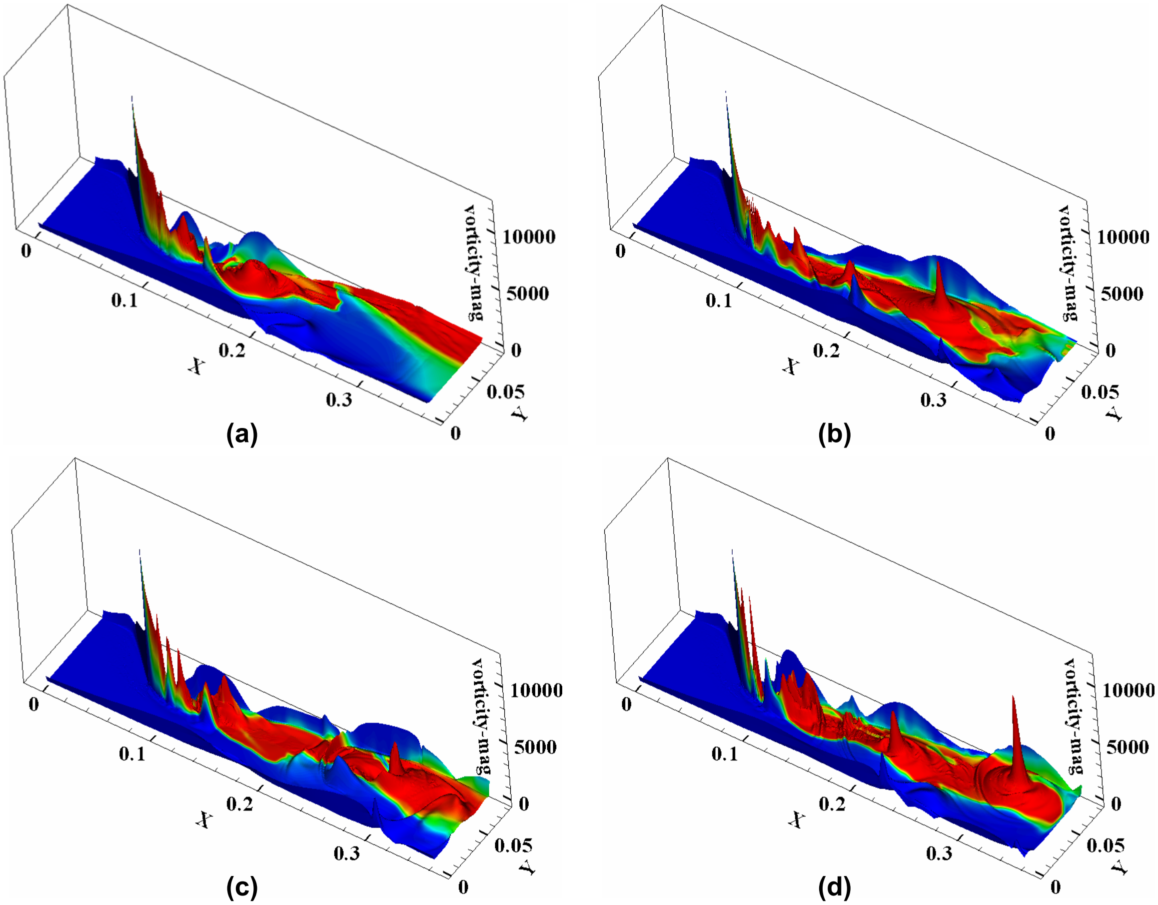

Figure 5.14: Plot of vorticity magnitude transport colored by vapor volume fraction for the nozzle type A , θ = 10°. Numerous small scale vortices present near the nozzle throat were captured and were observed to coaelasce as they convected downstream

A plot of vorticity magnitude with superimposed vapor fraction is shown in Fig. (5.14). Notice presence of high vorticity peaks near the throat section in Fig. (5.14(a-d)). The illustration clearly indicates accumulation of high vapor fraction where vorticity has typically spiked. The strong impact of coalescence of multiple vortices with different strengths on the cavitation clusters is detailed from these plots of transient interaction of large-scale vortex structures with vapor transport.

5.3.7.2 Formation of vortex cavities

The mechanism of rush-out of bubbly cloud into the main stream due to the arrival of re-entrant flow motion near the leading edge of the divergent portion has been well captured by our new model. As shown in Fig. (5.15(b)), the bubbly vapor cloud indicated by A' forms a small scale vortex cavity and coalesces with preceding small vortex cavities on the separated shear layer to grow into a larger scale.

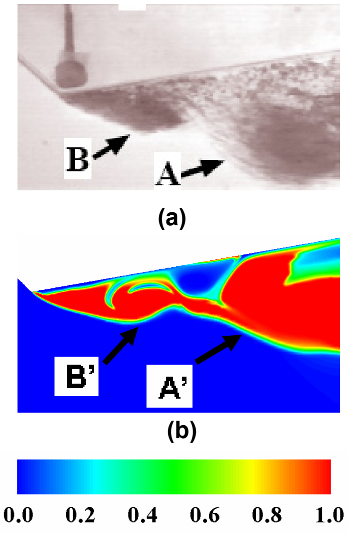

Figure 5.15: Detection of vortex cavities. (a) Experimental observations of Sato et al. [272] (b) Numerical simulation results. Arrow heads shown for comparison purposes.

Experimental observations are provided in Fig. (5.15(a)) while corresponding numerical simulation results are presented in Fig. (5.15(b)). As clearly seen from Fig. (5.15), our computations based on the unsteady formalism capture the formation and convection of vortex cavities very well. The length of cavity B observed in (5.15(a)) matches well with the simulated cavity length as shown in Fig. (5.15(b)). The transient shear layer rollup influencing the cavitation cloud propagation downstream has been well accommodated. A schematic representing the process of cavity-vortex interaction and re-entrant jet motion is shown in Fig. (5.16).

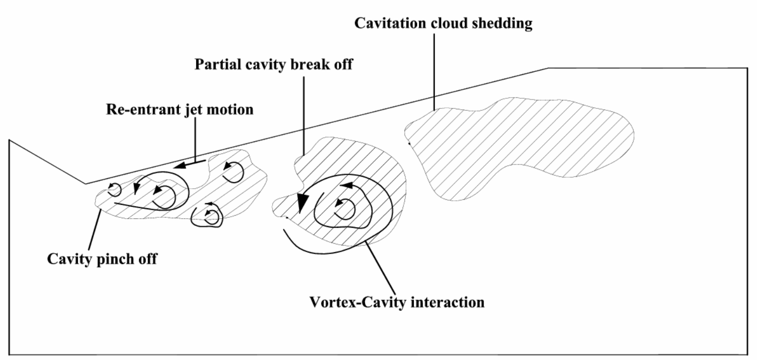

Figure 5.16: Schematic of a cloud cavitation mechanism indicating various events of cavity pinchoff, vortex-cavity interaction and cloud shedding

5.3.7.2.1 Transition effects near leading edge region

Having effectively captured the vortex cavities, we now compare some unsteady evolution of cavitation dynamics simulated by our model with the available experimental observations.

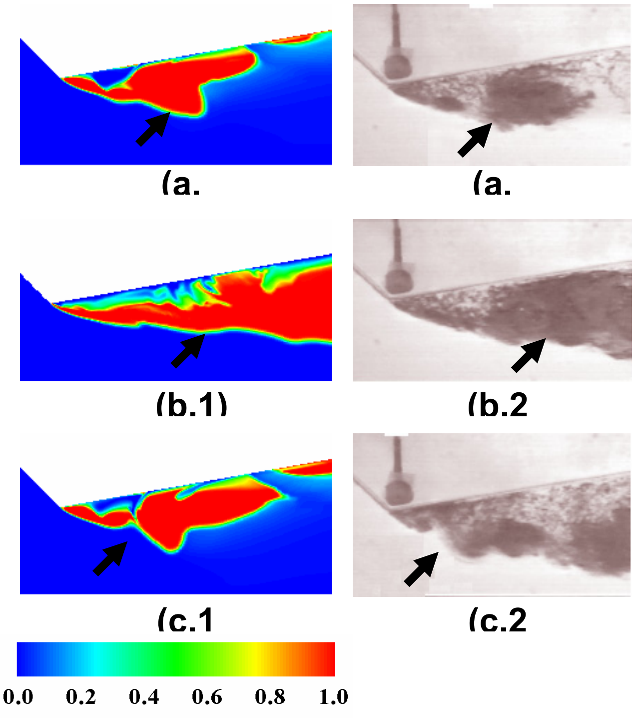

Figure 5.17: Comparing the experimentally [272] detected transient cloud cavitation phenomena with numerical computations.

Convection of cavities engulfed within vortices is shown in Fig. (5.17(a.1)). The overall structure matches well with the experimental observation shown in Fig. (5.17(a.2)). With time advancement, the expanding fluid creates diffusion effects, resulting in cluster coalescence seen as thick cavity regions in Fig. (5.17(b.1)). Multitude of unsteady vortical structures results in cluster stretching leading to smaller cavity structures. A very good comparison of a new vortex cavity formation and the resulting cluster dynamics was obtained (Fig. (5.17(c.1)) & Fig. (5.17(c.2))).

5.3.7.2.2 Effect of re-entrant jet motion

As strongly suggested in the literature, the re-entrant motion induces intrinsic instability in the expanding cavity regions [170-174]. This effect captured by our simulations is shown in Fig. (5.18).

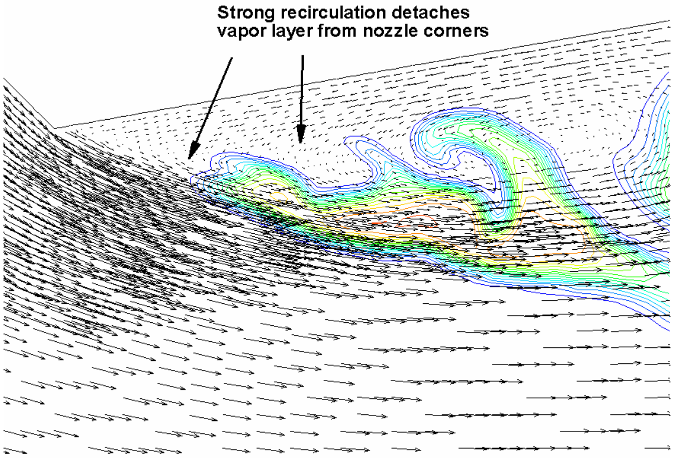

Figure 5.18: Plot of velocity vectors indicating the influence of reverse flow on vapor layer detachment from the nozzle walls. Contour color lines indicate vapor volume fraction.

In the initial stages of the simulation, no re-entrant jet was observed leading to growth of cavities along the wall as seen in Fig. (5.18(a)). However, appearance of re-entrant jet motion strongly disrupted the cavitation growth. The vapor layers were detached from the nozzle walls as the re-entrant jet propagated upstream. The re-entrant flow motion was unsteady and hence resulted in fluctuations in the cavity length closer to the wall. Observations from the experiments of Sato et al. [272] indicated separation of intense cloud cavitation regions from the nozzle walls. The computed magnitude of flow reversal velocities closer to the throat regions were as strong as the bulk flow velocity. Experiments on flow reversal intensities indicated similar characteristics [172].

5.3.7.3 Computations with Nozzle-B

With increased divergent section angle, the flow separation was more prominent. Transient plots of vapor volume fraction contours are shown in Fig. (5.19). Observe from Fig. (5.19(a)) that the resulting cavity formation, due to flow expansion, was not favored close to the wall due to strong adverse pressure gradients detaching the vapor layers [171]. The cavity clusters continued to interact with the vortical structures and resulting in their elongation, Figs. (5.19(b) & (c)) and later, Fig. (5.19(d)), formation of larger cavities downstream. Similar to the smaller divergent angle type nozzle, larger cavities split into smaller fragments and were convected downstream within the flow as shown in Figs. (5.19(d) – (g)). As flow expansion occurred, the diffusion of the cavitation clusters occurred bringing them closer to the nozzle walls as seen in Figs. (5.19(h) – (k)).

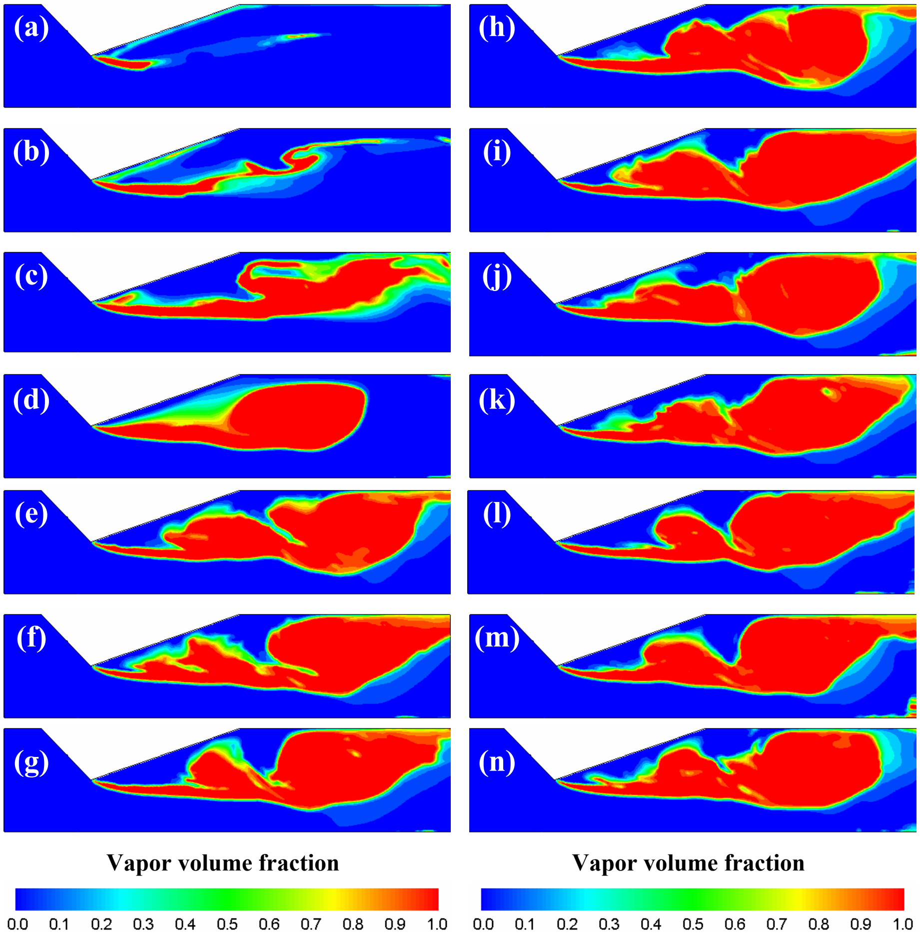

Figure 5.19: Transient evolution of vapor volume fraction for nozzle type B with $\theta = 18^{o}$. Flow characteristics include Re = 2.7X10^6 and $\sigma_c = 6.5$.

Strong shear layer interactions cause cavity roll-up, Fig. (5.19(l)), which then merge with the large scale structure resulting in bigger cavities. These events are illustrated in Figs. (5.19(l) – (n)). Due to increased slope of the tunnel wall, the vortex shedding phenomenon is modifed distinctly. The interaction of the vortex shedding with the cavitation clusters for nozzle-B is shown in Fig. (5.20).

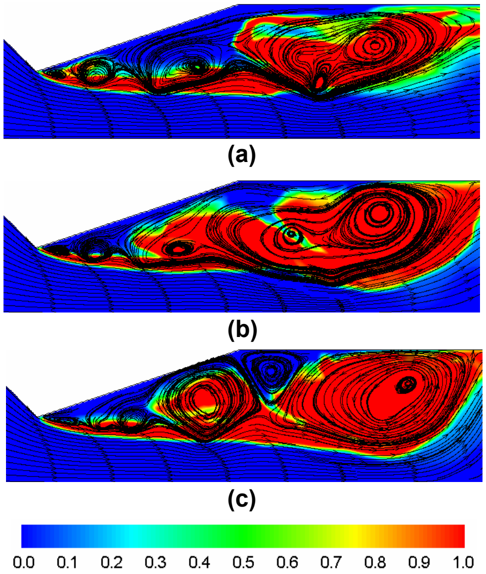

Figure 5.20: Cavity vortex interactions for increased divergent angle ($\theta = 18^o$).

Transient evolution of vapor fraction engulfed in vortical structures is depicted in Figs. (5.20(a-c)). As the mixture flow enters the constant channel height section downstream we observe only large scale vortices as a result of smaller vortices coalescence enforced by the phenomena of viscous diffusion. We plot the vorticity magnitude, superimposed on vapor fraction, at different time instants in Fig. (5.21).

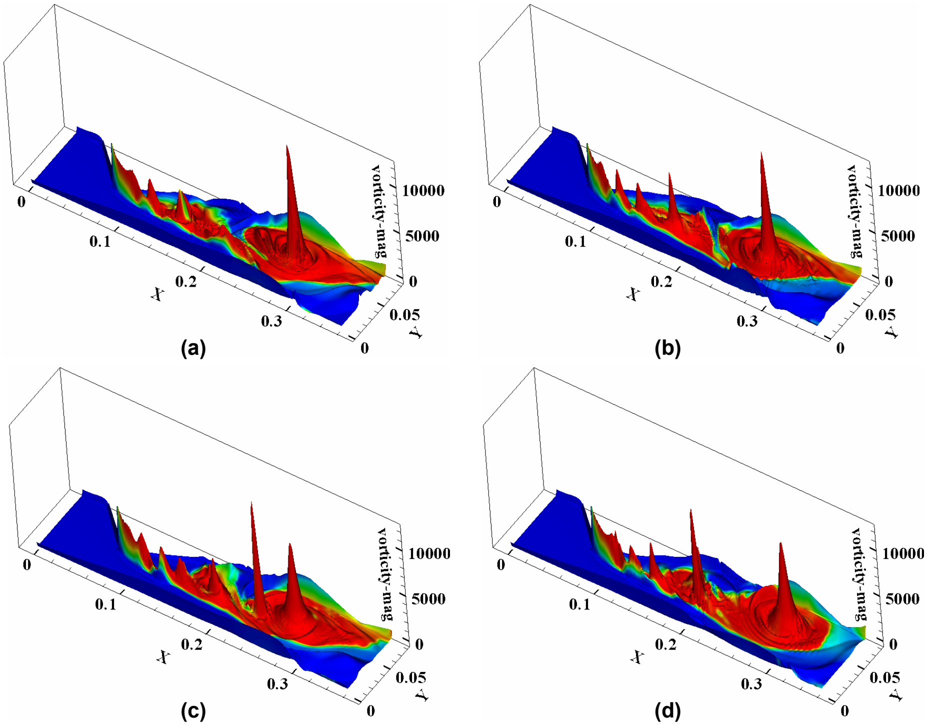

Figure 5.21: Plot of vorticity magnitude for nozzle type B. Large scale vortex structures are observed downstream towards the nozzle exit with increased cavitation intensity.

Notice the shift in higher vorticity components further downstream as compared to the structures observed in nozzle-A with smaller divergent angles. The modifications in flow structure bring along pronounced variation in the vapor distribution in the domain. No fixed cavitation near the throat and further downstream is observed. Distances *He*/2 and further downstream, cavitation interaction with multi-scale vortices embedded in the flow causes the development of larger cavities indicative of transitional cavity flow phenomena (Fig. (5.21)). Extending beyond *He* downstream the cavity length and width increase in a pronounced manner providing a measure of diffusion controlled flow regime.

5.3.7.3.1 Near wall cavitating flow structure using nozzle-B

The effect of adverse pressure gradient has a deep impact on the distribution of cavity clusters in the downstream portion of the nozzle. As the vapor layer expands in the low pressure region close to the walls, presence of steep pressure gradients act against the vapor growth leading to their quick detachment. We plot the velocity vectors with contours of vapor fraction in Fig. (5.22(a)) to identify this effect. Due to this effect, the stability of the vapor layer is compromised and fluctuating characteristics are observed with unsteady cavity attachment and detachment process in the near wall region. Strong re-entrant flow affecting the bubbly cavitation cloud separation near the throat is shown in Fig. (5.22(b)). The thickness of the cavitation layer is decreased to diffusion of re-entrant liquid flow into the clusters affecting their collapse.

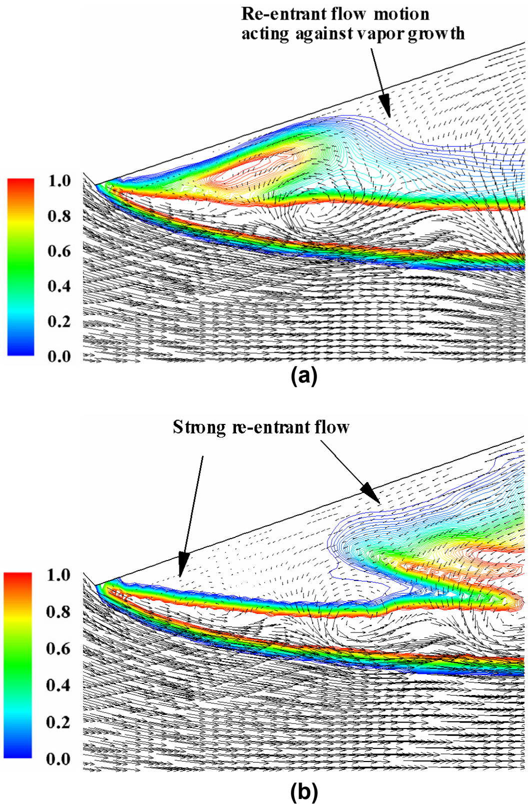

Figure 5.22: Vector plot showing enhanced flow reversal mechanism curbing the growth of cavity in the near nozzle wall region.

A comparison of the collapse region simulated using the numerical model with the experimental data is shown in Fig. (5.23).

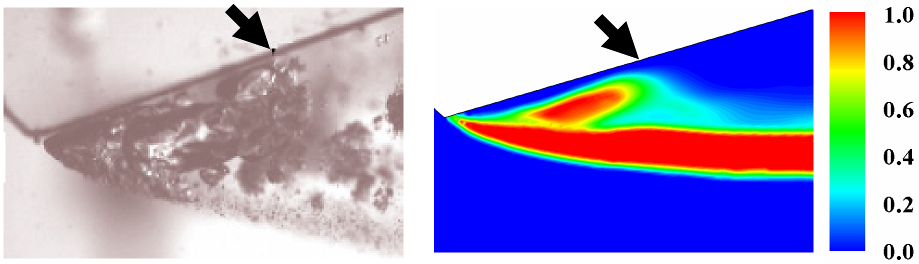

(a) (b)

Figure 5.23: Observing the activity of cavity clusters near the leading edge of the nozzle divegent section for nozzle type B (a) experimental results [272] (b) numerical simulation indicating contour plot of vapor volume fraction. Arrow heads depicts effective capturing of the cavity collapse regions.

The strong influence of adverse pressure gradient negating vapor diffusion is well handled by the model. However, the thickness of the cavitation layer is over predicted during the initial simulation stage owing to the suppressing influence of viscous and surface tension forces on the bubble dynamics [34, 185, 190]. Also, holding the bubble density constant irrespective of the vapor concentration may not be entirely appropriate and an accurate transport function is required to completely model the bubble distribution in the flow field.

5.3.8. Concluding remarks

A new numerical methodology for tracking events of cavitation is presented in Sections (5.3). The model introduces effect of liquid-vapor mixture compressibility in regions of cavitation into a predominantly incompressible bulk liquid flow. In comparison with the experiments, the model was able to predict qualitatively accurate cloud cavitation shedding and non-linear vortex interaction phenomena. Within a locally compressible framework, mechanisms of cavitation cluster coalescence, pinch off, growth and collapse of partial cavities were well attuned. Prediction of vortex cavities formation and diffusion showed remarkable similarities with the experimental observations. The simulation showed its capability of simulating various descriptions involving sheet and cloud cavitation phenomena. Firstly, the mechanism of re-entrant jet formation and the effect of adverse pressure gradient on the sheet development along the nozzle walls aligned well with well established instability theories that explain cavitation cluster growth and shedding process. Following this, the magnitude of re-entrant jet was demonstrated to be of the order of the bulk flow velocity. Finally, generation of a local pressure depression resulting from a cavity pinch-off resulted in the closure of the sheet. A secondary jet like liquid rushing behavior impinging on the nozzle walls perturbing the rear end of the cavity was observed. The re-entrant jet motion appeared to be complex due to the localized perturbations. With different nozzle configurations, the cloud cavitation behavior was influenced appreciably. Cavitation clusters were concentrated at the vortex centers and diffused as they propagated downstream. Vortex merging process resulted in extension of vapor regions as they convected towards the nozzle exit. The present simulation does not take into account the presence of non-condensable gases which can alter the cavitation dynamics distinctly. In addition, a transport equation for the bubble number density is necessary to improve coupling with the bulk flow regime. Overall, this model can be applied with ease to any existing eulerian formulation to track cavitation events and feedback the concerned effects.

5.4 Coupled Internal-External Nozzle calculations

The flexibility of the Cavitation-Induced-Momentum-Defect methodology described in Section (5.3) lies in its ability to be linked to any Eulerian flow solver by providing the necessary properties of the cavitating mixture. In the current section, the CIMD approach is employed to track events of cavitation and to model their effects on a liquid jet discharging from a planar nozzle into ambience. Volume-of-Fluid methods are used for tracking the liquid-gas interface confronted in the exterior nozzle zone. This testing process is carried out to validate the extension of CIMD to multiphase flows. The experimental setup of Akira et al. [278] is used for validation purposes. In their experiments, sharp corned nozzles were used with varying inlet flow Reynolds number to scrutinize cavitation effects. The physical domain used in the experiments and the corresponding computational domain for CFD calculations are shown in Fig. (5.24). The nozzles used by Akira et al. [278] were planar with a 1 mm thickness. Using the planar assumption with symmetry, for ease of computation, two-dimensional CFD computations are performed in the current study. The computational domain in the external region extends upto 10 nozzle hole height in the flow direction, while a domain length of 5 nozzle diameters are engaged in the orthogonal y-direction as indicated in Fig. (5.24).

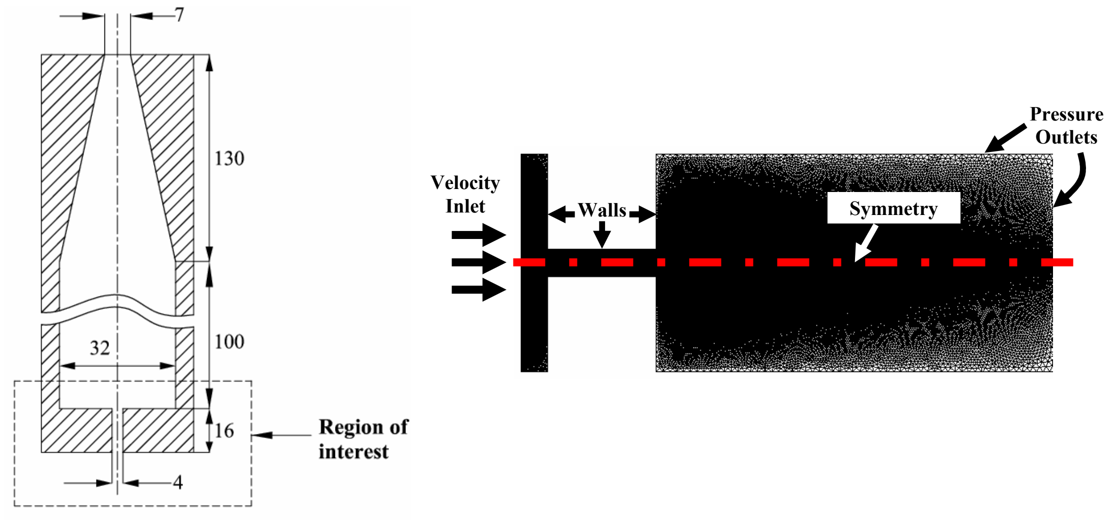

(a) (b)

Figure 5.24: Physical and computational domain from the experiments of Akira et al. [278]

For validation purposes, Akira et al. [278] defined the cavitation number (σ_c) and Reynolds number Re as

$$\sigma_c = \frac{P_a - P_v}{\frac{1}{2}\rho_L U^2} \tag{5.58}$$

$$\mathrm{Re} = \frac{U_N W_N}{\nu_L} \tag{5.59}$$

where W_N represents the length of the nozzle sac and is taken as the characteristic length scale and U_N the mean velocity of the liquid inside the nozzle is assumed to be the fundamental velocity scale. Details of two test cases presented here for validation purposes are given in Table (5.1).

Table 5.1 List of test cases used for validating the CIMD approach to multiphase flows

Mean velocity in the nozzle (m/s)	**Reynolds number (Re)**	**Cavitation number (σ_c)**
17.0	*68000*	*0.69*
17.5	*70000*	*0.65*

Numerical simulations of the coupled cavitating flow with liquid jet disintegration process are carried out using the commercial software code Fluent [241]. Mesh generation procedure for CFD computations are carried out using GAMBIT [241]. Unstructured triangular meshes are used for the computations and appropriate grid fineness is preserved to minimize diffusion effects and enhance the interface tracking process. A closer view of the unstructured mesh created near the nozzle entrance and exit regions are shown in Fig. (5.25). Volume-of-Fluid multiphase model in combination with a Geometric reconstruction scheme for interface tracking the water-air interface is adopted. User defined functions computing relevant momentum and vapor scalar source terms are connected to Fluent using an interpreted method.

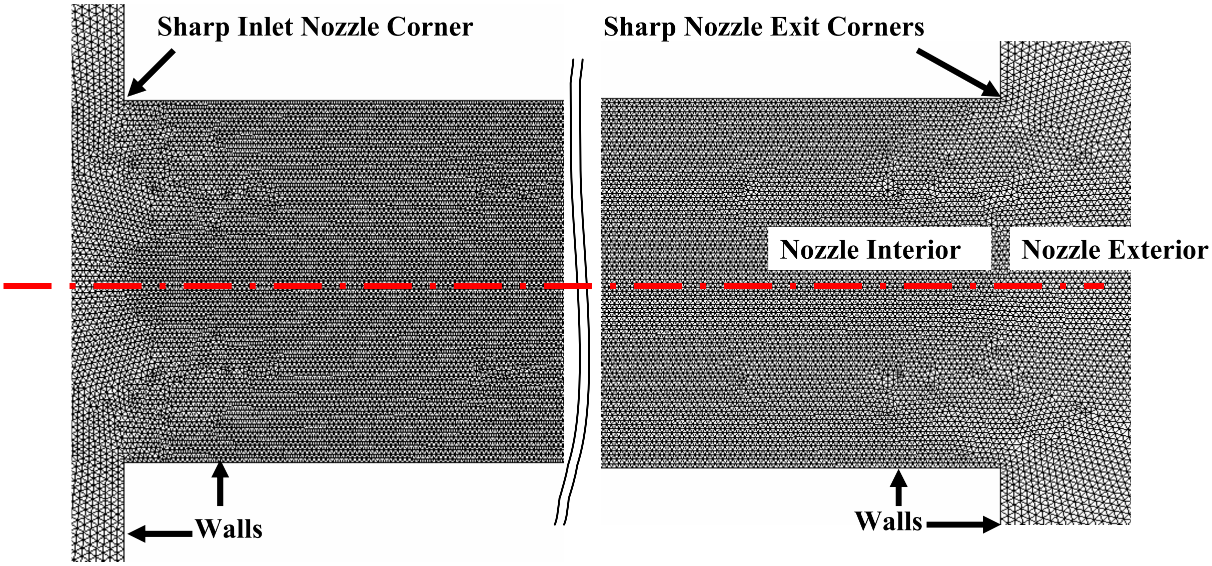

Figure 5.25: Closer view of the computational grids used in the coupled internal-external nozzle flow calculations

The equations governing the CIMD methodology are solved only if the cell is completely filled with water. This is particularly true, since water-air-vapor mixture cannot co-exist in a given cell. Bubble number density of 10^{14} / m^3 used in Section (5.3) are retained in the present computations.

5.4.1 Numerical solver controls

As a result of embedding a user defined vapor transport equation in a multiphase flow solver, problems arise in their discretization within the multiphase framework. Section (5.3.7) detailed the numerical validation of the CIMD strategy in a domain comprising of a single fluid. Higher order momentum and scalar discretization were opted since the process involved no inclusion of a second phase, although a pseudo second phase, the vapor, existed in the domain. In the current scenario, existence of a gas phase necessatitates inclusion of a higher order surface reconstruction scheme which demands strong stability in the liquid and gas flow for accurate computation. Constrained by the stability issues imposed by the interface tracking strategy, a lower first order upwinding process is adopted for momentum equations. However to capture the transient cavitation effects, a second order upwinding scheme is used for discretization of the scalar variable [138, 150]. Attempts to use a QUICK scheme for scalar equations to track the cavitation events with higher sensitivity were unsuccessful largely due to its destabilization effect within the VOF scheme. Pressure discretization is carried out using a body-weighted force method, typically used for in scenarios concerning interfacial dynamics. The source terms generated by the vapor scalar adds further complexity to the stability of momentum equations in addition to the existing confusions created by the surface tension term. The CIMD approach based on a momentum source/sink defect correction methodology is appropriately treated as a body force in the current model. Furthermore, the under-relaxation factor for the scalar variable is reduced to 0.0005 to ensure stability of the computation. For including the flow turbulence effects, an RNG k-ε model is incorporated without any corrections for the density variable in the low viscosity regions to ensure stability in the computations. Adaptive time stepping procedures are adopted to provide stability to the computations. The simulations are run in the Superdome HP clusters at the University of Kentucky in a parallel fashion in an 8 way mode. Results obtained from the simulations are presented in the preceding section.

5.4.2 Results: Liquid jet disintegration with cavitation effects

5.4.2.1 Simulations with Re = 68000, σ_c = 0.69

Figure (5.26(a-h)) describes transient evolution of the cavitation scalar within the nozzle interior for Re = 68000 and σ_c = 0.69, while simultaneous propagation of the liquid fraction outside the nozzle is depicted in Fig. (5.26(a’-h’)). Instabilities steming from the engagement of liquid with the ambient gas are markedly visible from the contour plots of liquid volume fractions. The highly transient vapor inception, growth and convection process are captured by the CIMD methodology as shown in Figure (5.26(i)(a)-(c)).

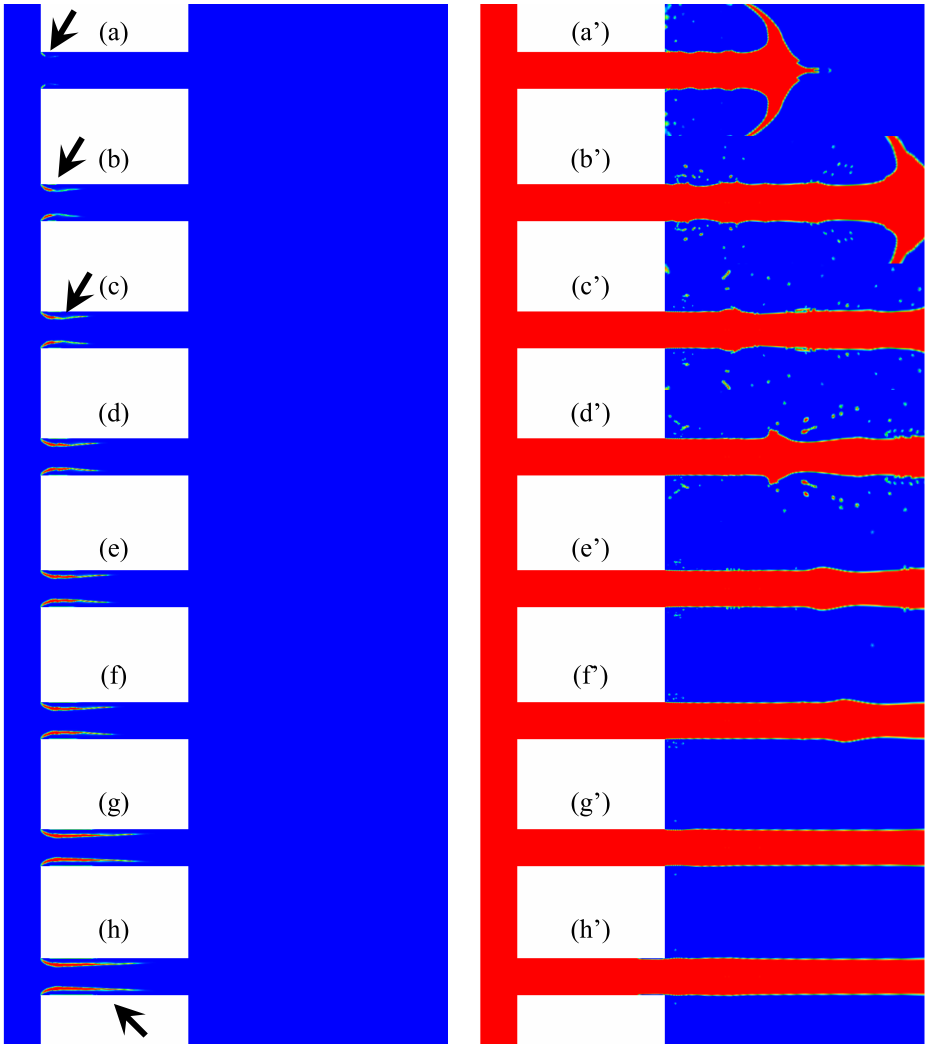

(i) (ii)

Figure 5.26: Simulataneous transient evolution of (i) vapor scalar (ii) liquid jet in the compuational domain for Re = 68000, $\sigma_c = 0.69$.

In the current case, the cavitation layer collapse occurs inside the nozzle and no events of supercavitation are recognized. A closer view of the partial cavitation process modeled by the CIMD approach is detailed in Fig. (5.27).

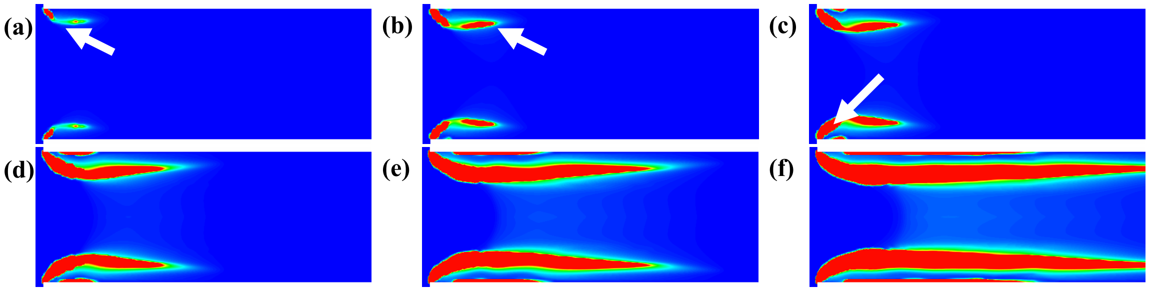

Figure 5.27: Evolution of vapor region within the nozzle sac predicted by the CIMD strategy close to the nozzle entrance regions. Nozzle exit regions are omitted for clarity purposes. Flow direction is from left to right. Color: Red – vapor, Blue – Water.

The transient CIMD model predicts, vapor inception, Fig. (5.27(a)), detachment, Fig. (5.27(b)), diffusion and transport process, Fig. (5.27(c)-(f)) within the liquid phase very effectively. The use of higher order discretization method for the vapor fraction scalar helps capture the flux direction sensitive transport process. Since the CIMD approach is strongly coupled to any variation in the pressure variable, presence of vapor clusters in the recirculation regions in the near nozzle entrance regions, generated by intense pressure gradients, are well accommodated.

5.4.2.2. Simulations with Re = 70000, σ_c = 0.65

Increasing the Reynolds number of the jet with lowered cavitation number results in intensification of the cavitation clusters within the nozzle, recognized from the vapor contour plots presented in Fig. (5.28). The axial length of the cavitation zones extend farther towards the nozzle exit. Intense cavitation bubbles grow along the nozzle walls till they reach the exit section representing a fully developed cavitation process. Due to the boundary effects, some unsteadiness in the cavity clusters prevails near the nozzle exit region. Evolution of liquid jets into the ambient and the resulting interfacial dynamics are visualized in Fig. (5.28(ii)). The instabilities in the liquid jets, as a result of flow modification generated by the cavitation dynamics within the nozzle interior zone, are marked in Fig. (5.28(ii)b-f). Wavy jet structures are detected with temporal evolution of the liquid jet in the nozzle exterior.

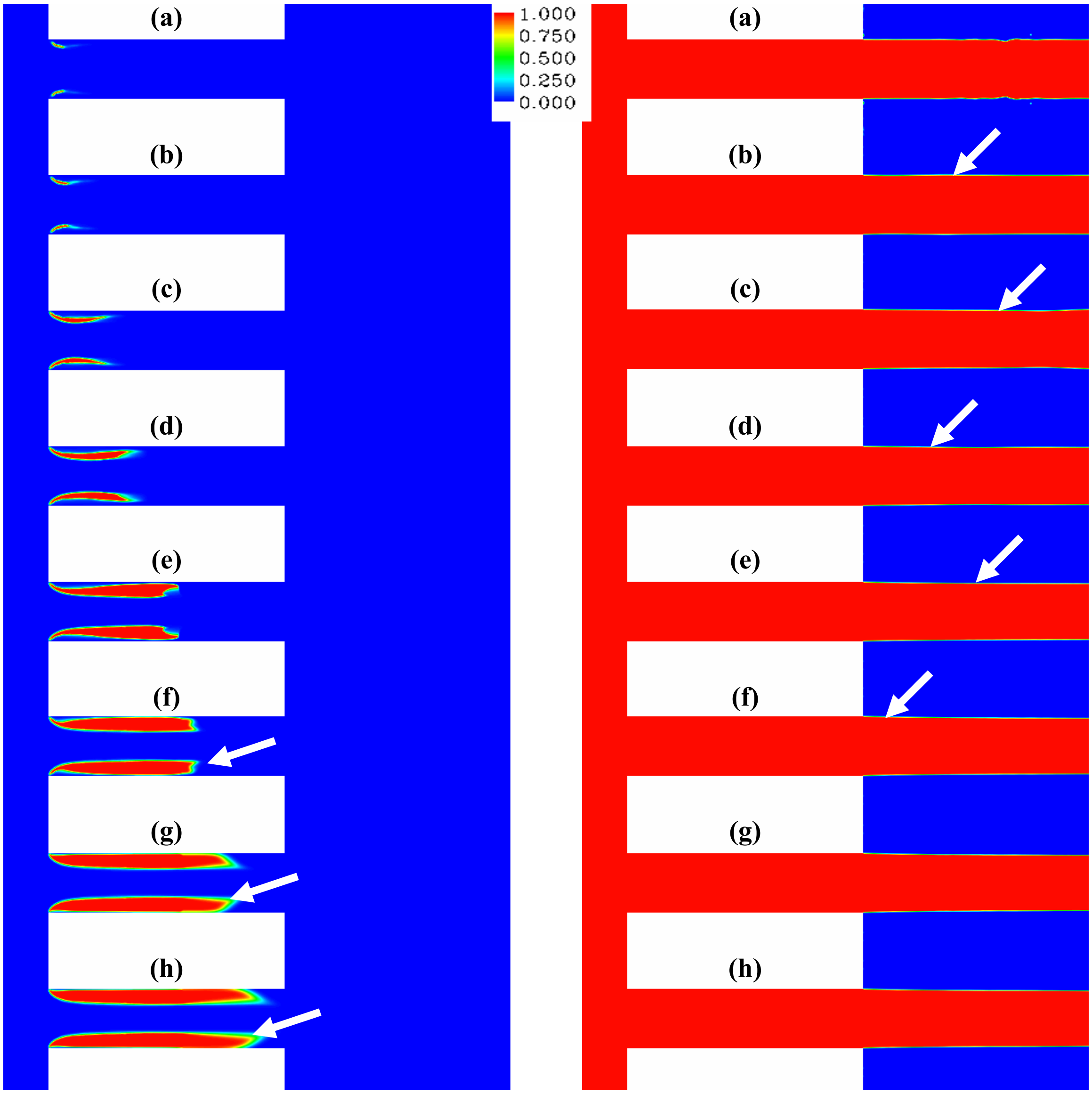

(i) (ii)

Figure 5.28: Transient evolution of (i) cavitation vapor fraction (ii) liquid volume fraction in the computational domain with Re = 70000, $\sigma_c = 0.65$.

Magnified view of the vapor dynamics in the near nozzle entrance zone is detailed in Fig. (5.29). In comparison to Fig. (5.27), the thickness of the cavitation layer is markedly pronounced. This is attributed to flow Reynolds number effect: Increase in Reynolds number results in amplification of shear rates near the nozzle entrance regions. Since the shear rates are intricately coupled with the pressure gradients, which in turn dictate cavitation rates, strong vapor formation events are encountered near the sharp corners. Undulations in the evolving cavity flow near the nozzle corners are detected by the model (Fig. (5.29 (a-b))).

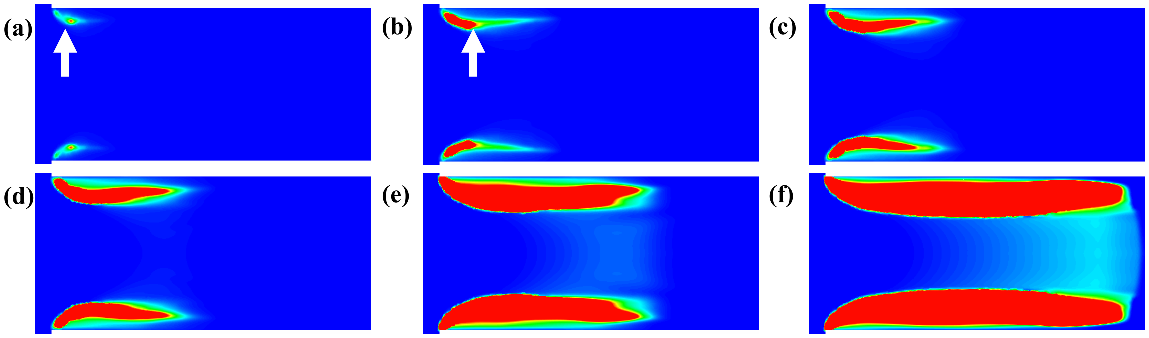

Figure 5.29: Growth of cavitation clusters near the nozzle entrance region with Re = 70000, $\sigma_c = 0.65$.

5.4.2.3 Comparison with experimental observations

The two computations presented in Section (5.4.2.1) and (5.4.2.1) are validated qualitatively against the high quality spatial images obtained by Akira et al. [278]. The comparisons presented in Fig. (5.30) shows very good agreement between the real-time cavitation studies against the CIMD based cavitation model.

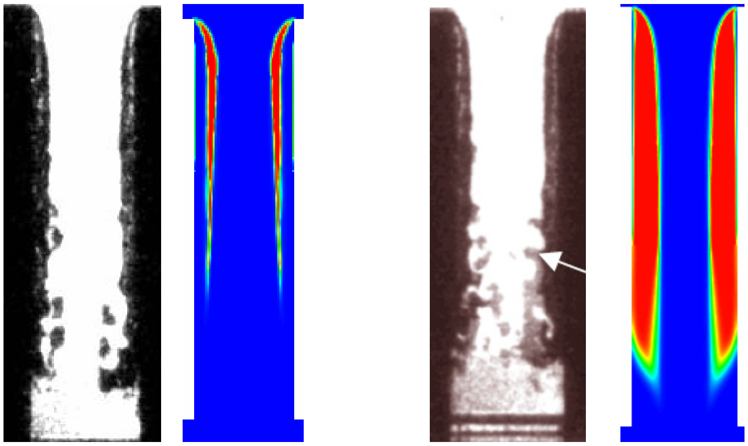

(a) (b) (a) (b)

(i) (ii)

Figure 5.30: Comparison of numerical simulations with the experimental data [278] (i) Re = 68000, $\sigma_c = 0.69$, (ii) Re = 70000, $\sigma_c = 0.65$

In the low Reynolds number case, Re = 68000, the cavitation cluster length is under-predicted by the model by about 15%. In the case of Re = 70000, the CIMD based prediction of the cavity length matches exactly with the experimental data, although the thickness of the vapor sheet is strictly over-predicted. Both the deviations are attributed to the varied approximations used in the model such as constant bubble number density and first order bubble growth effects. Further, the model does not include any effect of immersed gas nuclei which, under low pressures, can alter the pressure content of the bubble appreciably and modify the vapor dynamics.

Another comparison presented in Fig. (5.31) acknowledges the shear-rate sensitivity of the CIMD model. Under both Reynolds number cases, the visualization of cavity sheet separation from the nozzle walls is tracked efficiently by the CIMD based cavitation model. This is attributed to the incorporation of the local vapor relaxation effect in the CIMD model which implicitly treats the drag force encountered by the vapor phase in regions of high shear. Also, the predicted smoothness of the vapor scalar in the nozzle entrance regions devoid of any perturbed interface features compares identical to the experimental observations [278] as shown in Fig. (5.31).

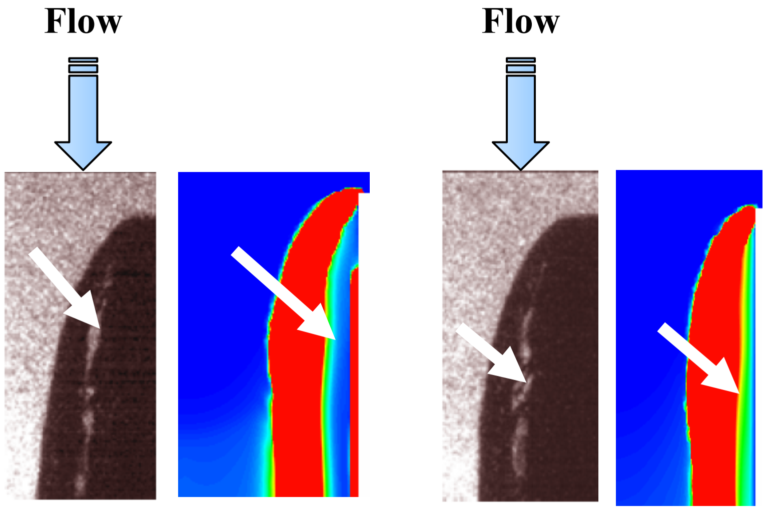

(a) **(b)** **(a)** **(b)**

(i) (ii)

Figure 5.31: Cavitation phenomena in the nozzle entrance regions for (i) Re = 68000, $\sigma_c = 0.69$, (ii) Re = 70000, $\sigma_c = 0.65$ [278]

The results presented in Section (5.3.10) reveal the capability of the present model to be extended to multiphase computation scenarios. Although, the CIMD model identified the partial and fully developed cavitation regimes, the VOF based interface tracking approach with turbulence effects captured only the wavy jet regime and little disintegration of liquid jet was observed in the flow with Re = 68000. However, for a flow Reynolds number of 70000, experiments of Akira et al. encountered spray regime which is not well established with the current VOF model. Influence of high turbulent viscosity is suspected to play a role in liquid-gas instability suppressions.

5.5 Closure

We have developed new cavitation models in both a compressible framework and later extended to an incompressible regime. The models have been validated against experimental observations giving an account of their predictive capability. The cavitation-induced-momentum defect approach is extended within a two-phase flow configuration involving liquid jet discharge into a free air environment resulting in its subsequent disintegration. The differential cavitation effects arising from varying flow Reynolds numbers are well captured by the CIMD based cavitation model. Based on this study, the preceding chapter is dedicated to carrying out computations in the atomizer configuration proposed in Chapter 4. Copyright © Vedanth Srinivasan 2006.

Chapter 6

Numerical Simulation of Jet Disintegration using CIMD Strategy and New Prototype Design

6.1 Simulations of jet disintegration using a two-zone approach

The major methodology employed in the current study concerns the use of a two-zone discrete modeling approach to design a new spray applicator. A schematic of the two-zone approach is presented in Fig. (6.1).

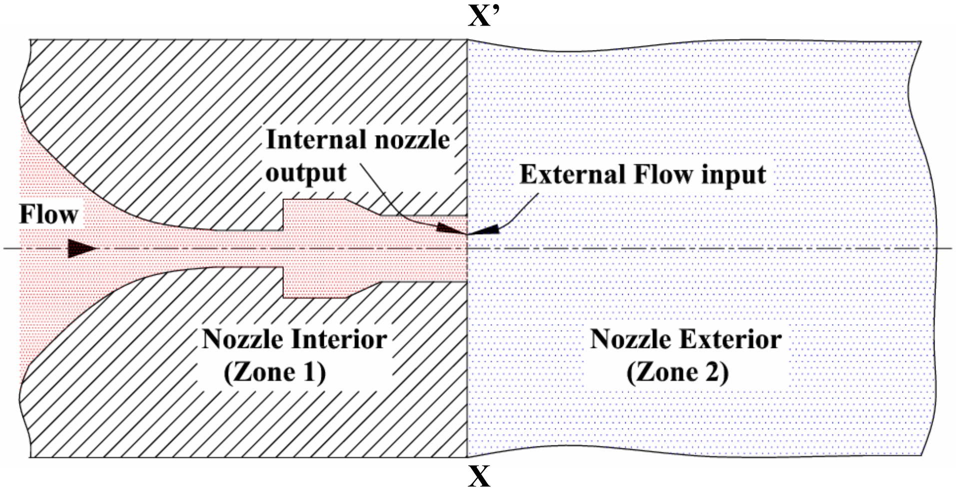

Figure 6.1: Two-zone approach used for simulating disintegration of liquid jet emanating an atomizer

Utilizing a multiphase cavitation model, wide range of numerical simulations were reported in Chapter 4 detailing the interior nozzle geometry characterization, while Chapter 3 discussed various disintegration phenomena subjected to specific initial modulation conditions. Associating the information on modulated liquid jets with the internal cavitating flow dynamics, configuration C_3 is adopted to obtain enhanced breakup of cavitating forced liquid jets. At this juncture, we are provided with the internal nozzle geometry based on which the exterior drop formation process requires to be modeled. Simulations of the exterior jet disintegration process subjected to the interior nozzle flow design obtained from C_3 configuration is carried out by extracting the details of the relevant flow variables at the nozzle exit section X-X' as described in Fig. (6.1).

The fundamental design of the atomizer demands that the flow passing through the nozzle exit section be pulsated through the use of a high-frequency (ultrasonic) horn. Furthermore, several processes such as horn motion induced vorticity transport, shear layer formation near the backward-facing step etc. inherent to the current configuration, can potentially induce additional perturbations characteristics on their own, superimposed on the explicit pulsation provided by the horn motion. This effect is illustrated in Fig. (6.2).

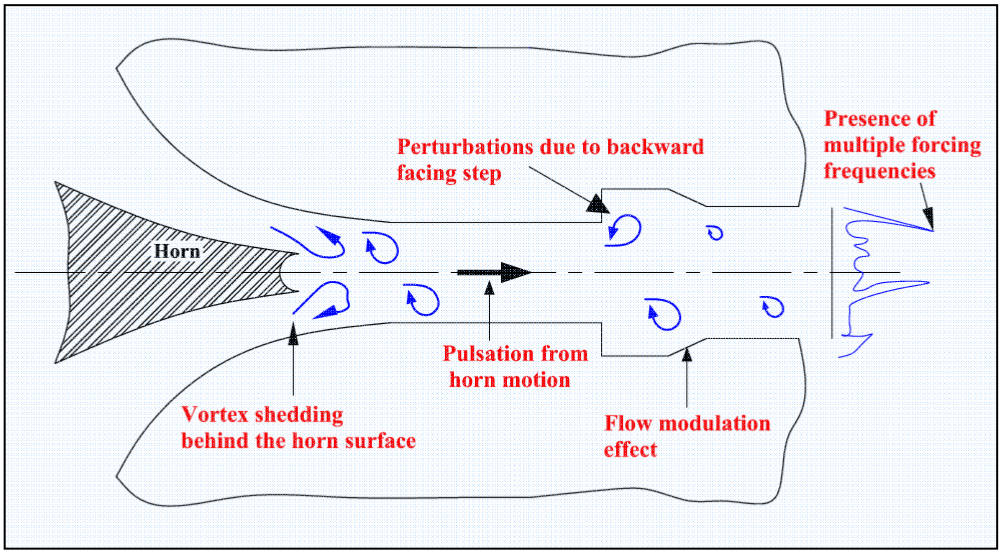

Figure 6.2: Schematic of various perturbations present in the nozzle flow

To address the multiple forcing issues, time history information of the velocity is extracted and analyzed. Figure (6.3) shows the variation in axial-velocity magnitude of the liquid-vapor mixture exiting the atomizer configuration C_3.

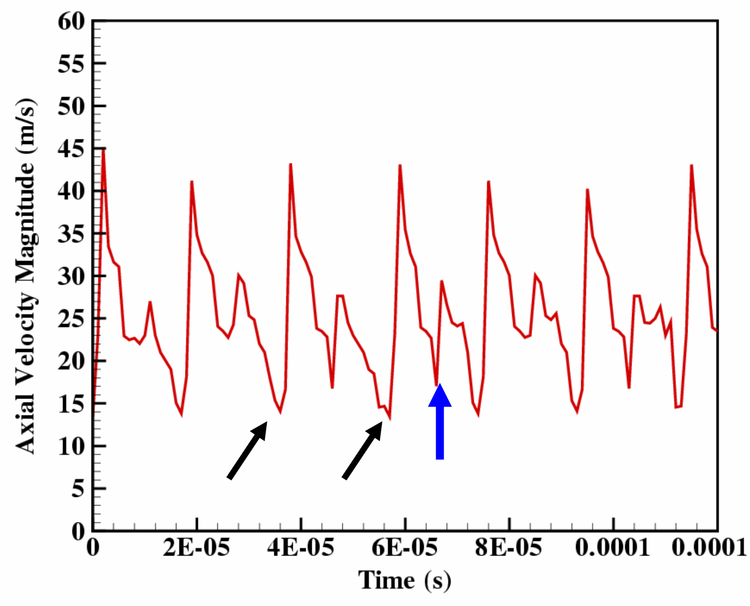

Figure 6.3: Time history of the axial velocity of the liquid jets emanating from the C_3 configuration discussed in Section (4.8.3.2). Primary collapse events are marked by balck arrow heads while secondary perturbations are distinguished using a blue arrowhead.

Notice that collapse of the supercavitating vapor regime is encountered in the lower velocity peaking as marked in Fig. (6.3). Time separation between the two peaks is of the order of 1.76×10^{-5} seconds. Computing the frequency of collapse, we obtain a collapsing effect every 1.2 cycles of the horn motion inclusive of all the coalescence, diffusion and transport effects of the liquid-vapor mixture flow. Performing a Fast Fourier transform operation on the velocity signal results in the characterization of compounded multiple frequencies in the exiting liquid jets. As shown in Fig. (6.4(a)), two power peaks at a frequency of 68000 Hz and 110 KHz are detected.

The effect of the second high frequency perturbation on the velocity perturbation is clearly distinguished in Fig (6.3).

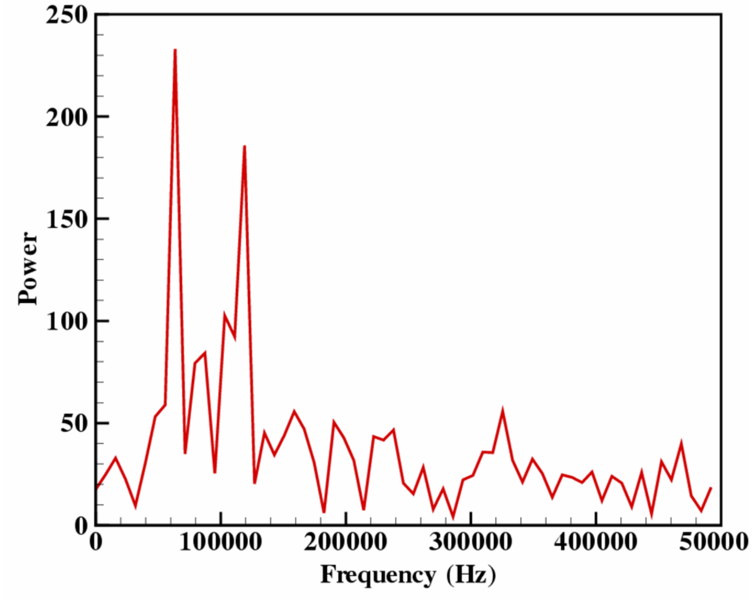

Figure 6.4: Frequency plots with 2 different frequencies

The existence of multiple frequencies indicated potential occurrence of a phase jump phenomena in the modulated jets appearance in the exterior domain. The time history data presented in Fig. (6.3) is fitted with two frequency sinusoidal perturbation frequencies; the frequencies obtained from the FFT operation with relevant signal strengths. In this connection, two numerical simulations are reported: firstly, simulations are carried out with the fundamental forcing frequency of 68 KHz, neglecting the secondary forcing frequency of 110 KHz. The mean velocity of the liquid jet and the modulation amplitude details are extracted from the time history as 28 m/s and 0.4 respectively. Preceding this computation, additional peak frequency (~110 KHz) is incorporated into the inlet boundary by utilizing the fitted velocity-history data.

6.1.1 Effect of multiple frequencies on forced liquid jets

Observe from Fig. (6.5(a) and (b)), application of different frequency modes in the exiting liquid jets result in distinct breakup characteristics.

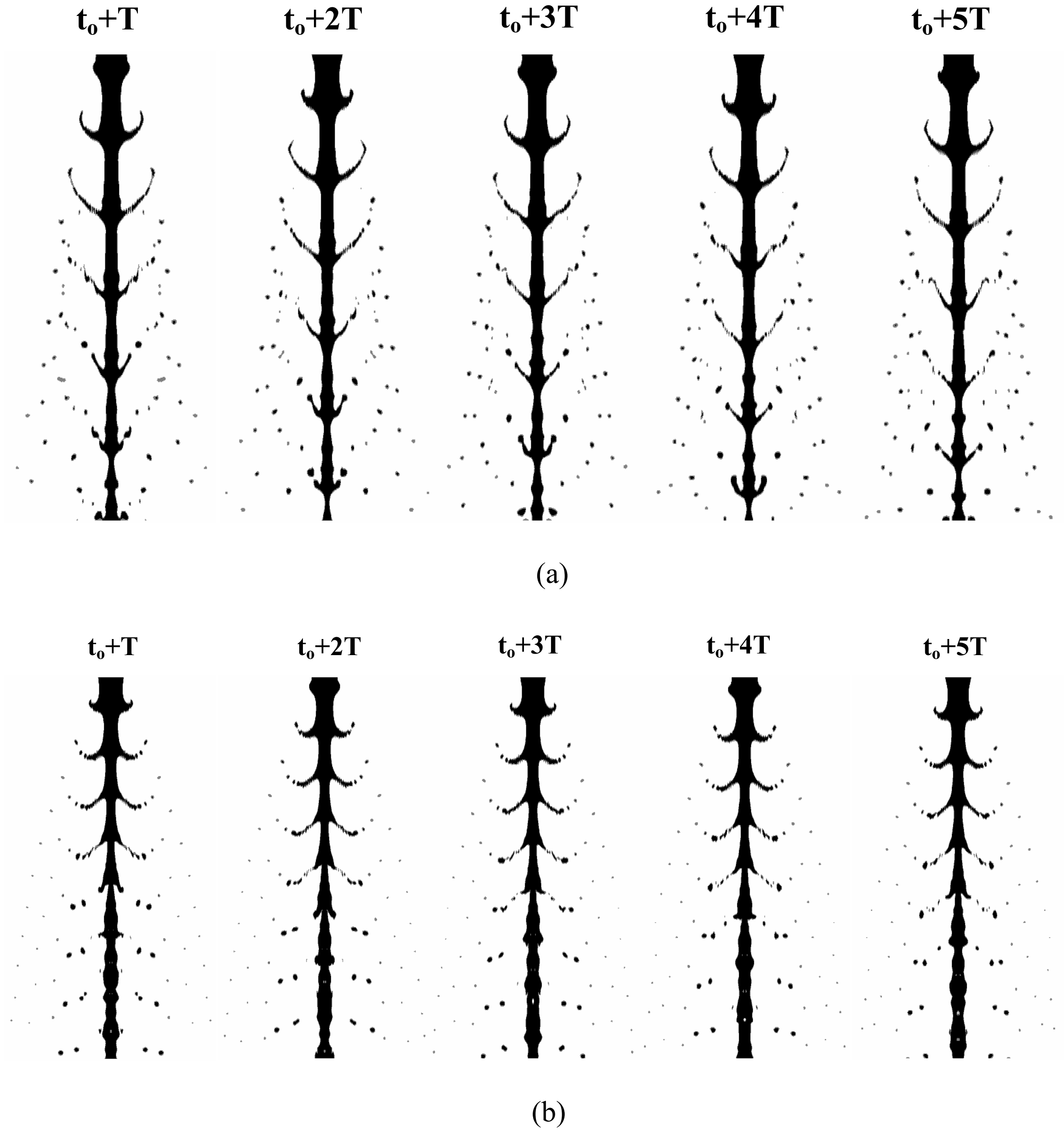

(a)

(b)

Figure 6.5: Numerical simulations of modulated liquid jet emanating from the exit of atomizer configuration C_3 with (a) single forcing frequency (b) multiple frequencies

With single forcing frequency acting on the jet, coalescence of the central liquid core is predominantly detected resulting in a reduced breakup mode. Also the effect of frequency configuration on the nature of ligament orientation is singularized. Figure (6.5(a)) shows characteristic upstream directed bells, while Fig. (6.5(b)) supports a downstream bell configuration. This is attributed to the conjoint non-linear effects rising from the multiple frequency perturbations. Yet another striking feature signalized in these compuations pertains to the length of the ligaments formed by these two configurations: A single dominant frequency in the appropriate initial condition range results in elongated ligaments breaking up into fine droplets while presence of multiple frequencies suppresses ligament formation and results in large droplet size distribution. Elevated enhancement of the liquid-gas interfacial instability owing to the presence of the high frequency secondary perturbation is numerically concluded. In both cases, however, reproducibility of the liquid structures is retained.

The simulations using a two-zone approach strongly supports the fact that discrete zoning methodology can suppress vital information concerning fluid flow statistics such as vortex phenomena and additional perturbations that might have been initiated within the nozzle. In this concern, a full internal-external coupled approach to address jet disintegration process is envisioned.

6.2 Numerical simulations with Internal-External Coupled Approach

The two-zone approach presented in Section (6.1) indicated the severe consequence of applying discrete zoning approach for investigating the disintegration behavior of round liquid jets. Consequently, in order to completely predict the overall disintegration process, utilization of a coupled internal-external nozzle flow methodology is undeniable.

6.2.1 Boundary conditions modeling for coupled computations

The requirement of specifying accurate boundary conditions is instrumental in obtaining physically realistic solutions within the relevant accuracy limits [138, 146, 150]. The overall cavitating atomizer system designed in this study comprises of a moving horn structure placed in a nozzle flow to aggrandize cavitating conditions within the nozzle and impose forced modulations on the exiting liquid jets. However, complexity arises in unifying the moving horn structure information into the coupled computations owing to sensitive mesh adaptation and remeshing strategies. To alleviate any problems associated with the horn structure effect, flow variable details are extracted from a section very close to the horn surface. This process is described schematically in Fig. (6.6). The 'inlet boundary' for characterizing the jet breakup lies within the nozzle region, in this case at a distance of 1mm from the nozzle exit.

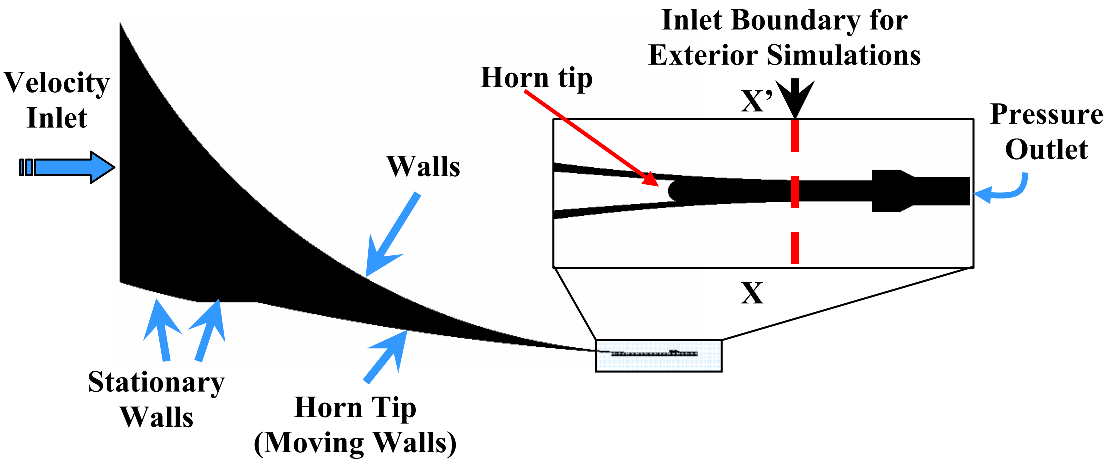

Figure 6.6: Inlet data for numerical simulation is taken at a section X-X' where the constant diameter throat section begins in the interior nozzle design

Typically, the section X-X' represents the beginning of a constant diameter nozzle throat section detailed in the C_3 atomizer configuration. By this process, any flow perturbations resulting from the horn vibration and associated dynamics can be distinctly treated and later, be applied to the nozzle downstream zone towards the exterior region. As carried out before, the numerical simulations are provided with a mean axial-velocity magnitude at the nozzle central axis, based on which a velocity profile is constructed. For providing data input to the coupled computations, time history of the axial-velocity magnitude is obtained from the numerical simulations of the C_3 atomizer configuration. Details of the time history are presented in Fig. (6.7(a)). Fast-Fourier transform operation is carried out to separate discrete operating frequencies. Result of the FFT operation is shown in Fig. (6.7(b)).

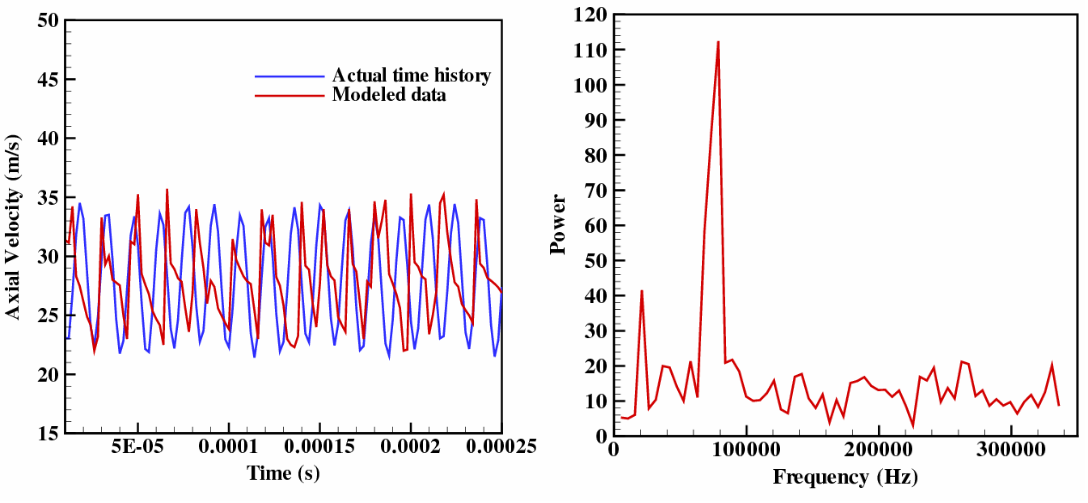

(a) (b)

Figure 6.7: (a) Actual time history and modeled data using discrete frequency combinations (b) Fourier transform of the actual time history

Similar to the observations made from the exit velocity evolution, presence of multiple frequencies is detected in the regions near the oscillating horn. Despite peaking of a large number of frequencies, two strong forcing frequencies are singularized from Fig. (6.7(b)). This operation concludes that, mechanisms associated with horn oscillations such as shear layers, flow modulation between the horn and nozzle walls etc, indeed, perturb the flow structure. For computational ease of implementing the boundary conditions, the actual time history data is modeled by compounding two sinusoidal waveforms with peak frequencies obtained from FFT operation. With the inclusion of the interior nozzle regions for coupled computations, the effects of cavitation assumptions are critical. To achieve this objective, the CIMD approach previously extended to VOF based multiphase simulations, detailed in Section (5.3), is treated here. In what follows next, coupled computations with no-modulation effects are detailed to separate the impact of modulations and later, followed by implementation of the cavitation effects. From the boundary data description from Section (6.2.1), the flow Reynolds number in the 'coupled configuration inlet', based on the mean velocity (as characteristic velocity scale) and throat diameter, assumed as the characteristic length scale, is computed as 5250. For a cylindrical nozzle flow, transitions from laminar to turbulent regimes are experienced in the range of 2300 to 4000. The current value of Reynolds number lies in the initial turbulent regime. Based on the study characterizing the importance of turbulence models in simulating the jet breakup process in Section (3.4.3), turbulence effects are strictly ignored. Hence, the only dissipative mechanism experienced by the computations stem from the viscous forces of the liquid, the ambient gas and the cavitating vapor mixture.

6.2.2 Computational methodology and simulation domain

Computational domain constructed for carrying out the coupled computations is presented in Fig. (6.8). Using the continuity assumption, given the diameter of the inlet boundary (150μm) and the exit orifice diameter (200μm) with a mean inlet flow velocity of 30 m/s, the Reynolds number of the exiting liquid jets, with out any cavitation effects, can be approximated to 4000. Clearly this is value lies in the laminar-turbulent transition regime and hence neglecting the turbulence effects can be considered beneficiary. Also, using the air density, the exiting gas-Weber number can be calculated as 4.44 which are strictly in the axi-symmetric jet evolution regime [11]. Hence, use of axi-symmetric approximations is valid and would substantially help minimize the computational effort. The disintegration simulations are carried out in openFoam running in a single-node 4 way linux PC. A total number of 250,000 grid cells were used in the domain. Mesh sizes ~ 2µm were made available near the exit of the nozzle to capture sharp transition effects and instabilities. The computational methodology used in the breakup modeling investigation has already been described in Section (3.2). In addition, the matrices arising from the discretization of the additional vapor scalar transport equation are solved using BICCG procedures. The vapor scalar equation is solved in a segregated manner following the velocity iteration loop. By using this approach, any momentum change initiated by the CIMD approach would be identified by the pressure correction loop in the PISO procedure.

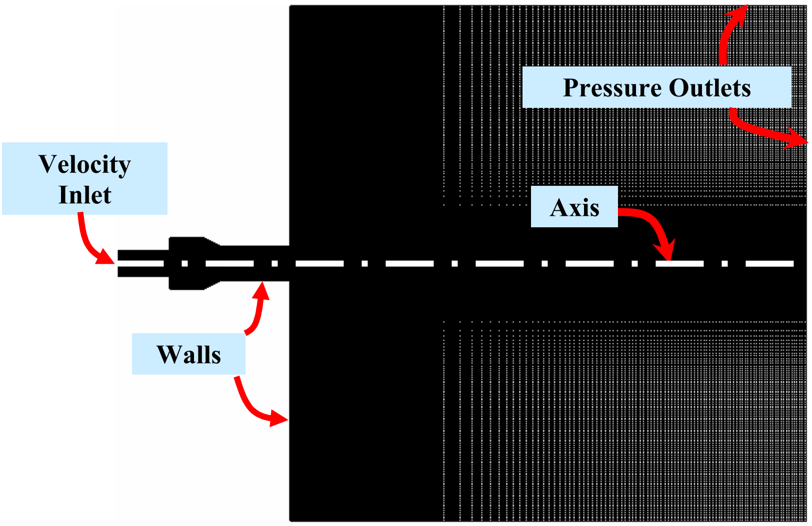

(a)

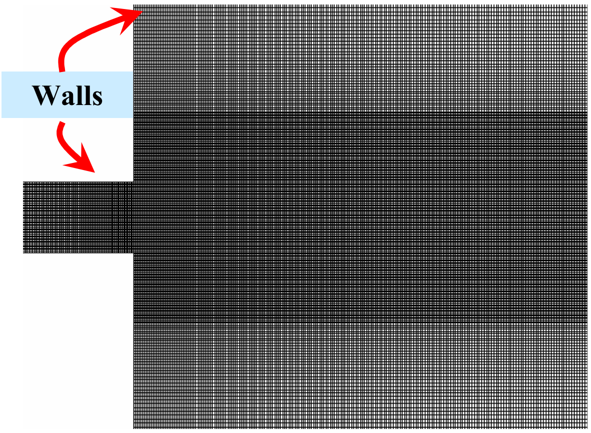

(b)

Figure 6.8: (a) Computational domain for coupled computations (b) Fine grid requirements near the nozzle exit for accurate tracking of liquid-gas interface instabilities

Inlet and outlet conditions are treated using velocity inlet and pressure outlets; implementation of inlet boundary conditions detailed in Section (6.2.2). Based on the computed Reynolds number, a turbulent velocity profile is constructed at the inlet. Standard atmospheric pressure conditions are assumed for the computations. In the case of cavitating flow simulations, a higher pressure value in the entire domain is initialized to avoid any occurrence of unrealistic cavitation events. Water, air and vapor properties are assumed for liquid, gas and vapor phases respectively at STP.

6.2.3 Coupled-Computation with no-modulation effects

The coupled internal and external nozzle flow simulations presented in Fig. (6.9) show transient evolution of the non-modulated liquid jet into the gas domain. No cavitation and turbulence effects are imposed; hence any disintegration events intercepted can be attributed to the geometry and aerodynamic effects alone.

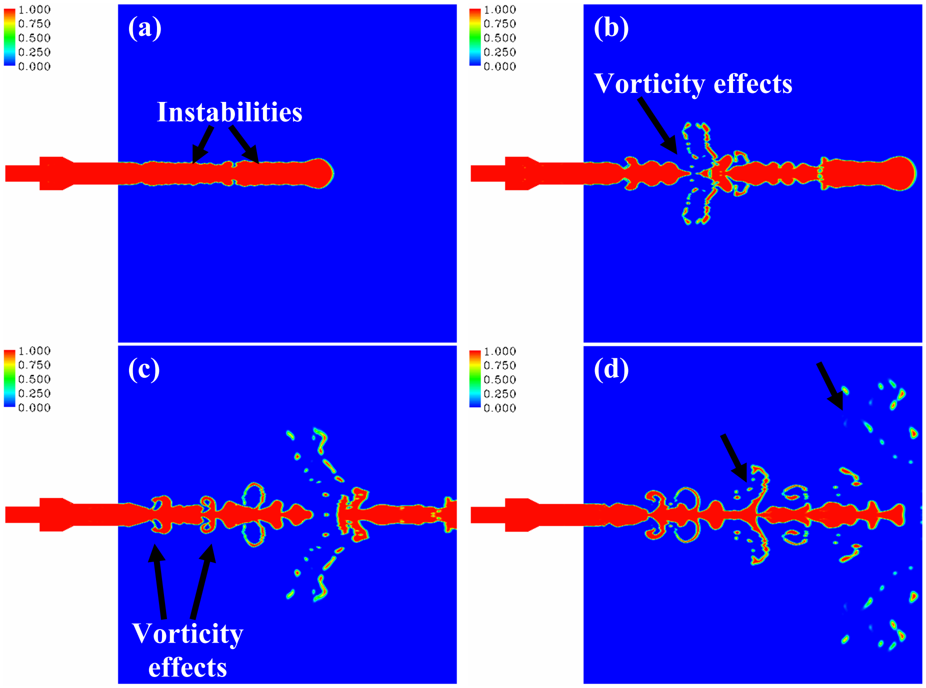

Figure 6.9: Coupled internal-external nozzle region simulation of the C_3 atomizer design using interface capturing methods with no-pulsation and cavitation effects.

The liquid-gas instability is escalated by the atomizer design which creates intense vortex activities within the nozzle owing to the presence of the backward facing step profile. The effect of vorticity in expediting the breakup process can be readily argued using Fig. (6.10). Presence of strong shear effects and vorticity components in the domain is visualized in Fig. (6.10). Notice the presence of vortex diffusion and concentrated accumulation, as they are released into the free shear region (Fig. (6.10(b)). The vortex shedding inside the nozzle is repetitive and results in constant ejection of eddy packets immersed in the liquid jets into the nozzle exterior. Upon exiting the nozzle, these vortex cores expand and result in destabilization of the liquid interface promoting breakup process. Comparing Fig. (6.9(c)) and Fig. (6.10(c)), the effects of vortex structures are clearly signalized. Furthermore, observe that the disintegrated fragments are caught in the vortex cores and are transported in the domain following regions of strong vortex presence as shown in Fig. (6.9(d)) and Fig. (6.10(d)).

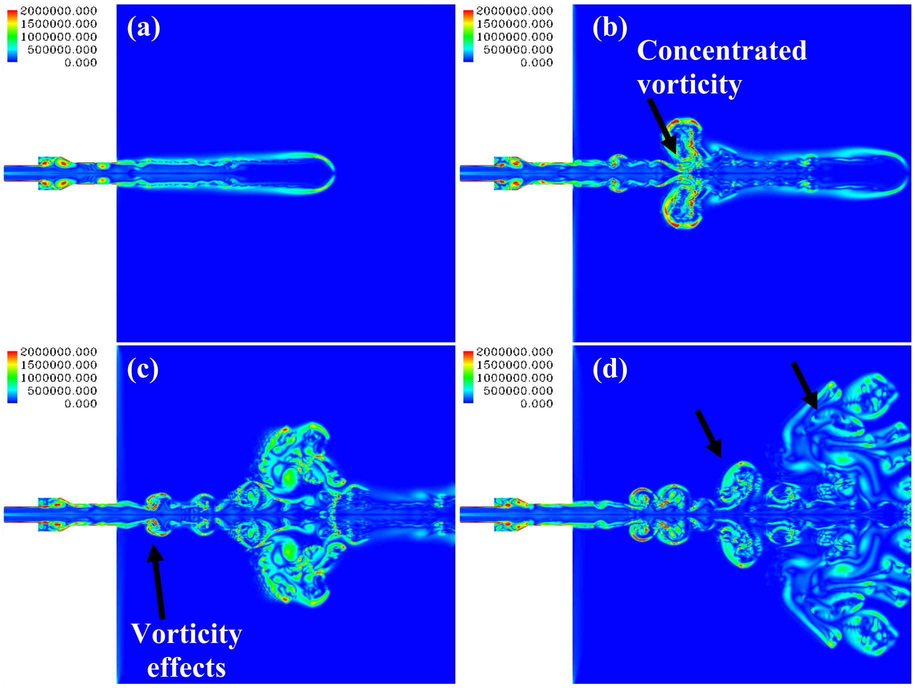

Figure 6.10: Contours of vorticity magnitude generated by the non-pulsated liquid flow in the C_3 atomizer configuration.

6.2.4 Coupled computations with pulsation effect

Figure (6.11) shows transient propagation of the forced liquid jets discharged from the C_3 atomizer configuration into the gas domain. The velocity at the domain inlet is taken from the modeled data shown in Fig. (6.7). The nature of the breakup processes, as recognized from Fig. (6.11), are similar to the results obtained by employing a discrete zoning approach with multiple representative frequencies, Fig. (6.5(b)). The reproducible liquid jet structures generated by the modulated jets, (Fig. (6.11(1-3))), are disrupted by the flow instabilities transported from within the nozzle, leading to amplified perturbations as seen in Fig. (6.11(4-6)). A truly remarkable feature of the coupled computation is its ability to accommodate interfering and mutually interacting frequency perturbations. This effect is identified by the orientation of the ligament structures in the domain.

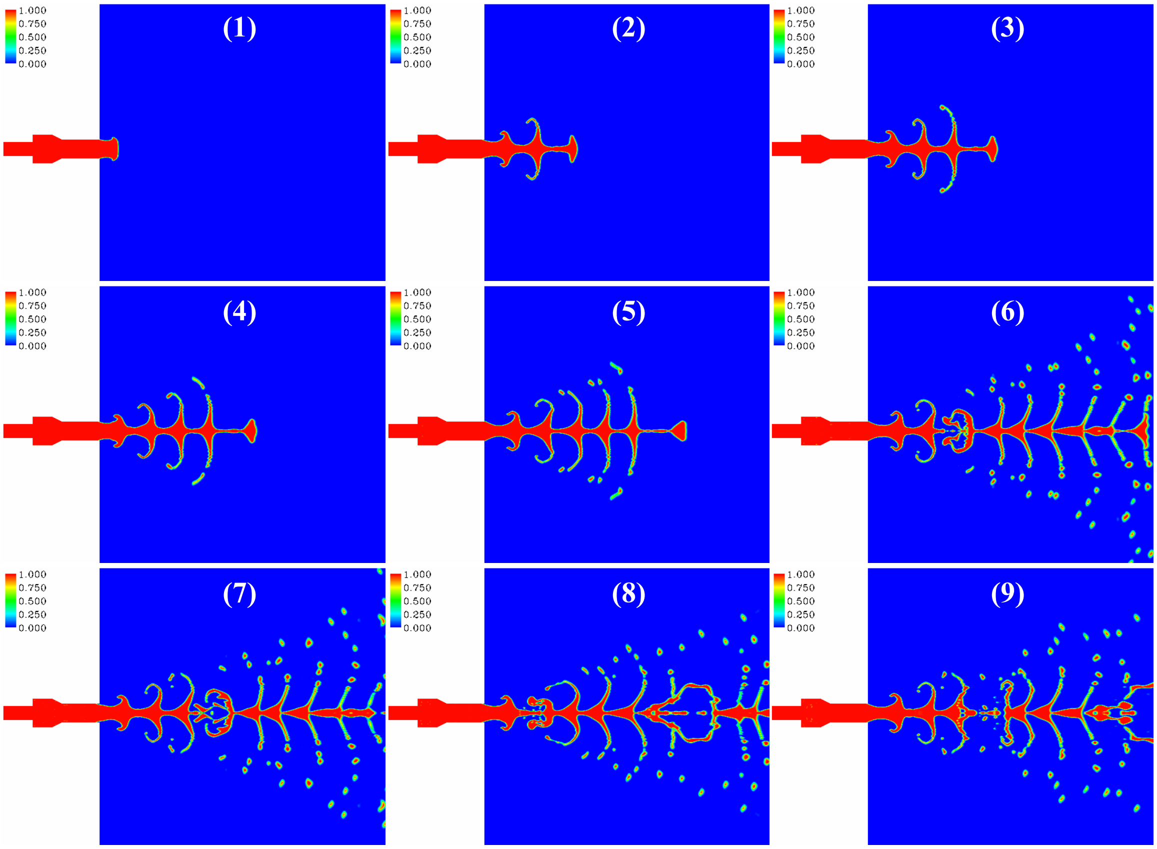

Figure 6.11: Transient evolution of modulated liquid jets emanating from a C_3 type atomizer configuration

As noted earlier, jets modulated with a single perturbation frequency resulted in a downstream directed spray structure while the inclusion of multiple frequencies dramatically altered the spray structure into an upstream directed configuration, resulting in elongated ligaments. In the coupled scenario, the ligaments in the first 5 nozzle diameters are bent upstream while ligaments, found progressing further downstream, are more orthogonally inclined. Few downstream directed ligament structures are encountered near the domain exit. The non-linearity of the breakup process in the appropriate frequency range is not eliminated. The strong pulsation effects along the liquid core are prevalent and easily distinguishable from Fig. (6.11(7-9)). No distinct breakup length measure is perceivable from the simulation results. Rather, a continuous stream of liquid elements is always present along the liquid core. The overall disintegration process shows strong reproducibility and presence of coherent structures as visualized from the vorticity plots in Fig. (6.12(c)).

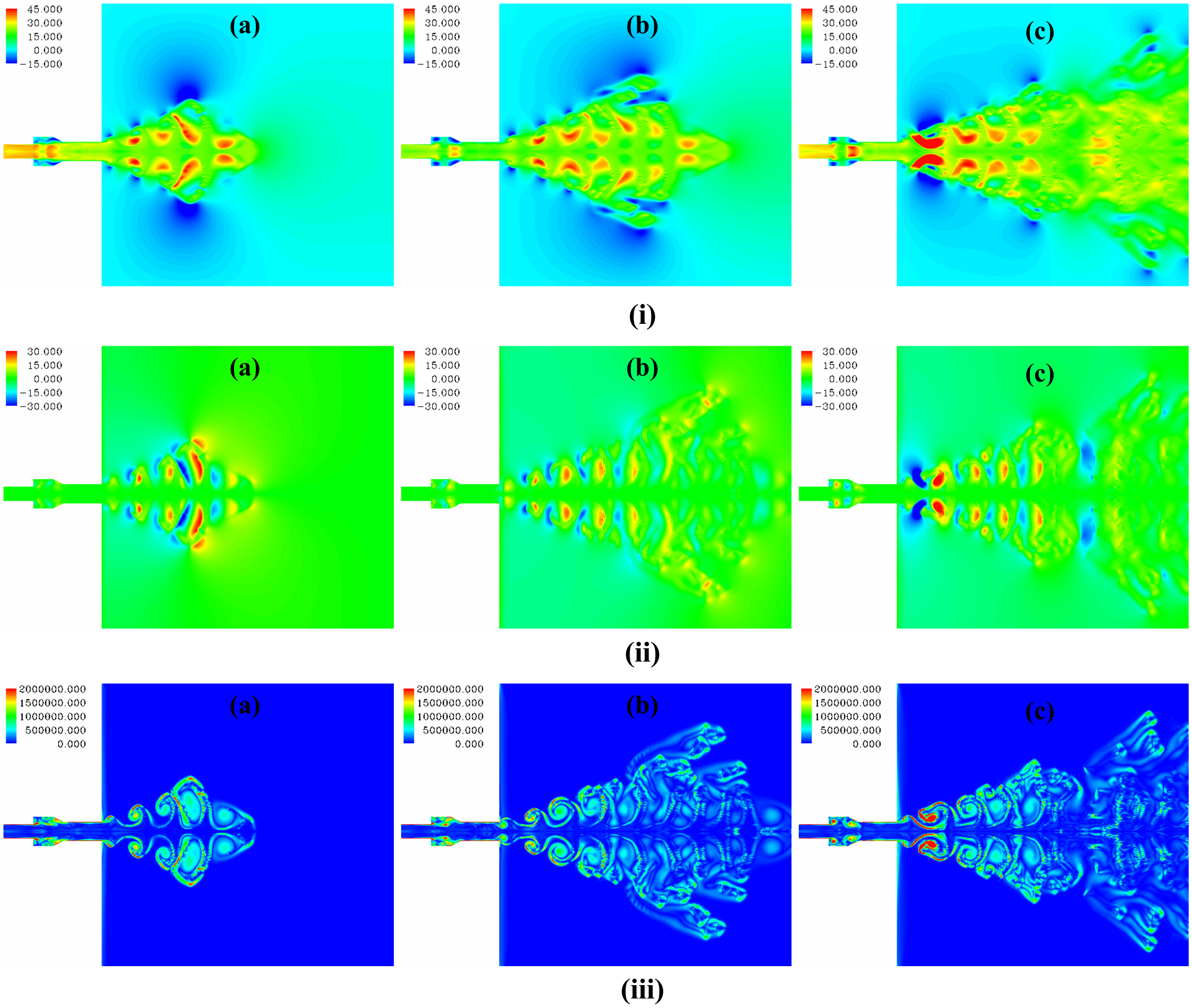

Figure 6.12: Contour plots of (i) axial-velocity magnitude (ii) radial velocity and (iii) vorticity magnitude in the computational domain operating under a forced liquid jet configuration

6.2.5. Additive cavitation effects on forced liquid jets

Section (6.2.3) addressed the breakup response of a steady liquid jet injected into ambience from the C_3 atomizer nozzle configuration. Improving on the steady state injection assumption, Section (6.2.4) was devoted to identify the impact of modulations on the disintegration process. In the present section, a complete description of a velocity modulated liquid jet including the transient effects of cavitation dynamics is discussed. Before delving into the current objective, the breakup process of a steady liquid injection case discussed in Section (6.2.3) is re-evaluated with cavitation effects. Using an incompressible cavitation model [237], the strong presence of cavitation in a steady flow situation within the C_3 atomizer configuration was earlier demonstrated in Section (4.8.3.1) within the Fluent framework. However, owing to Fluent's limitation in carrying out three phase computations, we employ the CIMD approach for treating the cavitation effects. Due to the transient formulation of the CIMD strategy, only unsteady computations are permitted.

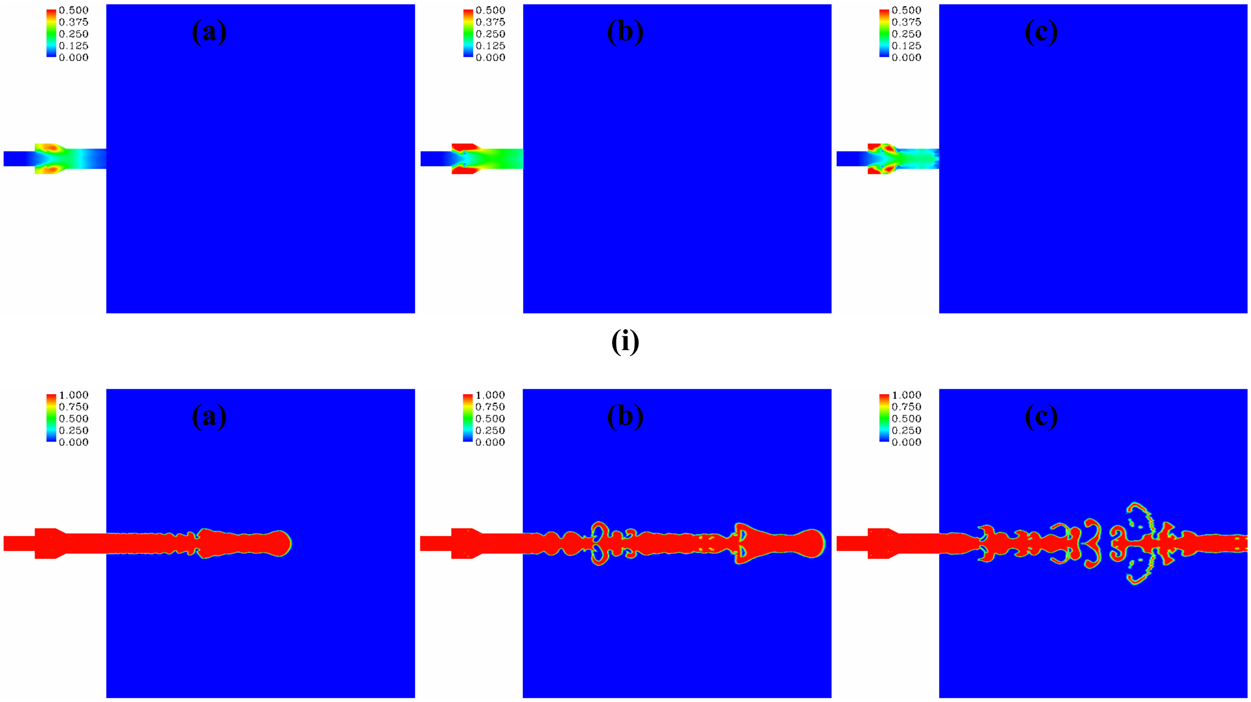

(i)

(ii)

Figure 6.13: Numerical simulation of un-modulated cavitating liquid jets injected from the C_3 atomizer configuration

Figure (6.13) shows the transient evolution of the un-modulated liquid jet from the C_3 atomizer configuration into the free shear gas domain. The CIMD model recognizes the low pressure contents residing within the nozzle and activates the vapor transport equation. The distribution of the vapor phase in the computational domain is indicated in Fig. (6.13(i)); simultaneous evolution of the liquid jet downstream of the nozzle is perceived from Fig. (6.13(ii)). The magnitude of the cavitating vapor zones within the nozzle reaches a maximum limit of 0.6. These values indicated by the CIMD models do not belong to the same category of vapor distribution characterization described using Fluent's mixture model. The Fluent's model computes effective continuity equation such that the compounded vapor and liquid fraction sum to one. This implies that, in the event a given computational cell is comprised of vapor fraction 0.6, the liquid zone remaining in the cell takes the value of 0.4. However, the CIMD approach is a pressure perspective of visualizing the cavitation vapor regions using the analytical model of Schmidt et al. Vapor fraction of one in the CIMD strategy sense can be obtained only when the pressure falls below a critical vapor pressure computed using the fluid properties such as in equation (5.42). This critical pressure to obtain complete vapor presence is far below the critical vaporization pressure for liquids such as water. In the current model, recognize that a magnitude of 0.6 still accounts for considerable cavitation events although the strict critical limit is not achieved by the atomizer configuration subjected to the present flow configurations. To comprehend the impact of cavitation dynamics imposed by the CIMD model, comparisons are drawn with the current computations with those presented in Section (6.2.3).

6.2.5.1 Cavitation effects in steadily injected liquid jets

The effect of imposing cavitation assumption on the liquid jet instability and the ensuing breakup process is clearly identified by comparing the results from Section (6.2.5.1) with Section (6.2.3). The results describled in Fig. (6.14) relates to the initial development of the liquid jet in the gas domain where the cavitation forces are strongly felt. As the simulations evolved temporally, the impact of vorticity and other aerodynamic entities destabilized the liquid jets making it hard to assess the influence of cavitation. The destabilizing effect of cavitation dynamics can be distinctly identified by equating a non-cavitation based jet breakup, Fig. (6.14(i)a), with the jet breakup process involving cavitation dynamics, Fig. (6.14(ii)a).

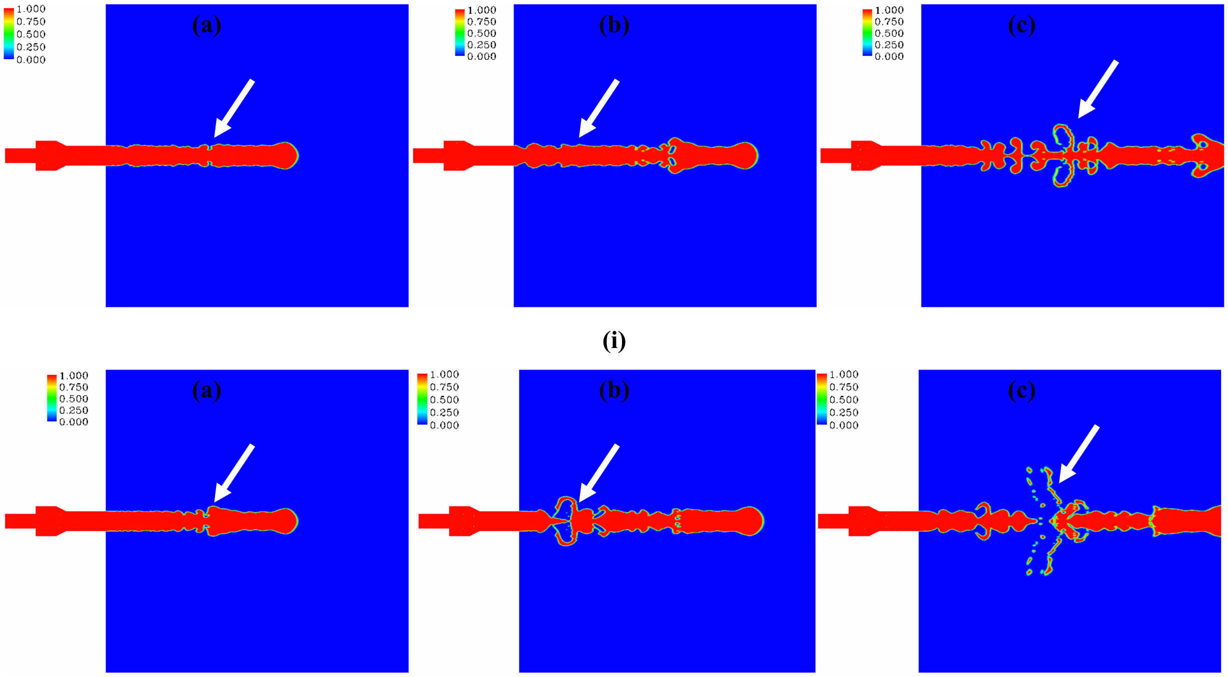

(i)

(ii)

Figure 6.14: Comparison of jet instability and breakup process in steady liquid jets issuing from the C_3 atomizer configuration under (a) No cavitation effects (b) cavitation effects

The presence of additional wrinkle like features, indicated in the figure by arrowhead, in the cavitating jet case underscores the implemented CIMD model effect. The multiplying effect of this initited instability can be tracked in the rest of the results presented. With the inclusion of the cavitation model, accelerated jet disintegration is conceived (Fig. (6.14(ii)-c).

6.2.6 Simulation of cavitating forced liquid jets

The numerical experiments conducted in Section (6.2.5.1) clearly acknowledged the instability proliferation mechanism of the cavitation model on the liquid jet evolution. With this background, forced oscillations are incorporated at the inlet of the computational domain investigated in Section (6.2.5). Time evolution of the liquid jet breakup under the modulated cavitating conditions are presented in Fig. (6.15).We can detect a drastic reduction in the breakup length from Fig. (6.15) in comparison to the case presented with no cavitation effects in Fig. (6.11)). The effect of the imposed CIMD model is to supply additional deformation forces, as a source term, to the governing motions as a function of rate of change of the cavitation vapor scalar. The instabilities generated by these deformation forces result in accelerated growth of the liquid-gas surface waves resulting in elongated ligaments exposed to gas drag. Furthermore, notice that the drop sizes obtained from the computations, within the primary breakup zone, are of the order of 30μm showing similarity to the drop sizes in atomization regime (where the drop sizes are several order of magnitudes smaller than the jet diameter). Employing the CIMD strategy to mimic cavitation effects, the simulations indicates breakup length of liquid jets as small as 2 nozzle diameters.

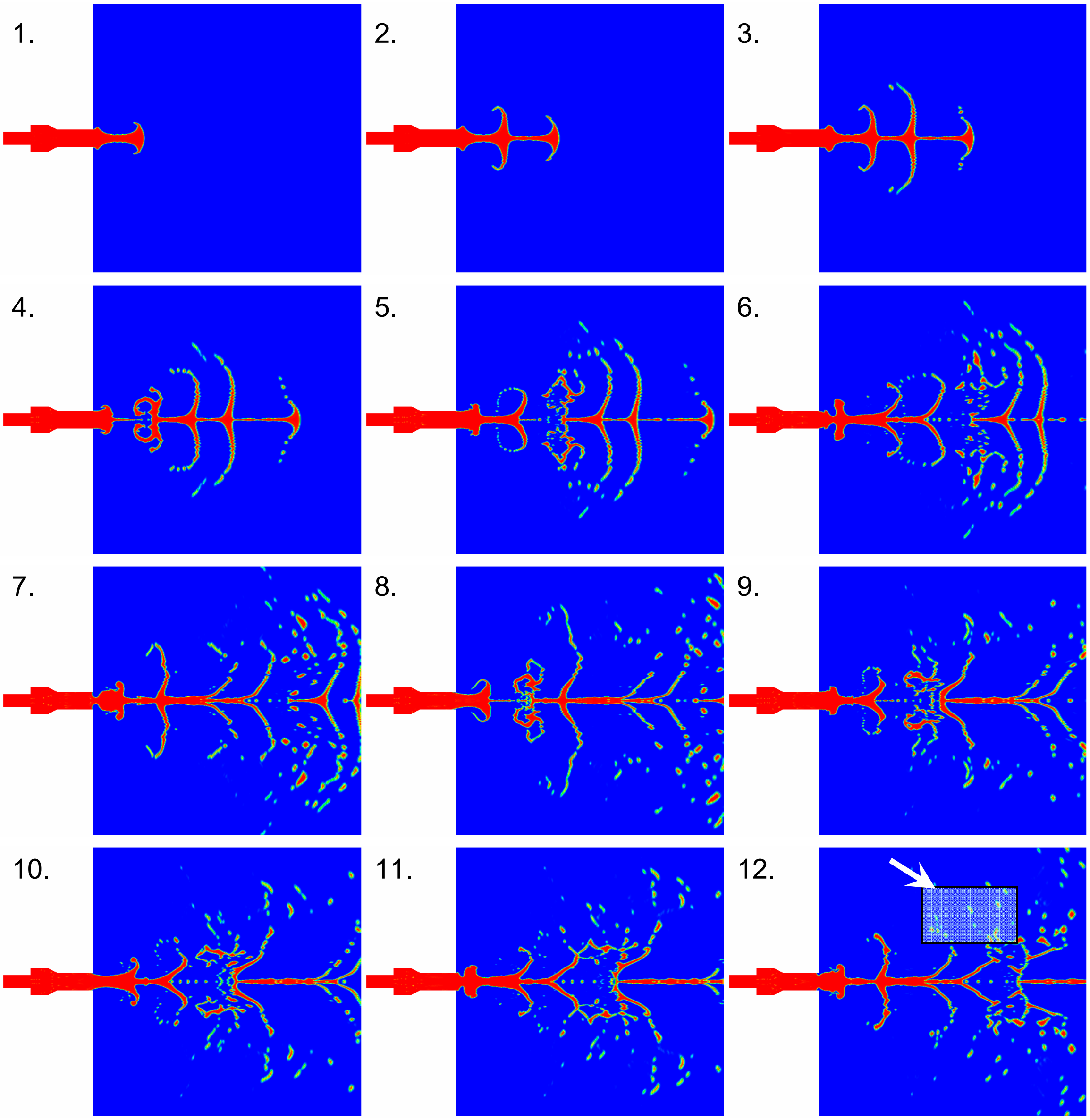

Figure 6.15: Transient evolution of forced liquid jets emanating from C_3 atomizer configuration under cavitation effects. Very small droplets in the primary breakup region are generated.

The evolution of vapor scalar in a simultaneous fashion is described in Fig. (6.16). Note that during the initial stages of cavitation no appreciable destabilizing effects are detected in the jet evolution(Fig. (6.15(1-3)). With escalation of the cavitation process, Fig. (6.16(4-6)), leading to events of supercavitation, the momentum defect strategy appropriately adds the relevant source terms arising from the cavitation growth and collapse behavior, resulting in a dramatic change in the liquid jet structure in the nozzle exterior, Fig. (6.15(4-6)). At this juncture, the influence of cavitation dynamics within the nozzle on the exterior spray formation is well singularized. Progressing further into the simulation, proliferated cavitation clusters enhance momentum exchange process within the liquid flow and appreciably alter the overall velocity gradients within the nozzle. As a result, strong fluctuations are enforced due to the cavitation transport superimposed on the already existing modulation effects, leading to an overall ramification of the breakup process as shown in Fig. (6.15(7-9)).

Notice that the cavitation clusters transported in the computational domain stay confined within the nozzle interior. As already explained, the present model cannot handle presence of three phases, liquid-gas-vapor in a given cell, since the presence of gas would negate any effect of vapor presence. As the liquid jet exits the nozzle interior, the pressure in the ambience is far higher than the internal liquid pressure. This effect is complicated by the modulation parameters imposed on the liquid jet. The CIMD method is highly sensitive to pressure field perturbation and hence, an increase in pressure variable beyond the critical vaporization pressure is detected as a collapse event. Another competing effect modifying the cavitation distribution is the low diffusive nature in regions of higher pressure. Confronted with these factors, the vapor scalars become non-existent in regions just outside the orifice exit section.

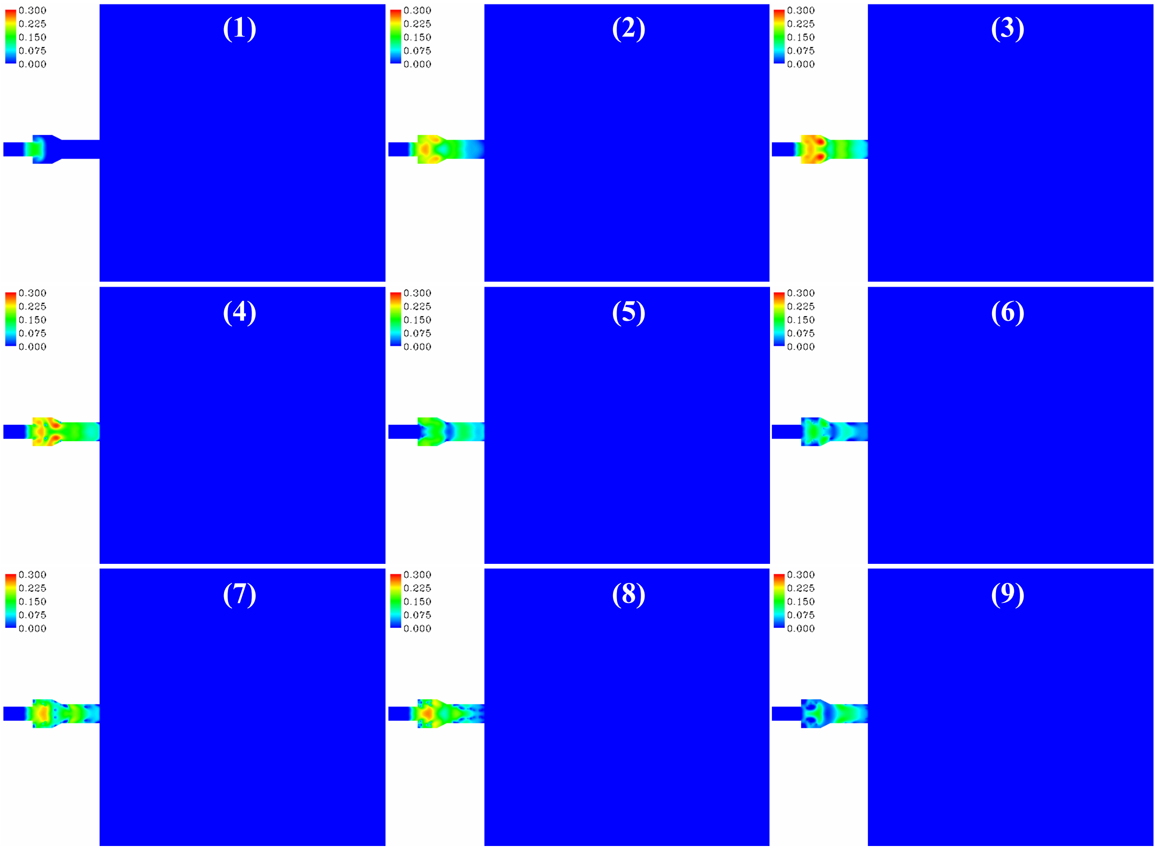

Figure 6.16: Contours of vapor volume fraction present visualized in the computational domain.

The overall flow structure, the axial and radial velocity components, prevailing in the simulation domain is presented in Fig. (6.17) to address the flow structure distortion generated by the cavitation process. As a result of intense liquid jet surface realignment due to rapidly changing internal forces such as the pulsation force, surface tension and the cavitation force, enhanced jet breakup was conceived earlier. Due to the intense breakup the flow structure looks more distorted. This is similar to the effect reported by Shavit [81], where he describes the mutual interaction of the gas and liquid phase fluctuations on one another. In the present case, domination of the liquid phase distortion over the fluctuations triggered by the gas phase is evident.

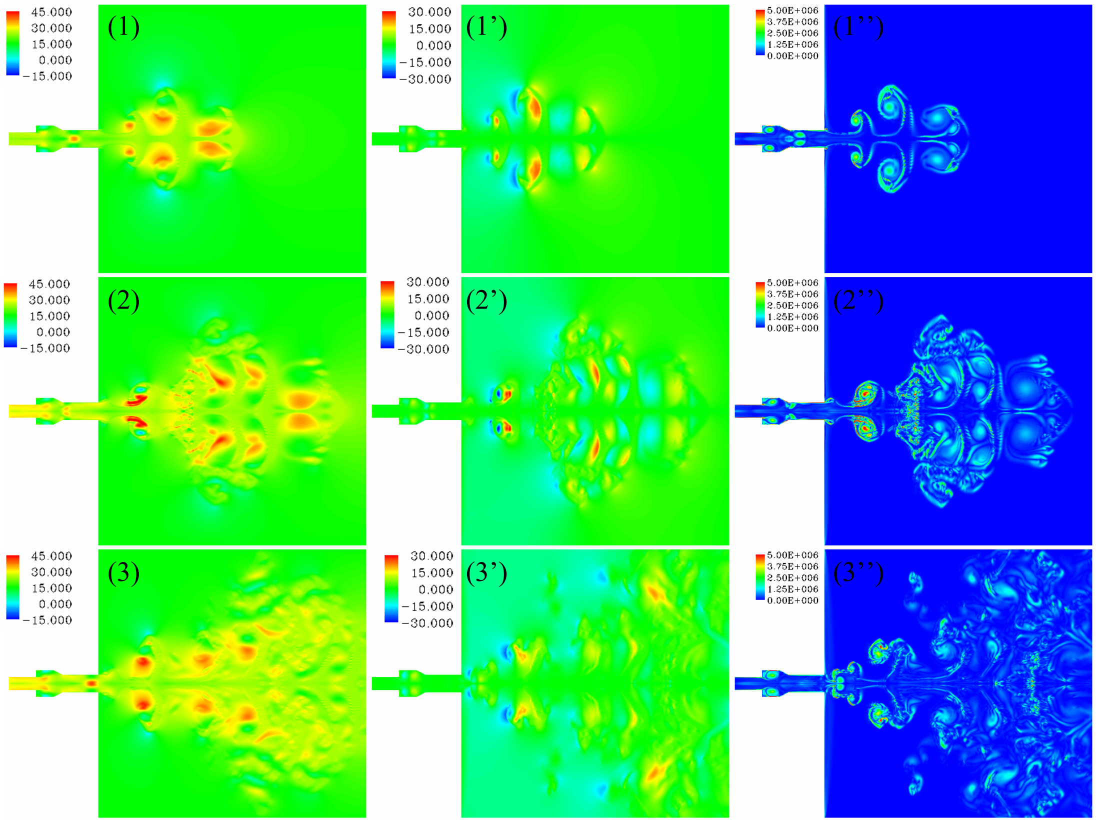

Figure 6.17: Contour plots of axial velocity (1-3), radial-velocity (1'-3') and vorticity magnitude (1''-3'') in the computational domain.

Figure (6.17) portrays strong axial and radial component fluctuations within the nozzle interior and further downstream. The primary reason for visualization of distorted vortex structures in the nozzle exit is attributed to the aggravated levels of radial velocity components generated within the nozzles and just outside as seen in Fig. (6.17(1'-3')). Similar trends are noticed with the axial-velocity components just at the exit of the nozzle. The fundamental difference between the present flow structure (Fig. (6.18)) and the non-cavitating flow case (Fig. (6.18)) is the inclusion of the cavitation induced force term. The phenomena of vortex stretching mechanisms and shear enhancement processes, based on which the atomizer configuration is built on is demonstrated in Fig. 6.18.

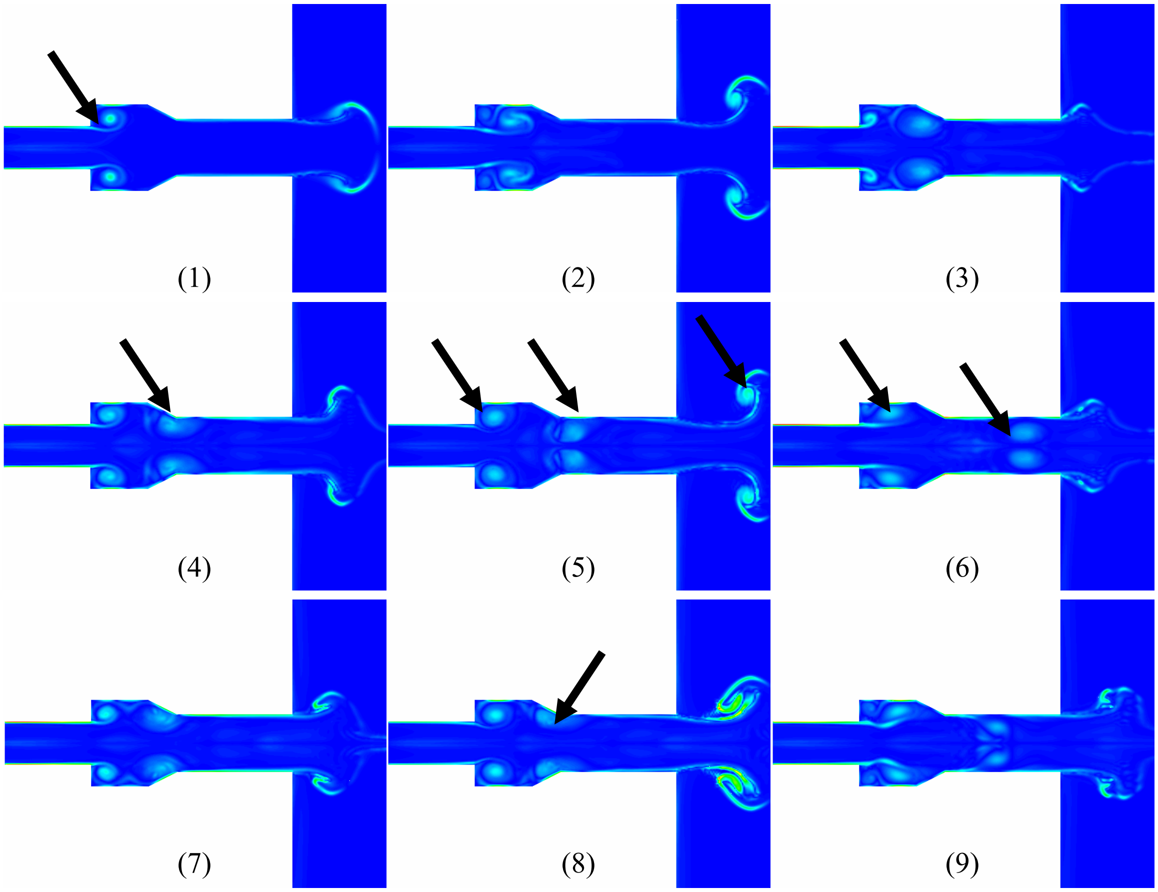

Figure 6.18: Vorticity transport within the C_3 atomizer configuration under the influence of forced modulations

The fundamental vorticity generation and transport mechanism is described in Fig. (6.18). Notice, from Fig. (6.18(1)), strong formation of vortices as a result of shear layer effect near the backward facing step region inside the nozzle. In addition, the exit nozzle region creates a free shear rollup effect and hence a second vortex shedding mechanism can be spotted in the nozzle exterior (Fig. (6.18(2))). The vortices generated near the residence chamber are distinctly seen stretched Fig. (6.18(3-5)) and convected Fig. (6.18(5-6)) into the main core liquid flow. The overall vorticity mechanism that enhances overall liquid jet instability is identified from Fig. (7-9). Recall that these vortex mechanisms are immersed within the liquid jet exiting the nozzle; upon exit they expand due to the removal of the wall constraint and accelerate radial energy transfer mechanisms bringing about changes to the liquid–gas interface topology; an effect demonstrated in Section (6.2.3).

6.3 Prototype development: Ultrasonically Cavitating atomizer prototype development

Motivated by the possibility of generating very small drop sizes distributed uniformly in the domain by the action of coherent structures, the design of a new spray applicator is furnished in this section. The atomizer design is built on the C_3 atomizer configuration previously tested for cavitating characteristics in Section (4.8.3.2) followed by disintegration tests under steady-cavitating, modulated-cavitating conditions.

Schematic of the new spray applicator design is shown in Fig. (6.19). Front view and side view of the applicator are described.

The essential parts of the spray applicator include

(1) Cavitation enhancer module (comprises of the Backward facing step profile with the flow modulation chamber)
(2) Nozzle profile
(3) Spray applicator support
(4) Piezo support device
(5) Rear fluid entry port support
(6) Piezo-actuator (for realizing horn motion) and
(7) other relevant supporting mechanical components (A), (B), (C)

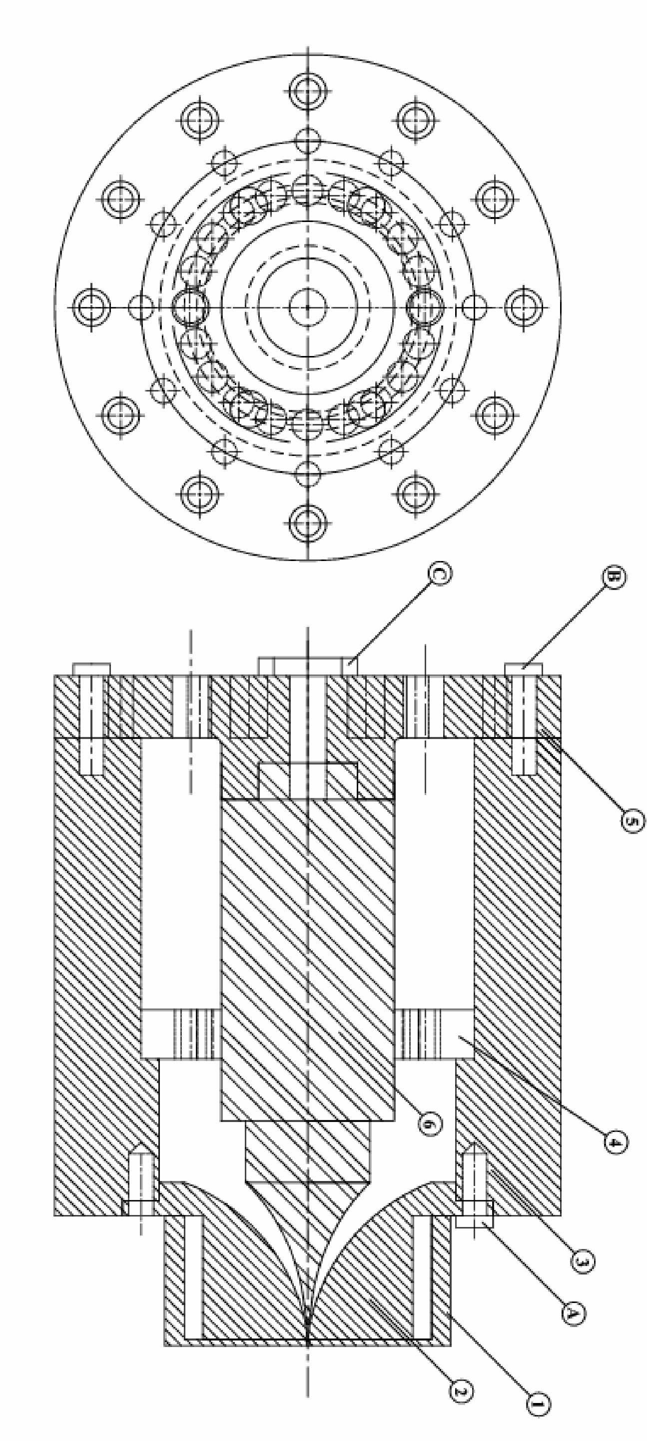

Figure 6.19: Ultrasonically cavitating atomizer prototype design © Vedanth Srinivasan, Abraham J. Salazar, Kozo Saito, Department of Mechanical Engineering, University of Kentucky, 2006.

A complete three-dimensional exploded view of the novel spray applicator is shown in Fig. (6.20).

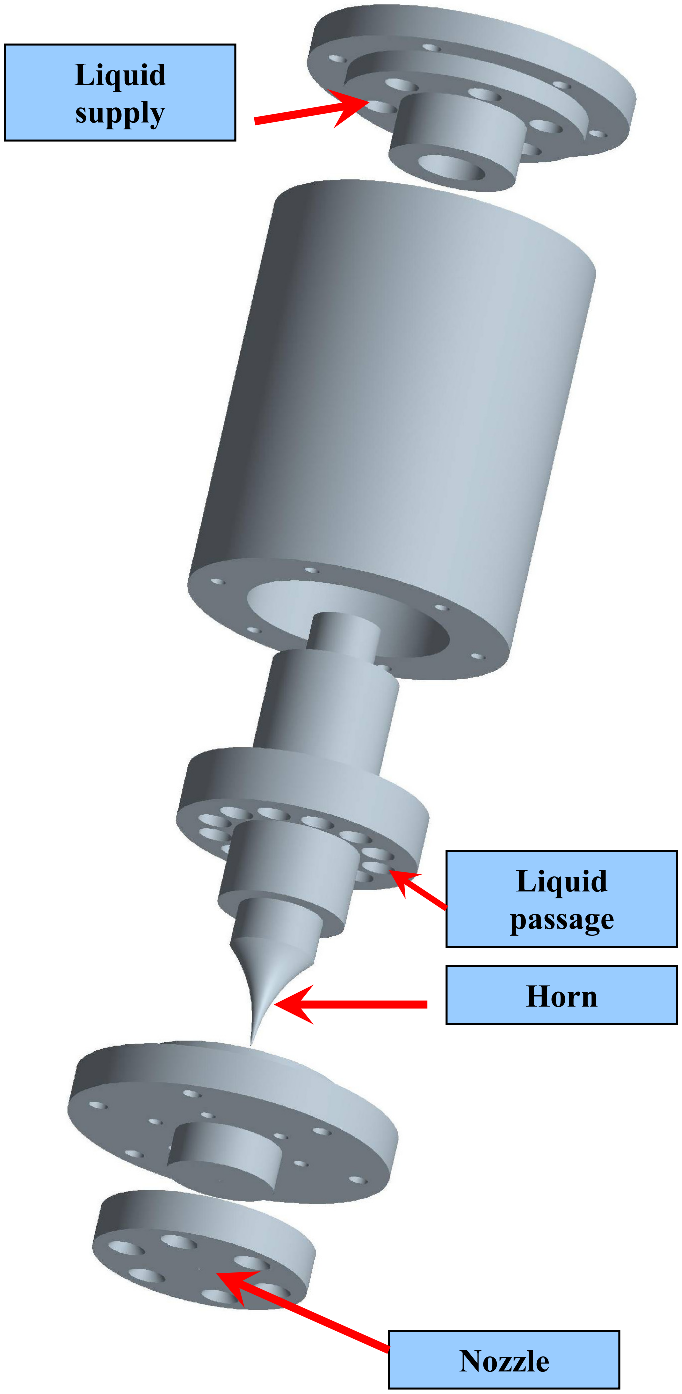

Figure 6.20: Exploded view of the atomizer prototype © Vedanth Srinivasan, Abraham J. Salazar, Kozo Saito, Department of Mechanical Engineering, University of Kentucky, 2006.

In order to ensure proper functioning of the prototype, it is required that the overall flow field within the sprayer configuration be carefully designed. For example, presence of strong re-circulating flow would result in increased energy requirement for the applicator operation. Moreover cautioned efforts are required to ensure instability free flows in the current design, since the atomizer incorporates strong effects of horn motion dynamics and cavitating flow phenomena. All the simulations presented in Chapter 4 described regions close to the nozzle exit and the horn surface providing deep insight to the cavitating flow structure. However, any global flow field representation was not properly addressed. In this section, the global flow field simulated in the C_3 atomizer configuration shown in Fig. (6.21) is elaborately discussed. Transient plots of axial-velocity magnitudes are shown to provide descriptive information of regions where the flow has changed direction.

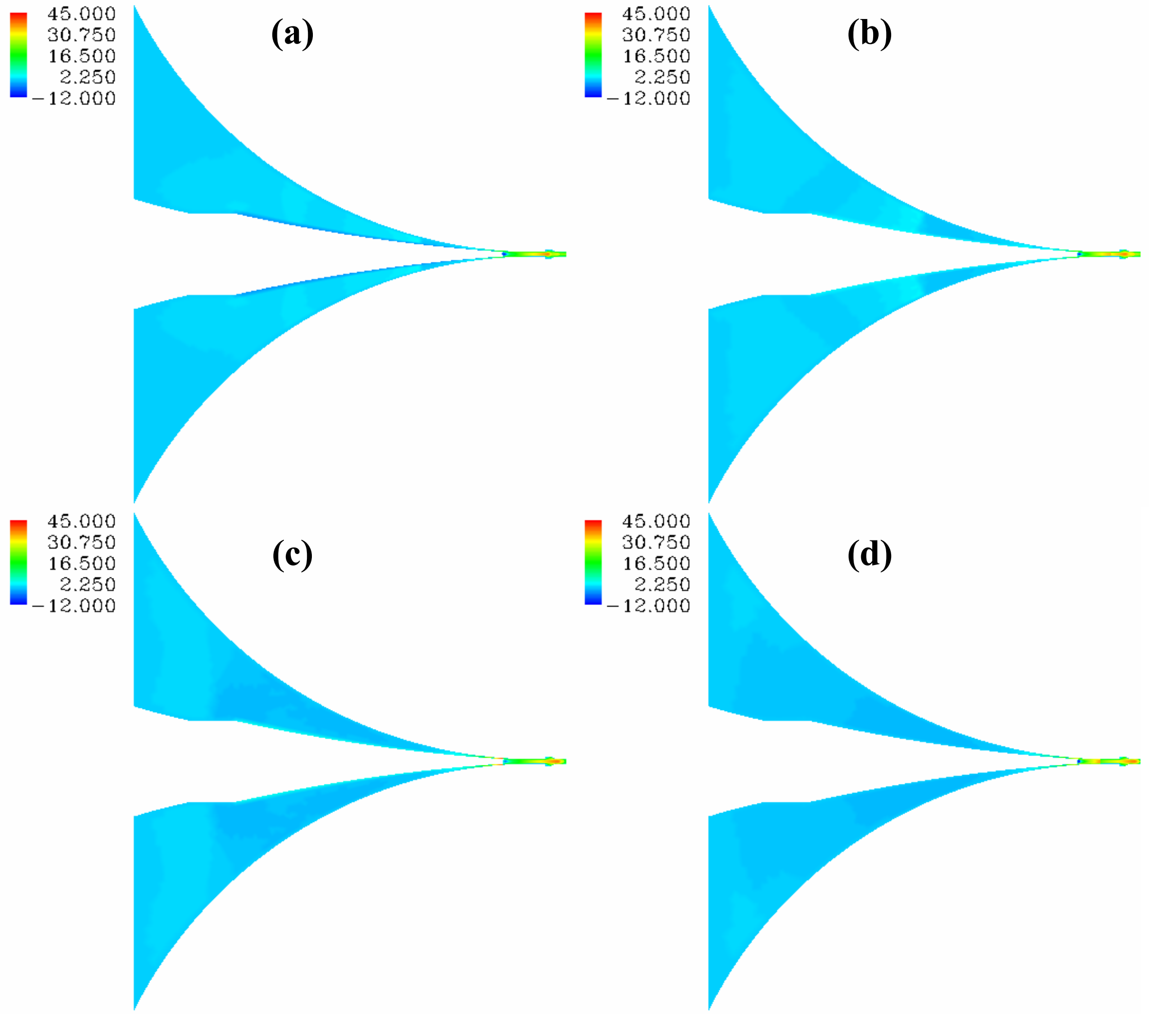

Figure 6.21: Contour (smoothed) plots of axial velocity in the C_3 atomizer configuration

Observe from Fig. (6.21), no strong presence of flow reversal is detected. On the other hand, regions close to the oscillating horn surface experiences some appreciable shear which induces localized flow reversal mechanisms. For more detailed observation, we present contour plots of axial-velocity regions less than zero representing zones of flow reversals. The plots shown in Fig. (6.22), clearly identifies existence of flow reversals in the flow acceleration zones. The flow reversal mechanisms are brought about by the high frequency horn motion which generates strong regions of vorticity near its surface. The induced vortices due to alternating horn motion are then propagated by their interaction with the local fluid flow.

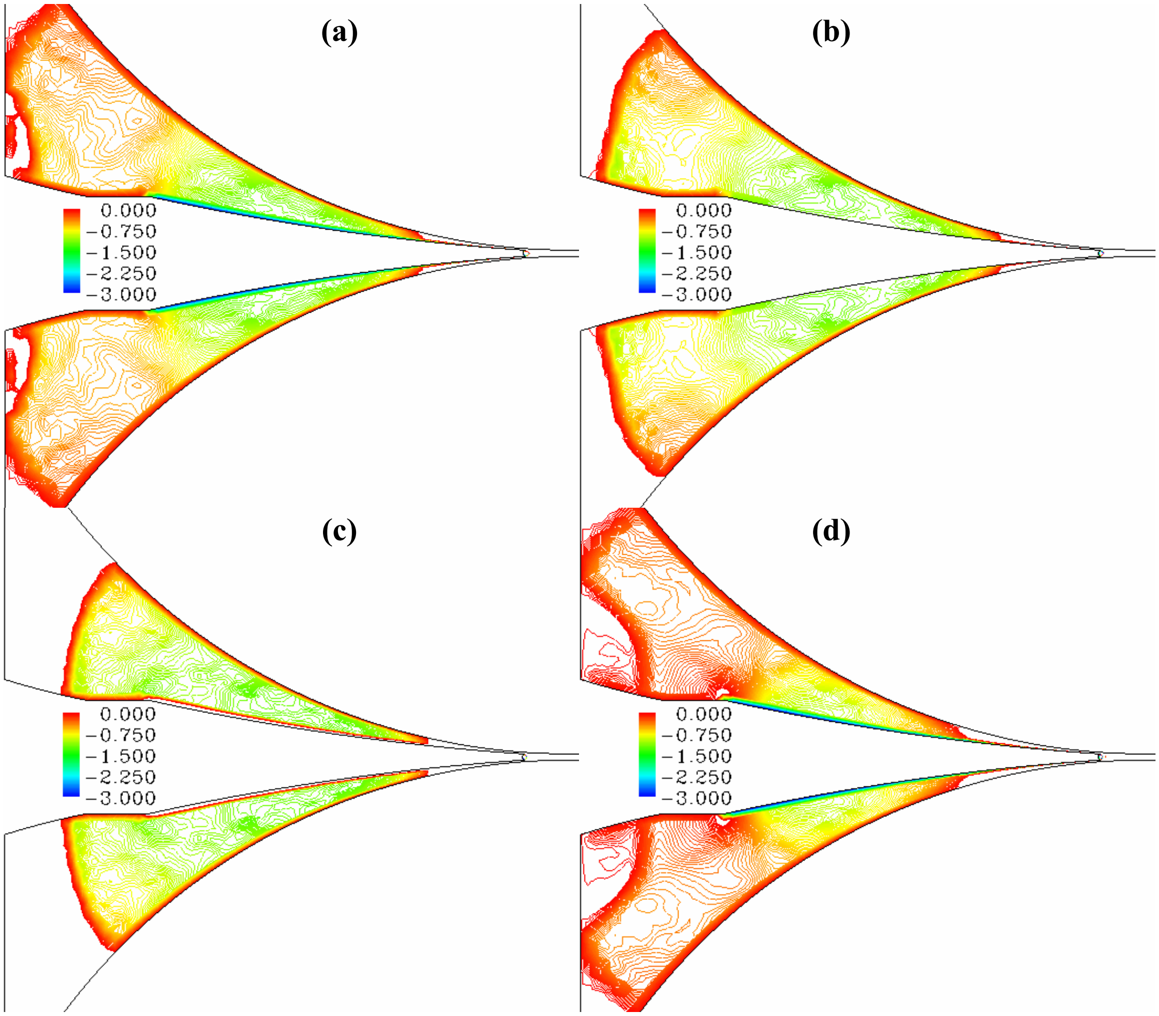

Figure 6.22: Contour plots of axial-velocity magnitude to indicate regions of flow reversal typically encountered in the C_3 atomizer configuration

6.4 Closure

The disintegration characteristics of liquid jets emanating from the C_3 atomizer configuration adopted in Chapter 4 is addressed through a series of numerical experiments with inclusion of modulation and cavitation effects. The Cavitation-Induced-Momentum-Defect correction approach performs commendable performance in detecting regions of cavitation within the nozzle. Moreover, as seen from the discussions earlier, the cavitation effects were seen strongly associated with the vortex structures, an effect that was not well accommodated in Fluent's cavitation routine. Importantly, identify that no turbulence effects have been included in the model which would enact a dual role within the system by augmenting the instability of the liquid jets within the nozzle due to shear enhancement and cross-stream velocity components while in the exterior spray region, it would supply additional dissipation to the liquid-gas interface leading to complex characteristics. The current studies based on axi-symmetric transient simulations of the cavitating atomizer reveal very strong potential for generating small drop sizes. The motion of the droplets along the vortex cores was visualized from the simulations. In this effect, the cavitation and vortex structures within the liquid enact to improve breakup phenomena while the distribution of the disintegrated droplets travel in the coherent structures generated by the pulsed jets themselves. More detailed analysis is required to identify finer details on the intensity of the coherent structures generated by the pulsed jets and their subsequent dissipation. Moreover, the current study focuses only on the primary breakup zone, upto 10-15 nozzle diameters, within which a very highly intense breakup has been achieved by uniting the effect of velocity modulation and cavitation effects. As a result, numerical models which are computationally less intensive, such as the discrete lagrangian tracking schemes, can be used further downstream to obtain a detailed information concerning the fate of these droplets generated by the primary breakup.

Chapter 7

Conclusions and Future Recommendations

7.1 Closure

This research work has been concerned with the design and development of a new spray applicator design for obtaining atomization of low viscosity Newtonian liquids such as water. In this context, a thorough review of the effect of cavitation compounded with other influencing parameters such as nozzle turbulence and geometry effects, on the disintegration behavior of round liquid jets was presented in Chapter 2. To develop an energy efficient atomizer design, use of high frequency oscillations by means of horn structure, placed inside the nozzle interior, combined with the naturally occurring cavitation phenomena was envisioned. In dealing with the methodology to envisage the new atomizer prototype, experimental and numerical methods are encountered. Distinguishing the differences existing between the two procedures, the later was adopted owing to its flexile nature to accommodate different design scenarios. Furthermore, the numerical treatment has been found to possess a very enticing complementing nature to the experimental methods.

The motion of the vacillating horn structure induces pressure perturbations on exiting liquid jets, as a result of which, multitude of fluid structures are obtained. In order to evaluate the impression of the pulsation characteristics on the development of a wide gamut of jet structures, numerical methods were entertained. Before delving into the numerical strategy, details concerning the characteristic behavior of modulated jets were analyzed by deriving analytical relations.

7.1.1 On modulated liquid jets

The analytical approximations, demonstrated in Chapter 3, were derived based on low modulation assumptions discarding the injected fluid properties. In higher modulation regimes, the analytical models fall short due to severe non-linearities exhibited by the liquid-gas multiphase systems. To work out a complete representation of the liquid jet disintegration process, numerical methods to solve full set of fluid flow governing motions, the Navier-Stokes equations, were considered. The presence of a liquid interface in a predominant gas phase presents additional complexity in treating their evolution within the domain. To resolve this confusion, Volume-of-Fluid based interface tracking scheme was adopted. Within this routine, a Compressive Interface Capturing Scheme for Arbitrary Meshes (CICSAM) procedure has been employed to capture the liquid-gas interfacial dynamics. This sub-routine was programmed in C++ into a finite volume based openFoam open source code. The VOF method was tested for its predictive capability in tracking events of primary breakup process confronted, in the first few nozzle diameters, by a turbulent liquid jet discharging into a pressurized environment. Obtaining qualitatively satisfying results by direct comparison with experimental observations, the VOF model was later used in conjunction several turbulence models to test the latter's influence in combination with the CICSAM strategy for monitoring interfacial dynamics. Proceeding further, the VOF methods were used for simulating modulated liquid jets. In this account, firstly, the scaling laws governing the evolution of forced liquid jets were validated using numerical methods. Indeed, different (Newtonian) liquids sprayed under similar Strouhal and Weber numbers were observed to form similar structures, differences arising in their disintegration modes owing to the resistive liquid properties such as surface tension, viscosity etc. Further, the modulated liquid jets induced coherent structures in the gas phases as a result of matching interfacial dynamics. Also, the liquid jets modulated with finite amplitude and frequency were seen reproducible, an effect previously experimented by several authors.

Gaining confidence on the use of VOF schemes, numerical studies on generating sprays by modulating high speed jets were taken up. The investigations indicated long breakup lengths resulting from the use of high speed jets, since the wavelength of the imposed perturbations are longer and hence, the jet modulation regions widely separated. Later, series of numerical studies concerning the effect of modulation amplitude and frequency on low velocity jets were carried out. The effects of modulation amplitude on the liquid jet disintegration and the spray cone angle generated were established. The effect of frequency (the Strouhal number) was observed to play a dual role. At low frequencies, combined with higher amplitudes, jet disintegration were favored. With increase in the imposed frequencies, even at higher amplitudes, jet disintegration is suppressed and droplet chains were generated. Severe non-linearities were encountered by combining high modulation amplitudes with low velocity jets. The masking effect of the frequency over the modulation amplitude was discussed and the chapter closure provided range of velocities for nozzle operation under which, sufficiently small drop sizes can be obtained.

7.1.2 Cavitation studies

Chapter 4 concerns cavitation studies at the single bubble level leading to a macroscopic ensemble approach. First, a new one-dimensional model based on nucleation theories is derived to study bubble dynamics in vibratory cavitation process. Following this analysis, simulations of multiple bubble system scenarios are presented and the relevant complexities detailed. Availability of several numerical methods for simulating cavitating flows in macroscopic environments was reviewed. Cavitation model based on a reduced bubble dynamic formulation was used within the commercial code Fluent framework for the present studies owing to its robust handling of a wide variety of fluid flows. Further, its capability is well established in handling dynamic meshing procedures which is a critical parameter affecting the novel atomizer design. With RNG *k-e* modeling assumptions for estimating turbulence effects, a detailed study on the impact of horn stroke length, frequency, fluid flow rate within the atomizer, nozzle design, horn tip position and the atomizer geometry scaling based on an initial arbitrary design has been presented. Following this detailed study, numerical simulations of sharp cornered nozzles were elaborated. Obtaining a wealth of information from these cavitation studies, a new atomizing nozzle design was created by incorporating Backward Facing Step (BFS) geometry. Extensive computations based on the new geometry indicated the potent contribution of BFS in effecting cavitation solutions. In particular, strong variations in the velocity and vapor distributions were obtained by modifying the height and width of the backward facing step profile. Among several designs exercising the BFS strategy, a nozzle configuration, C_3, providing optimized velocity distribution, as recommended in Chapter 3, was singularized for further studies.

7.1.3 Coupled approach vs Discrete zoning method

The use of a discrete two-zoning approach was taken up owing to the incapability of the existing solvers to accommodate more than two phases in VOF based simulations. For this purpose, a new cavitation model capable of being treated in a multiphase mixture was formulated. The formulation was carried out in two steps: first, a new cavitation model invoking Homogeneous Equilibrium Assumptions in a compressible framework were used in conjunction with a pressure correction equation to simulate cavitating injector flows using the openFoam C++ libraries available for continuum mechanics. Due to the inadequacy of the compressible assumptions in an incompressible flow domain, a new Cavitation-Induced-Momentum-Defect (CIMD) correction methodology was extended from the compressible analysis. The new model enforces compressible assumptions in regions of cavitation within an incompressible flow and solves a vapor transport model with appropriate source, diffusion and convective terms. The model, incoroporated into the commercial Fluent solver, was used to track cloud cavitation phenomena. The vapor dynamics prediced by the model compared well with the experimental results. Later, the CIMD method was engaged into a two-phase VOF model within the Fluent code and tested for its capability to be fully exploited into any Eulerian procedure. The resulting solutions matched closely with the experimental work.

7.1.4 Cavitating atomizer design and testing

The newly developed CIMD approach was used to study the disintegration phenomena faced by the pulsed liquid jet discharging from the atomizer design proposed in Chapter 4. Relevant boundary condition treatments were exposed. In particular, time history of the velocity profile, at the nozzle exit, of the C_3 atomizer configuration indicated that the collapse behavior of the cavitating flows, were indeed, in-phase with the imposed horn oscillations. The simulation of cavitating pulsed jets was modeled through a series of computations: First, a steady jet injected into the ambience from the given atomizer configuration was tested; secondly, cavitation model using the CIMD approach, was fed into the code, and a steady liquid jet with cavitation effects was evaluated. As a third step, pulsating liquid jets, with no cavitation effects, emanating from the proposed design was studied; finally, the CIMD model was employed to test the overall disintegration behavior of pulsed cavitating liquid jets. The results showed the combined influence of vortex mechanisms and cavitation induced deformation forces on the explosive atomization obtained. The breakup length, of the jet exiting from the atomizer configuration, was reduced close to 1-2 nozzle diameters. It is to be noted that a steady jet, based on the current geometry and liquid property, lies in the second-wind induced regime capable of generating drop sizes smaller than the jet diameter, yet far from the atomization regime. By use of pulsation and cavitation efforts, drop sizes several orders of magnitude smaller than the liquid jet diameter were obtained in the primary breakup zone of the disintegration process. Based on the testing of several atomizer models using the numerical approach, a basic prototype design was presented in Chapter 6.

7.1.5 Contributions of the dissertation

In summary, this study provided the following contributions to the research community:

(1) Numerical simulations of spherical viscous gas bubbles exposed to pulsating pressure fields with added complexity of their translation

(2) Numerical investigations on cavitation dynamics generated by moving structure placed in a liquid medium

(3) Numerical simulations of cavitating nozzle flows with aggressive dynamic meshing procedures for the evaluation of nozzle designs

(4) New cavitation bubble dynamics model using modified nucleation theories for investigating vibratory cavitation process

(5) Enhancement of new interface tracking routines and testing with different turbulence models for their predictive capabilities

(6) Numerical studies on the development of liquid structures generated by pulsed liquid jets

(7) Numerical evaluation of the scaling parameters encountered in forced liquid jets

(8) Development of a new compressible cavitation model based on Homogeneous Equilibrium Assumptions supplemented with a pressure correction equation

(9) Development of a new Cavitation-Induced-Momentum-Defect correction methodology for tracking events of cavitation

(10) Development of a new pseudo-three phase simulation procedure combining cavitation effects, using CIMD approach, and an interface tracking scheme (CICSAM)

(11) Design and development of new atomizer design incorporating Backward Facing Step configuration for enhanced disintegration of liquid jets.

7.2 Future work

7.2.1 Nozzle design procedures and experiments

The current nozzle design requires further testing and enhancement, particularly to analyze, in detail, the frequency effects imposed by the geometry and oscillating horn motion. From Chapter 6, the presence of multiple frequencies was spotted and their influence on the resulting spray structure was quantified. The resulting effects from the engagement of myriad of frequencies in the system, demands puissant considerations of the interior nozzle design for obtaining efficient spray formation process. Although a wide range of computations has been reported, some of these designs are fundamentally inspired the need to enhance turbulence and shear rates for destabilizing the exiting liquid jets. Further studies based on these principles can certainly augment the stress levels through a variety of means such as adding swirl motions, geometry corrections etc. More importantly, extensive experimental testing of the proposed atomizer configuration is recommended for optimization and validating the numerical models.

7.2.2 Advanced cavitation modeling

The CIMD approach is built strongly on the pressure variable distribution. The current formulation assumes a constant bubble number density of the vapor bubbles initially set in the given flow domain. This assumption can be solved by using a dynamic transport equation for bubble number density in the flow and then constructing the vapor volume fractions on the fly. Further, the model does not account for the surface tension and viscosity effects of the individual bubbles in monitoring their growth and collapse. These assumptions have to be reevaluated in a wide variety of flows such as in Non-Newtonian flows, multi component flows, flows with varying liquid properties etc.

Explicit evaluation of the CIMD based momentum defect has not been carried out in the code. Rather, only the overall difference in the flow structure and breakup behavior (in interfacial flows with disintegration effects) has been obtained. More detailed considerations of the momentum correction magnitudes relevant to the cavitating regimes would help in enhancing the approximations used in the methodology.

7.2.3 Dimensional effects in liquid disintegration studies

All the simulations presented in the present study, concerning the interfacial dynamics such as the breakup process, are carried out in an axi-symmetric fashion supported by theories on breakup modes from literature. In order to completely quantify the droplet distribution and full scale three dimensional effects such as vortex stretching, turbulence distortions, a complete three dimensional simulation studies are required. Many a times, three dimensional phenomena such as surface instabilities in the rotational sense, are critical in expediting the breakup process and their dismissal using a two dimensional axi-symmetric assumptions can lead to wide deviations from the actual spray generation process.

Adding to this, the simulations reported in Chapter 6, do not account for the turbulence effects due to the increased computational effort and modeling discrepancies; the support for their exclusion stemming from the studies presented in Chapter 3, on the effect of using various turbulence models. However, turbulence generated by cavitation effects and the pulsating flows cannot be discarded due to the strong intercoupling nature of the involved phases.

In sum, some detailed effects of three-dimensionality, turbulence and cavitation needs to be addressed in the future.

Appendix

A.1 Nomenclature

We	Weber Number	[dimensionless]
Oh	Ohnesorge number	[dimensionless]
Re	Reynolds number	[dimensionless]
D	Diameter	[m]
L	Length	[m]
U	Velocity	[m/s]
$B.L$	Breakup length	[m]
Ca	Proportionality Constant	[m]
T	Taylor number	[dimensionless]
Sr	Strouhal number	[dimensionless]
f	Frequency	[1/s]
$\bar{U}$	Mean velocity	[m/s]
t	Time	[s]
r	Radial co-ordinate	[m]
x, y ,z	Co-ordinate	[m]
P	Pressure	[N/m^2]
V	Volume	[m^3]
A	Area	[m^2]
u, v	Velocity	[m/s]
$\tilde{u}$	Non-dimensional velocity	[dimensionless]
z	Length scale	[m]

St	Strouhal number	[dimensionless]
R	Radius	[m]
M	Modulation amplitude	[dimensionless]
T	Time period	[s]
T	Temperature	[K]
F	Force	[N]
S	Surface area	[m^2]
G	Turbulent energy	[m^2/s^2]
H	Heaviside function	[dimensionless]
Ma	Mach number	[dimensionless]
Sp	Source term	[kg/m^{3}s]
$\dot{R}$	Bubble wall velocity	[m/s]
h	Enthalpy	[J/kg]
Gb	Gibbs function	
b	void fraction	[dimensionless]
Rp	Net phase change rate	[kg/m^{3}s]
Re	Evaporation rate	[kg/m^{3}s]
Rc	Condensation rate	[kg/m^{3}s]
E	Mass exchange coefficient	[Kg/ ms]
q	mass fraction	[dimensionless]
Y	Dilational term	[kg/ms^3]
ap	Horn acceleration	[m/s^2]
Γ	Amplitude	[m]

LS	Stroke length	[m]
D	Strain rate tensor	[1/s]
HP	Discretization operator	[operator]
aa	Matrix coefficient	[Ns/m^4]
Fa	Face flux	[N/m^3]
Fc	Momentum change	[Kg/m^{2}s^2]
Di	Mass exchange coefficient	[Kg/ms]
tk	Thermal conductivity	[W/m/k]
fd	Drag function	[dimensionless]
Ax	Acceleration	[m/s^2]
En	Energy	[Kg m^2/s^2]
He	Mean height	[m]
w	Polytropic constant	[dimensionless]
W	Work	[Kg m^2/s^2]
rd	Horizontal Distance	[m]
yd	Vertical Distance	[m]
W	Prandtl number	[dimensionless]
Z	Compressibility	[s^2/m^2]
m	Mass	[Kg]
fi	Fiddle factor	[dimensionless]
i	Number of molecules	[dimensionless]
c	Courant number	[dimensionless]
l	Wave length	[m/s]

K	Wave number	[1/m]
a	speed of sound	[m/s]
N	Number density	[1/m^3]
C	Constant	[dimensionless]
n	Normal vector	[m]
$\overline{S}$	Strain rate	[1/s]
k	Turbulent kinetic energy	[m^2/s^2]
eps	Epsilon	[m^2/s^3]
φ	Constant	[dimensionless]
κref	Reflection coefficient	[dimensionless]
ϖ	Non-dimensional time	[dimensionless]
v	Kinematic viscosity	[m^2/s]
ζ	Non-dimensional radius	[dimensionless]
θ	Angle	[degrees]
Φo	Viscous dissipation	[kg/ms^3]
∇	Differential operator	[1/m]
ζk	time	[s]
Δ	Difference operator	[operator]
Γ	amplitude	[m]
σ	Surface tension	[N/m]
δ	Delta function	[operator]
κ	Curvature	[1/m]
ε	Modulation amplitude	[dimensionless]

Δ	Length scale	[m]
μ	Viscosity	[Ns/m^2]
τ	Shear stress	[N/m^2]
γ	Volume fraction	[dimensionless]
β	blending factor	[dimensionless]
α	volume fraction	[dimensionless]
ω	Angular frequency	[1/s]
Θ	Distance	[m]
λ	Wave length	[m]
η	non-dimensional length	[dimensionless]
ψ	Fluid Compressibility	[s^2/m^2]
ΩE	Energy barrier	[Kg m^2/s^2]
μc	Chemical potential	[Kg m^2/s^2]
ρ	Density	[Kg/m^3]
Ξ	Arbitrary parameter	[dimensionless]
ζk	Delay time	[s]

Subscripts

l,L	liquid
g,G	gas
N	Normal
T	Tangential
o	Initial
v, V	Vapor

i,j,I,J	indices
x,y	Co-ordinate direction
1d	one-dimension
mo	modulated
s	Surface
n	Natural mode
U	Upstream
D	Donor
f,F	Face
A	Acceptor
CBC	Convection bounded criteria
UQ	Ultimate quickest
sgs	Sub-grid scale
e	eddy
KH	Kelvin-Helmholtz
rel	Relative
lig	Ligament
bulk	Bulk
w	Weber
t	Turbulent
c	Cavitation
B	Buoyancy
Go	Initial gas

a	ambient
res	Resonance
rev	Reversible
k	Kinetic energy
b, B	Bubble
pro	Prototype
en	Entrance
ex, $exit$	Exit
$cham$	Chamber
h	Horn
he	Horn-entrance
P	Point (cell)
Ne	Neighbor
$face$	Cell face
vl	vapor-liquid
m	Mixture
$Cell$	Computational cell
α	Vapor
∞	Infinity
B	Arbitrary variable

Superscripts

‘	Location
+, -	Right, left sides

References

[1] Lefebvre, A. H., Atomization and Sprays, Hemisphere Publishing Corporation, New York, NY, USA, 1989.

[2] Reitz, R.D., Atomization and other breakup regimes of a liquid jet, Ph.D thesis, Princeton Univ., Princeton, NJ. 231 pp, 1978.

[3] Reitz, R.D., Bracco, F.V., Mechanisms of Breakup of Round Liquid Jets, The Encyclopedia of Fluid Mechanics, Ed. N. Cheremisnoff, Vol. 3, pp. 233-49,1986

[4] Lin, S.P., Reitz, R.D., Drop and Spray Formation from a Liquid Jet, Ann. Rev. Fluid Mech., Vol. 30, pp.85-105, 1998.

[5] Reitz, R.D., Bracco, F.V., Mechanism of Atomization of a Liquid Jet, Phys. Fluids, 25(10), 1982.

[6] Sirignano, W.A., Fluid dynamics and transport of droplets and sprays, Cambdridge University press, 2005.

[7] Zhao, F. Q., Lai, M. C., Harrington, D. L., The Spray Characteristics of Automotive Port Fuel Injection – A Critical Review, SAE Paper 950506, 1995.

[8] Sirignano, W. A., Spray Combustion Review, Trans. ASME J. Fluids Eng., 115:345–378, 1993.

[9] Masters, K., Spray Drying, Second Edition, John Wiley and Sons, New York, NY, USA, 1976.

[10] Huimin, L., Science and engineering of droplets: Fundamentals and applications, Noyes publications, UK, 2000.

[11] Farago, Z., Chigier, N., Morphological classification of disintegration of round liquid jets in a coaxial air stream, Atomization and sprays, Vol. 2 (2), pp.137-153, 1992.

[12] Reitz, R.D, Bracco, F.V., On the Dependence of the Spray Angle and Other Spray Parameters on Nozzle Design and Operating Conditions, SAE Pap 790494, 1979.

[13] Carey, F. H., The Development of the Spill Flow Burner and Its Control System for Gas Turbine Engines, J. R. Aeronaut. Soc., Vol. 58(527), pp.737–753, 1954.

[14] Radcliffe, A., The Performance of a Type of Swirl Atomizer, Proc. Inst. Mech. Eng., Vol. 169, pp.93–106, 1955.

[15] Dombrowski, N., Munday, G., Spray Drying, Biochemical and Biological Engineering Science, Vol. 2, Chapter 16, Academic Press, New York, NY, USA, pp. 209–320, 1968.

[16] Dombrowski, N., Hasson, D., Ward, D. E., Some Aspects of Liquid Flow through Fan Spray Nozzles, Chem. Eng. Sci., Vol. 12, pp.35–50, 1960.

[17] Matsumoto, S., Crosby, E. J., Belcher, D. W., Rotary Atomizers: Performance Understanding and Prediction, in: Proc. of the Third Int. Conf. on Liquid Atomization and Spray Systems (Yule, A. J., and Eisenklam, P., eds.), Institute of Energy, London, UK, pp. 1A/1/1–21, 1985.

[18] Nukiyama, S., Tanasawa, Y., Experiments on the Atomization of Liquids in an Airstream, Trans. Soc. Mech. Eng. Jpn., Vol. 5(18), pp.62–75, 1939.

[19] Rizk, N. K., Lefebvre, A. H., Spray Characteristics of Plain-Jet Airblast Atomizers, Trans. ASME J. Eng. Gas Turbines Power, Vol. 106, pp.639–644, 1984

[20] Berger, H. L., Characterization of a Class of Widely Applicable Ultrasonic Nozzles, in: Proc. of the Third Int. Conf. on Liquid Atomization and Spray Systems (Yule, A. J., and Eisenklam, P., eds.), Institute of Energy, London, UK, pp. 1A/2/1–13, 1985.

[21] Cook, C.A., Charagundla, S.R., Presser, C., Dressler, J.L, Gupta, A.K., Effect of acoustic atomization on combustion emissions, American flame research committee Int. Symposium, Baltimore, MD, 1996.

[22] Brenn, G., Rensink, D., Durst, F., Influencing the breakup of fan-shaped liquid sheets by vibrational excitation, ILASS-Europe 2000, Darmstadt, 11-13, September 2000.

[23] Brenn, G., Prebeg, Z., Yarin, A.L., Spray formation through liquid sheet breakup controlled by vibrational excitation, ILASS-Europe 2002, Zaragoza 9-11 September 2002.

[24] Chung, I-ping, Presser, C., Dressler J.L., Effect of piezoelectric transducer modulation on liquid sheet disintegration, Atomization and sprays, Vol. 8, pp.479-502, 1998

[25] Takahashi, F., Schmoll, W.J., Dressler, J.L., Characterization of a velocity-modulation atomizer, Rev. Sci. Instrum., Vol. 65(11), November 1994.

[26] Takahashi, F., Schmoll, W.J., Dressler, J.L., Characteristics of a velocity-modulated pressure-swirl atomizing spray, J. Propulsion and power, Vol. 11, pp. 955-963, 1995

[27] Zhao, F.Q., Lai, M.C., Amer, A., Dressler, J.L., Atomization characteristics of pressure modulated automotive port injector sprays, Atomization and sprays, Vol. 6, pp. 461-483, 1996.

[28] Chung, I.P., Dunn-Rankin, D., Ganji, A., Characteristics of a spray from an ultrasonically modulated nozzle, Atomization and sprays, Vol. 7, pp. 295-315, 1997.

[29] Vijay, M.M., Pulsed jets: Fundamentals and applications. Proc. 5th Pacific Rim International Conference on Water Jet Technology. pp. 9-23. WJTSJ, Tokyo, Japan & ISWJT, Ottawa, Canada, 1998.

[30] Vijay, M.M.,. Design and development of a prototype pulsed water jet machine for the removal of hard coatings. Proc. 14th International Conference on Jetting Technology. pp.39-57, 1998.

[31] Vijay, M. M., Ultrasonically generated cavitating or interrupted jet. U. S. Patent No. 5,154,347, 1992.

[32] Vijay, M.M., Foldyna, J., Remisz, J.,Ultrasonic Modulation of High-Speed Water Jets. pp. 327- 332, 1992

[33] Knapp, R.T, Daily, J.W., Hammitt, F.G., Cavitation, McGraw-Hill, Newyork, 1970.

[34] Brennen, C.E., Cavitation and bubble dynamics, Oxford University Press, 1995.

[35] Batchelor, G.K., An Introduction to fluid dynamics, Cambridge University Press, 2000.

[36] Yule, A. J., Dunkley, J. J., Atomization of Melts for Powder Production and Spray Deposition, Clarendon Press, Oxford, UK, 1994.

[37] Sirignano, W. A., Fuel Droplet Vaporization and Spray Combustion Theory, Prog. Energy Combust. Sci., Vol. 9, pp.291–322, 1983.

[38] Plateau, J, Stattique Experimentale et Theoretique des Liquids Soumie Aux Seules Forces Moleicularies. Paris: Chanthier Vallars, 1873.

[39] Rayleigh, L., On the Instability of Jets, Proc. Lond. Math. Soc., Vol. 10, pp.4–13, 1878.

[40] Chandrasekhar, S., Hydrodynamic and hydromagnetic stability, NewYork, Dover, 1961.

[41] Weber, G., Zum Zerfall eines Flüssigkeitsstrahles, Z. Angew. Math. Mech., Vol. 11(2), pp.136–154, 1931.

[42] Ohnesorge, W., Formation of Drops by Nozzles and the Breakup of Liquid Jets, Z. Angew. Math. Mech., Vol. 16,pp. 355-358, 1936

[43] Taylor, G.I., Generation of ripples by wind blowing over viscous fluids. In The Scientific Papers of G.I. Taylor, ed. GK Batchelor, Vol.3, pp 244– 54. Cambridge: Cambridge Univ. Press, 1962.

[44] Chigier, N., Reitz, R.D., Regimes of Jet Breakup and Breakup Mechanisms (Physical Aspects) In Recent Advances in Spray Combustion: Spray Atomization and Drop Burning Phenomena, Ed KK Kuo, Vol.1, pp. 109-35, 1996.

[45] Wu, P.K.,Tseng, L.K., Faeth, G.M., Primary Breakup in Gas/Liquid Mixing Layers for Turbulent Liquids, Atomization & Sprays, Vol. 2, pp. 295-317, 1992.

[46] Sterling, M., Sleicher, C.A., The Instability of Capillary Jets, J. Fluid Mech., Vol. 68, pp. 477-495, 1975.

[47] Leroux, S., Dumouchel, C., Ledoux, M., The stability curve of Newtonian liquid jets, Atomization and sprays, Vol.6, pp. 623-647, 1996.

[48] Hiroyasu, H., Spray Breakup Mechanism from the Hole Type Nozzle and Its Applications, Atomization and Sprays, Vol. 10, pp. 511-521, 2000.

[49] Arai, M., Shimizu, M., Hiroyasu, H., Break-up length and spray angle of high speed jet, ICLASS-85, 1985.

[50] Haenlein, A., Disintegration of a Liquid Jet, NACA TN 659, (1932)

[51] McCarthy, M.J., Malloy, J.J., Review of Stability of Liquid Jets and the Influence of Nozzle Design," Chemical Engineering Journal, Vol. 7, 1974, pp. 1-20.

[52] Littaye, G., C.R Acad. Sci. Paris, Vol. 208, p.1705, 1939.

[53] Hiroyasu, H., Arai.M., Shimizu, M., The Breakup of High Speed Jet in a High Pressure Gaseous Atmosphere, Proceedings of the 2nd International Conference on Liquid Atomization and Spray Systems, Madison; Wis.; pp. 69-74, 1982

[54] Arai, M., Hiroyasu, H., Shimizu, M., Tabata, M., Disintegration Process and Spray Characterization of Fuel Jet Injected by a Diesel Nozzle, Society of Automotive Engineers Technical Paper Series, Paper No. 840275, 1984.

[55] Arai, M., Breakup Length and Spray Angle of High-Speed Jet, Proceedings of the 3rd ICLASS, London, PP. IB/4/1-10, 1985.

[56] Arai, M., Shimizu, M., Hiroyasu, H., Breakup Length and Spray Formation mechanism of a High Speed Liquid Jet, Proc. ICLASS-1988, pp. 177-184, 1988.

[57] Hiroyasu, H., Arai, M., Shimizu, M., Breakup Length of a Liquid Jet and Internal Flow in a Nozzle, Proc. ICLASS-91, pp. 123-133, 1991.

[58] Arai, M., Hiroyasu, H., Shimizu, M., Similarity between the Breakup Lengths of a High Speed Liquid Jet in Atmospheric and Pressurized Conditions, Proceedings of the International Conference on Liquid Atomization and Spray Systems, p. 61, 1991.

[59] Schmidt, D.P., Rutland, C.J., Corradini, M.L., Roosen, P., Genge, O., Cavitation in two dimensional asymmetric nozzles. SAE paper 1999-01-0518, 1999.

[60] Brzustowski, T.A., Newman, J.A., Behavior of liquid sprays at high pressures, 8th AIAA Aerospace sciences meeting, NY, January 19-21, AIAA-1970-8, 1970.

[61] Chehroudi, B., Bracco, F.V., On the intact core of full cone sprays, Soc. Automot. Eng. Tech. Pap. 850126, 1985

[62] Dan, T., Yamamoto, T., Senda, J., Fujimoto, H., Effect of nozzle configurations for characteristics of non-reacting diesel fuel sprays, Soc. Automot. Eng. Tech. Pap. 970355, 1997.

[63] Taylor, G.I., The dispersion of jets of metals at low melting point in water, in the scientific papers of Sir G.I. Taylor, Vol. III, ed. G.K. Batchelor (1963), 1940.

[64] Castleman, R. A., jr., The Mechanism of the atomization of liquids, Bur. Standards Jour. Rem-arch, March, pp. 369-376, 1931.

[65] Castleman, R. A., jr., The Mechanism of atomization accompanying solid injection, T. R. No. 440, N. A. C. A., 1932.

[66] Sauter, J., Investigation of atomization in carburetors, NACA TM,518, 1929.

[67] Ranz, W.E., On sprays and spraying, Dept. Engg, Res. Penn state university Bulletin 65, 1965.

[68] Dejuhasz, K.J., Dispersion of sprays in solid injection oil engines, Trans. ASME (OGP), Vol. 53, p.65 ,1931.

[69] Schweitzer, P.H., Mechanism of disintegration of liquid jets, J. Applied physics, Vol. 8, p. 513, 1937.

[70] Lee, D.W., Spencer, R.C., Preliminary Photomicrographic Studies of Fuel Sprays, NACA Technical Note 424, Washington, D.C., 1933.

[71] Lee, D.W., Spencer, R.C., Photomicrographic Studies of Fuel Sprays, NACA Tech. Note 454, Washington, D.C., 1933.

[72] Bergwerk, W., Flow pattern in diesel nozzle spray holes, Proc. Instn. Mech. Engrs., Vol. 173, p. 655, 1959.

[73] Grant, R. P., Middleman, S., Newtonian Jet Stability, AICHE, Vol. 12, pp. 669-678, 1966.

[74] Rupe, J.H., On the dynamic characteristics of free-liquid jets and a partial correlation with orifice geometry, Jet Prop. Lab Report No. 32-207, 1962.

[75] Mansour, A., Chigier, N., Turbulence characteristics in cylindrical liquid jets, Physics of Fluids, Vol. 6(10), pp. 3380-3391, 1994.

[76] Wu, P.-K., Faeth, G.M., Aerodynamic Effects in Primary Breakup of Turbulent Liquids, Atomization and Sprays, Vol. 3, No. 3, pp. 265–289, 1993.

[77] Hoyt, J.W, Taylor, J.J., Waves on Water Jets, Journal of Fluid Mechanics, Vol. 83, pp. 119-127, 1977.

[78] Sirignano, W.A., Mehring, C., Review of Theory of Distortion and Disintegration of Liquid Streams, Progress In Energy And Combustion Science, Vol. 26, pp. 609-655, 2000.

[79] Sallam, K.A., Dai, Z., Faeth, G.M., Liquid Breakup at the Surface of Turbulent Round Liquid Jets in Still Gases, International Journal Of Multiphase Flow, Vol. 28, pp. 427-449, 2002.

[80] Hoyt, J.W, Taylor, J.J., Turbulence Structure in a Water Jet Discharging in Air, Physics of Fluids, Vol. 20, Pt. 2, pp. S253-S257, 1977.

[81] Shavit, U., Gas-Liquid Interaction in the Liquid Breakup Region of Twin- Fluid Atomization, Experiments in Fluids, Vol. 31, pp. 550-557, 2001.

[82] Lasheras, J. C., Hopfinger, E. J., Liquid jet instability and atomization in a coaxial gas stream. Ann. Rev. Fluid Mech., Vol. 32, pp 275-308, 2000.

[83] Lasheras, J. C., Villermaux, E., Hopfinger, E. J., Breakup and atomization of a water jet by a high speed annular air stream. J. Fluid Mech. 357, p 351, 1998.

[84] Gordillo, J.M., Perez-Saborid, M.,Ganan-Calvo, A.M., Linear stability of co-flowing liquid-gas jets, Journal of Fluid Mechanics,Vol.448, pp. 23-51, 2001.

[85] Mayer, W. O. H, Coaxial Liquid Atomization of a Round Liquid Jet in a High Speed Gas Stream: a Phenomenological Study, Exp. In Fluids, Vol. 16, pp. 401-410, 1994.

[86] Phinney, R. E., The Breakup of a Turbulent Jet in a Gaseous Atmosphere, Journal of Fluid Mechanics, Vol. 60, pp. 689-701, 1973.

[87] Li, X., J. Shen, J., Absolute and convective instability of cylindrical liquid jets in co-flowing gas streams, Atomization Sprays Vol. 8, pp. 45-62, 1998.

[88] Lin., S.P., Breakup of Liquid Sheets and Jets, Cambridge University Press, 2003.

[89] Lin., S.P., Lian, Z.W., Mechanism of the Breakup of Liquid Jets, AIAA Journal, Vol 28, pp.120-126, 1990.

[90] Nurick, W.H., Orifice Cavitation and its Effects on Spray Mixing, Journal Fluids Eng., 1976.

[91] Northrup, R.P, Flow stability in small orifices, A.R.S. Paper, pp.49-51, 1951.

[92] Sadek, R., Communication on Flow Pattern in Nozzle Spray Holes and Discharge Coefficient of Orifices, Roc. Inst. Mech. Eng., Vol. 173, No.225, p.374, 1961.

[93] Chaves, H., Knapp, M., Kubitzek, A., Obermeier, F., Schneider, T., Experimental Study of Cavitation in the Nozzle Hole of Diesel Injectors Using Transparent Nozzles, SAE 950290, SP-1101, 1995

[94] Arcoumanis, C., Gavaises, M., Nouri, J. M., Abdul-Wahab, E., Horrocks, R.W., Analysis of the Flow in the Nozzle of a Vertical Multi Hole Diesel Engine Injector, SAE Paper 980811, 1998.

[95] Fujimoto, H., Nishikori, T., Hojyo, Y., Tsukamoto, T., Senda, J., Modeling of atomization and vaporization process in flash boiling spray, ICLASS 94, Rouen, France, July 1994.

[96] Tamaki, N., Shimizu, M., Nishida, K., Hiroyasu, Effects of cavitation and internal flow on atomization of a liquid jet, Atomization and sprays, Vol. 8, pp 179-197, 1998.

[97] He, L., Ruiz, H., Effect of cavitation on flow and turbulence in plain orifices for high-speed atomization, Atomization and sprays, Vol. 5, pp. 569-583, 1995.

[98] Ong, D., Yeh, C.P., Hoverman, T.J., Collicott, S.H., Effects of a small step in an orifice on liquid jet breakup, Atomization and sprays, Vol. 13, pp. 297-307, 2003.

[99] Nishida, K., Ceccio, S., Assanis, D., Tamaki, N., Hiroyasu, H., Characterization of cavitation flow in a simple hole nozzle, Proceedings of ICLASS-97, August 18-22, Seoul, 1997.

[100] Soteriou, C., Andrews, R. J., Smith, M., Direct Injection Diesel Sprays and the Effect of Cavitation and Hydraulic Flip on Atomization, SAE Paper, 950080, 1995.

[101] Badock, C., Wirth, R., Fath, A., Leipertz, A., Investigation of Cavitation in Real Size Diesel Injection Nozzles, Internal Journal Of Heat and Fluid Flow, Vol. 20, Pp. 538-544, 1999.

[102] Tomita, Y., Shima, A., On the impulse pressure accompanying spherical bubble collapse in liquids, Rep. Inst. High speed Mech., Vol. 31, N0. 281, 1975.

[103] Shkadov, V. Y. Wave flow regimes of a thin layer of viscous fluid subject to gravity, Izv. Akad. Nauk. SSSR, Mekh. Zhid. Gaza, No. 1, 43-51, 1967.

[104] Tanasawa, Y., Toyoda, S., On the Atomization of Liquid Jet Issuing from a Cylindrical Nozzle, The Technology Reports of the Tohoku University, Jpn., No. 19-2, pp. 135–156, 1955.

[105] De lange, D.F., De Bruin, G.J., Sheet cavitation and cloud cavitation, Re-entrant jet and three-dimensionality, Applied Sci. Research, Vol. 58, pp. 91-114, 1998.

[106] Schmidt, D.P., Rutland, C.J., Corradini, M.L., Roosen, P., Genge, O., Cavitation in two-dimensional asymmetric nozzles, SAE 1999-01-0518, 1999.

[107] Roosen, P., Unruh, O., and Behmann, M., Untersuchung und Modellierung des transienten Verhaltens von Kavitationserscheinungen bei ein- und mehrkomponentigen Kraftstoffen in schnell durchströmten Düsen, Rpt. – Institute for Technical Thermodynamics, RWTH Aachen, Germany, 1996.

[108] Gopalan, S., Katz, J., Flow structure and modeling issues in the closure region of attached cavitation, Physics of Fluids, Vol.12, 895-911, 2000.

[109] Crane, L., Birch, S., McCormack, P.D., The effect of mechanical vibration on the breakup of a cylindrical water jet in air, Br. J. Appl. Phys., Vol. 15, pp. 743-750, 1965.

[110] McCormack, P.D., Crane, L., Birch, S., An experimental and theoretical analysis of cylindrical liquid jets subjected to vibration, Br. J. Appl. Phys., Vol. 16, pp. 395-408, 1965.

[111] Meier, G.E.A., Loose, S., Stasicki, B., Unsteady liquid jets, Applied Scientific Research, Vol. 58, pp. 207-216, 1997.

[112] Seno, T., Kageyama, S., Ito, R., Effect of controlled pulsation on axi-symmetric behavior, Journal of Chemical Engg of Japan, Vol. 20, Nov. 2, 1997

[113] Chaves, H., Obermeier, F., Modeling the effect of modulations of the injection velocity on the structure of liquid jets, Spray 2002, Freiberg 21-22, November 2002.

[114] Geschner, F., Chaves, H., Obermeier, F, Investigation of different phenomena of the disintegration of a sinusoidally forced liquid jet, ILASS-Europe 2001, Zurich 2-6 September 2001.

[115] Geschner, F., Chaves, H., Obermeier, F., Non-dimensional map for the appearance of spray structures of a periodically excited liquid jet, DFG Schwerpunktprogramm FluidzerstÄaubung und SprÄuhvorgÄange DFG-Priority Program Atomization and Spray Processes, Dortmund, March 18-19, 2004

[116] Keller, J. B., Rubinow, S. I., and Tu, Y. O., Spatial Instability of a Jet, Physics of Fluids, Vol. 16(12), pp. 2052-2055, 1973.

[117] Lafrance, P., Nonlinear Breakup of a Liquid Jet, The Physics of Fluids, Vol. 17(10), pp. 1913-14, 1974.

[118] Nayfeh, A. H., Nonlinear Stability of a Liquid Jet, The Physics of Fluids, Vol. 13(4), pp. 841-847, 1970.

[119] Bogy, D.B., Wave propagation and instability in a circular Semi-infinite liquid jet harmonically forced at the nozzle, Journal of applied mechanics, Vol. 45, September 1978.

[120] Lee, H. C., Drop Formation in a Liquid Jet, IBM J. Res. Develop., v. 18, pp. 364-369, 1974.

[121] Sellens, R.W., A one-dimensional numerical model of capillary instability, Atomization and sprays, Vol. 2, pp. 239-251, 1992.

[122] Yi, Yong, Reitz, R.D., A one-dimensional breakup model for low-speed jets, Atomization and sprays, Vol. 12, pp. 667-685, 2002.

[123] Merrington, A.C., Richardson, E.G., The break-up of liquid jets, The proceedings of the physical society, Vol. 59(1), No. 331, 1947.

[124] Harlow, F.H, Welch, J. E, Numerical Calculation of Time-Dependent Viscous Incompressible Flow of Fluid with Free Surface, *Phys. of Fluids*, Vol. 8, pp. 2182-2189, 1965.

[125] Hirt, C.W., Nichols, B.D., Volume of Fluid (VOF) Method for the Dynamics of Free Boundaries," J. Computational Physics, Vol. 39, pp. 201-225, 1981.

[126] Yabe, T., Ishikawa, T., Wang, P.-Y., Aoki, T., Kadota, Y., and Ikeda, F., A Universal Solver for Hyperbolic Equations by Cubic-Polynomial Interpolation II. Two- and Three-Dimensional Solvers, Comput. Phys. Commun, Vol. 66, pp. 233-242, 1991.

[127] Sussman, M., Fatemi, E., Smeraka, P., and Osher, S., An Improved Level Set Method for Incompressible Two-Phase Flows, CompFluids, Vol. 27, pp. 663-680, 1998.

[128] Inamura, T., Tsutagawa, T., Cho, S.J, Masuya, G., Numerical simulation on liquid jet behavior issued into still air, Heat transfer – Asian research, Vol. 32, pp. 141-152, 2003.

[129] Inamura, T., Daikoku, M., Numerical simulation of droplet formation from coaxial twin-fluid atomizer, Atomization and sprays, Vol. 12, pp.247-266, 2002.

[130] Beck, J.C., Watkins, A.P., Simulation of water and other non-fuel sprays using a new spray model, Atomization and sprays, Vol. 13, pp. 1-26, 2003.

[131] Chatwani, A.U., Bracco, F.V., Computation of dense spray jets, ICLASS-85, 1985.

[132] Tauber, W., Computations of Atomization, Ph.D. Dissertation, The University of Michigan, 2001.

[133] Tauber, W., Tryggvason, G., Direct Numerical Simulations of Primary Breakup. Computational Fluid Dynamics Journal, Vol. 9, 2000

[134] Srinivasan, V., Salazar, A.J., Saito, K., Investigation of the primary breakup of round turbulent liquid jets using LES/VOF technique, Proceedings in 36th AIAA fluid dynamics conference and exhibit, San francisco, CA, June 5-8, 2006.

[135] Brackbill, J., Kothe, D. B., Ruppel, H.M., A Continuum Method for Modeling Surface Tension, J. Comput, Phys. Vol. 100, pp. 335-354, 1992.

[136] Ubbink, O., Numerical prediction of two fluid systems with sharp interfaces, PhD Thesis, University of London, 1997.

[137] Ubbink, O., Issa, R. I., A Method for Capturing Sharp Fluid Interfaces on Arbitrary Meshes, Journal of Computational Physics, Vol. 153, pp. 26-50, 1999.

[138] Versteeg, H.K., Malalasekera, W., An introduction to computational fluid dynamics, the finite volume method. Harlow: Longman Scientific & Technical., 1995

[139] Leonard, B.P., The Ultimate Conservative Difference Scheme Applied to Unsteady One-Dimensional Advection, Computer Methods in Applied Mechanics and Engineering, Vol. 88, pp.17-74, 1991.

[140] Darwish, M.S., Moukalled, F., Normalized variable and space formulation methodology for high-resolution schemes, Numer. Heat Tranf. B Fundam., Vol. 26, pp.79–96, 1994.

[141] Leonard, B.P, A stable and accurate modelling procedure based on quadratic interpolation, Comput. Methods Appl. Mech. Engrg. Vol. 19, pp. 58-98, 1979.

[142] Lafaurie, B., Nardone, C., Scardovelli, R., Zaleski, S., Zanetti, G., Modelling merging and fragmentation in multiphase flows with SURFER, J. Comp. Physics, Vol.113, pp.134-147, 1994.

[143] Jasak, H. Weller, H.G., Gosman, A.D., High resolution NVD differencing scheme for arbitrarily unstructured meshes, Int. J. Numer. Meth. Fluids, Vol. 31, pp 431-449, 1999.

[144] Weller, H.G., Tabor, G., Jasak, H., Fureby, C., A Tensorial Approach to Computational Continuum Mechanics using Object-Oriented Techniques, Computers in Physics, Vol. 12(6), pp. 620-631, 1998.

[145] Jasak, H., Weller, H.G., Interface-tracking capabilities of the InterGamma differencing scheme. Internal Report, CFD research group, Imperial College, London, 1995.

[146] Chung, T.J., Computational Fluid Dynamics, Cambridge University Press, 1st edition, 2002.

[147] Jasak, H., Error analysis and estimation for the Finite Volume method with applications to fluid flows, PhD. Thesis, Imperial College, University of London, 1996

[148] Issa, R.I., Solution of the implicitly discretized fluid flow equations by operator splitting, J. Comp. Phys., Vol. 62, 1986.

[149] Rhie, C., Chow., W., A numerical study of the flow past an isolated airfoil with trailing edge separation. AIAA Journal, Vol. 21, pp.1525—1532, 1982.

[150] Ferziger, J.H., Peric, M., Computational Methods for Fluid Dynamics, Springer-Verlag Berlin and Heidelberg GmbH & Co. K , 1996.

[151] Brocchini, M., Peregrine, D.H., The dynamics of strong turbulence at free surfaces, Part 2: Free-surface boundary conditions, J. Fluid Mechanics, Vol. 449, pp.255-290, 2001b.

[152] Wilcox, D.C., Turbulence Modeling for CFD, DCW Industries, 1993.

[153] Davidson, L., An Introduction to Turbulence Models, Rept. 97/2, Dept. of Thermo and Fluid Dynamics, Chalmers University of Technology, Göteborg, 1997.

[154] Banerjee, S., Modeling considerations for turbulent multiphase flows, Engineering turbulence modeling and experiments, edited by W. Rodi and E. N. Ganiac, Elsevier Science, NewYork, 1990. pp 831-866.

[155] Walker, D.T., and Chen, C.Y., Evaluation of Algebraic stress models in free-surface jet flows, Free-surface turbulence, edited by E.P. Rood and J. Katz, FED-Vol. 181, American Society of Mechanical Engineers, NewYork, pp.83-95, 1994.

[156] Hong, W.L., Walker, D.T., Reynolds-Averaged equations for free surface flows with application to High-Froude number jet spreading, Journal of Fluid Mechanics, Vol. 417, pp. 183-209 ,2000.

[157] Yoshizawa, A., Statistical modeling of a transport equation for the kinetic energy dissipation rate*, Phys. of Fluids,* Vol. 30, No. 3, pp. 628-631, 1987.

[158] Mayer, W. O. H., Branam, R., Atomization Characteristics on the Surface of a Round Liquid Jet, Experiments in Fluids, Vol. 36, pp. 528-539, 2004.

[159] Marmottant, P. Villermaux, E., On spray formation, J. Fluid Mech., Vol. 498, pp 73-111, 2004.

[160] Sallam, K.A., Faeth, G.M., Surface Properties During Primary Breakup of Turbulent Liquid Jets in Still Air, AIAA Journal, Vol. 41, No. 8, pp. 1514-1524, 2003.

[161] Lin., S.P., Creighton. B., Energy Budget in Atomization, Journal of Aerosol Science and Technology, Vol. 12, pp. 630-636, 1990.

[162] Herrmann, M., Modeling Primary Breakup: A Three Dimensional Eulerian Level Set/Vortex Sheet Method for Two-Phase Interface Dynamics, Center for Turbulence Research, Annual Research Briefs, pp. 185-196, 2002.

[163] Raynal, L., Instabilite et entrainement a` l'interface d'une couche de melange liquide-gaz. The`se de Doctorat, Universite´ Joseph Fourier, Grenoble, 1997.

[164] Varga, C.M., Lasheras, J.C., Hopfinger, E.J., Initial breakup of a small-diameter liquid jet by a high-speed gas stream, Vol. 497, pp. 405-434, 2003.

[165] Eggers, J., Nonlinear dynamics and breakup of free-surface flows, Reviews of Modern Physics, 69, 865-930, 1997.

[166] Scardovelli, R., Zaleski, S., Direct numerical simulation of free-surface and interfacial flow, Ann. Rev. of Fluid Mechanics, Vol. 31, pp. 567-603, 1999.

[167] Lozano, A., Garcia-Olivares, A., Dopazo, C., The instability growth leading to a liquid sheet breakup, Physics of Fluids, Vol. 10(9), pp. 2188-2197, 1998.

[168] Furness, R.A., Hutton, S.P., Experimental and theoretical studies of two dimensional-fixed cavities, J. Fluids Engg., pp. 515-522, 1975.

[169] Kubota, A., Kato, H., Yamaguchi H., Maeda, M., Unsteady structure measurement of cloud cavitation on a foil section using conditional sampling technique, J. of Fluids Eng., Vol. 111, pp. 204-210, 1989.

[170] Franc, J.P., Partial cavity instabilities and Re-entrant jet, CAV 2001, Int. sym. on cavitation, Pasadena, USA, June 20-23, 2001.

[171] Kawanami, Y., Kato, H., Yamaguchi, H., Tagaya, Y., Tanimura, M., Mechanism and control of cloud cavitation, J. Fluids Engg., Vol. 119, pp.788-795, 1997.

[172] Callenaere, M., Franc, J. P., Michel, J. M, Riondet, M., The Cavitation Instability Induced by the Development of a Re-entrant Jet, J. Fluid Mech., 444, pp. 223-256, 2001.

[173] Le, Q., Franc, J.P., Michel, J.M., Partial cavities: Global behavior and mean pressure distribution, J. Fluids Eng., Vol. 115, pp.243-248, 1993.

[174] De Lange, D.F., Bruin, G.J., Van Winjngaarden, L., On the Mechanism of Cloud Cavitation - Experiment and Modelling, Proc. 2nd Int. Symp. on Cavitation, pp. 45-49, 1994.

[175] Stutz, B., Reboud, J. –L., Two-phase flow structure of sheet cavitation, Physics of fluids, Vol. 9 (12), pp.3678-3686, 1997.

[176] Frenkel, J., Kinetic theory of liquids. Dover, New York, 1955.

[177] Skripov, V.P., Metastable Liquids. John Wiley and Sons, 1974.

[178] Coutier-Delgosha, O., Fortes-Patella, R., Reboud, J.L., Simulation of unsteady cavitation with a two-equations turbulence model including compressibility effects, J. of Turbulence, Vol. 3, 2002.

[179] Wu, J., Utturkar, Y., Senocak, I., Shyy, W., Arakere, N., Impact of Turbulence and Compressibility Modeling on Three-Dimensional Cavitating Flow Computations, AIAA, Paper 2003-4264, 2003.

[180] Rayleigh, L., On the pressure developed in a liquid during the collapse of a spherical cavity. Phil. Mag., Vol. 34, pp.94—98, 1917.

[181] Plesset, M.S., The dynamics of cavitation bubbles, ASME J. Appl. Mech., 16, pp.228-231, 1949.

[182] Poritsky, H., The collapse or growth of a spherical bubble or cavity in a viscous fluid. Proc. First Nat. Cong. in Appl. Math., pp.813-821, 1952.

[183] Plesset, M.S., Zwick, S.A., A nonsteady heat diffusion problem with spherical symmetry. J. Appl. Phys., Vol. 23, No. 1, pp. 95—98, 1952.

[184] Plesset, M.S., Prosperetti, A, Bubble dynamics and cavitation. *Ann. Rev. Fluid Mech.*, 9, pp.145—185, 1977.

[185] Feng, Z.C., Leal, L.G., Nonlinear Bubble Dynamics, Annu. Rev. Fluid. Mech., pp.201-43, 1997.

[186] Chakraborty, B.B., Tuteja, G.S., Motion of an expanding, spherical gas bubble in a viscous liquid under gravity, Phys. of Fluids (A), Vol. 5(8), p.1879, 1993.

[187] Theofanous T, Biasi L., Isbin H.S., Fauske H., Chem. Eng. Sci., Vol. 24,p. 885, 1969.

[188] Plesset, M.S, Hsieh, D.Y., Theory of gas bubble dynamics in oscillating pressure fields, Phys. Fluids Vol. 3, p.882, 1960.

[189] Leighton T. G., The Acoustic Bubble, ACADEMIC PRESS, London, 1996

[190] Blake, F.G, The onset of cavitation in liquids, Acoustics Res. Lab., Harvard Univ., Tech. Memo. No. 12.,1949.

[191] Willard G.W., Ultrasonically Induced Cavitation in Water: A Step-by-step Process, Journal of the Acoustical Society of America Vol. 25, pp.669-686, 1953.

[192] Lauterborn, W., Numerical investigation of nonlinear oscillations of gas bubbles in liquids, J. Acoust. Soc. Am. 59, 283, 1976.

[193] Hao, Y., Prosperetti, A., The dynamics of vapor bubbles in acoustic pressure fields, Phys.Fluids, Vol. (11), p.2008, 1999.

[194] Hao. Y., Prosperetti, A., Rectified heat transfer into translating and pulsating vapor bubbles, J. Acoust. Soc. Am., Vol. 112, 1787, 2002.

[195] Srinivasan, V., Salazar, A.J., Saito, K., On the dynamics of a translating and expanding spherical gas bubble in a viscous medium with oscillating pressure fields, revision submitted to Physics of Fluids, December 2006.

[196] Neppiras, E.A., Noltingk, B.E., Cavitation produced by ultrasonics: theoretical conditions for the onset of cavitation. Proc. Phys. Soc., London, 64B, pp.1032-1038, 1951.

[197] Noltingk, B.E., Neppiras, E.A., Cavitation produced by ultrasonics. Proc. Phys. Soc., London, 63B, pp.674—685, 1950.

[198] Flynn, H.G., Physics of acoustic cavitation in liquids. Physical Acoustics, 1B. Academic Press, 1964.

[199] Apfel, R.E., 1981., Acoustic cavitation prediction. J. Acoust. Soc. Am., Vol. 69, pp. 1624—1633, 1981.

[200] Williams, P.R., Williams, R.L., Cavitation and the tensile strength of liquids under dynamic stressing, Molecular Physics, Vol. 102, No. 19-20, pp.2091-2102, 2004.

[201] Shimada, M., Kobayashi, T., Matsumoto , Y., Dynamics of the cloud cavitation and cavitation erosion, ASME/JSME Joint fluids engineering conference, 1999.

[202] Kedrinskii, V.K., Negative pressure profile in cavitation zone at underwater explosion near free surface, Acta Astronautica, Vol. 3, pp. 623-632, 1976.

[203] Hansson, I., Morch, K.A., Comparison of the initial stage of vibratory and flow cavitation erosion, Proceedings of the Fifth Intl. Conference on Erosion by liquid and solid impact, Newhham College, UK, 3-6 September 1979.

[204] Hansson, I., Morch, K.A., Some aspects on the initial stage of ultrasonically induced cavitation erosion, Ultrasonics International 79, Proceedings of the conference, Graz, Austria, May 15-17, 1979.

[205] Kedrinskii, V.K., Nonlinear problems of cavitation breakdown of liquids under explosive loading (Review), Plenum publishing corporation, pp. 361-377, 1993.

[206] Hansson, I., Kedrinskii, V.K., Morch, K.A., On the dynamics of cavity clusters, J. Phys. D: Appl. Phys., Vol. 15, pp. 1725-1734, 1982.

[207] Colonius, T., d'Auria, F., Brennen, C.E., Acoustic saturation in bubbly cavitating flow adjacent to an oscillating wall, Physics of fluids, Vol. 12 (11), 2000.

[208] Delale, C.F., Hruby, J., Marsik, F., Homogeneous bubble nucleation in liquids: The classical theory revisited, J. Chem Physics, Vol. 118 (2), pp. 792-806, 2003.

[209] Konno, A., Kato, H., Yamaguchi, H., Maeda, M., On the collapsing behavior of cavitation bubble clusters, JSME International Journal Series B, Vol. 45(3), pp. 631-637, 2002.

[210] Takahira, H., Fujikawa, S., Akamatsu, T., Numerical investigation of nonlinear oscillations of two spherical gas bubbles in a compressible liquid, JSME Intl. journal II, Vol. 32(2), pp.163-172, 1989.

[211] Smereka, P., Banerjee, S., The dynamics of periodically driven bubble clouds, Physics of Fluids, Vol. 31 (12), December 1988.

[212] Fujikawa, S., Takahira, H., Dynamics of two non-spherical cavitation bubbles in liquids, Fluid dynamics research, Vol. 4, pp.179-184, 1988.

[213] Park, S., Weng, J.G., Tien, C.L., Cavitation and bubble nucleation using molecular dynamics simulation, Microscale thermophysical engineering, Vol. 4 (3), pp.161-175, July 2000.

[214] van Wijngaarden, L., One-dimensional flow of liquids containing small gas bubbles, Annu. Rev. Fluid Mech., Vol.4, pp.369-396, 1972.

[215] Ishii, R., Umeda, Y., Murata, S., Shishido, N., Bubbly flows through a coverging-diverging nozzle, Physics of Fluids A-Fluid Dynamics, Vol. 5(7), pp. 1630-1643, 1993.

[216] Delale, C.F., Okita, K., Matsumoto, Y., Steady-state cavitating nozzle flows with nucleation, Fifth Intl. symposium on cavitation - CAV 2003, CAV03-GS-4-001, Osaka, Japan, November 1-4, 2003.

[217] Wang, Y.,-C., Brennen, C., One-dimensional bubbly cavitating flows through a converging-diverging nozzle, Journal of Fluids Engineering – Transactions of the ASME, Vol. 120(1), pp. 166-170, 1998.

[218] Wang, Y.,-C., Stability analysis of one-dimensional steady cavitating nozzle flows with bubble size distribution, 1999 ASME/JSME FED Summer meeting, 1999.

[219] Chen, Y., Heister, S.D., A Numerical Treatment for Attached Cavitation," Journal of Fluids Engineering, Vol. 116, pp. 613-618, 1994.

[220] Kunz, R.F., Chyczewski, T.S., Boger, D. A., Stinebring, D. R., Gibeling, H. J. 1999, "Multi-Phase CFD Analysis of Natural and Ventilated Cavitation About Submerged Bodies," ASME Paper FEDSM99-7364, Proceedings of 3rdASME/JSME Joints Fluids Engineering Conference.

[221] Song, C., He, J., Numerical Simulation of Cavitating Flows by Single-Phase Flow Approach, 3rd Int. Symp. on Cavitation, Grenoble, France, pp. 295-300, 1998.

[222] Kubota, A., Kato, H., Yamaguchi, H., A New Modeling of Cavitation Flows: A Numerical Study of Unsteady Cavitation on a Hydrofoil Section, J. Fluid Mech., Vol. 240, pp. 59–96, 1992.

[223] Delannoy, Y., Kueny, J. L., Two Phase Flow Approach in Unsteady Cavitation Modeling, Cavitation and Multiphase Flow Forum, ASME, New York, 98, pp. 153–158, 1990.

[224] Chen, Y., Heister, S. D., Modeling Hydrodynamic Non Equilibrium in Cavitating Flows, ASME J. Fluids Eng., Vol. 118, pp. 172–178, 1996.

[225] Ventikos, Y., Tzabiras, G., A numerical Method for the Simulation of Steady and Unsteady Cavitating Flows, Comput Fluids, Vol. 29, pp. 63-88, 2000.

[226] Yuan, W., Sauer, J., Schnerr, G., Modeling and computation of unsteady cavitation flows in injection nozzles, Mec. Ind., Vol. 2, pp. 383-394, 2001.

[227] Yuan, W., Schnerr, H.G., Numerical simulation of two-phase flow in injection nozzles: Interaction of cavitation and external jet formation, J. Fluids Engg., Vol. 125(6), pp. 963-969, 2003.

[228] Sauer, J., Winkler, G., Schnerr, G.H., Cavitation and condensation – common aspects of physical modeling and numerical approach, Chemical engineering and technology, Vol.23 (8), pp. 663-666, 2000.

[229] Tamura, Y., Sugiyama, K., Matsumoto, Y., Physical modeling and solution algorithm for cavitating flow simulations, 15th AIAA CFD conference, 11-14 June 2001, Anaheim, CA, USA.

[230] Wallis, G.B., One-dimensional two-phase flow, McGraw-Hill, 1969.

[231] Schmidt, D.P., Rutland, C.J., and Corradini, M.L., A Fully Compressible Model of Small, High Speed, Cavitating Nozzle Flows, Atomization and Sprays, Vol. 9, pp. 255-276, 1999.

[232] Shin, B.R., Iwata, Y., Ikohagi, T., Numerical simulation of unsteady cavitating flows using a homogeneous equilibrium model, Computational mechanics, Vol. 30, pp. 388-395, 2003.

[233] Dumont, N., Simonin, O., Habchi, C., Numerical simulation of cavitating flow in diesel injectors by a homogenous equilibrium modeling approach, CAV 2001, Session B6, 2001.

[234] Turkel, E., Preconditioning methods for solving the incompressible and low speed compressible equations, J.of Comp. Phys., Vol. 72, pp. 277-298, 1987.

[235] Choi, D., Merkle, C. L., The application of preconditioning in viscous flows, Journal of Comp. Phys., Vol. 105, pp. 207-223, 1993.

[236] Van der Haul, D.R., Vuik, C., Wesseling, P., A conservative pressure-correction method for flow at all speeds, Computers and Fluids, Vol. 32(8), pp.1113-1132, 2003.

[237] Singhal, AK., Athavale, M.M., Li, H.Y., Jiang, Y., Mathematical Basis and Validation of the Full Cavitation Model, ASME J. Fluids Engg., Vol. 124, pp.617-624, 2002.

[238] Athavale, M.M., Li, H.-Y., Jiang, Y, Singhal, A.K., Application of the Full Cavitation Model to Pumps and Inducers, International Journal of Rotating Machinery, Vol. 8, pp.45-56, 2002.

[239] Merkle, C.L., Feng, J., Buelow, P.E.O., Computational Modeling of the Dynamics of Sheet Cavitation, Proc. 3rd International Symposium on Cavitation, Grenoble, France, 1998.

[240] Kunz, R.F., Chyczewski, T.S., Boger, D. A., Stinebring, D. R., Gibeling, H. J., Multi-Phase CFD Analysis of Natural and Ventilated Cavitation About Submerged Bodies, ASME Paper FEDSM99-7364, Proceedings of 3rdASME/JSME Joints Fluids Engineering Conference, 1999.

[241] Fluent 6.2 Manual, Fluent Inc., 2005.

[242] Kato, H., Thermodynamic effect on incipient and developed sheet cavitation, Intl. symposium on Cavitation inception, FED-Vol. 16, December 1984

[243] Manninen, M., Taivassalo, V., Kallio, S., On the mixture model for multiphase flow, VTT Publications 288, Technical Research Centre of Finland, 1996.

[244] Yakhot, V., Orszag, S.A., Renormalization group analysis of turbulence, J. Sci. Comput., Vol.1, p. 3, 1986.

[245] L. Schiller, Z. Naumann, A Drag Coefficient Correlation, Z.Ver. Deutsch. Ing., Vol. 77, p.318, 1935.

[246] Numachi, F., Effect of turbulence in free stream on cavitation incipience of hydrofoil, J. Fluids Engg., Vol. 97, pp. 180-190, 1975.

[247] Baur, T., Kongeter, J., The three-dimensional character of cavitation structures in a turbulent shear layer, XIX IAHR International symposium on Hydraulic Machinery and Cavitation, 9-11, Singapore, September 1998.

[248] Chahine, G.L., Nuclei effects on cavitation inception and noise, 25th symposium on naval hydrodynamics, Canada, 8-13, August 2004.

[249] Coutier-Delgosha, O., Fortes-patella, R., Reboud, J., Evaluation of the turbulence model : Influence on the numerical simulations of unsteady cavitation, J. Fluids Eng., Vol. 125, pp. 38-45, 2003b.

[250] Reboud, J.L., Stutz, B., Coutier, O., Two phase flow structure of cavitation : experiment and modeling of unsteady effects, 3rd Int. Symp. on Cavitation, Grenoble, France, 1998.

[251] Armaly, B.F., Durst, F., Pereira, J.C.F.,Schönung, B., Experimental and theoretical investigation of backward-facing step flow, J. Fluid. Mech., Vol. 127, pp. 473–496, 1983.

[252] Kaiktsis,L., Karniadakis, G.E., Orszag, S.A.,Unsteadiness and convective instabilities in two-dimensional flow over a backward-facing step, J. Fluid. Mech., Vol. 321, pp.157–187, 1996

[253] Barkley, D., Gomes, M.G.M., Henderson, R.D., Three-dimensional instability in flow over a backward-facing step, J. Fluid. Mech. Vol. 473, pp. 167–190, 2002.

[254] Denhamand, M. K., Patrick, M.A., Laminar flow over a downstream-facing step in a two- dimensional flow channel, Trans.Inst.Chem.Eng., Vol. 52, 361–367, 1974.

[255] Nagib, H.M., Reisenthel, P.H., Koga, P.J., On the dynamic scaling of forced unsteady separated flows, AIAA Shear flow control conference, AIAA-85-0553, March 12-14, Colorado, 1985

[256] Roos, F.W., Kegelman, J.T., Control of coherent structures in reattaching laminar and turbulent shear layers, AIAA Journal, Vol. 24, pp.1956-1963, 1986.

[257] Chun, K.B., Sung, H.J., Control of turbulent separated flow over a backward-facing step by local forcing, Experiments in Fluids, Vol. 21(6), 1996.

[258] Chun, K.B., Sung, H.J., Visualization of a locally-forced separated flow over a backward-facing step, Engineering and physics and astronomy, Vol. 25 (2), 1998.

[259] Saric, S., Jakirlic, S., Tropea, C., A periodically perturbed backward-facint-step flow by means of LES, DES and T-RANS: An example of flow separation control, Journal of Fluids Engg., Vol. 127, pp. 879-887, 2005.

[260] Laberteaux, K.R, Ceccio, S.L, Flow in the closure region of closed partial attached cavitation, 3rd International Symposium on Cavitation, April 1998, Grenoble, France, p. 197, 1998.

[261] Laberteaux, K.R., Ceccio, S.L., Mastrocola, V., Lowrance, J., High speed digital imaging of cavitating vortices, Exp. Fluids, Vol. 24, 1998.

[262] Laberteaux, K.R, Ceccio, S. I., Partial cavity flows: Part 1—Cavities forming on models without spanwise variation, J. Fluid Mech., Vol. 431, 2000.

[263] Laberteaux, K.R, Ceccio, S.L., Partial cavity flows: Part 2—Cavities forming on test objects with spanwise variation, J. Fluid Mech. 431, 2000.

[264] Yang, W.M., Chou, S.K., Shu, C., Li, Z.W., Xue, H., Combustion in micro-cylindrical combustors with and without a backward facing step, Applied Thermal engineering, Vol. 22, pp.1777-1787, 2002.

[265] Correa, S.M., Warren, R.E., Haller, F.F., Kaiser, W.O., Supersonic combustion of hydrogen jets behind a backward facing step, 28th AIAA aerospace meeting and exhibit, AIAA-1990-204, January 8-11, 1990.

[266] Chaturvedi, M.C., Flow characteristics of axisymmetric expansion, Journal of the hydraulics division, ASCE, pp.61-92, 1963.

[267] Gould, R.D., Stevenson, W.H., Thompson, H.D., Investigation of turbulent transport in an axisymmetric suddent expansion, AIAA Journal, Vol. 28(2), pp. 276-283, 1990.

[268] Belahadji, B., Franc, J. P., Michel, J.M., Cavitation in the rotational structures of a turbulent wake, J. Fluid Mech., Vol. 287, p.383, 1995.

[269] Thompson, K.W., Time Dependent Boundary Conditions for Hyperbolic Systems, J. of Computational Physics, Vol. 68, pp. 1-24, 1987.

[270] Poinsot, T. J., Lele, S.K., Boundary Conditions for Direct Simulations of Compressible Viscous Reacting Flows, J. of Computational Physics, Vol. 101, pp. 104-129, 1992.

[271] Tafreshi, V. H., Pourdeyhimi, B., Simulation of Cavitation and Hydraulic Flip inside Hydroentangling Nozzles, Textiles Research Journal , Vol. 74 (4) ,pp. 59-364, 2004.

[272] Sato., K., Shimojo, S., Detailed observations on a starting mechanism for shedding of cavitation cloud, Fifth international symposium of cavitation, CAV 2003, Japan, 2003.

[273] Furness, R.A., Hutton, S.P., Experimental and theoretical studies of two dimensional-fixed cavities, J. Fluids Engg., pp. 515-522, 1975.

[274] Kubota, A., Kato, H., Yamaguchi H., Maeda, M., Unsteady structure measurement of cloud cavitation on a foil section using conditional sampling technique, J. of Fluids Eng., Vol. 111, pp. 204-210, 1989.

[275] Stutz, B., Legoupil, S., X-ray measurements within unsteady cavitation, Experiments in fluids, Vol. 35, pp. 130-138, 2003.

[276] Le, Q., Franc, J.P., Michel, J.M., Partial cavities: Global behavior and mean pressure distribution, J. Fluids Eng., Vol. 115, pp.243-248, 1993.

[277] Yuan, W., Schnerr, G.H., Optimization of two-phase flow in injection nozzles—Interaction of cavitation and external jet formation, Proc. ASME FED, Montreal, Canada, July 14-18, ASME product, CD-ROM, 2002.

[278] Sou, A., Tomiyama, A., Hosokawa, S., Nigorikawa, S., Matsumoto, Y., LDV measurement of cavitating flows in a two-dimesional nozzle, Proc. Int. Symp. On Heat and Mass transfer in spray systems (SPRAY 2005), Turkey, 2005.

[279] Sou, A., Tomiyama, A., Hosokawa, S., Nigorikawa, S., Matsumoto, Y., Visualization of cavitation in a two-dimensional nozzle and liquid jet, 5th Intl. Conference on Multiphase flow, ICMF 2004, May 30-June 4, 2004, Japan.

[280] Sou, A., Tomiyama, A., Hosokawa, S., Nigorikawa, S., Matsumoto, Y., Cavitation and Internal flow in a two-dimensional nozzle, Japan-US seminar on Two-Phase flow dynamics, December 6-11, 2004, Nagahama, Japan.

Vita

Date of Birth: May, 25th 1981

Place of Birth: Chennai, India

Education:

Bachelor of Engineering in Mechanical Engineering, University of Madras, 2002

Honors:

Outstanding Graduate Student in the Department of Mechanical Engineering, 2004-2005

ILASS – Americas Student Fellowship award for presentation in ICLASS 2006, Kyoto, Japan, 2006

Kentucky Graduate Scholarship 2002-2006

Publications:

[1] Vedanth Srinivasan, Abraham J. Salazar, Kozo Saito, Numerical investigation on the disintegration of round turbulent liquid jets using LES/VOF techniques, submitted to Atomization and Sprays, November 2006.

[2] Vedanth Srinivasan, Abraham J. Salazar, Kozo Saito, Investigating the disintegration behavior of forced liquid jets using VOF techniques, 5th International symposium on scale modeling, September 13-16, Japan 2006.

[3] Vedanth Srinivasan, Abraham J. Salazar, Kozo Saito, Computational investigation of cavitating injectors flows using Homogeneous Equilibrium Model supplemented with a pressure correction equation, Paper 06-087, ICLASS 06, Kyoto, Japan, 2006.

[4] Vedanth Srinivasan, Abraham J. Salazar, Kozo Saito, Modeling the Effect of the Injection Velocity on the Disintegration of Round Turbulent Liquid Jets using LES/VOF Techniques, Paper 06-282, ICLASS 06, Kyoto, Japan, 2006.

[5] Vedanth Srinivasan, Abraham J. Salazar, Kozo Saito, Investigation of the primary breakup of round turbulent liquid jets using LES/VOF technique, Proceedings in 36th AIAA fluid dynamics conference and exhibit, San francisco, CA, June 5-8, 2006.

[6] Vedanth Srinivasan, Abraham J. Salazar, Kozo Saito, On the dynamics of a translating and expanding spherical gas bubble in a viscous medium with oscillating pressure fields, submitted to Physics of Fluids, May 2006.

[7]Vedanth Srinivasan, Abraham J. Salazar, Kozo Saito, Numerical simulation of cavitating injector flows using pressure correction techniques, submitted to Journal of Fluids Engineering, May 2006.

[8] Vedanth Srinivasan, Abraham J. Salazar, Kozo Saito, Computational investigation of the effect of velocity modulation on low-velocity round liquid jets, Proceedings in ILASS – Americas, Toronto, Canada, May 2006.

[9] Vedanth Srinivasan, Abraham J. Salazar, Kozo Saito, CFD investigation of an oscillating structure placed in a liquid medium, Proceedings in International Mechanical Engineering Congress and Exposition, Anaheim, CA, USA, November, 2004.